

International Advanced Researches and Engineering Journal

e-ISSN
2618-575X



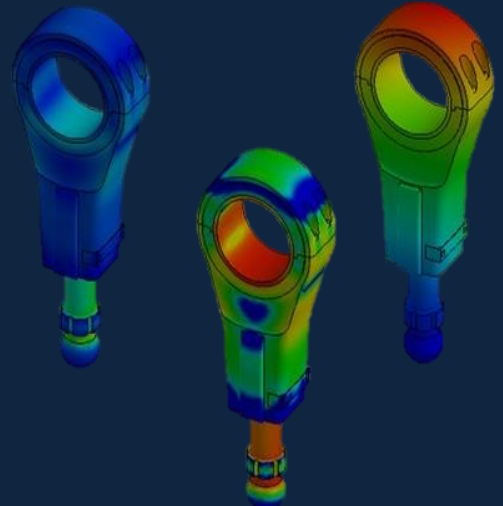
$$F=ma$$

$$E=mc^2$$

$$\int \frac{dy}{dx} dt$$

Volume	Issue
05	02

August, 2021





International Advanced Researches and Engineering Journal (IAREJ) is a double-blind peer-reviewed and publicly available online journal that has Editorial Board (<https://dergipark.org.tr/en/pub/iarej/board>). The editor in chief of IAREJ welcomes the submissions that cover theoretical and/or applied researches on **Engineering** and related science with Engineering. The publication language of the Journal is **English**. **Writing Rules** are given in Author Guidelines (<https://dergipark.org.tr/en/pub/iarej/writing-rules>). IAREJ publishes **original papers** that are research papers and technical review papers.

IAREJ publication, which is **open access**, is **free of charge**. There is no article submission and processing charges (APCs).

IAREJ is indexed & abstracted in:

Crossref (Doi beginning: 10.35860/iarej.xxxxxx)
Directory of Open Access Scholarly Researches (ROAD)
Directory of Research Journals Indexing (DRJI)
EBSCO
Google Scholar
Index Copernicus (ICI Journal Master List)
J-Gate
TUBITAK ULAKBIM TR Dizin (TR index)
WorldCAT

Authors are responsible from the copyrights of the figures and the contents of the manuscripts, accuracy of the references, quotations and proposed ideas and the Publication Ethics (<https://dergipark.org.tr/en/pub/iarej/page/4240>).

All rights of the issue are reserved by International Advanced Researches and Engineering Journal (IAREJ). IAREJ also allows the author(s) to hold the copyright of own articles.

©

IAREJ

15 August 2020



This is an open access issue under the CC BY-NC license (<http://creativecommons.org/licenses/by-nc/4.0/>).



e-ISSN: 2618-575X

Available online at www.dergipark.org.tr/en

INTERNATIONAL ADVANCED RESEARCHES
and
ENGINEERING JOURNAL

Journal homepage: www.dergipark.org.tr/en/pub/iarej

International
Open Access



Volume 05
Issue 02
August 2021

Table of Contents

Research Articles	Pages
Proposed new equations for calculation of thermophysical properties of nanofluids <i>Mahmut KAPLAN and Melda ÖZDİNÇ ÇARPINLIOĞLU</i>	142-151
Experimental investigation of the effects of different refrigerants used in the refrigeration system on compressor vibrations and noise <i>Zafer CİNGİZ, Ferzan KATIRCIOĞLU, Suat SARIDEMİR, Gökhan YILDIZ and Yusuf ÇAY</i>	152-162
Chemical characterization of waste tire pyrolysis products <i>Gediz UGUZ and Abdülkadir AYANOGLU</i>	163-170
Mathematical modeling and production of semi-active hand prosthesis from clear resin <i>Mehmet KAYRICI, Yusuf UZUN, Onur GÖK and Hüseyin ARIKAN</i>	171-180
Determination of the effect of artificial aging parameters on dry sliding wear resistance of 6013 aluminum alloy (Al-Mg-Si-Cu) <i>Mehmet AYVAZ</i>	181-187
Investigation of the temperature effect on the mechanical properties of 3D printed composites <i>Hamed TANABİ</i>	188-193
Investigation of friction performance and surface integrity of cryogenically treated AISI 430 ferritic stainless steel <i>Şenol ŞİRİN and Sıtkı AKINCIOĞLU</i>	194-201
Water absorption parameters of glass/epoxy composites based on dimension effect <i>Zeynal Abidin OĞUZ and Ahmet ERKLİĞ</i>	202-208
Dynamics of axially functionally graded pipes conveying fluid using a higher order shear deformation theory <i>Reza AGHAZADEH</i>	209-217
A numerical study of the natural convection of Al₂O₃-EG nanofluid in a square enclosure and impacts and a comparison of various viscosity and thermal conductivity models <i>Nese KEKLIKCIOGLU CAKMAK, Hasan Hüseyin DURMAZUCAR and Kerim YAPICI</i>	218-230
A GIS-based technique analysis of land use and land cover change detection in taluka Mirpur Mathelo: A case study in district Ghotki, Pakistan <i>Shoukat ALI SHAH and Madeeha KİRAN</i>	231-239
Prediction of market-clearing price using neural networks based methods and boosting algorithms <i>Aslı BORU İPEK</i>	240-246

Vibration reduction on a cantilever Timoshenko beam control subjected to combined effects of wind and earthquake loads using damped outriggers <i>Jules METSEBO, Buris Peggy NDEMANOU, André CHÉAGÉ CHAMGOUÉ and Guy Richard KOL</i>	247-259
Numerical assessment of the performance of different constitutive models used to predict liquefiable soil behavior <i>Selçuk DEMİR</i>	260-267
Application of Muskingum-Cunge Routing Method With Variable Parameters In A Gauged Creek Reach <i>Hülya ÇAKIR and M. Erol KESKİN</i>	268-274
Analysis and modified function projective synchronization of integer and fractional-order autonomous Morse jerk oscillator <i>Eric Donald DONGMO, Cyrille AÏNAMON, Alex Stéphane KEMNANG TSAFACK, Nasr SAEED, Victor KAMDOUM and Sifeu T. KİNGNĪ</i>	275-280
A new region-of-interest (ROI) detection method using the chan-ve-se algorithm for lung nodule classification <i>Ali CINAR, Bengisu TOPUZ and Semih ERGİN</i>	281-291
A comparative study on appliance recognition with power parameters by using machine learning algorithms <i>Yılmaz GÜVEN</i>	292-300
A novel formula derived by using ABC algorithm for calculation of the average fiber diameter of electrospun poly (ϵ-caprolactone) scaffolds <i>Çağdaş YILMAZ, Didem DEMİR, Nimet BÖLGEN KARAGÜLLE and Ali AKDAĞLI</i>	301-308

Review Articles	Pages
Review of machine learning and deep learning models in agriculture <i>Fatih BAL and Fatih KAYAALP</i>	309-323
A survey: blockchain utilization for securing healthcare system <i>Elnaz DADVAR and Kubra KALKAN</i>	324-333



e-ISSN: 2618-575X

INTERNATIONAL ADVANCED RESEARCHES
and
ENGINEERING JOURNAL

Journal homepage: www.dergipark.org.tr/en/pub/iarejInternational
Open Access Volume 05
Issue 02

August, 2021

Research Article

Proposed new equations for calculation of thermophysical properties of nanofluids

Mahmut Kaplan ^{a,*}  and Melda Özdiñç Çarpınlioğlu ^b 

^aAmasya University, Technology Faculty, Department of Mechanical Engineering, Amasya, 05100, Turkey

^bGaziantep University, Faculty of Engineering, Department of Mechanical Engineering, Gaziantep, 27310, Turkey

ARTICLE INFO

Article history:

Received 30 October 2020

Revised 08 February 2021

Accepted 05 March 2021

Keywords:

Brownian motion

Nanofluids

Particle sphericity

Relative dynamic viscosity

Relative thermal conductivity

ABSTRACT

A trial-error procedure is applied for the derivation of correlations to estimate the relative thermal conductivity (k_r) and dynamic viscosity (μ_r) of nanofluids using MATLAB. Thermophysical properties of particles and base fluids, particle diameter (d_p), sphericity, capping layer thickness, Brownian motion of a particle, temperature, and volume fraction (ϕ) are considered. The accuracy of predicting k_r and μ_r of nanofluids is developed using dimensionless parameters involving base fluid and particle characteristics. The results reveal that the estimated values are in a good agreement with the experimental data with a standard deviation of 2.16% and 8.16% for k_r and μ_r of nanofluids, respectively. Besides that, 97.5% of the predicted k_r values suit experimental data of k_r with a mean deviation of $\pm 5\%$, whereas 90.4% of the estimated μ_r values match the data of μ_r with a mean deviation of $\pm 10\%$. Therefore, the proposed new equations will be useful for numerical simulation studies and the engineering design of heat transfer devices such as refrigeration systems, solar collectors, and heat exchangers.

© 2021, Advanced Researches and Engineering Journal (IAREJ) and the Author(s).

1. Introduction

Nanofluids consist of addition of nanometer sized (0-100 nm) particles such as oxides, nitrides, carbides, metal, carbon-based materials and hybrid nanoparticles to base fluids containing water (W), ethylene glycol (EG), ethylene glycol-water (EG-W), oil, etc. Recent review papers on thermophysical properties of nanofluids illustrated that thermal conductivity and dynamic viscosity of nanofluids depend on various parameters including the Brownian velocity, particle size and shape, type of nanoparticle and base fluid, nanofluid temperature (T), particle volume fraction (ϕ), and surfactants [1-5].

The relative thermal conductivity (k_r) equals thermal conductivity of nanofluids over thermal conductivity of base fluids. Several researchers [6-18] have improved various correlations for predicting k_r of nanofluids. The Maxwell model [6] was improved to predict k_r of dilute suspensions of non-interacting spheres. Hamilton et al. [7] developed a model involving a shape factor by changing the Maxwell model. But both Maxwell's and Hamilton's

models do not consider the influence of temperature and particle size on k_r of nanofluids. Since the models considering only the influence of variation of ϕ fail to estimate k_r of nanofluids, many new models including different properties of nanofluids have been improved in recent decades. Koo et al. [8] and Vajjha et al. [10] used a two-term model considering the conventional static conductivity (Maxwell model) and the thermal conductivity thanks to Brownian effect including particle diameter (d_p), ϕ , T , and properties of base fluid. Patel et al. [11] suggested an empirical equation including change of thermal conductivity of base fluids and particles, T and d_p using the non-linear regression analysis. Hassani et al. [14] suggested a correlation including the size distribution of nanoparticles, the Brownian motion, ϕ and T using the Vaschy–Buckingham theorem.

The dynamic viscosity of nanofluids is also important for the heat transfer applications thanks to the internal resistance to fluid flow and a negative impact on the pumping power. The relative dynamic viscosity of

* Corresponding author. Tel.: +0-358-211-5053 ; Fax: +0-358-260-0070.

E-mail addresses: mahmut.kaplan@amasya.edu.tr (M. Kaplan), melda@gantep.edu.tr (M. Özdiñç Çarpınlioğlu)

ORCID: 0000-0003-2675-9229 (M. Kaplan), 0000-0002-7531-8000 (M. Özdiñç Çarpınlioğlu)

DOI: 10.35860/iarej.818668

This article is licensed under the CC BY-NC 4.0 International License (<https://creativecommons.org/licenses/by-nc/4.0/>).

nanofluids (μ_r) equals dynamic viscosity of nanofluids divided by dynamic viscosity of base fluids.

Various models [19-27] were suggested to predict μ_r of nanofluids. Einstein [19] was the first researcher who developed a theoretical model to estimate μ_r of the solid-liquid suspension for $\phi < 0.2\%$. Graham [20] presented a model to calculate μ_r depending on d_p and the minimum distance separating the sphere surfaces for low ϕ . Masoumi et al. [22] described a new correlation involving the Brownian motion of nanoparticles, d_p , particle density, dynamic viscosity of base fluid, and distance between centers of particles. Hosseini et al. [23] improved a model with capping layer thickness, hydrodynamic volume fraction and d_p on the nanoparticle and T . Corcione [12] proposed an equation accounting for d_p , equivalent molecular diameter of the base fluid and ϕ . Adio et al. [24] suggested a correlation considering d_p , ϕ , capping layer thickness and T by using dimensional analysis. The goal of the present paper is to represent new empirical correlating equations for predicting k_r and μ_r of W, EG and EG-W based nanofluids including spherical and cylindrical nanoparticles. Most of researchers have developed their models to estimate k_r of nanofluids with spherical particles using only their own data. On other hand, the models for estimating μ_r of nanofluids are relatively few compared to k_r models and most of them deal with only change of ϕ . But k_r and μ_r of nanofluids are dependent on many factors. Therefore, the suggested correlations will help to improve predicting k_r and μ_r of nanofluids with extending range by using different dimensionless parameters consisting of the Brownian velocity, thermophysical properties of base fluids and nanoparticles, d_p , ψ , T , and ϕ . A summary of different models on k_r and μ_r of nanofluids is presented in Table 1 and Table 2, respectively.

2. Methodology

2.1 Correlations for Relative Thermal Conductivity

The correlation for predicting k_r of nanofluids is derived from the experimental data [28, 29, 31-39] including spherical and cylindrical particles with W, EG and EG-W based nanofluids by trial error method using MATLAB.

A second-degree polynomial is used to describe k_r of nanofluids:

$$k_r = (\beta_2\phi^2 + \beta_1\phi)\Delta_{k_r} + \beta_0 \quad (1)$$

where the terms, β_2 , β_1 , and β_0 are the empirical constants, and Δ_{k_r} is the dimensionless term, which is multiplied by the constants, β_2 , and β_1 to express the impacts of base fluids and particles characteristics on k_r of nanofluids.

The term, Δ_{k_r} in Equation (1) can be written as:

$$\Delta_{k_r} = \left(\frac{k_p}{k_{bf}}\right)^{0.78} \left[\ln\left(\frac{k_p}{k_{bf}}\right)^{1.25} \right] \left(\frac{h}{d_p}\right)^{1.12} \left(\frac{T}{T_{ref}}\right)^{13.9} \left(\frac{c_{p_{bf}}}{c_{p_{ref}}}\right)^{5.35} \left(\frac{1}{\psi}\right)^{0.017(d_p/h)} \text{Re}^{0.1} \text{Pr}^{0.24} \quad (2)$$

where h is capping layer thickness and $h = 1$ nm [23], T_{ref} is a reference temperature and $T_{ref} = 293$ K, $c_{p_{bf}}$ and $c_{p_{ref}}$ are specific heat of base fluid and reference specific heat and $c_{p_{ref}}$ is equal to 4182.2 J/kg (specific heat of water at 293 K) [40].

The particle sphericity, ψ in Equation (2) is equal to the sphere surface area including equivalent volume as the actual particle [41]. $\psi = 0.5$ and $\psi = 1$ for cylindrical and spherical nanoparticles, respectively.

The nanoparticle Reynolds number is calculated by:

$$\text{Re} = \frac{\rho_b u_{Br} d_p}{\mu_{bf}} \quad (3)$$

where u_{Br} is the Brownian velocity, which is computed using the Koo and Kleinstreuer model accounting for the influence of the particle Brownian motion and interaction between particles and fluid molecules [8]:

$$u_{Br} = \sqrt{\frac{18k_b T}{\pi \rho_{bf} d_p^3}} \quad (4)$$

where k_b is the Boltzmann constant which is equal to 1.3806×10^{-23} .

The Prandtl number of the base fluids is calculated as

$$\text{Pr} = \frac{c_{p_{bf}} \mu_b}{k_{bf}} \quad (5)$$

The constants, β_2 , β_1 , and β_0 in Equation (1) and the exponents in Equation (2) are determined based on the experimental data [28, 29, 31-39] using MATLAB. For spherical particle with W based nanofluids and cylindrical particle with W, EG and EG-W based fluids, $\beta_2 = 0.00019$, $\beta_1 = 0.0045$, and $\beta_0 = 1.033$. For spherical particle with EG and EG-W based fluids $\beta_2 = -0.0008$, $\beta_1 = 0.0716$, and $\beta_0 = 1.011$.

2.2 Correlations for Relative Dynamic Viscosity

The correlation for predicting μ_r of nanofluids are derived from experimental data [24, 28, 35, 39, 43-48] including spherical and cylindrical particles with W, EG and EG-W based nanofluids by trial error method using MATLAB.

A second-degree polynomial is used to express μ_r of nanofluids:

$$\mu_r = (\eta_2\phi^2 + \eta_1\phi)\Delta_{\mu_r} + \eta_0 \quad (6)$$

where the terms, η_2 , η_1 , and η_0 are the empirical constants, and Δ_{μ_r} is the dimensionless term, which is multiplied by the

constants, η_2 , and η_1 to express the impacts of base fluids and particles characteristics on k_r of nanofluids.

The term, $\Delta\mu_r$ in Equation (6) can be written as:

$$\Delta\mu_r = \left(\frac{\rho_p}{\rho_{bf}}\right)^{2.4} \left(\frac{h}{d_p}\right)^{1.8} \left(\frac{T_{ref}}{T}\right)^8 \left(\frac{1}{\psi}\right)^6 Re^{-0.11} \quad (7)$$

where ρ_p and ρ_{bf} are particle and base fluid density. The constants, η_2 , η_1 , and η_0 in Equation (6) and the exponents in Equation (7) are determined based on the experimental data [24, 28, 35, 39, 43-48] using MATLAB. For spherical

particle with W based nanofluids and cylindrical particle with W, EG and EG-W based fluids, $\eta_2=0.3136$, $\eta_1=0.5165$, and $\eta_0=1.064$. For spherical particle with EG and EG-W based fluids, $\eta_2=0.1167$, $\eta_1=0.4717$, and $\eta_0=1.064$.

The thermophysical properties of the base fluids in Equations (2) and (7) are evaluated using the data taken from [40, 42] at the nanofluid temperature. The thermophysical properties of the nanoparticles used for all the calculations are given in Table 3.

Table 1. Various correlations on k_r nanofluids

Authors	Correlations	Remarks
Maxwell [6]	$k_r = \frac{2k_{bf} + 2(k_p - k_{bf})\varphi + k_p}{2k_{bf} - (k_p - k_{bf})\varphi + k_p}$	Nanofluids with spherical particles for low φ .
Hamilton et al. [7]	$k_r = \frac{(n-1)k_{bf} + (n-1)(k_p - k_{bf})\varphi + k_p}{(n-1)k_{bf} - (k_p - k_{bf})\varphi + k_p}$	n is a shape factor and $n = 3/\psi$.
Koo et al. [8]	$k_r = \frac{2k_{bf} + 2(k_p - k_{bf})\varphi + k_p}{2k_{bf} - (k_p - k_{bf})\varphi + k_p} + \frac{5 \times 10^4 \beta \rho_{bf} c_{p,bf} \varphi}{k_{bf}} \sqrt{\frac{k_b T}{\rho_p d_p}} f(T, \varphi)$ $\beta = 0.0137(100\varphi)^{-0.8229} \quad (\varphi < 1\%), \quad \beta = 0.0011(100\varphi)^{-0.7272} \quad (\varphi > 1\%),$ $f(T, \varphi) = (0.4705 - 6.04\varphi)T + 1722.3\varphi - 134.63 \quad \text{for CuO-W mixture.}$	$f(T, \varphi)$ is obtained the measured data of Das et al. [9].
Vajjha et al. [10]	$k_r = \frac{2k_{bf} + 2(k_p - k_{bf})\varphi + k_p}{2k_{bf} - (k_p - k_{bf})\varphi + k_p} + \frac{5 \times 10^4 \beta \rho_{bf} c_{p,bf} \varphi}{k_{bf}} \sqrt{\frac{k_b T}{\rho_p d_p}} f(T, \varphi)$ $\beta = 8.4407(100\varphi)^{-1.07304} \quad (\varphi = 1-10\%) \quad \text{for Al}_2\text{O}_3 \text{ and } (\varphi = 1-7\%) \quad \text{for ZnO}$ $\beta = 9.881(100\varphi)^{-0.9446} \quad (\varphi = 1-6\%) \quad \text{for CuO with 60-40\% EG-W}$ $f(T, \varphi) = (2.8217 \times 10^{-2} \varphi + 3.917 \times 10^{-3}) \frac{T}{T_0} - 3.069 \times 10^{-2} \varphi - 3.91123 \times 10^{-3}$	The ranges of d_p , T and φ are 29-77 nm, 298-363 K and 1-10%.
Patel et al. [11]	$k_r = 1 + 0.135 \left(\frac{k_p}{k_{bf}}\right)^{0.273} \varphi^{0.467} \left(\frac{T}{20}\right)^{0.547} \left(\frac{100}{d_p}\right)^{0.234}$	The ranges of d_p , T and φ are 10-150 nm, 293-343 K and 0.1-3% for nanoparticles with W, EG and transformer oil.
Corcione [12]	$k_r = 4.4 Re^{0.4} Pr^{0.66} \left(\frac{T}{T_{fr}}\right)^{10} \left(\frac{k_p}{k_{bf}}\right)^{0.03} \varphi^{0.66} + 1, \quad Re = \frac{\rho_{bf} u_{Br} d_p}{\mu_{bf}}, \quad Pr = \frac{c_{p,bf} \mu_{bf}}{k_{bf}}$	The ranges of d_p , T and φ are 10-150 nm, 294-324 K and 0.2-9% for Al ₂ O ₃ , CuO-W and EG, TiO ₂ -W and Cu-EG.
Azmi et al. [13]	$k_r = 0.8938 \left(1 + \frac{\varphi}{100}\right)^{1.37} \left(1 + \frac{T}{70}\right)^{0.2777} \left(1 + \frac{d_p}{150}\right)^{-0.0336} \left(\frac{\alpha_p}{\alpha_w}\right)^{0.01737}$	T is 394.5 K and the range of φ is 0-4% nm for Al ₂ O ₃ (50 nm), ZnO (100 nm) with W.
Hassani et al. [14]	$k_r = 1.04 + \varphi^{1.11} \pi_3^{0.33} \pi_4^{-1.7} \left[\pi_4^{1.7} - 262 \pi_3^{-0.33} + (135 \pi_5^{0.23} \pi_6^{0.82} \pi_7^{-0.1} \pi_8^{-7}) \right]$ $\pi_3 = \frac{k_p}{k_{bf}}, \quad \pi_4 = \frac{c_{p,bf} \mu_{bf}}{k_{bf}}, \quad \pi_5 = \frac{d_{ref}}{d_p}, \quad \pi_6 = \frac{v_{bf}}{d_p u_{Br}}, \quad \pi_7 = \frac{c_{p,bf}}{T^{-1} u_{Br}^2}, \quad \pi_8 = \frac{T_b}{T}$	The ranges of d_p , T and φ are 15-200 nm, 293-393 K and 0.005-14% for various nanofluids.
Garoosi [17]	$k_r = \frac{2k_{bf} + 2(k_p - k_{bf})\varphi + k_p}{2k_{bf} - (k_p - k_{bf})\varphi + k_p} + 3.762 \left(\frac{T}{T_0}\right)^{8.661} \left(\frac{d_p}{d_{bf}}\right)^{-0.4351} \left(\frac{k_p}{k_{bf}}\right)^{0.08235} \varphi^{0.64} e^{(-5.742\varphi)}$ $\omega = (1 + 0.8946 \times \varphi)$	Empirical correlation is valid for $0 \leq \varphi \leq 0.12$, $10 \text{ nm} \leq d_p \leq 5 \mu\text{m}$ and $288 \text{ K} \leq T \leq 360 \text{ K}$.
Arasu et al. [18]	$k_r = 0.9472 - 0.052\varphi + 0.001482T + 0.00663(\varphi T)$	The ranges of T and φ are 308-333 K and 0.1-0.4% for TiO ₂ with W.

Table 2. Various correlations on μ_r nanofluids

Authors	Correlations	Remarks
Einstein [19]	$\mu_r = 1 + 2.5\phi$	The model is valid for low ϕ ($\phi < 2\%$).
Graham [20]	$\mu_r = 1 + 2.5\phi + \frac{4.5}{\left(\frac{h}{a}\right)\left(2 + \frac{h}{a}\right)\left(1 + \frac{h}{a}\right)^2}$ $h/a = (2)[1 - (\phi/\phi_m)^{1/3}]/(\phi/\phi_m)^{1/3}$	h is minimum distance separating two spheres. a is radius of particle. ϕ_m is maximum packing spheres.
Chen et al. [21]	$\mu_r = \left(1 - \frac{\phi}{0.605} \left(\frac{a_a}{a}\right)^{1.2}\right)^{-1.5125}$	d_p is 25 nm. The ranges of T and ϕ are 293-333 K and 0-2% for TiO ₂ -EG.
Masoumi et al. [22]	$\mu_r = 1 + \frac{\rho_p v_{Br} d_p^2}{72C\delta\mu_{bf}}$	d_p is 13 and 28 nm. The ranges of T and ϕ are 290-340 K and 1-5% for Al ₂ O ₃ -W.
Hosseini et al. [23]	$\mu_r = \exp\left[m + \alpha\left(\frac{T}{T_0}\right) + \beta(\phi_h) + \gamma\left(\frac{d_p}{1+r}\right)\right], \phi_h = \phi\left[\frac{d_p + 2s}{d_p}\right]^3$	$T_0 = 20$ °C. d_p is 36 and 47 nm. The ranges of T and ϕ are 293-333 K and 0-10% for Al ₂ O ₃ -W.
Corcione [12]	$\mu_r = \frac{1}{1 - 34.87\left(\frac{d_p}{d_{bf}}\right)^{-0.3} \phi^{1.03}}, d_{bf} = 0.1\left(\frac{6M}{N\pi\rho_{bf0}}\right)^{1/3}$	The ranges of d_p , T and ϕ are 25-200 nm, 293-333 K and 0.01-7% for Al ₂ O ₃ -W and propylene glycol, TiO ₂ -W and EG, SiO ₂ -ethanol and Cu-EG.
Adio et al. [24]	$\mu_r = 1 + \left[a_0 + a_1\left(\frac{T}{T_0}\right) + a_2\left(\frac{d_p}{h}\right)\right]\phi + \left[a_3\left(\frac{d_p}{h}\right)^2 + a_4\left(\frac{T}{T_0}\right)^2 + a_5\right]\phi^2 + a_6\left(\frac{T}{T_0}\right)^2 \phi^{\frac{1}{3}}$ $a_0 = 7.0764, a_1 = -0.1246, a_2 = -0.0346, a_3 = -0.0024, a_4 = -1.2357, a_5 = 53.6946, a_6 = 0.0436$	d_p is 21, 105 and 125 nm. The range of T is 293-343 K and $\phi \leq 5\%$ for MgO-EG.
Garossi [17]	$\mu_r = 1 + 49.6 \times \left(\frac{d_p}{d_{bf}}\right)^{-0.414} \phi^{0.908} e^{(10.8\phi)}$	Empirical correlation is valid for $0 \leq \phi \leq 0.12, 10 \text{ nm} \leq d_p \leq 5 \mu\text{m}$.
Esfe et al. [27]	$\mu_r = 1.01171 + 0.0387\phi + 6.35 \times 10^{-5}T - 0.0010096\phi T - 0.00466\phi^2 + 2.127 \times 10^{-5}T^2 + 0.000107\phi^2 T + 4.527 \times 10^{-5}\phi T^2$	The ranges of T and ϕ are 298-323 K and 1-4% for AlN (Aluminium nitride) with EG.

Table 3. Thermophysical properties of nanoparticles

Nanoparticles	k (W/m K)	ρ (kg/m ³)
Al ₂ O ₃ [14]	40	3970
CuO [14]	20	6400
SiO ₂ [14]	1.2	2200
TiO ₂ [49]	8.95	4250
MgO [50]	48.4	3580
ZnO [51]	13	5600
Ag [17]	429	10500
Al [36]	237	2700
CNT, MWCNT [30, 52]	2000	2100

3. Results and Discussion

Figure 1 shows comparison of the predicted k_r values obtained from Equation (1) with experimental data including Al₂O₃-W [28, 29, 33], CuO-W [33], TiO₂-W [32], Ag-W [35] and CNT-W [31] with a d_p range of 13-150 nm, a T range of 295-323 K, a ϕ range of 0-18.1%.

Figure 2 illustrates comparison of the predicted k_r values obtained from Equation (1) with experimental data containing SiO₂-EG [39], ZnO-EG [34], Al-EG [36], Al₂O₃-20:80%, 40-60%, 60:40% EG-W [38], MWCNT-30:70% EG-W [37] with a d_p range of 5-50 nm, a T range of 293-303 K, a ϕ range of 0-5%.

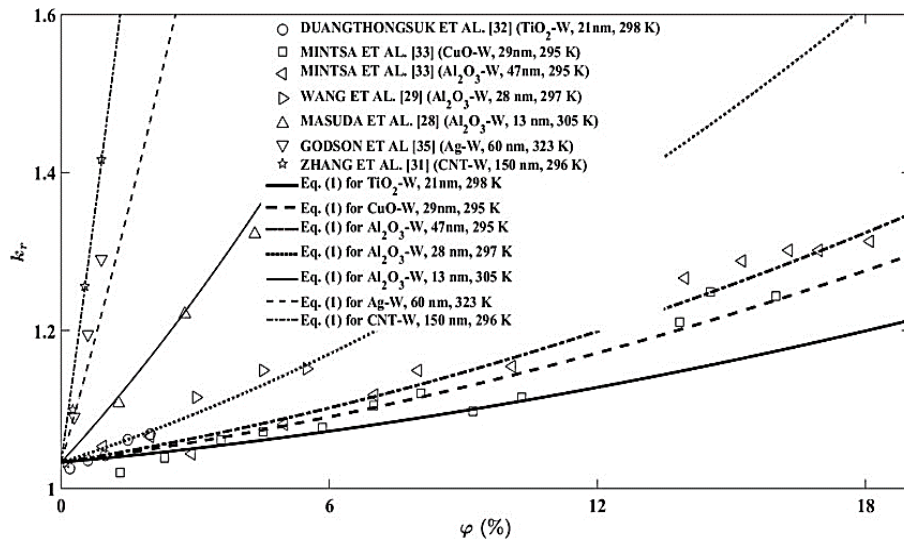


Figure 1. Comparison between the predicted values of k_r produced using Equation (1) and the values obtained by the experimental data of W based nanofluids

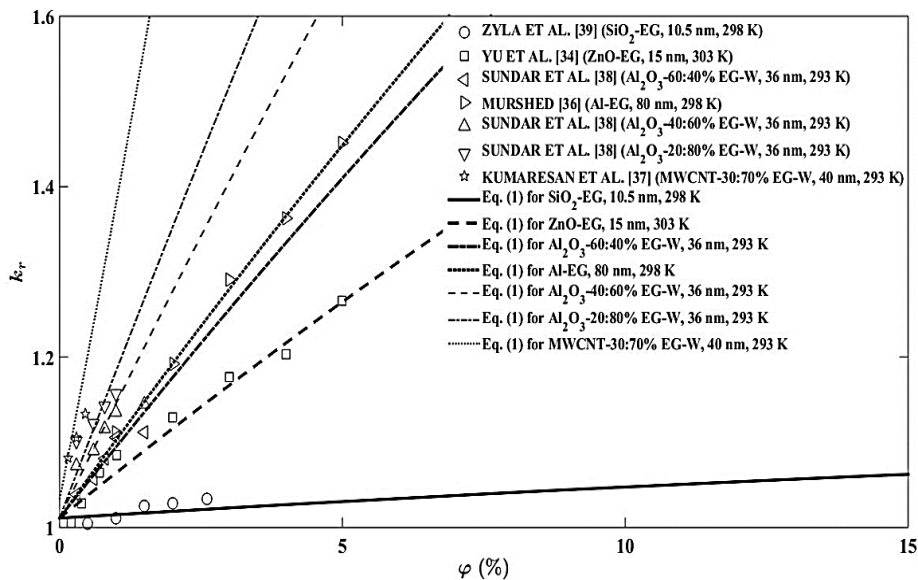


Figure 2. Comparison between the predicted values of k_r produced using Equation (1) and the values obtained by the experimental data of EG / EG-W based nanofluids

It is clear from Figures 1 and 2 that the predicted k_r values found using Equation (1) agree well with experimental data. Previous experimental studies illustrate that the type, shape, and size of nanoparticles affect k_r of nanofluids which generally increases with a reduction of nanoparticle's size. Figures 1 and 2 show that the suggested correlation estimates well k_r of nanofluids with different nanoparticle shapes, sizes, and types. The dimensionless parameters containing h , d_p , and ψ in Equation (2) improve estimation of different size of spherical and cylindrical nanoparticles. The maximum values of k_r are gained by nanofluids with higher thermal conductive particles such as Ag, CNT and MWCNT as shown in Table 3.

Like the experimental data in Figures 1 and 2, the predicted k_r values obtained by Equation (1) increase when

decreasing d_p and increasing T and ϕ . Moreover, dimensionless parameters including the nanoparticle's Brownian velocity and thermophysical properties of base fluids enhance predicting k_r of nanofluids with different weight ratios of EG-W mixtures as indicated in Figure 2.

In Figure 3, the predicted k_r values obtained using Equation (1) are compared with experimental k_r values of W, EG / EG-W based nanofluids. As shown in Figure 3, the estimated k_r values are very close to experimental k_r values with standard deviations of 2.16%.

In addition, 97.5% of the predicted data match experimental data with a mean deviation of $\pm 5\%$ as demonstrated in Figure 3.

Figures 4 shows comparison of the estimated values obtained from Equation (6) with experimental data including Al_2O_3 -W [28, 46], ZnO-W [44], Ag-W [35] and

MWCNT-W [45] with a d_p range of 9.2-75 nm, a T range of 293-323 K, a ϕ range of 0-20.4%.

Figures 5 illustrates comparison of the estimated values obtained from Equation (6) with experimental data containing SiO₂-EG [39], MgO-EG, [24] ZnO-EG [47], CuO -60:40% EG-W [43], MWCNT-50:50% EG-W [48] with a d_p range of 10.5-70 nm, a T range of 293-323 K, a ϕ range of 0-6.2%, respectively. Figures 4 and 5 indicate that the calculated μ_r values obtained Equation (6) are in good agreement with the experimental μ_r values. As demonstrated in Figures 4 and 5, the estimated μ_r values gained by Equation (6) confirm the general trends of μ_r of nanofluids that the values of μ_r increase when increasing ϕ and decreasing d_p and T .

The present correlation also takes account of the impact of particle shape on μ_r of nanofluids using ψ in Equation (7). Like the experimental data of μ_r in Figures 4 and 5, the

maximum μ_r values are obtained by nanofluids with cylindrical particles such as CNT and MWCNT. As demonstrated in Figure 5, the relative dynamic viscosity of nanofluids with different weight ratios of EG-W mixtures are predicted by using dimensionless parameters including u_{Br} , ρ_{bf} , and μ_{bf} .

In Figure 6, the predicted μ_r values obtained from Equation (6) are compared with experimental μ_r values of W, EG / EG-W based nanofluids. The predicted μ_r values calculated using Equation (6) match closely with experimental μ_r values of W, EG / EG-W based nanofluids with standard deviations of 8.16% as demonstrated in Figure 6. 90.4% and 96.2% of the predicted data suit experimental data with a mean deviation of $\pm 10\%$ and $\pm 20\%$, respectively. Two points of the calculated data are above a 20% of deviation.

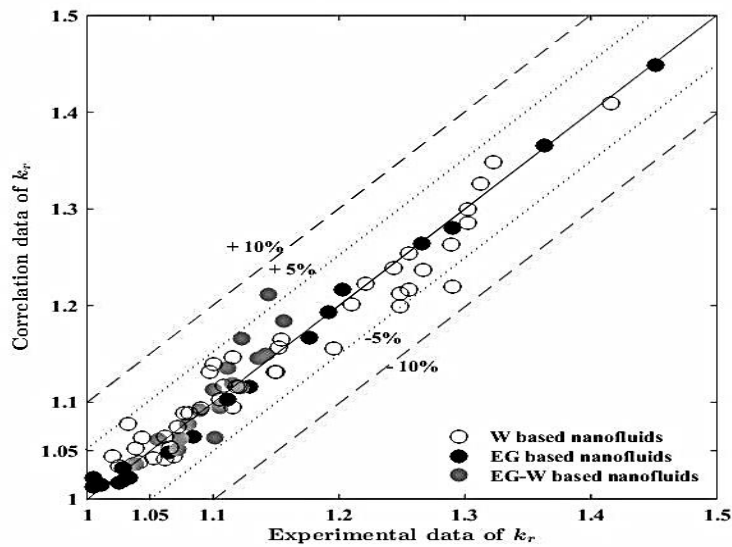


Figure 3. Comparison between the estimated values of k_r calculated using Equation (1) and the measured values of k_r for W, EG / EG-W based nanofluids

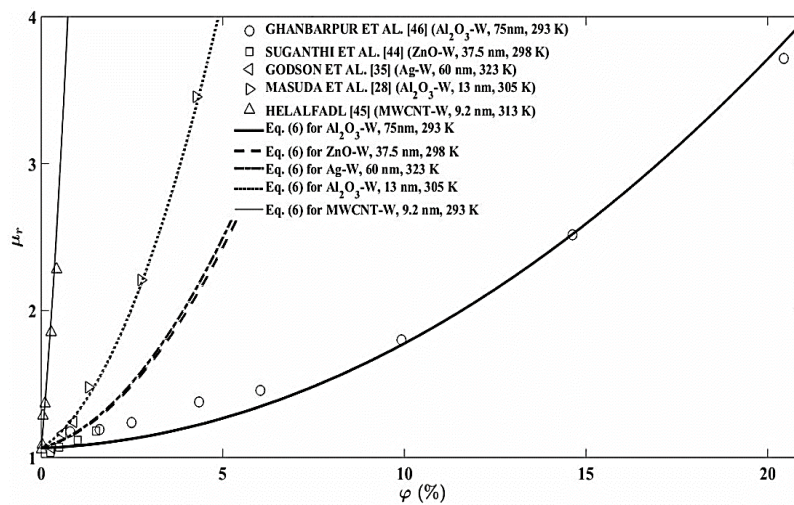


Figure 4. Comparison between the predicted values of μ_r generated using Equation (6) and the values obtained by the experimental data of W based nanofluids

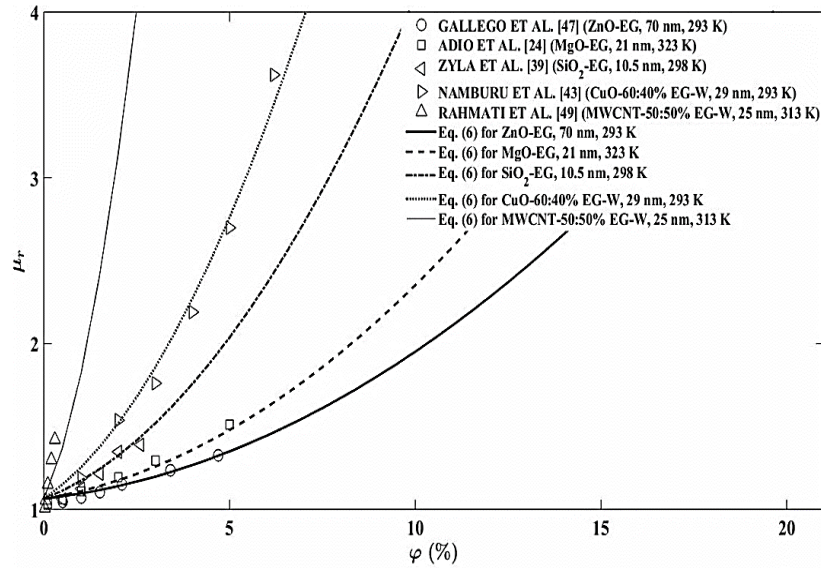


Figure 5. Comparison between the predicted values of μ_r generated using Equation (6) and the values obtained by the experimental data of EG / EG-W based nanofluids

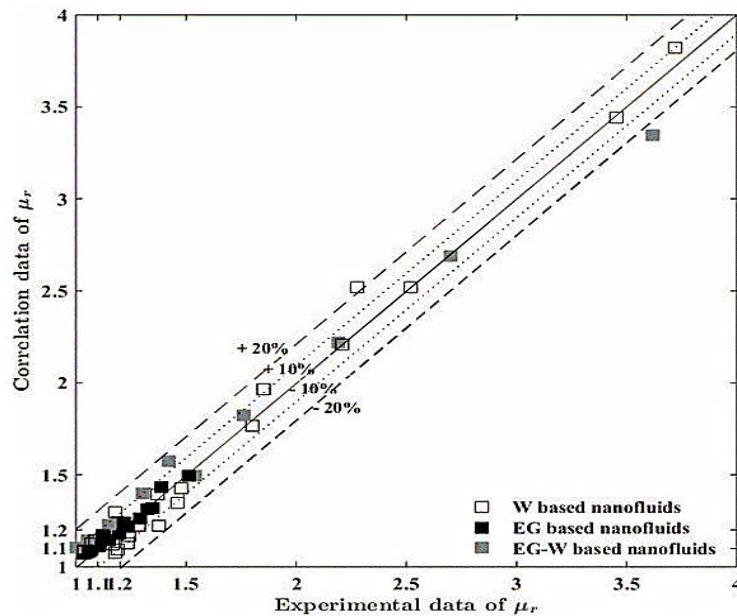


Figure 6. Comparison between the estimated values of μ_r calculated using Equation (6) and the measured values of μ_r for W, EG / EG-W based nanofluids

4. Conclusions

In this paper, k_r and μ_r of nanofluids are estimated by using the correlations with various dimensionless parameters related to the Brownian motion and properties of base fluids and nanoparticles as an extension study of [53]. The following results are achieved:

- Since k_r and μ_r of nanofluids depend on many factors, increasing number of parameters instead of using only ϕ and extending range of parameters in the correlations enhance accuracy of the results.
- Experimental results show that k_r generally increases when decreasing d_p and increasing k_p , T , and ϕ while μ_r generally increases when increasing ϕ and decreasing d_p and T . The suggested correlations suit this general trend.
- Adding $1/\psi$ in Equations (2) and (7) helps to improve the estimation of k_r and μ_r of nanofluids with cylindrical shape nanoparticles.
- The dimensionless parameters including particles Brownian motion and thermophysical properties of base fluids contribute to estimating k_r and μ_r of nanofluids for different weight ratios of EG-W mixtures.
- Owing to improving the correctness of predicting k_r and μ_r of nanofluids with spherical and cylindrical nanoparticles by using new dimensionless parameters,

Equations (1) and (6) will be useful tool in designing the nanofluids for various industrial applications.

Declaration

The authors declared no potential conflicts of interest with respect to the research, authorship, and/or publication of this article. The authors also declared that this article is original, was prepared in accordance with international publication and research ethics, and ethical committee permission or any special permission is not required.

Author Contributions

All authors conceived the study and developed the methodology. M. Kaplan performed the computations and wrote the manuscript. M. Özdiñç Çarpınlioğlu contributed to the final version of the manuscript.

Nomenclature

c_p	: Specific heat, J/kg K
d	: Nanoparticle diameter, nm
h	: Capping layer thickness, Nm
k	: Thermal conductivity, W/m K
k_b	: Boltzmann constant, 1.3806×10^{-23} J/K
T	: Temperature, K
Pr	: Prandtl number
Re	: Reynolds number
u_{Br}	: Brownian velocity (m/s)
β	: Empirical constant
Δ	: Correlation term
η	: Empirical constant
μ	: Dynamic viscosity, Pas
ρ	: Density (g/cm^3)
ϕ	: Volume fraction (%)
ψ	: Particle sphericity
bf	: Base fluid
p	: Particle
r	: Relative
ref	: Reference
AlN	: Aluminium nitride
CNT	: Carbon nanotubes
EG	: Ethylene glycol
$MWCNT$: Multiwalled carbon nanotubes
W	: Water

References

- Gupta M., V. Singh, R. Kumar, and Z. Said, *A review on thermophysical properties of nanofluids and heat transfer applications*. Renewable & Sustainable Energy Reviews, 2017. **74**: p. 638–670.
- Murshed S.M.S. and P Estellé, *A state of the art review on viscosity of nanofluids*. Renewable and Sustainable Energy Reviews, 2017. **76**: p. 1134-1152.
- Ahmadi M.H., A. Mirlohi, A.M. Nazari, and R. Ghasempour, *A review of thermal conductivity of various nanofluids*. Journal of Molecular Liquids, 2018. **265**: p. 181-188.
- Kaplan M. and M.O. Carpinlioglu, *An extensive review on nanofluids - based on available experimental studies*. Proceedings of 2nd International Symposium on Innovative Approaches in Scientific Studies: Samsun; 2018. p. 104-116.
- Munyalo J.M. and X. Zhang. *Particle size effect on thermophysical properties of nanofluid and nanofluid based phase change materials: A review*. Journal of Molecular Liquids, 2018. **265**: p. 77-87.
- Maxwell J.C., *A treatise on electricity and magnetism (volume 1)*. 1881, Clarendon press series.
- Hamilton R.L. and O.K. Crosser, *Thermal conductivity of heterogeneous two-component systems*. Industrial & Engineering Chemistry Fundamentals, 1962. **1**(3): p. 187–191.
- Koo J. and C. Kleinstreuer, *Laminar nanofluid flow in microheat-sinks*. International Journal of Heat Mass Transfer, 2005. **48**(13): p. 2652–2661.
- Das S., N. Putra, P. Thiesen, and W. Roetzel, *Temperature dependence of thermal conductivity enhancement for nanofluids*, Journal of Heat Transfer, 2003. **125**: p. 567–574
- Vajjha R.S. and D.K. Das, *Experimental determination of thermal conductivity of three nanofluids and development of new correlations*. International Journal of Heat Mass Transfer, 2009 **52**: p. 4675–4682.
- Patel H., T. Sundararajan, and S. Das, *An experimental investigation into the thermal conductivity enhancement in oxide and metallic nanofluids*. Journal of Nanoparticle Research, 2010. **12**(3): p. 1015–1031.
- Corcione M., *Empirical correlating equations for predicting the effective thermal conductivity and dynamic viscosity of nanofluids*. Energy Conversion and Management, 2011. **52**(1): p. 789–793.
- Azmi W.H., K.V. Sharma, R. Mamat, A.B.S. Alias, and I.I. Misnon, *Correlations for thermal conductivity and viscosity of water based nanofluids*. IOP Conference Series: Materials Science and Engineering, 2012. **36**(1): 012029.
- Hassani S., R. Saidur, S. Mekhilef, and A. Hepbasli, *A new correlation for predicting the thermal conductivity of nanofluids using dimensional analysis*, International Journal of Heat Mass Transfer, 2015. **90**: p. 121–130.
- Nadooshan A., *An experimental correlation approach for predicting thermal conductivity of water-EG based nanofluids of zinc oxide*. Physica E: Low-dimensional Systems and Nanostructures, 2017. **87**: p. 15–9.
- Kaplan M. and M.O. Carpinlioglu, *Correlations for calculation of relative thermal conductivity of nanofluids using dimensionless parameters*. ICAME 2019 - 5th International Conference on Advances in Mechanical Engineering, Istanbul, 2019. p. 1890-1896.
- Garooosi F., *Presenting two new empirical models for calculating the effective dynamic viscosity and thermal conductivity of nanofluids*. Powder Technology, 2020. **366**: 788–820.
- Arasu A.V., D.D. Kumar, and I.A Khan, *Experimental validation of enhancement in thermal conductivity of titania/water nanofluid by the addition of silver nanoparticles*. International Communications in Heat and Mass Transfer, 202. **120**: 104910.
- Einstein A., *A new determination of molecular dimensions*, Annals of Physics, 1906. **19**(2): p. 289–306.

20. Graham A.L., *On the viscosity of suspensions of solid spheres*. Applied Scientific Research, 1981. **37**: 275–286.
21. Chen H., Y. Ding, and C. Tan, *Rheological behaviour of nanofluids*, New Journal of Physics, 2007. **9**(10): 367.
22. Masoumi N., N. Sohrabi, and A. Behzadmehr, *A new model for calculating the effective viscosity of nanofluids*, Journal of Physics D: Applied Physics, 2009. **42**(5): 055501.
23. Hosseini S.M., A. Moghadassi, and D.E. Henneke, *A new dimensionless group model for determining the viscosity of nanofluids*. Journal of Thermal Analysis and Calorimetry, 2010. **100**(3): p. 873–877.
24. Adio S.A., M. Mehrabi, M. Sharifpur, and J.P. Meyer, *Experimental investigation and model development for effective viscosity of MgO–ethylene glycol nanofluids by using dimensional analysis, FCM-ANFIS and GA-PNN techniques*. International Communications in Heat and Mass Transfer, 2016. **72**: p. 71–83.
25. Akilu S., A.T. Bahita, and K.V. Sharma, *Experimental measurements of thermal conductivity and viscosity of ethylene glycol-based hybrid nanofluid with TiO₂-CuO/C inclusions*. Journal of Molecular Liquids, 2017. **246**: p. 396–405.
26. Kaplan M. and M.O. Carpinlioglu, *Correlations for calculation of relative dynamic viscosity of nanofluids using dimensionless parameters*. ICAME 2019 - 5th International Conference on Advances in Mechanical Engineering, Istanbul, 2019. p. 1897-1903.
27. Esfe M.F. and S.M. Motallebi, *Optimization, modeling, and prediction of relative viscosity and relative thermal conductivity of AlN nano-powders suspended in EG*. The European physical journal plus, 2021. **136**: 56.
28. Masuda H., A. Ebata, K. Teramae, and N. Hishinuma, *Alteration of thermal conductivity and viscosity of liquid by dispersing ultra-fine particles (Dispersion of γ -Al₂O₃, SiO₂, and TiO₂ ultra-fine particles*, Netsu Bussei (in Japanese), 1993. **4**: p. 227–233.
29. Wang X., X. Xu, and S.U.S. Choi, *Thermal conductivity of nanoparticles–fluid mixture*. Journal of Thermophysics and Heat Transfer, 1999. **13**(4): p. 474–480.
30. Liu M.S., M.C.C. Lin, I.T. Huang, C.C. Wang, *Enhancement of thermal conductivity with carbon nanotube for nanofluids*. International Communications in Heat and Mass Transfer, 2005. **32**(9): p. 1202–1210.
31. Zhang X., H. Gu, and M. Fujii, *Effective thermal conductivity and thermal diffusivity of nanofluids containing spherical and cylindrical nanoparticles*. Experimental Thermal and Fluid Science, 2007. **31**: p. 593–599.
32. Duangthongsuk W. and S. Wongwises, *Measurement of temperature-dependent thermal conductivity and viscosity of TiO₂-water nanofluids*, Experimental Thermal and Fluid Science, 2009. **33**(4): p. 706–714.
33. Mintsu H.A., G. Roy, C.T. Nguyen, and D. Doucet, *New temperature dependent thermal conductivity data for water-based nanofluids*. International Journal of Thermal Sciences, 2009. **48**(2): p. 363-371.
34. Yu W., H. Xie, L. Chen, and Y. Li, *Investigation of thermal conductivity and viscosity of ethylene glycol based ZnO nanofluid*. Including results for Thermochemica Acta, 2009. **491**(1): p. 92–96.
35. Godson L., B. Raja, D.M. Lal, and S. Wongwises, *Experimental investigation on the thermal conductivity and viscosity of silver-deionized water nanofluid*. Experimental Heat Transfer 2010. **23**(4): p. 317–332.
36. Murshed S.M.S., *Simultaneous measurement of thermal conductivity, thermal diffusivity, and specific heat of nanofluids*. Heat Transfer Engineering, 2012. **33**(8): p. 722–731.
37. Kumaresan V. and R. Velraj, *Experimental investigation of the thermo-physical properties of water–ethylene glycol mixture based CNT nanofluids*. Including results for Thermochemica Acta, 2012. **545**: p. 180–186.
38. Sundar L.S., E.V. Ramana, M.K. Singh, and A.C.M. Sousa, *Thermal conductivity and viscosity of stabilized ethylene glycol and water mixture Al₂O₃ nanofluids for heat transfer applications: an experimental study*, International Communications in Heat and Mass Transfer, 2014. **56**: p. 86–95.
39. Zyla G. and J. Fal, *Viscosity, thermal and electrical conductivity of silicodioxide–ethylene glycol transparent nanofluids: An experimental studies*, Including results for Thermochemica Acta, 2017. **650**: p. 106–113.
40. Bergman T.L., A.S. Lavine, F.P. Incropera, and D.P. DeWitt, *Fundamentals of heat and mass transfer*, 2011, John Wiley & Sons.
41. Li T., S. Li, J. Zhao, P. Lu, and L. Meng, *Sphericities of non-spherical objects*. Particuology, 2012. **10**: p. 97–104.
42. ASHRAE, *ASHRAE Handbook-Fundamentals*, 2001. American Society of Heating, Refrigerating and Air-conditioning Engineers Inc., Atlanta.
43. Namburu P.K., D.P. Kulkarni, D. Misra, and D.K. Das, *Viscosity of copper oxide nanoparticles dispersed in ethylene glycol and water mixture*. Experimental Thermal and Fluid Science, 2007. **32**(2): p. 397–402.
44. Suganthi K.S. and K.S. Rajan, *Temperature induced changes in ZnO – water nanofluid: zeta potential, size distribution and viscosity profiles*. International Journal of Heat Mass Transfer, 2012. **55**(25): p. 7969–7980.
45. Halefadi S., P. Estellé, B. Aladag N. Doner, and T. Maré, *Viscosity of carbon nanotubes water-based nanofluids: influence of concentration and temperature*. International Journal of Thermal Sciences, 2013. **71**: p. 111–117.
46. Ghanbarpour M., E.B. Haghigi, R. Khodabandeh, *Thermal properties and rheological behaviour of water based Al₂O₃ nanofluid as a heat transfer fluid*. Experimental Thermal and Fluid Science, 2014. **53**: p. 227-235.
47. Pastoriza-Gallego M. J., L. Lugo, D. Cabaleiro, J. L. Legido, and M.M. Piñeiro, *Thermophysical profile of ethylene glycol-based ZnO nanofluids*, The Journal of Chemical Thermodynamics, 2014. **73**: 23–30.
48. Rahmati A.R. and M. Reiszadeh, *An experimental study on the effects of the use of multi-walled carbon nanotubes in ethylene glycol/water-based fluid with indirect heaters in gas pressure reducing stations*. Applied Thermal Engineering, 2018. **134**: p. 107–117.
49. Oztop H.F. and E. Abu-Nada, *Numerical study of natural convection in partially heated rectangular enclosures filled with nanofluids*. International Journal of Heat Fluid Flow, 2008. **29**(5): p. 1326–1336.
50. Rabbani P., A. Hamzhepour, M. Ashjaee, M. Najafi, and E. Houshfar, *Experimental investigation on heat transfer of MgO nanofluid in tubes partially filled with metal foam*. Powder Technology 354 (2019) 734-742
51. Alawi O.A., N.A.C. Sidik, H.W. Xian, T.H. Kean, S.N. Kazi, *Thermal conductivity and viscosity models of metallic oxides nanofluids*. International Journal of Heat Mass Transfer, 2018. **116**: p. 1314–1325.

52. Jenei P., C. Balázs, Á. Horváth, K. Balázs, and J. Gubicza, *The influence of carbon nanotube addition on the phase composition, microstructure and mechanical properties of 316L stainless steel consolidated by spark plasma sintering*, Journal of Materials Research and Technology., 2019. **8**(1): p. 1141-1149.
53. Carpinlioglu M.O. and M. Kaplan., *A correlation approach for the calculation of thermal conductivity of nanofluids as a function of dynamic viscosity*. Journal of the Brazilian Society of Mechanical Sciences and Engineering, 2021, **43**(5): 242.



Research Article

Experimental investigation of the effects of different refrigerants used in the refrigeration system on compressor vibrations and noise

Zafer Cingiz^a , Ferzan Katircioğlu^b , Suat Sarıdemir^c , Gökhan Yıldız^{d,*}  and Yusuf Çay^e 

^aDepartment of Electricity and Energy, Düzce Vocational School, Düzce University, Düzce, Turkey

^bDepartment of Electronics and Automation, Düzce Vocational School, Düzce University, Düzce, Turkey

^cDepartment of Mechanical Engineering, Faculty of Engineering, Düzce University, Düzce, Turkey

^dDepartment of Mechanical Engineering, Graduate School of Natural and Applied Sciences, Düzce University, Düzce, Turkey

^eDepartment of Mechanical Engineering, Technology Faculty, Sakarya University of Applied Sciences, Sakarya, Turkey

ARTICLE INFO

Article history:

Received 12 January 2021

Revised 24 February 2021

Accepted 20 March 2021

Keywords:

Alternative refrigerants

Noise

Vibration

ABSTRACT

Vibration and noise are undesirable effects in daily life and energy-consuming systems. In this study, the effects of different refrigerants on noise and vibration in a sealed reciprocating compressor are discussed. The study compared the noise and vibration performances of refrigerants with lower ozone depletion potential (ODP) values compared to R22, which has a high ODP value. The study was carried out experimentally in two stages. Firstly, tests were conducted for the coefficient of performance (COP) of different refrigerants. Secondly, vibration and noise data were obtained experimentally for different refrigerants. The results obtained from the experiments showed that both the COP value and the compressor vibration and noise have different values for R22 refrigerant and other alternative refrigerants, but values close to R22 are obtained. It was observed that the compressor noise values and vibration values vary depending on the type of used refrigerant. Average vibration values were determined as 0.604 m/s² in R22, 0.603 m/s² in R438A, 0.593 m/s² in R417A, 0.622 m/s² in R422D and 0.637 m/s² in R422A. When the noise values are examined, it was measured as 61.327 dB for R22, 62.913 dB for R438A, 62.187 dB for R417A, 63.715 dB for R422D and 64.913 dB for R422A. R417A, which has a 99% similar noise value to R22, was determined as an alternative refrigerant. COP values were found as 4.07 in R22, 3.98 in R438A, 3.63 in R417A, 3.37 in R422D, and 3.18 in R422A. R438A showing 95% similarity for COP can be used as an alternative to R22. Generally, it was observed that the noise and vibration values are very close to each other for all refrigerants examined.

© 2021, Advanced Researches and Engineering Journal (IAREJ) and the Author(s).

1. Introduction

Noise pollution is a problem that significantly affects our health and social behavior in the developing world. The gradual increase in living standards and the shrinkage of living spaces have made the noise problem in the air conditioning and refrigeration sector important. Considering that these devices are used for almost 24 hours, acoustic and vibration properties are important in terms of quality of life. Especially at night and when

people seek a quiet environment and need a state of rest, the noise generated by these devices is disturbing.

Domestic and commercial refrigeration and air conditioning (HVAC) systems constitute an indispensable part of modern life in the world [1]. Although the area of use is wide, these devices are also used to protect perishable substances, regulate temperature-sensitive processes in industries, and provide a comfortable environment [2].

* Corresponding author. Tel.: +90-850-800-8181.

E-mail addresses: zafercingiz@duzce.edu.tr (Z. Cingiz), ferzankatircioglu@duzce.edu.tr (F. Katircioğlu), suatsaridemir@duzce.edu.tr (S. Sarıdemir), gokhan.yildiz1987@hotmail.com (G. Yıldız), yçay@subu.edu.tr (Y. Çay)

ORCID: 0000-0003-3796-755X (Z. Cingiz), 0000-0001-5463-3792 (F. Katircioğlu), 0000-0002-6028-1073 (S. Sarıdemir), 0000-0001-6039-9226 (G. Yıldız), 0000-0003-4007-6168 (Y. Çay)

DOI: 10.35860/iarej.859423

This article is licensed under the CC BY-NC 4.0 International License (<https://creativecommons.org/licenses/by-nc/4.0/>).

Compressors used in refrigeration and air conditioning systems are one of the most important sources of vibration and noise. The most important design parameter for reducing the noise emitted to the environment by the compressors used is possible by reducing the dynamic forces transmitted from the compressor to the casing.

Vibration and noise generated by compressors are transmitted to the compressor outer casing starting from its emergence, and from here it passes to the environment in the form of noise and/or vibration through the environment in which the compressor is located or the system elements.

Li et al. emphasized in their study that the vibration value is transmitted from the compressor to the system by pipes and mounting elements that connect the compressor to the structure. It was stated that the design of these elements significantly affects the dynamic performance of the system. In the study, a sequencing explaining the compressor vibration is defined by using the solid body model. It has been shown that if this sequencing is used, the number of points to be measured in the vibration test can be reduced. The specified analytical method was applied to a compressor system, the results were compared with the measurements, and consistency was observed [3].

Hamilton evaluated the vibration and noise problems in compressors in general terms. In this study, firstly the compressors used in refrigeration systems are grouped and the vibration and noise sources that occur in the compressors and their transmission routes to the environment are emphasized with their general characteristics. Basic sound and noise properties were mentioned. The importance of measuring noise in compressors was emphasized. The measurements that can be applied in the interior of the compressors, the purposes for which they will be carried out, and how the results will be handled were evaluated. The effects of the compressor outer casing on compressor noise were discussed. Besides, measurement techniques that can be used for vibration and noise control in compressors are discussed [4].

The design and production of quieter mechanical systems have been important studies in terms of acoustics and noise control. The noise of appliances in household appliances such as refrigerators is unpleasant and undesirable. The source of noise in refrigeration systems is generally due to the operation of the component in the system and the flow of the refrigerant in the pipes. Vibrations caused by flow in the pipes pose a problem during the design of refrigeration systems. To eliminate this disturbance of refrigeration systems, noise should be reduced or eliminated [5].

Lee et al. in their study conducted different experiments to analyze refrigerator sounds. During the experiments, tests were carried out on how the refrigerator sounds were perceived by humans. For the study, sound recordings were made at home and in a completely silent room using

two household refrigerators. Taking measurements from different sides of the refrigerator, it was determined that the main sound source is the compressor. Measurement records were taken from the moment the compressor started operating and the sounds generated were divided into various groups. These groups consist of the sounds during the start of the compressor, the sounds during the stable operation of the refrigerator, and the sounds that occur when the compressor stops. The voices in these groups were tested separately and analyzed [6].

Han et al. in their study dealt with noise originating from refrigerant at the evaporator inlet and the capillary pipe outlet in two different studies. The study showed that due to the transition from expansion to evaporation, bubble formation and interaction caused some degree of flow-induced noise [7] [8].

Jang et al. made a noise analysis of the rotary compressor in a domestic air conditioner. The suction pressure of the compressor is 9.12 kg/cm^2 and the discharge pressure is 33.45 kg/cm^2 . The noise originating from the compressor was examined in two categories as pressure pulse of the refrigerant and structural vibration. As a result of the experiments, it was observed that the refrigerant creates noise while leaving the discharge line, and this noise increases as the speed of the compressor increases [9].

Venkatappa et al. analyzed the noise values of R134a and R1234yf refrigerants caused by the refrigerant flow in the compressor in the automotive air conditioning system. As a result of experiments, the noise and vibration energy generated due to flow is significantly higher in R1234yf compared to R134a [10].

Considering the new technological developments in refrigeration systems and the improvement of the compressor, the noise originating from the refrigerant was almost eliminated. Also, for refrigeration system manufacturers, how to improve performance and reduce noise was always a big challenge. Many consumers complained about the noise originating from the refrigerant in refrigeration systems. For a refrigeration system company with annual sales of more than 1 million in China, the return of the product due to noise resulted in financial losses of over 20 million Yuan. Therefore, it is necessary to investigate and address the noise from originating refrigerant [11].

In a 100 m^2 flat in Korea, the noise characteristics of different types of a refrigerator in a real-life environment were investigated. It was determined that the noise level of the refrigerator in the living room is approximately 10 dB higher than the noise level in a quiet room in the same position. A semantic differential test was also conducted using various nomenclatures to evaluate the noise quality of the refrigerator [12].

The number of complaints about noise in living spaces

increases dramatically. Especially, there are concerns regarding the noise of electrical devices. The International Noise Control Engineering Institute has proposed noise labels for consumer and industrial products and researched how noise is labeled in various countries [13].

On the contrary other household appliances, users react sensitively to the noise generated by these appliances, as refrigerators operate all day. Consumer reports recommend that consumers control the noise ratio before purchasing a refrigerator. For this reason, the noise levels of the refrigerators should be reduced to create a quieter living environment [14].

Although the noise value in the refrigerator tested in a quiet room decreased, noise complaints and symptoms continue. Because of this, it is necessary to take into account the noise level, flaws, and consumer sensitivity of the refrigerators. Household device manufacturers usually measure refrigerator noise in a quiet room. However, the noise level, frequency characteristics, and differences in sound characteristics in house conditions are very different from environmental conditions. Therefore, the evaluation of refrigerator noise in people's living environments should be made. Also, the noise level is affected by background noise, noise duration, and frequency characteristics [12].

Compressors and fans are refrigerator noise sources that lead to consumer complaints. The refrigerator noise level in the living environment is approximately 40 dB. Some structural improvements to be made in the refrigerator system may reduce this noise level. For example, it was stated that the improvement in the form of rear and side panels reduces the compressor noise level by approximately 2 dB [14-16].

The method of refrigerator noise measurement in a quiet room according to ISO 3745 gives a different sound characteristic according to the noise level measured in living environments. Sound quality assessments and predictive models were proposed in various mechanical engineering applications such as automobiles, HVAC systems, and trucks used in cold transport [17-19].

Refrigeration and air conditioning systems are systems that use compressors and refrigerants. When the compressor in these devices operates, vibration occurs in the pipes due to the compressor. There are two main causes of this vibration: These are vibrations and mechanical vibrations caused by the refrigerant [20].

Pressure fluctuations consist in the compressor as a result of the closing and opening of the valve during the compression and suction of the refrigerant. The vibration occurs in the system pipes due to these fluctuations. Vibration caused by pressure fluctuations is one of the most important causes of compressor noise. Therefore, it is critical to anticipate and prevent vibration and noise [21-23].

The main cause of noise and vibration in refrigeration systems is the compressor. Therefore, it is a determining factor in the noise generated in refrigeration systems. Many scientists worked on reducing compressor vibration noise. Besides, influential methods such as improving the shape of the compressor outer layer before entering the dryer-filter, improving the suction muffler, and replacing the filter drier have been proposed. All of the driers and similar attempts have been found to significantly reduce the noise level of the refrigerator.

In this study, the effects of different refrigerants on noise and vibration in a sealed reciprocating compressor are discussed. Due to the high ozone depletion potential (ODP) of R22 used in the refrigeration system, the refrigerants with lower ODP are analyzed. The study is carried out experimentally in two stages. First, tests are conducted for the coefficient of performance (COP) of different refrigerants. Secondly, vibration and noise data are obtained experimentally for different refrigerants. As a result of the experiments, it is determined that the refrigerant that can be an alternative to R22 for both the COP and the compressor vibration and noise is detected.

2. Material and Method

The operation of the system is stopped by a relay because of the signal coming from the thermostat to the compressor, when the cabin temperature is reached at 0 °C. The refrigerant flow through the evaporator also increases, when the compressor stops running [5-6]. More refrigerant flows again into the evaporator due to the pressure difference between the condenser and the evaporator, in addition to the refrigerant that cannot complete its flow in the evaporator and is therefore trapped there. The refrigerant moves in both the liquid and vapor phases, but it has been found that the noise caused by the flow mainly consists of the liquid phase [20]. When the difference between the cooled space temperature and the set temperature reaches the set level, the compressor starts to operate again. Due to the rapid drop in pressure in the suction line, the liquid refrigerant flows towards the compressor. During this flow, the refrigerant stimulates the pipe walls, causing a temporary noise [21]. Flow begins from the discharge line of the refrigeration system to the suction line when the compressor stops. Besides, some of the refrigerants that evaporate due to increased pressure at a constant temperature condense in the evaporator. After a while, the heat charge in the evaporator comes to just sufficient to evaporate some of the liquid refrigerants until the compressor starts up. A large amount of liquid refrigerant evaporates due to the rapid drop in pressure, when the cycle starts [22]. The experimental steps in the study are given in Figure 1.

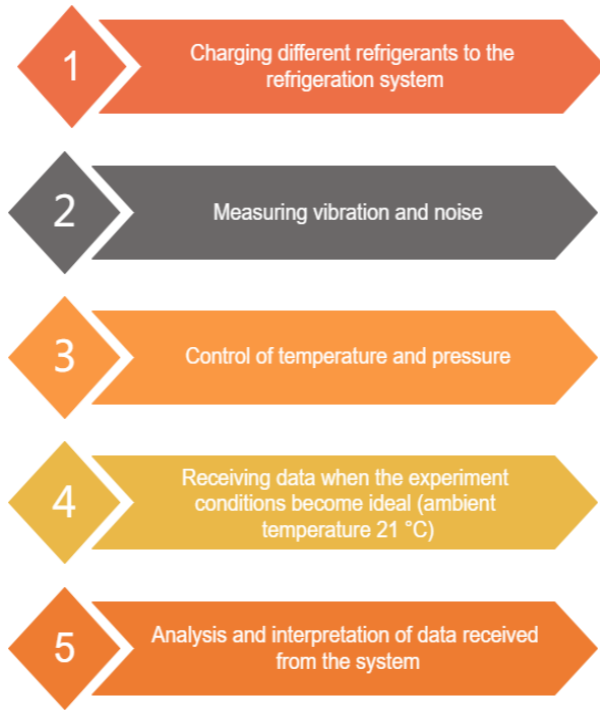


Figure 1. Flow chart for the experimental process

2.1 Refrigerants

In this study, R22, R438A, R417A, R422D, and R422A refrigerants were used. R22 is a suitable refrigerant for a variety of refrigeration and air conditioning applications with a wide variety of temperature preferences. Due to this property, it has become the most common refrigerant used in many applications after the removal of chlorofluorocarbons [24]. R422D is preferred for R22 refrigerant changes in the direct evaporation component. In most systems, it shows similar efficiency and performance values to R22 [25]. R417A is used instead of R22 in direct expansion constant air conditioning and refrigeration systems in medium temperature [26]. R422A is used in some low-temperature commercial refrigeration applications as an alternative to

R22. It provides lower pressure refrigerant temperatures compared to R22 and can extend the service life of the compressor. R438A, the other refrigerant used in the test system, is used as an alternative to R22 indirect evaporation systems [25]. R438A provides similar refrigeration performance and energy efficiency to R22 when operating at a lower compressor discharge temperature, similar evaporator, and condenser pressures. R22, direct expansion (DX) refrigeration and air conditioning systems were successfully realized renewal by using R438A as refrigerant [27]. The compositions and basic thermodynamic properties of the five refrigerants used in the experimental setup are given in detail in Table 1.

2.2 Experimental Setup

The experimental system was designed based on the vapor compression refrigeration cycle. In the experimental system, a commercial type refrigeration system operating with R22 and alternatives R438A, R417A, R422D, and R422A refrigerants was manufactured. The experimental rig of refrigeration system is given in Figure 2. Each refrigerant to be tested was charged as 900 g, the compressor was purged with nitrogen before charging and vacuuming was performed. To be able to perform the experiments in a stable environment and to examine the performances of different refrigerants more realistically, the experiments were carried out in a closed environment with a constant outside temperature. To measure temperatures in the system, instant measurements were made with K-type thermocouples connected to the inputs and outputs of each main element of the system. Pressure measurements were carried out with pressure transmitters. All components and measurement devices used in the designed experimental system were given in Figure 3, and their technical specifications were given in Table 2.

Table 1. Environmental and physical properties of tested refrigerants [28]

Specification	R22	R438A		R417A		R422D		R422A	
Refrigerant Composition (Mass %)	R22	R125	45%	R125	46.60%	R125	65.1%	R125	85.1%
		R134a	44.2%	R134a	50%	R134a	31.5%	R134a	11.5%
		R600	1.7%	R600	3.4%	R600a	3.4%	R600a	3.4%
		R601a	0.6%						
		R32	8.5%						
Molecular Weight (kg/kmol)	86.5	99.1		106.8		109.9		116	
Critical Temperature (°C)	96.2	85.3		87.1		79.6		71.7	
Critical Pressure (bar)	49.9	43		40.45		39.18		37.54	
Oil	MO	MO/AB/POE		MO/AB/POE		MO/AB/POE		MO/AB/POE	
ODP	0.05	0		0		0		0	
GWP	1810	2264		2346		2730		3140	

MO: Mineral Oil AB: Alkaline benzene POE: Polyol ester

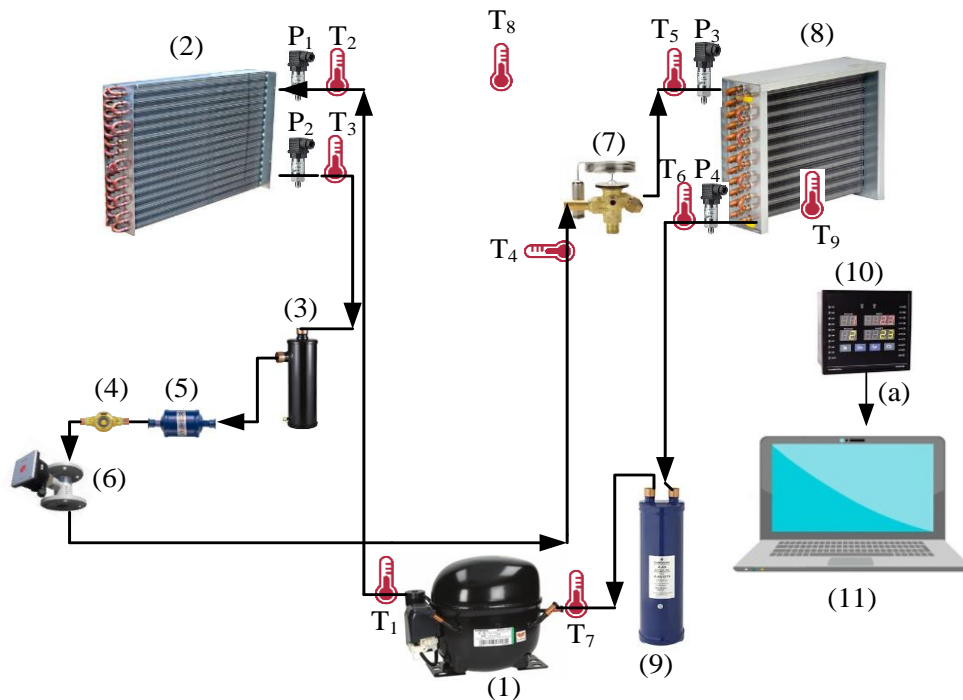


Figure 2. Experimental rig of refrigeration system

2.3 Vibration Measurement

Accelerometer was placed at the top of the compressor and vibration data were taken from this point depending on time. First of all, the accelerometer was fixed with

adhesive on the compressor and connected to the data acquisition device. Compressor vibration data were taken with a Bruel & Kjaer 4527 model piezoelectric accelerometer that can measure in three axes (x, y, z). The x-axis of the accelerometer indicates the direction perpendicular to the direction of movement of the piston in the working plane of the piston, the y-axis the direction in which the piston moves, and the z-axis in the normal directions of the working. The accelerometer was connected to four-channel VIBROTEST 80 model data acquisition devices capable of FFT analysis. The device has Bruel & Kjaer software and hardware system. Vibration signals up to 5 kHz were received for 20 seconds for each refrigerant test. Measurements were taken in the Hanning window at 6400 resolution over time. The characteristics of the triaxial accelerometer were given in Table 2.



1	Compressor	10	Scanner ve Alarm Device	T ₃	Thermocouple (Condenser Outlet Temperature)
2	Condenser	11	Computer	T ₄	Thermocouple (TEX Inlet Temperature)
3	Liquid Receiver	P ₁	Condenser Inlet Pressure Sensor	T ₅	Thermocouple (Evaporator Inlet Temperature)
4	Sight Glass	P ₂	Condenser Outlet Pressure Sensor	T ₆	Thermocouple (Evaporator Outlet Temperature)
5	Drier-Filter	P ₃	Evaporator Inlet Pressure Sensor	T ₇	Thermocouple (Compressor Inlet Temperature)
6	Flowmeter	P ₄	Evaporator Outlet Pressure Sensor	T ₈	Thermocouple (Ambient Temperature)
7	Thermostatic Expansion Valve	a	Data Transfer	T ₉	Thermocouple (Cooling Cabin Temperature)
8	Evaporator	T ₁	Thermocouple (Compressor Outlet Temperature)		
9	Accumulator	T ₂	Thermocouple (Condenser Inlet Temperature)		

Figure 3. All components and measuring equipment used in the experimental system

Table 2. Specifications of components and sensors in the experimental system

Component and Sensors	Voltage	Current	Technical Specifications
Compressor	220-240V		Embraco NEU 6215 GK - Hermetic reciprocating, Refrigerant: R22, Power: 1/2 Hp
Condenser	220-240V		Karyer KT- with airflow, 3/4 Hp
Evaporator	220-240V		Karyer KT- with airflow, 1/2 Hp
Expansion Valve			DuNan TEX TIS externally balanced union, One way PS 46 bar, Refrigerant: R22, Operating range: -40/+10 °C
Liquid Receiver			ESS-LRY, Pressure: 32 bar, Operating range: 0/+70 °C, Volume: 1.1 L
Accumulator			SAN XIN SX-204
Drier-Filter			Sanhua DTG, Welded, Operating range: -40/+120 °C
Sight Glass			SARCOOL Welded
Converter			Ordel SBA200- USB-RS485, USB 1.1 ve 2.0 compatible PC connection 300...3M Baud Communication speeds support Ordel OPIK16
Process Monitoring, Recording and Control Program			Variables can be monitored, changed, and saved on the computer, 128 channels can be defined to one parameter each, Each channel can be viewed as digital, analog, and graphic, Records can be kept in Microsoft Database (mdb) format., These can be opened with Microsoft ACCESS or Microsoft EXCEL programs
Universal Input Scanner and Alarm Device	100-240V AC/DC		Ordel SCN100-03/0/2/0/11, Number of entries: 20, 2 Piece 4 Digit Numeric and 2 Piece 2 Digit Numeric Display, 22 LED Displays Universal Sensor Input (TC, RT, mA, mV, V), Accuracy: ±0.2% Gas charging station with digital scales
Gas Filling Device	220V		Vacuum pumped (3 m ³ /h), Balance sensitivity: ±5 gram Operating temperature: 8- 49 °C Pressure Range: 15- 30 bar
Flowmeter	12-24V DC	4-20 mA	Bass- TDSS.004.015.D.A.10.S.S.N.N Measuring range: 0.6... 4.5 l/dk, Accuracy: 1% T.S. Temperature: -40...120°C, Pressure: 63 bar max. Keller PA-21Y, for refrigeration groups
Pressure Transmitter	8-28V	4-20 mA	Pressure range: 0-30 bar Accuracy: 1%, Operating range: -20....+85°C Ordel KTTE 2x0.5T 2K- K Type
Thermocouple			Cross-section: 2 x 0.5 mm ² Single wire, welded end Insulation: Teflon + Teflon, Cable length: 2 m
Thermostat	230V AC		EVCO- EVKB 21- Digital Hold with defrost NTC: -40/+105 °C, Relay Output: 1 piece16 A, Digital Input: 1
Accelerometer			Three axis, Brüel&Kjaer 4527, Frequency range: 0.3-10000 Hz, Accuracy: 3 mV/g, Temperature range: -30/180°C, Resonance frequency: 30 kHz
Noise Measuring Device			Svantek SV 104, Filters: A, C, Z Measuring range: 55 dbA RMS/ 140.1 dbA peak, Frequency range: 30 kHz-8 kHz, Dynamic range: 95 dB
Data acquisition device			Vibrotest 80, FFT analysis can be done, four-channel, Brüel&Kjaer 4527 program

2.4 Noise Measurement

Noise is one of the most important problems in home and work life, which occurs in all air conditioning and refrigeration systems and is ignored. The dosimeter is used to determine the level of exposure to noise of people in an environment with noisy devices. The dosimeter also detects the level where the noise is at its highest level. In this study, compressor noise was measured with a Svantek 104 model dosimeter shown in Figure 4. For this, the measuring device is fixed very close to the compressor. The process of obtaining vibration and noise data from the test system is shown in Figure 5.

2.5 Uncertainty Analysis

The total uncertainty value of the experimental study was calculated by the following equations. In the equation, W_R is

the total uncertainty of the study (%), R and w are the uncertainty function and the dimensional factor, respectively. In the same equation, W_n expresses the uncertainties in the independent variables [29, 30].

$$W_R = \left[\left(\frac{\partial R}{\partial x_1} w_1 \right)^2 + \left(\frac{\partial R}{\partial x_2} w_2 \right)^2 + \dots + \left(\frac{\partial R}{\partial x_n} w_n \right)^2 \right]^{1/2} \quad (1)$$



Figure 4. Noise measuring device

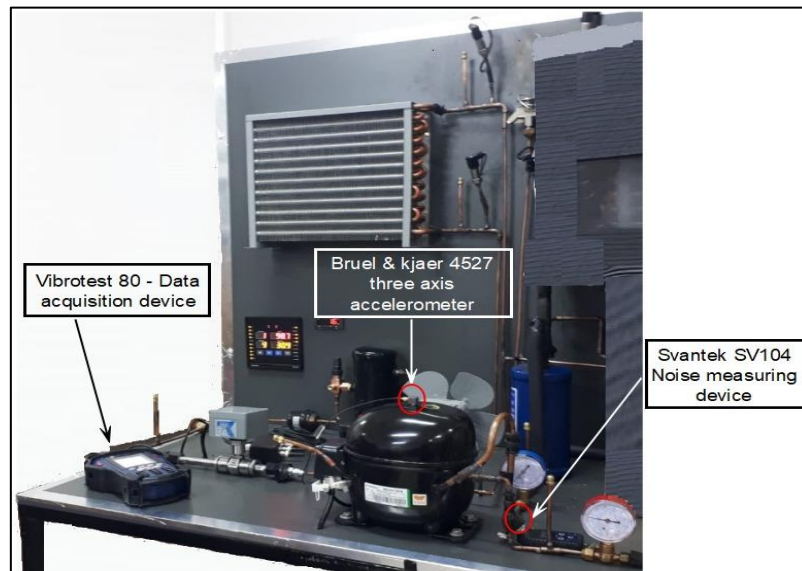


Figure 5. Vibration and noise measurement process from the experimental system

3. Results and Discussion

The uncertainty was calculated as 1.5% for the COP and the noise value as 2%. In this study, the variation of noise and vibration characteristics depending on the compressor load was experimentally investigated. Experiments were done with R22 and alternative refrigerants. 16384 data were taken for each measurement. When the compressor is loaded with different refrigerants, to compare the vibration amplitude values of the compressor, the root mean square (RMS) of the data taken from each axis has been calculated according to Equation (2) [31].

$$a_{RMS} = \sqrt{\frac{1}{N} \sum_{k=1}^N a_k^2} \quad (2)$$

Here; a_{RMS} : Root mean square of acceleration signals (g), a_k : k^{th} acceleration value for time-domain signals, N: Total acceleration value (N:16384).

The results of the data obtained from x, y, and z axes for the compressor used different refrigerants in the loaded position, arranged according to Equation (2), are given in Table 3. As can be seen from the measurements, especially when R22 and alternative refrigerants are used in the regime, the compressor RMS values in all axes were obtained very close to each other.

As seen in Table 3, for all refrigerants when the compressor is operating, the smallest RMS value on the x-

axis is obtained with R422D, while the highest RMS value is obtained in R22. While the smallest RMS value on the y-axis was obtained with R417A, the largest was obtained with R422A. While the smallest RMS value on the z-axis is obtained with R22, the largest was obtained with R422D.

Using the data in Table 3, average vibration values (a_t) in all axes (x, y, z) were calculated according to Equation 3.

$$a_t = \sqrt{a_{(x)}^2 + a_{(y)}^2 + a_{(z)}^2} \quad (3)$$

Here; a_t = Average vibration value, $a_{(x)}$ = RMS value in x direction, $a_{(y)}$ = RMS value in y-direction, $a_{(z)}$ = RMS value in z-direction.

Average vibration values (a_t) for all refrigerants were given in Figure 6. Average noise values were given for all refrigerants in Figure 7. While the highest average vibration values were obtained with R422A, the smallest average vibration value was obtained with R417A. This situation depends on the lowest COP value of R422A. The low COP value of R422A caused the compressor to operate at higher speeds, increasing the average vibration and noise values.

In Figure 7, the noise values of alternative refrigerants increase, respectively, R417A, R438A, R422D, and R422A when compared with R22 refrigerant. The noise values obtained as a result of the measurement are 99% similar for R417A, 97% for R438A, 96% for R422D, and 94% for R422A according to the refrigerant R22.

Table 3. RMS values for different refrigerants

	Axis	Refrigerants				
		R22	R438A	R417A	R422D	R422A
Compressor	(x), (CH1)	0.146219	0.137383	0.117344	0.097732	0.110746
	(y), (CH2)	0.110678	0.1146197	0.107061	0.154545	0.185198
	(z), (CH3)	0.108183	0.111886	0.128004	0.136984	0.111478

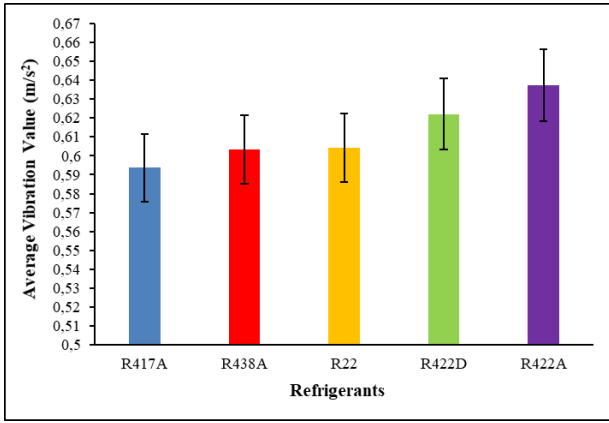


Figure 6. Average vibration values for different refrigerants

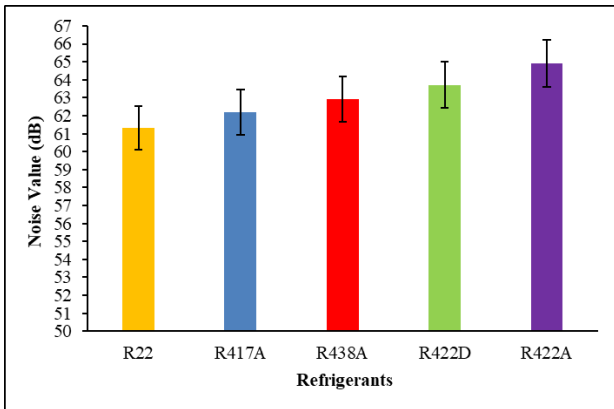


Figure 7. Change of noise according to different refrigerants

As seen in Table 1, the fact that refrigerants R438A, R417A, R422D, and R422A, which are preferred as alternatives to R22, have low hydrocarbon content by weight, keeps these mixtures at low flammability and makes them compatible with MO and AB. Besides, the used refrigerants have a similar safety level (A1) with R22. In most cases, the fact that there is no need to change the type of lubricant and the existing component during renewal and replacement shows that there are no major differences in the COP, noise, and vibration values of the used refrigerants.

One of the main reasons for the noise and vibration in the compressor is the cavitation level inside the pump. The higher the flow rate, the higher the cavitation level. Under the cavitation process, vapor bubbles increase due to the lower fluid pressure than vapor pressure. Increasing pressure

fluctuations due to cavitation in the compressor cause an increase in vibration and noise. For this reason, the pressure value of the fluid in the suction and discharge line is important [32-35]. As seen in Figure 6, R417A with lower suction pressure has the lowest average vibration value.

When the experimental results of the refrigerants in Table 4 were examined, it was seen that the cooling capacity, operating pressures, discharge temperatures, and power consumption of the refrigerants used were close to each other in terms of vibration and noise values as seen in Figure 6 and Figure 7. COP values of different refrigerants are given in Figure 8.

COP is a very important indicator of refrigeration system performance. The higher the COP value, the higher the efficiency of the refrigeration system. COP values were found to be 4.07 for R22, 3.88 for R438A, 3.63 for R417A, 3.37 for R422D, and 3.18 for R422A. As seen in Figure 8, it showed similarity 95% for R438A, 89% for R417A, 83% for R422D, and 78% for R422A compared to R22. COP values showed that none of the refrigerants selected were as efficient as R22. However, their COP values revealed that each would be considered as a potential alternative for empowerment and change. While it has comparable COP with other refrigerants, the low cooling capacity of R417A makes it less attractive. R422D and R422A refrigerants with lower COP are seen as the least alternative to R22 refrigerant. R438A refrigerant was determined to be the best alternative to R22. The relationship between noise and vibration values of different refrigerants and COP is given in Figure 9.

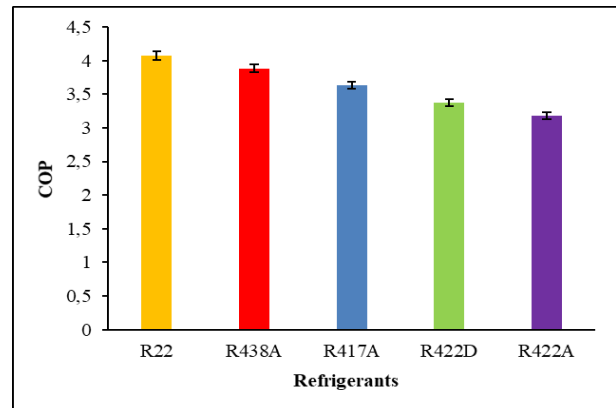


Figure 8. Change of COP for different refrigerants

Table 4. Experimental results of refrigerants

Refrigerants	COP	Cooling Capacity (kW)	Electricity Consumption (kWh)	Evaporation Pressure P ₁ (bar)	Condensation Pressure P ₂ (bar)	Discharge Temperature (°C)
R22	4.07	1.12	0.32	1.94	12.49	91.5
R438A	3.88	0.94	0.28	1.88	12.14	73.4
R417A	3.63	0.85	0.27	1.81	10.93	71
R422D	3.37	0.76	0.26	1.92	12.57	70.8
R422A	3.18	0.69	0.25	1.97	14.22	70.2

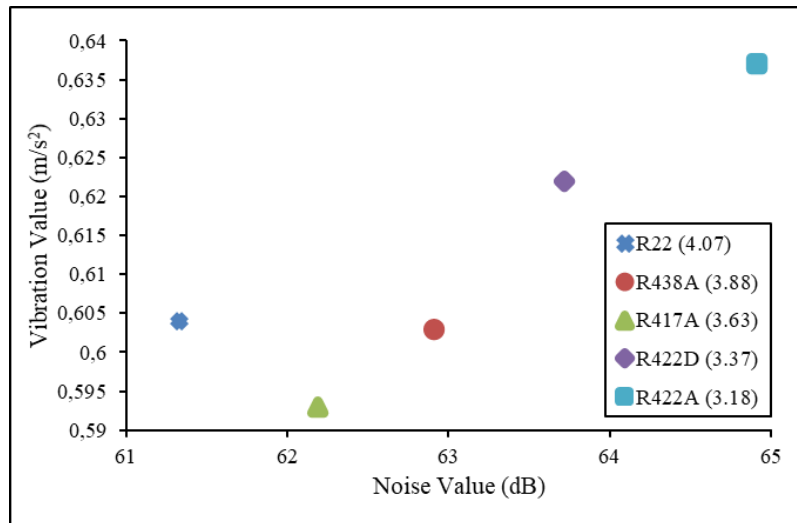


Figure 9. COP, vibration, and noise relationship graph for refrigerant

As seen in Figure 9, the relationship with the COP of the refrigerants between vibration and noise values is seen. R22 refrigerant with the highest COP value has the least vibration and noise. It is followed by R438A, R417A, R422D, and R422A refrigerants. It was observed that the vibration and noise values of the refrigerants are compatible with the COP.

4. Conclusions

The most important design parameter to reduce the noise and vibration emitted by the compressors used in refrigeration and air conditioning systems can be by reducing the forces transmitted from the compressor to the casing. In this study, the dynamic behavior of the reciprocating and sealed compressors, which form the backbone of the systems used for cooling purposes and which are mostly used in these systems, have been investigated. Thus, it has been possible to examine the dynamic behavior of compressors in the starting and regime states.

In this study, in which vibration and noise variation depending on the load were examined in a reciprocating sealed compressor, the average vibration and noise values of the compressor were determined by analyzing the data obtained from the x, y, and z axes. It was observed that the compressor noise values and vibration values vary depending on the type of refrigerant used. R417A, which has a 99% similar noise value to R22, was determined as an alternative refrigerant. R438A showing 95% similarity for COP can be used as an alternative to R22. It was observed that the noise and vibration values are very close to each other for all refrigerants examined. These close values obtained are also close in COP. This proximity showed that R22 and its alternative refrigerants can be used interchangeably without any changes in the system. Compressor vibrations and noise are partially affected by the refrigerant change in the system. This study showed that the refrigerants used in the experiments can be used as an alternative to R22 in terms of vibration and noise in the

refrigeration system.

Hermetic reciprocating compressors are the type of compressor that is widely used almost everywhere in the air conditioning and refrigeration industry. In this study, experiments were conducted by charging five different refrigerant systems using the vibration and noise analysis method, and vibration and noise data were obtained from the experiments. It is thought that the study will contribute to the knowledge and literature of those dealing with the detection of imbalance and other problems, vibration and noise analysis caused by refrigerants in hermetic reciprocating compressors used in air conditioning and refrigeration systems. Maintaining these compressors, which serve as the most effective parts of air conditioning and refrigeration processes, ensures that they maintain their performance and efficiency. It is very important to predict the malfunctions that may occur in the compressors, to keep production down and maintenance costs to a minimum. At the same time, whether there is a difference in terms of the refrigerants used shows the importance of the study. As a result of the study, it was seen that vibration and noise analysis of the hermetic reciprocating compressor is an important method in detecting malfunctions that may occur. Considering the studies in the literature, it is foreseen that vibrations and noises can be analyzed with a smart system without the need for expert interpretation, and malfunctions or maintenance processes can be predicted with a smart decision support system. In future studies, it is aimed to develop a modern fault detection, diagnosis, and maintenance system using machine learning methods and to work on increasing the performance of the system.

Declaration

The authors declared no potential conflicts of interest with respect to the research, authorship, and/or publication of this article. The authors also declared that this article is original, was prepared in accordance with international

publication and research ethics, and ethical committee permission or any special permission is not required.

Author Contributions

G. Yıldız developed the methodology. S. Sarıdemir and Y. Çay performed the analysis. Z. Cingiz and F. Katircioğlu supervised and improved the study.

Acknowledgment

This study was supported by Düzce University Scientific Research Projects (Project no: 2019.21.02.983), Turkey.

Nomenclature

a_t	: Average vibration value
$a_{(x)}$: RMS value in x-direction
$a_{(y)}$: RMS value in y-direction
$a_{(z)}$: RMS value in z-direction
a_{RMS}	: Root mean square of acceleration signals
a_k	: kth acceleration value for time-domain signals
AB	: Alkaline benzene
AC	: Alternating current
CH	: Channel
COP	: Coefficient of performance
DC	: Direct current
DX	: Direct expansion
FFT	: Fast Fourier transform
GWP	: Global warming potential
HVAC	: Heating, ventilation, and air conditioning system
MO	: Mineral oil
N	: Total acceleration value
ODP	: Mineral oil
POE	: Polyol ester
R	: Uncertainty function
RMS	: Root mean square
TEX	: Thermostatic expansion valve
V	: Volt
w	: Dimensional factor
W_R	: Total uncertainty
W_n	: Uncertainties in the independent variables

References

- Ceylan, İ., G. Yıldız, A. E. Gürel, A. Ergün, and A. Tosun, *The effect of malfunctions in air handling units on energy and exergy efficiency*. Heat Transfer Research, 2020. **51**(11): 1007-1028..
- United Nations Development Programme UNDP. "20 years of success: Montreal protocol on substances that deplete the ozone layer.," [cited 2020 29 October]; Available from: <http://www.un.org.kh/undp/knowledge/publications/20-years-of-success-montreal-protocol-on-substances-that-deplete-the-ozone-layer-2>.
- Li, W. L., and V. Eyo, *Dynamic Analysis of a Compressor Mounting System*. International Compressor Engineering Conference, 1996.
- Hamilton, J. F., *Measurement and control of compressor noise*, West Lafayette, Purdue University, USA, 1988.
- Celik, S., and E. C. Nsofor, *Studies on the flow-induced noise at the evaporator of a refrigerating system*. Applied Thermal Engineering, 2011. **31**(14-15): p. 2485-2493.
- Lee, C., Y. Cho, B. Baek, S. Lee, D. Hwang, and K. Jo, *Analyses of refrigerator noises*. In Proceedings of the IEEE International Symposium on Industrial Electronics, 2005: p. 1179-1184.
- Han, H. S., W. B. Jeong, M. S. Kim, and T. H. Kim, *Analysis of the root causes of refrigerant-induced noise in refrigerators*. Journal of Mechanical Science and Technology, 2009. **23**(12): p. 3245-3256.
- Han, H. S., W. B. Jeong, M. S. Kim, S. Y. Lee, and M. Y. Seo, *Reduction of the refrigerant-induced noise from the evaporator-inlet pipe in a refrigerator*. International Journal of Refrigeration, 2010. **33**(7): p. 1478-1488.
- Jang, S., Choung, H., Park, S., and Lee, S. *Investigation on noise of rotary compressors using fluid-structure interaction*. Journal of Mechanical Science and Technology, 2019. **33**(11): p. 5129-5135.
- Venkatappa, S., M. Koberstein, and Z. Liu, *NVH Challenges with Introduction of New Refrigerant HFO-1234yf*. SAE Technical Paper, 2017. (2017-01-0172)
- Xia, Y., Y. Liu, Y. Liu, Y. Ma, C. Xiao, and T. Wu, *Experimental study on reducing the noise of horizontal household freezers*. Applied Thermal Engineering, 2014. **68**(1-2): p. 107-114.
- Jeon, J. Y., J. You, and H. Y. Chang, *Sound radiation and sound quality characteristics of refrigerator noise in real living environments*. Applied Acoustics, 2007. **68**(10): p. 1118-1134.
- Berry, B. F., *The work of I-INCE Technical Study Group 2 on noise labels for consumer and industrial products*. Noise and Health, 2003. **5**(18): p. 21.
- Kim, K. M., *Study of efficiency and noise improvement in a reciprocating compressor for refrigerator*. The Magazine of the Society of Air-Conditioning and Refrigerating Engineers of Korea, 1995. **24**(1): p. 71-81.
- Yoo, W. H., C. G. Back, and J. H. Song, *The search for relations between compressor noise and refrigerator noise*, in Korean Society of Noise and Vibration Engineering, Autumn Conference. 1996: p. 32-36.
- Seo, S. H., T. H. Kwak, C. J. Kim, J. K. Park, and K. S. Cho, *Noise and vibration reduction of a household refrigerator*. Proceedings of the HVAC Refrigeration Engineering, 2000. p. 1133-1140.
- Lee, J. K., Y. W. Park, and J. B. Chai, *Development of a sound quality index for the evaluation of an intake noise of a passenger car*. Transactions of the Korean Society for Noise and Vibration Engineering, 2005. **15**(8): p. 939-944.
- Khan, M. S., and C. Hogstrom, *Determination of sound quality of HVAC systems on trains using multivariate analysis*. Noise Control Engineering Journal, 2001. **49**(6): p. 276-283.
- Khan, M. S., and C. Dickson, *Evaluation of sound quality of wheel loaders using a human subject for binaural recording*. Noise Control Engineering Journal, 2002. **50**(4): p. 117-126.
- Oh, H. E., D. J. Park, and W. B. Jeong, *Numerical and experimental study on the reduction of refrigerant pressure pulsation within compressor pipes*. Journal of Sound and Vibration, 2019. **438**: p. 506-519.
- Park, J., and S. Wang, *Noise reduction for compressors by modes control using topology optimization of eigenvalue*. Journal of Sound and Vibration, 2008. **315**(4-5), p. 836-848.

22. Birajdar, R., R. Patil, and K. Khanzode, *Vibration and noise in centrifugal pumps-Sources and diagnosis methods*, in 3rd International Conference on Integrity, Reliability, and Failure, 2009: p. 20-24.
23. Kim, B. L., J. Y. Jung, and I. K. Oh, *Modified transfer path analysis considering transmissibility functions for accurate estimation of vibration source*. Journal of Sound and Vibration, 2017. **398**: p. 70-83.
24. Linde. *Linde gas*. [Accessed 26 May, 2020]; Available from: https://www.linde-gas.com/en/products_and_supply/refrigerants/h_cfc_refrigerants/r22/index.html.
25. Bock Compressor. *Bock Compressor, Alternative Refrigerants Information on use of R2*. [Accessed 16 April, 2020]; Available from: http://www.bock.de/media/files/PDF/Produktinformationen/96151_Alternative-refrigerants_R22_Gb.pdf.
26. Climalife IDS Refrigeration Limited. *Climalife IDS Refrigeration Limited*. [Accessed 15 April, 2020]; Available from: <https://www.climalife.co.uk/docs/ISCEON-MO29Retrofit-Guidelines-V2.pdf>.
27. Allgood, C. C., and C. C. Lawson, *Performance of R-438A in R-22 refrigeration and air conditioning systems*, in International Refrigeration and Air Conditioning Conference: 2010, USA.
28. Cingiz, Z., F. Katircioğlu, Y. Çay, and A. Kolip, *Buhar Sıkıştırılmalı Soğutma Sisteminde R22 Alternatifi Soğutucu Akışkanların Termodinamik Analizi*. Politeknik Dergisi, 2020. **23**(4): p. 1205-1212.
29. Ağbulut, Ü., A. E. Gürel, and S. Sarıdemir, *Experimental investigation and prediction of performance and emission responses of a CI engine fuelled with different metal-oxide based nanoparticles–diesel blends using different machine learning algorithms*. Energy, 2021. **215**: 119076.
30. Sarıdemir, S., G. Yıldız, and H. Hanedar, *Effect of diesel-biodiesel-methanol blends on performance and combustion characteristics of diesel engine*. Düzce Üniversitesi Bilim ve Teknoloji Dergisi, 2021. **9**(1): p. 189-201.
31. Ağbulut, Ü., M. Karagöz, S. Sarıdemir, and A. Öztürk, *Impact of various metal-oxide based nanoparticles and biodiesel blends on the combustion, performance, emission, vibration and noise characteristics of a CI engine*. Fuel, 2020. **270**: p. 117521.
32. Al-Obaidi, A. R., *Experimental comparative investigations to evaluate cavitation conditions within a centrifugal pump based on vibration and acoustic analyses techniques*. Archives of Acoustics, 2020. **45**(3): p. 541-556.
33. Al-Obaidi, A. R., and R. Mishra, *Experimental investigation of the effect of air injection on performance and detection of cavitation in the centrifugal pump based on vibration technique*. Arabian Journal for Science and Engineering, 2020. **45**(7): p. 5657-5671.
34. Al-Obaidi, A. R., *Detection of cavitation phenomenon within a centrifugal pump based on vibration analysis technique in both time and frequency domains*. Experimental Techniques, 2020. **44**(3): p. 329-347.
35. Al-Obaidi, A. R., and H. Towsyfyhan, *An experimental study on vibration signatures for detecting incipient cavitation in centrifugal pumps based on envelope spectrum analysis*. Journal of Applied Fluid Mechanics, 2019. **12**(6): p. 2057-2067.

**Research Article****Chemical characterization of waste tire pyrolysis products****Gediz Uguz^a** and **Abdulkadir Ayanoglu^{b,*}** ^aOndokuz Mayıs University, Faculty of Engineering, Department of Chemical Engineering, 55139, Samsun, Turkey^bMardin Artuklu University, Vocational School, Mechanical and Material School, 47200, Mardin, Turkey

ARTICLE INFO

Article history:

Received 07 January 2021

Revised 10 March 2021

Accepted 20 April 2021

Keywords:

Gasoline like fuels

Diesel like fuels

Pyrolysis of waste tire

ABSTRACT

The significance of tire disposal, an attractive waste to convert into burning oil or absorber etc., has been increasing day by day. However, if it does not change into a useful form, it will damage the nature and the living things. Thus, pyrolysis, a well-known method, which is used to convert recycle tire waste into gas, liquid and char. On the other hand, the waste pyrolysis oil or waste tire oil (WTO) has a substantial available calorific value similar to those of fossil fuels. Due to pyrolysis reaction, high amount of sulfur is detected in the WTO; therefore, another step of explosion applied to WTO to decrease sulfur and also re-upgrade quality of oil with such catalysts as Calcium Oxide (CaO) and Natural Zeolite (NZ) at a ratio from 2 to 10 with an increase of 2 for each step, individually. It is noticed that distillation test is a key analysis for separation discrimination of rich or lean quality fuel. As a consequence of mixture of catalyst-WTO reactions, the best curve was observed at a 10% CaO-WTO mixture which was close to diesel#2 and the mixture was separated into two new fuels as light (Gasoline Like Fuel or abbreviated as GLF) and heavy one (Diesel Like Fuel or shortened as DLF) due to temperature differences. According to distillation, FT-IR, NMR and UV-vis were used to analyze WTO, GLF and DLF for defining their characterization as well. Thus, the characterization result data of samples have quasi-equivalent with standard petroleum in open literature, and can be combusted in engine as well.

© 2021, Advanced Researches and Engineering Journal (IAREJ) and the Author(s).

1. Introduction

The world has come across a renew aspect by lowering traditional energy sources, so the energy gap requires to be filled by waste or natural sources. Unfortunately, waste materials (waste tire, waste oil, garbage etc.) are required to be utilized by minimizing their harmful effects by recycling methods [1-2].

Recently, the amount waste tires (WTs) has increased due to the increase in transportation. However, tires have been worn out or abraded because of road problems or other factors. Thus, high amount of WTs has been discarded to environment, which causes harmful problems throughout human life and ecosystem [3]. The US disposes 500 million tones WT every year [4]. And the amount of tire disposed in Australia for each year is 51 million tones [5].

Owing to high amounts of the residual, the WTs have been used for landfill to minimize ecotoxicology problems [5]. The cement kiln and incinerators use 35 % of total WTs as fuel while 38% is recovered to utilize in civil engineering usage by shredded chips or granulates of WTs. [6]. Mechanical, biological, thermal incineration, chemical and pyrolysis or catalytic pyrolysis methods have been used for WTs in order to recycle them into useful products [7].

Therefore, pyrolysis is a green and clean technique, which can be applied to WTs in order to obtain useful products (non-condensable gas, liquid and solid material) as a result of high temperature and pressure applied at several conditions [8-10]. Based on depolymerization of the WTs, pyrolysis has brought in complex-mixture of organics (paraffin, olefins, terpenes, mono-polyaromatics,

* Corresponding author. Tel.: +90 482 213 00 02; Fax: +90 482 213 66 44.:

E-mail addresses: gediz.uguz@omu.edu.tr (G.Uguz), a.ayanoglu1@gmail.com (A. Ayanoglu)

ORCID: 0000-0002-6796-6067 (G.Uguz), 0000-0002-5835-558X (A. Ayanoglu)

DOI: 10.35860/iarej.856112

This article is licensed under the CC BY-NC 4.0 International License (<https://creativecommons.org/licenses/by-nc/4.0/>).

nitrogen and sulfur compounds with heterocycles and oxygenates) like chemical contents of fuels. The initial product of WTs was non-condensable gas which can be burned directly in energy generating systems, because of high heating value. Other one, the solid product, could be activated by nitrogen (N_2) or carbon dioxide (CO_2) flow gases to upgrade as absorbent materials. Besides, the liquid has disgusting odor, low power of hydrogen (pH), low heating value and high sulfur amount which causes air pollution, high corrosion in engine with less burning capacity. Due to tire oil problems, it was treated with catalyst to improve properties of oil for burning [11–14].

Ayanoglu and Yumrutas pyrolyzed WTs particles to oil and then mixed with catalysts to obtain well-quality fuels which have similarity to fuels. Moreover, each sample was analyzed through chemical and physical tests to check their comprehensive with petroleum fuels [15]. Kebritchi et al. [16] studied WTs pyrolysis to compare its yield and properties with other fuels. Furthermore, Ground Tire Rubber (GTR) and Reclaim Rubber (RR) were converted at 400–600 °C. The alkanes/aromatic ratios of FT-IR results and elemental analyses were close to each other. 1H -NMR and ^{13}C -NMR spectra were declared at different concentrations of aromatics, and they exhibited similarities due to each property. Lopez et al. [17] investigated natural and synthetic rubber of WTs conversion in conical spouted bed reactor between 425–600 °C. The liquid was tested by gas chromatography and mass spectrometry (GC-MS), two-dimensional gas chromatography (GCxGC) with distillation and elemental tests.

The present study aims to characterize GLF and DLF with GF and DF in order to delineate organic compositions by means of FT-IR, NMR and UV-Vis methods which can be utilized in chamber of combustion. Each of analysis determined structure of composition with detection of organic compounds under advanced technology of instrumental analysis.

2. Material and Methods

2.1. Raw Material

WTs were cut into small particles (1mm) which were replaced in the reactor for organic decompositions [18]. The simple schematic representation of cycling paths of WTs is declared at Figure 1.

2.2. Pyrolysis System

The batch pyrolysis system consists of a main reactor, auto control, thermocouple, blender, safety valve, heat exchanger and container (Figure 2). A cylindrical reactor has a dimension of $\varnothing 30 \times 40$ cm with 5 cm glass wool insulation. Additionally, a 5 kW electrical heater is used to verify temperature from room temperature to demanded values. Furthermore, the blender is used for homogenous temperature variations. The last part of the system is heat exchanger which liquefies gas into oil.

2.3. Reaction of Pyrolysis

The main advantages of pyrolysis system are to be cheap according to its parts, which minimized energy consumption and maximized desired products. Furthermore, the pyrolysis has other contribution to decrease residual of solid by increasing condensable (oil) and non-condensable (gas) fractions via heating rates, catalysts, pressure and other parameters for minimizing harmful and polluting effects because of high amount of sulfur [19–21].

WTs were converted into gas, liquid (WTO) and solid at first step of pyrolysis at a heating rate of 5 °C/min. And then, WTO was reacted with of CaO and NZ individually at mass ratios of 2,4,6,8 and 10. Each sample was distilled to compare with diesel fuel (DF). Consequently, 10% CaO-WTO sample curve was fairly close to DF. However, the sample had a lower boiling temperature than DF.

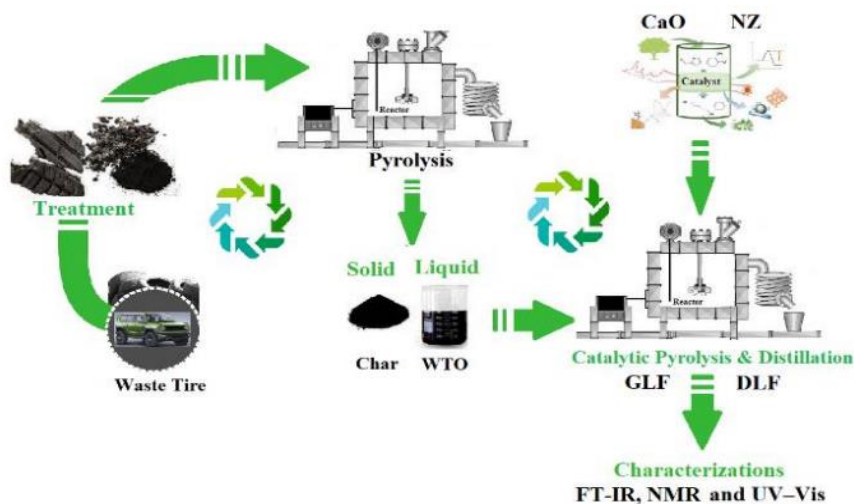


Figure 1. Cycling paths of WTs

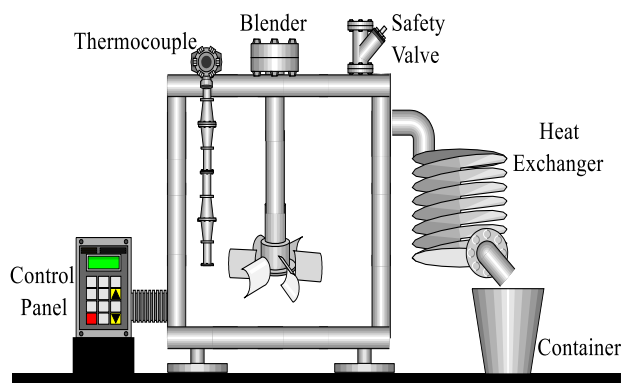


Figure 2. The batch pyrolysis system

Thus, the sample was divided into two new fuel samples at 54 °C to 150 °C which labelled as gasoline like fuel (GLF) and another one from 150 °C to 360 °C which was stated as Diesel like fuel (DLF) [22-24].

2.4 Fourier Transform Infrared Spectroscopy (FT-IR) Method

The physico-chemical properties with performance and emissions of fuel have been influenced by different composition amount of hydrocarbon. The compositions of fuel include different numbers of carbon which are combined with various elements to form new types of hydrocarbons at different ratios which can be classified as iso-paraffins, aromatics, naphthene, olefins (alkenes): diolefins (alkins) [25]. The FT-IR is used to characterize bond structures of functional groups.

In this study, FT-IR was used to define functional groups and bands by a simple analytical technique which was related with kind of stretching and bending vibrations of substances [26].

FT-IR spectra were recorded between 4000-650 cm^{-1} range with a resolution of 4 cm^{-1} for 4 scans at room temperature by a Perkin Elmer Spectrum-Two spectrometer for WTO, DLF, DF, GLF and GF, and the chemical structure was observed.

2.5 Nuclear magnetic resonance spectroscopy (^{13}C -NMR, ^1H -NMR)

NMR has a special characterization analytical technique to satisfy available chemical compound structures of renewable or conventional fuels. Besides, NMR has a good technique to find aromatic and aliphatic hydrogen and carbon atoms in fuel sample. The resonance peaks area were characterized by the amount of ^1H or ^{13}C atoms related with chemical compositions at spectra [31]. The qualitative composition of WTO, DLF, GLF, DF and GF were determined in terms of high-resolution technique. Due to high resolution, NMR spectroscopy provided detailed information on chemistry of petroleum fuels as proton and carbon [32]. The ^1H , ^{13}C , ^{19}F , ^{31}P , ^{11}B , APT and DEPT core probes were used

by Agilent Premium Compact NMR600 MHz spectrometer. The deuterated chloroform (CDCl_3) was used to dissolve sample at internal standard of NMR. ^1H and ^{13}C spectra were recorded from -2.00 ppm to 10.00 ppm and 20.00 ppm to 200 ppm, respectively at 600 MHz frequency.

2.6 Ultraviolet–Visible Spectroscopy Analysis (UV-Vis)

UV–vis spectra is used to detect the electronic properties of molecules. Each organic spectrum is taken via light into its structure to determine different aromatic compounds in samples at visible and ultraviolet fields [33].

In this study, UV absorption spectra of WTO, DLF, DF, GLF and GF were analyzed by using Agilent Technologies Cary 60 UV–Vis Spectrophotometer in the wavelength range of 900-200 nm, at 1 nm intervals, at room temperature and scanned by using standard 1 cm quartz cuvettes which are filled with samples for obtaining spectra. Additionally, samples were diluted by ethanol to define the measurable absorbance interval in the spectrophotometer since samples absorbed light in high UV range to obtain spectra.

3. Results and Discussion

3.1 The physical properties of products

A good indicator was physico-chemical analyses that were applied to all samples. The initial product (WTO) was tested to measure calorific value and carbon amount which was close to standard fuel except sulfur ratio. And a second step of pyrolysis was carried out by adding catalysts (2, 4, 6, 8 and 10 % of CaO and NZ separately) to WTO to minimize sulfur and increase features of new mixture samples [18].

The distillation was a good key for fuel properties to notice best curve which was 10% CaO-WTO for the sample, while the mixture had to be extracted into two parts by boiling points of 54 °C-150 °C as GLF and 150 °C-360 °C as DLF. Moreover, the carbon percentages, density, flash point, and HHV of GLF and DLF were

close to fossil fuels. But, DLF sulfur amount require to be decreased by utilizing a novel process. Finally, GLF and DLF features were benefited for conventional engines [18].

3.2 Fourier Transform Infrared Spectroscopy (FT-IR)

The conventional fuels have complex ingredients as paraffins (alkanes), olefins (alkenes), diolefins (alkynes), naphthenic (cycloalkanes), and aromatic hydrocarbons (benzene derivatives), sulfur, oxygen, and nitrogen molecules which cannot directly and easily break into components [30]. Due to conventional fuel ingredients, WTO has same complicated structure as well as aliphatic, aromatic, hetero-atom and polar compounds. For instance, WTO contains aromatic hydrocarbons compounds such as benzene, toluene, xylene, styrene and limonene. And also, the hydrocarbon groups of alkanes which cause an increase in cetane number. Thus, the alkanes amount was preferred to be high in fuel as an advantageous factor [31]. Figures 3 and 4 indicate FT-IR absorbance spectra which aim to show functional group individually while Figures 5 and 6 indicate FT-IR transmittance spectra which target to define conflict functional group of samples. The observed peaks defined alkenes group for each sample. The functional groups, which were found in literature and compared with all samples, were tabulated at Table 1.

As seen in Table 1, IR spectra have been explained deeply in some researches, as represented in Ref. [32–35]. The wave number ranging between 3700 and 3200 cm^{-1} were defined O–H stretching which was shown in the hydroxyl compounds as alcohols, phenols and carboxylic acids. Another absorption between 3000 and 2800 cm^{-1} was determined as $-\text{CH}_3$, $-\text{CH}_2$, and C-H functional groups to be specified by aliphatic group of alkanes [36–37]. The peak of 3677 cm^{-1} was seen at O-H stretching for GLF, DLF, DF and GF. The peaks of 2962 cm^{-1} and 2925 cm^{-1} were related with C-H stretching which were vibrated to hybridized at sp^3 layers. This aliphatic and aromatic compound were obviously indicated of alkane groups [38]. The peak around 1608 cm^{-1} was allocated at C=C stretching of aromatics and alkenes [39]. Other peaks were observed between 1455, 1376 and 1247 cm^{-1} due to vibration of aliphatic C-H molecules. The C-H stretching (alkanes), C=C stretching (alkenes) and C-H bending (alkanes) were observed at all peaks of samples. Besides, 1150 and 1100 cm^{-1} peaks were described at C-H in plane bending of aromatics. Furthermore, aromatic hydrocarbons were underwent chemical reaction with oxygen at high temperatures more than aliphatic hydrocarbons [40]. The wave number ranges were altered between 1020 and 845 cm^{-1} to define C=C stretching of alkenes.

The peak of 891 cm^{-1} was determined C=C stretching which was presented in GLF, DLF and gasoline. The residual aromatic groups were arranged at 768 cm^{-1} , 742 cm^{-1} , 729 cm^{-1} and 693 cm^{-1} which were seen at sharp medium peaks of C-H cyclic deformations. The peak of C–H cyclic deformations were detected in all samples except DF [40]. The peaks of all samples revealed the main structure of hydrocarbons and their characteristics by FT-IR spectrum analysis.

3.3 Nuclear magnetic resonance spectroscopy (^{13}C -NMR, ^1H -NMR)

NMR principal has been found on average molecular compounds for aromatic, olefin and aliphatic hydrocarbons. The latter structures have a mean of various functional groups number, which were detected at the NMR spectra [41]. The WTO, DLF, DF, GLF and GF were analyzed by ^1H -NMR spectra. The characteristic spectral area was defined by aromatic, olefin and aliphatic of proton signals at high and low fields. The ^1H -NMR spectra were separated into spectral regions by signals which were determined by aromatic, olefin and aliphatic hydrocarbons, as shown in Figure 7. ^1H -NMR spectra defined the aromatic and aliphatic groups in samples.

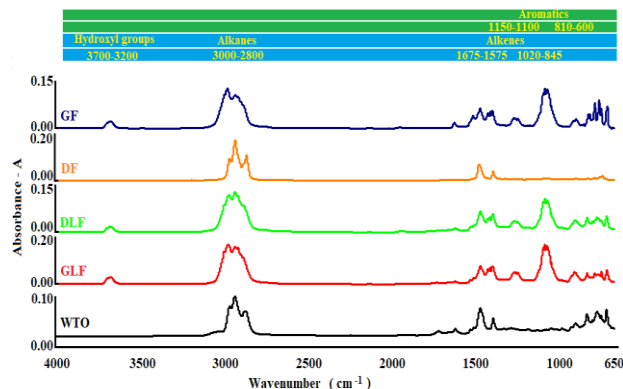


Figure 3. FT-IR split absorbance (A) spectra of WTO, DLF, DF, GLF and GF

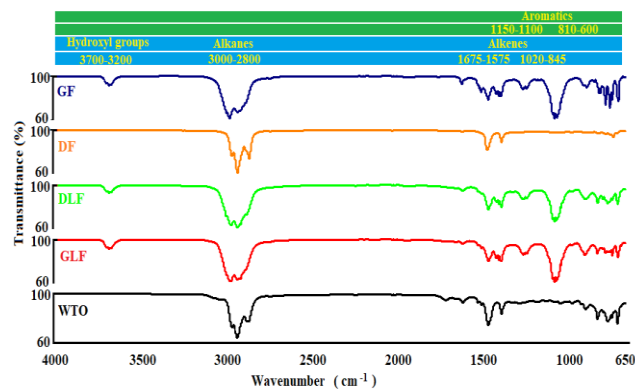


Figure 4. FT-IR split transmittance (%) spectra of WTO, DLF, DF, GLF and GF

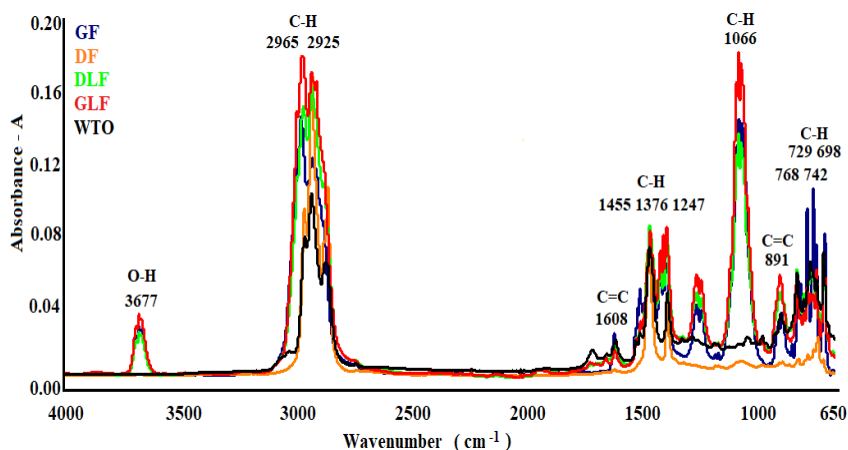


Figure 5. FT-IR overlay absorbance (A) spectra of WTO, DLF, DF, GLF and GF

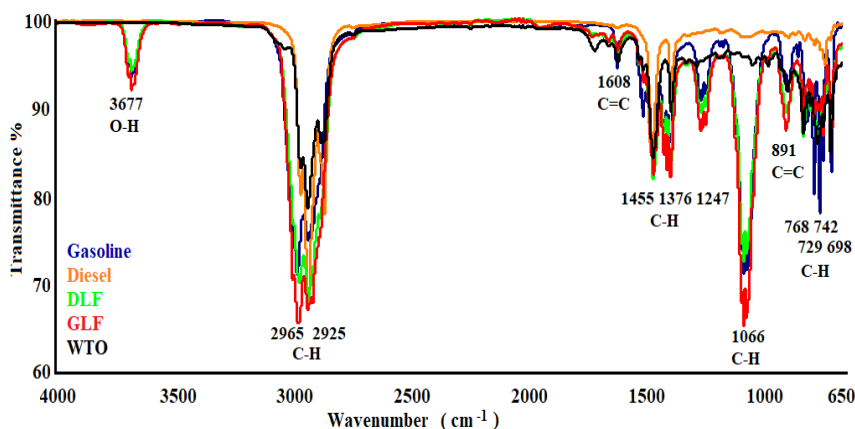


Figure 6. FT-IR overlay transmittance (%) spectra of WTO, DLF, DF, GLF and GF

Table 1. FT-IR functional groups and compounds of WTO, DLF, DF, GLF and GF [32-35]

Wavenumber ranges (cm ⁻¹)	Wavenumber (cm ⁻¹)	Functional group	Groups	Samples
3700-3200	3677	O-H stretching	hydroxyl	GLF, DLF, gasoline
3000-2800	2962,2925	C-H stretching	alkanes	Whole samples*
1675-1575	1608	C=C stretching	alkenes	Whole samples*
1525-1115	1455,1376,1247	C-H bending	alkanes	Whole samples*
1150-1100	1066	C-H in plane bending	aromatics	GLF, DLF, gasoline
1020-845	891	C = C stretching	alkenes	Whole samples*
810-600	768,742,729,693	C-H cyclic deformations	aromatics	DLF, GLF, WTO, gasoline

*Whole samples: WTO, DLF, diesel, GLF and gasoline.

As seen in Table 2, DLF, GLF and GF were analyzed by 1H-NMR that aromatic peaks were observed between 9.00-6.00 ppm of 1H chemical shift. The aliphatic alkane and aliphatic alkene peaks were detected at a range of 1.74-0.88 ppm and 6.00-1.70 ppm, respectively. Moreover, 1H chemical shift was identified in all samples (WTO, DLF, DF, GLF and GF). The samples were also tested by 13C-NMR spectroscopy to obtain more detail of their chemical structure. 13C nuclei of NMR sample spectra are seen in Figure 8.

13C-NMR spectroscopy presents more detail on broad chemical shifts interval data (0-200 ppm) [41]. 13C-NMR spectra have large numbers of distinguishable signals to

define carbon groups (i.e. methyl, methylene, methylene) and information about their locations which were assigned at various typical regions [42]. Thus, 13C-NMR informs about presence of aromatic and aliphatic carbon in samples which have an agreement with FT-IR spectra. In Table 2, 13C-NMR analysis was identified aromatic peaks from 150.00 to 125.00 ppm by 13C chemical shift for DLF, GLF, DF and GF. And also, alkane and alkene of aliphatic compounds were seen in all samples which were detected via 13C chemical shift range of during interval of 27.99-13.69 ppm and 150-110 ppm, respectively.

Table 2. ^1H -NMR and ^{13}C -NMR spectral regions for single components and structural groups of WTO, DLF, DF, GLF and GF [43, 44]

Class	^1H chemical shift (ppm)	^{13}C chemical shift (ppm)	Formulas	Samples
Aromatics	9.00-6.00	150.00-125.00	Ar-H	GLF, DLF, GF
Deuterated chloroform	7.27	77.36	CDCl_3	Whole samples*
Aliphatics Alkenes	6.00-1.70	150-110	$\text{C}=\text{C}$	Whole samples*
Aliphatics Alkanes	1.74-0.88	27.99-13.69	$\text{C}-\text{C}$	Whole samples*

*Whole samples: WTO, DLF, diesel, GLF and gasoline.

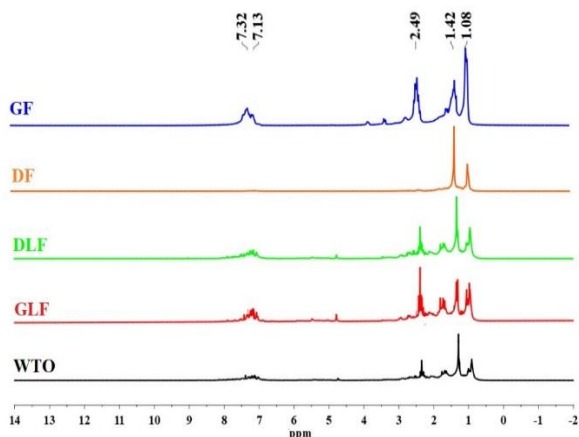


Figure 7. ^1H -NMR spectra of WTO, DLF, DF, GLF and GF

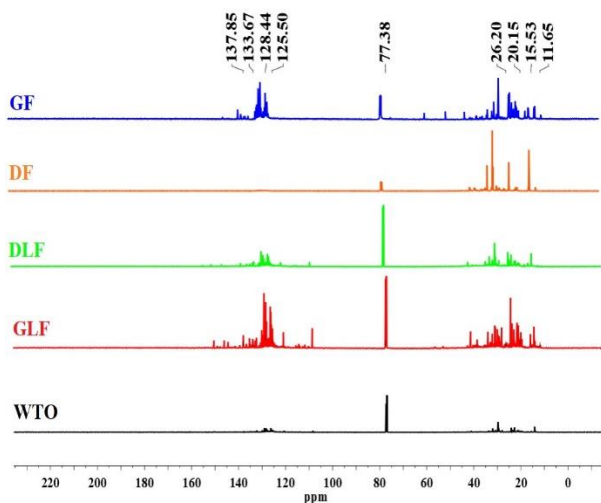


Figure 8. ^{13}C -NMR spectra of WTO, DLF, DF, GLF and GF

3.7. Ultraviolet–Visible Spectroscopy Analysis (UV-Vis)

UV-vis spectrometry is used for high accuracy quantity analysis for limited application interval due to range of absorption. Thus, organic compounds were enlightened on visible and ultraviolet fields to observe absorption spectrum for functional sample groups. The absorbance curves of diluted samples were observed at wavelength of 700–200 nm as seen in Figure 9. The curves were plotted by UV-Vis spectra data to compare samples' shape and slope which have similarity with chemical compounds of fossil fuels [45]

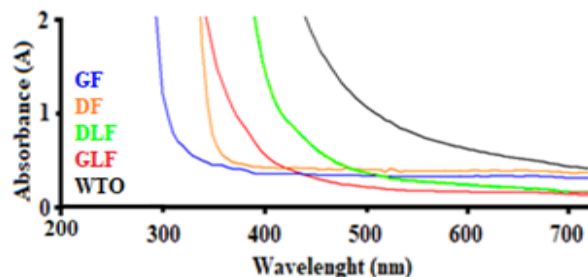


Figure 9. UV-vis absorbance spectra of WTO, DLF, DF, GLF and GF

3. Conclusions

WTs was liquefied into affluent organic products as gas, oil and solid. Especially, the physical and chemical features with calorific value of WTO were near to DF, except for sulfur. Thus, CaO and NZ catalysts reacted with different mass ratios to decrease sulfur quantity. Then, the new products compared with DF. 10 % CaO -WTO mixture curve was close to DF. Due to boiling points, the mixture sample was separated into light (GLF) and heavy (DLF) fractions. Both of GLF and DLF were very similar to GF and DF. However, some available characterization analyses were done for GLF and DLF via FT-IR, NMR and UV-Vis which was explained as items:

- FT-IR spectrum analyses of GLF and DLF had peaks which demonstrated fundamental structure of hydrocarbons, similar to standard fuels.
- ^1H -NMR and ^{13}C -NMR spectra of GLF and DLF had aromatic and aliphatic carbon groups which were compatible with FT-IR spectra which were close to gasoline and diesel fuel.
- UV-Vis spectra GLF and DLF had a similarity as visible and ultraviolet fields with standard petroleum fuels.

Declaration

The authors declare no potential conflicts of interest with respect to the research, authorship, and/or publication of this article. The authors also declare that this article is original, and was prepared in accordance with international publication and research ethics, and no ethical committee permission or special permission is required.

Author Contributions

G. Uguz and A. Ayanoglu have equal contribution and responsibility for the study.

Acknowledgment

The authors wish to thank Tuna Demirci for the TGA, DÜBİT, Düzce University, Düzce, Turkey.

References

- Chorazy, T., Čáslavský, J., Žvaková, V., Raček, J., Hlavínek P. *Characteristics of Pyrolysis Oil as Renewable Source of Chemical Materials and Alternative Fuel from the Sewage Sludge Treatment*. Waste and Biomass Valorization, 2020. **11**(1): p. 4491–4505.
- Lira, H.N.F., Rangel, E.T., Suarez, P.A.Z. *Diesel-Like Fuels and Lubricating Grease Preparation from an Industrial Oily Waste*. Waste and Biomass Valorization, 2019. **9**(9): p. 2459–2470.
- Wang, K., Xu, Y., Duan, P., Wang, F., XianguXu, Z. *Thermo-chemical conversion of scrap tire waste to produce gasoline fuel*. Waste Management, 2019. **86**(1): p. 1–12.
- Berrueco, C., Esperanza, E., Mastral, F.J., García-Bacaicoa, P., Ceamanos, J. *Pyrolysis of waste tyres in an atmospheric static-bed batch reactor: Analysis of the gases obtained*. Journal of Analytical and Applied Pyrolysis, 2005. **74**(1): p. 245–253.
- Sathiskumara, C., Karthikeyan, S. *Recycling of waste tires and its energy storage application of by-products – a review*. Sustainable Materials and Technologies, 2019, **22**(1): p. 00125.
- Moulin, L., Bounaceur, S.D.S.A., Soudais, M.H.Y. *Assessment of Recovered Carbon Black Obtained by Waste Tires Steam Water Thermolysis: An Industrial Application*. Waste and Biomass Valorization, 2017. **8**(8): p. 2757–2770.
- Panda, A.K., Singh, R.K., Mishra, D.K. *Thermolysis of waste plastics to liquid fuel. A suitable method for plastic waste management and manufacture of value added products-A world prospective*. Renewable and Sustainable Energy Reviews, 2010. **74**(1): p. 233–248.
- Galvagno, S., Casciaro, G., Casu, S., Martino, M., Mingazzini, C., Russod, A., Portofino, S. *Steam gasification of tyre waste, poplar, and refuse-derived fuel: A comparative analysis*. Waste Management, 2009. **29**(2): p. 678–689.
- Sienkiewicz, M., Kucinska-Lipka, J., Janik, H., Balas, A. *Progress in used tyres management in the European Union: A review*. Waste Management, 2012. **32**(10): p. 1742–1751.
- Kyari, M., Cunliffe, A., Williams, P.T. *Characterization of oils, gases, and char in relation to the pyrolysis of different brands of scrap automotive tires*. Energy and Fuels, 2005. **19**(3): p. 1165–1173.
- Arabiourrutia, M., Lopez, G., Elordi, G., Olazar, M., Aguado, R., Bilbao, J. *Product distribution obtained in the pyrolysis of tyres in a conical spouted bed reactor*. Chemical Engineering Science, 2007. **62**(18): p. 5271–5275.
- Roy, C., Chaala, A., Darmstadt, H. *Vacuum pyrolysis of used tires end-uses for oil and carbon black products*. Journal of Analytical and Applied Pyrolysis, 1999. **51**(1): p. 201–221.
- Mohan, A., Dutta, S., Madav, V. *Characterization and upgradation of crude tire pyrolysis oil (CTPO) obtained from a rotating autoclave reactor*. Energy Conversion and Management, 2017. **250**(1): p. 339–351.
- Williams, P.T. *Pyrolysis of waste tyres: A review*. Waste Management, 2013. **33**(8): p. 1714–1728.
- Ayanoglu, A., Yumrutaş, R. *Production of gasoline and diesel like fuels from waste tire oil by using catalytic pyrolysis*. Energy, 2016. **103**(1): p. 456–468.
- Kebritchi, A., Firoozifar, H., Shams, K., Jalali-Arani, A. *Effect of pre-devulcanization and temperature on physical and chemical properties of waste tire pyrolytic oil residue*. Fuel, 2013. **112**(21): p. 319–325.
- Lopez, G., Olazar, M., Amutio, M., Aguado, R., Bilbao, J. *Influence of tire formulation on the products of continuous pyrolysis in a conical spouted bed reactor*. Energy and Fuels, 2009. **23**(11): p. 5423–5431.
- Ayanoglu, A., Yumrutaş, R. *Rotary kiln and batch pyrolysis of waste tire to produce gasoline and diesel like fuels*. Energy Conversion and Management, 2016. **111**(1): p. 261–270.
- Wang, W.C., Bai, C.J., Lin, C.T., Prakash, S. *Alternative fuel produced from thermal pyrolysis of waste tires and its use in a diesel engine*. Applied Thermal Engineering, 2016. **93**(1): p. 330–338.
- Martínez, J.D., Murillo, R., García, T., Veses, A. *Demonstration of the waste tire pyrolysis process on pilot scale in a continuous auger reactor*. Journal of Hazardous Materials, 2013. **261**(1): p. 637–645.
- Quek, A., Balasubramanian, R. *Liquefaction of waste tires by pyrolysis for oil and chemicals - A review*. Journal of Analytical and Applied Pyrolysis, 2013. **101**(1): p. 1–16.
- Ilkiliç, C., Aydin, H. *Fuel production from waste vehicle tires by catalytic pyrolysis and its application in a diesel engine*. Fuel Processing Technology, 2011. **92**(5): p. 1129–1135.
- Arpa, O., Yumrutaş, R., Demirbas, A. *Production of diesel-like fuel from waste engine oil by pyrolytic distillation*. Applied Energy, 2010. **87**(1): p. 122–127.
- Arpa, O., Yumrutaş, R., Argunhan, Z. *Experimental investigation of the effects of diesel-like fuel obtained from waste lubrication oil on engine performance and exhaust emission*. Fuel Processing Technology, 2010. **91**(10): p. 1241–1249.
- Singh, A.P., Mukherji, S., Tewari, A.K., Kalsi, W.R., Sarpal, A.S. *Determination of benzene and total aromatics in commercial gasolines using packed column GC and NMR techniques*. Fuel, 2003. **82**(1): p. 23–33.
- Atabani, A.E., Mekaoussi, M., Uguz, G., Arpa, O., Ayanoglu, A., Shobana, S. *Evaluation, characterization, and engine performance of complementary fuel blends of butanol–biodiesel–diesel from Aleurites moluccanus as potential alternative fuels for CI engines*. Energy and Environment, 2020. **31**(5): p. 755–784.
- Kushnarev, D.F., Afonina, T.V., Kalabin, G.A., Presnova, R. N., Bogdanova, N.I. *Investigation of the composition of crude oils and condensates from the south of the Siberian platform using ¹H and ¹³C NMR spectroscopy*. Petroleum Chemistry: USSR, 1989. **29**: p. 149–159.
- Mondal, S., Yadav, A., Kumar, R., Bansal, V., Das, S.K., Christopher, J., Kapur, G.S., *Molecular-Level Structural Insight into Clarified Oil by Nuclear Magnetic Resonance (NMR) Spectroscopy: Estimation of Hydrocarbon Types and Average Structural Parameters*. Energy and Fuels, 2017. **31**(7): p. 7682–7692.

29. Shen, Y., Shuai, S., Wang, J., Xiao, J. *Optimization of gasoline hydrocarbon compositions for reducing exhaust emissions*. Journal of Environmental Sciences, 2009. **21**(9): p 1208-1213.
30. Muhammad, A., Azeredo, R. B. V. *¹H NMR spectroscopy and low-field relaxometry for predicting viscosity and API gravity of Brazilian crude oils – A comparative study*. Fuel, 2014. **130**(9): p 126-134.
31. Poveda, J. C., Molina, D. R. *Average molecular parameters of heavy crude oils and their fractions using NMR spectroscopy*. Journal of Petroleum Science and Engineering, 2012. **84**(1): p 1-7.
32. Shimamoto, G.G., Tubino, M. *Alternative methods to quantify biodiesel in standard diesel-biodiesel blends and samples adulterated with vegetable oil through UV-Visible spectroscopy*. Fuel, 2016. **186**(1): p 199-203.
33. Zanier, A., Jäckle, H.W. *Heat capacity measurements of petroleum fuels by modulated DSC*. Thermochimica Acta, 1996. **287**(2): p 203–212.
34. Çakmak, A., Özcan, H. *Benzin İçin Oksijenli Yakıt Katkuları*. Journal of Polytechnic, 2018. **21**(4): p 831–840.
35. Taleb, D.A., Hamid, H.A., Deris, R.R.R., Zulkifli, M., Khalil, N.A., Yahaya, A.N.A. *Insights into pyrolysis of waste tire in fixed bed reactor: Thermal behavior*. Materials Today: Proceedings, 2020. **31**(1): p 178–186.
36. Islam, M. R., Haniu, H., Beg, M. R. A. *Liquid fuels and chemicals from pyrolysis of motorcycle tire waste: Product yields, compositions and related properties*. Fuel, 2008. **87**(13): p 3112–3122.
37. Williams, P.T., Besler, S., Taylor, D.T. *The pyrolysis of scrap automotive tyres. The influence of temperature and heating rate on product composition*. Fuel, 1990. **69**(12): p 1474–1482.
38. González, J.F., Encinar, J.M., Canito, J.L., Rodríguez, J.J. *Pyrolysis of automobile tyre waste. Influence of operating variables and kinetics study*. Journal of Analytical and Applied Pyrolysis, 2001. **58**(1): p 667–683.
39. Siddiqui, M.N. *Conversion of hazardous plastic wastes into useful chemical products*. Journal of Hazardous Materials, 2009. **167**(1-3): p 728–735.
40. Istadi, I., Buchori, L., Suherman, S. *Plastic Waste Conversion To Liquid Fuels Over Modified-Residual Catalytic Cracking Catalysts: Modeling and Optimization Using Hybrid Artificial Neural Network – Genetic Algorithm*. Reaktor, 2011. **13**(3): p 131-139.
41. Mangesh, V.L., Padmanabhan, S., Tamizhdurai, P., Ramesh, A. *Experimental investigation to identify the type of waste plastic pyrolysis oil suitable for conversion to diesel engine fuel*. Journal of Cleaner Production, 2020. **246**(1-2): p 119066.
42. Corro, G., Flores, A., Pacheco-Aguirre, F., Pal, U., Bañuelos, F., Ramirez, A., Zehe, A. *Biodiesel and fossil-fuel diesel soot oxidation activities of Ag/CeO₂ catalyst*. Fuel, 2020. **250**(1): p 17–26.
43. Burri, J., Crockett, R., Hany, R., Rentsch, D. *Gasoline composition determined by ¹H NMR spectroscopy*. Fuel, 2004. **83**(2): p 187–193.
44. Rakhmatullin, I.Z., Efimov, S.V., Tyurin, V.A., Al-Muntaser, A.A., Klimovitskii, A.E., Varfolomeev, M.A., Klochkov, V.V. *Application of high resolution NMR (¹H and ¹³C) and FTIR spectroscopy for characterization of light and heavy crude oils*. Journal of Petroleum Science and Engineering. 2018. **168**(1): p 256–262.
45. Mohammed, M., Atabani, A., Uguz, G., Lay, C., Kumar, G., Al-Samaraae, R. *Characterization of Hemp (Cannabis sativa L.) Biodiesel Blends with Euro Diesel, Butanol and Diethyl Ether Using FT-IR, UV-Vis, TGA and DSC Techniques*. Waste and Biomass Valorization, 2020. **11**(1): p 1097-1113.



Research Article

Mathematical modeling and production of semi-active hand prosthesis from clear resin

Mehmet Kayrıci ^a , Yusuf Uzun ^{b,*} , Onur Gök ^c  and Hüseyin Arıkan ^a 

^aDepartment of Mechanical Engineering, Faculty of Seydisehir Ahmet Cengiz Engineering, Necmettin Erbakan University, Konya 42370, Turkey

^bDepartment of Computer Engineering, Faculty of Seydisehir Ahmet Cengiz Engineering, Necmettin Erbakan University, Konya 42370, Turkey

^cDepartment of Machinery and Metal Technologies, Seydişehir Vocational School, Necmettin Erbakan University, Konya 42370, Turkey

ARTICLE INFO

Article history:

Received 30 November 2020

Revised 25 February 2021

Accepted 13 April 2021

Keywords:

Finite element method

Hand prosthesis

Kinematic

Kinetic

ABSTRACT

In this study, the static, kinematic and dynamic behaviors of a semi-active hand prosthesis were analyzed numerically. Finite Elements method was used in static analysis and analytical method was used in kinematic and dynamic analysis. The mathematical model of the hand was created in kinematic and dynamic analysis. Using the mathematical model obtained, torque values of 0, 15, 30, 45, 60, 75, 90 degrees were calculated according to the different position angles of the fingers. Examination was performed for 4 fingers (index finger, middle finger, ring finger, little finger) and 5 kg of force was applied to the fingertips perpendicular to the finger plane. In this examination, the forces are divided into 25% for the index finger, 35% for the middle finger, 25% for the ring finger and 15% for the little finger. The results obtained for forces at different angles under the specified conditions were explained. As a result of all these stages, the prosthetic hand was designed. The design was calculated as linear statically by the finite element method. As a result of the study, a semi-active prosthetic hand was produced considering the calculation findings. Clear resin was used as material.

© 2021, Advanced Researches and Engineering Journal (IAREJ) and the Author(s).

1. Introduction

Biomechanics is a discipline that examines the internal and external interactions of systems designed using engineering principles [1]. Today, biomechanics has gained great importance with the development of engineering science. Thanks to the rapid developments in technology, many applications have been developed in this area. Although the limb has a complex structure, it is possible for a prosthetic hand to approach the mobility of the real hand limb with the use of developing technology [2]. Bionic limbs are vital for people with limb loss. Hand limbs are very important for the individual's sensitivity in environmental interaction. Loss of the upper limb causes physical and psychological impairment in the life of an amputated person. Studies show that 67% of upper extremity losses are male and in the fertile age range of 16-

54. However, it has emerged that 35% of them do not use the prostheses they have [3]. Poulliquen et al. suggested that the problem of lack and difficulty of use caused by psychological or lack of appearance and functionality can be solved by cosmetic improvement, comprehension, and high controllability [4]. Kerpa et al. in order to realize human-robot cooperation in housework, they worked on a robot arm that can be controlled by physiological sensors and sometimes manually [5]. Butz et al. performed the stress model in the finger joints for activities such as writing on the keyboard, playing the piano, holding a pencil, carrying weight and opening a jar [6]. Undesired limb losses for any reason not only affect the minimum quality of life of people in their daily life, but also cause a great devastation in human psychology [7, 8]. The most important reason for this is that the human hand is both a sense organ and one of the most important limbs that help

* Corresponding author. Tel.: +90-332-582-6000.

E-mail addresses: mkayranci@erbakan.edu.tr (M. Kayrıci), yuzun@erbakan.edu.tr (Y. Uzun), ogok@erbakan.edu.tr (O. Gök),

harikan@erbakan.edu.tr (H. Arıkan)

ORCID: 0000-0003-1178-5168 (M. Kayrıci), 0000-0002-7061-8784 (Y. Uzun), 0000-0003-1160-1963 (O. Gök), 0000-0003-1266-4982 (H. Arıkan)

DOI: 10.35860/iarej.833538

This article is licensed under the CC BY-NC 4.0 International License (<https://creativecommons.org/licenses/by-nc/4.0/>).

us meet our minimum life needs. Loss of the limb inevitably impedes the individual's freedom of movement [9]. Today, approaching the functionality of the real human hand with mechanical, cosmetic, electronic and control mechanisms will be possible with interdisciplinary studies.

A wide range of technologies should be considered when designing and developing a prosthetic hand. In the design, not only the idea of facilitating human life, but also factors such as mental health of people, ability to grasp objects well, adaptation of the material to the body, ability to act independently, movement speed and grasping should be taken into consideration [10]. Butz et al. used a two-dimensional geometry method to determine the resulting joint and tendon forces of the hand in their model designed for the analysis of finger forces. Since the static force analysis resulted in an uncertain system, the method developed by Weightman and Amis (1982) [11] was used with the assumption that force ratios at tendon junctions are scaled proportionally to cross-sectional areas [6]. It should be well known that all bone, muscle and tendon structures of the human hand add realistic features to the limb. Atasoy et al. studied the mechanical structure of the index finger [12]. The human hand has 24 degrees of freedom kinematically. The grasping movement of the hand structure is performed by tendons attached to joints and nerves that stimulate the hand muscles [13]. Prosthetic hands such as Otto Bock 6 or VASI 7-11 are devices that hold two fingers opposite a thumb. Prosthetic hands designed in this way have some limitations. Since they are limited to opening and closing movements within a single degree of freedom, they have a limited mechanical function [7]. It appears that a large number of prosthetic hands have been developed in recent years [14]. To design a good hand limb, this limb must first be modeled mathematically [15]. Despite the complexity of the human hand, it is possible to model the finger joints kinematically [16]. Cobos et al. made some studies on hand kinematics and obtained some equations as a result of these studies [17]. Ryew and Choi designed a kinematically 2 degree of freedom joint design [18]. Zhe Xu and Emanuel Todorov designed a 3D hand design at Washington University and produced a hand functionally very close to the finger limbs [19]. José Alfredo Leal-Naranjo et al. analyzed the 3-arm hand structure (thumb, index finger, middle finger) statically and dynamically using the finite element method [20]. Gregor Harih et al. examined the finger model in the 3-dimensional finite element method and as a result found the contact force of the finger limb. Recently, studies on how to use the finite element method in mechanical design in biomedical field have been started [21]. Antoanela N. et al., by examining the bone structure of the finger limb using the finite element method, concluded that using experimental and numerical studies together is effective in

understanding the behavior of the limb [22].

The main purpose of this study is to model the human hand dynamically according to physical bases, to explain the system mathematically with certain variables and to produce an optimized hand model according to these findings. To achieve this, a mathematical model of a finger limb must be kinematically constructed. The static loads on the pin elements were calculated by examining the hand model with the linear static method using the finite element method and the prosthesis was designed in a healthier way. Another aim of this study is to reduce the raw material cost in manual production. Cost is a very important factor in prosthetic hand production.

2. Material and Method

2.1 Equipment and materials

Solidworks software was used to create the CAD model of the prosthetic hand. The CAD geometry of the finger limb to be analyzed statically with this CAD program has been made as a solid design. After static analysis and finite element mathematical modeling, Cosmos Works software was used to perform linear static analysis. A Formlab Form2 3D printer model was used to produce a prosthetic hand. The technical features of the 3D printer used were shown in Table 1. The printer used was provided by 3D fab.

The thickness was chosen as 25 microns for a total production time of 12 hours. Finger models produced were invested in alcohol. In accordance with the recommendation of the resin and the printer manufacturer, the models, which were rigid with alcohol, were then cured by exposure to ultraviolet light. The CAD geometry obtained from the SolidWorks software was converted to STL format and produced with a prosthetic hand printer. Clear resin material is used as printing material. The mechanical properties of the material used were shown in Table 2. The clear resin material used was provided by the 3bfab company.

Table 1. 3D printer features used

Attributes	Values
Dimensions	35x33x52 cm
Operation Temperature	35 °C maximum
Power Requirements	100–240 V, 2A 50/60 hz, 65W
Laser Properties	EN 60825-1, 405nm, 250W
Technology	Stereolithography (SLA)
Print Area	14.5 × 14.5 × 17.5 cm
Layer Thickness	25, 50, 100, 200 microns

Table 2. Mechanical properties of celar resin used

Attributes	Values
Type of material	Clear resin
Tensile Strength	65 MPa
Young's Modulus	2.8 GPa
Heat Deflection Temperature	0.45 MPa, 289 °C

The material used in the tendon design was supplied from the UK Open Bionics company. Mechanical properties of the material were given in Table 3.

The spring material and mechanical properties placed on the joints to provide the opening mechanism of the hand mechanism were shown in Table 4. These springs were supplied by Sakarya Yay Mak.

A total of 5 linear motors were used for the finger controls of the prosthetic hand. Motor selections were provided by Open Bionics company based on dynamic calculation results. The mechanical properties of the supplied motors were given in Table 5.

Schematic representation of the materials used in the prosthesis was shown in Figure 1. The hand prosthesis, which grips with the motion of tendon and linear motors, was opened with the tension force of the springs.

2.2 Kinematic and dynamic analysis

The human hand anatomically has 8 carpal bones, 5 metacarpal bones and 14 phalanges bones [22]. There are 14 joints that connect the phalanges bone group and provide the planar movement of the fingers. These joints are marked in red in Figure 2.

In this study, the mathematical model of the index, middle, ring and little finger in kinematic and dynamic terms is obtained by assuming that the motion is planar. Kinematic and dynamic mathematical modeling was done by analytical method.

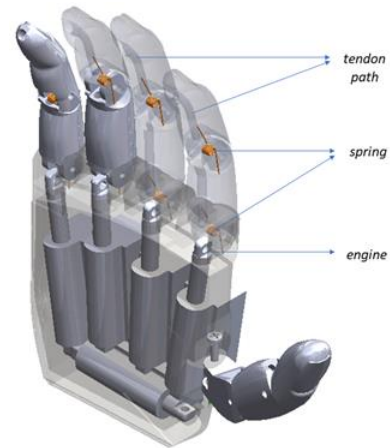


Figure 1. Schematic representation of the materials used on the prosthesis

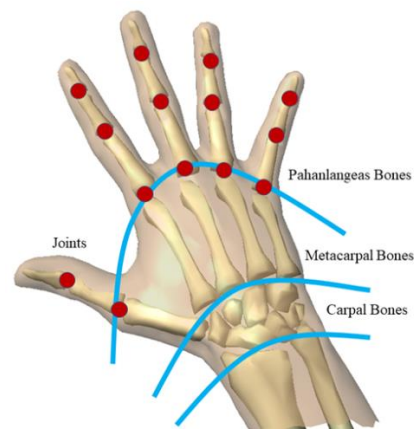


Figure 2. Anatomical hand structure [15]

Table 3. Mechanical properties of tendon material

Attributes	Values
Maximum tensile load	45.35 kg
Tendon diameter	0.75 mm

Table 4. Mechanical properties of spring material

Attributes	Values
Type of material	Stainless Steel
Spring Diameter	0.9 mm
Winding Number	6
Spring inner diameter	2.1 mm
Spring span	180 degrees
k stiffness value	163 N / mm

Table 5. Mechanical properties of motors.

Attributes	Values
Gearing Option	63:1
Peak Power Point	30 N; 8 mm/s
Peak Efficiency Point	12 N; 12 mm/s
Max Speed (no load)	15 mm/s
Max Force (lifted)	45 N
Max Side Load	10 N
Back Drive Load	25 N
Stroke	20 mm

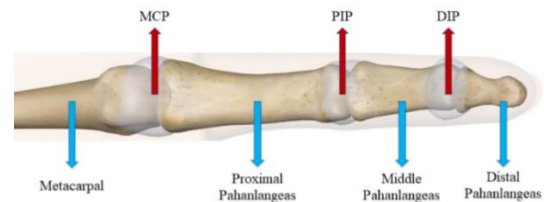


Figure 3. Anatomical finger structure [26]

There are 3 joints in the bones of the phalanges group in human anatomy (except the thumb). As shown in Figure 3, these are the MCP joint connecting the metacarpal to the proximal phalangeal, the PIP joint connecting the proximal phalangeal to the middle phalangeal, and the DIP joint connecting the middle phalanges to the distal phalanges [24, 25].

In the study, kinematic equations of a finger were obtained first and the working range was determined. To create the kinematic model of the hand, the equations of motion of the finger model must be obtained. Finger anatomy consists of cylindrical and spherical structures. DIP, PIP and MCP connections can be thought of as a single degree of freedom rotary connection. The assumptions made on the finger model in the kinematic analysis were shown in Figure 4.

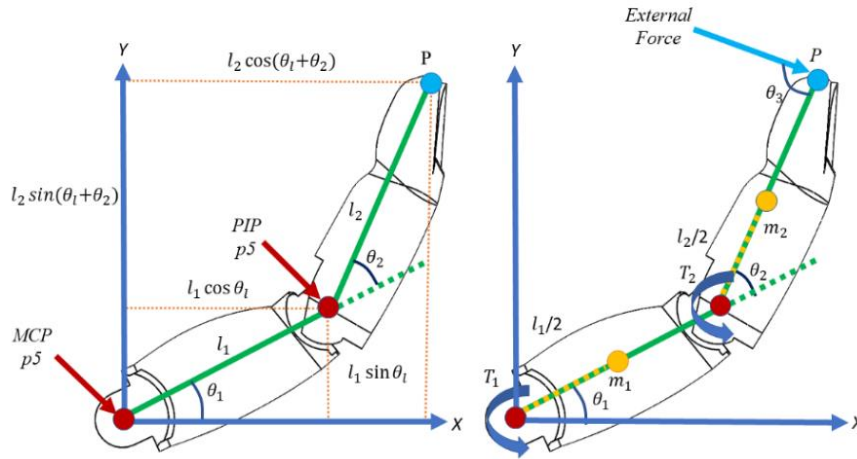


Figure 4. Kinematic and dynamic finger model

In the finger model in the figure, the MCP joint was accepted at the origin point, while the DIP joint was accepted as the fixed limb. Where, l_1 and l_2 are the lengths of the finger limbs of the kinematic finger model. The P denotes the position at the end point of the kinematic finger model. In space, an object has six degrees of freedom. If the degree of freedom in space was expressed by the formula, it is possible to express it as shown in Equation (1).

$$W = 6n - 5p5 - 4p4 - 3p3 \quad (1)$$

In Equation (1), W represents the degree of freedom, n is the number of mobile limbs, $p5$ is one degree of freedom, $p4$ is two degrees of freedom, and $p3$ is three degrees of freedom, the moving limbs. The two-dimensional degree of freedom in the plane is as expressed in Equation (2).

$$W = 3n - 2p5 - p4 \quad (2)$$

The finger model in Figure 4 is a two degree of freedom mechanism. In Equation (3), Denavit-Hartenberg method was used to express P position kinematically. For the two-limb finger model in Figure 4, this equation can be written as Equation (A1) in Appendix. In the three-jointed finger model, the transformation matrices for all joints can be extracted as specified in Appendix with Equations (A2), (A3), (A4).

$${}^0_N T = {}^0_1 T {}^1_2 T {}^2_3 T \dots {}^{N-1}_N T \quad (3)$$

From these equations, P_x and P_y positions specified in Equation (4) was obtained.

$$\begin{aligned} P_x &= l_1 \cos \theta_1 + l_2 \cos (\theta_1 + \theta_2) \\ P_y &= l_1 \sin \theta_1 + l_2 \sin (\theta_1 + \theta_2) \end{aligned} \quad (4)$$

For dynamic analysis modeling boundary conditions, internal and external forces were determined. Internal forces are masses of the finger limb. External force is the $F_{external}$ force applied separately for each finger limb. These boundary conditions were given in Table 6.

Table 6. Finger physical sizes

Fingers	m_1	m_2	$F_{external}$	l_1	l_2
Index finger	0.005	0.004	12.5N	0.037m	0.040m
Middle finger	0.006	0.005	17.5N	0.042m	0.046m
Ring Finger	0.006	0.004	12.5N	0.039m	0.033m
Little finger	0.003	0.003	7.5N	0.040m	0.035m

For the dynamic analysis, the mass center positions of the finger limbs were found with Equations (5) and (6). Afterwards, the speeds of these positions for the kinetic energy calculation were found by Equation (7) and (8).

$$\begin{bmatrix} x_1 \\ y_1 \end{bmatrix} = \begin{bmatrix} \frac{l_1}{2} \cos \theta_1 \\ \frac{l_1}{2} \sin \theta_1 \end{bmatrix} \quad (5)$$

$$\begin{bmatrix} x_2 \\ y_2 \end{bmatrix} = \begin{bmatrix} l_1 \cos \theta_1 + \frac{l_2}{2} \cos (\theta_1 + \theta_2) \\ l_1 \sin \theta_1 + \frac{l_2}{2} \sin (\theta_1 + \theta_2) \end{bmatrix} \quad (6)$$

$$\begin{bmatrix} \dot{x}_1 \\ \dot{y}_1 \end{bmatrix} = \begin{bmatrix} -\frac{l_1}{2} \sin \theta_1 \dot{\theta}_1 \\ \frac{l_1}{2} \cos \theta_1 \dot{\theta}_1 \end{bmatrix} \quad (7)$$

$$\begin{bmatrix} \dot{x}_2 \\ \dot{y}_2 \end{bmatrix} = \begin{bmatrix} -l_1 \sin \theta_1 \dot{\theta}_1 - \frac{l_2}{2} (\dot{\theta}_1 + \dot{\theta}_2) \sin (\theta_1 + \theta_2) \\ l_1 \cos \theta_1 \dot{\theta}_1 + \frac{l_2}{2} (\dot{\theta}_1 + \dot{\theta}_2) \cos (\theta_1 + \theta_2) \end{bmatrix} \quad (8)$$

After these calculations, the total kinetic energy formula Equation (A5) was obtained. After calculating potential energy with Equation (A6), $T_{internal1}$ and $T_{internal2}$ equation sets specified in Equations (A8) and (A9) for the finger limb under the influence of internal forces were found by using the Lagrange equation specified by Equation (A7). Finally, the torque values under the influence of internal and external forces were obtained using T_{total1} and T_{total2} Equation (A10).

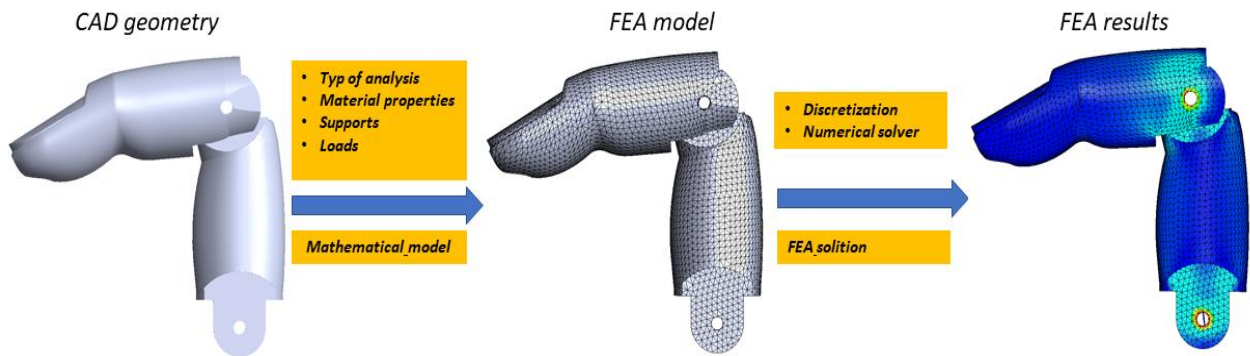


Figure 5. Static analysis processes

With these mathematical equations obtained, torque values for different angle positions (for 0, 15, 30, 45, 60, 75 degrees) were calculated separately for the index, middle, ring and little finger.

2.2 Static analysis

After kinematic and dynamic analysis, finger limb was statically analyzed by finite element method. Solidworks simulation finite element package program was used for this study. Analysis modeling was done with linear static analysis acceptance. It is assumed that displacement against the load is linear.

This is because the part up to plastic deformation is to be examined. It is important for the stress values and distribution in the structure of the finger limb that remains under force. Firstly, CAD geometry was created for static analysis. A mathematical model was created from the CAD geometry created afterwards. Resin material, linear elastic isotropically, the mechanical properties of the material were introduced to the package program, and the degree of freedom limitations and forces were applied. After these steps, the analysis was run and the results shown in Figure 5 were obtained.

For degree of freedom limitations, zero degrees of freedom are defined on the hinge surfaces at the bottom of the finger model and these surfaces are built-in support. 1.25 kg load is made and shown as a force perpendicular to the finger surface. In Figure 6, the Tet element is used as the mathematical model. The mathematical model used is 10 nodes for each element. In the Solidworks simulation program, the most sensitive solution network was created with 10-node element structure. The total number of nets used is 162139. The percentage of the item with an aspect ratio of less than 3 is 99.5%. Solid mesh is used as the mesh type. The real pin element is not used in the analysis model. This is to reduce the number of contacts and networks. The pin element has been defined by the program. Contact surfaces are defined between parts. No penetration contact type has been defined for these contact surfaces and the parts are prevented from intermingling. Since the reaction forces between the contact surfaces are an important factor for the stress values that will occur in the finger model, this contact

definition has been made.

3. Results and Discussion

In the study, a single degree of freedom rotary connection type defined as P5 was used for finger connections by reducing the finger movement to planar dimension. The prosthetic hand and movement functions produced were given in Figures 7 and 8.

Thus, kinematic and dynamic analyzes of the fingers were made under different boundary conditions. The torque values calculated according to the angles and forces of the index finger were shown in Table 7.

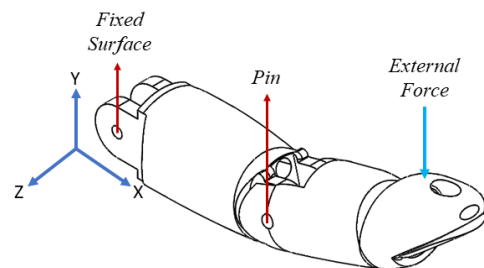


Figure 6. Boundary conditions applied for static analysis



Figure 7. Images of the produced prosthetic hand in the open position

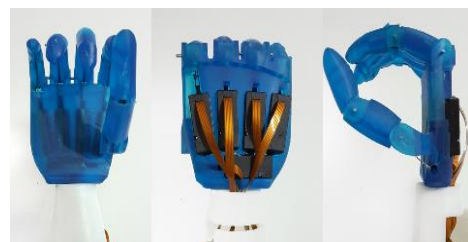


Figure 8. Images of produced prosthetic hand in closed position

Table 7. Torque values calculated for index finger

θ_1	θ_2	θ_3	F_{dis}	T_{total1}	T_{total2}
0°	0°	90°	12,5N	0,982Nm	0,512Nm
15°	15°	90°	12,5N	0,966Nm	0,508Nm
30°	30°	90°	12,5N	0,919Nm	0,496Nm
45°	45°	90°	12,5N	0,844Nm	0,476Nm
60°	60°	90°	12,5N	0,747Nm	0,449Nm
75°	75°	90°	12,5N	0,634Nm	0,416Nm
90°	90°	90°	12,5N	0,512Nm	0,377Nm

Torque values calculated according to angles and forces of the middle finger was shown in Table 8. Torque values calculated according to angles and forces of the ring finger was shown in Table 9. Torque values calculated according to angles and forces of the little finger was shown in Table 10.

The torque forces to the MCP and PIP joints are graphically explained in Figure 9. Maximum torque values were obtained at the middle finger. Minimum torque values were observed on the little finger. The torque values of index and ring fingers were close to each other for all boundary conditions.

Table 8. Torque values calculated for middle finger

θ_1	θ_2	θ_3	F_{dis}	T_{total1}	T_{total2}
0°	0	90°	17,5N	1,564Nm	0,820Nm
15°	15°	90°	17,5N	1,538Nm	0,814Nm
30°	30°	90°	17,5N	1,464Nm	0,795Nm
45°	45°	90°	17,5N	1,346Nm	0,764Nm
60°	60°	90°	17,5N	1,191Nm	0,721Nm
75°	75°	90°	17,5N	1,012Nm	0,669Nm
90°	90°	90°	17,5N	0,820Nm	0,607Nm

Table 9. Torque values calculated for the ring finger

θ_1	θ_2	θ_3	F_{dis}	T_{total1}	T_{total2}
0°	0	90°	12,5N	1,004Nm	0,510Nm
15°	15°	90°	12,5N	0,987Nm	0,506Nm
30°	30°	90°	12,5N	0,938Nm	0,483Nm
45°	45°	90°	12,5N	0,859Nm	0,472Nm
60°	60°	90°	12,5N	0,757Nm	0,444Nm
75°	75°	90°	12,5N	0,638Nm	0,408Nm
90°	90°	90°	12,5N	0,510Nm	0,366Nm

Table 10. Torque values calculated for the little finger

θ_1	θ_2	θ_3	F_{dis}	T_{total1}	T_{total2}
0°	0	90°	7,5N	0,522Nm	0,268Nm
15°	15°	90°	7,5N	0,513Nm	0,266Nm
30°	30°	90°	7,5N	0,488Nm	0,260Nm
45°	45°	90°	7,5N	0,448Nm	0,249Nm
60°	60°	90°	7,5N	0,395Nm	0,235Nm
75°	75°	90°	7,5N	0,331Nm	0,217Nm
90°	90°	90°	7,5N	0,268Nm	0,195Nm

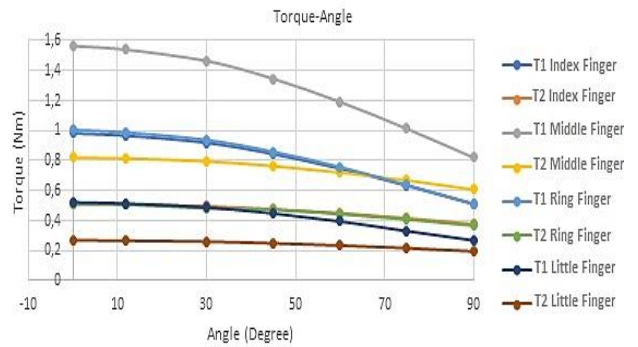


Figure 9. T1 and T2 graphics according to the position angles of the fingers

In the static analysis of the study, the maximum stress values were obtained in the joint region according to the vonmises error criteria and the results are shown in Figures 10, 11, 12, 13, 14, 15 and 16, respectively.

As seen in Figure 17, this value in the joint region ranges from 35 MPa to 18 MPa. These values are the nodal stress values.

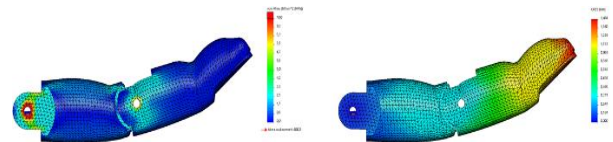


Figure 10. Stress and displacement graph for $\theta_1 = 0^\circ$ and $\theta_2 = 0^\circ$ configurations

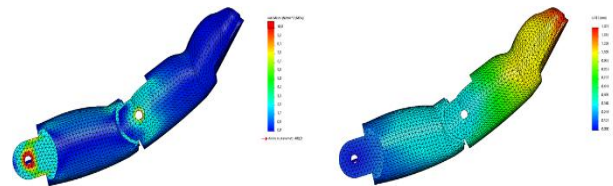


Figure 11. Stress and displacement graph for $\theta_1 = 15^\circ$ and $\theta_2 = 15^\circ$ configurations

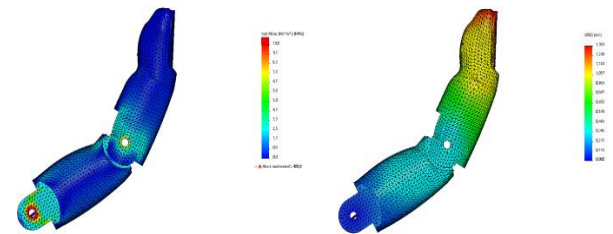


Figure 12. Stress and displacement graph for $\theta_1 = 30^\circ$ and $\theta_2 = 30^\circ$ configurations

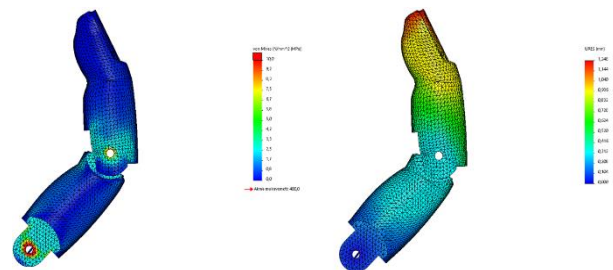


Figure 13. Stress and displacement graph for $\theta_1 = 45^\circ$ and $\theta_2 = 45^\circ$ configurations

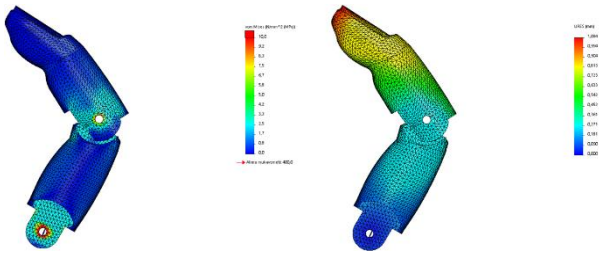


Figure 14. Stress and displacement graph for $\theta_1 = 60^\circ$ and $\theta_2 = 60^\circ$ configurations

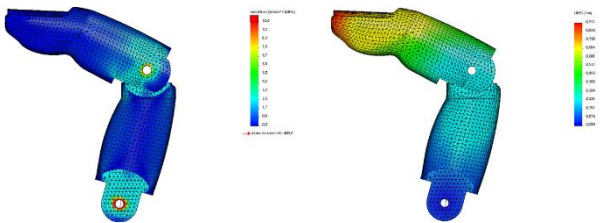


Figure 15. Stress and displacement graph for $\theta_1 = 75^\circ$ and $\theta_2 = 75^\circ$ configurations

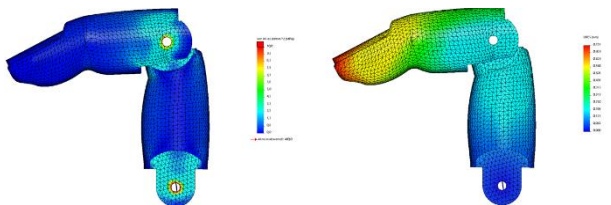


Figure 16. Stress and displacement graph for $\theta_1 = 90^\circ$ and $\theta_2 = 90^\circ$ configurations

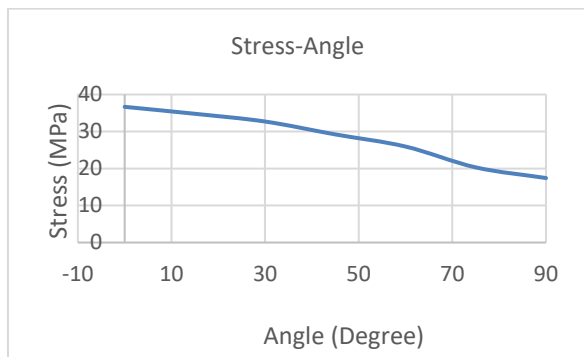


Figure 17. Stress graph according to the position angles of the index finger

The displacement values were calculated between 1.473 mm and 0.751. The graphic of the displacement of the index finger relative to the angle of change specified in the range of Figures 8 and 14 was shown in Figure 18.



Figure 18. Displacement graph according to the position angles of the index finger

Special silicone hands were prepared to have a realistic appearance after 3D scanning and editing. Human skin color, hair and nail details were taken into consideration in the production of silicone covers. When the products on the market were examined, there are two types of silicone sleeves. The first of these is the silicone used in prosthetic hands. Silicone hands were passed over the prosthesis, both closing the mechanical image of the prosthesis and creating a realistic image by working with it. The second is passive silicone hand coating. They were used only for display purposes and the wall thickness is quite high. In this study, both silicone hands were studied in the prosthesis. Both silicone hands can be used on the go, as the design is unique. However, the project continued with other silicone gloves, as it was seen that the motors consume too much power for passive silicone gloves with high wall thickness.

4. Conclusion

The prosthetic hand was produced and assembled on a 3D printer using clear resin. The production took about 7 hours, and the production and quality control of the whole process was provided for around 20 hours together with the assembly and trials. Production was made with extremely low costs in terms of cost. As shown in Figures 7 and 8, the prosthetic hand was tested on an amputated person using a silicon sheath. Glass holding position was studied during the trial. Finger speed settings were calibrated in the trials, and thumb movement was provided manually by the person. As a result of the trials, the hand held the glass normally and let it go. This prosthetic hand provided the amputee's cosmetic, appearance and control sensitivity that did not attract much attention in the society and positively affected the person.

In our future studies, we hope to do studies with electromyography or a completely neural network.

Declaration

The author(s) declared no potential conflicts of interest with respect to the research, authorship, and/or publication of this article. The author(s) also declared that this article is original, was prepared in accordance with international publication and research ethics, and ethical committee permission or any special permission is not required.

Author Contributions

M. Kayrıci prepared experimental setup. Y. Uzun contributed to data collection phase and wrote the manuscript. O. Gök performed the analysis and mathematical modelling. H. Arıkan made proofreading of manuscript.

Acknowledgment

This study was supported by the Scientific Research Projects Coordination Unit of Necmettin Erbakan University [Grant No: 161731002].

References

1. Gürgül, S., Uzun, C., and Erdal, N., *Kemik biyomekanigi*. Gaziosmanpaşa Üniversitesi Tıp Fakültesi Dergisi, 2016. **8**(1): p. 18-34.
2. Naranjo, J., Miguel, C., Romero, M., and Saez L., *Structural numerical analysis of a three fingers prosthetic hand prototype*. International Journal of Physical Sciences, 2013. **8**(13): p. 526-536.
3. Clement, R.G., Bugler, K.E., and Oliver, C.W., *Bionic prosthetic hands: A review of present technology and future aspirations*. Surgeon, 2011. **9**(6): p. 336-340.
4. Poulighen, M., Bernard, A., Marsot, J., and Chodorge, L., *Virtual Hands And Virtual Reality Multimodal Platform To Design Safer Industrial Systems*. Computers in Industry, 2007. **58**(1): p. 46-56.
5. Kerpa, O., Osswald, D., Yigit, S., Burghart, C., and Woern, H., *Arm-hand control by tactile sensing for human robot co-operation*. Proc.Humanoids'2003, **1**(1): p. 1-12.
6. Butz, K.D., Merrell, G., and Nauman, E.A., *A biomechanical analysis of finger joint forces and stresses developed during common daily activities*. Computer Methods in Biomechanics and Biomedical Engineering, 2012. **15**(2): p. 131-140.
7. Dechev, N., Cleghorn, W.L., and Naumann, S., *Multiple finger, passive adaptive grasp prosthetic hand*. Mechanism and Machine Theory, 2001. **36**(10): p. 1157-1173.
8. El Kady, A.M., Mahfouz, A.E., and Taher, M.F., *Mechanical design of an anthropomorphic prosthetic hand for shape memory alloy actuation*. In: 2010 5th Cairo International Biomedical Engineering Conference, CIBEC 2010, 2010. p. 1157-1173.
9. Kuran, B., *El rehabilitasyonu*. 1995, Nobel Tıp Kitapları.
10. Durand, R., Pantoja-Rosero, B., and Oliveria, V., *A general mesh smoothing method for finite elements*. Finite Elements in Analysis and Design, 2019. **158**(1): p. 17-30.
11. Weightman, B., and Amis, A.A., *Finger joint force predictions related to design of joint replacements*. J Biomed Eng., 1982. **4**(3): p. 197-205
12. Atasoy, A., Kuchimov, S., Toptas, E., Kaplanoglu, E., Takka, S., and Ozkan, M., *Finger design for anthropomorphic prosthetic hands*. 2014 18th National Biomedical Engineering Meeting, BIYOMUT 2014, 2015. p. 1-3.
13. Özkan, S.S., Karayel, D., Atalı, G., and Gökbayrak, I., *Esnek Algılayıcı Kontrollü Robot El Tasarımı ve Gerçeklenmesi*. Academic Platform Journal of Engineering and Science, 2017. p. 35-40.
14. Carozza, M.C., Cappiello, G., Stellin, G., Zacccone, F., Vecchi, F., Micera, S., and Dario, P., *On the development of a novel adaptive prosthetic hand with compliant joints: experimental platform and emg control*. 2005 IEEE/RSJ International Conference on Intelligent Robots and Systems, 2005. p. 1271-1276.
15. Anatomical hand structure. [cited 2020 29 Nov]; Available from: <http://pulpbits.net/4-human-skeleton-hand-diagrams/animation-of-skeleton-hands>.
16. Lin, J., Wu, Y., and Huang, T.S., *Modeling the constraints of human hand motion*. Proceedings, Workshop on Human Motion, HUMO, 2000. **7**(2): p. 121-126.
17. Cobos, S., Ferre, M. and Sánchez-Urán, M.A., Ortego, J., and Peña, C., *Efficient human hand kinematics for manipulation tasks*. In: 2008 IEEE/RSJ International Conference on Intelligent Robots and Systems, IROS, 2008. **8**(3): p. 2246-2251.
18. Ryew, S., and Choi, H., *Double active universal joint (dauj): Robotic joint mechanism for humanlike motions*. IEEE Transactions on Robotics and Automation, 2001. **17**(2): p. 290-300.
19. Xu, Z., and Todorov, E., *Design of a highly biomimetic anthropomorphic robotic hand towards artificial limb regeneration*. Proceedings - IEEE International Conference on Robotics and Automation, 2016. **12**(2): p. 3485-3492.
20. Joseacute, A.L.N., Christopher, R.T.S.M., Manuel, F.C.R., and Ez Luis, M.N.S., *Structural numerical analysis of a three fingers prosthetic hand prototype*. International Journal of Physical Sciences, 2013. **8**(3): p. 526-536.
21. Harih, G., Tada, M., and Dolšak, B., *Justification for a 2d versus 3d fingertip finite element model during static contact simulations*. Computer Methods in Biomechanics and Biomedical Engineering, 2016. **19**(3): p. 1409-1417.
22. Antoanela, N., Ardelean, D., and Srl, T., *The application of the finite element method in the biomechanics of the human upper limb and of some prosthetic components*. WSEAS Transactions on Computers, 2009. **8**(2): p. 1296-1305.
23. Gray, H., Warwick, R., and Williams, P.L., *Gray's Anatomy*. 1973, 35 ed., Longman.
24. Kouchi, M., and Tada, M., *Digital Hand: Interface Between the Robot Hand and Human Hand*. Human Inspired Dexterity in Robotic Manipulation, Academic Press, 2018. **11**(3): p. 11-26.
25. Vishwakarma, P., and Sharma, A., *3d finite element analysis of milling process for non-ferrous metal using deform-3d*. Materials Today, Proceedings, 2019. **26**(2): p. 2726-2733.
26. Anatomic finger structure. [cited 2020 29 Nov]; Available from: <https://en.wikipedia.org/wiki/Thumb>. Web. 29 Nov 2020.

Appendix

$${}^i-1T_i = \begin{bmatrix} \cos \theta_i & -\sin \theta_i & 0 & a_{i-1} \\ \sin \theta_i \cos \alpha_{i-1} & \cos \theta_i \cos \alpha_{i-1} & -\sin \alpha_{i-1} & -\sin \alpha_{i-1} d_1 \\ \sin \theta_i \sin \alpha_{i-1} & \cos \theta_i \sin \alpha_{i-1} & \cos \alpha_{i-1} & \cos \alpha_{i-1} d_1 \\ 0 & 0 & 0 & 1 \end{bmatrix} \tag{A1}$$

For the 1st joint, ($i=1$), ${}^{i-1}T_i = {}^{1-1}T_1 = {}^0T_1$

$${}^0T_1 = \begin{bmatrix} \cos \theta_1 & -\sin \theta_1 & 0 & a_0 \\ \sin \theta_1 \cos \alpha_0 & \cos \theta_1 \sin \alpha_0 & -\sin \alpha_0 & -\sin \alpha_0 d_1 \\ \sin \theta_1 \sin \alpha_0 & \cos \theta_1 \sin \alpha_0 & \cos \alpha_{1-1} & \cos \alpha_0 d_1 \\ 0 & 0 & 0 & 1 \end{bmatrix} = \begin{bmatrix} \cos \theta_1 & -\sin \theta_1 & 0 & 0 \\ \sin \theta_1 & \cos \theta_1 & 0 & 0 \\ 0 & 0 & 1 & 0 \\ 0 & 0 & 0 & 1 \end{bmatrix} \tag{A2}$$

For the 2nd joint, ($i=2$), ${}^{i-1}T_i = {}^{2-1}T_2 = {}^1T_2$,

$${}^1T_2 = \begin{bmatrix} \cos \theta_2 & -\sin \theta_2 & 0 & a_{2-1} \\ \sin \theta_2 \cos \alpha_{2-1} & \cos \theta_2 \cos \alpha_{2-1} & -\sin \alpha_{2-1} & -\sin \alpha_{2-1} d_2 \\ \sin \theta_2 \sin \alpha_{2-1} & \cos \theta_2 \cos \alpha_{2-1} & \cos \alpha_{2-1} & \cos \alpha_{2-1} d_2 \\ 0 & 0 & 0 & 1 \end{bmatrix} = \begin{bmatrix} \cos \theta_2 & -\sin \theta_2 & 0 & l_1 \\ \sin \theta_2 & \cos \theta_2 & 0 & 0 \\ 0 & 0 & 1 & 0 \\ 0 & 0 & 0 & 1 \end{bmatrix} \tag{A3}$$

For the 3rd joint, ($i=3$), ${}^{i-1}T_i = {}^{3-1}T_3 = {}^2T_3$

$${}^2T_3 = \begin{bmatrix} \cos \theta_3 & -\sin \theta_3 & 0 & a_{3-1} \\ \sin \theta_3 \cos \alpha_{3-1} & \cos \theta_3 \sin \alpha_3 & -\sin \alpha_{3-1} & -\sin \alpha_{3-1} d_3 \\ \sin \theta_3 \sin \alpha_{3-1} & \cos \theta_3 \sin \alpha_3 & \cos \alpha_{3-1} & \cos \alpha_{3-1} d_3 \\ 0 & 0 & 0 & 1 \end{bmatrix} = \begin{bmatrix} 1 & 0 & 0 & l_2 \\ 0 & 1 & 0 & 0 \\ 0 & 0 & 1 & 0 \\ 0 & 0 & 0 & 1 \end{bmatrix}$$

${}^0T_3 = {}^0T_1 {}^1T_2 {}^2T_3$

$${}^0T_3 = \begin{bmatrix} \cos \theta_1 & -\sin \theta_1 & 0 & 0 \\ \sin \theta_1 & \cos \theta_1 & 0 & 0 \\ 0 & 0 & 1 & 0 \\ 0 & 0 & 0 & 1 \end{bmatrix} \begin{bmatrix} \cos \theta_2 & -\sin \theta_2 & 0 & l_1 \\ \sin \theta_2 & \cos \theta_2 & 0 & 0 \\ 0 & 0 & 1 & 0 \\ 0 & 0 & 0 & 1 \end{bmatrix} \begin{bmatrix} 1 & 0 & 0 & l_2 \\ 0 & 1 & 0 & 0 \\ 0 & 0 & 1 & 0 \\ 0 & 0 & 0 & 1 \end{bmatrix} \tag{A4}$$

$${}^0T_3 = \begin{bmatrix} \cos \theta_{12} & -\sin \theta_{12} & 0 & l_1 \cos \theta_1 + l_2 \cos \theta_{12} \\ \sin \theta_{12} & \cos \theta_{12} & 0 & l_1 \sin \theta_1 + l_2 \sin \theta_{12} \\ 0 & 0 & 1 & 0 \\ 0 & 0 & 0 & 1 \end{bmatrix}$$

Kinetic energy;

$$S = S_1 + S_2 = \frac{1}{2} m_1 (\dot{x}_1^2 + \dot{y}_1^2) + \frac{1}{2} m_2 (\dot{x}_2^2 + \dot{y}_2^2)$$

$$= \frac{1}{8} m_1 l_1^2 \dot{\theta}_1^2 + \frac{1}{2} m_2 \left[l_1^2 \dot{\theta}_1^2 + \frac{l_2^2}{4} (\dot{\theta}_1 + \dot{\theta}_2)^2 + l_1 l_2 \cos \theta_1 \dot{\theta}_1 (\dot{\theta}_1 + \dot{\theta}_2) (l_1 l_2 \cos \theta_1 \dot{\theta}_1 (\dot{\theta}_1 + \dot{\theta}_2) \cos(\theta_1 + \theta_2)) \right] \tag{A5}$$

Potential energy;

$$V = V_1 + V_2 = m_1 g Y_1 + m_2 g Y_2 = m_1 g \frac{l_1}{2} \sin \theta_1 + m_2 g \left[(l_1 \sin \theta_1 + \frac{l_2}{2} \sin(\theta_1 + \theta_2)) \right] \tag{A6}$$

$L = S - V$

$$= \frac{1}{8} m_1 l_1^2 \dot{\theta}_1^2 + \frac{1}{2} m_2 \left[l_1^2 \dot{\theta}_1^2 + \frac{l_2^2}{4} (\dot{\theta}_1 + \dot{\theta}_2)^2 + l_1 l_2 \cos \theta_1 \dot{\theta}_1 (\dot{\theta}_1 + \dot{\theta}_2) (l_1 l_2 \cos \theta_1 \dot{\theta}_1 (\dot{\theta}_1 + \dot{\theta}_2) \cos(\theta_1 + \theta_2)) \right] - m_1 g \frac{l_1}{2} \sin \theta_1 + m_2 g \left[(l_1 \sin \theta_1 + \frac{l_2}{2} \sin(\theta_1 + \theta_2)) \right] \tag{A7}$$

$$\left(\frac{\partial L}{\partial \theta_1} \right) = - \left(\frac{m_1}{2} + m_2 \right) g l_1 \cos \theta_1 - m_2 g \frac{l_2}{2} \cos(\theta_1 + \theta_2)$$

$$\frac{\partial L}{\partial \dot{\theta}_1} = \left(\frac{m_1}{4} + m_2 \right) l_1^2 \dot{\theta}_1 + \frac{l_2^2}{4} m_2 l_2^2 (\dot{\theta}_1 + \dot{\theta}_2) + \frac{1}{2} m_2 l_1 l_2 (2\dot{\theta}_1 + \dot{\theta}_2) \cos \theta_2$$

$$\frac{d}{dt} \left(\frac{\partial L}{\partial \dot{\theta}_1} \right) = \left(\frac{m_1}{4} + m_2 \right) l_1^2 \ddot{\theta}_1 + \frac{1}{4} m_2 l_2^2 (\ddot{\theta}_1 + \ddot{\theta}_2) + \frac{1}{2} m_2 l_1 l_2 (2\ddot{\theta}_1 + \ddot{\theta}_2) \cos \theta_2 - \frac{1}{2} m_2 l_1 l_2 \dot{\theta}_2 (2\dot{\theta}_1 + \dot{\theta}_2) \sin \theta_2 \tag{A8}$$

$$\begin{aligned}
\left(\frac{\partial L}{\partial \theta_2}\right) &= -\frac{1}{2}m_2l_1l_2\dot{\theta}_1(\dot{\theta}_1 + \dot{\theta}_2)\sin\theta_2 - m_2g\frac{l_2}{2}\cos(\theta_1 + \theta_2) \\
\left(\frac{\partial L}{\partial \dot{\theta}_2}\right) &= \frac{1}{4}m_2l_2^2(\dot{\theta}_1 + \dot{\theta}_2) + \frac{1}{2}m_2l_1l_2\dot{\theta}_1\cos\theta_2 \\
\frac{d}{dt}\left(\frac{\partial L}{\partial \dot{\theta}_2}\right) &= \frac{1}{4}m_2l_2^2(\ddot{\theta}_1 + \ddot{\theta}_2) + \frac{1}{2}m_2l_1l_2\ddot{\theta}_1\cos\theta_2 - \frac{1}{2}m_2l_1l_2\dot{\theta}_1\dot{\theta}_2\sin\theta_2 \\
T_{internal1} &= \frac{d}{dt}\left(\frac{\partial L}{\partial \dot{\theta}_1}\right) - \left(\frac{\partial L}{\partial \theta_1}\right) \\
&= \left(\frac{m_1}{4} + m_2\right)l_1^2\ddot{\theta}_1 + \frac{1}{4}m_2l_2^2(\ddot{\theta}_1 + \ddot{\theta}_2) + \frac{1}{2}m_2l_1l_2(2\ddot{\theta}_1 + \ddot{\theta}_2)\cos\theta_2 - \frac{1}{2}m_2l_1l_2\dot{\theta}_2(2\dot{\theta}_1 + \dot{\theta}_2)\sin\theta_2 + \\
&\left(\frac{m_1}{2} + m_2\right)gl_1\cos\theta_1 + m_2g\frac{l_2}{2}\cos(\theta_1 + \theta_2) \\
T_{internal2} &= \frac{d}{dt}\left(\frac{\partial L}{\partial \dot{\theta}_2}\right) - \left(\frac{\partial L}{\partial \theta_2}\right) \\
&= m_2\frac{l_2^2}{4}(\ddot{\theta}_1 + \ddot{\theta}_2) + \frac{1}{2}m_2l_1l_2\ddot{\theta}_1\cos\theta_2 - \frac{1}{2}m_2l_1l_2\dot{\theta}_1\dot{\theta}_2\sin\theta_2 + \frac{1}{2}m_2l_1l_2\dot{\theta}_1(\dot{\theta}_1 + \dot{\theta}_2)\sin\theta_2 + \\
&m_2g\frac{l_2}{2}\cos(\theta_1 + \theta_2)
\end{aligned} \tag{A9}$$

$$\begin{bmatrix} T_{total1} \\ T_{total2} \end{bmatrix} = \begin{bmatrix} T_{internal1} \\ T_{internal2} \end{bmatrix} + \begin{bmatrix} F_{external1} \\ F_{external2} \end{bmatrix} \begin{bmatrix} Pxy1 \\ Pxy2 \end{bmatrix} \tag{A10}$$



Research Article

Determination of the effect of artificial aging parameters on dry sliding wear resistance of 6013 aluminum alloy (Al-Mg-Si-Cu)

Mehmet Ayvaz^{a,*} 

^aVocational School of Manisa Technical Sciences, Manisa Celal Bayar University, Manisa 45140, Turkey

ARTICLE INFO

Article history:

Received 11 December 2020

Revised 12 February 2021

Accepted 05 March 2021

Keywords:

Aluminum

AA 6013

Artificial aging

Pin-on-disc

Dry sliding

ABSTRACT

In this study, the effect of artificial aging parameters, applied to AA6013 aluminum alloys commonly used in the automotive and aerospace sectors, on wear resistance was examined. For this purpose, AA6013 aluminum alloy samples were solutionized at 575 °C for 60 minutes and then they were artificially aged for 2, 4, and 6 hours at 180 and 200 °C temperatures. Mean hardness was measured as 66.6 HV in the solutionized samples taken. It was determined that as a result of artificial aging, α -AlFeMnSi intermetallic phase precipitation were formed between α -Al grains. By the effect of precipitation hardening, an increase in hardness was observed in all artificially aged samples; the highest hardness was found as an average of 149.3 HV in AA6013 samples aged artificially for 2 hours at 200 °C. A general decrease in the friction coefficients of samples aged at both 180 °C and 200 °C was observed along with the artificial aging temperature. The lowest specific wear rate was determined as $3.542 \times 10^{-3} \text{ mm}^3/\text{Nm}$ in the AA6013 sample aged artificially for 2 hours at 200 °C.

© 2021, Advanced Researches and Engineering Journal (IAREJ) and the Author(s).

1. Introduction

Compared to steel and its alloys, aluminum and its alloys have been used in the automotive industry and in the aerospace industry since 1910 due to their high specific strength, corrosion resistance, and easy workability [1, 2]. Furthermore, the mechanical, physical, and chemical properties of heat-treatable 2XXX (Al-Cu), 6XXX (Al-Mg-Si) and 7XXX (Al-Zn-Mg) aluminum alloys can be improved by artificial aging. This precipitation hardening in aluminum alloys was coincidentally detected by Wilm in 1906 [3]. This phenomenon was also explained by Guinier and Preston independently of each other in 1938 [4, 5].

In 6XXX series Al-Mg-Si aluminum alloys, at the early stages of artificial aging, Mg and Si begin to precipitate from super-saturated solid solution (SSSS) formed with the solutionizing annealing, and then Guinier–Preston GP zones occur. In later stages, needle-like β'' (Mg_5Si_6) and rodlike β' phases are formed, respectively. As a result of long-term heat treatment, these metastable phases turn into stable β -

$\text{Mg}_2\text{Si}+\text{Si}$ phases [6, 7].

The 6013 aluminum alloy, a Cu-added Al-Mg-Si-Cu alloy of the 6XXX series, was first produced in the 1970s for the automotive sector with the aim of improving fuel efficiency. In later years, as a result of tests carried out at Lockheed and Alcoa Laboratories, the 6013 aluminum alloy was found to provide higher corrosion resistance despite having almost similar mechanical properties to the 2024 aluminum alloy used in aircraft, and it has begun to be used by Lockheed as structural aircraft material [8]. During aging in the Al-Mg-Si-Cu aluminum alloy, the needle-like β'' phase transforms into the rodlike β^+ lathlike $Q'-\text{Al}_5\text{Cu}_2\text{Mg}_8\text{Si}_6$ phases. In the final stage, these phases also turn into $Q+\beta-\text{Mg}_2\text{Si}+\theta-\text{Al}_2\text{Cu}+\text{Si}$ precipitate phases [9-11]. In addition, higher strengths are obtained by providing a smaller and finer distribution of precipitates formed by the addition of copper. This is because copper additions lead to smaller and finer dispersed precipitates [9].

Erdogan et al. applied artificial aging to 6013 aluminum alloy samples, which were solutionized at 530 °C, in a

* Corresponding author. Tel.: +90 232 260 1001; Fax: +90 232 260 1004.

E-mail addresses: m.ayvaz@cbu.edu.tr, author.m.ayvaz@gmail.com (M. Ayvaz)

ORCID: 0000-0002-9671-8679 (M. Ayvaz)

DOI: 10.35860/iarej.839108

This article is licensed under the CC BY-NC 4.0 International License (<https://creativecommons.org/licenses/by-nc/4.0/>).

microwave oven for 3 different periods of 1, 3, and 5 hours at 190 °C. The highest hardness values were obtained in samples aged artificially for 3 hours around 70 HV, and the highest corrosion resistance was also obtained in these samples. It was reported that FeAl intermetallic phases improved both mechanical properties and corrosion resistance. [12].

After taking 5068, 6061, and 6013 aluminum alloys into the solution at 530 °C, Zeid artificially aged them for 30 minutes at 175 °C and then compared their mechanical properties and corrosion resistance. In the study, Mg₂Si with orientation (420), (422) and (511) was detected in natural and artificially aged AA 6013 alloy. After the aging heat treatment, the highest hardness values were obtained in 6013 aluminum alloy. In addition, 6013 and 6061 aluminum alloys exhibited higher corrosion resistance than 5086 [13].

In their study, Liu et al. took 6013 aluminum alloy samples into the solution at 560 °C for 2 hours, then artificially aged them at 191°C and different periods between 10 min-24 h, and examined their mechanical properties. The highest hardness value was measured as approximately 111 HV in the sample aged for 4 h. They also found the highest yield and tensile strength in this sample to be 258 and 310 MPa, respectively [14].

After taking 6013 aluminum alloys into the solution at 560 °C for 8 hours, Akyüz and Şenaysoy aged them artificially at 180°C for 1,3, 6, 9, 12, and 24 hours. 6 hours of artificial aging revealed optimum values in terms of time and mechanical properties. As a result of machinability experiments, they determined that the shear force increased with aging time [15]. In another study conducted with the same aging heat treatment parameters, they examined the mechanical and machinability properties of 6013 and 6082 aluminum alloys comparatively. In tests carried out with a shear rate of 60 m·min⁻¹, as a result of aging, lower shear forces were measured and higher surface quality was obtained in 6013 aluminum alloy with higher mechanical properties compared to 6082 aluminum alloy [16].

One of the limits of use of aluminum alloys is low wear resistance. In many studies in the literature, the mechanical properties, machinability, and corrosion resistance of the 6013 aluminum alloy after artificial aging heat treatment have been examined and optimal heat treatment parameters have been identified. However, the effect of artificial aging on the tribological properties and wear resistance of the 6013 aluminum alloy have not been revealed and optimal parameters have not been determined. In this study, the relationship between aging heat treatment and wear resistance was revealed.

2. Materials and Method

First, 6013 aluminum alloy samples were cut in a way that they would be Ø30 mm and 10 mm thickness. The lower and upper surfaces of the cut samples were sanded with 180-1200

grit sandpapers. The prepared samples were solutionized for 60 minutes at 575 °C in the Protherm brand Ash furnace and then cooled in the water at room temperature. Artificial aging heat treatment was applied for 2, 4, and 6 hours at temperatures of 180 °C to one part of the samples were solutionized and at 200 °C to the other part of the samples. Spectral analysis of the used AA6013 aluminum alloy samples is given in Table 1.

Micro-hardness measurements of the samples solutionized and aged were performed with the Vickers hardness tester (Future-Tech Corp FM-700, Tokyo, Japan). In these tests, which were implemented in accordance with ASTM E384–17 standards, measurements were repeated at least 5 times for each sample with a sinking time of 10 seconds under a 50gf load. The wear test surfaces of the samples were polished with 3 and 1 µm diamond polishers. Then, wear tests of these samples were then carried out on the CSM Tribometer model wear tester (Anton Paar, Switzerland) in accordance with ASTM G99–17 standard. Tests were conducted with dry sliding, under 10 N Load, with a sliding speed of 20 cm·sec⁻¹. 100Cr6 balls with a diameter of 6 mm were used as counter elements in the tests (Figure 1).

For metallographic examinations, 6013 aluminum alloy samples, whose surfaces were sanded and polished, were etched with Keller solution (2.5 ml HNO₃, 1.5 ml HCl, 1 ml HF, 95 ml water). Microstructure and wear surface examinations of the samples were carried out with the ZEISS GeminiSEM 500 FE-SEM model (ZEISS, Oberkochen, Germany) scanning electron microscope (SEM).

Table 1. Chemical composition (wt.%) of AA6013 aluminum alloy samples

Element	Wt %
Al	95.96
Si	0.903
Cu	0.767
Mg	1.002
Mn	0.412
Fe	0.645
Zn	0.179
Cr	0.036
Other	0.096

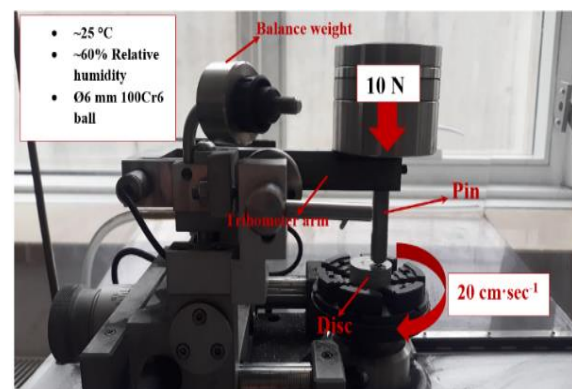


Figure 1. Pin-on-disc tribometer

3. Results and Discussion

Microhardness values of samples solutionized and artificially aged for 2, 4, and 6 hours at 180 and 200 °C are presented in Figure 2. The microhardness value of solutionized AA6013 aluminum alloy was determined as 66.6 HV on average. In samples aged artificially at 180 °C, as aging time increased, an increase in the microhardness values of AA6013 samples occurred; the microhardness values for these samples were measured on average as 89.8, 112.6, and 117.2, respectively. Hardness increase, occurring as a result of precipitation and precipitation hardening emerging due to artificial aging, is a well-known mechanism [10, 17-19]. The increase in hardness reaches the peak point at different artificial aging times, and at the end of aging time, a decrease occurs again. This case was clearly seen in the samples aged artificially at 200 °C. In AA6013 aluminum alloy samples that were aged artificially at 200 °C, microhardness values were measured as 149.3, 142.8, and 130.6 HV for aging times of 2, 4, and 6 hours, respectively. It is known that the T6 heat treatment of AA6013 is performed for 4 hours at 190 °C [20].

In this study, by heat treatment performed for 2 hours at 200 °C, peak artificial aging was achieved and a 2.2 times increase in microhardness was obtained in these samples compared to the solutionized samples.

In Figure 3a-f, SEM images of the microstructures of the samples aged artificially for 2, 4, and 6 hours at temperatures of 180 and 200 °C are shown. When the internal structures are examined, precipitate formations in the α -Al matrix are seen in all samples. The SEM images of this precipitate was taken from sample of it aged artificially for 4 hours at 180 °C and an EDS analysis was performed (Figure 4). The precipitate formed by artificial aging had almost round

structure and was in sizes of 1-1.5 μ m. EDS analysis showed that this precipitate was an α -AlFeMnSi intermetallic compound. In their study, Barbosa et al. determined that α -AlFeMnSi precipitates of 800-900 nm in the round structure were formed as a result of artificial aging processes that were realized at different times at 180 °C [11]. They also reported that the Mn/Fe ratio in that precipitate was 0.58 ± 0.12 . In this study too, this ratio was determined to be approximately 0.55.

In Figure 5, for post wear-tests, volume losses and specific wear rates of solutionized sample and samples aged artificially for 2, 4 and 6 hours at 180 and 200 °C are given. The specific wear rate of solutionized the sample was determined as $\sim 6.12 \times 10^{-3}$ mm³/Nm. In samples artificially aged for 2 and 4 hours at 180 °C, whereas there was a decrease in specific wear rates, no significant wear resistance was observed. Specific wear rates for these samples were $\sim 5.90 \times 10^{-3}$ and 5.38×10^{-3} mm³/Nm, respectively. With $\sim 18\%$ reduction, the specific wear rate in the sample aged artificially for 6 hours at 180 °C became $\sim 5.01 \times 10^{-3}$ mm³/Nm. By artificial aging heat treatment performed for 2 hours at 200 °C, the specific wear rate of the AA6013 aluminum alloy sample decreased by $\sim 42\%$ and became $\sim 3.54 \times 10^{-3}$ mm³/Nm. After aging treatments performed for 4 and 6 hours at this temperature, specific wear rates were determined as $\sim 4.64 \times 10^{-3}$ and 5.60×10^{-3} mm³/Nm, respectively. Previous studies have generally reported that wear resistance of the aluminum alloy increases with peak aging and there is a relationship between hardness and wear resistance [21-23]. In 6XXX series aluminum alloys, Mg₂Si, Al₂Cu and AlFeSi precipitates formed with artificial aging play an important role in this increase in hardness and wear resistance [22, 24, 25].

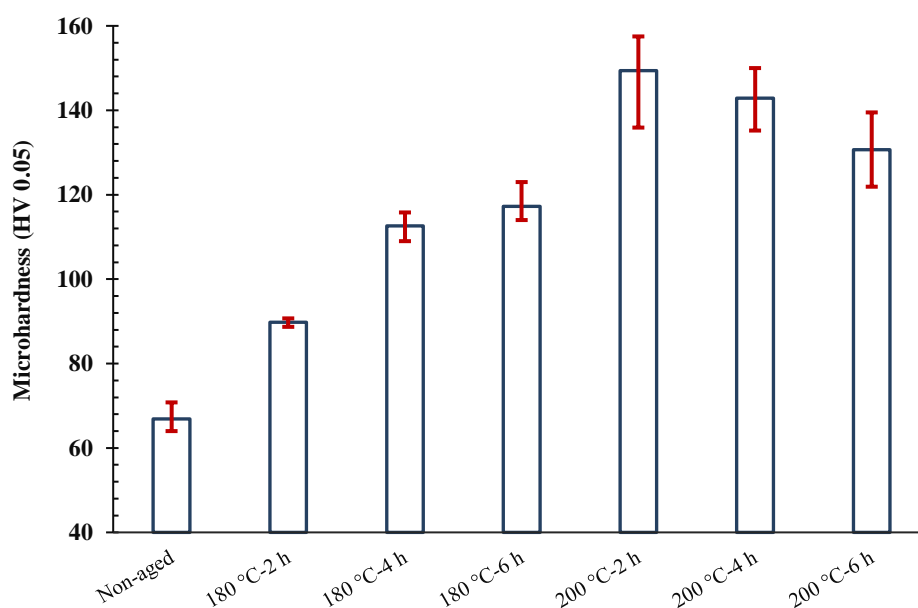


Figure 2. Microhardness of AA6013 samples solutionized and aged artificially

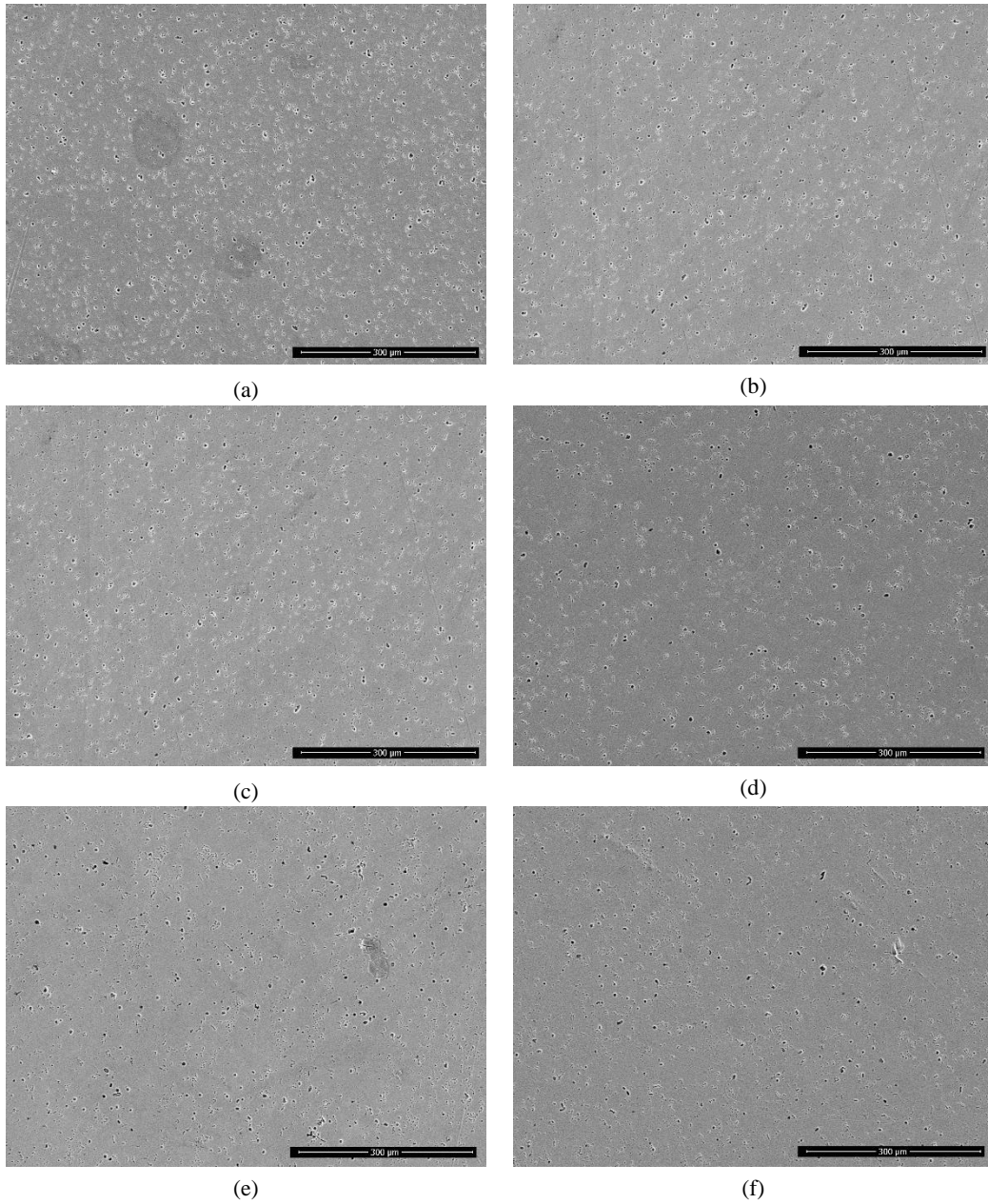


Figure 3. SEM images of internal structures of artificially aged samples: a) 180 °C-2h, b) 180 °C-4h, c) 180 °C-6h, d) 200 °C-2h, e) 200 °C-4h and f) 200 °C-6h.

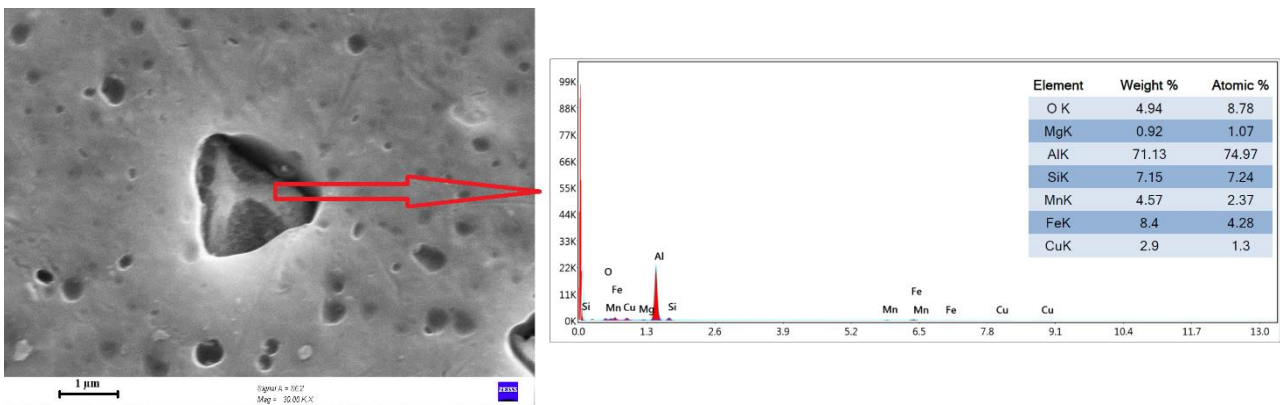


Figure 4. SEM image and EDS analysis of α -AlFeMnSi precipitate in the sample aged artificially for 4 hours at 180 °C.

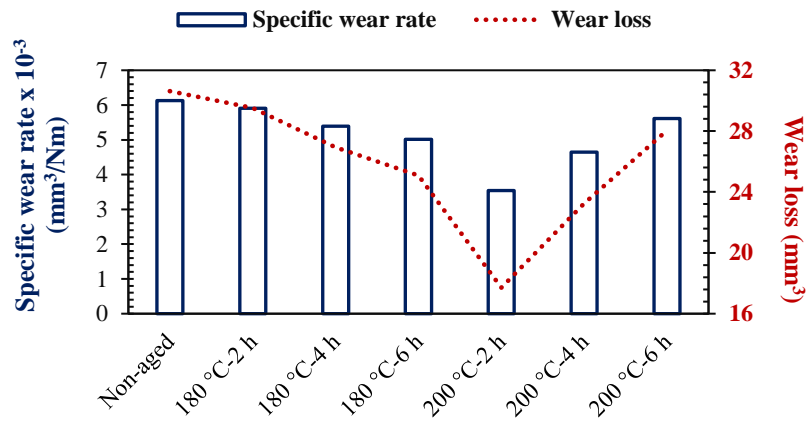


Figure 5. Wear losses and specific wear rates of solutionized and aged AA6013 aluminum alloy samples.

Figure 6 shows SEM images taken from the wear surfaces of AA6013 aluminum alloy samples that have been solutionized and aged. It can be seen in these SEM images

that in the solutionized sample and in the samples aged for 2, 4 and 6 hours at 180 °C after being solutionized, the dominant wear type is delamination wear (Figures 6a-d)

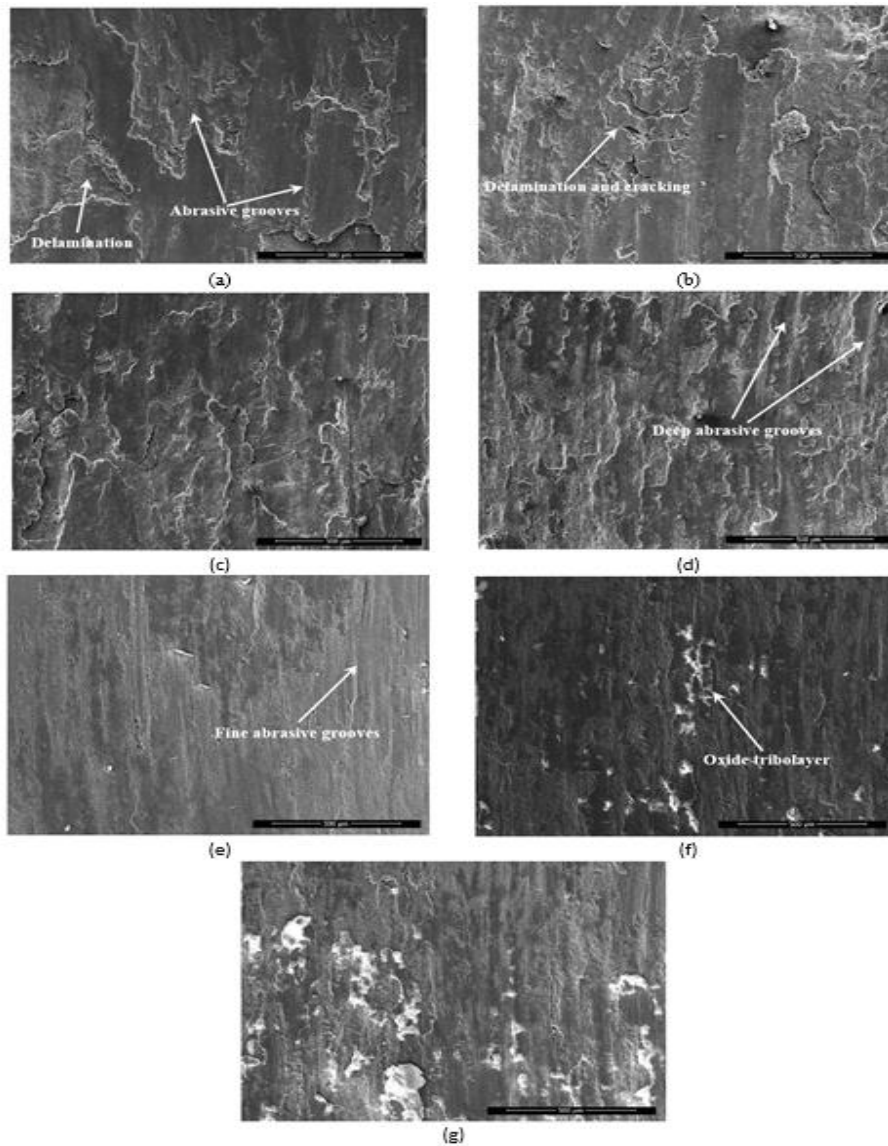


Figure 6. SEM images of wear surfaces of the heat treated AA6013 samples: a) solutionized, b) 180 °C-2h, c) 180 °C-4h, d) 180 °C-6h, e) 200 °C-2h, f) 200 °C-4h and g) 200 °C-6h.

Abrasive wear scratches in these samples also indicate the presence of abrasive wear. In the sample to which aging process has been applied at 200 °C for 2 hours, the width of the wear trace appears to be narrower compared to other samples (Figure 6e). In addition, delamination wear has almost never occurred in this sample. But traces of abrasive wear are also evident in this sample. Moreover, on the wearing surface, intense crack formation, which occurs as a result of plastic deformation resistance increasing with increased hardness, is observed. Plastic deformation and flow traces are again observed in samples aged for 4 and 6 hours at 200 °C (Figures 6f, g). In addition, oxidative wear traces and tribolayers were identified on the wear surfaces of these samples and this was also detected by EDS analysis results obtained from the surface of the sample, which was aged for 4 hours at 200 °C (Figure 7).

In Figure 8, sliding distance dependent friction coefficients of the samples aged for 2, 4, and 6 hours at 180 °C and 200 °C are given. The mean friction coefficient of the solutionized sample was determined as 0.502. In samples that underwent artificial aging heat treatment at 180 °C for 2 and 4 hours, the mean friction coefficients were also found to be 0.503 and 0.502, respectively. In the sample aged artificially for 6 hours, on the other hand, the mean friction coefficient decreased slightly and became 0.470. Similarly, in the samples aged artificially at 200 °C, the lowest mean coefficient of friction was measured as 0.440 in the sample aged artificially for 6 hours. Among all samples solutionized and aged artificially, the highest mean friction coefficient was determined in the sample aged artificially for 2 hours at 200 °C. In addition, when graphs of change in the sliding distance dependent friction coefficient were examined, it was seen that the running-in period decreased and the steady-state was reached in a shorter time with an increase in artificial aging temperature and time.

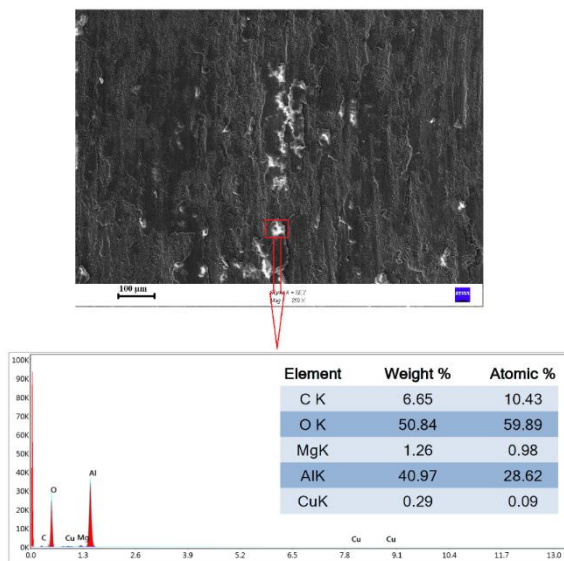


Figure 7. EDS analysis results obtained from the surface of the sample, which was aged for 4 hours at 200 °C

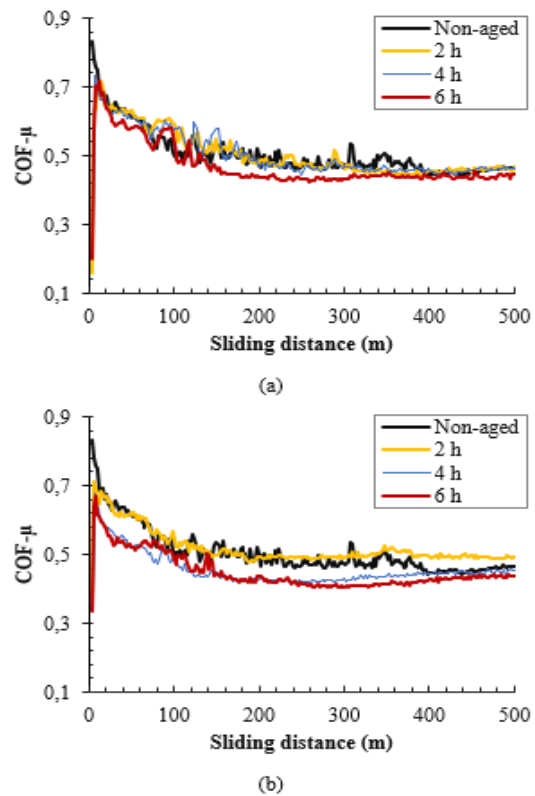


Figure 8. Sliding distance dependent friction coefficients of the artificial aged samples

4. Conclusion

As a result of microstructural and tribological investigations of the non-aged and artificial aged AA6013 samples, the determined results are as follows:

- The hardness of the solutionized sample is 66 HV.
- Peak-aged samples are samples aged artificially for 2 hours at 200 °C. The hardness of these samples is 149.3 HV.
- By artificial aging, α -AlFeMnSi precipitates that have a low Mn/Fe ratio, 1-1.5 μm diameter, and almost round structure are formed.
- The sample that has the highest friction coefficient ($\mu=0.517$) and the lowest specific wear rate ($\sim 3.54 \times 10^{-3} \text{ mm}^3/\text{Nm}$) is the sample aged artificially for 2 hours at 200 °C.
- In AA6013 samples, while plastic deformations and delamination type wear are observed as hardness decreases, abrasive wear becomes dominant as hardness increases (against 60-65 HRc 100Cr6 ball counterpart).

Declaration

The author declared no potential conflicts of interest with respect to the research, authorship, and/or publication of this article. The author also declared that this article is original, was prepared in accordance with international publication and research ethics, and ethical committee permission or any special permission is not required.

Author Contributions

M. Ayvaz is responsible for all section of the study.

References

1. Atilio I., Braga, V., Siqueira, R. H. M., Carvalho, S. M., Lima, M. S. F., *Comparing the weldability of AA6013-t4 aluminium alloy on DP600 dual-phase steel with laser welding and resistance spot welding*, Journal of the Brazilian Society of Mechanical Sciences and Engineering, 2020. **42**(71): p. 1-12.
2. Şimşek, İ., Şimşek, D., Özyürek, D., *The effect of different sliding speeds on wear behavior of ZrO₂ reinforcement aluminium matrix composite materials*. Internatioal Advanced Researches and Engineering Journal, 2020. **4**(1): p. 1-7.
3. Wilm, A., *Physico-metallurgical investigations of aluminium alloys containing magnesium*. Metallurgie, 1911. **8**: p. 255-227.
4. Guinier, A., *Structure of age-hardened aluminium-copper alloys*. Nature, 1938. **14**: p. 569–570.
5. Preston, G. D., *The diffraction of x-rays by age-hardening aluminium copper alloys*. Proceedings of the Royal Society of London, 1938. **167**(931): p. 526-538.
6. Dutta, I., Allen, S.M., *A calorimetric of precipitation in commercial aluminum alloy 6061*. Journal of Materials Science Letters, 1991. **10**: p. 323-326.
7. Pogatscher, S., Antrekowitsch, H., Leitner, H., Ebner, T., Uggowitzer, P. J., *Mechanisms controlling the artificial aging of Al–Mg–Si alloys*. Acta Materialia, 2011. **59**: p. 3352-3363.
8. Kaneko, R.S., Bakow, L., Lee, E.W., *Aluminum alloy 6013 sheet for new U.S. navy aircraft*. JOM, 1990. **42**: p. 16-18.
9. Staab, T.E.M., Krause-Rehberg, R., Hornauer, U., Zschech, E., *Study of artificial aging in AlMgSi (6061) and AlMgSiCu (6013) alloys by Positron Annihilation*. Journal of Material Science, 2006. **41**: p. 1059–1066.
10. Buha, J., Lumley, R.N., Crosky, A.G., Hono, K., *Secondary precipitation in an Al–Mg–Si–Cu alloy*. Acta Materialia, 2007. **55**: p. 3015-3024.
11. Barbosa, C., Rebello, J.M.A., Acselrad, O., Dille, J., Delplancke, J.-L., *Identification of precipitates in 6013 aluminum alloy (Al–Mg–Si–Cu)*. International Journal of Materials Research, 2002. **93**(3): p. 208-211.
12. Erdoğan, M., Tekin, R., Kaya, M., *Mikrodalga fırında suni yaşlandırılan 6013 alüminyum alaşımın korozyon davranışının incelenmesi (Investigation of corrosion behavior of 6013 aluminum alloy aged artificially in microwave oven)*. Pamukkale Üniversitesi Mühendislik Bilimleri Dergisi, 2014. **20**(1): p. 25-30.
13. Abo Zeid, E.F., *Mechanical and electrochemical characteristics of solutionized AA 6061, AA6013 and AA 5086 aluminum alloys*. Journal of Materials Research and Technology, 2019. **8**(2): p. 1870-1877.
14. Liu, M., Jiang, T., Wang, J., Liu, Q., Wu, Z., Yu, Y., Skaret, P.C., Roven, H. J., *Aging behavior and mechanical properties of 6013 aluminum alloy processed by severe plastic deformation*. Transactions of Nonferrous Metals Society of China, 2014. **24**: p. 3858-3865.
15. Akyüz, B., Şenaysoy, S., *Effect of the aging process on mechanical properties and machinability in AA6013 aluminum alloys*. Scientific Research and Essays, 2015. **10**(2): p. 17-78.
16. Akyüz, B., Şenaysoy, S., *Effect of aging on mechanical properties and machining on aluminum alloys*. Bilecik Şeyh Edebali Üniversitesi Fen Bilimleri Dergisi, 2014. **1**(1): p. 1-9.
17. Cuniberiti, A., Tolley, A., Castro Riglos, M.V., Giovachini, R., *Influence of natural aging on the precipitation hardening of an AlMgSi alloy*. Materials Science and Engineering A, 2010. **527**: p. 5307-5311.
18. Esmaeili, S., Wang, X., Lloyd, D.J., Poole, W.J., *On the precipitation-hardening behavior of the Al–Mg–Si–Cu alloy AA6111*. Metallurgical and Materials Transactions A, 2003. **34**: p. 751-763.
19. Murayama, M., Hono, K., *Pre-precipitate clusters and precipitation processes in Al–Mg–Si alloys*. Acta Materialia, 1999. **47**(5): p. 1537-1548.
20. Heat Treating, ASM Handbook, Volume 4 (1991): *Heat Treating of Aluminum Alloys*.
21. Das, S., Pelcastre, L., Hardell, J., Prakash, B., *Effect of static and dynamic ageing on wear and friction behavior of aluminum 6082 alloy*. Tribology International, 2013. **60**: p. 1-9.
22. Meyveci, A., Karacan, İ., Çalığülü, U., Durmuş, H., *Pin-on-disc characterization of 2xxx and 6xxx aluminum alloys aged by precipitation age hardening*. Journal of Alloys and Compounds, 2010. **491**: p. 278-283.
23. Baydoğan, M., Çimenoglu, H., Kayali E.S., *A study on sliding wear of a 7075 aluminum alloy*. Wear, 2004. **257**: p. 852-861.
24. Gavgali, M., Totik, Y., Sadeler, R., *The effects of artificial aging on wear properties of AA 6063 alloy*. Materials Letters, 2003. **57**: p. 3713-3721.
25. Meriç, C., Atik, E., Kaçar, H., *Effect of aging on abrasive wear of deformable aluminum alloy AA6351*. Metal Science and Heat Treatment, 2004. **46**(3-4): p. 110-114.

**Research Article**

Investigation of the temperature effect on the mechanical properties of 3D printed composites

Hamed Tanabi ^a 

^aMechanical Engineering Department, University of Turkish Aeronautical Association, Ankara, Turkey

ARTICLE INFO

Article history:

Received 17 January 2021

Revised 20 February 2021

Accepted 01 March 2021

Keywords:

Additive manufacturing

FDM

Fiber reinforcement

Structural analysis

3D print

ABSTRACT

Short fiber reinforced additively manufactured components are lightweight yet durable materials with a wide range of potential applications in various industries such as aerospace and automotive. The fabricated specimens may be subjected to various thermal conditions ranging from -20 up to 60 °C during their service life. This study aims to investigate the effect of temperature on mechanical properties of the 3D printed short glass-fiber-reinforced polyamide 6 (GFPA6) composites and ABS as an unreinforced polymer. In accordance with ASTM D638, tensile test specimens were fabricated using Fused Deposition Modeling (FDM) technique. The fabricated samples were subjected to tensile load to investigate the stiffness and strength while temperatures set to -20, 20, 40, and 60 °C. The mechanisms of failure were identified based on fracture surface microscopic analysis. The glass fiber reinforced PA6 showed higher stiffness and strength up to 56% and 59% compare to ABS. At elevated temperatures, specimens showed a large deformation with a significant decline in tensile strength. It was observed that the dominant failure mechanism for ABS was the breakage of the deposited filaments while fiber pull-out was the dominant failure mechanism for GFPA6 material.

© 2021, Advanced Researches and Engineering Journal (IAREJ) and the Author(s).

1. Introduction

Additive manufacturing as a revolutionary technology has found so many applications in fabricating structural parts ranging from customized small to high performance parts. The benefits of this technology involve easy and fast prototyping of parts with complex shapes, low waste of raw materials, and affordable cost. Among the available additive manufacturing processes, Fused Deposition Modeling (FDM), is more interested respect to the low cost of the technology, minimal waste of material together with ease of access and use [1, 2]. In FDM, three-dimensional parts are fabricated using a layer-by-layer deposition of a thermoplastic polymer such as Poly Lactic Acid (PLA), nylon, Acrylonitrile butadiene styrene (ABS), and polycarbonate. Lack of toughness, strength, and unstable mechanical properties make the end-use FDM parts made from pure polymers, to be unreliable for structural and functional engineering applications [3]. However, this issue has been addressed by introducing fiber reinforced

filaments for FDM. In recent years, the study on printing process conditions and final properties of FDM parts reinforced with short or continuous carbon, glass, and aramid fibers is under extensive investigation [4–6].

In [7], continuous carbon fiber was used to reinforce FDM printed ABS, while PLA was used in [5, 8]. The mechanical characterization of the printed composites indicated that the bending and tensile strengths were increased respectively by up to 35% and 108% in comparison with pure PLA while delamination together with matrix cracking were found as the dominant failure modes [9].

Mohammadizadeh et al. [3] Studied the mechanical and structural behavior of the continuous carbon fiber reinforced 3D printed components under static and dynamic loadings. The presented results show that specimens printed with fiber inclusion exhibit superior mechanical properties compared with those fabricated with pure polymer. Also, fiber breakage, fiber pull-out,

* Corresponding author. Tel.: +90-312-589-6100.

E-mail addresses: htanabi@thk.edu.tr (H. Tanabi)

ORCID: 0000-0002-0911-6849 (H. Tanabi)

DOI: 10.35860/iarej.862304

This article is licensed under the CC BY-NC 4.0 International License (<https://creativecommons.org/licenses/by-nc/4.0/>).

and delamination were indicated as the dominant failure mechanisms.

The impact damage performance of FDM printed continuous glass, carbon, and aramid fiber reinforced thermoplastic composites was studied in [10]. The authors found that while the printed parts with carbon fiber reinforced nylon results in a brittle structure, the impact performance of the nylon reinforced with glass fibers was improved significantly.

Yasa and Ersoy [11] investigated the mechanical properties and dimensional accuracy of the short carbon fiber reinforced nylon composites fabricated by FDM. They showed that using appropriate compensation techniques the dimensional accuracy for some features can be enhanced. The presented results for tensile tests show that compared to unreinforced nylon, the elastic modulus and yield strength were greatly enhanced at the cost of ductility.

Yu et al. [12] used X-ray microscopy to characterize the internal morphologies of 3D-printed composites. They used Modified Kelly-Tyson model considering the void volume fraction to predict the tensile strength of 3D-printed composites. Fiber length, fiber orientation, and void content were determined using morphology characterization through X-ray microscopy.

The properties such as high dimensional stability, high level of strength, and stiffness at an affordable cost make fiber reinforced filaments an interesting material that opens new application fields in FDM printing [13, 14]. For instance, these high-performance 3D printing filaments are used in fabricating light-weight Unmanned Aerial Vehicle (UAV) structures as well as their payloads [15–17]. It is worth noting that aero-structures may be subjected to a wide range of temperatures during their service life. For example, a gimbal (the platform that is used for stabilizing the optic and thermal cameras on a UAV) should be able to show stable performance in a temperature ranging from $-20\text{ }^{\circ}\text{C}$ to $60\text{ }^{\circ}\text{C}$. Thus, the structures made using FDM method should also be able to meet the desired structural requirements in the mentioned temperature range. Although the working temperature is a critical challenge in the application of FDM based polymers in aerospace structures; there is no study in open source literature on this field.

This study aims to address this issue by investigating the mechanical properties of FDM specimens made of fiber reinforced polymer filament at various temperatures. The study starts with the explanation of the samples material and their manufacturing process in section 2. Then the tensile test procedure is explained in detail in section 3. In section 4, the experimental results are presented together with the discussion of these results. Finally, in section 5, key findings and conclusions obtained from this study are presented.

2. Material and sample preparation

2.1 Characterization of Filaments

Thermo-gravimetric analysis (TGA) was used to identify the glass fiber mass fraction in the GF30-PA6 filament. The variation of the filament weight was measured in the $15\text{ }^{\circ}\text{C}$ to $1000\text{ }^{\circ}\text{C}$ temperature interval with the temperature rate of $10\text{ }^{\circ}\text{C}/\text{min}$. TGA was conducted under a nitrogen atmosphere.

2.2 Fabrication of Samples

Test specimens were fabricated in accordance with ASTM D638-Type I, using the fused deposition modeling technique. As material, ABS and XSTRAND GF30-PA6 filament (1.75 mm diameter, developed by Owens) were used. XSTRAND GF30-PA6 is a polyamide base filament reinforced with short glass fibers. Properties such as good chemical and UV resistance and high wear resistance make polyamide reinforced filaments an interesting material for 3D printing purposes. The GF30-PA6 filaments are moisture sensitive so to ensure constant material properties the material was dried in an oven at $60\text{ }^{\circ}\text{C}$ for 48 hours.

The geometry of test specimens was generated using the SolidWorks software package. The model geometry was exported as a stereolithography file (STL) and loaded into a 3D printer slicing software package, namely “Z-Suite” then the process parameters were adjusted. Samples were fabricated by Zortrax M 200 printer. Due to the abrasive nature of fiber reinforced filaments, a hard steel nozzle diameter of 0.4 mm was used as the extruder. The printing speed is set to 40 mm/s with a layer height of 0.19 mm for all layers. Infill density, bed, and nozzle temperatures are set to 100% (solid), $80\text{ }^{\circ}\text{C}$, and $255\text{ }^{\circ}\text{C}$, respectively. For ABS material printing speed, bed and nozzle temperatures are set to 35 mm/s, $80\text{ }^{\circ}\text{C}$, and $275\text{ }^{\circ}\text{C}$, respectively. To improve 3D printer bed adhesion, a thin layer of glue stick was applied on the bed just before printing.

The arrangement of the models in slicing software and printed samples is shown in Figure 1. In total, 40 test coupons were fabricated for mechanical characterization.

2.3 Mechanical Characterization

Uniaxial tensile tests were performed on samples (fabricated as outlined in section 2.1) according to ASTM D638 under displacement control by straining at a rate of 1 mm/min using a universal tensile test machine (Tenson). Tensile tests were performed at -20 , 20 , 40 , and $60\text{ }^{\circ}\text{C}$. Test samples were kept in an oven or a freezer for 30 minutes in temperatures the same as their test temperatures. During the test, a heating pad with a control unit (Tk heat clamp, New Era) was used for heating the test samples up to 40 and $60\text{ }^{\circ}\text{C}$. On the other hand, a freeze spray (RS PRO Aerosol) was used to lower the temperature to around $-20\text{ }^{\circ}\text{C}$. To keep the temperature around the desired value ($-20\pm 5\text{ }^{\circ}\text{C}$), the

spraying was performed during the test, continuously.

To measure the temperature of the samples, a noncontact infra-red thermometer (AN200, Exttech) was used. The experimental setup is shown in Figure 2.

3. Results and discussion

3.1 Thermo-gravimetric Analysis of the Filaments

TGA results are presented in Figure 3. According to the TGA results the reinforcement fiber content in the filament was determined to be 27%.

3.2 Mechanical Characterization

Table 1 presents the results of the tensile test for eight test configurations. The presented results are an average of 5 tests. At room temperature, the tensile strength of ABS samples was measured as 32 ± 2 MPa. The strains at tensile strength and breaking point are 3.6% and 4.8%, respectively. In [18], the elastic modulus, average tensile strength and corresponding strain for ABS were reported as 1.7 GPa, 29.5 MPa and 2.3%, respectively. In [19], tensile strength was measured as 34 MPa, and strain at break was reported as 8.6%. In [20] Young’s modulus, tensile strength, and strain at failure were reported as 1.9 GPa, 32.8 MPa, and 9%. However, in both [19] and [20] a wide scattering was observed in the reported strain value (around $\pm 3\%$). It is worth noting that the obtained mechanical properties can diverge significantly depending on the supplier and their filament fabrication process [2].

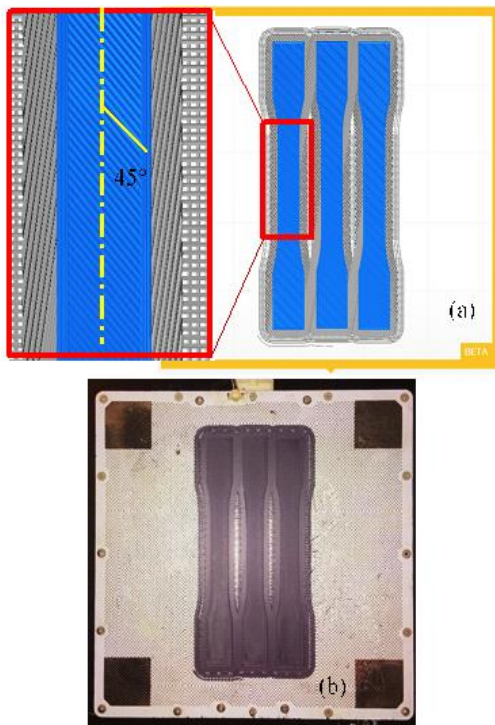


Figure 1. (a) Arrangement of the models in slicing software, Solid layers are oriented $\pm 45^\circ$, (b) Fabricated samples

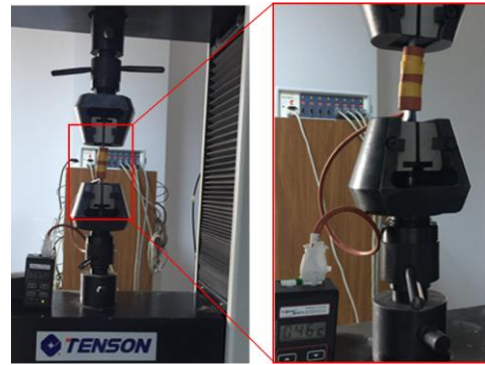


Figure 2. Tensile test and heating setups

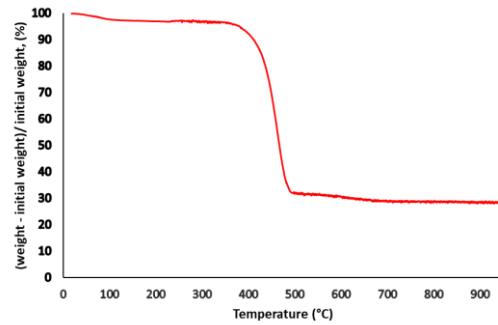


Figure 3. TGA analysis results of GFPA6 filaments

In all tests, elastic modulus decreases by increasing the temperature. For ABS material, the highest average modulus was measured at -20°C while by increasing temperature the elastic modulus was reduced significantly. Average tensile strength was also reduced by increasing the temperature, however, similar results were obtained at -20 and 20°C . For short glass fiber reinforced polyamide (GFPA6), a little variation in elastic modulus was observed for the tests performed at -20 and 20°C . However, average tensile strength is significantly affected by temperature and while a tensile strength of 70 ± 3 MPa was obtained at -20°C , it was measured as 51 ± 3 MPa, 30 ± 2 MPa, and 26 ± 2 MPa at 20 , 40 , and 60°C , respectively. For all test conditions, GFPA6 shows higher stiffness and tensile strength with respect to ABS.

For GFPA6, fracture strain is significantly increased by increasing the test temperature but is not affected at low (-20°C) temperature. For ABS, fracture strain does not vary too much in the temperature range of -20 to 40°C , but by increasing the temperature up to 60°C the fracture strain reaches 7.4%. Figure 4 shows stress versus strain diagrams of ABS and GFPA6 at various temperatures.

3.3 Characterization of the Fractured Surface

To determine the failure mechanism, all specimens were examined using an optical microscope. The images were obtained from the fracture surface of the samples. Optical microscopic images of the fractured surface of ABS and GFPA6 specimens are shown in Figure 4 and Figure 5, respectively.

Table 1. Uniaxial tensile test results for ABS and glass fiber reinforced PA6 at various temperatures

Sample	Material	Temperature (°C)	E (GPa)	S_{ut} (MPa)	ϵ (%)
ABS/-20C	ABS	-20±5	2.4±0.3	31±2	4.2±0.1
ABS/20C	ABS	20±2	1.6±0.3	32±2	4.8±0.2
ABS/40C	ABS	40±2	1.2±0.3	22±2	5.3±0.3
ABS/60C	ABS	60±2	1.1±0.2	15±3	7.4±0.5
GFPA6/-20C	GF30PA6	-20±5	3.0±0.3	70±3	5.0±0.1
GFPA6/20C	GF30PA6	20±2	2.5±0.2	51±3	5.2±0.1
GFPA6/40C	GF30PA6	40±2	1.5±0.2	30±2	9.8±0.3
GFPA6/60C	GF30PA6	60±2	1.3±0.2	26 ±2	8.4±0.3

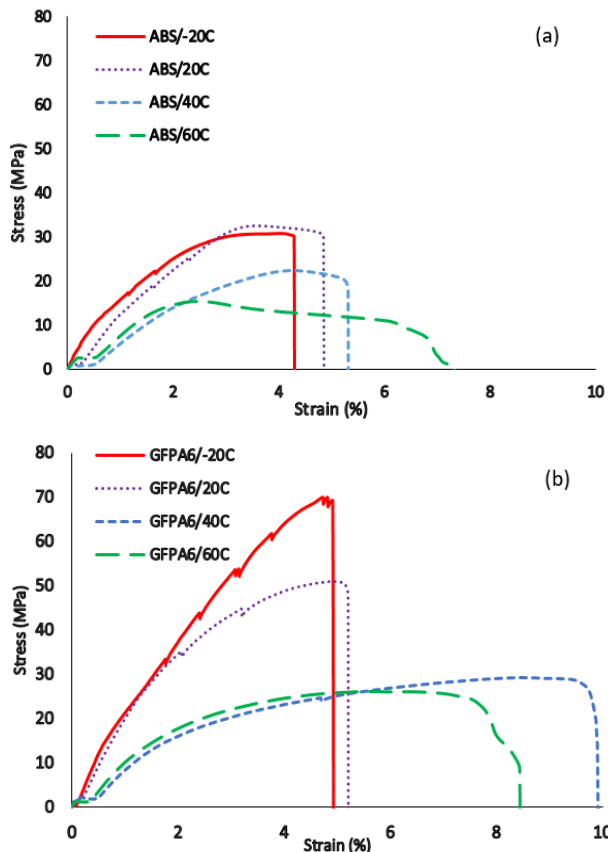


Figure 4. Stress vs strain diagram of a) ABS, and b) GFPA6

As it is shown in Figure 5, a local necking (narrowing in cross-section) is observed in ABS samples at 60 °C. The effect of this issue can also be traced on the stress vs. strain diagram of these samples (Figure 4a).

This phenomenon was not observed in GFPA6 samples. On the other hand, while a local fracture is seen in ABS/40C and ABS/60C specimens, fractured filaments are noticed in all over gauge length for ABS/-20C and ABS/20C (Figure 4). In all ABS test specimens, the fractured surface was perpendicular to the loading axis (Figure 5) while an oblique fracture surface was observed in GFPA6 samples (Figure 6).

The existence of voids and pores in 3D printed parts is unavoidable, though the shape, size, and distribution are highly dependent on the process parameters [21]. The internal structure and, in turn, the mechanical properties of the printed part are affected by these voids [22]. Internal voids result in a weak binding force between the deposited materials and serve as sites of cracks initiation and growth

through the fabricated structure by FDM process. The crack nucleation and propagation are manifested with fiber breakage, fiber pull-out, and delamination [3]. The fracture mechanism in ABS samples is fiber breakage while glass fiber pullout seems to be the main fracture mechanism in GFPA6 specimens. Chopped glass fibers in GFPA6, owing to higher elastic modulus, carry the highest load on the specimen. Thus, fiber pull-out is dominant

Takahashi et.al [23] showed that fiber pull-outs in loading direction is the main failure mechanism in short fiber reinforced polymers. Furthermore, they found that the number of pulled out fibers increases with increasing temperature. This phenomenon can be used to describe the variation in tensile strength of GFPA6 where at elevated temperatures the matrix-reinforcement fiber bonding strength is decreased thus, more fibers are pulled out even under low axial loads. In contrast, at low temperature (here is -20 °C) more axial load needs to overcome the matrix-reinforcement fiber bonding strength.

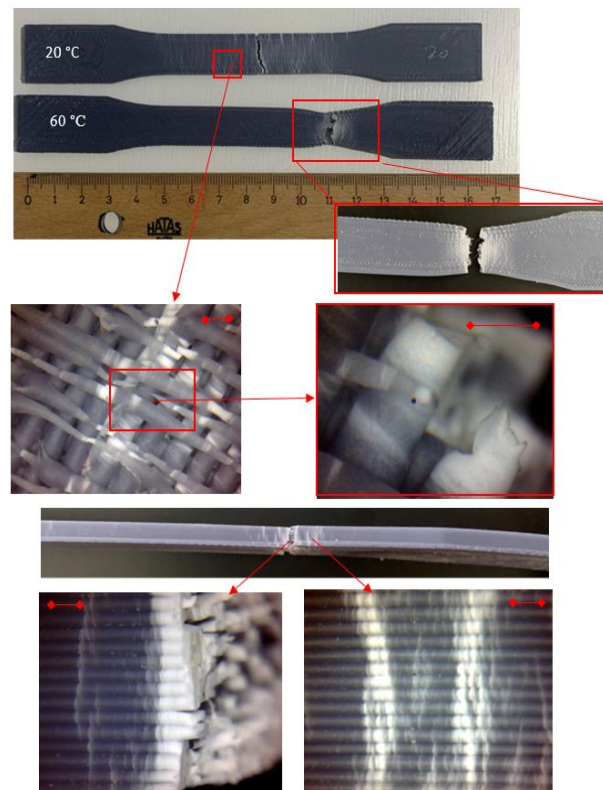


Figure 5. Optical images of ABS components after tensile test. Scale bar is 0.5 mm

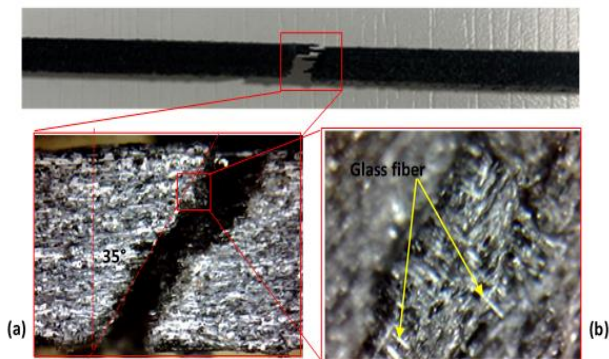


Figure 6. Optical images of GFPA6 component after the tensile test. The optic zoom is (a) 20X, (b) 400X

4. Conclusions

In this study, the effect of temperature on mechanical properties of 3D printed short glass fiber reinforced polyamide and ABS specimens under uniaxial tensile load were investigated experimentally. The fracture mode of the FDM printed composite samples was investigated using an optical microscope. Considering the experimental results the following conclusions were drawn from this work:

- Higher stiffness and strength up to 56% and 59% compare to ABS was obtained using glass fiber reinforced PA6.
- Both ABS and glass fiber reinforced PA6 specimens become stiffer at -20 C.
- At elevated temperatures, test specimens show a large deformation with a significant decline in tensile strength.
- For ABS, the breakage of the deposited filaments is the dominant failure mechanism.
- Reinforcement fiber pull-out was known as the dominant failure mechanism for GFPA6 material.

Declaration

The author declared no potential conflicts of interest with respect to the research, authorship, and/or publication of this article. The author also declared that this article is original, was prepared in accordance with international publication and research ethics, and ethical committee permission or any special permission is not required.

Author Contributions

H. Tanabi is responsible for all section of the study.

References


1. Dey A. and Yodo N. , *A systematic survey of FDM process parameter optimization and their influence on part characteristics*. Journal of Manufacturing and Materials Processing, 2019. 3(3).
2. Daminabo S.C., Goel S., Grammatikos S.A., Nezhad H.Y. and Thakur V.K., *Fused deposition modeling-based additive manufacturing (3D printing): techniques for polymer material systems*. Materials Today Chemistry, 2020. 16: p. 100248.
3. Mohammadzadeh M., Imeri A., Fidan I. and Elkelany M., *3D printed fiber reinforced polymer composites - Structural analysis*. Composites Part B, 2019. 175: p. 107112.
4. Mortazavian S. and Fatemi A., *Effects of fiber orientation and anisotropy on tensile strength and elastic modulus of short fiber reinforced polymer composites*. Composites Part B, 2015. 72: p. 116–129.
5. Tian X., Liu T., Yang C., Wang Q. and Li D., *Interface and performance of 3D printed continuous carbon fiber reinforced PLA composites*. Composites Part A: Applied Science and Manufacturing, 2016. 88: p. 198–205.
6. Justo J., Távora L. and París F., *Characterization of 3D printed long fibre reinforced composites*. Composite Structures, 2018. 185: p. 537–548.
7. Ning F., Cong W., Qiu J., Wei J. and Wang S., *Additive manufacturing of carbon fiber reinforced thermoplastic composites using fused deposition modeling*. Composites Part B: Engineering, 2015. 80: p. 369–378.
8. Li N., Li Y. and Liu S., *Rapid prototyping of continuous carbon fiber reinforced polylactic acid composites by 3D printing*. Journal of Materials Processing Technology, 2016. 238: p. 218–225.
9. Heidari-Rarani M., Rafiee-Afarani M. and Zahedi A.M., *Mechanical characterization of FDM 3D printing of continuous carbon fiber reinforced PLA composites*. Composites Part B: Engineering, 2019. 175: p. 107147.
10. Caminero M.A., Chacón J.M., García-moreno I. and Rodríguez G.P., *Impact damage resistance of 3D printed continuous fibre reinforced thermoplastic composites using fused deposition modelling*. Composites Part B, 2018. 148: p. 93–103.
11. Yasa E. and Ersoy K., *Dimensional Accuracy and Mechanical Properties of Chopped Carbon Reinforced Polymers Produced by Material Extrusion Additive Manufacturing*. Materials, 2019. 12(3885).
12. Yu S., Hyeong Y., Yeon J. and Hyung S., *Analytical study on the 3D-printed structure and mechanical properties of basalt fiber-reinforced PLA composites using X-ray microscopy*. Composites Science and Technology, 2019. 175: p. 18–27.
13. Attaran M., *The rise of 3-D printing: The advantages of additive manufacturing over traditional manufacturing*. Business Horizons, 2017. 60(5): p. 677–688.
14. Ngo T.D., Kashani A., Imbalzano G., Nguyen K.T.Q. and Hui D., *Additive manufacturing (3D printing): A review of materials, methods, applications and challenges*. Composites Part B: Engineering, 2018. 143: p. 172–196.
15. Azarov A. V, Antonov F.K., Golubev M. V, Khaziev A.R. and Ushanov S.A., *Composite 3D printing for the small size unmanned aerial vehicle structure*. Composites Part B, 2019. 169: p. 157–163.
16. Chen W. and Zhang Y., *Development and application of 3D printing technology in various fields*. Journal of Physics: Conference Series, 2019. 1303(1).
17. Moon S.K., Tan Y.E., Hwang J. and Yoon Y.J., *Application of 3D printing technology for designing light-weight unmanned aerial vehicle wing structures*. International Journal of Precision Engineering and Manufacturing - Green Technology, 2014. 1(3): p. 223–228.
18. Tymrak B.M., Kreiger M. and Pearce J.M., *Mechanical properties of components fabricated with open-source 3-D printers under realistic environmental conditions*. Materials and Design, 2014. 58: p. 242–246.

19. Torrado A.R., Shemelya C.M., English J.D., Lin Y., Wicker R.B. et al, *Characterizing the effect of additives to ABS on the mechanical property anisotropy of specimens fabricated by material extrusion 3D printing*. Additive Manufacturing, 2015. **6**: p. 16–29.
20. Cantrell J., Rohde S., Damiani D., Gurnani R., Disandro L. et al, *Experimental Characterization of the Mechanical Properties of 3D Printed ABS and Polycarbonate Parts*. 2017. **3**: p. 89–105.
21. Wang J., Xie H., Weng Z., Senthil T. and Wu L., *A novel approach to improve mechanical properties of parts fabricated by fused deposition modeling*. Materials and Design, 2016. **105**: p. 152–159.
22. Wang X., Zhao L., Ying J. and Fuh H., *Effect of Porosity on Mechanical Properties of 3D Printed Polymers: Experiments and Micromechanical Modeling Based on X-ray Computed Tomography Analysis*. Polymers (Basel), 2019. **11**(7): p. 1154.
23. Takahashi R., Shohji I., Seki Y. and Maruyama S., *Mechanical Properties of Short Fiber-Reinforced*. In: International Conference on Electronics Packaging (ICEP). JIEP, Toyama, pp 778–781.



e-ISSN: 2618-575X

INTERNATIONAL ADVANCED RESEARCHES
and
ENGINEERING JOURNAL

Journal homepage: www.dergipark.org.tr/en/pub/iarejInternational
Open Access Volume 05
Issue 02

August, 2021

Research Article

Investigation of friction performance and surface integrity of cryogenically treated AISI 430 ferritic stainless steel

Şenol Şirin ^{a,*}  and Sıtkı Akıncioğlu ^a 

^aDüzce University, Department of Machine and Metal Technologies, Gumusova Vocational School, Düzce, 81850, Turkey

ARTICLE INFO*Article history:*

Received 13 January 2021

Revised 09 February 2021

Accepted 21 February 2021

Keywords:

AISI 430 ferritic stainless steel

Ball-on-disk test

Friction coefficient

Shallow cryogenic treatment

ABSTRACT

In this study, the effect of shallow cryogenic treatment on the friction coefficient of AISI 430 ferritic stainless steel was investigated. The friction coefficient experiments were carried out in a ball-on-disc wear tester under 5 N load at 400 rpm. As a result of the tests, the study examined the surface topography of the wear traces, the abrasion profile, microscopic images of the wear traces, and the hardness change of the wear traces. After applying shallow cryogenic treatment, the friction coefficient of the samples was increased by 7.5%. The micro hardness value around the wear traces of the cryogenic (Cryo) samples was 28.4% higher than the value for the commercial samples. The width of the wear trace of the Cryo samples was reduced by 44%. The average roughness value of the wear trace was 33.3% improved in the Cryo sample compared to the commercial sample.

© 2021, Advanced Researches and Engineering Journal (IAREJ) and the Author(s).

1. Introduction

Mechanical components used in various fields can be exposed to both mechanical wear and corrosion at the same time [1]. Because of features such as high corrosion and wear resistance as well as their attractive appearance, stainless steels are widely preferred and used in many sectors. Stainless steels generally contain iron, chromium, and nickel and due to the chromium, they exhibit resistance to corrosion [2,3]. Stainless steels, known as corrosion-resistant steels in the aviation industry, appeal to a wide milieu, ranging from the food industry to the chemical industry, and from nuclear applications to the machinery sector [4]. Stainless steel materials can be classified in five different groups according to their chemical and crystal structures: austenitic, ferritic, martensitic, duplex, and precipitation hardening stainless steels. Ferritic stainless steels stand out compared to other stainless steels due to their low cost / high benefit ratio. Because of the high chromium content in ferritic stainless steels, they exhibit very high corrosion resistance, and their iron content renders them magnetic [5]. The most widely known grades of ferritic stainless steels are AISI

430 and AISI 442. In applications where corrosion and wear occur simultaneously, mechanical friction caused by plastic deformation leads to unwanted wear on the material surface [6].

In recent years, cryogenic treatment (-80 °C ~ -196 °C) has been frequently used to improve the wear resistance, toughness, and hardness of the materials [7]. Different gases (nitrogen, helium, oxygen, neon, etc.) are used in cryogenic treatments, which can be classified as deep cryogenic treatment (-140 °C ~ -196 °C) and shallow cryogenic treatment (-80 °C ~ -140 °C) [8]. As a result of studies conducted, the residual austenite in the microstructure of steels is known to transform into martensite under cryogenic treatment. The wear resistance in the steel increases because of this transformation. For example, in his study, Akıncioğlu [3] stated that shallow cryogenic treatment significantly boosted the material wear resistance, hardness, and electrical conductivity of AISI 410 stainless steel. Moreover, cryogenic treatment application is seen in many fields such as space and aviation research, in food storage, and in the transportation sector [9]. Studies performed by applying cryogenic treatment are mentioned below.

* Corresponding author. Tel.: +90 380 731 20 45; Fax: +90 380 731 31 24.

E-mail addresses: senolsirin@duzce.edu.tr (Ş. Şirin), sitkiakincioglu@duzce.edu.tr (S. Akıncioğlu)

ORCID: 0000-0002-3629-9003 (Ş. Şirin), 0000-0003-4073-4837 (S. Akıncioğlu)

DOI: 10.35860/iarej.859730

This article is licensed under the CC BY-NC 4.0 International License (<https://creativecommons.org/licenses/by-nc/4.0/>).

Kızılkaya and Ovalı conducted a series of experiments to determine the mechanical properties of AISI 4140 steel using shallow cryogenic treatment. In this context, they prepared five different samples that were poured and cured, and then cryogenic treatment was applied for 2 h, 4 h, and 6 h after the treatment. First, the notch impact test was performed on the prepared samples, and then abrasive wear tests (pin-on-disk) were applied at three different loads (5 N, 10 N, and 15 N) and at three different sliding distances (95 m, 190 m, and 285 m). At the end of their experimental work, the researchers obtained the lowest wear rate in the sample that was cryogenically treated for 6 h. They achieved the maximum friction coefficient by applying a force of 5 N on the sample that had been cryogenically treated for 6 h [10]. Şirin et al. applied shallow cryogenic treatment to AISI 430 ferritic stainless steel at different holding times and investigated the effect on mechanical properties. Tensile strength tests were applied to four different samples cryogenically treated for 0 h, 6 h, 12 h, and 24 h. They reached the maximum tensile strength (455 N/mm²) with the samples that were treated for 24 h [11]. In his thesis, Yamanoğlu [12] examined the abrasive wear resistance of DIN 1.2379 and DIN 1.2080 cold work tool steels subjected to deep cryogenic treatment at -140 °C. The study included commercial, quenched, quenched + cryogenically treated, and quenched + tempered cold work tool steels. The 12-h deep cryogenic (-140 °C) treatment was the most desirable. According to the test results, he claimed that the wear resistance was dependent on the load and the amount of wear and that the lowest wear loss was found at a 10-N load in the quenched + cryogenically treated samples. Akıncioğlu [3] investigated the effect of shallow cryogenic treatment on the microstructure, hardness, and electrical conductivity of AISI 410 stainless steel. In this context, shallow cryogenic (-80 °C) treatment was applied to AISI 410 stainless steel samples for 24 h, 48 h, 72 h, and 96 h. The researcher claimed that the hardness value of the 96-h sample had increased by 4% and the electrical conductivity by 300% compared to the commercial (untreated) sample. Sert [13] investigated the changes in the microstructure and tribological properties of AISI M2 tool steel subjected to different heat treatment applications. In the experiment, three different samples were used: quenched + tempered, quenched + deep cryogenically treated + tempered, and quenched + tempered + deep cryogenically treated + tempered. It was stated that the carbide grain size and distribution in the microstructure were better in the deep

cryogenically treated samples. According to the tribology test results, it was stated that the wear rate and friction coefficients of the cryogenically treated samples were lower than for the other samples.

A review of the literature yielded a number of studies investigating the mechanical and tribological characteristics of various materials following cryogenic treatment. These studies concluded that the microstructure, hardness, friction coefficient, etc. were improved in shallow or deep cryogenically treated material [14]. However, to date, no study had been carried out to examine the total effects of shallow cryogenic treatment on AISI 430 ferritic stainless steel in terms of the friction coefficient. In addition, the surface quality and topography of the wear traces on this steel had not been adequately studied. Accordingly, this study investigated the friction coefficient, surface quality, and wear trace topography of shallow cryogenically treated AISI 430 ferritic stainless steel.

2. Material and Methods

In the experiments, 40 × 60 × 4-mm samples of AISI 430 ferritic stainless steel (EN 1.4016, Nom. X6Cr17) were used. Tables 1 and 2, respectively, give the chemical composition of the test samples and the mechanical properties of AISI 430.

Pre-experiment samples were prepared as untreated (Commercial) and cryogenically treated for 24 h (Cryo). The shallow cryogenic treatment was applied to the Cryo samples in the cryogenic treatment unit (Figure 1-a) at a 24-h holding time. During the treatment, in order to prevent unwanted micro cracks in the AISI 430 ferritic stainless steel, the samples were gradually brought to -80 °C and at the end of the treatment, gradually returned to room temperature. The Turkeyus ball-on-disc tribometer (Figure 1-b) was used to determine the friction coefficient. For the experiments, Ø6-mm DIN 100Cr6 balls were selected and a new ball was used in each experiment.

The tests were performed on the ball-on-disk friction tester according to the ASTM G99-05 standard, at room temperature (23 °C), a constant 20-mm trace diameter, under 5 N load and 6 Hz sampling frequency, and at a speed of 418.9 m/min.

Table 1. Chemical composition of AISI 430 ferritic stainless steel test samples [11]

C	Si	Mn	Cr	Ni	Mo	Al	Balance
0.046	0.25	0.44	17.1	0.15	0.18	0.01	Fe

Table 2. Mechanical properties of AISI 430 ferritic stainless steel at room temperature [15]

Density	Elastic Module	Tensile Strength	Yield Strength	Elongation	Hardness
(g/cm ³)	(GPa)	(MPa)	(MPa)	(%)	(HV)
7.8	200	459	373	22	162

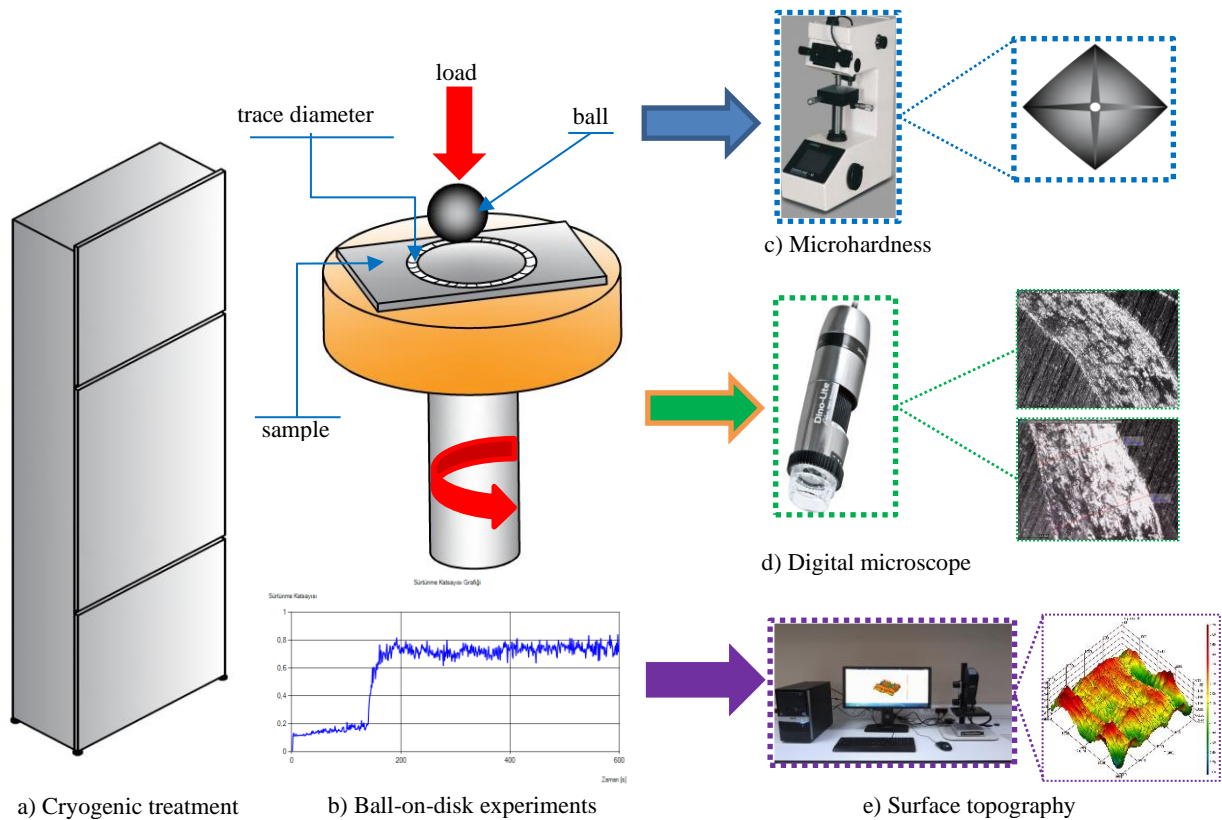


Figure 1. Experimental setup: a) Cryogenic treatment, b) Ball-on-disc experiments, c) Microhardness measurement, d) Wear trace width measurement, e) Surface topography measurement

Before and after the test, the samples were cleaned with an ethyl alcohol solution and dried.

After the friction tests, 10 microhardness measurements were taken at distances starting at $50\ \mu\text{m}$ from the wear trace and moving towards the outer edge of the material. Microhardness measurements, at a test load determined as 100 g and a dwell-time of 19 s, were carried out using the Metkon DUROLINE M microhardness tester (Figure 1-c). Before the hardness measurements, the device was calibrated with a measuring block gauge and the average of measurements from three different points was used. The Dino-Lite AM7915MZT digital microscope (Figure 1-d) was used for the analysis of wear traces and determination of wear trace widths. Before carrying out the measurements, accuracy was ensured by calibrating the instrument with a digital microscope calibration gauge. The Phase View surface topography device (Figure 1-e) was used for the three-dimensional examination of the deterioration in the wear traces. The same wear trace sections were examined in all samples. The experimental setup and equipment used in the experiments are given in Figure 1.

3. Results and Discussion

3.1. Evaluation of average friction coefficient

The friction coefficient test was carried out under a constant load of 5 N at a speed of 400 rpm. The results obtained depending on the test period are given in Figure

2. The figure shows that the average friction coefficient varied depending on the time. A higher coefficient of friction was obtained in the Cryo samples compared to the non-treated Commercial samples.

It is thought that the friction coefficients increased because of the increased toughness and hardness of the cryogenically treated samples [15]. Especially after 100 s, the peak trend for the friction coefficient was observed in both test samples. The friction coefficient of the Commercial samples was determined as 0.587 after the ball-on-disc friction coefficient experiments. The Cryo sample friction coefficient increased by 18.25% compared to Commercial samples. Meng et al. applied cryogenic treatment to Fe-12Cr-Mo-V-1,4C tool steel at -50 and $-180\ ^\circ\text{C}$ [16]. It was concluded that the most important factor contributing to the increase in wear resistance was the reduction of residual austenite and the formation of a homogeneous martensitic structure resulting from the cryogenic treatment. Similar findings were obtained in our study. The increase in the friction coefficient in the Cryo samples can be explained by the transformation of residual austenite to martensite.

Plastic deformation of metals occurs when dislocations progress through the crystalline structure. Dislocations are defined as linear defects within the microstructure. The strength, hardness, and mechanical properties of metals are explained by the density of dislocations in the microstructure and the interaction of dislocations with

other defects. Tyshchenko et al. [17] reported that with cryogenic treatment, plastic deformation occurred during martensitic transformation in tool steel. They found that the plastic deformation caused the carbide particles to partially dissolve. This plastic deformation captured stationary carbon atoms by moving dislocations, providing a suitable environment for the nucleation of new η -carbide particles. Deformation hardening occurs as a result of the interaction of dislocations with each other and various obstacles that make the movement of the dislocations difficult [18]. Any factor that makes the movement of dislocations in the microstructure of metals difficult will lead to an increase in the strength of the material. It can be said that the friction coefficient of the Cryo samples was increased due to the deformation hardening caused by the cryogenic treatment.

3.2. Evaluation of the microhardness

In order to determine the change in micro hardness, measurements were taken at distances around the wear traces formed as a result of the wear tests. The changes in micro hardness depending on the measured distances are given in Figure 3. Hardness values were measured higher close to the wear trace at a distance of 50- μm . Moving away from the wear trace, the hardness values decreased,

and the lowest hardness values were reached at a distance of 500 μm , as the farthest point from the wear trace. It can be said that this hardness increase resulted from the wear trace and the material trapped around it due to the wear load.

Hardness values of the Commercial and Cryo samples at a distance of 50 μm from the wear trace were measured as 321.8 HV and 230.1 HV, respectively. The hardness increase around the wear trace of the Cryo sample was 28.4%. The hardness change rate of the Cryo sample between 50 μm and 500 μm (181.4 HV) was 43.6%. Plastic deformation applied to metals in the cold deformation zone leads to deformation hardening. Cold deformation occurs at temperatures lower than half the melting temperature of the metals (usually at room temperature). The deformation process in this temperature range causes strain hardening in the metallic structure. Kalsi et al. [19] investigated the effect of cryogenic treatment and stated that it increased the hardness of many steels. Yang et al. [20] found that the hardness of 13Cr2Mn2 V high chromium white iron samples was increased by deep cryogenic treatment. The increased hardness was attributed to the transformation of residual austenite into martensite and to the increased secondary carbides precipitated in the matrix.

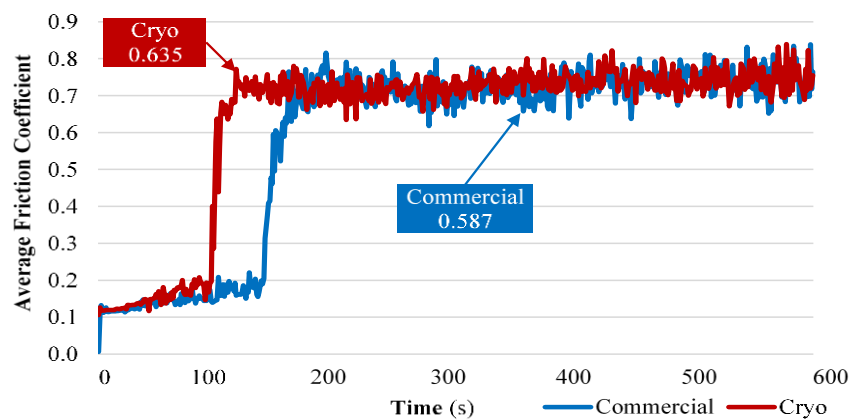


Figure 2. Change in friction coefficient depending on time

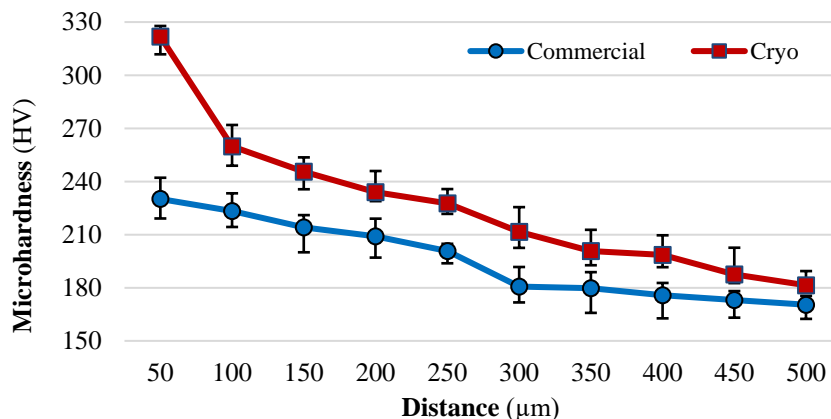


Figure 3. Change in micro hardness depending on measuring distance

Akhbarizadeh et al. [21] attributed the increase in the hardness of D6 steel to the homogeneous carbide distribution and high chromium carbon concentration as a result of deep cryogenic treatment. Benseley et al. [22] found that the hardness of En353 steel increased 3.48% after deep cryogenic treatment. They explained that the increase in hardness was caused by the residual austenite transformed into martensite. They concluded that cryogenic treatment applied to steels generally affects the hardness positively. The increase in hardness was largely explained by the conversion of residual austenite into martensite, and the precipitation of carbides that were homogeneously distributed throughout the microstructure.

In this study, the hardness increase occurring as a result of shallow cryogenic treatments was realized by the more regular microstructure formed in the AISI 430 ferritic stainless steel.

The width of the wear traces of the samples can be seen in Figure 4, which shows that the wear traces in the Cryo samples are narrow. The wear trace width of the Cryo samples decreased by 44% compared to the Commercial samples. This can be attributed to the change in the microstructure and the increase in hardness of the samples after shallow cryogenic treatment. This can be explained by the cold hardening that occurred when rolling pressure was applied to the samples under friction. Akhbarizadeh et al. found that the increase of hardness in D6 steel Cryo samples was caused by the formation of a homogeneous microstructure and the decrease of austenite [21]. With cryogenic treatment at low temperatures, the austenite and martensite lattice structure shrinks. This constriction forces the carbon atoms to dissolve. New carbides are produced at higher temperatures, leading to a more homogeneous distribution of carbides [16, 23].

3.3. Evaluation of worn surface characteristics

Figure 5 shows microscope images of the wear traces obtained after the ball-on-disc wear tests of the AISI 430

ferritic stainless steel. Deflections and pits can be seen in these images. Deflections are more pronounced in the Commercial sample. The traces are slighter and more homogeneous in the Cryo samples. This can be attributed to the higher friction coefficient and hardness values of the shallow cryogenically treated samples. Meng et al. [16] explained that the rate of wear can be controlled by controlling the crack nucleation under the surface, which is related to the strength and toughness of the materials. Residual austenite can prevent crack propagation by changing the growth direction of a progressive crack or by largely absorbing the energy. Cryogenic treatment is known to promote corrosion resistance because of the precipitation of fine η -carbides rather than because the retained austenite was removed.

The surface topography of the wear traces formed after wear tests of the AISI 430 ferritic stainless steel was examined. The surface topography images of the Commercial sample (Figure 6-a) show that the trace profile has a more pitted surface. This situation coincides with the formation of debris observed in the microscopic images of the traces (Figure 5). The low hardness values of the Commercial samples caused more wear. In addition, their softer structure compared to the Cryo samples caused the formation of deflections and pits on the worn surfaces. The trace profile was relatively smoother in the Cryo samples. Shallower wear traces can be seen in the Cryo samples compared to the Commercial samples [21]. The R_a values found for the wear traces of the Commercial and Cryo samples were measured as $0.4012 \mu\text{m}$ and $0.2678 \mu\text{m}$, respectively. The wear trace average roughness value of the Cryo sample was 33.3% improved over the Commercial sample. This result can be attributed to the harder, homogeneous microstructure of the samples because of the shallow cryogenic treatment.

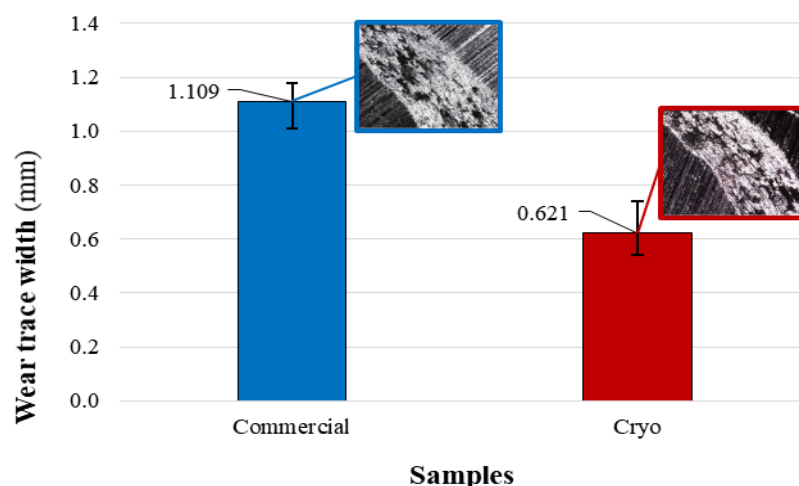


Figure 4. Change in wear trace width after the experiment

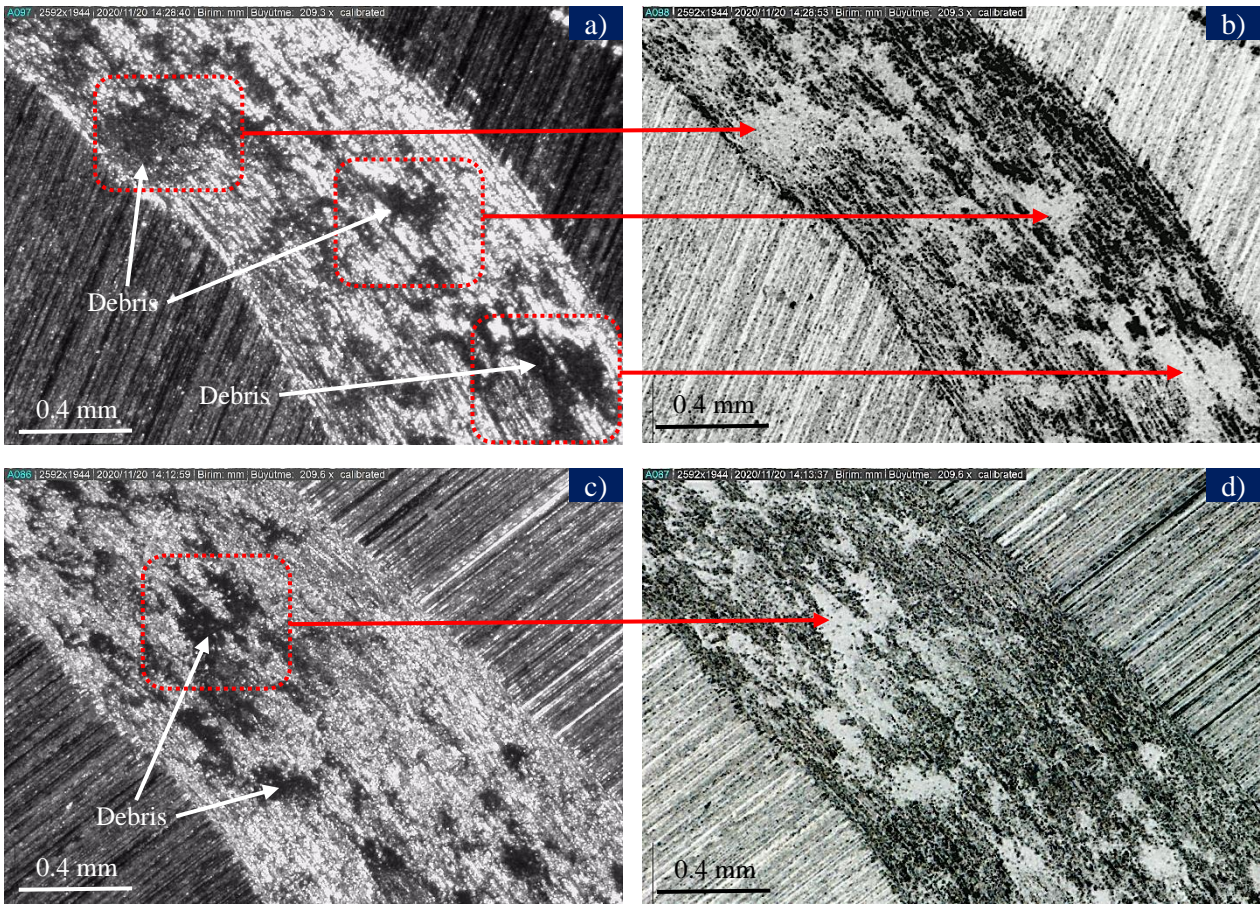


Figure 5. AISI 430 ferritic stainless steel surface photos after wear tests: a) Commercial, b) Commercial (negative photo), c) Cryo, d) Cryo (negative photo)

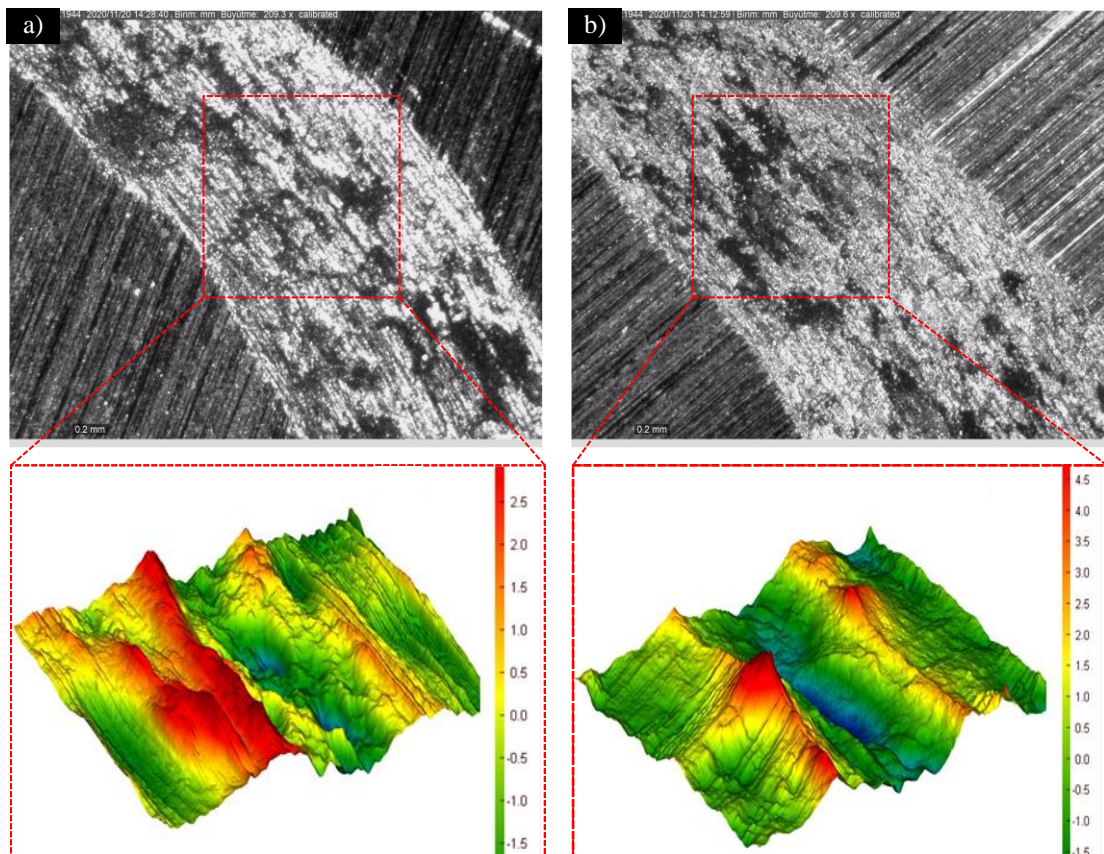


Figure 6. Wear trace topography: a) Commercial sample, b) Cryo sample

4. Conclusions

The study investigated the effects of the shallow cryogenic treatment on the friction coefficient, microhardness, and surface wear of the AISI 430 ferritic stainless steel and the following results were obtained.

- A higher friction coefficient was obtained in the Cryo samples than in the Commercial samples. The friction coefficients were determined as 0.635 and 0.587 in the Cryo and Commercial samples, respectively.
- The *Ra* values of the Commercial and Cryo samples were measured as 0.4012 μm and 0.2678 μm , respectively. The wear trace roughness of the Cryo sample was improved by 33.3% compared to the commercial sample.
- Wear traces were more pronounced in the Commercial samples. The traces were more homogeneous and there were fewer depressions in the Cryo samples.
- The shallow cryogenic treatment reduced the wear trace width on the AISI 403 stainless steel. The wear trace width of the shallow cryogenically treated Cryo samples was reduced by 44% compared to the Commercial samples.
- Hardness values decreased as the distance away from the wear trace increased. The hardness increase around the Cryo sample wear traces was 28.4% higher than for the Commercial samples.
- It was concluded that a positive contribution had been made by the shallow cryogenic treatment in terms of the mechanical properties of the AISI 430 ferritic stainless steel.
- In further studies on AISI 430 ferritic stainless steel, the effect of shallow cryogenic treatment applied at different temperatures and different waiting times can be investigated.

No in-depth studies had yet been conducted on the friction performance of shallow cryogenically treated AISI 430 ferritic stainless steel, as investigated in this study. Additionally the aim of this study was to provide a contribution to the literature in the form of a comprehensive study of the surface integrity of AISI 430 ferritic stainless steel after wear testing.

Declaration

The authors declare that they have no potential conflicts of interest with respect to the research, authorship, and/or publication of this article. The authors also declare that this article is original and was prepared in accordance with international publication and research ethics, and that no ethical committee or special permission was required.

Author Contributions

Ş. Şirin: Conceptualization, Investigation, Resources, Methodology, Writing - editing. S. Akıncıoğlu: Writing -

review, Validation, Software, Data curation, Supervision.

References

1. Labiapari, W.S., Ardila, M.A.N., Costa, H.L. and de Mello, J.D.B., *Micro abrasion-corrosion of ferritic stainless steels*. Wear, 2017. **376**: p. 1298-1306.
2. Mermi, G. 2012. *Paslanmaz çelik malzemenin iç mimari uygulamalarında sürdürülebilirlik açısından değerlendirilmesi*. Yüksek Lisans Tezi, Haliç Üniversitesi, Fen Bilimleri Enstitüsü, **85s**, İstanbul.
3. Akıncıoğlu, S., *Sığ kriyojenik işlemin AISI 410 paslanmaz çeliğin fiziksel özelliklerine etkisinin araştırılması*. Düzce Üniversitesi Bilim ve Teknoloji Dergisi, 2019. **7**(3): p. 985-993.
4. Çelik, E., Kıvak, T. ve Şirin, Ş., *Dubleks paslanmaz çeliğin farklı soğutma/yağlama yöntemleri altında tornalanmasında kesme sıcaklığının optimizasyonu*. in ISMS2019: Ankara. p. 15-17.
5. Pekşen, H. 2020. *AISI 430 paslanmaz çeliğinin işlenebilirliğinin deneysel olarak incelenmesi*. Yüksek Lisans Tezi, Karabük Üniversitesi, Fen Bilimleri Enstitüsü, **78s**, Karabük.
6. Landolt, D., Mischler, S., Stemp, M. and Barril, S., *Third body effects and material fluxes in tribocorrosion systems involving a sliding contact*. Wear, 2004. **256**(5): p. 517-524.
7. Çiçek, A., Kara, F., Kıvak, T. and Ekici, E., *Evaluation of machinability of hardened and cryo-treated AISI H13 hot work tool steel with ceramic inserts*. International Journal of Refractory Metals and Hard Materials, 2013. **41**: p. 461-469.
8. Akıncıoğlu, S., Gökkaya, H. and Uygur, İ., *The effects of cryogenic-treated carbide tools on tool wear and surface roughness of turning of Hastelloy C22 based on Taguchi method*. The International Journal of Advanced Manufacturing Technology, 2016. **82**(1-4): 303-314.
9. Sundaram, M.M., Yıldız, Y. and Rajurkar K.P., *Experimental study of the effect of cryogenic treatment on the performance of electro discharge machining*. in MSEC2009: Indiana, USA. p. 4-7.
10. Kızılkaya, E. and Ovalı, İ., *AISI 4140 çeliğine uygulanan sığ kriyojenik işleminin mekanik özellikler üzerindeki etkisi*. Gazi Üniversitesi Fen Bilimleri Dergisi Part C: Tasarım ve Teknoloji, 2018. **6**(1): p. 137-148.
11. Şirin, Ş., Akıncıoğlu, S. and Gül, H., *Kriyojenik işlem zamanının AISI 430 çeliğinin mekanik özelliklerine etkisi*. İleri Teknoloji Bilimleri Dergisi, 2018. **7**(3): p.66-71.
12. Yamaoğlu, O. 2015. *Soğuk iş takım çeliklerinin aşınma direnci üzerinde kriyojenik işlemin etkisi*. Yüksek Lisans Tezi, Fen Bilimleri Enstitüsü, Gazi Üniversitesi, **97s**, Ankara.
13. Sert, A., *AISI M2 takım çeliğinin mikroyapısı ve mekanik davranışları üzerine derin kriyojenik ısıtma işleminin ve temperlemenin etkisi*. Dokuz Eylül Üniversitesi Mühendislik Fakültesi Fen ve Mühendislik Dergisi, 2020. **22**(66): p. 801-811.
14. Baldissera, P., *Deep cryogenic treatment of aisi 302 stainless steel: Part I-hardness and tensile properties*. Materials & Design, 2010. **31**(10): p. 4725-4730.
15. Akıncıoğlu, S., Gökkaya, H. and Uygur, İ., *A review of cryogenic treatment on cutting tools*. The International Journal of Advanced Manufacturing Technology, 2015. **78**(9-12): p. 1609-1627.
16. Meng, F., Tagashira, K., Azuma, R. and Sohma, H., *Role of*

- eta-carbide precipitations in the wear resistance improvements of Fe-12Cr-Mo-V-1.4 C tool steel by cryogenic treatment.* ISIJ international, 1994. **34**(2): p. 205-210.
17. Tyshchenko, A.I., Theisen, W., Oppenkowski, A., Siebert, S., Razumov, O. N., Skoblik, A.P., Sirosh, V.A., Petrov, Yu.N. and Gavriljuk, V.G., *Low-temperature martensitic transformation and deep cryogenic treatment of a tool steel.* Materials Science and Engineering: A, 2010. **527**(26), p. 7027-7039.
 18. Li, S., Deng, L., Wu, X., Wang, H., Min, Y. and Min, N., *Effect of deep cryogenic treatment on internal friction behaviors of cold work die steel and their experimental explanation by coupling model.* Materials Science and Engineering: A, 2010. **527**(29-30): p. 7950-7954.
 19. Kalsi, N.S., Sehgal, R. and Sharma, V.S., *Cryogenic treatment of tool materials: a review.* Materials and Manufacturing Processes, 2010. **25**(10): p. 1077-1100.
 20. Yang, H.S., Jun, W., Bao-Luo, S., Hao-Huai, L., Sheng-Ji, G. and Si-Jiu, H., *Effect of cryogenic treatment on the matrix structure and abrasion resistance of white cast iron subjected to destabilization treatment.* Wear, 2006. **261**(10): p. 1150-1154.
 21. Akhbarizadeh, A., Shafyei, A. and Golozar, M.A., *Effects of cryogenic treatment on wear behavior of D6 tool steel.* Materials & Design, 2009. **30**(8): p. 3259-3264.
 22. Bensely, A., Prabhakaran, A., Lal, D.M. and Nagarajan, G., *Enhancing the wear resistance of case carburized steel (En 353) by cryogenic treatment.* Cryogenics, 2005. **45**(12): p. 747-754.
 23. Molinari, A., Pellizzari, M., Gialanella, S., Straffelini, G. and Stiasny, K.H., *Effect of deep cryogenic treatment on the mechanical properties of tool steels.* Journal of materials processing technology, 2001. **118**(1-3): p. 350-355.

**Research Article**

Water absorption parameters of glass/epoxy composites based on dimension effect

Zeynal Abidin Oğuz ^{a,*} , and Ahmet Erklığ ^b 

^aGeneral Directorate of State Hydraulic Works, 02040, Adiyaman, Turkey

^bDepartment of Mechanical Engineering, Gaziantep University, Gaziantep 27310, Turkey.

ARTICLE INFO*Article history:*

Received 08 February 2021

Revised 10 March 2021

Accepted 24 March 2021

Keywords:

Distilled water

Hydrothermal aging

Sea water

S-glass/epoxy

ABSTRACT

In this study, the water uptake parameters of S glass/epoxy samples have been assessed experimentally. The glass/epoxy specimens were manufactured by the vacuum assisted resin transfer method (VARIM) have been kept in distilled water and sea water at 25°C and 70°C temperatures for 1000 hours in a hydrothermal aging cabin. The water gain behavior of samples with different length/width (L/w) ratios has been investigated based on criteria such as different water types and different temperatures. Furthermore, the water uptake trend of samples has been assessed analytically based on the Fick's law in addition to the experimental method. The results have shown that the L/w ratio, water type, and temperature have an important influence on the water gain character of glass/epoxy composites. The experimental weight measurements showed that temperature increase was caused to more water absorption in both water types. Furthermore, it was noted the increase in L/w ratio was caused to more water sorption. Moreover, experimental and analytical results have shown that water intake trends consistent in both methods.

© 2021, Advanced Researches and Engineering Journal (IAREJ) and the Author(s).

1. Introduction

Compared to traditional materials, superior features, for example, high specific strength, high specific stiffness, well corrosion resistance, excellent resistance to chemical attack have increased the interest in composite materials [7,22,23]. However, the high water absorption disadvantage of composite materials compared to traditional materials has led researchers to work on the hydrothermal, hygrothermal aging issues. Many studies have been looked into the water intake character of composite materials, as the water molecules absorbed by the polymer composites play a plasticizer role and disrupt the fiber/resin structure and cause deterioration of the fiber/matrix interface.

The effect of hydrothermal/hygrothermal aging on the mechanical characteristics of composites has been studied extensively in the literature. However, researches on the water gain character based on dimension effect is limited.

In this section, the information will be given about similar studies that can be associated with this study.

Boukhoulda et al. [1] studied the moisture gain behavior of glass/polyester samples experimentally and theoretically. Composite samples were kept in hygrothermal conditions with 50°C temperature and 95% relative humidity for 289 days. The moisture gain trend of glass/polyester composites was evaluated according to the Carter-Kibler's model and Fick's law, in addition to experimental study. It was found that Carter-Kibler's model showed excellent accordance with experimental results for this study. Also, the maximum moisture gain ratio of glass/polyester composites was found above 0.7%. Abdel-Magid et al. [2] investigated the aging performance of the E-glass/epoxy samples in hydrothermal conditions. Composites were immersed in distilled water 25°C and 65°C for 500, 1000, and 3000 hours. It was found that an increment in temperature and aging period was caused to an increase in the water intake ratio of composite samples. The maximum weight gain ratio was found as 0.9% and

* Corresponding author. Tel.: +90-416-216-4312 (7162); Fax: +90-416-216-9853.

E-mail addresses: oguzzeynal02@gmail.com (Z. A. Oğuz), erklig@gantep.edu.tr (A. Erklığ)

ORCID: 0000-0002-8566-2331 (Z. A. Oğuz), 0000-0003-3906-3415 (A. Erklığ)

DOI: 10.35860/iarej.875841

This article is licensed under the CC BY-NC 4.0 International License (<https://creativecommons.org/licenses/by-nc/4.0/>).

1.73% for 500 hours and 1000 hours aging period, respectively at room temperature. Furthermore, the maximum weight gain ratio of samples immersed at 65°C for 3000 hours was found as 7.8%.

Soykok et al. [3] analyzed the aging period and temperature effects on the water sorption character of glass fiber/epoxy composite experimentally. Samples were immersed in water at 50°C, 70°C, and 90°C temperatures for 168 and 336 hours. Moisture uptake ratios did not change with increasing time for 50°C and 70°C temperatures, although the moisture uptake ratio of composites aged at 90°C increased with an increasing aging period. The maximum moisture gain ratios of specimens immersed at 50°C and 70°C were reported as 0.31% and 0.71%, respectively. Also, the maximum moisture ratios of specimens immersed at 90°C were found as 0.76% and 0.97% for 168 and 336 hours aging periods, respectively.

Jiang et al. [4] investigated the hydrothermal/hydrothermal character of the different parts of the bridge deck was manufactured by glass-fiber-reinforced polymer composite. Composite parts immersed in two different hydrothermal aging condition with 50% and 96% relative humidity at 20°C and 40°C. Further, specimens were kept in water at 20°C and 40°C. The aging period was limited to 24 days for this study. Researchers observed that the maximum moisture uptake ratios and aging behavior of different parts of the glass-fiber-reinforced bridge deck were changed with varied aging conditions and temperature. It was noticed that increased humidity and temperature led to more water absorption. Besides, samples aged in a hydrothermal environment absorbed more moisture than samples aged in a hydrothermal environment.

Jiang et al. [5] assessed the shape factor on the water sorption parameters of the sandwich FRP composite deck. Samples with square and rectangular shapes were exposed to hydrothermal and hydrothermal environments with different temperatures and relative humidity degree. At the end of 250 days immersing time, researchers observed that the maximum water gain ratio of square samples kept in water (20°C) and 50% relative humidity (20°C) was bigger than rectangular samples. However, it was found that the maximum water gain ratio of square samples kept in water (40°C) and 96% relative humidity (40°C) was smaller than rectangular samples.

Chakraverty et al. [6] investigated the water sorption character of the glass fiber reinforced epoxy (GRE) samples by using hydrothermal and hydrothermal aging conditions. The E-glass/epoxy composites were aged in distilled water at 65°C for 120 days and exposed to hydrothermal condition with 95% relative humidity at 60°C for 90 days. Similar water sorption tendencies were noticed for both hydrothermal and hydrothermal aging

conditions. The maximum water intake ratios were found as 1.642% and 1.682% for hydrothermal and hydrothermal aging conditions, respectively.

The effect of aging in sea water and distilled water on the water uptake character of glass/vinyl ester samples was investigated by Larbi et al. [21]. Composite samples aged at 40°C in both water types. It was revealed the sea water absorption rate of composites kept in sea water was higher than composites kept in distilled water. Maximum water gain ratios of samples were nearly 1.3% and 0.8% for sea water and distilled water aging, respectively.

Mourad et al. [8] assessed the hydrothermal aging influence of the glass composites by using different resin systems. Glass/epoxy and glass/polyurethane composite samples aged in sea water at 25°C and 65°C for 12 months. The weight gain rate of both composite groups was recorded to increase as the aging period increased. The maximum water gain ratios were found as 2.5% and 5% for glass/epoxy samples aged at 25°C and 65°C, respectively. Further, the maximum water gain ratios were found as 3.2% and 4.7% for glass/polyurethane composites aged at 25°C and 65°C, respectively.

Bulut et al. [20] investigated the influence of nano-particle inclusion on the mechanical, thermal, and water intake behavior of intraply carbon/aramid samples. It was reported from the study the inclusion of nano-silica and nano-clay was caused to more water absorption.

In summary, since the water/moisture absorbed by composite materials disrupts the structure of the fiber/resin system, many studies have been conducted by researchers on how much water/moisture composites absorb in different environments. In these studies, many ideas have been developed on criteria such as water types, temperature, and aging time. However, these criteria have not been studied based on the dimension effect in the literature. Furthermore, it is essential to examine water absorption behavior in order to guess not only the outcomes of the water absorbed, but also how to minimize water sorption. Hence, the hydrothermal aging effect on the glass/epoxy composites based on dimension effect has been evaluated in this study. Two composite groups with different L/w (length/width) ratios were exposed to distilled water and sea water for 1000 hours. The water absorption behavior results of glass/epoxy composites were evaluated with criteria such as temperature and water type based on L/w ratio.

2. Materials and Procedures

2.1 Materials

In this study, plain woven S-glass fabric, with an areal density of 202 g/m², was used as a reinforcement phase in the composite. Also, an epoxy MGS L 285 resin with MGS H 285 hardener was used as a matrix system. The properties of reinforcements and resin systems are

illustrated in Table 1 and Table 2, respectively. The reinforcement materials were provided from Dost Kimya, Istanbul, Turkey.

2.2 Manufacturing Process

The vacuum assisted resin infusion method (VARIM) was used to create the composite specimens in this study. The composite samples were fabricated at laboratory conditions by twelve ply laminates of plain-woven glass fabrics. The resin/curing agent ratio was used at a ratio of 100/40 according to the manufacturer's recommendation. The epoxy and curing agent was mixed for 5-10 minutes with a special apparatus attached to the mixer at 1000 rpm. The designation of VARIM method and manufacturing process are showed in Figure 1 a) and b), respectively.

Table 1. Mechanical and physical properties of reinforcements

Material	Specifications	Dimensions
Glass Fabric	Areal Density	202 g/m ²
	Fabric thickness	0.15 mm
	Tensile Strength	3000-5000 (MPa)
	Elastic Modulus	72-82 (GPa)

Table 2. Physical properties of resins systems

Material	Specifications	Dimensions
MGS L 285	Density	1.18-1.23 g/cm ³
	Viscosity	600-900 mPa.s
MGS H 285	Density	0.94-0.97 g/cm ³
	Viscosity	50-100 mPa.s

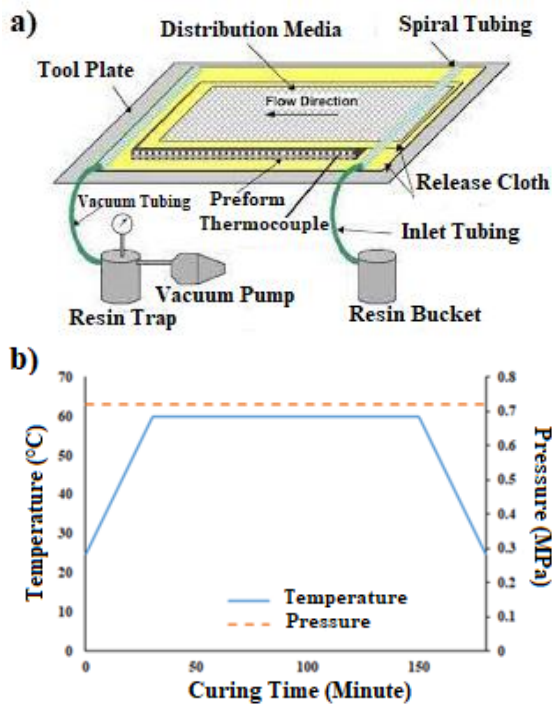


Figure 1. a) Designation of VARIM method [9] b) Production process

The composite plates were produced as 350×500 (mm²) plates. Samples of each test class were simultaneously produced to avoid different plate thicknesses. The test specimens were cut with the help of the CNC router based on the two different L/w ratios. By keeping the length measurement constant, composite samples with 2 different widths were cut as L/w ratios were 10 and 15. The thickness of glass/epoxy samples was recorded as 2.24±0.02 mm.

2.3 Hydrothermal Aging

The glass/epoxy samples were kept in sea water (SW) and distilled water (DW) at 25°C and 70°C temperatures for 1000 hours. Because of the geographical position, there is not able to obtain seawater continuously from the sea, artificial sea water was created using natural sea salt with a density of 3.5 percent, based on the average global ocean salt concentration. Since this rate deteriorates due to heating, periodical rate control has been performed with a suitable densitometer, and water and salt have been added as needed. The aging cabin is illustrated in Figure 2.

To prevent restriction of water absorption during the test, the samples that would be immersed in water before the test was not sandpapered due to the sandpapering process could prevent water absorption. Furthermore, to maximize the water absorption, a suitable separator was used to prevent the contact of the samples in order to achieve water sorption from all surfaces.

Depending on ASTM D5229/D5229M-14 [10], hydrothermal aging was performed in which the water absorption amount M_t can be determined as below

$$M_t = \frac{m_t - m_0}{m_0} \times 100 \quad (1)$$

where m_t and m_0 are the weight at time t and the first weight of the specimen, respectively.

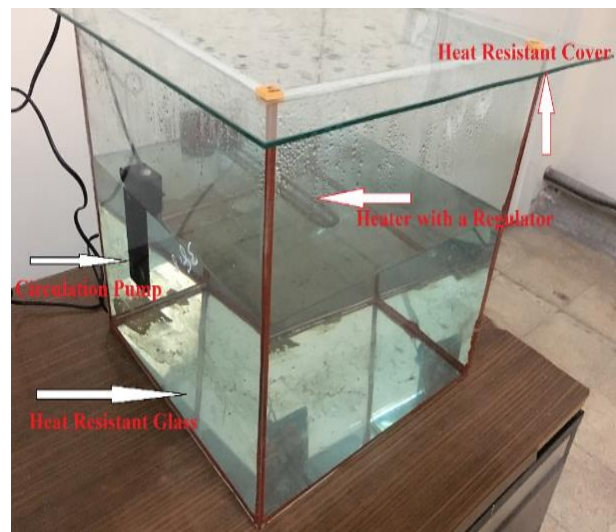


Figure 2. Hydrothermal aging cabin

Furthermore, using Fick's law as a theoretical basis, the water sorption potential of samples was determined. With thickness h , Fick's law yields the following equation [11].

$$\frac{M_t}{M_m} = 1 - \frac{8}{\pi^2} \sum_{n=0}^{\infty} \frac{1}{(2n+1)^2} \exp \left[-\frac{(2n+1)^2 \pi^2 D t}{h^2} \right] \quad (2)$$

where M_t and M_m are the water gain at time t and the overall water gain at equilibrium plateau, respectively and D is the diffusion coefficient.

Shen and Springer [12] simplified the equation 2 based on Dt/h^2 ratio as:

$$\frac{M_t}{M_m} = \left\{ \frac{4}{h} \sqrt{\frac{Dt}{\pi}} \right. \quad \text{for } \frac{Dt}{h^2} < 0.05 \quad (3)$$

$$\left. \frac{M_t}{M_m} = \left\{ 1 - \frac{8}{\pi^2} \exp \left[-\frac{\pi^2 D t}{h^2} \right] \right. \quad \text{for } \frac{Dt}{h^2} > 0.05 \quad (4)$$

The diffusion coefficient (D) of samples can be determined using the following formula:

$$D = \pi \left(\frac{h}{4M_m} \right)^2 k^2 \quad (5)$$

where k is the initial slope of the plot M_t versus square root of time, \sqrt{t} .

Due to the water intake experiments involve water intake from all surfaces, the estimated value of D from equation (5) causes to mistake [13,14]. For the correct diffusion coefficient, a correction factor can be calculated for the edge effect, so the corrected diffusion coefficient D_c can be counted as;

$$D_c = D \left(1 + \frac{h}{L} + \frac{h}{w} \right)^{-2} \quad (6)$$

where w and L are the width and length of the sample, respectively [14].

A nomenclature is given to the samples showing the parameters studied. For instance, 15-DW25 is a specimen that was manufactured with an L/w ratio of 15 and aged in distilled water at 25°C temperature, whereas 10-SW70 is a specimen that was manufactured with an L/w ratio as 10 and aged in sea water at 70°C temperature.

3. Results and Discussions

The theoretical mass change line (M_t) and experimental mass change line (M_e) of glass/epoxy composites immersed in hydrothermal conditions at 25°C and 70°C are illustrated in Figure 3 and Figure 4, respectively. The water uptake lines of samples were plotted against the square root of an aging period in figures.

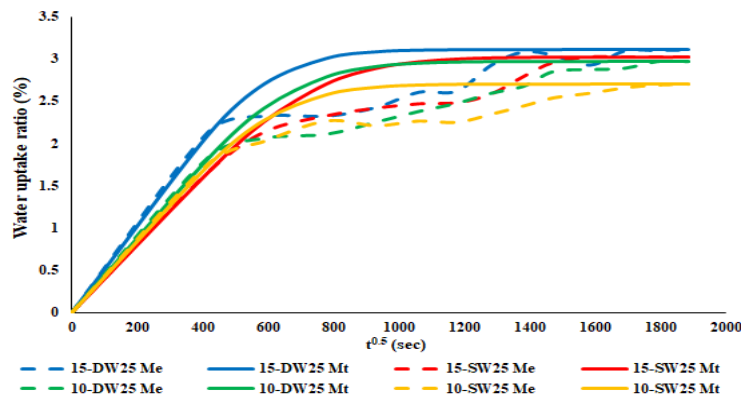


Figure 3. Water uptake ratio of composites aged at 25°C

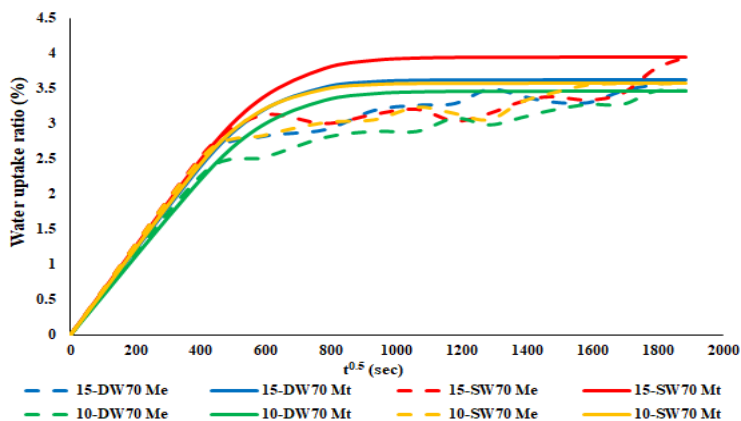


Figure 4. Water uptake ratio of composites aged at 70°C

It is clear from Figures 3 and 4 that water uptake rates of composites are time-dependent. The findings revealed the water sorption of glass/epoxy samples increased rapidly in the early period of the aging period. As the aging time prolonged, the rate of water absorption started to decrease and gradually approached the near saturation point. The main reasons for this situation can be explained as void/pore presence on the composite surface and the difference in humidity between the composite material and the aging environment [15].

Furthermore, it is clear from Figure 3 and Figure 4 that experimental and analytical weight gain ratio showed compatible results each other. For both temperature and water types based on L/w ratio, glass/epoxy composites showed a Fickian like absorption tendency. The small discrepancies between experimental and analytical mass changes of samples can be associated with integrative effects of the matrix, micro-pores, and interface between fiber/matrix are present [16].

When the two groups with different L/w ratios were evaluated separately, it was seen that the temperature increase directly affected the increment of the maximum water gain rate of glass/epoxy composites for both water types, as seen in Figure 5. The high temperature was caused to deteriorate the resin/matrix system. Deterioration of fiber/matrix interface was caused by to increase of voids/pores at high temperature [2]. One of the most significant considerations that disrupts the matrix and fiber/matrix structure is high temperature. Cracks and voids tend to increase in structures that deteriorate at high temperatures. Excessive water absorption occurs as voids and cracks fill with water [17].

Moreover, the comparison of distilled water aging and sea water aging results revealed that samples aged at 25°C absorbed more distilled water, while samples aged at 70°C absorbed more sea water, with negligible weight gain ratio

differences. It can be said the overall water intake rates of glass/epoxy samples are not exact results. Because the immersing period of samples was limited as 1000 hours for this study. Hence, further immersing period can change the small differences between distilled water and sea water results. The more sea water sorption can be associated with the pH level that causes micro-cracks in the matrix [21]. The amount of water that fills the micro-cracks causes the sea water to be absorbed more. In addition, since salt particles restrict the free movement of sea water molecules [13,18], it has been observed in some studies in the literature that sea water absorption is less than distilled water.

The periodical weight measurements showed that the L/w ratio of composite samples has directly affected the water absorption of the samples. Glass/epoxy samples with different L/w ratio aged under the same conditions showed that increase of L/w ratio was caused to more water absorption in both water types and temperatures, as seen in Figure 5. The maximum water gain ratios for distilled water aging were found as 3.106% and 2.965% for 15-DW25 and 10-DW25, respectively. The similar water uptake trend was noticed for sea water aging at 25°C. The maximum water gain ratios were found as 3.025% and 2.701% for 15-SW25 and 10-SW25, respectively. Furthermore, the experimental measurements revealed that the difference between the maximum water absorption amounts of composite samples with different L/w ratio was greater at 70°C compared to 25°C. The maximum water gain ratios for distilled water aging were found as 3.621% and 3.464% for 15-DW70 and 10-DW70, respectively. A similar water gain trend with distilled water aging was observed in sea water aging at 70°C. The maximum water gain ratios for distilled water aging were found as 3.955% and 3.580% for 15-SW70 and 10-SW70, respectively.

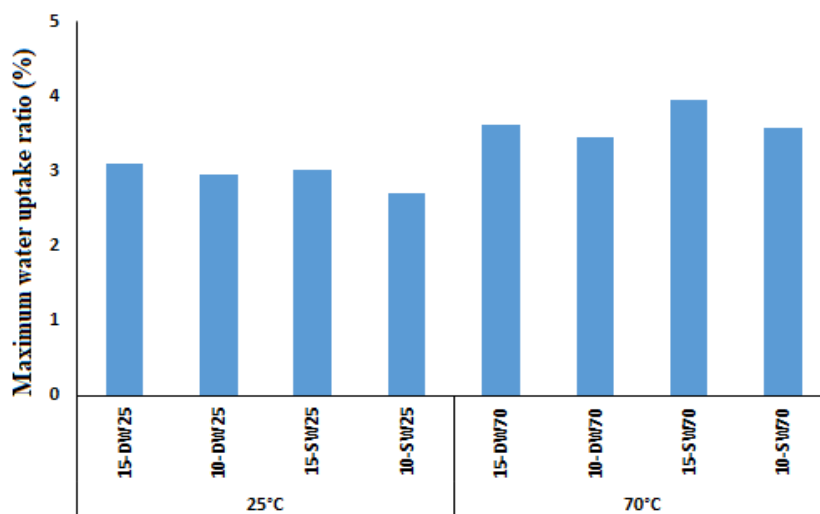


Figure 5. Maximum water uptake ratio of glass/epoxy composites

The diffusion coefficient (D) that displays how much water molecules can penetrate the composite samples is one of the most major factors of Fick's model [19].

Although the diffusion coefficient results did not give regular results as well as the results of the maximum water absorption rate, they showed consistent results in itself. Increasing L/w ratio of glass/epoxy composites aged at both temperatures in distilled water was caused an increase in diffusion coefficient values. The findings showed results consistent with the literature [4,5]. However, sea water results showed the opposite trend from distilled water aging results. The diffusion coefficients of glass/epoxy composites are displayed in Figure 6.

The diffusion coefficients of composites aged at 25°C temperature were found as 2.706×10^{-6} , 2.187×10^{-6} , 1.733×10^{-6} and 2.848×10^{-6} for 15-DW25, 10-DW25, 15-SW25 and 10-SW25, respectively. In addition, the diffusion coefficients aged at high temperature showed a similar tendency with 25°C. The diffusion coefficients of composites aged at 70°C temperature were found as 2.962×10^{-6} , 2.424×10^{-6} , 2.541×10^{-6} and 3.152×10^{-6} , for 15-DW70, 10-DW70, 15-SW70 and 10-SW70, respectively.

The corrected diffusion coefficients (Dc) of composite samples were found as smaller than diffusion coefficients as expected because of edge factor, as seen in Figure 6. Further, the Dc of composites showed a similar trend with D results. Increase of L/w ratio was caused to increase of Dc values for distilled water aging whereas, an opposite tendency was observed in sea water aging results. The corrected diffusion coefficients of glass/epoxy samples immersed in distilled water were found as 1.916×10^{-6} , 1.732×10^{-6} , 2.086×10^{-6} and 2.234×10^{-6} for 15-DW25, 10-DW25, 15-DW70 and 10-DW70, respectively. In addition, the corrected diffusion coefficients of composite

samples immersed in sea water were found as 1.227×10^{-6} , 1.919×10^{-6} , 1.799×10^{-6} and 2.483×10^{-6} for 15-SW25, 10-SW25, 15-SW70 and 10-SW70, respectively.

4. Conclusion

In this study, the water sorption parameters of glass/epoxy samples based on dimension effect were investigated. The results revealed that water type, temperature and L/w ratio of samples affected the water sorption behavior of glass/epoxy samples. It was observed that maximum water absorption rates of glass/epoxy specimens immersed in distilled water were higher than specimens immersed in sea water in all conditions. Further, the experimental results showed that temperature increase was caused to more water absorption in both water aging conditions. Besides, the experimental and analytical weight measurements showed consistent results. Also, the increase of L/w ratio was caused to more water absorption in both water types and temperature. The overall water intake ratios of samples aged at 25°C were found as 3.106%, 2.965%, 3.025%, and 2.701% for 15-DW25, 10-DW25, 15-SW25, and 10-SW25, respectively. In addition, the maximum water intake ratios of samples at 70°C were found as 3.621%, 3.464%, 3.955%, and 3.580% for 15-DW70, 10-DW70, 15-SW70, and 10-SW70, respectively. Moreover, the increase of L/w ratio was caused to increase of diffusion coefficient of specimens immersed in distilled water. However, the decrease of L/W ratio was caused to increase of diffusion coefficient of specimens immersed in distilled water. As a result, the effect of sample sizes on water absorption, which is an important parameter for design, has been observed in this study.

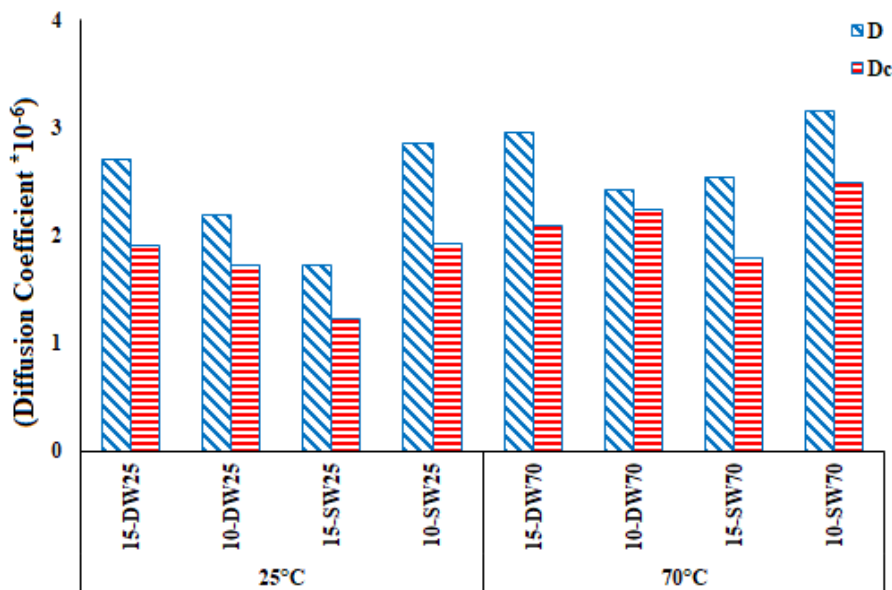


Figure 6. Diffusion coefficients of glass/epoxy composites

Declaration

The author(s) declared no potential conflicts of interest with respect to the research, authorship, and/or publication of this article. The author(s) also declared that this article is original, was prepared in accordance with international publication and research ethics, and ethical committee permission or any special permission is not required.

Author Contributions

Z.A. Oğuz: Investigation, methodology, writing original draft preparation. A. Erklığ: Investigation, supervision, writing, reviewing and editing.

Acknowledgement

This work was supported by the Gaziantep University Scientific Research Project Governing Unit (BAPYB) with an MF.DT.19.08 project number. This article has been produced from the Ph.D. thesis "Hydrothermal aging effects on mechanical properties of hybrid composites". Thesis author and supervisor names are Zeynal Abidin OĞUZ and Ahmet ERKLİĞ, respectively.

References

- Boukhoulda, F.B., L. Guillaumat, J.L. Lataillade, E. Adda-Bedia and A. Lousdad, *Aging-impact coupling based analysis upon glass/polyester composite material in hygrothermal environment*. Materials and Design, 2011. **32**: p. 4080-4087.
- Abdel-Magid, B., S. Ziaee, K. Gass and M. Schneider, *The combined effects of load, moisture and temperature on the properties of E-glass/epoxy composites*. Composite Structures, 2005. **71**: p. 320-326.
- Soykok, İ.B., O. Sayman and A. Pasinli, *Effects of hot water aging on failure behavior of mechanically fastened glass fiber/epoxy composite joints*. Composites: Part B, 2013. **54**: p. 59-70.
- Jiang, X., H. Kolstein and F.S.K. Bijlaard, *Moisture diffusion in glass-fiber-reinforced polymer composite bridge under hot/wet environment*. Composites: Part B, 2013. **45**: p. 407-416.
- Jiang, X., H. Kolstein, F.S.K. Bijlaard, X. Qiang, *Effects of hygrothermal aging on glass-fibre reinforced polymer laminates and adhesive of FRP composite bridge: Moisture diffusion characteristics*. Composites: Part A, 2014. **57**: p. 49-58.
- Chakraverty, A.P., U. K. Mohanty, S. C. Mishra and B. B. Biswal, *Effect of hydrothermal immersion and hygrothermal conditioning on mechanical properties of GRE composite*. IOP Conf. Series: Materials Science and Engineering, 2017. **178**: p. 1-12.
- Özbek, Ö., *Axial and lateral buckling analysis of Kevlar/epoxy fiber-reinforced composite laminates incorporating silica nanoparticles*. Polymer Composites, 2021. **42**, p: 1109-1122.
- Mourad, A.H.I., B. M. Abdel-Magid, T. El-Maaddawy, M. E. Grami, *Effect of seawater and warm environment on glass/epoxy and glass/polyurethane composites*. Appl Compos Mater, 2010. **17**: p. 557-573.
- Wei, B., H. Cao, S. Song, *Degradation of basalt fibre and glass fibre/epoxy resin composites in seawater*. Corrosion Science, 2011. **53**(1): p. 426-431.
- ASTM D5229 *Standard Test Method for Moisture Absorption Properties and Equilibrium Conditioning of Polymer Matrix Composite Materials*.
- Jost, W. 1960, *Diffusion in solids, liquids, gases* New York: Academic Press.
- Shen, C.H., G. S. Springer, *Moisture absorption and desorption of composite materials*. Journal of Composite Material, 1976. **10**: p. 1-20.
- Abd El-baky, M. A., M. A. Attia, *Water absorption effect on the in-plane shear properties of jute-glass-carbon-reinforced composites using losipescu test*. Journal of CompositeMaterials,2018.doi:10.1177/0021998318809525
- Collings T. A., S. M. Copley, *On the accelerated ageing of CFRP*, Composites, 1983. **14**(3): p. 180-188.
- Nayak R.K, B.C. Ray, *Influence of seawater absorption on retention of mechanical properties of nano-TiO2 embedded glass fiber reinforced epoxy polymer matrix composites*. Archives of Civil and Mechanical Engineering 2018. **18**(4): p. 1597-1607.
- Bian L, J. Xiao, J. Zeng, S. Xing, *Effects of seawater immersion on water absorption and mechanical properties of GFRP composites*. Journal of Composite Materials 2012. **46**(25): p. 3151-3162.
- Soykok İ.F, O. Sayman and A. Pasinli, *Effects of hot water aging on failure behavior of mechanically fastened glass fiber/epoxy composite joints*. Compos Part B Eng 2013. **54**: p. 59-70.
- Yan L, N. Chouw, *Effect of water, seawater and alkaline solution ageing on mechanical properties of flax fabric/epoxy composites used for civil engineering applications*. Construction and Building Materials 2015. **99**: p. 118-127.
- Yahaya R., S.M. Sapuan, M. Jawaid, Z. Leman, E.S. Zainudin, *Effect of fibre orientations on the mechanical properties of kenaf-aramid hybrid composites for spall-liner application*. Defence Technology 2015. **12**(1): p. 52-58.
- Bulut, M., M. Alsaadi, A. Erklığ, *The effects of nanosilica and nanoclay particles inclusion mode II delamination, thermal and water absorption of intraply woven carbon/aramid hybrid composites*. International Polymer Processing, 2020. **35**(5): p. 367-375.
- Larbi, S., R. Bensaada, S. Djebali, A. Bilek. *Experimental and Theoretical Study on Hygrothermal Aging Effect on Mechanical Behavior of Fiber Reinforced Plastic Laminates*. International Journal of Mechanical, Aerospace, Industrial, Mechatronic and Manufacturing Engineering 2016. **10**(7): 1239-1242.
- Özbek, Ö., N.F. Doğan, Ö.Y. Bozkurt. *An experimental investigation on lateral crushing response of glass/ carbon intraply hybrid filament wound composite pipes*. Journal of the Brazilian Society of Mechanical Sciences and Engineering, 2020. **42**: 389, doi: 10.1007/s40430-020-02475-3.
- Doğan, N.F., A. Erklığ. *On the effect of nano particle inclusion in fiber reinforced composite tensile and flexural behavior*. International Advanced Researches and Engineering Journal, 2018. **2**(3): p. 240-244.

**Research Article**

Dynamics of axially functionally graded pipes conveying fluid using a higher order shear deformation theory

Reza Aghazadeh ^{a,*} 

^aDepartment of Aeronautical Engineering, University of Turkish Aeronautical Association, Ankara 06790, Turkey

ARTICLE INFO*Article history:*

Received 10 February 2021

Revised 15 April 2021

Accepted 26 April 2021

Keywords:

Axially functionally graded material
Critical flow velocity
Differential quadrature method
Fluid conveying pipes
Refined pipe model

ABSTRACT

This study presents a novel approach for addressing dynamical characteristics of fluid conveying axially functionally graded pipes. The variation of material properties of the pipe along axial direction is taken into account according to a power-law function. Owing to a unified expression for displacement field, the developed model can be recast into classical Euler – Bernoulli and Timoshenko tube models as well as a newly developed higher order shear deformable tube model; the latter satisfies zero-shear conditions on free surfaces, and hence yields more realistic results. The system of partial differential equations governing dynamics of fluid conveying axially functionally graded pipes is derived through utilization of Hamilton's principle. Differential quadrature scheme is used to discretize the system of differential equations and generate numerical results. Detailed numerical investigations of the current fluid-solid interaction problem elucidate the effects of material gradation pattern, transverse shear deformation distribution profile along radial direction and fluid velocity on the natural frequencies of fluid conveying functionally graded pipes. The critical fluid velocity, which is a significant design parameter, can also be determined by means of developed procedures in this study.

© 2021, Advanced Researches and Engineering Journal (IAREJ) and the Author(s).

1. Introduction

Fluid conveying tubes/pipes are fundamental mechanical components which are extensively used in various engineering fields such as oil industries, heat exchangers, micro- and nano-technologies and so on. Due to their widespread applications, mechanical analyses of these elements have attracted researchers' considerable attention. The stability analyses and dynamics of fluid conveying pipes (FCPs) are generally investigated within the scope of a fluid structure interaction (FSI) problem. Most of the recently developed models for predicting dynamical behavior of FCPs have their basis on a study by Paidoussis [1]. According to Paidoussis [1] FCPs may exhibit two forms of instabilities as the fluid flow velocity increases, namely, flutter and divergence. A conservative system which is supported at both ends undergoes a static instability via divergence and a non-conservative cantilever pipe loses its stability in the form large amplitude vibrations known as flutter. These two

phenomena have been investigated in numerous studies and have raised a great deal of interest in recent years.

In a number of studies linear [2, 3] and nonlinear [4, 5] free vibrations of FCPs have been studied. The aim of free vibration analyses is to compute natural frequencies for various flow velocities and boundary conditions and hence to examine stability of FCPs. ElNajjar and Daneshmand [6] investigated the possibility of improving the stability of vertical and horizontal FCPs by attaching one or more additional springs and/or masses at various points along the pipe. In a study by Dagli and Ergut [7], Rayleigh theory is used to examine the influence of nonclassical boundary conditions on dynamic behavior of FCPs. Abdollahi, Dehghani Firouz-abadi [8] focused on stability and flexural vibration analyses of rotating pipes undergoing simultaneous external and internal fluid loadings. In some studies, using damping devices such as eddy-current dampers, the effort have been made to stabilize FCPs when the flow velocity inside them reaches the critical value [9].

* Corresponding author. Tel.: +90-312-589-6132.

E-mail addresses: raghazadeh@thk.edu.tr

ORCID: 0000-0003-4549-7068

DOI: 10.35860/iarej.878194

This article is licensed under the CC BY-NC 4.0 International License (<https://creativecommons.org/licenses/by-nc/4.0/>).

In recent years, by advances in material science and manufacturing technologies, functionally graded materials (FGMs) have found wide variety of applications from aerospace [10] to biomedical industries [11]. FGMs belong to a novel class of composite materials which are manufactured by combining the best features of two or more constituents. The volume fractions of constitutional phases vary according to a predefined profile and in the desired direction. Nowadays, these advanced composites are manufactured in various forms such as beams, plates and shells and can be reinforced by smart materials [12-15]. The superior mechanical properties of FGMs such as low stress concentration, high designability, enhanced performance in harsh and corrosive environments, and suitability for passive control purposes have made them an ideal candidate to be used in technological applications such as a fluid conveying macro- and micro-pipes. Consequently, there has been a considerable focus on stability analyses of FCPs made of FGMs. Although there are large number of studies available in the literature focusing on mechanical behavior of radially, i.e. through-the-thickness, functionally graded pipes [16-23], a few effort is made to deal with axially functionally graded pipes (AFGPs) conveying fluid. However, for complicated engineering applications and especially for control purposes, AFGPs are more preferable than radial ones. Note that modeling and analysis procedures of AFGPs are somewhat different from those employed for materials possessing through-the-thickness variations in properties. For example, unlike radial ones, the stiffness and inertia coefficients appearing in governing system of equations for AFGPs are functions of longitudinal coordinate which consequently need special treat while implementing the numerical technique. Further, new terms including the length-wise derivatives of these coefficients exist in the system of equations. In order to investigate the behavior of fluid conveying AFGPs, An and Su [24] utilized integral transform technique to numerically solve the system of governing equations. Zhou, Dai [25] studied the effects of longitudinal gradation of material properties on linear dynamics of cantilevered AFGPs aiming at enhancing stability of such systems. In some studies related to stability and dynamics of the AFGPs thermal loads [26] and nonlinear effects [27] are also taken into account. A study by Mirtalebi, Ebrahimi-Mamaghani [28] is devoted to dynamical stability and intelligent control of AFGPs by use of design flexibility of FGMs.

In all abovementioned studies as well as most researches available in the literature, the displacement field of pipe are expressed based on classical Euler-Bernoulli or Timoshenko beam models. It is worth mentioning Euler-Bernoulli model ignores transverse shear stress, and Timoshenko pipe model presumes it to be constant through the thickness. Therefore, both of these traditional theories

use strictly simplifying assumptions. In order to properly express displacement field, refined beam models, which satisfy no-shear conditions on the free surfaces, are developed recently. For the beams having rectangular cross-sections, various refined shear deformable models can be found in the literature [29, 30], however, there are few number of studies regarding higher order annular tubes satisfying transverse shear conditions. In this respect, Zhang and Fu [31] took the shear deformation considerations into account and established a higher order pipe model (HOPM). They also carried out static, free vibration and wave propagation analyses using newly developed model and made comparisons between new results and those of conventional approaches. To the best of author's knowledge, there is no report on the analyses of fluid conveying AFGPs on the basis of HOPM in the available technical sources. The works utilizing higher order pipe theory are merely restricted to pure structural problems of pipes/tubes. Babaei and Reza Eslami [32] employed HOPM in conjunction with modified couple stress theory to put forward a nonclassical model for investigating vibrations of buckled functionally graded tubes in thermal environment. In some studies higher order shear deformable pipe model is used to derive an accurate size-dependent system of equations for pipes based on nonlocal elasticity [33, 34]. In another study by Zhong, Fu [35] statics and dynamics of functionally graded tubes under thermal loads are studied based on refined pipe model.

The aim of the current study is to derive governing equations and associated boundary conditions regarding free vibration problem of AFGPs conveying fluid. Owing to a unified expression for displacement field used in this study, the system can be reduced to any of conventional or higher order models, i.e. Euler-Bernoulli, Timoshenko, and higher order pipe model. The latter model, to the best of author's knowledge, is used in analysis of fluid conveying pipes for the first time. The higher order pipe model satisfies shear free conditions on inner and outer surfaces and hence can result in more realistic prediction of mechanical behavior of pipes. Further, the rotary inertia is not neglected in the derivations. The pipe is assumed to be functionally graded in longitudinal direction in which material properties smoothly vary from upstream to downstream according to a power-law function. The current study seems to be one of the few number of researches investigating effects of through-the-length variations of constituents of FCPs. Differential quadrature method (DQM) is used as a numerical solution method to obtain natural frequencies in different fluid velocities. The generated results clearly elucidate the influences of fluid velocity, material gradation patterns, and geometrical dimensions upon critical flow velocity and natural frequencies of fluid conveying AFGPs.

2. Formulation

Illustrated in Figure 1 is the configuration of an AFGP conveying fluid of velocity Γ with inner and outer radii denoted by r_i and r_o , respectively, and its length is designated by L . The volume fractions of pipe constituents vary smoothly from upstream, i.e. left side, to downstream, i.e. right side. The displacement field for the pipe domain at any time t can be expressed as the following unified form:

$$u_1(x_1, x_3, t) = u(x_1, t) - x_3 w_{,x_1} + f(x_2, x_3) \gamma(x_1, t) \quad (1.a)$$

$$u_2(x_1, x_3, t) = 0 \quad (1.b)$$

$$u_3(x_1, x_2, x_3, t) = w(x_1, t) \quad (1.c)$$

where u_1 , u_2 and u_3 designate the displacements of desired point along x_1 , x_2 and x_3 directions, respectively. u and w denote the displacement of any point located on mid-surface $x_3 = 0$, along x_1 and x_3 directions, respectively; “,” stands for partial derivative, γ is transverse shear strain of any hypothetical point on the neutral axis x_1 and can be stated in terms of bending rotation ϕ as

$$\gamma(x_1, t) = w_{,x_1}(x_1, t) + \phi(x_1, t), \quad (2)$$

Shape function f is utilized to delineate through-the-thickness distribution pattern of transverse shear strain. Conventional pipe models, namely Euler – Bernoulli pipe model (EBPM), Timoshenko pipe model (TPM), as well as the higher order pipe model (HOPM) [31] can be retrieved by choosing one of the following expressions for f :

$$\text{EBPM: } f(x_2, x_3) = 0 \quad (3.a)$$

$$\text{TPM: } f(x_2, x_3) = x_3 \quad (3.b)$$

$$\text{HOPM: } f(x_2, x_3) = x_3 + \frac{x_3}{(r_o^2 + r_i^2)} \left(\frac{r_o^2 r_i^2}{r^2} - \frac{r^2}{3} \right) \quad (3.c)$$

Note that the shear stress is neglected in EBPM; TPM presumes transverse shear to be constant through the thickness of the pipe; and a nonlinear shear strain and stress distribution pattern is achievable by using HOPM.

In order to establish equations of motion and boundary conditions governing dynamics of the AFGP conveying fluid Hamilton’s principle is used. It postulates that

$$\delta \int_{t_1}^{t_2} (K - U) dt = 0. \quad (4)$$

U and K here are total strain energy and kinetic energy, respectively. Strain energy U of a pipe occupying

a domain Ω is written as:

$$U = \frac{1}{2} \int_{\Omega} (\sigma_{ij} \varepsilon_{ij}) dV, \quad (5)$$

where σ_{ij} and ε_{ij} are components of classical stress and strain tensors. ε_{ij} is expressed in the form of the following strain-displacement relation

$$\varepsilon_{ij} = \frac{1}{2} (u_{i,j} + u_{j,i}), \quad (6)$$

and σ_{ij} can be evaluated by means of the following constitutive relation

$$\sigma_{ij} = 2\mu \varepsilon_{ij} + \lambda \delta_{ij} \varepsilon_{kk} \quad (7)$$

where λ and μ are Lamé’s constants and can be expressed in terms of modulus of elasticity E and Poisson’s ratio ν as follows

$$\lambda = \frac{E\nu}{(1+\nu)(1-2\nu)}, \quad \mu = \frac{E}{2(1+\nu)} \quad (8)$$

The total kinetic energy comprising those of pipe motion and fluid flow can be written in the form

$$K = K_p + K_f \quad (9)$$

where K_p and K_f are kinetic energies of pipe and fluid, respectively and can be expressed as

$$K_p = \frac{1}{2} \int_{\Omega} \rho \left\{ \left(\frac{\partial u_1}{\partial t} \right)^2 + \left(\frac{\partial u_2}{\partial t} \right)^2 + \left(\frac{\partial u_3}{\partial t} \right)^2 \right\} dV, \quad (10.a)$$

$$\begin{aligned} K_f &= \frac{1}{2} \int_{\Omega_f} \rho_f \{ \vec{v}_f \cdot \vec{v}_f \} dV_f \\ &= \frac{1}{2} \int_L \rho_f A_f \{ \vec{v}_f \cdot \vec{v}_f \} dx_1 = \frac{1}{2} \int_L m_f \{ \vec{v}_f \cdot \vec{v}_f \} dx_1. \end{aligned} \quad (10.b)$$

Ω_f is the fluid domain inside the pipe; ρ and ρ_f denote mass densities of the pipe and the fluid, respectively. A_f stands for the cross-sectional area of fluid flow, and $m_f = \rho_f A_f$ is the mass per unit length of the fluid. \vec{v}_f is the fluid velocity which can be expressed as the sum of velocity of the pipe \vec{v}_p and flow velocity Γ relative to the pipe

$$\vec{v}_f = \vec{v}_p + \Gamma \vec{e} \quad (11)$$

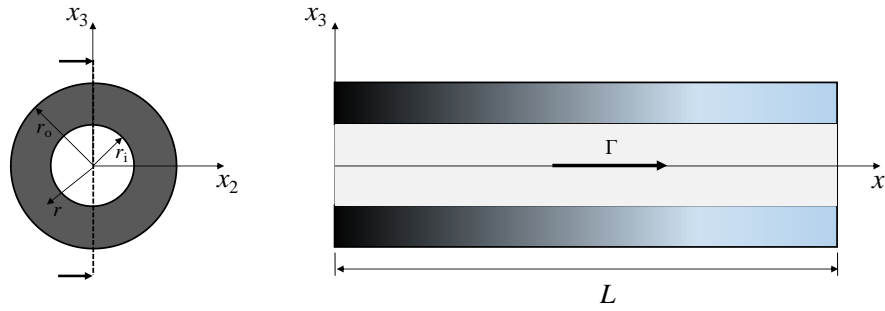


Figure 1. Fluid conveying AFGP

$\bar{\tau}$ here is the unit vector tangent to the pipe. The components of \bar{v}_p are the time derivatives of displacement field given by Eq. (1).

Note that, in the present study, a typical material property of the pipe, denoted by Z , including E , ν , μ , and ρ , is assumed to be axially varying from upstream, $x_1 = 0$, to downstream, $x_1 = L$, according to the following power-law function

$$Z(x_1) = Z_0 \left(1 + \left(\frac{Z_L}{Z_0} - 1 \right) \left(\frac{x_1}{L} \right)^\alpha \right) \quad (11)$$

α is the power-law index which characterizes the distribution profile of the material properties along axial direction of the pipe. Subscripts 0 and L designate the material properties of the pipe at $x_1 = 0$ and $x_1 = L$, respectively.

Introducing expressions for U and K and associated relations into Hamilton's principle yields the following system of governing partial differential equations:

δu :

$$A \frac{\partial}{\partial x_1} \left(\eta(x_1) \frac{\partial u}{\partial x_1} \right) = \rho(x_1) A \frac{\partial^2 u}{\partial t^2} + m_f \frac{\partial^2 u}{\partial t^2}, \quad (12.a)$$

δw :

$$\begin{aligned} & (2F_{22} - I - F_{33}) \frac{\partial^2}{\partial x_1^2} \left(\eta(x_1) \frac{\partial^2 w}{\partial x_1^2} \right) + k_s (F_{55} + F_{77}) \\ & \frac{\partial}{\partial x_1} \left(\mu(x_1) \frac{\partial w}{\partial x_1} \right) - (F_{33} - F_{22}) \frac{\partial^2}{\partial x_1^2} \left(\eta(x_1) \frac{\partial \phi}{\partial x_1} \right) \\ & + k_s (F_{55} + F_{77}) \frac{\partial}{\partial x_1} (\mu(x_1) \phi) - m_f \Gamma^2 \frac{\partial^2 w}{\partial x_1^2} \\ & = (2F_{22} - I - F_{33}) \frac{\partial}{\partial x_1} \left(\rho(x_1) \frac{\partial^3 w}{\partial x_1 \partial t^2} \right) + \rho(x_1) A \frac{\partial^2 w}{\partial t^2} \\ & + (F_{22} - F_{33}) \frac{\partial}{\partial x_1} \left(\rho(x_1) \frac{\partial^2 \phi}{\partial t^2} \right) - (c_f - 1)^2 I_f \frac{\partial^4 w}{\partial x_1^2 \partial t^2} \\ & - c_f (c_f - 1) I_f \frac{\partial^3 \phi}{\partial x_1 \partial t^2} + m_f \frac{\partial^2 w}{\partial t^2} + 2m_f \Gamma \frac{\partial^2 w}{\partial x_1 \partial t}, \end{aligned} \quad (12.b)$$

$\delta \phi$:

$$\begin{aligned} & (F_{33} - F_{22}) \frac{\partial}{\partial x_1} \left(\eta(x_1) \frac{\partial^2 w}{\partial x_1^2} \right) - k_s (F_{55} + F_{77}) \mu(x_1) \frac{\partial w}{\partial x_1} \\ & + F_{33} \frac{\partial}{\partial x_1} \left(\eta(x_1) \frac{\partial \phi}{\partial x_1} \right) - k_s (F_{55} + F_{77}) \mu(x_1) \phi \\ & = \rho(x_1) (F_{33} - F_{22}) \frac{\partial^3 w}{\partial x_1 \partial t^2} + \rho(x_1) F_{33} \frac{\partial^2 \phi}{\partial t^2} \\ & + c_f (c_f - 1) I_f \frac{\partial^3 w}{\partial x_1 \partial t^2} + c_f^2 I_f \frac{\partial^2 \phi}{\partial t^2}, \end{aligned} \quad (12.c)$$

and the boundary conditions read

$$\delta u = 0 \quad \text{or} \quad A \eta(x_1) \frac{\partial u}{\partial x_1} = 0, \quad (13.a)$$

$$\begin{aligned} \delta w = 0 \quad \text{or} \quad & (2F_{22} - I - F_{33}) \frac{\partial}{\partial x_1} \left(\eta(x_1) \frac{\partial^2 w}{\partial x_1^2} \right) \\ & + k_s (F_{55} + F_{77}) \mu(x_1) \frac{\partial w}{\partial x_1} - (F_{33} - F_{22}) \frac{\partial}{\partial x_1} \left(\eta(x_1) \frac{\partial \phi}{\partial x_1} \right) \\ & + k_s (F_{55} + F_{77}) \mu(x_1) \phi - m_f \Gamma^2 \frac{\partial w}{\partial x_1} \\ & = (2F_{22} - I - F_{33}) \rho(x_1) \frac{\partial^3 w}{\partial x_1 \partial t^2} - (F_{33} - F_{22}) \rho(x_1) \frac{\partial^2 \phi}{\partial t^2} \\ & - (c_f - 1)^2 I_f \frac{\partial^3 w}{\partial x_1 \partial t^2} - c_f (c_f - 1) I_f \frac{\partial^2 \phi}{\partial t^2} + m_f \Gamma \frac{\partial w}{\partial t}, \end{aligned} \quad (13.b)$$

$$\begin{aligned} \delta \frac{\partial w}{\partial x_1} = 0 \quad \text{or} \quad & (I + F_{33} - 2F_{22}) \eta(x_1) \frac{\partial^2 w}{\partial x_1^2} \\ & + (F_{33} - F_{22}) \eta(x_1) \frac{\partial \phi}{\partial x_1} = 0, \end{aligned} \quad (13.c)$$

$$\begin{aligned} \delta \phi = 0 \quad \text{or} \quad & (F_{33} - F_{22}) \eta(x_1) \frac{\partial^2 w}{\partial x_1^2} + F_{33} \eta(x_1) \frac{\partial \phi}{\partial x_1} = 0, \end{aligned} \quad (13.d)$$

η , I_f , and c_f here are utilized for the sake of brevity by

letting $\eta(x_1) = \lambda(x_1) + 2\mu(x_1)$, $I_f = \rho_f \pi r_i^4 / 4$, and $c_f = f / x_3$ computed at $r = r_i$. k_s is the shear correction factor and is taken as unity for EBPM and HOPM, and for Timoshenko beam model when used for annular cross-section is given as follows [36]

$$k_s = \frac{6(\zeta^2 + 1)^2 (1 + \nu)^2}{(7 + 12\nu + 4\nu^2)(\zeta^4 + 1) + (34 + 48\nu + 16\nu^2)\zeta^2} \quad (14)$$

where $\zeta = r_i / r_o$. The stiffness and inertia parameters appeared in Eqs. (13) and (14) are as follows

$$\begin{aligned} & \{A, I, F_{22}, F_{33}, F_{55}, F_{77}, F_{15}, F_{66}, F_{99}, F_{68}, F_{88}\} \\ & = \int_A \left\{ 1, x_3^2, x_3 f, f^2, f_{,x_3}^2, f_{,x_2}^2, f_{,x_3}^2, f_{,x_3 x_3}^2, f_{,x_2 x_3}^2, \right. \\ & \left. f_{,x_3 x_3} f_{,x_2 x_2}, f_{,x_2 x_2}^2 \right\} dA \end{aligned} \quad (15)$$

3. Numerical Solution

In the present paper, differential quadrature method (DQM) is employed to discretize and solve the system of differential equations comprising governing equations and boundary conditions [37]. The fundamental idea of DQM is to approximate m^{th} derivative of a function by a weighted sum of functional values at all sampling points. For this purpose, after dividing the domain $0 \leq x \leq L$ by using number of nodes N , the m^{th} derivative of a function $z(x, t)$ with respect to x at a desired point x_i is written as:

$$\frac{\partial^m z(x, t)}{\partial x^m} \Big|_{x=x_i} = \sum_{j=1}^N c_{ij}^{(m)} z(x_j, t), \quad i = 1, 2, \dots, N. \quad (16)$$

$c_{ij}^{(m)}$ are the weighting coefficients. Utilization of differential quadrature technique formulated by Eq. (16) transforms the equations of motion and boundary conditions to the following form:

$$\begin{aligned} & \begin{bmatrix} \mathbf{0} & \mathbf{0} \\ \mathbf{M}_{db} & \mathbf{M}_{dd} \end{bmatrix} \begin{Bmatrix} \dot{\mathbf{d}}_b \\ \dot{\mathbf{d}}_d \end{Bmatrix} + \begin{bmatrix} \mathbf{0} & \mathbf{0} \\ \mathbf{C}_{db} & \mathbf{C}_{dd} \end{bmatrix} \begin{Bmatrix} \dot{\mathbf{d}}_b \\ \dot{\mathbf{d}}_d \end{Bmatrix} \\ & + \begin{bmatrix} \mathbf{K}_{bb} & \mathbf{K}_{bd} \\ \mathbf{K}_{db} & \mathbf{K}_{dd} \end{bmatrix} \begin{Bmatrix} \mathbf{d}_b \\ \mathbf{d}_d \end{Bmatrix} = \mathbf{0} \end{aligned} \quad (17)$$

where \mathbf{K} , \mathbf{C} , and \mathbf{M} are stiffness, damping, and mass matrices respectively. Subscripts b and d represent boundary and internal nodes, respectively. \mathbf{d} is dynamic displacement vector defined by

$$\mathbf{d} = \mathbf{d}^* e^{i\omega t}, \quad (18)$$

ω and \mathbf{d}^* in Eq. (18) represent eigenvalue and corresponding eigenvector, respectively. Although \mathbf{d}^* is a vector containing unknown amplitudes associated with u , w , and ϕ , in the current study, due to the following two reasons, axial displacement u is not taken into account in computations: 1) Inspecting governing equations and boundary conditions, it can be observed that the equations related to the axial displacement, i.e. Eqs. (12.a) and (13.a), are fully decoupled from other displacements and hence, it can be treated separately; 2) The magnitude of axial displacements are smaller than transverse ones by one order [1] and consequently they are less significant and can be neglected. Therefore, \mathbf{d}^* is comprised of unknown w and ϕ values at grid points

$$\mathbf{d}^* = \left\{ \left\{ w_p^* \right\}^T, \left\{ \phi_p^* \right\}^T \right\}^T, \quad \text{for } p = 1, 2, \dots, N \quad (19)$$

Substituting Eq. (18) into Eq. (17) leads to standard generalized eigenvalue problem as follows

$$\left\{ \mathbf{K} + \omega \mathbf{C} + \omega^2 \mathbf{M} \right\} \mathbf{d}^* = \mathbf{0}. \quad (20)$$

The nontrivial solution of Eq. (20) is obtained by equating determinant of coefficient matrix in Eq. (20) to zero

$$\det \left\{ \mathbf{K} + \omega \mathbf{C} + \omega^2 \mathbf{M} \right\} = \mathbf{0}. \quad (21)$$

It should be noted that eigenvalues ω which are computed through solving Eq. (21) are generally complex values in the form $\omega = \text{Re}(\omega) + i \text{Im}(\omega)$. The imaginary and real parts of eigenvalue are related to the oscillation frequency and decaying rate, respectively. $\text{Re}(\omega) > 0$ indicates that the system is unstable whereas the stability condition exists when $\text{Re}(\omega) < 0$.

4. Numerical Results

A simply supported fluid conveying AFGP is considered to carry out numerical analyses. The pipe is assumed to be functionally graded in longitudinal direction made of Epoxy at the right end with following properties: $E_L = 1.44$ GPa, $\nu_L = 0.38$, and $\rho_L = 1000$ kg/m³. In order to elucidate the axial material gradation effect on dynamical behavior of the pipe clearly, a material with following constants is chosen for the left hand side: $E_0 / E_L = 2$, $\nu_0 = \nu_L$ and $\rho_0 / \rho_L = 2$. In this study, for convenience, materials at the upstream and downstream ends will be called MAT1 and MAT2, respectively. The density of fluid used in numerical analysis is $\rho_f = 1000$ kg/m³ which is equal to that

of water. Unless otherwise mentioned the geometrical dimensions are taken as $r_o = 5$ cm, $r_i / r_o = 0.8$.

Plotted in

Figure 2 are the distribution profiles of material properties along dimensionless longitudinal direction x_1 / L , for different values of gradient index α . As it can be observed, a homogeneous Epoxy pipe is achieved by letting $\alpha = 0$ while as α approaches infinity a pipe made of fully MAT1 can be represented. For other values of power-law index a nonlinear pattern is seen for through-the-length variation of material properties except for $\alpha = 1$ which indicates a linear distribution profile. Further inspection of

Figure 2 reveals that at any distance x_1 , the higher is the α -value, the larger is the modulus of elasticity and density.

In order to examine the accuracy of procedures and techniques employed in the current study and also conduct convergence analysis, critical flow velocities Γ_{cr} , at which instability occurs, for a homogeneous and axially functionally graded fluid conveying pipes are tabulated in Table 1. The details on how to determine Γ_{cr} are discussed in the subsequent paragraphs. The accuracy of the procedures developed can be verified by observing excellent conformity between the results produced in the present study for homogeneous pipe with those provided by Wang [38]. Although for homogeneous pipe the convergence is achieved by choosing $N = 11$, for an AFGP, 17 grid points must be employed.

Figure 3 shows first eigenvalue of fluid conveying AFGP versus flow velocity Γ , computed in different values of material power-law index α . The results are generated based on HOPM. In order to be able to comment on the results, it should be noted that when $Re(\omega) > 0$ and

$Im(\omega) = 0$ the fluid conveying pipe loses its stability due to static divergence which is generally the case in conservative pipes. The smallest flow velocity at which this condition occurs is called critical flow velocity Γ_{cr} . Thus, inspecting Figure 3, it is obvious that for the current conservative (supported at both ends) FSI problem the instability is of the divergence type. Moreover, in all material gradation patterns characterized by α , the trend is preserved. In subcritical flow region, $\Gamma < \Gamma_{cr}$, the pipe is stable. $Im(\omega)$ value computed at $\Gamma = 0$ represents natural frequency of a pipe with still water acting as a core medium where the problem is unaffected by the dynamics of fluid flow. An increase in fluid velocity results in corresponding decrease in natural frequency, i.e. imaginary part of eigenvalue, which causes the pipe configuration to approach unstable state. In order to justify this fact, it should be mentioned that the centrifugal force term $m_f \Gamma^2 \partial^2 w / \partial x_1^2$ appeared in Eq. (12.b) resembles the term resulting from axial compressive load in a beam problem. Therefore, it can be physically realized that, with increasing the flow velocity the stiffness of the pipe is diminished; in sufficiently large values of Γ the destabilizing centrifugal force overcomes the restoring flexural force and as a result divergence instability, which can also be simply called as buckling, occurs. In addition to foregoing findings, it can be seen that larger value of α which represents a pipe with higher stiffness, yields greater value of frequency and correspondingly larger Γ_{cr} . Moreover, it follows from Figure 3 that, the dynamic flutter instability occurs at velocities beyond Γ_{cr} where real and imaginary parts of ω are simultaneously positive.

Table 1. Critical flow velocities Γ_{cr} of homogeneous and AFGP conveying fluid predicted by EBPM, $L / r_o = 40$, $r_o = 100$ μ m.

Gradient index α	Present, $N = 9$	Present, $N = 11$	Present, $N = 13$	Present, $N = 15$	Present, $N = 17$	Present, $N = 19$	Wang [38]
$\alpha = 0.0$, MAT2	45.258	45.261	45.261	45.261	45.261	45.261	45.262
$\alpha = 2.0$	76.395	76.146	76.082	76.066	76.062	76.062	-

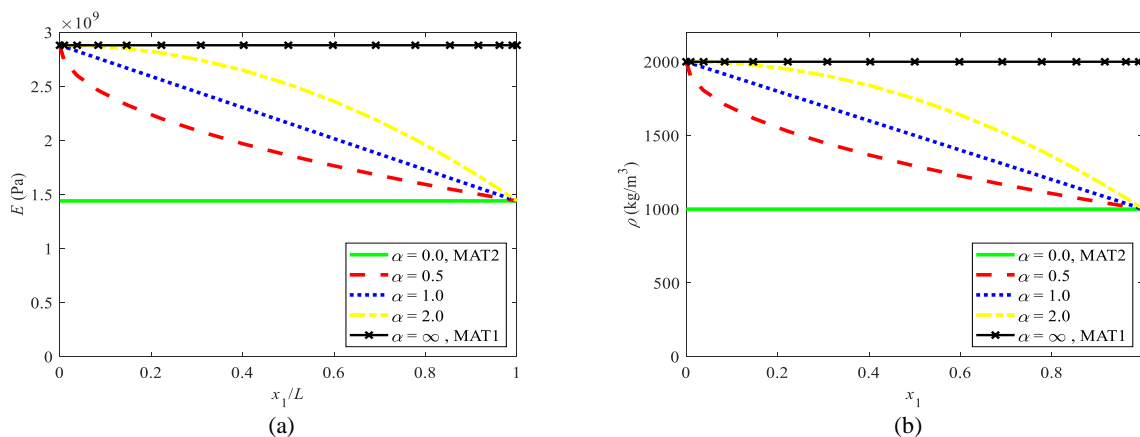


Figure 2. Through-the-length distribution of material properties of an AFGP with $L / r_o = 40$, (a) modulus of elasticity E and (b) mass density ρ .

To study the role of geometrical parameters in the dynamics of fluid conveying AFGP, the results provided in Figure 3 are regenerated in Figure 4 by only changing length to outer radius ratio L / r_o from 40 to 60. The same conclusions mentioned in the foregoing paragraph can be drawn from Figure 4. Comparing Figure 3 with Figure 4 reveals that a longer pipe has smaller stiffness and hence possesses smaller values of natural frequencies and critical flow velocities.

Plotted in Figure 5 are the real and imaginary parts of eigenvalues computed for a thicker fluid conveying AFGP with $r_i / r_o = 0.6$. It can clearly be observed that the frequencies are increased remarkably by increasing the thickness of the pipe. This fact is expectable because the higher the thickness is the stiffer the pipe becomes.

To investigate the effects of shear deformation on the dynamical behavior of AFGP, Table 2 tabulates critical flow velocities predicted by different tube models, namely EBPM, TPM and HOPM. As it is concluded from previous results, Γ_{cr} is an increasing function of α . Since EBPM neglects transverse shear stresses, it overestimates critical flow velocities. HOPM considers a proper through-the-thickness shear stresses distribution profile and hence its results are more accurate. Although Γ_{cr} predicted by TPM are close to those computed by HOPM, a slightly smaller critical flow velocity are obtained by HOPM.

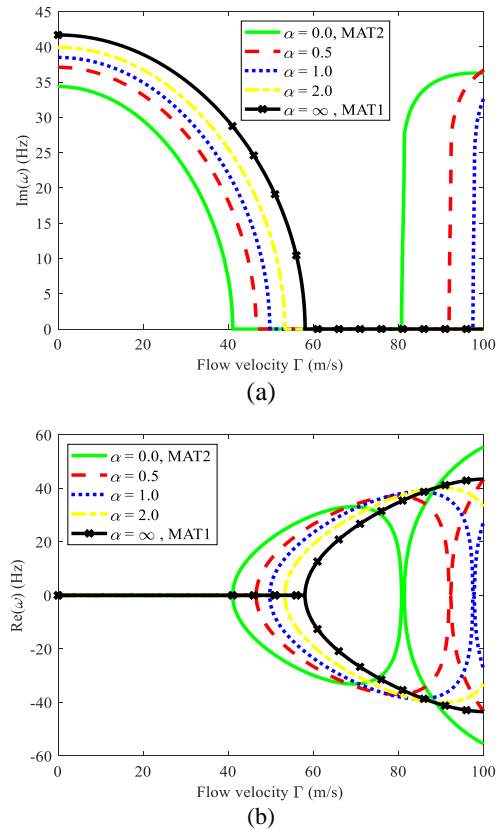


Figure 4. (a) Imaginary and (b) real parts of first eigenvalue of AFGP conveying fluid versus flow velocity Γ , $L / r_o = 60$.

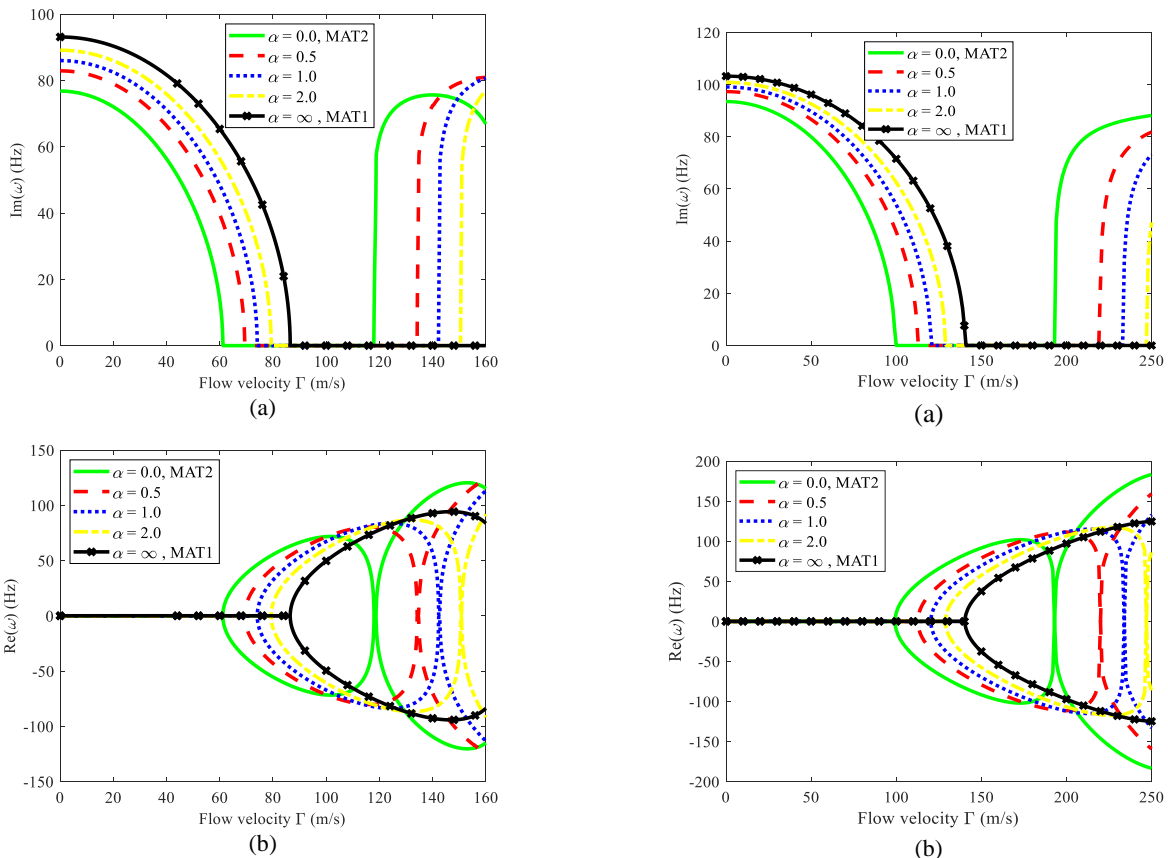


Figure 3. (a) Imaginary and (b) real parts of first eigenvalue of AFGP conveying fluid versus flow velocity Γ , $L / r_o = 40$.

Figure 5. (a) Imaginary and (b) real parts of first eigenvalue of AFGP conveying fluid versus flow velocity Γ , $L / r_o = 40$, $r_i / r_o = 0.6$.

Table 2. Critical flow velocities Γ_{cr} of AFGP conveying fluid predicted by different tube models, $L/r_o = 40$

Model	$\alpha = 0.0$, MAT2	$\alpha = 0.5$	$\alpha = 1.0$	$\alpha = 2.0$	$\alpha = \infty$, MAT1
HOPM	61.15	69.37	74.09	79.32	86.48
EBPM	61.93	70.27	75.09	80.45	87.58
TPM	61.25	69.51	74.22	79.46	86.62

5. Conclusion

A new model for dynamical analysis of AFGPs conveying fluid is presented by employing a unified displacement field. The longitudinal variations in material properties of FCP is taken into account by employing a power law function. Using the formulation and procedures developed in the current study, it is possible to retrieve pipe models based on different theories such as Euler-Bernoulli, Timoshenko and higher order shear deformation. HOPM, which for the first time is employed in dynamics of FCPs, delineates through-the-thickness distribution profile of the transverse shear stress more realistically and therefore yields more accurate results. The DQM is utilized to conduct parametric analyses and hence to reveal the effects of geometrical and material parameters on system eigenvalues at different flow velocities.

Power law index α determines the distribution profile of the material properties through the length of pipe. The results show that it has significant effect on dynamics of fluid conveying AFGPs which can be used as an important design parameter especially in control applications. Higher values of α results in improved eigenvalues and increase critical flow velocities for divergence instability.

The differences observed between the eigenvalue results of traditional pipe models and those of HOPM postulates that employing a refined higher order tube model, which takes into account the shear deformation considerations properly, is indispensable for an accurate prediction of mechanical responses. The frequencies predicted by EBPM and TPM are larger than those generated by HOPM. EBPM yields the largest values of $\text{Re}(\omega)$ because it disregards transverse shear stresses.

It is possible to capture the influences of different material and geometrical parameters upon dynamical characteristics of AFGPs conveying fluid using the techniques developed in the current study. Owing to the superior features of functionally graded materials, the results provided in this paper can be utilized for intelligibly design and control purposes. This study also aims at providing a foundation for futures works on mechanical analyses, design, control, and optimization of FSI systems.

Declaration

The author declared no potential conflicts of interest with respect to the research, authorship, and/or publication of this article. The author also declared that this article is

original, was prepared in accordance with international publication and research ethics, and ethical committee permission or any special permission is not required.

Author Contributions

R. Aghazadeh is responsible for all section of the study.

References

- Paidoussis, M.P., *Fluid-Structure Interactions: Slender Structures and Axial Flow*. 1998, London: Academic Press.
- Lee, U. and J. Park, *Spectral element modelling and analysis of a pipeline conveying internal unsteady fluid*. Journal of Fluids and Structures, 2006. **22**(2): p. 273-292.
- Xu, M.R., S.P. Xu, and H.Y. Guo, *Determination of natural frequencies of fluid-conveying pipes using homotopy perturbation method*. Computers & Mathematics with Applications, 2010. **60**(3): p. 520-527.
- Zhang, T., et al., *Nonlinear dynamics of straight fluid-conveying pipes with general boundary conditions and additional springs and masses*. Applied Mathematical Modelling, 2016. **40**(17): p. 7880-7900.
- Tang, Y., Y. Zhen, and B. Fang, *Nonlinear vibration analysis of a fractional dynamic model for the viscoelastic pipe conveying fluid*. Applied Mathematical Modelling, 2018. **56**: p. 123-136.
- ElNajjar, J. and F. Daneshmand, *Stability of horizontal and vertical pipes conveying fluid under the effects of additional point masses and springs*. Ocean Engineering, 2020. **206**: p. 106943.
- Dagli, B.Y. and A. Ergut, *Dynamics of fluid conveying pipes using Rayleigh theory under non-classical boundary conditions*. European Journal of Mechanics - B/Fluids, 2019. **77**: p. 125-134.
- Abdollahi, R., R. Dehghani Firouz-abadi, and M. Rahmani, *On the stability of rotating pipes conveying fluid in annular liquid medium*. Journal of Sound and Vibration, 2021. **494**: p. 115891.
- Szmidt, T., D. Pisarski, and R. Konowrocki, *Semi-active stabilisation of a pipe conveying fluid using eddy-current dampers: state-feedback control design, experimental validation*. Meccanica, 2019. **54**(6): p. 761-777.
- Mahamood, R.M. and E.T. Akinlabi, *Types of Functionally Graded Materials and Their Areas of Application*, in *Functionally Graded Materials*, R.M. Mahamood and E.T. Akinlabi, Editors. 2017, Springer International Publishing: Cham. p. 9-21.
- Petit, C., L. Montanaro, and P. Palmero, *Functionally graded ceramics for biomedical application: Concept, manufacturing, and properties*. International Journal of Applied Ceramic Technology, 2018. **15**(4): p. 820-840.
- Safaei, B., *The effect of embedding a porous core on the free vibration behavior of laminated composite plates*. Steel and Composite Structures, 2020. **35**(5): p. 659-670.
- Moradi-Dastjerdi, R., et al., *Buckling behavior of porous*

- CNT-reinforced plates integrated between active piezoelectric layers*. Engineering Structures, 2020. **222**: p. 111141.
14. Fan, F., S. Sahmani, and B. Safaei, *Isogeometric nonlinear oscillations of nonlocal strain gradient PFGM micro/nanoplates via NURBS-based formulation*. Composite Structures, 2021. **255**: p. 112969.
 15. Aghazadeh, R., S. Dag, and E. Cigeroglu, *Modelling of graded rectangular micro-plates with variable length scale parameters*. Structural engineering and mechanics: An international journal, 2018. **65**(5): p. 573-585.
 16. Tang, Y. and T. Yang, *Post-buckling behavior and nonlinear vibration analysis of a fluid-conveying pipe composed of functionally graded material*. Composite Structures, 2018. **185**: p. 393-400.
 17. Liu, H., Z. Lv, and H. Tang, *Nonlinear vibration and instability of functionally graded nanopipes with initial imperfection conveying fluid*. Applied Mathematical Modelling, 2019. **76**: p. 133-150.
 18. Zhu, B., et al., *Static and dynamic characteristics of the post-buckling of fluid-conveying porous functionally graded pipes with geometric imperfections*. International Journal of Mechanical Sciences, 2021. **189**: p. 105947.
 19. Dehrouyeh-Semnani, A.M., et al., *Nonlinear thermo-resonant behavior of fluid-conveying FG pipes*. International Journal of Engineering Science, 2019. **144**: p. 103141.
 20. Khodabakhsh, R., A.R. Saidi, and R. Bahaadini, *An analytical solution for nonlinear vibration and post-buckling of functionally graded pipes conveying fluid considering the rotary inertia and shear deformation effects*. Applied Ocean Research, 2020. **101**: p. 102277.
 21. Deng, J., et al., *Stability analysis of multi-span viscoelastic functionally graded material pipes conveying fluid using a hybrid method*. European Journal of Mechanics - A/Solids, 2017. **65**: p. 257-270.
 22. Reddy, R.S., S. Panda, and G. Natarajan, *Nonlinear dynamics of functionally graded pipes conveying hot fluid*. Nonlinear Dynamics, 2020. **99**(3): p. 1989-2010.
 23. Zhu, B., et al., *Nonlinear free and forced vibrations of porous functionally graded pipes conveying fluid and resting on nonlinear elastic foundation*. Composite Structures, 2020. **252**: p. 112672.
 24. An, C. and J. Su, *Dynamic Behavior of Axially Functionally Graded Pipes Conveying Fluid*. Mathematical Problems in Engineering, 2017. **2017**: p. 6789634.
 25. Zhou, X.-w., H.-L. Dai, and L. Wang, *Dynamics of axially functionally graded cantilevered pipes conveying fluid*. Composite Structures, 2018. **190**: p. 112-118.
 26. Ebrahimi-Mamaghani, A., et al., *Thermo-mechanical stability of axially graded Rayleigh pipes*. Mechanics Based Design of Structures and Machines, 2020: p. 1-30.
 27. Lu, Z.-Q., et al., *Nonlinear vibration effects on the fatigue life of fluid-conveying pipes composed of axially functionally graded materials*. Nonlinear Dynamics, 2020. **100**(2): p. 1091-1104.
 28. Mirtalebi, S.H., A. Ebrahimi-Mamaghani, and M.T. Ahmadian, *Vibration Control and Manufacturing of Intelligibly Designed Axially Functionally Graded Cantilevered Macro/Micro-tubes*. IFAC-PapersOnLine, 2019. **52**(10): p. 382-387.
 29. Şimşek, M. and J.N. Reddy, *Bending and vibration of functionally graded microbeams using a new higher order beam theory and the modified couple stress theory*. International Journal of Engineering Science, 2013. **64**: p. 37-53.
 30. Aghazadeh, R., E. Cigeroglu, and S. Dag, *Static and free vibration analyses of small-scale functionally graded beams possessing a variable length scale parameter using different beam theories*. European Journal of Mechanics - A/Solids, 2014. **46**: p. 1-11.
 31. Zhang, P. and Y. Fu, *A higher-order beam model for tubes*. European Journal of Mechanics - A/Solids, 2013. **38**: p. 12-19.
 32. Babaei, H. and M. Reza Eslami, *Size-dependent vibrations of thermally pre/post-buckled FG porous micro-tubes based on modified couple stress theory*. International Journal of Mechanical Sciences, 2020. **180**: p. 105694.
 33. She, G.-L., et al., *Nonlinear bending and vibration analysis of functionally graded porous tubes via a nonlocal strain gradient theory*. Composite Structures, 2018. **203**: p. 614-623.
 34. She, G.-L., et al., *On buckling and postbuckling behavior of nanotubes*. International Journal of Engineering Science, 2017. **121**: p. 130-142.
 35. Zhong, J., et al., *Nonlinear bending and vibration of functionally graded tubes resting on elastic foundations in thermal environment based on a refined beam model*. Applied Mathematical Modelling, 2016. **40**(17): p. 7601-7614.
 36. Hutchinson, J.R., *Shear Coefficients for Timoshenko Beam Theory*. Journal of Applied Mechanics, 2000. **68**(1): p. 87-92.
 37. Sahmani, S. and B. Safaei, *Large-amplitude oscillations of composite conical nanoshells with in-plane heterogeneity including surface stress effect*. Applied Mathematical Modelling, 2021. **89**: p. 1792-1813.
 38. Wang, L., *Size-dependent vibration characteristics of fluid-conveying microtubes*. Journal of Fluids and Structures, 2010. **26**(4): p. 675-684.

**Research Article****A numerical study of the natural convection of Al₂O₃-EG nanofluid in a square enclosure and impacts and a comparison of various viscosity and thermal conductivity models****Nese Keklikcioglu Cakmak^{a,*} , Hasan Hüseyin Durmazucar^a and Kerim Yapici^b** ^aDepartment of Chemical Engineering, Faculty of Engineering, Sivas Cumhuriyet University, Sivas, Turkey,^bDepartment of Chemical Engineering, Faculty of Engineering, Süleyman Demirel University, Isparta, Turkey

ARTICLE INFO

Article history:

Received 02 January 2021

Revised 15 May 2021

Accepted 09 June 2021

*Keywords:*Al₂O₃

Finite volume method

Fourth-order linear scheme

Lid-driven cavity

Nanofluid

Natural convection

Thermal conductivity

Viscosity

ABSTRACT

In the current study, heat transfer enhancement in an enclosure was investigated by utilizing Al₂O₃-EG nanofluid. In the numerical solutions, the solid-liquid mixture equations were applied for the enclosure that composed alumina-ethylene glycol nanofluid, in terms of the two-dimensional buoyancy-driven convection. Various viscosity and thermal conductivity models were utilized for the purpose of assessing heat transfer improvement. The purpose of this study was to reveal the impacts caused by uncertainties in the viscosity and thermal conductivity of the nanofluid on laminar natural convection heat transfer occurring in a square enclosure. The temperatures of the right and left vertical walls of the enclosure were kept constant as T_c and T_h, respectively, whereas the thermal insulation of the other walls was performed. The discretization of the governing equations was performed by utilizing the finite volume method and the SIMPLE algorithm. Calculations were made for the Rayleigh number (10³-10⁶) and the volume fraction of alumina nanoparticles, φ= 0-5%. In this study, many parameters affecting heat transfer by natural convection were investigated in the enclosure containing Al₂O₃-EG nanofluid, and it was found that nanofluid viscosity was the most efficient factor for heat transfer rate.

© 2021, Advanced Researches and Engineering Journal (IAREJ) and the Author(s).

1. Introduction

Because of its broad range of applications in the cooling of nuclear reactors, chemical processes, micro/mini-channel heat sinks, automobiles, solar energy collections, electronic system components, and heat exchangers, natural convection heat transfer represents a significant phenomenon in engineering systems [1-7]. In such systems, heat transfer increase is important for energy and industrial conservation. The fact that the thermal conductivity of conventional heat transfer fluids, including oil, ethylene glycol (EG), and water is low is regarded to be the main restriction on improving the performance and compactness of such thermal systems. Researchers conduct comprehensive studies for the purpose of revealing novel ways to meet the industrial requirements in the field of these thermal systems. The idea of Maxwell

to suspend micrometer or metallic millimeter-sized particles to be able to improve the thermal conductivity of fluids is broadly known [8]. Nevertheless, it is not possible to utilize these particles in micro-devices since they can lead to a number of significant issues, including the abrasion of the heat transfer device such as a pipeline, cooling channels, etc., blocking of the flow channels, and increasing in the pressure decrease in the fluid. Thus, fluids containing large suspended particles have limited practical applications in enhancing heat transfer. Nevertheless, modern nanotechnology presents significant opportunities for producing materials that have a mean size of 100 nanometer or below. The above-mentioned particles may disperse well in traditional working fluids for the purpose of generating a new heat transfer fluid type, which is known under the name of nanofluid [9]. There is a strong dependence of the management and

* Corresponding author. Tel.: +90-346-219-1010 / 2232 ; Fax: +90-346-219-1010.

E-mail addresses: nkeklikcioglu@cumhuriyet.edu.tr (N. Keklikcioglu Cakmak), hdurmaz@cumhuriyet.edu.tr (H.H. Durmazucar), kerimyapici@gmail.com (K. Yapici)

ORCID: 0000-0002-8634-9232 (N. Keklikcioglu Cakmak), 0000-0003-2454-7003 (H. H. Durmazucar), 0000-0002-3902-9375 (K. Yapici)

DOI: 10.35860/iarej.852562

This article is licensed under the CC BY-NC 4.0 International License (<https://creativecommons.org/licenses/by-nc/4.0/>).

miniaturization of engineering systems in thermal terms on the enhancement of working fluids' thermal behaviors. Comprehensive research has been conducted recently on a novel technique developed to enhance heat transfer by utilizing nano-scale particles that are dispersed in a base fluid, which is as also called nanofluid. Nanofluids, as new heat transfer fluids, may take a significant part in enhancing the thermal effectiveness of engineering devices, including cooling systems and heat exchangers. Comprehensive studies were carried out in the last ten years on convective heat transfer by utilizing nanofluids [10, 11]. Some researchers have carried out studies to improve the heat transfer-related properties of forced convection applications. On the contrary, not enough attention has been paid to enhancing heat transfer in applications regarding natural convection. As a first, Khanafer et al. [12] conducted a research on natural convection heat transfer inside a nanofluid-filled rectangular enclosure. A numerical natural convection simulation modeled as two-dimensional is presented for a nanofluid-filled vertical enclosure. The study showed that thanks to the volumetric fraction emerging in copper nanoparticles in the water at a specified Grashof number, an increase occurred in heat transfer through the enclosure. Hwang et al. [13] theoretically investigated the natural convection caused by the temperature change between the lower and upper walls and the adiabatic sidewalls in a rectangular cavity with water- Al_2O_3 nanofluids. They found that the increased nanoparticle size caused the deterioration of the natural rate of convection in the enclosure. Abu-Nada [14] investigated the impact of different characteristics of Al_2O_3 -water nanofluids on natural convection in a circular medium. The researcher determined that for $Ra \geq 10^4$, the heat transfer increased as the concentration of nanoparticles increased. However, improvement occurred in heat transfer at $Ra = 10^3$. By using nanofluids for different related parameters, Oztop and Abu-Nada [15] studied the improvement of heat transfer in a rectangular enclosure. The researchers stated that the reason for the improvement of heat transfer was the increased heater size and the Rayleigh (Ra) number. Corcione et al. [16] conducted the analysis of heat transfer in an enclosure, which was filled with a nanofluid, and obtained the findings indicating that an increase in nanoparticle concentration caused an increase in the performance of the heat transfer. Furthermore, the scholars revealed that as the average nanofluid temperature and width of the enclosure increased and the size of the nanoparticle decreased, the heat transfer increased. Mahalakshmi et al. [17] carried out a quantitative research related to the natural convective heat transfer in an enclosure with a center heater by utilizing nanofluids. They showed that an increase occurred in heat transfer with the increased heater length in both horizontal and

vertical positions for the increased Rayleigh numbers. Especially a more significant increase was observed in heat transfer due to a heater located in a vertical position of a maximum length. Yıldız et al. [18] conducted a comparative research to examine the thermal conductivity model on mono and hybrid nanofluids. A recently conducted numerical study demonstrated a lower thermal conductivity acquired by utilizing a number of theoretical and numerical models in comparison with their study because of ignoring a number of significant factors, such as nanoparticles' shapes and sizes.

Nevertheless, the results of experimental research related to the subject are contradictory [13, 19-21]. Accordingly, the dispersion of nanoparticles in a base fluid can lead to a considerable decrease, not the improvement, in the natural convection heat transfer in enclosures. Putra et al. [22] investigated the natural convection heat transfer of nanofluids experimentally in a horizontal cylinder. In their study, heating and cooling were performed from two ends, respectively. They found that with the use of CuO / water and Al_2O_3 / water nanofluids, the natural convective heat transfer undergoes a definite degradation depending on the cylinder's particle density, aspect ratio, and concentration. It was also found that with particle concentration, an increase occurred in the deterioration and it was more considerable in terms of CuO nanofluids. For instance, it was identified that at the 5×10^7 Rayleigh number, there were 150% and 300% reductions in the Nusselt number for 4 wt% of Al_2O_3 and CuO, respectively. Similar to Putra et al. [22], Wen and Ding [19] revealed a reduction in the coefficient of the natural convective heat transfer in comparison with pure water. Moreover, an increase was observed in the deterioration in question with nanoparticle concentration. For their observations, the researchers suggested a number of potential techniques, including the convection induced by a difference in concentration, interactions between particle-particle and particle-fluid, and modified dispersion characteristics.

For the mentioned difference among the numerical estimations and experimental findings with regard to the natural convection heat transfer efficiency of utilizing nanofluids in enclosures, the potential factors that ensures contribution can be vary in terms of the shape and size of particles, the distribution of particles, and uncertainty observed in the thermo-physical properties of nanofluids, particularly the effective dynamic viscosity and thermal conductivity. Therefore, the goal of this research is to investigate, through numerical simulations, the impacts of uncertainties because of employing various formulate in terms of the efficient thermal conductivity and dynamic viscosity of the Al_2O_3 -EG nanofluid on the properties related to the natural convection heat transfer occurring in a vertical square enclosure. In addition, in a part of this study, an evaluation of thermophysical properties, such as

thermal conductivity and viscosity, obtained by using experimental data on heat transfer in natural convection are presented.

2. Problem Statement and Mathematical Formulation

Figure 1 presents the physical models discussed in this study, the related boundary conditions, and geometric dimensions. Figure 1 is utilized with the aim of examining the natural convection heat transfer. A square cavity having stationary walls is investigated. Temperatures of the right and left walls belonging to the cavity are kept steady as cold (TC) and hot (TH), respectively. On the other hand, the walls at the bottom and top are kept as adiabatic. In terms of a series of the Rayleigh numbers, the analysis of the flow and heat transfer phenomena was performed for the case of natural convection. In the case, Al₂O₃-EG nanofluid was considered.

The thermophysical characteristics of Al₂O₃ nanoparticles and EG are shown in Table 1.

Utilizing the Boussinesq approximation and ignoring the viscous dissipation impact, the mathematical model for natural convection was obtained. For the Cartesian coordinate in two dimensions, it is possible to write the dimensionless governing equations in the following way:

$$\frac{\partial u}{\partial x} + \frac{\partial v}{\partial y} = 0 \tag{1}$$

$$u \frac{\partial u}{\partial x} + v \frac{\partial v}{\partial y} = -\frac{1}{\rho_{nf}} \frac{\partial p}{\partial x} + \nu_{nf} \left(\frac{\partial^2 u}{\partial x^2} + \frac{\partial^2 u}{\partial y^2} \right) \tag{2}$$

$$u \frac{\partial v}{\partial x} + v \frac{\partial v}{\partial y} = -\frac{1}{\rho_{nf}} \frac{\partial p}{\partial y} + \nu_{nf} \left(\frac{\partial^2 v}{\partial x^2} + \frac{\partial^2 v}{\partial y^2} \right) + g\beta_{nf}(T - T_c) \tag{3}$$

$$u \frac{\partial T}{\partial x} + v \frac{\partial T}{\partial y} = \alpha_{nf} \left(\frac{\partial^2 T}{\partial x^2} + \frac{\partial^2 T}{\partial y^2} \right) \tag{4}$$

The above-mentioned governing equations are obtained by utilizing the non-dimensional quantities presented below:

$$\begin{aligned} x' &= \frac{x}{H}, & y' &= \frac{y}{H}, & u' &= \frac{uH}{\alpha_f}, & v' &= \frac{vH}{\alpha_f}, \\ p' &= \frac{pH^2}{\rho_{nf}\alpha_f^2}, & \theta &= \frac{T-T_c}{T_H-T_c} \end{aligned} \tag{5}$$

where quantities shown with a prime mark refer to the dimensional forms of the primitive variables. In Equation 6, calculation of the dimensionless Prandtl (Pr) and Rayleigh (Ra) numbers are shown.

Figure 1 demonstrates the natural convection-related boundary conditions. It is seen that on every wall of the square cavity, the boundary condition of no-slip velocity is implemented. Regarding the non-dimensional temperature (θ), on the left wall ($\theta=1$) and the right wall ($\theta=0$), a constant boundary condition is set.

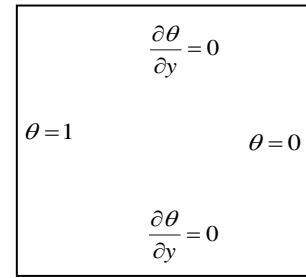


Figure 1. The natural convection problem

Table 1. Thermophysical characteristics of fluid (EG) and Al₂O₃ nanoparticles [23, 24]

	ρ	c_p	k	μ	β
	kgm ⁻³	Jkg ⁻¹ K ⁻¹	Wm ⁻¹ K ⁻¹	kgm ⁻¹ s ⁻¹	K ⁻¹
Al₂O₃	3970	765	40	-	0.85x10 ⁻⁵
Ethylene Glycol	1114	2415	0.252	0.0161	5.7x10 ⁻⁴

$$Ra = \frac{g\beta\Delta TH^3}{\nu\alpha} \quad Pr = \frac{\nu}{\alpha} \tag{6}$$

While keeping the walls at the top and bottom as adiabatic, a zero-flux boundary condition is implemented. Furthermore, the solution of problems related to the natural convection is achieved by utilizing Al₂O₃-EG nanofluid as a working fluid. In order to solve Al₂O₃-EG nanofluid, the approach of homogeneous single-phase is employed, and thus, the Al₂O₃-EG nanofluid replaces the physical characteristics of the Newtonian fluid mentioned above. It is possible to write the non-dimensional governing equations in the way presented below:

$$\frac{\partial u'}{\partial x'} + \frac{\partial v'}{\partial y'} = 0 \tag{7}$$

$$u' \frac{\partial u'}{\partial x'} + v' \frac{\partial v'}{\partial y'} = -\frac{\partial p'}{\partial x'} + \frac{\mu_{nf}}{\rho_{nf}\alpha_f} \left(\frac{\partial^2 u'}{\partial x'^2} + \frac{\partial^2 u'}{\partial y'^2} \right) \tag{8}$$

$$\begin{aligned} u' \frac{\partial v'}{\partial x'} + v' \frac{\partial v'}{\partial y'} &= -\frac{\partial p'}{\partial y'} \\ &+ \frac{\mu_{nf}}{\rho_{nf}\alpha_f} \left(\frac{\partial^2 v'}{\partial x'^2} + \frac{\partial^2 v'}{\partial y'^2} \right) \\ &+ \frac{\beta_{nf}}{\beta_f} Ra Pr \theta \end{aligned} \tag{9}$$

$$u' \frac{\partial \theta}{\partial x'} + v' \frac{\partial \theta}{\partial y'} = \frac{\alpha_{nf}}{\alpha_f} \left(\frac{\partial^2 \theta}{\partial x'^2} + \frac{\partial^2 \theta}{\partial y'^2} \right) \tag{10}$$

In these equations, *nf* refers to the features of the Al₂O₃-EG nanofluid. On the other hand, *f* denotes the characteristics of

the base fluid (EG). The non-dimensional quantities given in Equations from 7 to 10 are described by utilizing base fluid characteristics and they are also presented in Equation 6.

The governing flow equations are discretized by using the finite volume method. The second-order central differencing scheme is utilized to approximate the diffusion terms in the governing equations. On the other hand, the non-uniform form of the four-point fourth-order interpolation scheme proposed by Yapici and Obut [25] is utilized to be able to approximate convective terms.

Various correlations related to the physical characteristics of the Al₂O₃-EG nanofluid are introduced in the literature. In the present research, 2 cases formed by combining 8 different viscosity and 2 different thermal conductivity correlation model equations presented in tables 2 and 3 were investigated. While the combination of 8 various viscosity models was formed with the thermal conductivity model proposed by Maxwell [8] in the first case, the combination of 8 various viscosity models with the thermal conductivity model proposed by Chandrasekar et al. [26] was formed in the second case.

Where ϕ denotes the volume fraction of Al₂O₃ nanoparticles in the base fluid (EG). By utilizing the mixing rule, the heat capacity ($C_{p_{nf}}$), thermal expansion coefficient (β_{nf}), density (ρ_{nf}), and molecular weight (M_{nf}) of the Al₂O₃-EG nanofluid are assessed [26]:

$$\rho_{nf} = (1 - \phi)\rho_f + \phi\rho_p \quad (11)$$

$$C_{p_{nf}} = \frac{(1 - \phi)C_{p_f}\rho_f + \phi C_{p_p}\rho_p}{\rho_{nf}} \quad (12)$$

$$\beta_{nf} = \frac{(1 - \phi)\beta_f\rho_f + \phi\beta_p\rho_p}{\rho_{nf}} \quad (13)$$

$$M_{nf} = (1 - \phi)M_f + \phi M_p \quad (14)$$

The first three (1, 2, 3) models used as the viscosity model in Table 2 are theoretically obtained conventional effective viscosity models and are valid for spherical particles in the micro-dimension, where there is no interaction between particles. Furthermore, the model used as the thermal conductivity model is the effective thermal conductivity model proposed by Maxwell theoretically. The other viscosity models are the correlation equations experimentally obtained by the researchers. The fourth and fifth viscosity models in Table 2 are experimental correlation equations. The fourth model was derived for nanofluid formed with 47nm Al₂O₃ nanoparticles, and the fifth model was derived for nanofluid formed with 36 nm Al₂O₃ nanoparticles and water fluid. The experimental viscosity measurement was performed by a piston-type viscometer.

Table 2. Thermal conductivity and viscosity models utilized in numerical analysis (Case 1)

Model	Researcher	Viscosity	Thermal conductivity
I	(Brinkman, 1952) [27]	$\frac{\mu_{nf}}{\mu_f} = (1 - \phi)^{-2.5}$	
II	(Einstein, 1956) [28]	$\frac{\mu_{nf}}{\mu_f} = (1 + 2.5\phi)$	
III	(Batchelor, 1977) [29]	$\frac{\mu_{nf}}{\mu_f} = (1 + 2.5\phi + 6.5\phi^2)$	
IV	(Nguyen, 2008) [30]	$\frac{\mu_{nf}}{\mu_f} = (1 + 2.5\phi + 1.5\phi^2)$	
V	(Nguyen, 2008) [30]	$\frac{\mu_{nf}}{\mu_f} = (0.904e^{0.1483\phi})$	$\frac{k_{nf}}{k_f} = \frac{(k_p + 2k_f) - 2\phi(k_f - k_p)}{(k_p + 2k_f) - \phi(k_f - k_p)}$ (Maxwell, 1881) [8]
VI	(Chandrasekar et al., 2010) [26]	$b=5300, n=2.8$ $\frac{\mu_{nf}}{\mu_f} = \left(1 + b\left(\frac{\phi}{1 - \phi}\right)^n\right)$	
VII	(Maiga et al., 2004) [31]	$\frac{\mu_{nf}}{\mu_f} = (1 + 7.3\phi + 123\phi^2)$	
VIII	Experimentally obtained in this study	$\frac{\mu_{nf}}{\mu_f} = (1 + 2.5\phi + 107.2\phi^2)$	

Table 3. Thermal conductivity and viscosity models utilized in numerical analysis (Case 2)

Model	Researcher	Viscosity	Thermal conductivity
I	(Brinkman, 1952) [27]	$\frac{\mu_{nf}}{\mu_f} = (1 - \varphi)^{-2.5}$	
II	(Einstein, 1956) [28]	$\frac{\mu_{nf}}{\mu_f} = (1 + 2.5\varphi)$	
III	(Batchelor, 1977) [29]	$\frac{\mu_{nf}}{\mu_f} = (1 + 2.5\varphi + 6.5\varphi^2)$	
IV	(Nguyen, 2008) [30]	$\frac{\mu_{nf}}{\mu_f} = (1 + 2.5\varphi + 1.5\varphi^2)$	
V	(Nguyen, 2008) [30]	$\frac{\mu_{nf}}{\mu_f} = (0.904e^{0.1483\varphi})$	$\frac{k_{nf}}{k_f}$
VI	(Chandrasekar et al., 2010) [26]	$b=5300, n=2.8$ $\frac{\mu_{nf}}{\mu_f} = \left(1 + b \left(\frac{\varphi}{1 - \varphi}\right)^n\right)$	$= \left(\frac{C_{pnf}}{C_{pf}}\right)^{-0.023} \left(\frac{\rho_{nf}}{\rho_f}\right)^{1.358} \left(\frac{M_f}{M_{nf}}\right)^{0.126}$
VII	(Maiga et al., 2004) [31]	$\frac{\mu_{nf}}{\mu_f} = (1 + 7.3\varphi + 123\varphi^2)$	
VIII	Experimentally obtained in this study	$\frac{\mu_{nf}}{\mu_f} = (1 + 2.5\varphi + 107.2\varphi^2)$	

When the nanoparticle size was 47 nm and the nanoparticle volumetric fraction was 1%, 4%, 9%, and 12%, the relative viscosity values were 1.12, 1.6, 3, and 5.3, respectively. When the nanoparticle size was 36 nm and the nanoparticle volumetric fraction was 2.1%, 4.3%, 8.5%, and 12.2%, the relative viscosity values were 1.1, 1.4, 2, and 3.1, respectively. As a result, it was emphasized that the dynamic viscosity of the nanofluid increased with the increased nanoparticle volumetric fraction and the results obtained from 36 nm and 47 nm were close to each other, except for the high nanoparticle volumetric fraction. Furthermore, the experimentally obtained results were compared to the Einstein and Batchelor models, and it was stated that there was an inconsistency between them. The sixth viscosity model given in Table 2 was experimentally obtained for the nanofluid prepared at different nanoparticle volumetric fractions (0.33%-5%) with 43nm Al₂O₃ nanoparticles and water base fluid. A Brookfield cone and plate viscometer were used. While it was indicated that the nanofluid viscosity increased with the nanoparticle volumetric fraction when the nanoparticle volumetric fraction was 2% at most, a nonlinear relationship was revealed between an increase in the nanofluid viscosity and nanoparticle volumetric fraction when the nanoparticle volumetric fraction was more than 2%. It was argued that the reason for the formation of this situation might be more significant hydrodynamic

interaction between particles when the nanoparticle volumetric fraction was more than 2%. The seventh viscosity model given in Table 2 is a model obtained by Maiga et al. [31] by the correlation of the results experimentally acquired by Wang et al. [32]. They obtained the experimental results by measuring with a viscometer for nanofluids prepared at different nanoparticle volumetric fractions (1 – 6%) with 28 nm Al₂O₃ nanoparticles and water base fluid. The experimentally obtained results were calculated with the least-squares curve, and the dynamic viscosity of the nanofluid was obtained. It was concluded that the increase in the viscosity of the Al₂O₃-water nanofluid was almost 20%-30% when the nanoparticle volumetric fraction was 3%.

The eighth viscosity model given in Table 2 is the correlation equation obtained for the nanofluid at different nanoparticle volumetric fractions (1-5%), experimentally created in this study with 80 nm Al₂O₃ nanoparticles and ethylene glycol base fluid. All rheological measurements were carried out by a stress controlled Kinexus cone and plate rheometer under constant shear rate.

The viscosity models used in Table 3 are the same as the viscosity models in Table 2, and the used thermal conductivity model is the thermal conductivity model experimentally obtained by Chandrasekar et al. (2010) [26]. The measurement of the thermal conductivity of the nanofluid was performed by a Decagon KD2 Pro device

when the volumetric fraction was 3% at most. When the nanoparticle size was 43 nm and the nanoparticle volumetric fraction was 0.33%, 0.75%, 1%, 2%, and 3%, the thermal conductivity increase percentages were 1.64, 3.28, 3.43, 7.52, and 9.7, respectively. As a result, it was revealed that the thermal conductivity value of the nanofluid increased linearly with the increased nanoparticle volumetric fraction in the nanofluid, and the correlation equation was obtained. The thermal conductivities of the nanofluids prepared in the present research were measured experimentally, and the obtained correlation equation was found to be consistent with the thermal conductivity correlation equation proposed by Chandrasekar et al. (2010) [26].

3. Results and Discussion

In Tables 4 and 5, for model 1, the results obtained with four different Ra numbers (103, 104, 105, 106) were presented in the case of only heat transfer by natural convection in a square cavity geometry at five different nanoparticle volumetric fractions (1%, 2%, 3%, 4%, 5%) of the Al_2O_3 - EG nanofluid. The results were obtained for the Prandtl (Pr) number of 0.71, and u_{max} and y_{max} also, respectively, indicate the maximum value and position of the horizontal velocity component obtained along $x=0.5$ from the center of geometry. Similarly, v_{max} and x_{min} indicate the maximum value and position of the vertical velocity component obtained along $y=0.5$ from the center of the geometry. The Nu number, the measure of heat transfer, was calculated by taking the derivative of the temperature distribution along the heated wall according to component x. Nu_{max} and Nu_{min} show the maximum and minimum Nu numbers and positions computed along the hot wall. Nu_{avg} gives the average value acquired as a result of integrating the Nu number calculated along the hot wall. Nu_{avg}/Nu_{EG} shows the ratio of the average value obtained by integrating the Nu number computed along the hot wall to the calculated Nu number of the pure ethylene glycol base fluid.

Although there are many studies in the literature on nanofluids, there are few studies on the rheology of nanofluids [33-41]. In the studies conducted with nanofluids, some researchers [42, 43] argued that nanofluids behave in accordance with Newton's rule, while the others [33, 44-47] suggested that nanofluids exhibit a non-Newtonian behavior. In Figure 2, when the temperature of the Al_2O_3 -EG nanofluid was 25 °C, the variation of the viscosity increase in percentage with the nanoparticle volumetric fraction was examined in different models. As can be seen from Figure 2, a considerable difference was observed in the viscosity increase of the nanofluid in the models with the increased nanoparticle volumetric fraction. For example, when the nanoparticle volumetric fraction was 5%, the viscosity increase of the nanofluid in model 6 was 140%, whereas this increase was almost 12% in model 4. The reason for this situation is the fact that the viscosity value of the nanofluid

computed in the equation in model 6 was significantly higher compared to the viscosity value of the nanofluid in the equation in model 4. Furthermore, it draws attention that the viscosity increase with the increase in the nanoparticle volumetric fraction in models 5, 6, 7, and 8 was significantly higher compared to the other models. As seen from Figure 2, it is evident that the increase in the nanofluid viscosity is a function of the nanoparticle volumetric fraction. While a linear relationship was observed between the nanoparticle volumetric fraction and viscosity in models 1, 2, and 3, a nonlinear relationship was observed in the other models. The first three models are traditionally used viscosity models, and as previously mentioned, are similar to the experimental and valid data at low nanoparticle volumetric fractions. The reason for the increase in viscosity with the nanoparticle volumetric fraction, especially in models 5, 6, 7, and 8, is a result of the experimentally obtained correlation equations of these models. It is clearly observed that the viscosity increases of the experimental models are different from each other. The nanoparticles in each model and the sizes of these nanoparticles are different from each other. With the effect of the hydrodynamic force on the solid nanoparticle surface, the viscosity increases of the nanoparticles, which are accepted to be very well dispersed in the base fluid, can be affected. Since these hydrodynamic forces acting on nanoparticles of different sizes will also be different, the viscosity increase in the models may be different. For example, the viscosity increase of the nanofluid formed by Al_2O_3 with the particle size of 43 nm and water base fluid in model 6 is significantly higher in comparison with the viscosity increase of the nanofluid formed with 80 nm Al_2O_3 and ethylene glycol base fluid in model 8. Based on this, it is possible to conclude that the nanofluid viscosity increases with the decreasing nanoparticle size, similarly to the results obtained in the study by Gallego et al. (2011) [30].

For the purpose of determining the variation in the amount of heat transfer by natural convection in the square cavity geometry with the Al_2O_3 -EG nanofluid, the change was given as the ratio of the average Nu number computed along the hot wall versus the nanofluid concentration to the calculated Nu number of the ethylene glycol base fluid at four different Ra numbers, 10^3 , 10^4 , 10^5 , and 10^6 , in Figure 3 (Case 1).

As is known, at low Ra numbers, heat transfer occurs with the conduction mechanism in a square cavity geometry. In Figure 3(a), upon examining the change in the average Nu number calculated along the hot wall, which is regarded as a measure of the amount of change in the heat transfer rate with the nanoparticle volumetric fraction of the Al_2O_3 -EG nanofluid at low Ra numbers (Ra , 10^3), with the ratio to the calculated Nu number of the ethylene glycol base fluid, the heat transfer rate slightly decreased with the increased nanoparticle volumetric fraction in models 5, 6, 7, and 8, while the heat transfer rate increased a little bit with the

increased nanoparticle volumetric fraction in the other models. The reason why the change here was not too high was not too much variation in the heat transfer rate due to the fact that the heat transfer was realized by the conduction mechanism at $Ra, 10^3$, the viscosity had no impact on the heat transfer rate in this case, and the used thermal conductivity model equation was common although the viscosity equations used in the models were different. In other words, at low Ra numbers, the thermal conductivity model to be used becomes important and determines the amount of increase to be obtained from numerical analysis.

Although the heat transfer occurs by the conduction mechanism at low Ra numbers, the heat transfer is realized by the convection mechanism when the Ra number is 10^4 and higher. In this case, contrary to the case of 10^3 , the viscosity

models used in numerical analysis become more important. It is determined that an increase occurs in the heat transfer rate with the increased Ra number at any nanoparticle volumetric fraction at the values of the Ra number of $10^4, 10^5$, and 10^6 in all models. This can be understood better from the variation of the viscosity increase with the nanoparticle volumetric fraction for different models given in Figure 3.

Figure 4 demonstrates the change in the average Nu number calculated along the hot wall versus the nanofluid concentration with the ratio to the calculated Nu number of the ethylene glycol base fluid, by considering Case 2.

The difference between the figures given here and Figure 3 (Case 1) is that the used thermal conductivity model is different. The thermal conductivity model utilized here is the correlation equation obtained from the experimental data.

Table 4. Variation of the results obtained with four different Rayleigh (Ra) numbers for model 1 with nanoparticle volumetric fraction ($Ra=10^3$ and 10^4)

a) $Ra=10^3$

\emptyset (%)	u_{max}	y_{max}	v_{max}	x_{min}	Nu_{max}	y_{min}	Nu_{min}	y_{max}	Nu_{avg}	Nu_{avg}/Nu_{EG}
0	3.65810344	0.81093875	3.69029864	0.81786953	1.50945640	0.99900	0.69286702	0.08123783	1.12034418	1.17369131
1	3.55160036	0.81093875	3.58008800	0.81786953	1.50021670	0.99900	0.70568006	0.08123783	1.12144911	1.13961232
2	3.44621050	0.81093875	3.47204208	0.81786953	1.49382303	0.99900	0.72039430	0.08123783	1.12451816	1.10581402
3	3.34173214	0.81093875	3.36482122	0.81786953	1.48659235	0.99900	0.73457529	0.08123783	1.12708440	1.07232775
4	3.23854643	0.81093875	3.25990584	0.81786953	1.48173333	0.99900	0.75032610	0.07687971	1.13128025	1.03920069
5	3.13630700	0.81093875	3.15496296	0.81786953	1.47357076	0.99900	0.76378893	0.07687971	1.13328362	1.00645089

b) $Ra=10^4$

\emptyset (%)	u_{max}	y_{max}	v_{max}	x_{min}	Nu_{max}	y_{min}	Nu_{min}	y_{max}	Nu_{avg}	Nu_{avg}/Nu_{EG}
0	16.29452242	0.81786953	19.756268	0.8738399	3.69290540	0.9990	0.5679865	0.1206406	2.2785332	1
			26	6		0	3	0	6	
1	16.11105023	0.81786953	19.399180	0.8738399	3.66917206	0.9990	0.5721555	0.1206406	2.2672798	0.995061134
			71	6		0	1	0	9	
2	15.92145724	0.81786953	19.039341	0.8738399	3.64520741	0.9990	0.5764388	0.1206406	2.2558217	0.990032417
			56	6		0	8	0	9	
3	15.72580521	0.81093875	18.676477	0.8738399	3.62036448	0.9990	0.5806721	0.1206406	2.2437942	0.984753788
			41	6		0	5	0	6	
4	15.52400302	0.81093875	18.310216	0.8738399	3.59390922	0.9990	0.5846574	0.1261600	2.2307792	0.979041794
			43	6		0	7	4	9	
5	15.31629111	0.81093875	17.949511	0.8681833	3.56666093	0.9990	0.5886025	0.1261600	2.2172295	0.973095091
			7	2		0	5	4	3	

Table 5. Variation of the results obtained with four different Rayleigh (Ra) numbers for model 1 with nanoparticle volumetric fraction (Ra=10⁵ and 10⁶)

c) Ra=10⁵

Ø (%)	u _{max}	y _{max}	v _{max}	x _{min}	Nu _{max}	y _{min}	Nu _{min}	y _{max}	Nu _{avg}	Nu _{avg} /Nu _{EG}
0	36.74544379	0.84416170	73.78080601	0.92735897	8.54684085	0.99900	0.63786674	0.07687971	4.73379300	1
1	36.53469939	0.8441617	72.70857581	0.92735897	8.49586659	0.99900	0.64247331	0.07687971	4.71802856	0.996669808
2	36.31567196	0.8441617	71.61593655	0.92735897	8.44227153	0.99900	0.64692121	0.07687971	4.7007131	0.993011967
3	36.08907074	0.8441617	70.52711549	0.92312029	8.38646177	0.99900	0.65124959	0.07687971	4.68203683	0.98906666
4	35.85850926	0.83780294	69.44880317	0.92312029	8.32860549	0.99900	0.65543709	0.08123783	4.66193879	0.984821007
5	35.62693937	0.83780294	68.35299158	0.92312029	8.26920694	0.99900	0.65951823	0.08123783	4.64058323	0.980309707

d) Ra=10⁶

Ø (%)	u _{max}	y _{max}	v _{max}	x _{min}	Nu _{max}	y _{min}	Nu _{min}	y _{max}	Nu _{avg}	Nu _{avg} /Nu _{EG}
0	84.55612499	0.889992	235.94073	0.96049229	19.759115	0.99900	0.7555784	0.0395077	9.25328477	1
1	83.93812107	0.889992	233.05367	0.95722975	19.643750	0.99900	0.7600232	0.0395077	9.23065441	0.997554343
2	83.29366501	0.889992	230.13741	0.95722975	19.522327	0.99900	0.7642888	0.0395077	9.20515637	0.994798777
3	82.62374944	0.889992	227.15080	0.95722975	19.395606	0.99900	0.7683834	0.0395077	9.17704325	0.991760599
4	81.93223668	0.884743	224.09775	0.95722975	19.263244	0.99900	0.7723086	0.0395077	9.14621627	0.988429136
5	81.24754884	0.884743	220.98254	0.95722975	19.126735	0.99900	0.7760718	0.04277025	9.1128608	0.984824423

In Figure 4(a), upon examining the change in the average Nu number calculated along the hot wall, which is evaluated as a measure of the amount of change in the heat transfer rate with the nanoparticle volumetric fraction of the Al₂O₃-EG nanofluid at low Ra numbers (Ra = 10³) with the ratio to the calculated Nu number of the ethylene glycol base fluid, a linear increase is determined in the heat transfer rate with the increased nanoparticle volumetric fraction in all models. The difference between the increasing Ra number and models closed, and the amounts of increase converged. Similarly, to the variation in Case 1, the heat transfer rates of the models (5, 6, 7, 8) created with the experimentally obtained viscosity correlation equations are observed to decrease with the nanoparticle volumetric fraction. Furthermore, even if the thermal conductivity model changes, the change in the amount of increase and decrease does not change with the nanoparticle volumetric fraction. In this case, it becomes clear that nanofluid viscosity models are more important than nanofluid thermal conductivity models.

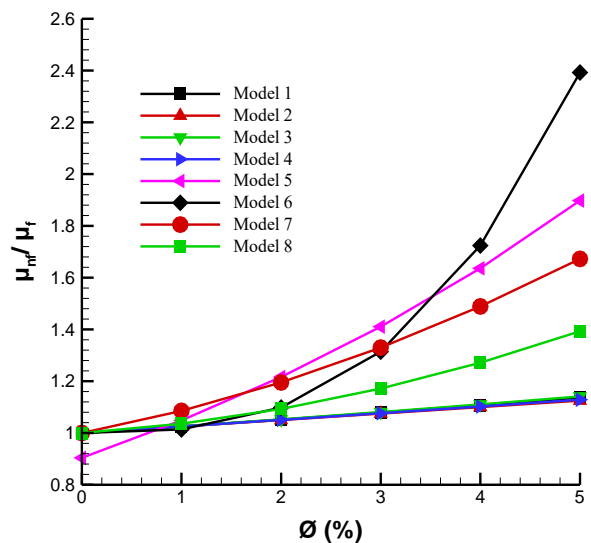


Figure 2. Variation of the relative viscosity increase with the Al₂O₃ nanoparticle volumetric fraction in percentage for different models

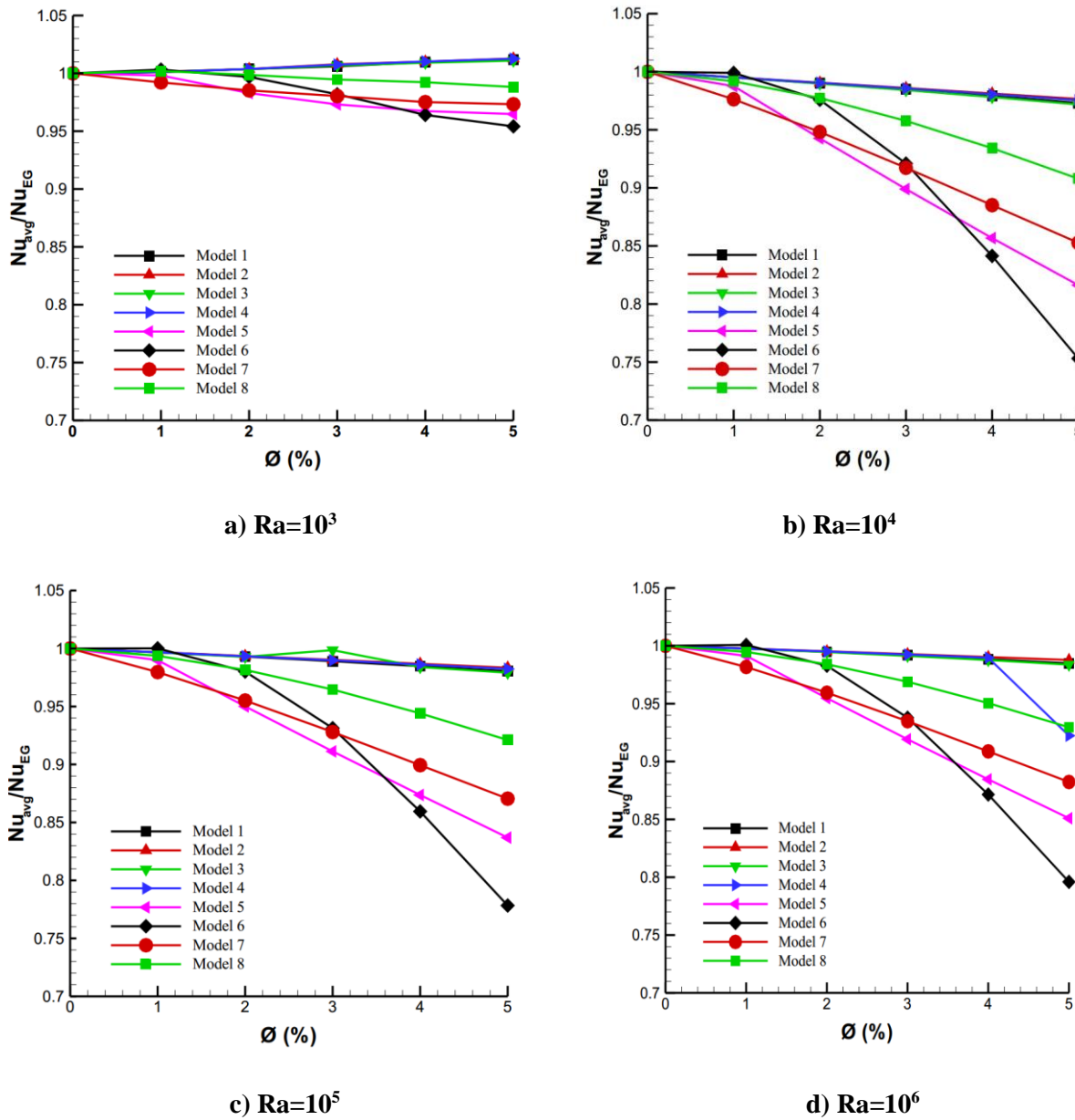


Figure 3. Variation of the ratio of the average Nu number computed along the hot wall to the Nu number calculated for pure ethylene glycol with the Al₂O₃ nanoparticle volumetric fraction in the square cavity geometry for different models. (Case 1)

Figures 5 and 6 demonstrate the impact of the nanoparticle volumetric fraction on the streamlines and isotherms at Ra numbers including 10^3 and 10^6 for three different models. In the figures, it is observed that only one vortex occurred in the streamlines at all Ra numbers and in all models (models 2, 6, 8). Since heat transfer by conduction is in question at a value of $Ra = 10^3$, the temperature contour isotherms are observed to advance almost parallel to the vertical walls. It draws attention that the structure of the vortexes formed in the center with the increased Ra number tends to be elliptical, and with the increased Ra number, the flow power efficiency increases in all models, and the boundary layer becomes more noticeable. It is revealed that the isotherms and streamlines are more severe around the hot and cold walls at a value of $Ra 10^6$. With the increase in the Ra number, the

circulation intensity increases and, thus, the amount of heat transfer also increases. Moreover, it is observed that thermal boundary layers are generated on the walls with the same temperature with an increase in the Ra number.

The increase in the circulation intensity with the increased Ra number in the same model and at the same nanoparticle volumetric fraction can be understood from the increase in the value of ϕ in Table 6. As is seen from Table 6, the value of ϕ was found to be higher almost at all Ra numbers and all nanoparticle volumetric fractions in model 2 in comparison with models 6 and 8. In the graph of the variation of viscosity increase with the nanoparticle volumetric fraction in Figure 2, the viscosity of model 2 varies linearly with the nanoparticle volumetric fraction, whereas the viscosity of models 6 and 8 varies as the second-order polynomial

function. In other words, at the same nanoparticle volumetric fraction, the viscosity increase value obtained from models 6 and 8 is significantly higher than the viscosity increase value obtained from model 2. Accordingly, as a result of the simulation performed with model 2, there was more mixing due to low viscosity in the square cavity, and the streamline value increased due to this situation.

Figure 7 shows the streamlines and isotherms at the constant nanoparticle volumetric fraction (5%) obtained from model 8 and at Ra numbers 10^3 and 10^6 . At the value of $Ra=10^3$, the temperature contour isotherms are observed to run almost parallel to the vertical walls. It is noteworthy that

this situation changes at higher Ra numbers and the isotherms run parallel to the horizontal walls. It is observed that the structure of the vortices formed in the center with the increase in the Ra number tends to be elliptical and the isotherms and streamlines around the hot and cold walls are more severe, especially at the value of $Ra 10^6$. With the increase in the Ra number, the circulation intensity increases, and, thus, the amount of heat transfer also increases. When the Ra number is 10^3 and 10^6 , the values of are 0.834, and 17.810, respectively. As a result, it is found that an increase occurs in the circulation intensity with the increased Ra number.

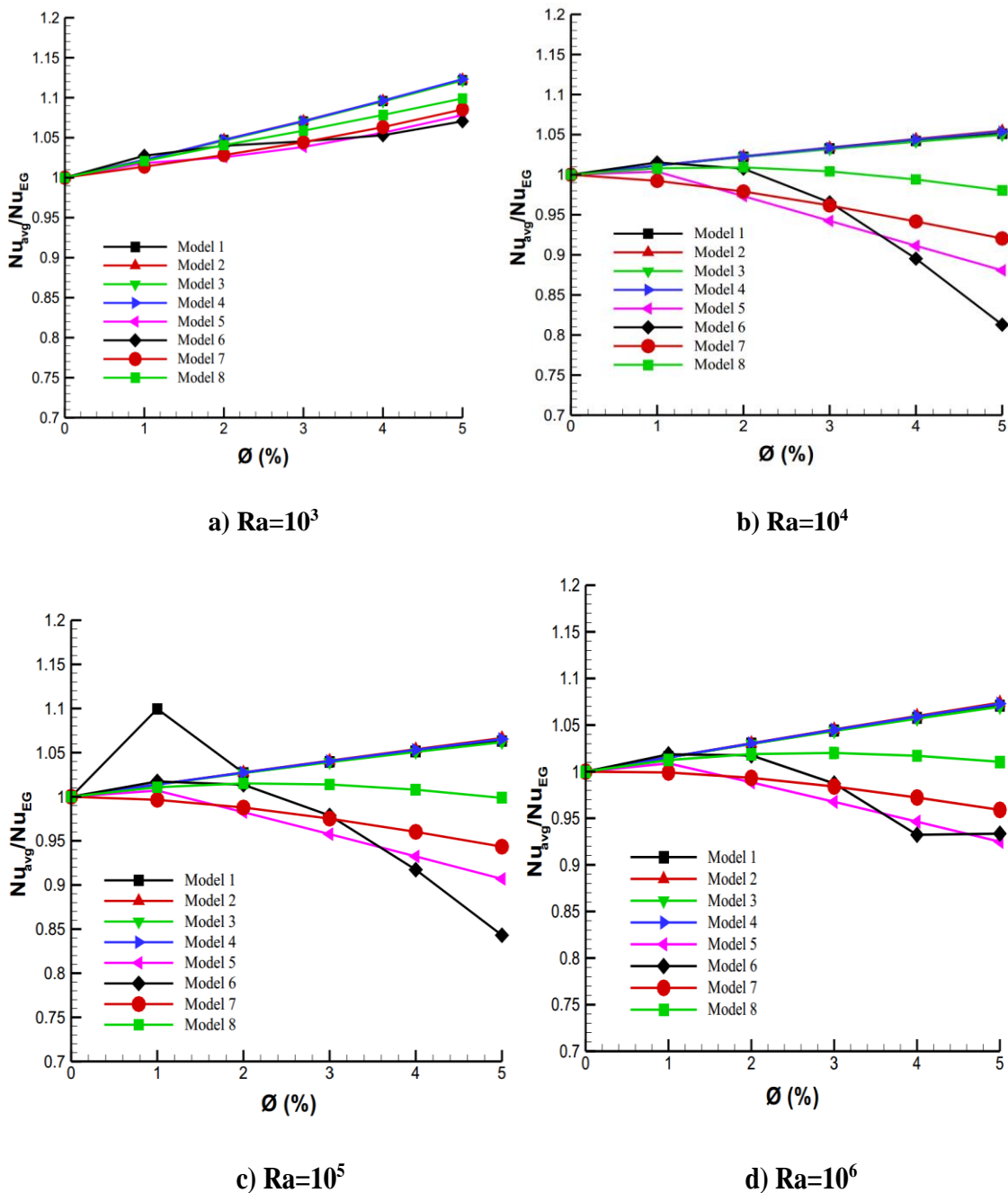


Figure 4. Variation of the ratio of the average Nu number computed along the hot wall to the Nu number calculated for pure ethylene glycol with the Al₂O₃ nanoparticle volumetric fraction in the square cavity geometry for different models. (Case 2)

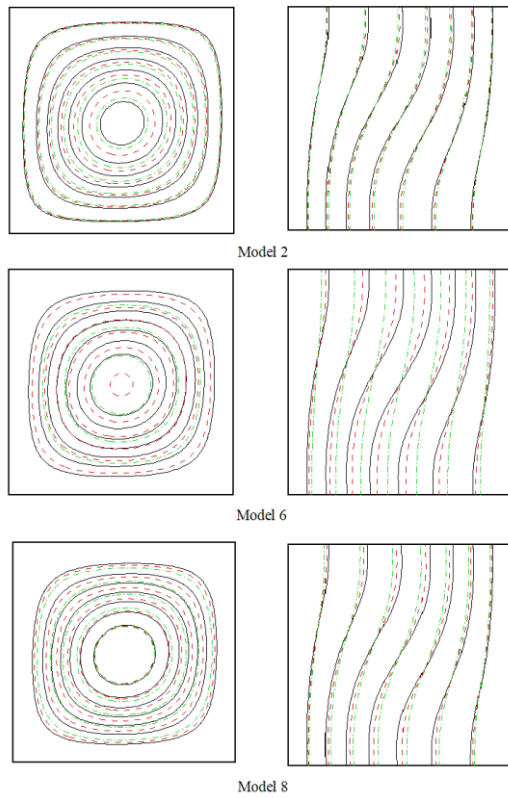


Figure 5. Streamlines (on the left) and isotherms (on the right) obtained from three various models for the Ra number of 103. Straight line: The base fluid is pure ethylene glycol; Dashed line: volumetric fraction $\phi = 3\%$; Dot-dashed line: volumetric fraction $\phi = 5\%$

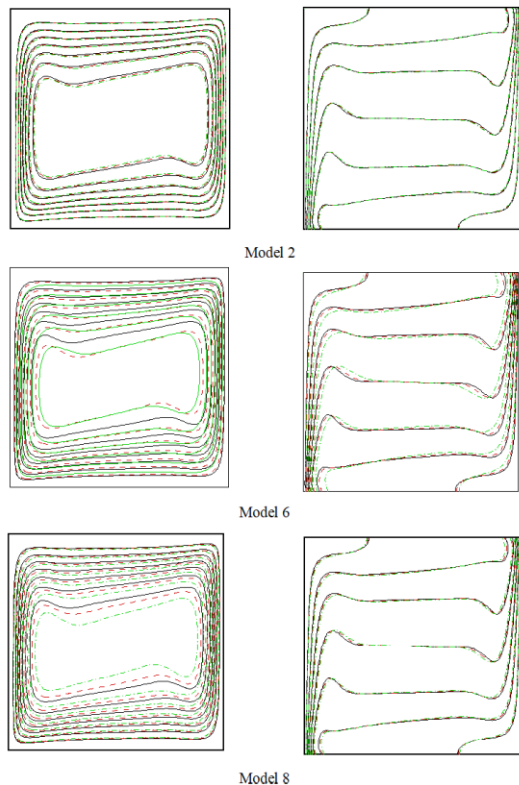


Figure 6. Streamlines (on the left) and isotherms (on the right) obtained from three various models for the Ra number of 106. Straight line: The base fluid is pure ethylene glycol; Dashed line: volumetric fraction $\phi = 3\%$; Dot-dashed line: volumetric fraction $\phi = 5\%$

Table 6. Variation of $|\psi_{mid}|$ values with the nanoparticle volumetric fraction and models for four different Rayleigh (Ra) numbers

	Model 2	Model 6	Model 8
	$ \psi_{mid} $	$ \psi_{mid} $	$ \psi_{mid} $
Ra = 10³			
$\phi = 0$	1.17369131	1.17369131	1.17369131
$\phi = 3$	1.07601917	0.89604768	0.99567184
$\phi = 5$	1.01605693	0.49698172	0.8343271
Ra = 10⁴			
$\phi = 0$	5.17565661	5.17565661	5.17565661
$\phi = 3$	5.01141879	4.55546043	4.81458625
$\phi = 5$	4.90059342	3.28177697	4.41558277
Ra = 10⁵			
$\phi = 0$	10.87485547	10.87485547	10.87485547
$\phi = 3$	10.78205462	10.22409723	10.54075466
$\phi = 5$	10.71546039	8.70841675	10.12306774
Ra = 10⁶			
$\phi = 0$	18.79429992	18.79429992	18.79429992
$\phi = 3$	18.72688246	17.91086387	18.3730733
$\phi = 5$	18.67433262	15.76604599	17.81044532

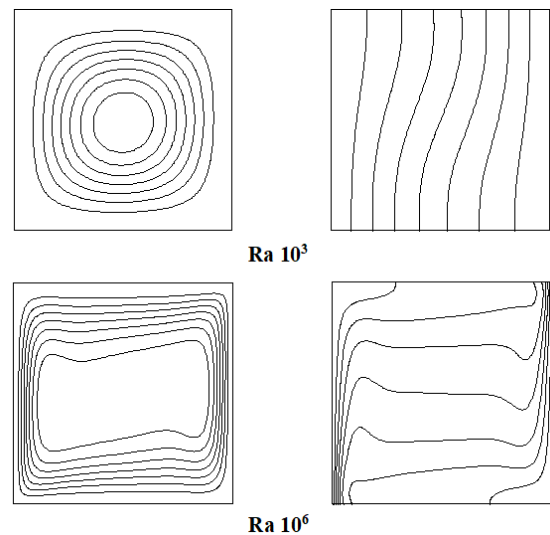


Figure 7. Streamlines (on the left) and isotherms (on the right) at the Ra number of 10³ and 10⁶ obtained from model 8 for the nanoparticle volumetric fraction of 5%

4. Conclusions

In this study, the numerical analysis of natural convection heat transfer in cavity that had two dimensions was performed. As a medium for heat transfer, Al₂O₃-EG nanofluid and incompressible Newtonian fluid were utilized.

With the aim of solving governing equations that have two dimensions, a non-uniform four-point fourth-order scheme was used and applied by utilizing the finite volume method. The systematical analysis of natural convection heat transfer was conducted for different Rayleigh numbers, different models for different concentrations of nanoparticles for the nanofluid case. The conclusions presented below were obtained based on the numerical tests:

- At low Ra numbers, a very slight increase was observed in the heat transfer rate with the increased nanoparticle fraction in models 1, 2, and 3, whereas a very slight decrease was observed in the other models. In this case, the change was not too much because the thermal conductivity equation was more significant than the viscosity equations at low Ra numbers and the thermal conductivity equation used in the models was common. In other words, the thermal conductivity model to be used at low Ra numbers gains importance and determines the result to be obtained from numerical analysis.
- Since heat transfer is conducted by the convection mechanism at high Ra numbers, in this case, the viscosity will increase with the increased nanoparticle volumetric fraction, and, thus, the fluid's mobility will decrease, and the heat transfer rate will also decrease. A decrease was observed in the heat transfer rate with the increased nanoparticle volumetric fraction in all of the experimental correlation models (5, 6, 7, 8), and, as a result, the viscosity models gained importance at high Ra numbers.
- It was revealed that an increase occurred in the heat transfer rate with the increasing Ra number at the fixed nanoparticle volumetric fraction.
- In Case 2, the heat transfer rate was found to be higher in all models in comparison with Case 1 at the constant nanoparticle volumetric fraction and constant Ra number, and the fit between the models was observed to be better in comparison with Case 1.
- Since the change trends of the models with the increased nanoparticle volumetric fraction were almost the same at high Ra numbers in Case 1 and Case 2, it was revealed that the used viscosity model was superior to the thermal conductivity model.

Declaration

The authors declared no potential conflicts of interest with respect to the research, authorship, and/or publication of this article. The authors also declared that this article is original, was prepared in accordance with international publication and research ethics, and ethical committee permission or any special permission is not required.

Author Contributions

N. Keklikcioglu Cakmak developed the methodology, and planned the study. N. Keklikcioglu Cakmak wrote the

manuscript. K. Yapici and H. H. Durmazucar participated analysis and made proofreading of manuscript.

Acknowledgment

This study supported by The Scientific Research Project Fund of Sivas Cumhuriyet University under Research Project (project number: M-489).

References

1. Baïri, A., E. Zarco-Pernia, and J.-M.G. De María, *A review on natural convection in enclosures for engineering applications. The particular case of the parallelogrammic diode cavity*. Applied Thermal Engineering, 2014. **63**(1): p. 304-322.
2. Tyagi, H., P. Phelan, and R. Prasher, *Predicted efficiency of a low-temperature nanofluid-based direct absorption solar collector*. Journal of solar energy engineering, 2009. **131**(4).
3. Mahian, O., et al., *A review of the applications of nanofluids in solar energy*. International Journal of Heat and Mass Transfer, 2013. **57**(2): p. 582-594.
4. Tyagi, H., *Radiative and combustion properties of nanoparticle-laden liquids*. 2008: Arizona State University.
5. Çakmak, N.K., *Experimental study of thermal conductivity of boric acid-water solutions*. 2019. **50**(17): p. 1675-1684.
6. Hussein, A.K., et al., *The effect of the baffle length on the natural convection in an enclosure filled with different nanofluids*. Journal of Thermal Analysis and Calorimetry, 2020.
7. Said, Z., et al., *Recent advances on nanofluids for low to medium temperature solar collectors: energy, exergy, economic analysis and environmental impact*. Progress in Energy and Combustion Science, 2021. **84**: p. 100898.
8. Maxwell, J.C., *A treatise on electricity and magnetism*, Clarendon. Oxford, 1881. **314**: p. 1873.
9. Choi, S.U. and J.A. Eastman, *Enhancing thermal conductivity of fluids with nanoparticles*. 1995, Argonne National Lab., IL (United States).
10. Bazdar, H., et al., *Numerical investigation of turbulent flow and heat transfer of nanofluid inside a wavy microchannel with different wavelenghts*. Journal of Thermal Analysis and Calorimetry, 2020. **139**(3): p. 2365-2380.
11. Keklikcioglu, O., T. Dagdevir, and V. Ozceyhan, *Heat transfer and pressure drop investigation of graphene nanoplatelet-water and titanium dioxide-water nanofluids in a horizontal tube*. Applied Thermal Engineering, 2019. **162**: p. 114256.
12. Khanafer, K., K. Vafai, and M. Lightstone, *Buoyancy-driven heat transfer enhancement in a two-dimensional enclosure utilizing nanofluids*. International journal of heat and mass transfer, 2003. **46**(19): p. 3639-3653.
13. Hwang, K.S., J.-H. Lee, and S.P. Jang, *Buoyancy-driven heat transfer of water-based Al₂O₃ nanofluids in a rectangular cavity*. International Journal of Heat and Mass Transfer, 2007. **50**(19-20): p. 4003-4010.
14. Abu-Nada, E., *Effects of variable viscosity and thermal conductivity of Al₂O₃-water nanofluid on heat transfer enhancement in natural convection*. International Journal of Heat and Fluid Flow, 2009. **30**(4): p. 679-690.
15. Oztop, H.F. and E. Abu-Nada, *Numerical study of natural convection in partially heated rectangular enclosures filled*

- with nanofluids. International journal of heat and fluid flow, 2008. **29**(5): p. 1326-1336.
16. Corcione, M., M. Cianfrini, and A. Quintino, *Enhanced natural convection heat transfer of nanofluids in enclosures with two adjacent walls heated and the two opposite walls cooled*. International Journal of Heat and Mass Transfer, 2015. **88**: p. 902-913.
 17. Mahalakshmi, T., et al., *Natural convective heat transfer of Ag-water nanofluid flow inside enclosure with center heater and bottom heat source*. Chinese Journal of Physics, 2018. **56**(4): p. 1497-1507.
 18. Yıldız, Ç., M. Arıcı, and H. Karabay, *Comparison of a theoretical and experimental thermal conductivity model on the heat transfer performance of Al₂O₃-SiO₂/water hybrid-nanofluid*. International Journal of Heat and Mass Transfer, 2019. **140**: p. 598-605.
 19. Wen, D. and Y. Ding, *Formulation of nanofluids for natural convective heat transfer applications*. International Journal of Heat and Fluid Flow, 2005. **26**(6): p. 855-864.
 20. Ho, C., et al., *Natural convection heat transfer of alumina-water nanofluid in vertical square enclosures: an experimental study*. International Journal of Thermal Sciences, 2010. **49**(8): p. 1345-1353.
 21. Keklikcioglu Cakmak, N., Durmazucar, H , Yapıcı, K . *A numerical study of mixed convection heat transfer in a lid-driven cavity using Al₂O₃-water nanofluid* . International Journal of Chemistry and Technology, 2020. **4**(1): p. 22-37.
 22. Putra, N., W. Roetzel, and S.K. Das, *Natural convection of nano-fluids*. Heat and mass transfer, 2003. **39**(8-9): p. 775-784.
 23. Abu-Nada, E., Z. Masoud, and A. Hijazi, *Natural convection heat transfer enhancement in horizontal concentric annuli using nanofluids*. International Communications in Heat and Mass Transfer, 2008. **35**(5): p. 657-665.
 24. Kim, C.S., K. Okuyama, and J.F. de la Mora, *Performance evaluation of an improved particle size magnifier (PSM) for single nanoparticle detection*. Aerosol Science & Technology, 2003. **37**(10): p. 791-803.
 25. Yapıcı, K. and S. Obut, *Benchmark results for natural and mixed convection heat transfer in a cavity*. International Journal of Numerical Methods for Heat & Fluid Flow, 2015.
 26. Chandrasekar, M., S. Suresh, and A.C. Bose, *Experimental investigations and theoretical determination of thermal conductivity and viscosity of Al₂O₃/water nanofluid*. Experimental Thermal and Fluid Science, 2010. **34**(2): p. 210-216.
 27. Brinkman, H., *The viscosity of concentrated suspensions and solutions*. The Journal of Chemical Physics, 1952. **20**(4): p. 571-571.
 28. Einstein, A., *Investigations on the Theory of the Brownian Movement*. 1956: Courier Corporation.
 29. Batchelor, G., *The effect of Brownian motion on the bulk stress in a suspension of spherical particles*. Journal of fluid mechanics, 1977. **83**(1): p. 97-117.
 30. Nguyen, C., et al., *Viscosity data for Al₂O₃-water nanofluid—hysteresis: is heat transfer enhancement using nanofluids reliable?* International journal of thermal sciences, 2008. **47**(2): p. 103-111.
 31. Maïga, S.E.B., et al., *Heat transfer behaviours of nanofluids in a uniformly heated tube*. Superlattices and Microstructures, 2004. **35**(3-6): p. 543-557.
 32. Wang, X., X. Xu, and S.U. Choi, *Thermal conductivity of nanoparticle-fluid mixture*. Journal of thermophysics and heat transfer, 1999. **13**(4): p. 474-480.
 33. Ding, Y., et al., *Heat transfer of aqueous suspensions of carbon nanotubes (CNT nanofluids)*. International Journal of Heat and Mass Transfer, 2006. **49**(1-2): p. 240-250.
 34. Yapıcı, K., et al., *Rheological characterization of polyethylene glycol based TiO₂ nanofluids*. Korea-Australia Rheology Journal, 2014. **26**(4): p. 355-363.
 35. Wang, L., H. Chen, and S. Witharana, *Rheology of nanofluids: a review*. Recent patents on nanotechnology, 2013. **7**(3): p. 232-246.
 36. Sharma, A.K., A.K. Tiwari, and A.R. Dixit, *Rheological behaviour of nanofluids: a review*. Renewable and Sustainable Energy Reviews, 2016. **53**: p. 779-791.
 37. Tiwari, A.K., et al., *4S consideration (synthesis, sonication, surfactant, stability) for the thermal conductivity of CeO₂ with MWCNT and water based hybrid nanofluid: An experimental assessment*. Colloids and Surfaces A: Physicochemical and Engineering Aspects, 2021. **610**: p. 125918.
 38. Tiwari, A.K., et al., *3S (Sonication, surfactant, stability) impact on the viscosity of hybrid nanofluid with different base fluids: An experimental study*. Journal of Molecular Liquids, 2021. **329**: p. 115455.
 39. Keklikcioglu Cakmak, N., *The impact of surfactants on the stability and thermal conductivity of graphene oxide de-ionized water nanofluids*. Journal of Thermal Analysis and Calorimetry, 2020. **139**(3): p. 1895-1902.
 40. Keklikcioglu Cakmak, N., Temel, Ü , Yapıcı, K, *Examination of Rheological Behavior of Water-Based Graphene Oxide Nanofluids* Cumhuriyet Science Journal, 2017. **38**(4): p. 176-183.
 41. Cakmak, N.K., et al., *Preparation, characterization, stability, and thermal conductivity of rGO-Fe₃O₄-TiO₂ hybrid nanofluid: An experimental study*. Powder Technology, 2020. **372**: p. 235-245.
 42. Das, S.K., N. Putra, and W. Roetzel, *Pool boiling characteristics of nano-fluids*. International journal of heat and mass transfer, 2003. **46**(5): p. 851-862.
 43. Prasher, R., et al., *Measurements of nanofluid viscosity and its implications for thermal applications*. Applied physics letters, 2006. **89**(13): p. 133108.
 44. He, Y., et al., *Heat transfer and flow behaviour of aqueous suspensions of TiO₂ nanoparticles (nanofluids) flowing upward through a vertical pipe*. International journal of heat and mass transfer, 2007. **50**(11-12): p. 2272-2281.
 45. Kwak, K. and C. Kim, *Viscosity and thermal conductivity of copper oxide nanofluid dispersed in ethylene glycol*. Korea-Australia Rheology Journal, 2005. **17**(2): p. 35-40.
 46. Studart, A.R., et al., *Rheology of concentrated suspensions containing weakly attractive alumina nanoparticles*. Journal of the American Ceramic Society, 2006. **89**(8): p. 2418-2425.
 47. Tseng, W.J. and K.-C. Lin, *Rheology and colloidal structure of aqueous TiO₂ nanoparticle suspensions*. Materials science and engineering: A, 2003. **355**(1-2): p. 186-192.

**Research Article**

A GIS-based technique analysis of land use and land cover change detection in taluka Mirpur Mathelo: A case study in district Ghotki, Pakistan

Shoukat Ali Shah ^{a,*}  and Madeeha Kiran ^b 

^aInstitute of Water Resources Engineering and Management, Mehran University of Engineering and Technology, Jamshoro, Sindh, Pakistan

^bSchool of Environmental Science, Northeast Normal University, China

ARTICLE INFO

Article history:

Received 29 December 2020

Revised 06 March 2021

Accepted 28 March 2021

Keywords:

Change detection

GIS

Landsat imagery

Land use land cover

Mirpur Mathelo

Remote sensing

ABSTRACT

Land use and land cover changes at the regional scale are necessary for a wide range of uses, including land planning, global warming, erosion, and landslide, etc. In this study, Land use and land cover change detection were studied by using remote sensing and GIS in taluka Mirpur Mathelo, Ghotki. For this purpose, ArcGIS 10.3 software was used. Firstly, supervised classification performance was applied to Landsat imageries which were acquired in 2013-2020. Image classification of six bands of Landsat imageries was carried out via a maximum likelihood classification process with the help of ground truthing data and signature file for both images 2013-2020 year. The second part focused on the land use and land cover change detection was evaluated with overlapping of the images. The results of the study indicated that severe land use and land cover change detection has occurred in the area during 2013-2020. The total relative change in the settlement is 2439.45 ha (1.94%) during the years. 592.38 ha (0.47%) changed in the vegetation cover. A total change of 3.16 ha (3.16 %) in the sand area. While barren land/plain -5094.63 ha (-4.06%) changed during the years. -1906.2 ha (-1.52%) shortage in the water body. It has been seen that decrease in barren land/plain and waterbody which has been converted into more in the sand and some portion in agriculture.

© 2021, Advanced Researches and Engineering Journal (IAREJ) and the Author(s).

1. Introduction

Human activity on the earth's surface and its adaptation around the sphere is commonly known as land use and land cover (LULC). Human activity and increasing population impact on finite resources of cultivated area, forest field, urban area, and manufacturing industries. More area of agricultural land is required to be cultivated with growing human inhabitants which will also affect and shrinkage in quality and quantity of resources of the earth. [1] studied that the empirical examination by the investigators from diverse fields concluded that land use and land cover change has come to be important in agriculture, environment, ecology, geography, forestry, geology, and hydrology. Land cover change detection plays several essential characters in global environmental changes because the variance has certainly disturbed the

sustainability, biodiversity, and relations between earth and the atmosphere. Proper planning, management, and utilization of natural resources are considered while studying land use and land cover changes [2]. Although, analysis of LULC from the past to present and it is simulating the future changes is significant for local and regional authorities. Unfortunately, traditional methods and techniques for land cover mapping especially in developing countries such as Pakistan are very poor, time-consuming and costly. Considering these difficulties, the attention of researchers has been directed towards GIS and remote sensing technology for monitoring LULC changes. This technology has been increasingly applied in the LULC mapping, analysis and urban development due to its cost-effectiveness and high efficiency [3, 4]. LULC changes have turned into a vital component in a present

* Corresponding author. Tel.: +92-303-249-9292, +92-333-366-5063

E-mail addresses: sarkar.sain151@gmail.com (S.A. Shah), madeehajanwery@yahoo.com (M. Kiran)

ORCID: 0000-0002-6723-9898 (S.A. Shah), 0000-0001-6061-642X (M. Kiran)

DOI: 10.35860/iarej.849130

This article is licensed under the CC BY-NC 4.0 International License (<https://creativecommons.org/licenses/by-nc/4.0/>).

strategy for the management of natural resources as well as to check environmental changes [5]. The accurate and timely information on the spatial distribution of land cover changes over a wide area is more convenient with this powerful technique [6-8]. RS and GIS have a wide range of usage in the agricultural fields [9]. Many approaches have been created and applied for change detection to monitor land cover changes by remotely sensed information and data for image differencing, post-classification comparison, vegetation index variation [10]. These methods were found to be the most accurate reliable and time-saving by a variety of different studies that offered advantages of representation of nature and physiographical changes. To obtain accurate and timely spatial data as well as analyzing LULC changes in a study area RS imageries and GIS are very useful tools [11, 12]. Multi-temporal data acquisition from remote sensing are very effective in mapping and change detection of agricultural area, urban, waterbody, barren land, and landscape to planning and managing. Therefore, for valuable and sustainable improvement, the policymakers, land-use managers, executives and municipal authorities need these techniques and tools to monitor how the land is used and understand the development and directions of different kinds of land users, in particular, urban land use in the past, present and future. It was also suggested to the policymaker with scientific change assessment to understand the natural state of the study area and the complex relation between the physiographic and man-made features. Keeping in view, in the present research study geospatial technique was used to reveal the significance of land cover changes over the study area, which helped to assess the change directions and dynamics. Taking into account, the aim of the study to analyze the land use and land cover change detection by using GIS and remote sensing techniques that were applied in MPM taluka of district Ghotki.

The purpose of this research study is to map the land use and land cover of MPM taluka to detect the changes from the last eight years that have been taken place. The following particular objectives of the research study are pursued to achieve the targets.

- To map land use and land cover classification scheme.
- To determine land use land cover change detection from 2013 to the 2020 year.
- To check the NDVI and vegetation index from 2013 to the 2020 year.

2. Materials and Methods

2.1 Location of Study Area

The research study was carried out in MPM taluka of district Ghotki, Sindh. MPM located on Latitude N: 28 02' 00" and Longitude E: 69 33' 00" Figure 1. The altitude of taluka 71 m above sea level. It covers an area of 125568

ha (1255.68 km²). The taluka is also headquarters of district Ghotki and administratively subdivided into 11 Union Councils i.e. Mirpur I, Mirpur II, Dhangro, Jahan Khan Unar, Islam Khan Lashari, Gari Chakar, Sono Pitafi, Jarwar, Yaro Lund, Wahi Ghoto, Dino Mako. The topography of MPM taluka is divided into two main clear physical parts i.e. Cultivated area and Desert area. Desert area covers nearly half of the area of taluka and consists of windblown dunes known as Acharo Thar (White desert) that starts from Sanghar district to Cholistan (Punjab) along with Indian border state of Rajasthan. It goes along southern belt of the district Ghotki. The taluka is bounded by Rahimyar Khan district of Punjab province in the northeast, Kashmore district in the west and north-west, Sukkur district in south and southwest and Rajasthan, India in the east.

2.2 The Population of Taluka MPM

The total population of taluka MPM has been reported in the census [13] as (327,944) in which Rural 227,184 and Urban 100,760.

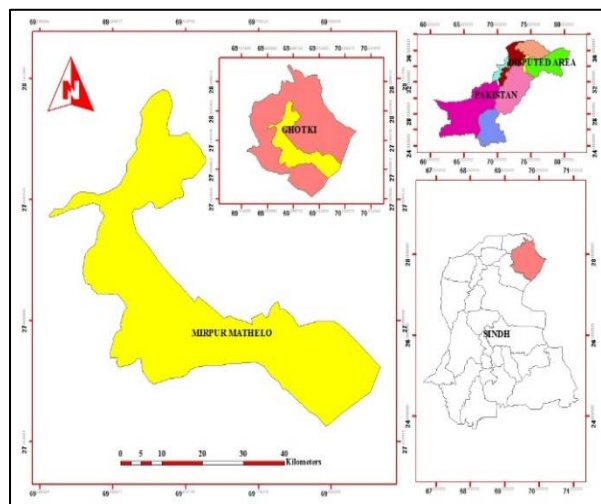


Figure 1. Location of MPM taluka, District Ghotki, Sindh, Pakistan

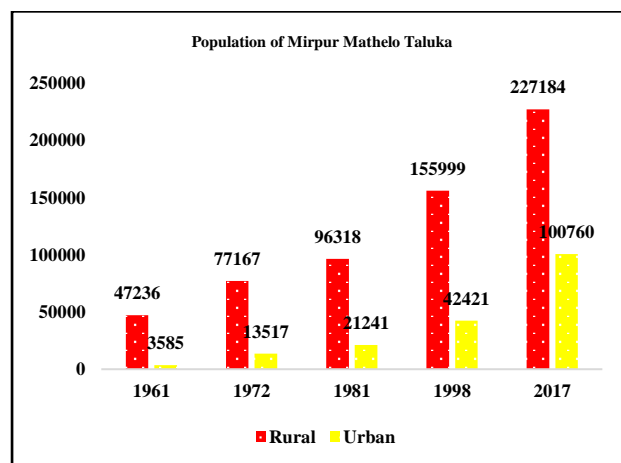


Figure 2. The population of MPM according to Census 1961 to 2017

2.3 Climate and Irrigation

MPM taluka is warm and has very little annual rainfall. The minimum temperature falls to 7°C in January is the coldest month. The maximum temperature is 45°C in May and June are the hottest months. Precipitation is highly erratic with an annual average of approximately 130 mm. Most of the inhabitants are engaged in agriculture. Wheat, cotton, vegetables, and fruits are the major crops in the study area. The climate is appropriate for growing vegetable crops and fruits such as dates, banana, mangoes, carrot, lemon, reddish, cabbage, onion, spinach, green chillies, etc [14]. The agricultural land has been irrigated by Masu wah which off-takes from Ghotki feeder canal which originates from Guddu barrage and some other network of distributaries, minors and also irrigated by Government and private tubewells.

2.4 Data Used

To identify changes over a period 2013-2020 required temporal Landsat satellite imageries. For mapping, the land use and land cover and change detection. Two images 2013 and 2020 that were cloud-free were acquired from remote sensing satellite Landsat 8 OLI/TIRS. The study area lies on the Path 151 Row 41. The Landsat 8 OLI/TIRS images were downloaded from USGS (GloVis) (<http://glovis.usgs.gov>) earth resource observation system data centre. All visible and infrared bands except the thermal infrared were included in the analysis of the imageries of the 2013-2020 year. The Topographic map was used and digitized to create a spatial database. This process was carried out using geospatial tools ArcGIS 10.3. software.

2.5 Ground Trothing Data

Ground trothing data/sampling points were collected from taluka MPM. The union councils were considered easily and timely to conduct field surveys for the collection of coordinates for different land use in the area of study (Figure 3). The geographical map of MPM taluka was followed and randomly sampling points (Longitude and Latitude) were taken with the Garmin 62s GPSMAP device. It is a handheld navigator by Garmin. The main function of the device is to navigate through even the most remote regions and terrain. By using this device settlements, vegetation, barren land, orchards, waterbody, sandy area, etc. sampling points were taken. A total of 110 ground sampling points were collected for five categories (Table.1) including 25 samples of vegetation, 20 samples of barren land/plains, 31 samples of settlements, 19 samples of Waterbody, and 15 samples of Sand, respectively. After the collection of sampling points, the collected data were prepared into MS Excel format and added into Landsat imageries for analysis and accuracy assessment to get the required objectives.

Table 1. Description of LULC categories

S. No	Class / Categories	No. of Samples	Description
1	Settlements	31	Built-up, Commercial areas, Buildings, Cities, Roads, Villages, Industries, etc.
2	Vegetation	25	Crops land, Pastures, Trees, Orchards, Grass, Plantation etc.
3	Waterbody	19	Ponds, Streams, Reservoirs, Canals, Minors, etc.
4	Barren land	20	Un cultivated area, Exposed soils, Landfills, Saline, Silt, etc.
5	Sand	15	Sandy area Thar (Achro)

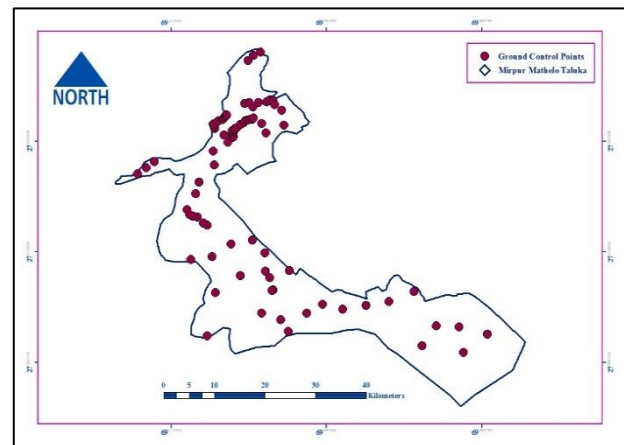


Figure 3. Ground Trothing Survey/sampling points of MPM taluka

2.6 Classification of RS Images

The boundary of the study area was digitized using ArcGIS 10.3 tool and overlapped onto satellite imageries. Two un-classified images 2013 and 2020 (Figure 4) were exported to ArcGIS 10.3 for map composition and cross-classification, tabulation, and land use and land cover changing modelling. The extraction of the Mask process was applied. During the process of image classification, a maximum likelihood classification algorithm was used for supervised classification to determine the classes. This practice has been used in various studies for RS image classification [15-19]. For supervised classification the signature file was made for each image, the pixels of the images were arranged into classes based on the signature by using classification decision. The cross-classification was done with re-classified maps. Before preprocessing and classification of satellite imageries, extensive randomly sampling points during field surveys and interviews were conducted in taluka. To find change detection with the help of image analysis, the post-classification comparison method is widely used in the world. In the present study, the quantitative method of change detection i.e. post-classification method was carefully chosen to find land use and land cover in the research study area.

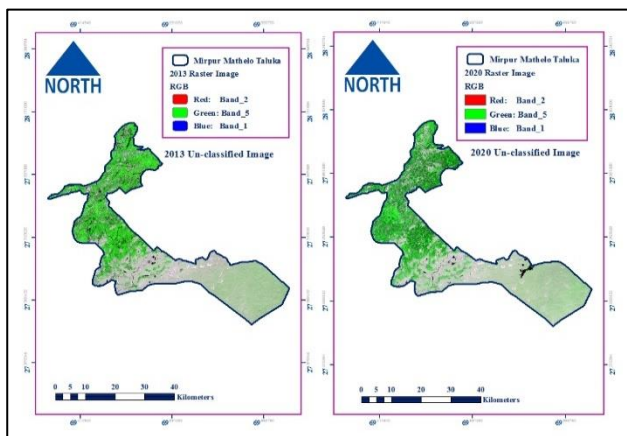


Figure 4. Un-Classified images (2013-2020) of MPM taluka

2.7 Change Detection Analysis 2013-2020 Years in MPM Taluka

Change detection is a process of recognizing the differences in the state of an object or phenomenon by observing it at different periods. The significance of change detection is to determine which land use and land cover is changing to the other. The researcher's widely used this technique for change detection is to overlay images, change vector analysis, image rationing, classification comparisons of land cover statistics, principal component analysis, and the differencing of NDVI [20]. The classification comparisons of land cover statistics were used in this study. The areas where covered by each land cover type for the various periods have been compared. Afterward, changes directions (positive and negative) in each land cover type have been determined.

2.8 NDVI of MPM Taluka

The normalized difference vegetation index (NDVI) is an identical index allowing to make an image showing greenness and biomass [21, 22]. It is a standard for comparing vegetation greenness between satellite images [23]. The index takes benefit of the contrast of characteristics between 2 bands from a multispectral raster dataset the chlorophyll pigment absorption in the red band and the high reflectivity of plant material in the near infrared NIR band. Extremely low or negative values present areas with no vegetation at all, such as clouds, water, snow. Very low values present an area of little to no vegetation such as rocks, concrete or bare soil. Moderate values present areas of shrubs and grassland. High values present forest areas and lush green. NDVI specifies a measure of healthy vegetation and ranges in value from -1 to 1. Values closer to 1 present green vegetation. NDVI was considered from Landsat 8 data using band 4 (red) and band 5 (near infrared) using Equation (1).

$$NDVI = \frac{\text{Near Infrared (Band 5)} - \text{Red Band (Band 4)}}{\text{Near Infrared (Band 5)} + \text{Red Band (Band 4)}} \quad (1)$$

3 Results and Discussion

3.1 Classification of Satellite Imageries

To study, the application of GIS and RS tools, land use and land cover analysis, and change detection in MPM taluka were determined. Different illustrative samples were collected to generate a signature file. A supervised classification method was followed and then the maximum likelihood classification algorithm was applied for the 2013 and 2020 year imageries. The images were grouped into five classes i.e. settlement, vegetation, waterbody, barren land, and sand. The total classified area 125568 ha of taluka has been calculated, which was later divided into land use and land cover (Table 2). Classified images 2013 and 2020 year (Figures 5 and 6) were analyzed and determined the area with settlement 25264 ha (20.1%) and 27703.4 ha (22.1%). The vegetation during the years was calculated as 35978 ha (28.7%) and 36569.9 ha (29.1%). The sand-covered an area of 52870 ha (42.1%) and 56839.1 ha (45.3%). Barren Land covered an area of 7726.8 ha (6.2%) and 2632.14 ha (2.1%). The waterbody determined in an area during the years was 3729.8 ha (3%) and 1823.58 ha (1.5%).

Table 2. Area covered under categories 2013-2020 of MPM taluka

Classification category	2013		2020	
	Area ha	Area %	Area ha	Area %
Settlements	25264	20.1	27703.4	22.1
Vegetation	35978	28.7	36569.9	29.1
Sand	52870	42.1	56839.1	45.3
Barrenland	7726.8	6.2	2632.14	2.1
Waterbody	3729.8	3.0	1823.58	1.5
Total	125568	100	125568.2	100

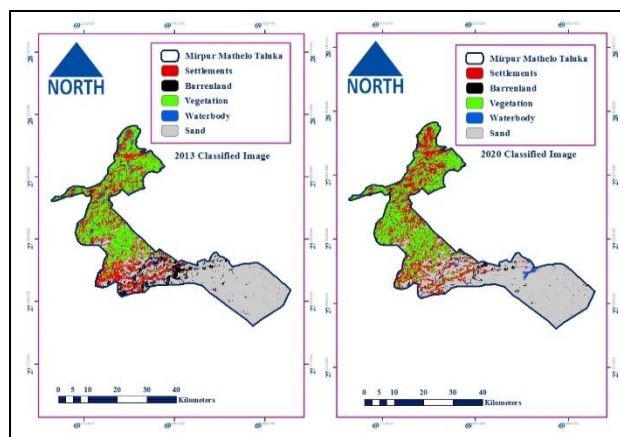


Figure 5. Classified images (2013-2020) of MPM taluka

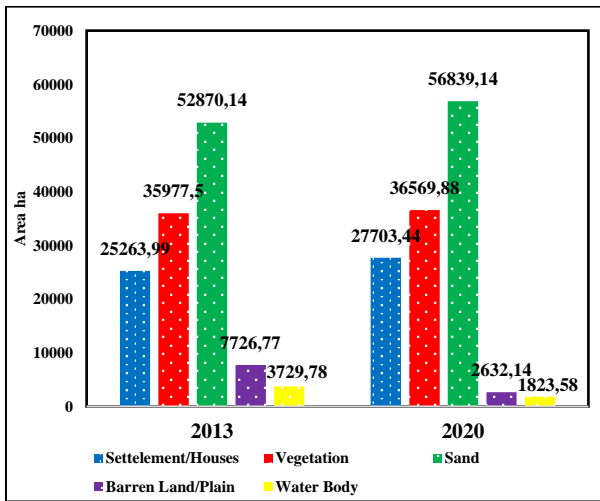


Figure 6. Clustered column chart for Area under LULC (2013-2020) of MPM

3.2 NDVI of 2013 and 2020 Imageries of MPM Taluka

Figure NDVI of MPM taluka calculated for both imageries shown in Figure 7. The peak NDVI for the image of 2013 and 2020 year was 0.508 and 0.533. It has been confirmed that the normalized difference vegetation index of an area increases with the height and maturity of vegetation and crops.

3.3 LULC change detection in MPM Taluka

Based on the analysis, the involvement of several facts and figures, the modern tools GIS, remote sensing imageries, ground trothing survey, and existing study area conditions, we have done LULC change detection and categorized the study area into five classes i.e. settlements, vegetation, sand, barren land, and waterbody. The land use and land cover change detection was calculated from the imageries with overlapping of 2013 and 2020 year (Figure 8).

Settlements:

LULC changes are relatively more pronounced in the MPM taluka, one of which is the massive increase in residential areas. Comprising mostly of residential and commercial establishments, the total area under the settlement was increased by 2439.45 ha (1.94%) in Taluka.

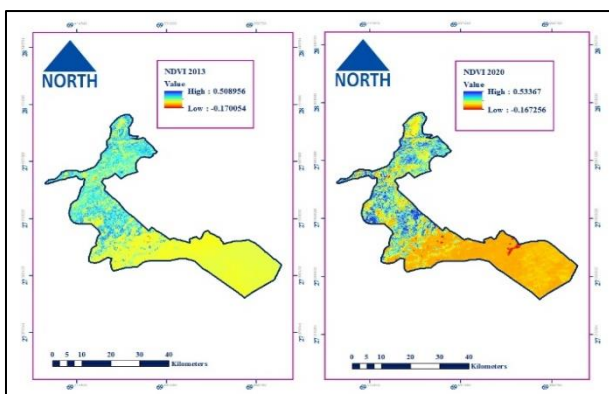


Figure 7. NDVI (2013-2020) images of MPM Taluka

The built-up expansion has been mostly encroaching the agricultural land and barren land near to cities. Particularly expanding along the roads and peripheral zones, the increasing urbanization adversely affects environmental quality in the taluka. Urbanization, population growth, market forces, and other activities of development are a principal factor of LULC change in the area.

Sand:

Sand is the first largest category of LULC. This class was considered the most change class during the 2013 to 2020 years. It has been increased by 3969 ha (3.16%). This is mainly due to climatic factors, especially wind. The movement of sand one place to another due to wind is a complex process that involves different types of grain movement that occurred less or more simultaneously. The environmental factors mostly wind and air factors which pulverize the sand to the agricultural and plain areas of the taluka. This change class only along with the sandy areas of the taluka.

Vegetation:

Vegetation is the second largest of all identified classes in this study. The agricultural land revealed a continuously raised throughout the study period. The total area under this class was increased to 592 ha (0.47%) from 2013 to the 2020 year. This increase is not a huge change in the study area considering the population. This is mainly because in the period from 2013 to 2020 there were no cropping patterns and advanced technology used to increase agricultural growth. The main reason peoples are only focusing on settlements and built-up houses and shifted from villages to cities. Other factors such as economic returns from the cash crops and climate change have also played a role in shifting land from one use to another.

Barren land:

The barren land category is among the small LULC categories of this classification. The barren land decreased from 2013 to the 2020 year -5094.63 ha (-4.06%) in the study area. It has been experiencing positive changes, this category was considerably reduced due to built-up and agricultural land increased in the study area.

Waterbody:

The area under open water has reduced to almost half Figure 8. There was a decline in the total share of this LULC -1906.2 ha (-1.52%) in Table 3. Climatic change and anthropogenic impacts on water bodies are the most stressed natural resources in the study area. On the other hand, morphological changing in irrigation canals and distributaries and loss of area owing to human intervention and fluctuations in the water budget. The lining of canals and distributaries and less rainfall in the area also impact on the shortage of water.

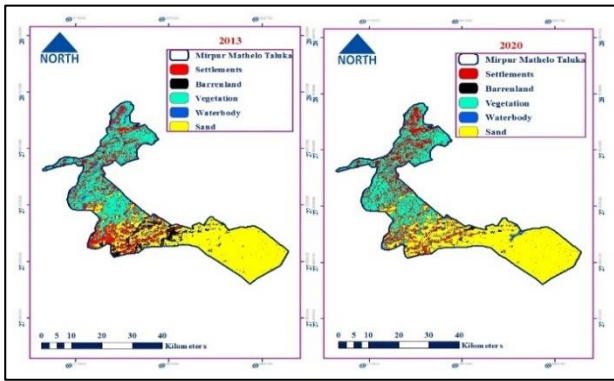


Figure 8. LULC change detection (2013-2020) of MPM taluka

Table 3. Land use and land class (2013-2020) images of MPM taluka

Class	Area (ha) 2013	Area (ha) 2020	Change Diff Area (ha) 2013-2020	Change Diff %
Settlements	25264	27703	2439.45	1.94
Vegetation	35978	36570	592.38	0.47
Sand	52870	56839	3969	3.16
Barren Land	7726.8	2632	-5094.63	-4.06
Water Body	3729.8	1824	-1906.2	-1.52

(-) indicates a decrease in Area

Figure 9 shows the pictorial view of LULC change detection between 2013-2020. Table 4 presents change detection of MPM taluka that how much area of land cover has converted into another land cover area between 2013-2020. Figures 10 and 11 show column clusters chart and graph details of LULC change detection (2013-2020), respectively.

3.4 Vegetation mask of MPM taluka

The vegetation mask of MPM taluka is presented in Figure 12 which shows the overall vegetation in 2013 and 2020 year. It is cleared in the image that the green colour shows the area under flora and the white colour indicates the area under settlements, roads, barren land and cities, ponds, etc. The Landsat imageries of 2013 and 2020 (Table 5) year indicated that the total estimated area of vegetation mask was about 35978 ha (28.6%) and 36570 ha (29.12%) of the total geographical area while no vegetation mask area was 89590.7 ha (71.3%) and 88998.3 ha (70.8%) of the total geographical area. The overall difference in the 2013-2020 year vegetation mask was increased to 592 ha (0.47%).

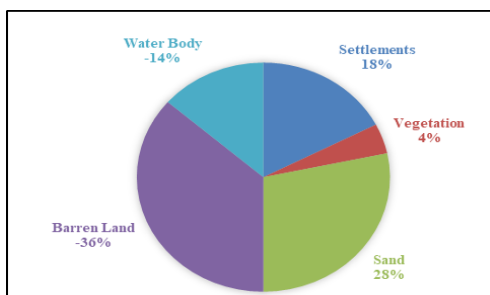


Figure 9. Pictorial view of LULC change detection between 2013-2020

Table 4. LULC (2013-2020) change detection of MPM taluka

Land use land class change 2013-2020	Area (ha)
Barren land – Barren land	1721.6099
Barren land - Sand	4544.4403
Barrenland - Settlements	1085.5777
Barrenland - Vegetation	45.81358
Barren land - Waterbody	166.41821
Sand – Barren land	228.00401
Sand - Sand	51456.838
Sand - Settlements	808.32976
Sand - Vegetation	8.6104422
Sand - Waterbody	471.4239
Settlements – Barren land	449.56551
Settlements - Sand	961.52241
Settlements - Settlements	16651.234
Settlements - Vegetation	6850.0159
Settlements - Waterbody	217.47599
Vegetation - Barrenland	17.000329
Vegetation - Sand	2.3412793
Vegetation - Settlements	7183.5386
Vegetation - Vegetation	28857.708
Vegetation - Waterbody	143.07478
Waterbody – Barren land	47.945613
Waterbody - Sand	3.2509999
Waterbody - Settlements	1833.547
Waterbody - Vegetation	971.45384
Waterbody - Waterbody	775.30934

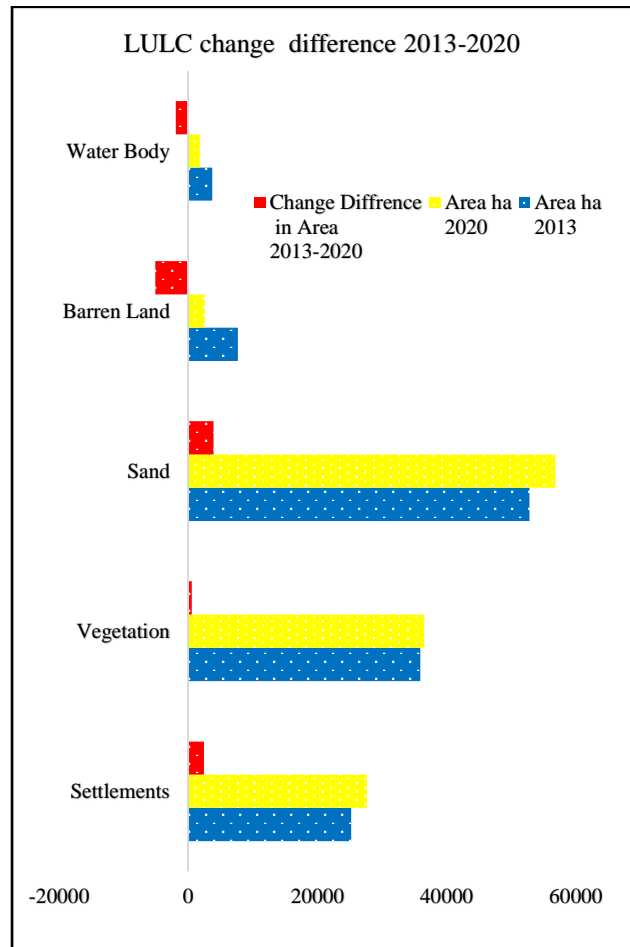


Figure 10. Column cluster chart of LULC (2013-2020) change detection of MPM taluka

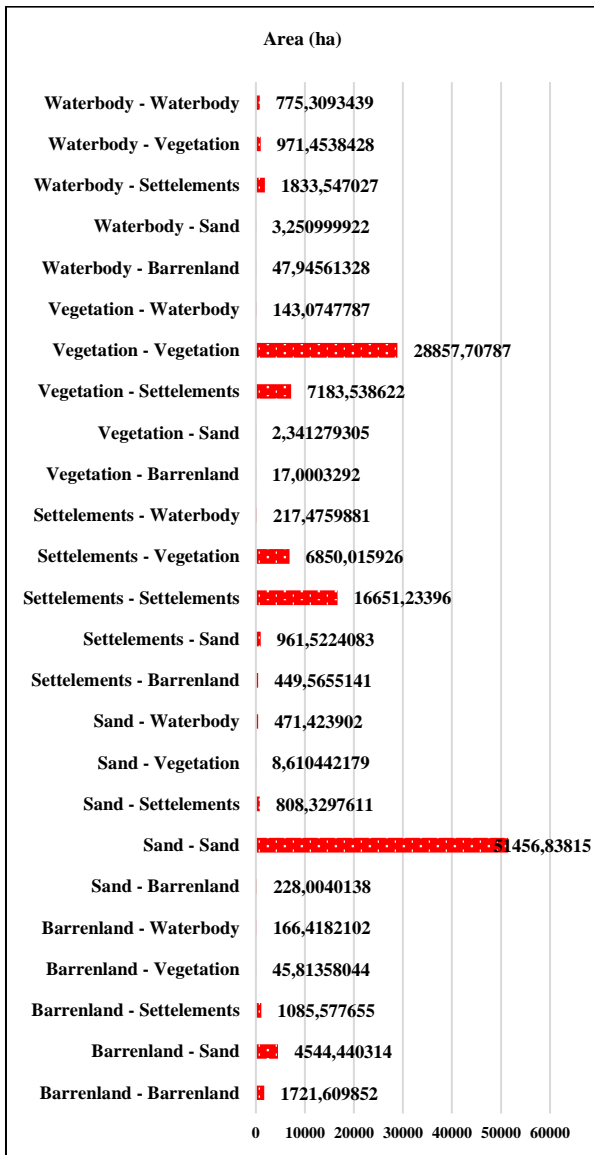


Figure 11. Column cluster graph of LULC (2013-2020) change detection of MPM taluka

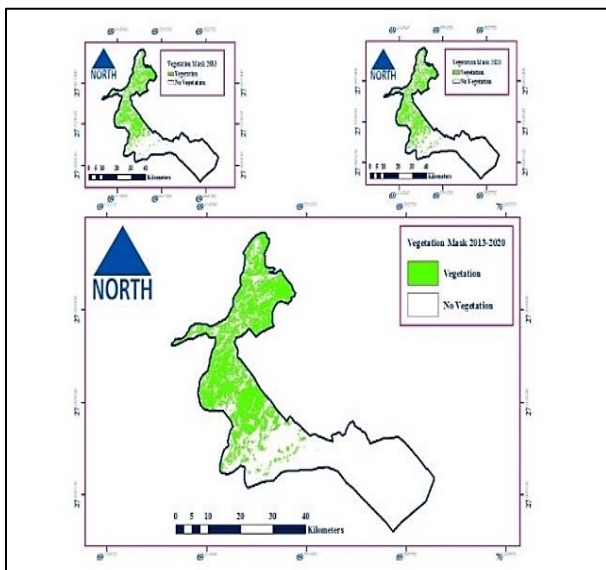


Figure 12. Vegetation Mask (2013-2020) of MPM taluka

Table 5. Vegetation Mask (2013-2020) of MPM taluka

Year	Vegetation Mask Area (ha) of MPM 2013-2020			
	Vegetation Area (ha)	Percentage of Geographic Area (ha)	No Vegetation Area (ha)	Percentage of Geographic Area (ha)
2013	35978	28.65	89590.7	71.35
2020	36570	29.12	88998.3	70.88
Diff 2013-2020	592.00	0.47	-592.40	-0.47
Total G Area (ha)	125568			

4. Conclusions

The objectives of this study were to deliver a recent outlook for land use and land cover change detection that took place from 2013 to 2020 years in MPM taluka. GIS and remote sensing technique provided significant information on the nature of land cover changes particularly the area and Spatio-temporal distribution of different land cover changes. During this period, the analyzed results give interesting observations.

The total relative change in a settlement is 2439.45 ha (1.94%). From 2013 to the 2020 year the settlements have been increased, peoples started migrating villages to cities for business and other work. It has indicated the impact of population and development activities over the study area. There was a total change in the sand area 3969 ha (3.16 %) was noted. A significant rise in the sand area from the barren land area due to no-cultivation of barren land or no management of land for purpose of agriculture or settlements. The main reason was also noted the climatic factors affecting this portion i.e wind which takes a grain of sand one place to another.

Barren land decreased to -5094.63 ha (-4.06%), Waterbody estimated as -1906.2 ha (-1.52%) according to facts and figures and confirmed from irrigation department that shortage of irrigation water for agricultural land during some previous years. While the waterbody ponds area converted into settlements and uses in agricultural land to fill the gap of food and cash crops with the growth of population.

Vegetation increased as 592.38 ha (0.47%). The vegetation area during 2013-2020 years increased on some portions. But there was also less use of advanced agricultural technology due to small owner of the land, they can not bear expenditure to prepare the land for different cropping patterns.

The results of classes proved that supervised classification is a more versatile method for land cover change detection and on the hand, this technique of

classification is easy to use and benefits of vectors make this method is useful.

Remotely sensed imageries specified convenience to investigate the LULC changes in a given time interval. Updated information of LULC mapping gives the most important information and facts for sustainable, accurate planning and management. It provides prediction regarding the amount, state, composition and configuration of the changes which can be used as an early warning for proper planning for decision making. These facts and figures helped to land use manager and policymakers to set up sustainable development that was facing the rapid expansion of urbanization. Remote sensing and GIS are suitable tools for revising, renovating the land use maps and then manage land cover changes based on analyzed and up to date information. The above-mentioned problems, significant and necessity of LULC changes monitoring and analyzing regarding the facts future planning should be done. The updated information of land cover changes give help to policymakers to aware the past, current and future situation to establish the necessary decision and policies about incremental trend of urbanization/settlements and decrease the possible negative consequences in the future as well as help in complex adaptive measures. In other words, this study provide input to policymakers to examine and understand the scenarios of LULC changes and formulating an effective and eco-friendly land use policy in the MPM taluka.

Declaration

The authors declare that there is no conflict of interest regarding the publication of this manuscript. Besides, the ethical issues, including plagiarism, informed consent, misconduct, data fabrication and/or falsification, double publication or submission, and redundancy have been completely observed by the authors.

Author's Contribution

S.A. Shah and M. Kiran significantly contributed to this study.

Nomenclature

GIS	: Geographic Information System
GloVis	: Global Visualization
LULC	: Land Cover Land Classification
MPM	: Mirpur Mathelo
OLI	: Operational Land Imager
PBS	: Pakistan Bureau of Statistics
RS	: Remote Sensing
TIRS	: Thermal Infrared Sensor
UC	: Union Council
USGS	: United States Geological Survey

References

1. Weng, Q., *A remote sensing-GIS evaluation of urban expansion and its impacts on the temperature in the Zhujiang Delta, China*. Int J Remote Sens, 2001. **22**(10): p. 1999-2014.
2. Asselman, N.E.M. Middelkoop, H. *Floodplain sedimentation quantities, Patterns and processes*. Earth Surf. Process. Landf, 1995. **20**(6): p. 481-499.
3. Reveshty M.A., *The assessment and predicting of land use changes to the urban area using multi-temporal satellite imagery and GIS: A case study on Zanjan, Iran (1984-2011)*. Journal of Geographic Information System, 2011. **3**(4): p. 298-305.
4. Wang, Y., Zhang, X., *A dynamic modelling approach to simulating socio-economic effects on landscape changes*. Ecological Modelling, 2001. **140**(1-2): p. 141-162.
5. Harshika, A. K. and Sopan, I., *Land use land cover classification and change detection using high-resolution temporal satellite data*. Journal of Environment, 2012. **1**(4): p. 146-152.
6. Mas, J.F., *Monitoring land-cover changes: Comparison of change detection techniques*. Int. J. Remote Sensing, 1999. **20**: p. 139-152.
7. Shi, H., Yu, K., Feng, Y., Dong, X., Zhao, H. and Deng, X., *RS and GIS-based analysis of landscape pattern changes in Urban-Rural Ecotone: A case study of Daiyue District, Tai'an City, China*. Journal of Landscape Research, 2012. **4**(9): p. 20-23.
8. Efreem, G., *Landuse, and land cover dynamics and rural livelihood perspective in the semi-arid areas of Central Rift Valley of Ethiopia*. Faculty of Forest Sciences, Department of Forest Resource Management Umea. Sweden: Swedish University of Agricultural Sciences. Doctoral Dissertation, 2010.
9. Yeh, A.G.O. and Li, X., *Principle component analysis of stacked multi-temporal images for the monitoring of rapid Urban expansion in the Pearl River*. Int. J. Remote Sensing, 1998. **19**(8): p. 1501-1518.
10. Lu, D., Mausel, P. and Brondizio, E., *Change detection techniques*. Int. J. Remote Sens., 2004. **25**(12): p. 2365-2407.
11. Reis, S., *Analyzing land use/land cover changes using remote sensing and GIS in Rize, North-East Turkey*. Sensors, 2008. **8**(10): p. 6188-6202.
12. Pervez, W., Uddin, V., Khan, S.A. and Khan. J.A., *Satellite-based land use mapping: Comparative analysis of Landsat-8, Advanced Land Imager, and big data Hyperion imagery*. J. Appl Remote Sens, 2016. **10**(2): 026004.
13. PBS (2017). *Blockwise Provisional Summary results of the 6th Population and Housing Census*. Pakistan Bureau of Statistics. [cited 2020 20 December]; Available from: <http://www.pbscensus.gov.pk>.
14. Shah, S.A. and Siyal, A.A., *GIS-based approach estimation of area under Wheat and other major Rabi crops in district Ghotki and corresponding irrigation water requirement*. ACTA Scientific Agriculture, 2019. **3**(12): p. 59-70.
15. Mundia, C.N. and Aniya, M., *Analysis of land use/cover changes and urban expansion of Nairobi city using remote sensing and GIS*. Int. J. Remote Sensing, 2005. **26**: p. 2831-2849.
16. Dibs, Hayder., *Maximum likelihood for land-use/land-cover mapping and change detection using Landsat satellite images: A case study "South of Johor"*. International

Journal of Computational Engineering Research, 2013.
3(6): p. 26-33.

17. Han, J., Hayashi, Y., Cao, X., and Imura, H., *Evaluating land-use change in rapidly urbanizing China: A case study of Shanghai*. Journal of Urban Planning and Development, 2009. **135**(4): p. 166-171.
18. Myneni, R.B., *A large carbon sink in the woody biomass of northern forests*. Proceeding of the National Academy of Sciences of the United States of America. 2001. **98**(26): p. 14784-14789.
19. Chen, D., and Brutsaert, W., *Satellite sensed distribution and spatial patterns of vegetation parameters over a tallgrass prairie*. Journal of the Atmospheric Sciences. 1998. **55**(7): p. 1225-1238.
20. Weng, Q., & Lo, C.P., *Spatial analysis of urban growth impacts on vegetative greenness with Landsat TM data*. Geocarto International, 2001. **16**(4): p. 17-25.

**Research Article****Prediction of market-clearing price using neural networks based methods and boosting algorithms****Aslı Boru İpek** ^{a,*} ^aAdana Alparslan Türkeş Science and Technology University, Faculty of Engineering, Department of Industrial Engineering, Adana, 01250, Turkey

ARTICLE INFO

Article history:

Received 11 November 2020

Revised 01 February 2021

Accepted 02 March 2021

Keywords:

ANN

Boosting algorithms

Market-clearing price

CNN

Energy

ABSTRACT

The development of Turkey's industry is contributing to a significant rise in electrical energy demand. Also, electricity is one of the critical elements in the household sectors. Therefore, the planning and managing of electrical energy is of great importance to support economic growth. In addition, effective prediction of market-clearing prices (MCP) is critical topic to meet the increasing energy demand and provide basis for decision making process. In this paper, MCP is predicted using artificial neural network (ANN), convolutional neural network (CNN), and also three boosting algorithms including extreme gradient boosting (XGBoost), categorical boosting (CatBoost), and adaptive boosting (AdaBoost). Various performance metrics are employed to evaluate the prediction performance of proposed methods. The results showed that proposed methods provide reasonable prediction results for energy sector. Hence, producers and consumers can use these methods to determine the bidding strategies and to maximize their profits.

© 2021, Advanced Researches and Engineering Journal (IAREJ) and the Author(s).

1. Introduction

The world energy consumption is increasing exponentially in parallel with population growth, industrialization, and technological progress. Energy is taken into account as a prime agent in wealth creation and a significant influence in economic growth as well [1]. Especially, electric energy consumption has been one of the most significant indicators of economic and social growth.

The Turkish energy policy primarily focuses on the reliable and timely assurance of energy supply under economic and clean terms [1]. As a consequence of the rapid growth in Turkey's population, urbanization and industrialization especially prompted the need for electrical energy to rise regularly. Therefore, the electrical energy sector continues to expand and liberalize in Turkey [2].

Since electricity is an indispensable element of daily life, one of the goals of almost all countries is to provide consumers with continuous and reliable electrical system. This can only be possible with the correct planning and management of the electricity supply system that require effective modeling and prediction capability. Due to the

unique characteristics of the electricity sector, it may be difficult to develop prediction models that are suitable for the different subsystems it carries. In literature, many prediction methods have been developed to evaluate the electricity. However, it is almost impossible to generalize and use them in demand prediction of any country. Hence, the development of methods that will include the unique characteristics of countries will provide more realistic prediction of electricity demand [3]. Most studies indicated that the key goal is to ensure sufficient electricity and fulfill potential needs. At this point, prediction is highly significant in the successful implementation of energy policies [4].

The worldwide electricity industry has undergone a change. The utilities owned by the government have been privatized. To be competitive in electricity market, policy makers and market managers need to research, evaluate and monitor the actions of market participants. At this point, strategic bidding problem should be solved to maximize profit. In the strategic bidding problem, MCP plays an important role because it defines which blocks will be

* Corresponding author. Tel.: +90 322 455 0000-2079.

E-mail addresses: aboru@atu.edu.tr (A. Boru İpek)

ORCID: 0000-0001-6403-5307 (A. Boru İpek)

DOI: 10.35860/iarej.824168

This article is licensed under the CC BY-NC 4.0 International License (<https://creativecommons.org/licenses/by-nc/4.0/>).

nominated by the market clearing process [5]. It is also stated that the prices formed in the day-ahead electricity market are the reference prices for other markets. The reference price means that the prices formed in the day-ahead electricity market reflect the supply and demand balance of market in a very close time to the delivery time of the electricity. One of the markets where MCPs are considered as reference prices is the balancing power market [6].

MCP is one of the most significant power market indicators. In the energy market, prediction of MCP has a critical role for any decision making process. Effective MCP prediction not only has critical roles in planning and management of energy market, but also improves the profit in energy market.

Electric energy that is a form of energy is used at a high rate today because it is efficient and rapidly transmittable resource. Planning on supply-demand, transmission-distribution and pricing that occur with the use of electrical energy is of great importance [7]. Kilic [1] analyzed the major energy sources of Turkey and the significance of their use in the energy sector. Akbalık and Kavcıoğlu [2] reviewed and analyzed the energy sector considering the technological, environmental, and financial structure in Turkey. In addition, supply and demand of global energy were evaluated based on the energy types. The distribution of public and private sector in Turkey was also discussed.

In the energy sector, accurate prediction is important in terms of providing the energy supply. However, prediction can be difficult due to the presence of random factors. In literature, various methods are proposed to improve the prediction results in electricity market. Bilgili [8] predicted the net electricity consumption of Turkey by means of linear regression, nonlinear regression models, and the ANN. The results demonstrated that the performance of the ANN provided better results than other proposed methods. Marvuglia and Messineo [9] predicted the residential electricity consumption using an Elman network. In the study, several Elman networks were analyzed and the best network was determined according to the prediction error. Sensitivity analysis was applied to provide a better insight for inputs. Es et al. [10] evaluated the performance of the ANN and multiple linear regression models in the net energy demand prediction of Turkey. Başoğlu and Bulut [3] developed a new prediction method including the ANN and expert systems to predict the demand of short-term electricity in Turkey. Errors that may occur due to random elements of the ANN have been minimized with the help of an expert system. Expert system can take into account random elements and seasonal effects that occur in different forms at different times. The results demonstrated that prediction accuracy of proposed method was high. Kocadayı et al. [7] predicted the annual electricity consumption by means of the ANN. It was seen that the

electricity consumption prediction results of the ANN model are very close to the real value. Nugaliyadde et al. [11] used the recurrent neural network and a long short term memory network to predict electricity consumption. The prediction results of proposed methods were compared with other prediction models to show the predictive ability of methods.

Tutun et al. [4] estimated future independent factors using predicted scenario approaches. Then, two new models with linear and quadratic behavior were applied for the prediction of net electricity consumption. Kaya et al. [12] presented the relationship between internet usage and electricity consumption for Turkey. In the paper, the number of internet users, gross domestic product (GDP), and annual percentage changes in electricity consumption were utilized. An autoregressive distributed lag model was employed. Accordingly, increasing the amount of internet users and growth in GDP has positive and statistically important impacts on the growth of electricity consumption in Turkey. Çamurdan and Ganiz [13] used publicly available data to create decision tree, linear regression and random forest models for electricity demand prediction. Li and Zhang [14] presented a novel optimized GM (1, 1) method to improve electricity consumption forecasts. Note that GM (m, n) represents a grey prediction model in which the differential equation order is m and variable number is n. In the model, data transformation was firstly applied for the original data sequence. Then, the background value was optimized by means of combination interpolation optimization. Finally, prediction model was created and evaluated. Two case studies were utilized to analyze the performance of the method. Sun et al. [15] proposed a monthly power consumption comprehensive prediction model. The model is capable of processing data for any type of seasonal variation factor. In addition, the change rate of seasonal component and trend component smoothness can be controlled. The actual monthly electricity consumption data was utilized to assess the efficiency of prediction model.

In the electricity market, long-term electricity purchases and sales are made through bilateral agreements. The electricity reference price that formed in the day-ahead market is important for market participants in determining the prices of bilateral agreements, making energy investments and determining energy trade risks. The day-ahead market provides a chance for market participants to eliminate the energy imbalances that may occur for the next day. The prices formed in the day-ahead market are accepted as the electricity reference price (MCP) due to their closeness to real time [16].

Producers and customers need information about price prediction to plan their bidding strategies. Producers with low ability to alter MCPs need day-ahead price prediction to make optimum self-scheduling and derive bidding

strategy in the pool. For the same reasons as the producers, retailers, and large consumers need day-ahead MCPs. However, MCPs are volatile in deregulated power markets [17]. Therefore, various methods were developed to provide better strategy for producers and customers. Gao et al. [18] proposed the three-layer back propagation network to predict the MCP and market clearing quantity. Considering truncated historical prices and untreated spiking data, two methods were created. It was determined that the truncated method had better accuracy. Georgilakis [17] developed a methodology for the prediction of MCP in California power market considering three steps. Firstly, the ANN was employed to predict the day-ahead load. Secondly, the persistence method was utilized to predict the MCPs. Finally, the ANN was employed to predict the MCPs. Two case studies including without price spikes and with price spikes were applied. Singhal and Swarup [19] employed the ANN to predict the MCP for daily energy market. Pre-processing and post-processing were applied to improve the ANN performance. It was observed that proposed method gives good results for normal trend. On the other hand, performance of the model gradually degraded for days with price spikes. Şenocak and Kahveci [16] used the adaptive network based fuzzy inference systems (ANFIS) and the ANN to predict the MCP. It was determined that the prediction performance of the ANFIS was better than the ANN. Anamika and Kumar [20] used the ANN and the regression method to predict the MCP in deregulated electricity markets. It was determined that the regression model was better than the ANN method in MCP prediction of Indian electricity markets. Anamika and Kumar [21] applied the ANN on different groups to predict hourly MCPs in the Indian electricity exchange. To eliminate outliers or price spikes and normalize the rest, data was also preprocessed. Kabak and Tasdemir [22] used the ANN to create a Turkey's electricity day-ahead price prediction model that was utilized for supply and demand curves. It was determined that prediction error of model was lower if it was considered daily rather than hourly.

Yan and Chowdhury [23] proposed a model based on multiple support vector machine (SVM) containing a SVM classification module and a SVM regression module to predict hourly electricity MCP. Price patterns can also predicted by proposed model. Prabavathi and Gnanadass [5] used a mathematical model to solve the bidding function for suppliers and customers. In the paper, step bidding function was used to find the MCP. It was determined that MCP can be higher when demand is increased. Cheng et al. [24] proposed a novel grey prediction model to predict the mid-term electricity MCP. In the study, two improved GM (0, N) models whose parameters were determined by an improved particle swarm optimization were employed. In addition, a novel whitenization method was utilized to define the value of definite prediction. Tür [25] presented

the analysis of the MCP and the system marginal price for consumers. Yanar and Akay [26] used the multilayer perceptron, recurrent neural network, CNN, and long short term memory to predict the MCP. From the literature it is apparently seen that a large number of studies are available. However, no single best prediction approach is available. Any method may not guarantee reasonable accuracy for all prediction situations. Therefore more improvement is required to increase the prediction accuracy. For the particular situations, it was also decided that each method has its own advantages. Further developments are required in the methods.

In this paper, MCP prediction is taken into account to cope with the challenges of electricity industry. Prediction models are created using XGBoost, CatBoost, AdaBoost, ANN, and CNN. Furthermore, the performances of the proposed methods are compared to evaluate the prediction results. Thus, a comparative analysis was provided on XGBoost, CatBoost, AdaBoost, ANN, and CNN to help academicians, economists, and statisticians selecting the best model for MCP prediction. It is seen that this line of study is highly contingent upon reliable prediction of MCP in Turkey. The contribution of this paper can be summarized as follows. Firstly, boosting algorithms including XGBoost, CatBoost, and AdaBoost are used to predict the MCP in Turkey. Secondly, ANN and CNN are employed for MCP prediction in Turkey. Thirdly, the performance of proposed methods is compared to evaluate the prediction.

2. Proposed Methods

In this paper, dataset covers the period from 01.07.2009 up to 01.03.2020. The dataset was downloaded from EPIAŞ (Market & Financial Settlement Center) [27]. Count (its value is 3897), mean (its value is 165.7), standard deviation (its value is 59.4), minimum (its value is 19.1), first quartile (its value is 130.3), second quartile (its value is 153.8), third quartile (its value is 180.2), and maximum (its value is 687) are evaluated as descriptive statistics of the MCP. Density plot and histogram of daily MCP dataset is also given in Figure 1 where the y-axis is in terms of density.

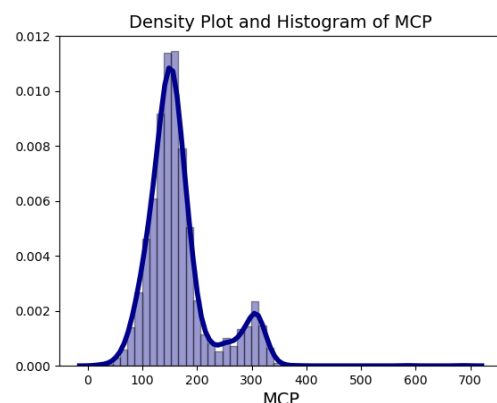


Figure 1. Density plot and histogram of daily MCP dataset

In this paper, boosting algorithms and neural network based methods are used to predict daily MCP. Note that the parameters of proposed methods are determined using trial and error method. In there, Mean Squared Error (MSE) was used as performance measurements to determine the parameters of proposed methods. Details about the proposed methods are given in following subsections. Note that processor is Intel (R)Core (TM) i7-8700CPU@3.70GH and Random-Access Memory (RAM) is 64 GB.

2.1 XGBoost

XGBoost can be described as a scalable end-to-end tree boosting system. It is used as an open-source package [28]. In XGBoost, weak classifiers are aggregated to create a powerful model. XGBoost can be represented as follows for a given dataset with n samples and m features ($D = \{(x_i, y_i)\} (|D| = n, x_i \in \mathbb{R}^m, y_i \in \mathbb{R})$).

$$\hat{y}_i = \sum_{k=1}^K f_k(x_i), f_k \in F \quad (1)$$

where $F = \{f(x) = w_{q(x)}\} (q: \mathbb{R}^m \rightarrow T, w \in \mathbb{R}^T)$ denotes the space of classification and regression trees (CART). $q(x)$ maps an input x to CART leaf node. The weight on the node represented as w and the total leave numbers in the tree is T . The XGBoost summarizes all weights provided from each CART and outputs a final score. Details about the XGBoost can be found in [29]. XGBoost utilizes a new regularization technique to control the overfitting that is the difference between XGBoost and other gradient boosting. Hence, XGBoost is faster and more robust during tuning of the method [30].

In XGBoost, the value of `colsample_bytree` (the subsample ratio of columns when constructing each tree) is 1. Maximum depth of a tree is determined as 3. In addition, `reg_alpha` (L2 regularization term on weights) and `reg_lambda` (L1 regularization term on weights) are specified as 1.3 and 1.1, respectively. `min_child_weight` (minimum sum of instance weight needed in a child) is 1. Finally, learning rate is assigned as 0.1. Note that dataset is divided into two separate parts as training (80%) and testing (20%).

2.2 CatBoost

CatBoost is a new gradient boosting decision tree algorithm. CatBoost can be used to overcome gradient bias. Multiple categorical features can be combined by CatBoost. A greedy way is utilized in CatBoost to integrate all categorical features and their combinations in the current tree. Random permutations of the training data are produced in CatBoost. To enhance the robustness of algorithm, multiple permutations can also be employed. CatBoost utilizes oblivious trees as base predictors [31-32]. CatBoost is an ensemble of symmetric decision trees that

have less parameters, faster training and testing, and higher accuracy in their symmetry structure [33]. In this paper, the learning rate is taken as 1 and depth is 4 for proposed CatBoost algorithm.

2.3 AdaBoost

The application of AdaBoost can be briefly explained as follows. Its adaptation is that the sample weight of previous weak classifier is strengthened. To train the next new weak classifier, the updated sample of the weight is again used. Population is used to train the new weak classifier in training phase. New sample weights are generated. These procedures continue until a particular condition is satisfied such as maximum number of iterations. It can be said that multiple weak classifiers combined into a strong classifier in AdaBoost. The strong classifier is determined using following equation.

$$F(x) = \sum_{k=1}^T \alpha_k f_k(x) \quad (2)$$

The strong classifier is represented as $F(x)$ while the weak classifier is denoted as $f_k(x)$. The weak classifier weight is α_k and weak classifier number is T . Details about the AdaBoost can be found in [34]. The main advantages of AdaBoost are fast, simple, and easy to program [35]. In this study, the number of estimators, learning rate, and maximum depth are determined as 170, 1.518, and 3, respectively.

2.4 ANN

ANN includes the input layer and the output layer, and also hidden layer(s) which help(s) catch nonlinearity. ANN is constructed with the aim of processing the input information and transmitting the information via various connections. ANN has a powerful connection between the variables of input and output. Thus, ANN is able to model a dynamic non-linear relationship and to extract dependency of input-outputs. It is easy to propose the prediction model in the ANN. However, the performance of the ANN directly depends on the parameters.

In this paper, Adam is selected among available optimizers in Keras. Two hidden layers are used in the ANN. The number of neuron in first hidden layer is specified as 32 while the number of neuron in second hidden layer is specified as 64. The epoch number is utilized as 500. In addition, rectified linear activation function (ReLU) is used as the activation function. Note that dataset is divided into two separate parts as training (80%) and testing (20%).

2.5 CNN

The term "convolutional neural system" demonstrates that the system uses a mathematical linear operation named convolution. CNN included at least one convolutional layer

and then followed by at least one fully connected layer as in a typical multi-layer ANN. Convolutional layer that defines the output of associated inputs is the main element in CNN. Fully connected layer seeks to build the predictions from the activations. In addition, sub-sampling layers between those two layers can exist [36]. Reducing the parameter numbers in the ANN is the most important feature of CNNs. Another significant feature of the CNN is to acquire abstract features as input propagates to deeper levels [37].

In this paper, settings of the common parameters of the CNN with the ANN are all the same. Thus, Adam is selected among available optimizers. Two hidden layers are used. The number of neuron in first hidden layer is specified as 32 while the number of neuron is specified as 64 in second hidden layer. The epoch number is utilized as 500. In addition, ReLU is used as the activation function. Note that dataset is divided into two separate parts as training (80%) and testing (20%).

3. Results and Discussion

Planning and management of the energy require effective modeling and prediction. The better prediction means more accurate investments and more satisfied customers. However, prediction is not an easy process in energy sector; it requires the consideration of very complex details. In this study, XGBoost, CatBoost, AdaBoost, ANN, and CNN are used to predict the MCP. The results of performance measures are given in Table 1.

Root-mean-square error (RMSE), mean squared error (MSE), mean absolute error (MAE), and central processing unit (CPU) time are used to compare the proposed methods. Thus, RMSE, MSE, MAE, and CPU are used to determine which prediction method performed the best under different

conditions. In literature, various performance measures are used to judge the prediction capability of the methods. Many researchers have also asserted that there are no universally applicable features for the accuracy measures. Thus, no measure is valid in all conditions and different measures treat different aspects of accuracy [38].

The results of this study demonstrated that AdaBoost required significantly less CPU time. The potential reason for AdaBoost algorithm gives less CPU time is that it has no parameters to tune. CatBoost gives the best value according to the MSE and MAE. CNN gives the best value according to the RMSE and MSE. It is also determined that the values of the RMSE, MSE, and MAE are relatively close in proposed methods. The MAE informs about the average size of prediction errors when negative signs are ignored. MSE and RMSE ensure a quadratic loss function and measure the uncertainty in prediction [39]. Note that the lower the values of the RMSE, MSE, and MAE, the closer the predicted values are to the actual values. The comparison between true values of MCP and the predictive values of each method is given in Figure 2.

In this study, the association strength based on Pearson's test is also calculated as given in Figure 3 for XGBoost, CatBoost, AdaBoost ANN, and CNN, respectively. When the coefficient of Pearson's correlation is equal to 1, it demonstrated that a linear relationship is available between the prediction result and the actual data. When the coefficient of Pearson's correlation is equal to 0, it demonstrated that no relationship is available. The coefficient of Pearson's correlation for ANN and CNN is higher than other methods. In addition, CatBoost has the lowest value when compared with XGBoost, AdaBoost ANN, and CNN.

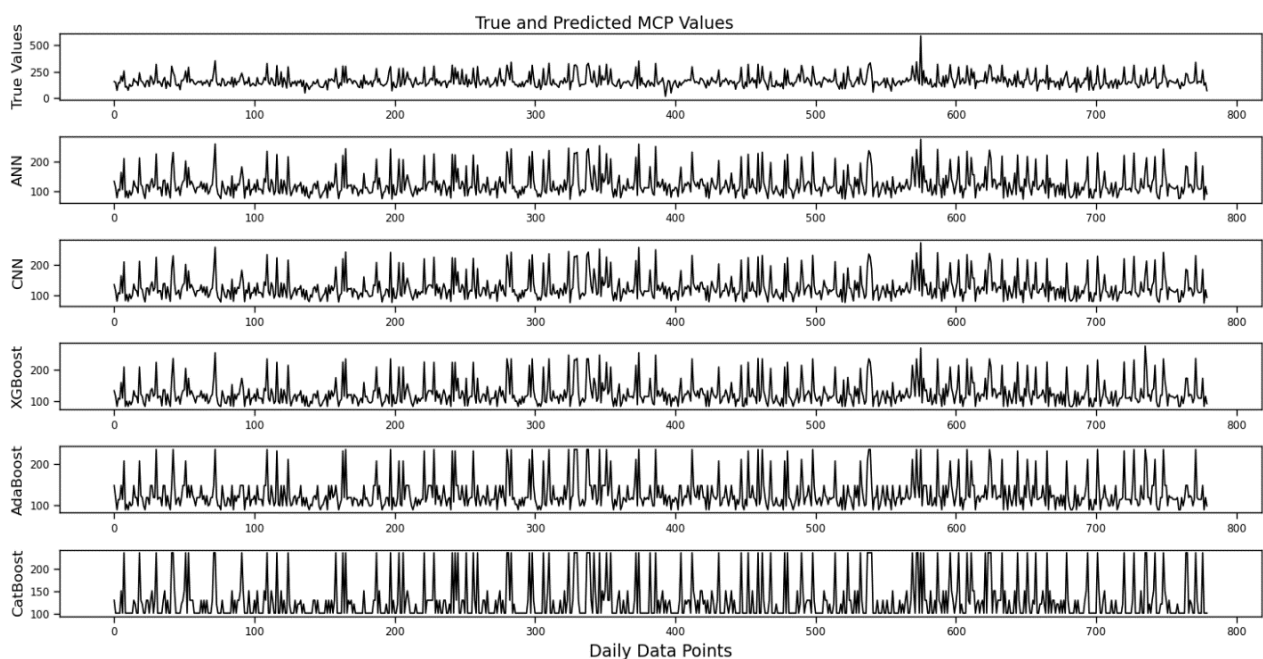


Figure 2. The true values of MCP and the prediction values of proposed methods

Table 1. The results of performance measures in proposed method

Methods	RMSE	MSE	MAE	CPU time (seconds)
XGBoost	0.0686	0.0047	0.0575	0.206
CatBoost	0.0671	0.0045	0.0558	0.441
AdaBoost	0.0690	0.0048	0.0559	0.035
ANN	0.0691	0.0049	0.0594	230.998
CNN	0.0664	0.0045	0.0568	243.925

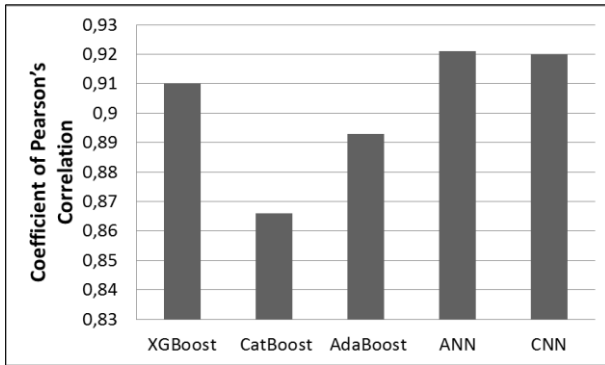


Figure 3. The coefficient of Pearson's correlation for proposed methods

4. Conclusion

Electricity is utilized in almost all kinds of human activity, such as industrial development, transportation, illumination, agriculture, residential, and heating. Electricity consumption is increasing every year. Therefore, prediction constitutes the significant part of the countries' energy policies. Due to the increasing population and industrialization, effective prediction is needed to meet the increasing energy demand. However, prediction in energy sector is a difficult task because of the uncertain and volatile nature. In this paper, MCP is predicted using XGBoost, CatBoost, AdaBoost, ANN, and CNN. Then, performances of proposed methods are compared to show the differences between methods. According to the results of CPU time, AdaBoost can be selected. It can be also said that the values of RMSE, MSE, and MAE are relatively close in proposed methods. However, the best value of MSE and MAE is provided by the CatBoost. CNN also provides the best value according to RMSE and MSE. Overall results of the study showed that all proposed methods can be successfully used to manage electricity usage and determine the bidding strategy. In future work, other optimization methods such as nondominated sorting genetic algorithm II can be employed when optimizing the parameters of methods in order to get better performance on prediction.

Declaration

The author declared no potential conflicts of interest with respect to the research, authorship, and/or publication of

this article. The author also declared that this article is original, was prepared in accordance with international publication and research ethics, and ethical committee permission or any special permission is not required.

Author Contributions

A. Boru İpek developed the methodology, performed the analysis and wrote the manuscript.

References





- Kiliç, A. M., *Turkey's main energy sources and importance of usage in energy sector*. Energy Exploration & Exploitation, 2006. **24**(1): p. 1–17.
- Akbalik, M., and Kavcıoğlu, Ş., *Energy sector outlook in Turkey*. Dumlupınar University Journal of Social Science, Special Issue of XIV. International Symposium on Econometrics, Operations Research and Statistics, 2014. p. 97–118.
- Başoğlu, B., and Bulut, M., *Kısa dönem elektrik talep tahminleri için yapay sinir ağları ve uzman sistemler tabanlı hibrit sistem geliştirilmesi*. Journal of the Faculty of Engineering & Architecture of Gazi University, 2017. **32**(2): p. 575–583.
- Tutun, S., Chou, C.-A., and Canıyılmaz, E., *A new forecasting framework for volatile behavior in net electricity consumption: A case study in Turkey*. Energy, **93**(2), 2015. p. 2406–2422.
- Prabavathi, M., and Gnanadass, R., *Electric power bidding model for practical utility system*. Alexandria Engineering Journal, 2018. **57**(1): p. 277–286.
- Ceyhan, G., *Türkiye'de elektrik piyasa takas fiyatı ve sistem marjinal fiyatı farkı üzerine istatistiksel bir çalışma*, 2016. [cited 2020 25 September]; Available from: https://blog.metu.edu.tr/e162742/files/2016/08/PTF_vs_SMF_original.pdf.
- Kocadayı, Y., ErKaymaz, O., and Uzun, R., *Estimation of Tr81 area yearly electric energy consumption by artificial neural networks*. Bilge International Journal of Science and Technology Research, **1**(Special Issue), 2017. p. 59–64.
- Bilgili, M., *Estimation of net electricity consumption of Turkey*. Journal of Thermal Science & Technology, 2009. **29**(2): p. 89–98.
- Marvuglia, A., and Messineo, A., *Using recurrent artificial neural networks to forecast household electricity consumption*. Energy Procedia, 2012. **14**: p. 45–55.
- Es, H. A., Kalender, F. Y., and Hamzaçebi, C., *Yapay sinir ağları ile Türkiye net enerji talep tahmini*. Journal of the Faculty of Engineering and Architecture of Gazi University, 2014. **29**(3): p. 495–504.
- Nugaliyadde, A., Somaratne, U., and Wong, K. W., *Predicting electricity consumption using deep recurrent neural networks*. 2019. arXiv:1909.08182.
- Kaya, M. V., Doyar, B. V., and Demir, F., *The effects of internet usage and GDP on electricity consumption: the case of Turkey*. Yönetim ve Ekonomi, 2017. **24**(1): p. 185–198.
- Çamurdan, Z., and Ganiz, M. C., *Machine learning based electricity demand forecasting*. 2017 International Conference on Computer Science and Engineering (UBMK), Antalya, 2017. p. 412–417.

14. Li, K., and Zhang, T., *Forecasting electricity consumption using an improved grey prediction model*. *Information*, 2018. **9**: p. 204.
15. Sun, T., Zhang, T., Teng, Y., Chen, Z., and Fang, J., *Monthly electricity consumption forecasting method based on X12 and STL decomposition model in an integrated energy system*. *Mathematical Problems in Engineering*, 2019. 9012543: p. 1-16.
16. Şenocak, F., and Kahveci, H., *Periodic price averages forecasting of MCP in day-ahead market*. 2016 National Conference on Electrical, Electronics and Biomedical Engineering (ELECO), Bursa, 2016. p. 664–668.
17. Georgilakis, P. S., *Market clearing price forecasting in deregulated electricity markets using adaptively trained neural networks*. Hellenic Conference on Artificial Intelligence, 2006. p. 56–66.
18. Gao, F., Guan, X., Cao, X.-R., and Papalexopoulos, A., *Forecasting power market clearing price and quantity using a neural network method*. 2000 Power Engineering Society Summer Meeting (Cat. No. 00CH37134), Seattle, WA, 2000. **4**: p. 2183–2188.
19. Singhal, D., and Swarup, K. S. 2011. *Electricity price forecasting using artificial neural networks*. *Electrical Power and Energy Systems*, **33**(3): p. 550–555.
20. Anamika, and Kumar, N., *Market clearing price prediction using ANN in Indian electricity markets*. 2016 International Conference on Energy Efficient Technologies for Sustainability (ICEETS), Nagercoil, 2016. p. 454–458.
21. Anamika, and Kumar, N., *Market-clearing price forecasting for Indian electricity markets*. *Proceeding of International Conference on Intelligent Communication, Control and Devices, Advances in Intelligent Systems and Computing*, Springer, Singapore, 2017. **479**: p. 633–642.
22. Kabak, M., and Tasdemir, T., *Electricity day-ahead market price forecasting by using artificial neural networks: an application for Turkey*. *Arabian Journal for Science and Engineering*, 2020. **45**: p. 2317–2326.
23. Yan, X., and Chowdhury, N. A., *Mid-term electricity market clearing price forecasting: A multiple SVM approach*. *Electrical Power & Energy Systems*, 2014. **58**: p. 206-214.
24. Cheng, C., Luo, B., Miao, S., and Wu, X., *Mid-term electricity market clearing price forecasting with sparse data: a case in newly-reformed Yunnan electricity market*. *Energies*, 2016. **9**: p. 804.
25. Tür, M. R., *Mikro şebeke sistemlerine dayalı elektrik piyasasında fiyat oluşturulma senaryosu*. *Gazi Üniversitesi Fen Bilimleri Dergisi Part C: Tasarım ve Teknoloji*, 2019. **7**(1): p. 192–202.
26. Yanar, A., and Akay, M. F. *Prediction of electricity market clearing price using machine learning and deep learning*. *Ç.Ü Fen ve Mühendislik Bilimleri Dergisi*, 2020. **39**(9), p.137–141.
27. EPİAŞ, *Market & Financial Settlement Center*, [cited 2020 03 March]; Available from:
<https://rapor.epias.com.tr/rapor/xhtml/ptfSmfListeleme.xhtml>
28. Chen, T., and Guestrin, C., *XGBoost: A scalable tree boosting system*. *Proceedings of the 22nd ACM SIGKDD International Conference on Knowledge Discovery and Data Mining*, 2016. p. 785–794.
29. Qian, N., Wang, X., Fu, Y., Zhao, Z., Xu, J., and Chen, J., *Predicting heat transfer of oscillating heat pipes for machining processes based on extreme gradient boosting algorithm*. *Applied Thermal Engineering*, 2020. **164**: p. 114521.
30. Daoud, E. A., *Comparison between XGBoost, LightGBM and CatBoost using a home credit dataset*. *International Journal of Computer and Information Engineering*, 2019. **13**(1): p. 6–10.
31. Huang, G., Wu, L., Ma, X., Zhang, W., Fan, J., Yu, X., Zeng, W., and Zhou, H., *Evaluation of CatBoost method for prediction of reference evapotranspiration in humid regions*. *Journal of Hydrology*, 2019. **574**: p. 1029–1041.
32. Zhang, Y., Zhao, Z., and Zheng, J., *CatBoost: A new approach for estimating daily reference crop evapotranspiration in arid and semi-arid regions of Northern China*. *Journal of Hydrology*, 2020. **588**: p. 125087.
33. Liu, W., Deng, K., Zhang, X., Cheng, Y., Zheng, Z., Jiang, F., and Peng, J., *A semi-supervised tri-catboost method for driving style recognition*. *Symmetry*, 2020. **12**(3): p. 336.
34. Dong, X., Dong, C., Chen, B., Zhong, J., He, G., and Chen, Z., *Application of AdaBoost algorithm based on decision tree in forecasting net power of circulating power plants*. 2020 IEEE 4th Information Technology, Networking, Electronic and Automation Control Conference (ITNEC), Chongqing, China, 2020. p. 747–750.
35. Jinbo, S., Xiu, L., and Wenhua, L., *The application of AdaBoost in customer churn prediction*. 2007 International Conference on Service Systems and Service Management, 2007. p. 1–6.
36. Dhillon, A., and Verma, G. K., *Convolutional neural network: a review of models, methodologies and applications to object detection*. *Progress in Artificial Intelligence*, 2020. **9**: p. 85–112.
37. Albawi, S., Mohammed, T. A., and Al-Zawi, S., *Understanding of a convolutional neural network*. 2017 International Conference on Engineering and Technology (ICET), Antalya, 2017. p. 1–6.
38. Cameron, A.C., and Windmeijer, F.A.G. *An R-squared measure of goodness of fit for some common nonlinear regression models*. *Journal of Econometrics*, 1997. **77**(2): p. 329–342.
39. Makridakis, S., and Hibon, M., *Evaluating Accuracy (or Error) Measures*. 1995. [cited 2020 04 March]; Available from:
<http://www.insead.edu/facultyresearch/research/doc.cfm?id=46875>.



Research Article

Vibration reduction on a cantilever Timoshenko beam control subjected to combined effects of wind and earthquake loads using damped outriggers

Jules Metsebo ^{a*} , Buris Peggy Ndemanou ^b , Andre Cheage Chamgoue ^c  and
Guy Richard Kol ^{b,c} 

^aDepartment of Hydraulics and water Management, National Advanced School of Engineering, University of Maroua, P.O Box 46 Maroua, Cameroon

^bDepartment of Mechanical Petroleum and Gas Engineering, Faculty of Mines and Petroleum Industries, University of Maroua; P.O Box 08 Kaélé, Cameroon

^cSchool of Geology and Mining Engineering, University of Ngaoundere, P.O. Box 115, Meiganga, Cameroon

ARTICLE INFO

Article history:

Received 05 February 2021

Revised 01 April 2021

Accepted 20 April 2021

Keywords:

Fuzzy Logic

Method of lines

MR dampers

Outriggers

RMS

Timoshenko beam

ABSTRACT

This paper deals with the combined effects of wind and earthquake on the dynamic response of a cantilever structure. It is mainly composed of the core-structure, multi-outriggers with magnetorheological (MR) dampers localized at different levels along of the structure and perimeter columns. These control devices are semi-active in nature and exhibit a nonlinear behavior. One of their interesting characteristics is their ability to add supplementary energy dissipation to the structural system. Exposed to combined wind and earthquake loads, the core-structure is modelled using a Timoshenko cantilever beam. The stochastic approach based on the statistic properties is employed to estimate the degree excitations of the two natural hazards. The peak Root-Mean-Square (RMS) are evaluated to quantify the optimal location of damped outriggers. Defined as the control algorithm based on human reasoning, the Fuzzy logic is used to select the appropriate current that feeds the control devices. The obtained results indicate that the application of the fuzzy logic further minimizes the effects of bending-moment and shear force. All of these enhance the performance of the whole structural response and lead to a significantly reduction of excessive vibration to an acceptable level.

© 2021, Advanced Researches and Engineering Journal (IAREJ) and the Author(s).

1. Introduction

Many structural engineering structures, such as bridges, tall-buildings [1,2,40], railways [3] and nuclear power plants [4] around the world, still suffer from the vibrations induced by winds or earthquakes during their lifetime. In recent decades, these mentioned natural disturbances are considered as the most destructive. They are able to alter the physical property of the majority of infrastructures by causing the severe structural damage and human life losses. Generally, the dynamic loads of these natural phenomenon are applied in two directions (horizontal and vertical motions) along the engineering structures. Due to its effect on the performance of the structural system, the horizontal

movement has proven to be of a great importance for the design of the structural engineering [5].

To further increase the ability and resiliency of tall buildings to withstand against the external perturbations, the outrigger systems were developed in the tall buildings as an alternative solution [6]. Some cases of application of these structures already exist in Shanghai with a height of 632 meter [7] and The Burj Khalifa in Dubai with the height of 828 meters [8]. In a traditional design, this system is constituted of the core-structure characterizing the tall building behaviour, the outriggers associated with control devices and the perimeter columns. Hence, the understanding of this design has considerably increased the

* Corresponding author. Tel.: +237-699-484-135.

E-mail addresses: jmetsebo@gmail.com (J. Metsebo), ndemanoupeggy@gmail.com (B. P. Ndemanou), cham6ko@yahoo.fr (A. C. Chamgoue), kolguy_r@yahoo.fr (G. R. Kol)

ORCID: 0000-0002-4312-6856 (J. Metsebo), 0000-0003-2254-9830 (B. P. Ndemanou), 0000-0002-7422-8839 (A. C. Chamgoue),

0000-0002-9959-2709 (G. R. Kol)

DOI: 10.35860/iarej.875161

This article is licensed under the CC BY-NC 4.0 International License (<https://creativecommons.org/licenses/by-nc/4.0/>).

motivation of many researchers [9–11]. Huang et al. [12] proposed an analytical method to evaluate the dynamic response of a single damped outrigger system. Based on this approach, they obtained the optimal locations of outrigger to further reduce response. Yang et al. [13] used the finite element methods to assess the seismic performance. They indicated that the equivalent energy design procedure is an efficient method to design the outrigger system and helps to avoid the collapse at different levels of the earthquake. Zhou et al. [14] studied the analytical methods to investigate the earthquake response of an outrigger system. The authors applied this approach to determine the optimal location of the outrigger.

In view of further reinforcing the performance of the damped outriggers, the control devices are installed between the core-structure and perimeter columns. These control devices are either passive, active, semi-active nature. They can adjust the magnitude of the control force. A large number of theoretical and experimental studies have been done [15–19]. The results reveal that among the different types of control devices, MR dampers are a promising type. Because they include the active and passive properties and also require a low power to change the system's physical characteristic [20]. Despite all these encouraging results, they are however, characterized by an intrinsically non-linear behaviour, which can sometimes be a major disadvantage. To avoid any inconvenience, some suitable control algorithms were developed. They remedy to this situation by optimising the dynamics response of the MR dampers. In this context, one can note the algorithms such as Clipped optimal control [21,22], Bang-bang control [23,24], Lyapunov stability [25], genetic algorithm [26–28], sliding mode [29] and fuzzy logic [31–37]. In the present work, the fuzzy logic is directly applied to select the appropriate input current of the MR dampers. of the shear in investigating transverse vibrations [38]. It is defined as an extension of the Euler-Bernoulli theory [39]. It is in this way that, Ndemanou et al. examined the performance of magneto-rheological damper on the outrigger system. Their results indicated that at the position near the top of the structural system, the damper outrigger further improves the dynamic response of the structure. The drawback of aforementioned studies is the fact that the effects of outrigger dampers do not assessed on the bending moment and shearing force of the core-structure.

To analyse the structural response of the outrigger system, the core-structure is assumed to be elastic and homogeneous. Thus, Timoshenko cantilever beam will be used to model the core-structure. This model includes the rotatory inertia and the effect.

In this paper, the Timoshenko's beam formulation based on the partial differential equations is used to model the core-structure. The structural system will be subjected to combined wind and earthquake loads. It is assuming that the

perimeter columns are axially very stiff [15]. Therefore, the effect of its dynamic response will be assumed neglected during this investigation.

The aim of this study is to analyze how the different locations of damped outriggers significantly affect the bending moment, shear force and transversal displacement of the core-structure under the combination of two natural disturbances. Although, the mentioned above force occurs in a structure by further causing stresses. It is important to underline that the one of the most important points is to increase the beam's ability by dramatically reducing the undesirable vibrations.

2. Description of the Physical System

The structural system subjected to two natural hazards is schematically displayed in Figure 1. It is constituted of an elastic core-structure, the exterior columns and three damped outriggers localized at different positions x_1 , $x_1 + x_2$ and $x_1 + x_2 + x_3$ along the height of the structural system. The connection of all these elements is an effective means to work together and changing their dynamic response. In traditional configuration, the core-structure is a tall-building constituted of several floors. It is assumed as a uniform cantilever beam, so the ends are fixed at the bottom and free at the top. The damped outriggers denote the outriggers equipped of MR dampers and are assumed to be symmetrical in relation to the central line of the core-structure. The indicated control devices are mounted vertically between the core-structure and the perimeter column as shown in Figure 1. As can be seen, this whole structure is submitted to combined action of wind and earthquake loads. In the current state, only their component in the horizontal direction is considered. Hence, the wind flow presents an unsteady behaviour and distributed all along the height of the structure.

Unlike wind dynamics, the horizontal earthquake displacement also defined as a ground motion is rather applied to the base of the mechanical structure. It should be noted that in the present case, each of outriggers behaves as a rigid body. It is important to point up that the outriggers and the exterior columns have commonly a high stiffness.

3. Mathematical modelling

Varying with the coordinate along the beam and with time, the lateral displacement of the structure from equilibrium line is defined by the variable. In this case study, the influence of the perimeter columns on the dynamics of the core is not taken into consideration. As a result, the governing equation modelling the dynamics of the cantilever Timoshenko beam with damped outriggers submit to combined actions of vertical wind and horizontal earthquake loadings can be defined by the partial differential equation given as follows [26].

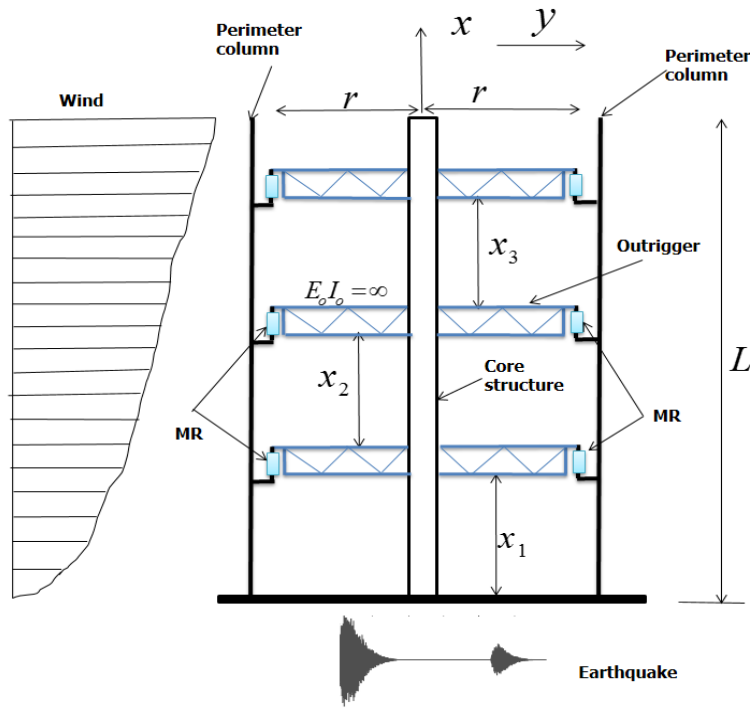


Figure 1. Schematic representation of the system under study: the simplified structure under the earthquake and wind loads

$$m \frac{\partial^2 y}{\partial t^2} + EI \frac{\partial^4 y}{\partial x^4} - mr^2 \left(1 + \frac{E}{k_s G} \right) \frac{\partial^4 y}{\partial x^2 \partial t^2} = f(x, t) - m \ddot{y}_g(t) + \frac{\partial M_a}{\partial x} \quad (1)$$

This above equation denotes transverse equation of motion. In this definition, m is the mass per unit length, ρ is the mass density of the beam, I is the moment of inertia of the cross-section area about the neutral axis, E is the elastic modulus; G is the shear modulus of elasticity. The dimensionless quantity k_s is the shear coefficient depending on the geometric of the cross-sectional area of the beam and depends on as well as of the Poisson's ratio. As indicated earlier, any information dynamics from perimeter columns linked to core-structure are not taken into account.

Note by passing that these defined geometrical characteristics are assumed constant.

Thus, within the Timoshenko theory configuration, the slope of the deflection curve $\left(\frac{\partial y}{\partial x} \right)$ is the sum of the angular rotation $\psi(x, t) = \psi$ of the beam cross-section due to the bending moment. and also of the angle due to shear distortion $\gamma(x, t)$, it follows that [41].

$$\frac{\partial y}{\partial x} = \psi(x, t) + \gamma(x, t) \quad (2)$$

Consequently, the bending moment is given by Equation (3).

$$M = -EI \frac{\partial \psi(x, t)}{\partial x} \quad (3)$$

The shearing force $Q(x, t) = Q$ along the beam length by the following equation:

$$Q = k_s AG \left(\frac{\partial y}{\partial x} - \psi \right) \quad (4)$$

As stated earlier, the shearing force is a force that occurs in a structure under external loads. As a result, reducing its effects will increase the resilience of the structure.

The angular rotation mentioned in Equations (2), (3) and (4) can be obtained through the following partial equation of motion:

$$\rho I \frac{\partial^2 \psi}{\partial t^2} = E.I \frac{\partial^2 \psi}{\partial x^2} + k_s GA \left(\frac{\partial y}{\partial x} - \psi \right) \quad (5)$$

The distributed moment generated by MR dampers is [42]:

$$M_a = 2r \sum_{i=1}^3 \delta(x - x_i) f_i(t) \quad (6)$$

The symbol $\delta(x - x_i)$ denotes the Dirac Delta function and has the property given as follows

$$\delta(x - x_i) = \begin{cases} \infty & x = x_i \\ 0 & x \neq x_i \end{cases} \quad (7)$$

The subscript i indicates the different points along the core-structure. As a result, x_i in equation (7) points out the places where the damped outriggers are installed.

As mentioned earlier, the MR devices are semi-active systems and also have the capacity to add the damping to the mechanical structure. They essentially exhibit a nonlinear behavior. Thus, a great number of studies in the literature have paid attention on the understanding of different accurate mathematical models that fully describe their dynamic response [43,44]. The mathematical form proposed by Yang et al. [45] is employed in this paper. Thus, it is defined as follows:

$$f_i(t) = m_r \ddot{y}(x_i, t) + c \left(\dot{y}(x_i, t) \right) \dot{y}(x_i, t) + k_1 y(x_i, t) + \alpha_1 z_b + f_0 \quad (8)$$

z_b is an evolutionary variable given by:

$$\dot{z}_b = -\gamma_a \left| \dot{y}(x_i, t) \right| z_b |z_b|^{n_o-1} + (\delta_a - \beta_a |z_b|^{n_o}) \dot{y}(x_i, t) \tag{9}$$

Where m_r is the equivalent mass which represents the MR fluid stiction phenomenon and inertial effect; k_1 is the accumulator stiffness and MR fluid compressibility; f_0 represents the damper friction force; $c \left(\dot{y}(x_i, t) \right)$ is the postyield plastic damping coefficient, γ_a , δ_a and β_a are the shape parameters of the hysteresis loops.

The damping coefficient is considered as follows:

$$c \left(\dot{y}(x_i, t) \right) = a_b \exp \left(- \left(a_c \left| \dot{y}(x_i, t) \right| \right)^p \right) \tag{10}$$

With a_b , a_c and p are positive constants.

Note that, an overdot denotes differentiation with respect to the time variable t .

Wind is a phenomenon of great complexity due to the many flow situations resulting from the interaction of wind with structures[46]. Thus, wind-induced vibrations may cause structural damage and have devastating effects on infrastructure [47]. Thus, the mathematical model of the dynamic wind loads can be established from an aero-elastic principle. Consequently, the aero-elastic force is given by the following expression [48,49].

$$f(x, t) = \frac{1}{2} \rho_a U^2 b \left[\varepsilon_0 + \frac{\varepsilon_1}{U} \left(\frac{\partial y}{\partial t} \right) + \frac{\varepsilon_2}{U^2} \left(\frac{\partial y}{\partial t} \right)^2 + \frac{\varepsilon_3}{U^3} \left(\frac{\partial y}{\partial t} \right)^3 \right] \tag{11}$$

Where ε_j ($j = 1,2,3$) are the aerodynamic coefficients relevant to square section, ρ_a is the air mass density. U is the wind velocity which can be considered as having two components

$$U = u_1 + u_2(t) \tag{12}$$

In which u_1 denotes the mean wind velocity, representing the steady component. The velocity fluctuation component $u_2(t)$ is a time varying part representing the turbulence that defined any movement of air at speeds very great, causing particles of air to move randomly in all directions.

By inserting (11) into (12) by applying the Taylor expansion, the Equation (11) can be rewritten as follows:

$$f(x, t) = f_{w1}(x, t) + f_{w2}(x, t)u_2(t) \tag{13}$$

Where:

$$f_{w1}(x, t) = \frac{1}{2} \rho_a b \left[\varepsilon_0 u_1^2 + \varepsilon_1 u_1 \left(\frac{\partial y}{\partial t} \right) + \varepsilon_2 \left(\frac{\partial y}{\partial t} \right)^2 + \frac{\varepsilon_3}{u_1} \left(\frac{\partial y}{\partial t} \right)^3 \right]$$

and

$$f_{w2}(x, t) = \frac{1}{2} \rho_a b \left[2\varepsilon_0 u_1 + \varepsilon_1 \left(\frac{\partial y}{\partial t} \right) - \frac{\varepsilon_3}{u_1^2} \left(\frac{\partial y}{\partial t} \right)^3 \right]$$

From Equation 12, it is clearly observed that the wind-induced vibrations on the whole structure mainly present a dissipative nonlinear. Moreover, its effects depend on the temporal and spatial fluctuations along the height of the structures.

Note by passing that the effects of turbulence on structural motion stability have become an important area in wind engineering [50].

The turbulent component of the wind flow used here, is assumed by the random processes of bounded variation with multiple spectrum peaks [51]. Consequently, the corresponding form is given by the following expression:

$$u_2(t) = \sum_{j=1}^{N_1} A_j \cos[\omega_j t + \sigma_j B_j(t) + \theta_j] \tag{14}$$

Where:

A_j are positive constants representing the amplitude of bounded noise, $B_j(t)$ are mutually independent unit Wiener processes, ω_j are representing center and σ_j are mutually independent random variables uniformly distributed in range $[0, 2\pi]$.

The spectral density of u_2 defined analytically can be found as:

$$S_w(\omega) = \sum_{j=1}^{n_1} \left(\frac{A_j^2 \sigma_j^2 \left(\omega^2 + \omega_j^2 + \frac{\sigma_j^4}{4} \right)}{4\pi \left[\left(\omega^2 - \omega_j^2 - \frac{\sigma_j^4}{4} \right)^2 + \sigma_j^4 \omega^2 \right]} \right) \tag{15}$$

It should be noted that the magnitude of the spectral density can be adjusted to approximate the well-known Dryden and Von Karman spectral of wind turbulence. By modifying the values of mentioned parameters as pointed up in the reference [52].

Figure 2 displays the two-side spectral density. The mathematical expression is developed in Equation (15). This gives a view on the repartition of the energy of the bounded noise.

As mentioned earlier, the same structure is also under earthquake loads. In this configuration, the mentioned variable $\ddot{y}_g(t)$ in Equation (1) defines the seismic events characterized by the ground acceleration.

It is worth pointing out that dot denotes derivative with respect to t . Thus, the governed equations are described as follows

$$\ddot{y}_g(t) = \left(2\xi_g \omega_g \dot{x}_g(t) + \omega_g^2 x_g(t) \right) e(t) \tag{16}$$

$$\ddot{x}_g(t) + 2\xi_g \omega_g \dot{x}_g(t) + \omega_g^2 x_g(t) = w(t) \tag{17}$$

Where $x_g(t)$ is the filter response, and $w(t)$ is the stationary Gaussian white noise with the following statistics:

$$\begin{cases} \langle w(t) \rangle = 0 \\ \langle w(t)w(\tau) \rangle = 2\pi S_0 \delta(t - \tau) \end{cases} \tag{18}$$

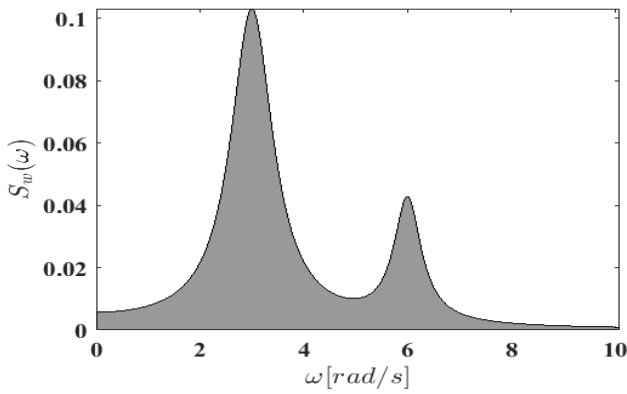


Figure 2. Spectral density of the bounded noise, with $A_1 = 0.8, A_1 = 0.4, \omega_1 = 3.0 \text{ rad/s } \omega_2 = 2\omega_1, \sigma_1 = 1.0, \sigma_2 = 0.8$

S_0 is the constant power spectral intensity of noise. $\langle \rangle$ denotes the angular brackets stand for ensemble averages [53].

The evolutionary power spectrum is given by:

$$S_g(\Omega, t) = |e(t)|^2 S_e(\Omega) \tag{19}$$

In which $e(t)$ is a deterministic envelope function of time. It is then given by the following form [54]:

$$e(t) = \begin{cases} e_{01}(t - t_1) \exp(-\lambda_1(t - t_1)) \\ 0 \\ e_{02}(t - t_2) \exp(-\lambda_2(t - t_2)) \end{cases} \tag{20}$$

Where e_{0j} and λ_j are positive constants that control intensity and non-stationary trend of the j th acceleration sequence.

The spectral density for the ground acceleration is defined as follows [55]:

$$S(\Omega) = S_0 \frac{\omega_g^4 + 4\xi_g^2 \omega_g^2 \Omega^2}{(\omega_g^2 - \Omega^2)^2 + 4\xi_g^2 \omega_g^2 \Omega^2} \tag{21}$$

Where ω_g is the dominant frequency of the soil, and ξ_g is the associated damping ratio of the soil layer.

4. Modal Equations and Numerical Results

To transform the partial form of the Equation (1) in the modal expression, let us consider the new dimensionless variables defined as follows:

$$X = \frac{x}{L}, \bar{u}_1 = \frac{u_1}{u_c}, a_1 = \frac{EI}{mL^4}, a_2 = \frac{r^2}{L^2} \left(1 + \frac{E}{k_s G}\right),$$

$$a_3 = \frac{E}{\rho L^2 \Delta X^2}, a_4 = \frac{k_s GA}{\rho I}, F(X, t) = \frac{1}{mL} f(x, t),$$

$$M^* = \frac{M_a}{mL^2}, \ddot{Y}_g = \frac{\ddot{y}_g}{L}, S_3 = \frac{\rho_a b \varepsilon_2 L b_5}{2m \times den}, S_4 = \frac{\rho_a b \varepsilon_3 L^2 b_6}{2m u_1 \times den},$$

$$S_5 = \frac{\rho_a b \varepsilon_0 u_c \bar{u}_1 b_4}{mL \times den}, S_6 = \frac{\rho_a b \varepsilon_1 b_1}{2m \times den}, S_7 = \frac{\rho_a b \varepsilon_3 L^2 b_6}{2m u_1^2 \times den},$$

$$\omega^2 = \frac{a_1 b_3}{den}, \eta_j = \frac{\phi'(X_j)}{den}, \zeta_a = \frac{2r}{L}, Z = \frac{z}{L}, \beta_L = \beta_a L^n$$

$$\gamma_L = \gamma_a L^n, den = b_1 - a_2 b_2 + \zeta_a \mu_m \sum_{j=1}^3 \phi(X_j) \phi'(X_j)$$

$$\mu_m = \frac{m_r}{mL}, f_a = \frac{1}{mL^2} f_0, \alpha_m = \frac{1}{mL} \alpha_l, K_1 = \frac{1}{mL} k_1,$$

$$C = \frac{1}{mL} c,$$

According to the relationships between the parameters, these leads to rewrite the Equation (1) of the dynamic of the structural system under the form:

$$\frac{\partial^2 Y}{\partial t^2} + a_1 \frac{\partial^4 Y}{\partial X^4} - a_2 \frac{\partial^4 Y}{\partial X^2 \partial t^2} = F(X, t) - \ddot{Y}_g(t) + \frac{\partial M^*}{\partial X} \tag{22}$$

It can be seen that the dimensionless expression only affects the spatial variable.

By considering that the transverse deflection of the beam can be written in term of product of two variables in the following form

$$Y = \phi(X)z(t) \tag{23}$$

In which, the function $\phi(X)$ is the spatial expression, $z(t)$ is the evolutionary displacement. Thus, the scheme for obtained this form has been detailed recently in reference [25]. In this paper, only the fundamental mode is considered because it contains more vibrational energy of the structural system.

By taking into account the internal damping, the mathematical manipulation of Equations (22) and (23) leads to modal equation given as:

$$\ddot{z} + \beta \dot{z} + \omega^2 z(t) = s_1 + s_2 \dot{z} + s_3 (\dot{z})^2 + s_4 (\dot{z})^3 + (s_5 + s_6 \dot{z} - s_7 (\dot{z})^3) u_2(t) - \sigma \ddot{Y}_g + \zeta_a \sum_{i=1}^3 \eta_i F_{m_i}(t) \tag{24}$$

From equation (24) it is well understood that, unlike seismic action, the effects of wind action on the structure increase the lateral deformation. Consequently, the mechanical system exhibits a nonlinear dynamic. This is due to the presence of nonlinear damping terms.

The dimensionless damping force of the control devices $F_{m_i}(t)$ can be written as follows:

$$F_{m_i}(t) = C (\dot{z} \phi(X_i)) \dot{z} \phi(X_i) + K_1 z \phi(X_i) + \alpha_m Z_{bi} + f_a$$

and

$$\dot{Z}_{bi} = -\gamma_L |\phi(x_i) \dot{z}| Z_{bi} |Z_{bi}|^{n-1} + (\delta_a - \beta_L |Z_{bi}|^n) \phi(x_i) \dot{z} \tag{25}$$

The damping coefficient can be rewritten as follows:

$$C (\dot{z} \phi(X_i)) = a_b^* \exp \left(- (a_c^* |\dot{z} \phi(X_i)|)^p \right)$$

To defined angular rotation the method of lines or semi-discretization method is applied on the Equation (5). It is a method is a procedure for obtaining the solution of the partial differential equations. This discretization approach is generally applied on the spatial variables. As a result, the Equation (5) can be expressed as:

$$\ddot{\psi}_n = a_3 (\psi_{n+1} - 2\psi_n + \psi_{n-1}) + a_4 (\phi'(x_n) z(t) - \psi_n) \tag{26}$$

The dimensionless boundary conditions can be written as follows:

$$X = 0 \rightarrow \psi_n = 0,$$

$$X = 1 \rightarrow \psi_{n+1} = \psi_{n-1}$$

This iteration method well-known in the literature is used to have the behavior of the system during the temporal evolution.

The core-structure considered in this study is assumed to have a total height $L = 300$ m. Its intrinsic properties are: Young’s modulus E of the material is 210 GPa, The shear Modulus of elasticity is $G = 81$ GPa, Poisson’s ratio ν is 0.3. The geometric properties are: mass of the core is $2 \times 10^5 \frac{kg}{m}$. The cross-section corresponds to $12 \text{ m} \times 12 \text{ m}$, thickness is 0.5 m and the shear coefficient $k_s = 0.435$. For the nonstationary ground acceleration, The intensities of the acceleration sequences at the first and second sequences $S_0 = 0.02 \text{ m}^2/\text{s}^3$ and $S_0 = 0.015 \text{ m}^2/\text{s}^3$, respectively. The parameters of the envelope functions are adopted as $e_{01} = 0.8155\lambda_1 = 0.3 \text{ s}^{-1}$ and $e_{02} = 0.9514$, $\lambda_2 = 0.35 \text{ s}^{-1}$ and the separating time interval between the sequences is 15 s. The interval time of the envelope function are $t_1 = 25 \text{ s}$, $t_2 = 40 \text{ s}$, $t_3 = 60 \text{ s}$.

Regarding the control devices, some of parameters are summarized in Table 1 [44]. These MR devices are able to generate the larger damping force [56]. Hence, in the present investigation, some values of parameters illustrated in Table 1 will be adjusted in order to have the appropriate values which defines a large-scale control device. From such devices are able to attenuate excessive vibrations of the structure under the optimal conditions. There are other parameters which do not depend on the input current and are therefore given by:

$$\gamma_a = 5179.04 \text{ m}^{-1}, \delta_a = 1377.9788,$$

$$\beta_a = 27.1603 \text{ m}^{-1}, p = 0.2442, k_1 = 20159.5 \text{ N/m}$$

It is interesting to indicate that the MR damper can be implemented in passive-off or passive-on mode. For each mode considered herein, the peak RMS of the shear force and bending-moment of the core-structure under combined wind and earthquake loads will be calculated to research to reasonable optimal location of the damper outriggers. Let us remind the readers that in configuration of the

outrigger system, one cannot refer our analysis to the comparison of controlled and uncontrolled cases. Because the damper outriggers are rigidly linked to core-structure and perimeter columns.

4.1 Passive-off

The passive off means the input current is zero. In other words, the MR damper is employed as a passive option. To assess the dynamic response of the structural system in this mode, the values of the control device will be selected in the first row in Table 1.

The next step is to apply the appropriate algorithm to numerically solve the Equations (24)-(26). Let us consider four positions of the damped outriggers defined as follows:

$$OL_1 = (0.4; 0.6; 0.8) ; OL_2 = (0.2; 0.7; 0.9) ; OL_3 = (0.3; 0.5; 0.9); OL_4 = (0.4; 0.7; 0.9).$$

Hence, it is worth investigate how the mentioned various positions of damper outriggers affect the shear force and bending-moment. The goal is to find the optimal position.

For this case, the length of an outriggers is $r = 4.0$.

Figure 3 and 5 clearly show the peak RMS of bending-moment and shear force at each point along of the core-structure, respectively. It appears that its different positions of damped outriggers rigidly connected to the core-structure affect significantly the moment-bending and shear force.

The results presented in Table 2 show that the bending-moment is very low at the point 0.1 of the core-structure and is high at the rest of points (0.2 up to 0.9) of the beam. It comes out that whatever the damped outriggers the value of the bending-moment is important at the point 0.3 of the mentioned structure. Looking closely at in Table 2, it is observed that the bending-moment is slightly small at location OL_4 compared to OL_1 , OL_2 and OL_3 .

The peak RMS values of the shear force in Figure 4 are shown in Table 3. The results indicate that the shear force is significantly important at the point 0.1 of the core-structure compared to the other points. The effects of the OL_4 of the damper outriggers are clearly weak on the core-structure than OL_1 , OL_2 and OL_3 .

Table 1. Damper parameter at various current levels

Current(A)	$\alpha_l(10^8 N)$	$\alpha_b(10^3 Ns/m)$	$a_b(10^3 s/m)$	$m_r(10^3 kg)$	no	$f_0(10^3 N)$
0.0237	1.3612	4,349,000	862.03	3,000	1.000	1,465.82
0.2588	2.2245	24,698,000	3,677.01	11,000	2.0679	2,708.36
0.5124	2.3270	28,500,000	3,713.88	16,000	3.5387	4,533.98
0.7625	2.1633	32,488,000	3,849.91	18,000	5.2533	4,433.08
1.0132	2.2347	24,172,000	2,327.49	19,500	5.6683	2,594.41
1.5198	2.2200	38,095,000	4,713.21	21,000	6.7673	5,804.24
2.0247	2.3002	35,030,000	4,335.08	22,000	6.7374	5,126.79

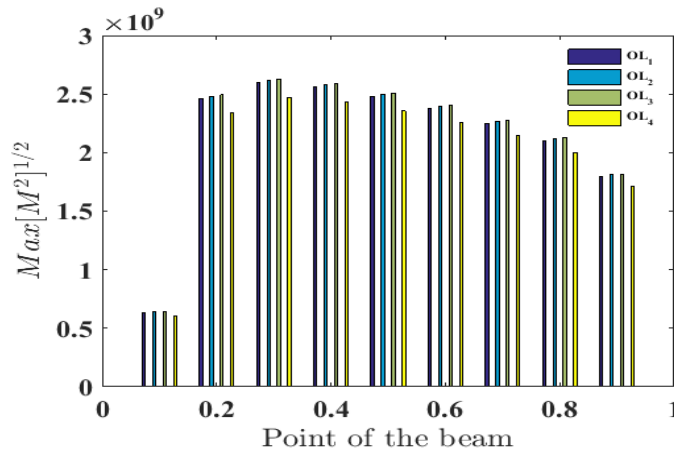


Figure 3. Peak RMS of bending moment at different points of the beam

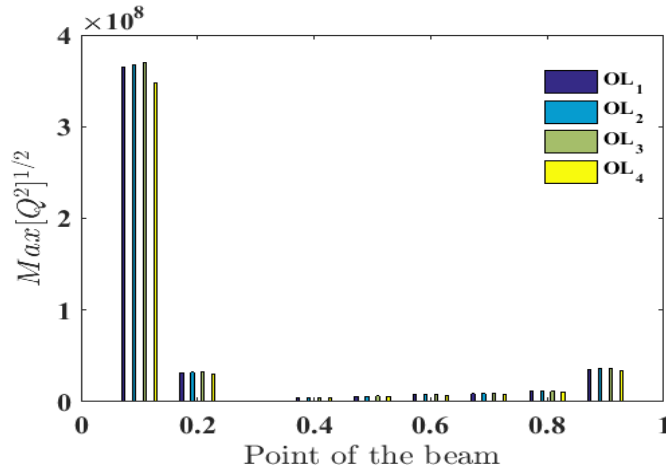


Figure 4. Peak RMS of shear force at different points of the beam

Table 2. Various peak values of RMS of the bending-Moment function of locations of damper outriggers.

$Max[M^2]^{1/2} \times 10^8$									
Outrigger location	Point of the beam								
	0.1	0.2	0.3	0.4	0.5	0.6	0.7	0.8	0.9
OL_1	6.34	24.64	25.98	25.58	24.78	23.74	22.51	21.02	17.96
OL_2	6.39	24.82	26.18	25.77	24.97	23.97	22.68	21.18	18.09
OL_3	6.42	24.93	26.29	25.88	25.08	24.03	22.78	21.27	18.18
OL_4	6.03	23.43	24.72	23.34	23.58	22.59	21.42	20.00	17.09

Table 3. Different peak values of RMS of the shear force in relation to locations of damper outriggers.

$Max[Q^2]^{1/2} \times 10^7$									
Outrigger location	Point of the beam								
	0.1	0.2	0.3	0.4	0.5	0.6	0.7	0.8	0.9
OL_1	36.53	3.18	0.025	0.42	0.61	0.76	0.87	1.14	3.56
OL_2	36.79	3.21	0.025	0.42	0.61	0.76	0.88	1.26	3.58
OL_3	36.96	3.22	0.025	0.42	0.62	0.77	0.89	1.16	3.60
OL_4	34.75	3.03	0.024	0.39	0.58	0.72	0.84	1.09	3.39

By summarizing the data in Table 1 and the results presented in Table 2, one can see that the location OL_4 of the damped outriggers is the optimal position. Because it

provides effective damping compared to other to reduce the bending-moment and shear force within the structural system.

4.2 Passive-on

One of the drawback associated with the MR damper is their nonlinear behaviour. It is due to its intrinsically characteristic that the appropriate algorithms used with MR damper are developed to suitable provide voltage or current that commands these control devices. Thus, in this present investigation, the fuzzy logic controller is employed to determine the appropriate output matched to inputs. According the principle of fuzzy logic, the different steps are: the fuzzification, the fuzzy inference associated with the control rules and defuzzification. The membership functions of the linguistic of inputs 1 (κ_1) and

2 (κ_2) are divided into six variables (i=1,2): Z*E*i (Zero), S*M*i (Small Medium), M*E*i (Medium), L*a*i (Large) , V*L*i (Very Large) and E*L*i (Extreme Large). Fuzzy variables defined as Z*E* (Zero), S*M* (Small Medium), M*E* (Medium), L*A*(Large) and V*L* (Very Large) are assigned to the output. The triangular and trapezoid membership functions used for all input and output are plotted. One can see that the two variables have different domain interval but having the same variables.

The fuzzy control rules are developed as shown in Table 4. The considered first set defines the RMS displacement and second one is the RMS velocity.

Table 4: Fuzzy control rules

		κ_1					
		Z <i>E</i> ₁	S <i>M</i> ₁	M <i>E</i> ₁	L <i>A</i> ₁	V <i>L</i> ₁	E <i>L</i> ₁
κ_2	Z <i>E</i> ₂	Z<i>E</i>	Z<i>E</i>	M<i>E</i>	S<i>M</i>	L<i>A</i>	V<i>L</i>
	S <i>M</i> ₂	Z<i>E</i>	S<i>M</i>	S<i>M</i>	M<i>E</i>	M<i>E</i>	L<i>A</i>
	M <i>E</i> ₂	M<i>E</i>	S<i>M</i>	M<i>E</i>	L<i>A</i>	L<i>A</i>	S<i>M</i>
	L <i>A</i> ₂	M<i>E</i>	M<i>E</i>	L<i>A</i>	L<i>A</i>	V<i>L</i>	L<i>A</i>
	V <i>L</i> ₂	M<i>E</i>	L<i>A</i>	L<i>A</i>	L<i>A</i>	V<i>L</i>	S<i>M</i>
E <i>L</i> ₂	L<i>A</i>	M<i>E</i>	V<i>L</i>	V<i>L</i>	L<i>A</i>	V<i>L</i>	

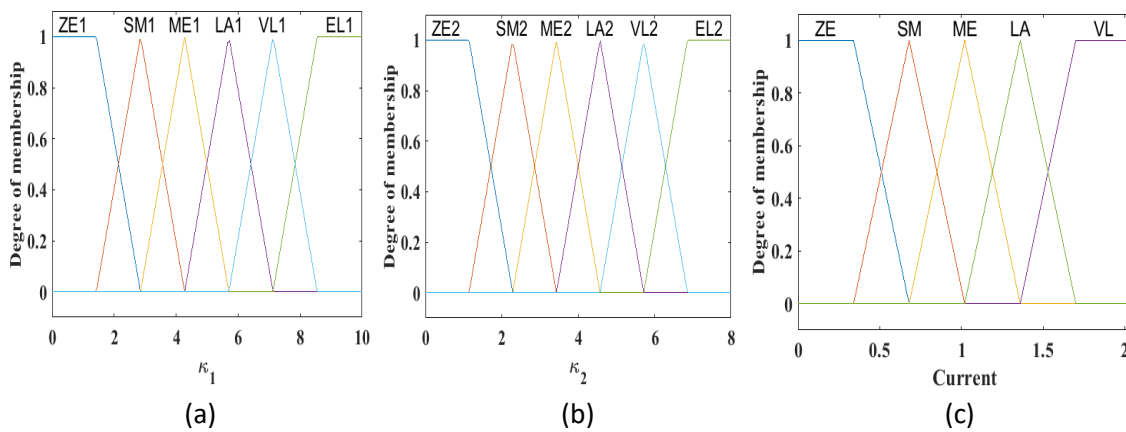


Figure 5. Membership functions for (a)-(b) inputs, (c) output

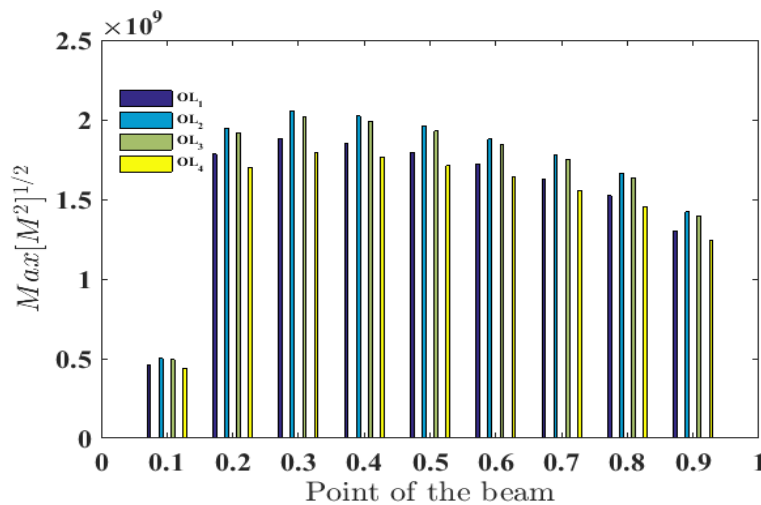


Figure 6. Peak RMS of the bending-Moment function of various points of the beam

Figure 6 shows the location effects of the damped outriggers on the bending-moment. It can be seen that the results are similar to the previous analysis. That is to say that moment is low at the point 0.1 and large at 0.3 of the core-structure.

Table 5 displays the various values of the RMS of the shear force. By focusing our attention on mentioned table, one can see that the coordinate OL₄ is still the optimal location as indicated in the previous analysis in Table 2. Because in this position the values of the bending-moment are slightly reduced than other locations. Thus, it is clearly observed that at this optimal location, the peak RMS of bending-moment is reduced up to 27% in the core-structure.

Here, the various peak RMS of the shear force in

Figure 7 are shown in Table 6. It comes out from the variation of locations of the damped outriggers affects the

shear force. Thus, the comparative data indicates that the position OL₄ of the damped outrigger further provides damping of the structural system. Therefore, it is more efficient than other position. One should be noted that the amplitude of reduction of the shear force can also reach the order of 27% in the core-structure.

To further investigate the performance of the damped outrigger on the dynamical response the whole structure. It is important to analyze the effects of the length of the outrigger on the dynamic of the structural system.

Figure 8 and 9 present the peak RMS of the bending moment and shear force versus the various points along of the core-structure, respectively. It is observed that at the point 0.1 the bending-moment is low and large for the shear force. Although at the point 0.3 of the beam the bending-moment is rather large and very low for the shear force.

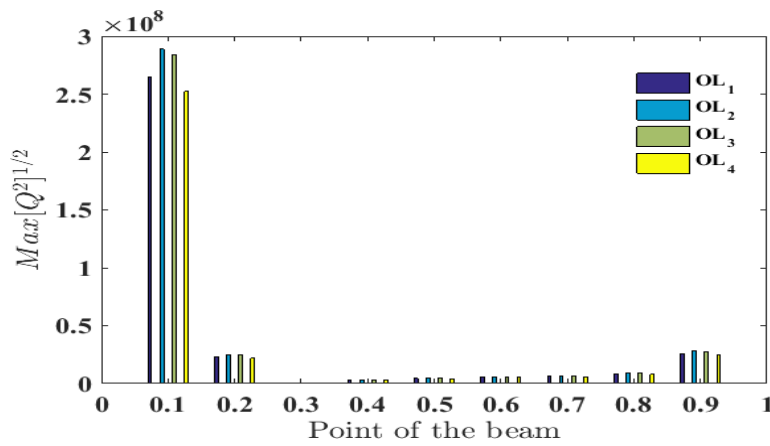


Figure 7. Peak RMS of the shear force function various points along the beam

Table 5. Peak RMS values of the bending-moment function to location of outriggers.

$Max[M^2]^{1/2} \times 10^8$									
Outrigger location	Point of the beam								
	0.1	0.2	0.3	0.4	0.5	0.6	0.7	0.8	0.9
OL ₁	4.59	17.84	18.82	18.52	17.95	17.19	16.30	15.22	13.00
OL ₂	5.01	19.48	20.55	20.23	19.60	18.78	17.80	16.63	14.21
OL ₃	4.93	19.16	20.21	19.90	19.28	18.48	17.51	16.36	13.98
OL ₄	4.38	17.01	17.95	17.67	17.12	16.40	15.55	14.52	12.41

Table 6. Peak RMS values of the shear force function to location of outriggers.

$Max[Q^2]^{1/2} \times 10^7$									
Outrigger location	Point of the beam								
	0.1	0.2	0.3	0.4	0.5	0.6	0.7	0.8	0.9
OL ₁	26.45	2.3	0.022	0.3	0.44	0.55	0.64	0.83	2.58
OL ₂	28.88	2.52	0.022	0.33	0.48	0.59	0.69	0.91	2.82
OL ₃	28.41	2.47	0.022	0.33	0.47	0.59	0.68	0.88	2.77
OL ₄	25.23	2.19	0.021	0.29	0.42	0.52	0.61	0.79	2.46

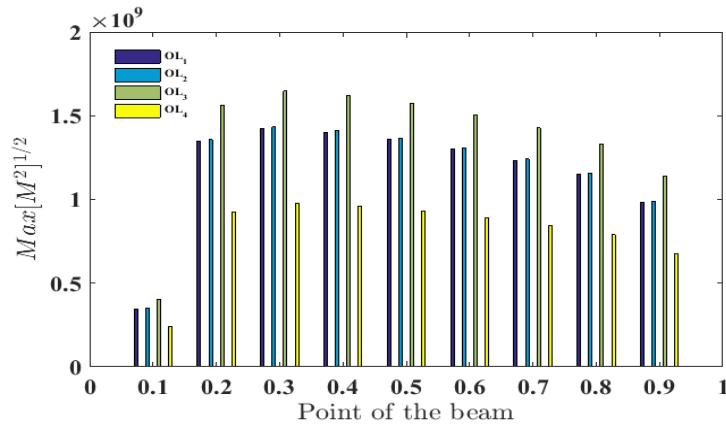


Figure 8. Peak RMS of the bending-moment function various points along the beam

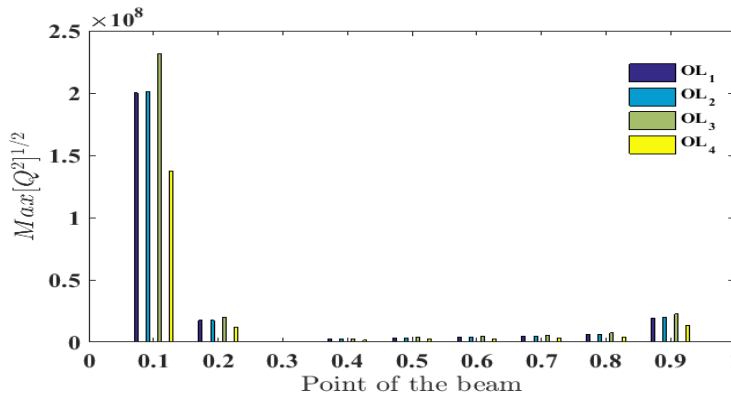


Figure 9. Peak RMS of the shear force function of various points along the beam with $r = 8.0$

Table 7 and 8 show the various peak RMS of the bending-moment and shear force in function locations of the damped outriggers, respectively. It can see that the increasing outrigger’s length can considerably reduce the bending-moment and shear force up to 45% of results from Table 5 Table 6.

Figure 10 displays outrigger’s length effects on the traversal displacement when damped outriggers are placed at the point of coordinate OL₄. It should be noted that at this position the damped outriggers are benefits and efficient than others. It is also observed the outrigger’s length considerably affects the dynamic response of the core-structure under combined wind and earthquake loads.

Table 7: Peak RMS values of the bending-moment function to location of outriggers

Outrigger location	$Max[M^2]^{1/2} \times 10^8$								
	Point of the beam								
	0.1	0.2	0.3	0.4	0.5	0.6	0.7	0.8	0.9
<i>OL1</i>	3.47	13.49	14.24	14.02	13.58	13.02	12.34	11.52	9.84
<i>OL2</i>	3.49	13.58	14.32	14.09	13.66	13.08	12.41	11.58	9.9
<i>OL3</i>	4.02	15.61	16.72	16.22	15.71	15.06	14.27	13.33	11.39
<i>OL4</i>	2.38	9.26	9.77	9.61	9.32	8.93	8.46	7.90	6.75

Table 8: Peak values RMS values of the shear force function to location of outriggers

Outrigger location	$Max[Q^2]^{1/2} \times 10^7$								
	Point of the beam								
	0.1	0.2	0.3	0.4	0.5	0.6	0.7	0.8	0.9
<i>OL1</i>	20.02	1.75	0.019	0.23	0.33	0.42	0.48	0.63	1.95
<i>OL2</i>	20.13	1.75	0.019	0.23	0.33	0.42	0.49	0.63	1.97
<i>OL3</i>	23.15	2.01	0.021	0.26	0.39	0.48	0.56	0.73	2.26
<i>OL4</i>	13.73	1.19	0.017	0.16	0.23	0.29	0.33	0.43	1.34

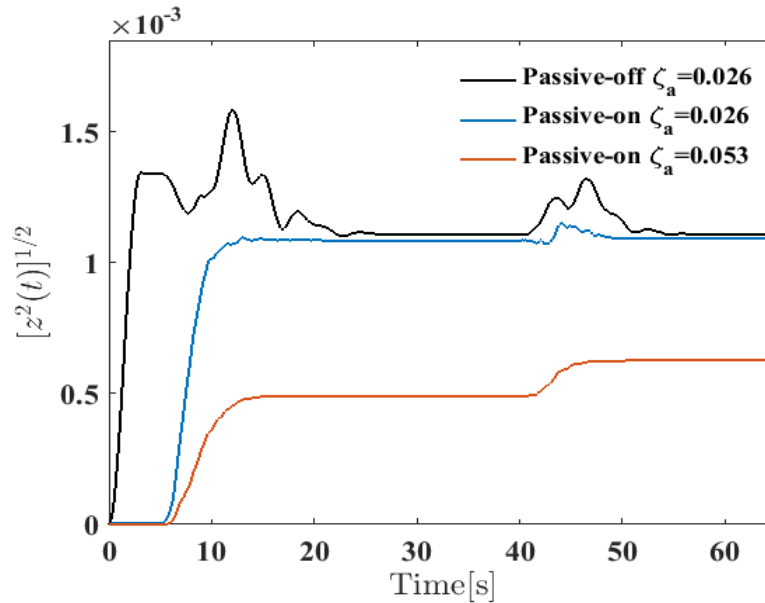


Figure 10. Variation of outrigger's length effects on RMS of displacement with the damped outriggers placed at the point OL₄

5. Discussions

The main investigation is to demonstrate how, the optimal position of damped outriggers can provide additional damping by attenuating the effects of the bending-moment and the shear force which may occur in the core-structure. Thus, to explore this phenomenon, different modes have been analysed.

In passive-off mode, the results show that the bending-moment and shear force at each point along the core-structure. It appears that this mentioned moment is significantly important at the point 0.1 and insignificant at the point 0.3 of the structure. Opposite to bending-moment, the shear force is rather insignificant at the point 0.1 and important at the point 0.3 of the core-structure. As discussed in earlier paragraph, the combined data reveal that the locations of the damped outriggers at the coordinate OL₄ further reduces the bending-moment and the shear force compared to other positions thus defined.

In passive-on mode, the Fuzzy logic algorithm used with MR damper to command the current is explored. It is observed that the application of this algorithm gradually decreases the effects of the bending-moment and shear force at any point along of the core-structure. In addition, the analysis of location effects of different damped outriggers indicates that the position OL₄ is better than OL₁, OL₂ and OL₃.

Note that the investigation of the attenuation of mentioned effects is not limited only to the two passive modes. An additional review of the length of the outrigger (geometric parameter) shows that:

- The length of the outrigger is an influencing factor, since an increasing of its value of this latter gradually decreases the effects of the moment-bending and the shear force of the core-structure;

- A significantly attenuation of the lateral deflection.
- In summary, it should be noted that the passive-on mode associated with variation of the length of the outrigger compared to passive-off mode considerably reduces the moment-bending and shear force effects of the core-structure under combined wind and earthquake loads up to 60%.

6. Conclusion

This paper investigates the effects of damped outriggers placed at various locations on the bending-moment and shear force of the core structure under combined wind and earthquake loads. Timoshenko theory, based on the partial differential equation has been explored to model the core-structure. It has been observed that the wind loads have significantly introduced the nonlinear dissipative of the mechanical structure.

The effects on different locations of damped outriggers have been analysed. The numerical results have revealed that;

- In passive off mode, analysis different data of peak RMS has shown that the position OL₄ like the optimal location where the damped outriggers should be installed on the core-structure. Since in this position, the damped outriggers mitigate the induced-vibration wind and earthquake excitation better than other locations;
- In passive on mode, the dynamics of the control devices have really enhanced the response of the bending-moment and shear force in all the points of the core-structure. This is due to the application of the fuzzy logic controller

Although the two modes are explored. The influence of the length of the outriggers has also been analysed. It comes out that a slightly increasing of its length effectively

strengthens the structural composition by reducing the bending-moment and shear force effects. It can also see how this positively affects the transverse displacement of the core-structure. Additionally, this analysis of this modification shows that the optimal location of outriggers remains unchanged.

Declaration

The author(s) declared no potential conflicts of interest with respect to the research, authorship, and/or publication of this article. The author(s) also declared that this article is original, was prepared in accordance with international publication and research ethics, and ethical committee permission or any special permission is not required.

Author Contributions

J. Metsebo proposed and modeled the system. B.P. Ndemanou and A.C. Chamgoue made the numerical analysis. G.R. Kol organized and structured the manuscript.

References

- Lin YK and Yang JN, *Multimode bridge response to wind excitations*. Journal of Engineering Mechanics, 1983. **109**(2): p. 586-603.
- Gu M and Quan Y, *Across-wind loads of typical tall buildings*. Journal of Wind Engineering and Industrial Aerodynamics, 2004. **92**(13): p. 1147-1165.
- Ali AM, Alexander J and Ray T, *Frequency-independent hysteretic dampers for mitigating wind-induced vibrations of tall buildings*. Structural Control and Health Monitoring, 2019. **e2341**: p. 1-22.
- Kang X, Jiang L, Bai Y and Caprani CC, *Seismic damage evaluation of high-speed railway bridge components under different intensities of earthquake excitations*. Engineering Structures, 2017. **152**: p. 116-128.
- Kubo T, Yamamoto T, Sato K, Jimbo M, Imaoka T and Umeki Y, *A seismic design of nuclear reactor building structures applying seismic isolation system in a high seismicity region – a feasibility case study in Japan-*. Nuclear Engineering and Technologies, 2014. **46**(5): p. 581–594.
- Taranath BS, *Wind and Earthquake Resistant Buildings*, 2004, USA. CRC Press.
- Fang C, Spencer BF, Xu J, Tan P and Zhou F, *Optimization of damped outrigger systems subject to stochastic excitation*. Engineering Structures, 2019. **191**: p. 280–291.
- Zhou Y, Zhang C and Lu X, *Earthquake resilience of a 632-meter super-tall building with energy dissipation outriggers*. Proceedings of the 10th National Conference on Earthquake Engineering, Earthquake Engineering Research Institute, Anchorage, AK, 2014.
- Baker B and Pawlikowski J, *The design and construction of the World's tallest building: The Burj Khalifa, Dubai*. Structural Engineering International, 2015. **25**(4): p. 389-394.
- Lu X, Liao W, Cui Y, Jiang Q, and Zhu Y, *Development of a novel sacrificial-energy dissipation outrigger system for tall buildings*. Earthquake Engineering and Structural Dynamics, 2019. **48**: p. 1661–1677.
- Lin P and Takeuchi T, *Seismic performance of buckling-restrained brace outrigger system in various configurations*. Japan Architectural Review, 2019. **2**: p. 392–408.
- Chen Y, McFarland DM, Wang Z, Spencer BF and Bergman LA, *Analysis of tall buildings with damped outriggers*. Journal of Structural Engineering, 2010. **136**(11): p. 1435-1443.
- Huang B and Takeuchi T, *Dynamic response evaluation of damped-outrigger systems with various heights*. Earthquake Spectra, 2017. **32**(2): p. 665-685.
- Yang TY, Atkinson J, Tobber L, Tung DP and Neville B, *Seismic design of outrigger systems using equivalent energy design procedure*. The Structural Design of Tall Special Buildings, 2020. **e1743**: p. 1-15.
- Zhou Y, Xing L and Zhou G, *Spectrum Analysis-Based Model for the Optimal Outrigger Location of High-Rise Buildings*. Journal of Earthquake Engineering, 2019. p. 1-26.
- Asai T and Watanabe Y, *Outrigger tuned inertial mass electromagnetic transducers for high-rise buildings subject to long period earthquakes*. Engineering Structures, 2017. **153**: p. 404–410.
- Tan P, Fang CJ, Chang CM, Spencer BF and Zhou FL, *Dynamic characteristics of novel energy dissipation systems with damped outriggers*. Engineering Structures, 2015. **98**: p. 128-140.
- Lu Z, He X and Zhou Y, *Performance-based seismic analysis on a super high-rise building with improved viscously damped outrigger system*. Structural Control and Health Monitoring, 2018. **e2190**: p. 1-21.
- Xing L, Zhou Y and Huang W, *Seismic optimization analysis of high-rise buildings with a buckling-restrained brace outrigger system*. Engineering Structures, 2020. **220**: 110959.
- Shan J, Shi Z, Gong N and Shi W, *Performance improvement of base isolation systems by incorporating eddy current damping and magnetic spring under earthquakes*. Structural Control and Health Monitoring, 2020. **e2524**: p. 1-20.
- Ndemanou BP and Nbandjo BRN, *Fuzzy magnetorheological device vibration control of the two Timoshenko cantilever beams interconnected under earthquake excitation*. The Structural Design of Tall and Special Buildings, 2018. **e1541**: p. 1-11.
- Yoshida O and Dyke S, *Seismic control of a nonlinear benchmark building using smart dampers*. Journal of Engineering Mechanics, 2004. **130**(4): p. 386-3892.
- Zafarani MM and Halabian AM, *A new supervisory adaptive strategy for the control of hysteretic multi-story irregular buildings equipped with MR-dampers*. Engineering Structures, 2020. **217**:110786.
- Rayegani A and Nouri G, *Application of Smart Dampers for Prevention of Seismic Pounding in Isolated Structures Subjected to Near-fault Earthquakes*. Journal of Earthquake Engineering, 2020. <https://doi.org/10.1080/13632469.2020.1822230>
- Jansen L and Dyke S, *Semi-active control strategies for MR dampers: comparative study*. Journal of Engineering Mechanics, 2000. **126**(8): 795–803.
- Ndemanou BP, Fankem ER and Nana Nbandjo BR (2017) *Reduction of vibration on a cantilever Timoshenko beam subjected to repeated sequence of excitation with magnetorheological outriggers*. The Structural Design of Tall and Special Buildings, 2017. **e1393**: p. 1-10.

27. Uz ME and Hadi MNS, *Optimal design of semi active control for adjacent buildings connected by MR damper based on integrated fuzzy logic and multi-objective genetic algorithm*. Engineering Structures, 2014. **69**: p. 135-148.
28. Braz-César MT, Folhento PLP and Barros RC, *Fuzzy controller optimization using a genetic algorithm for non-collocated semi-active MR based control of a three-DOF framed structure*. 13th APCA International Conference on Control and Soft Computing, CONTROLO, 2018.
29. Bozorgvar M and Zahrai SM, *Semi-active seismic control of buildings using MR damper and adaptive neural-fuzzy intelligent controller optimized with genetic algorithm*. Journal of Vibration and Control, 2019. **25**(2): p. 1-13.
30. Moon SJ, Bergman LA and Voulgaris PG, *Sliding mode control of cable-stayed bridge subjected to seismic excitation*. Journal of Engineering Mechanics, 2003. **129**(1): p. 71-78.
31. Ghaffarzadeh H, *Semi-active structural fuzzy control with MR dampers subjected to near-fault ground motions having forward directivity and fling step*. Smart Structures and Systems, 2013. **12**(6): p. 595-617.
- 32.** Kim HS, *Seismic response reduction of a building using top-story isolation system with MR damper*. Contemporary Engineering Sciences, 2014. **7**(21): p.979-986.
33. Ok SY, Kim DS, Park KS and Koh HM, *Semi-active fuzzy control of cable-stayed bridges using magneto-rheological dampers*. Engineering Structures, 2007. **29**(5): p. 776-788.
34. Ab Talib MH and Mat Darus IZ, *Intelligent fuzzy logic with firefly algorithm and particle swarm optimization for semi-active suspension system using magneto-rheological damper*. Journal of Vibration and Control, 2016. **23**(3): p. 501-514.
35. Li Z, Yang Y, Gong X, Lin Y, and Liu G, *Fuzzy control of the semi-active suspension with MR damper based on μGA* , IEEE Vehicle Power and Propulsion Conference Harbin, China, (VPPC '08), 2008. p. 1–6.
36. Dong XM and Yu M, *Genetic algorithm based fuzzy logic control for a magneto-rheological suspension*. Journal of Vibration and Control. 2014. **20**: p. 1343–1355.
37. Paksoy M, Guclu R and Cetin S, *Semiaactive self-tuning fuzzy logic control of full vehicle model with MR damper*. Advances in Mechanical Engineering. 2014. **6**:816813.
38. Timoshenko SP, *On the correction for shear of the differential equation for transverse vibrations of prismatic bars*. The London, Edinburgh, Dublin Philosophical Magazine and Journal of Science, 1921. **41**(215): p. 744–746.
39. Hutchinson JR, *Transverse vibrations of beams, exact versus approximate solutions*. Journal of Applied Mechanics, 1981. **48**(4):923.
40. Saeid F and Bahadır Yüksel S, *Investigation of nonlinear behavior of high ductility reinforced concrete shear walls*. International Advanced Researches and Engineering Journal, 2020. **04**(02): p. 116-128.
41. Kelly SG, *Advanced vibration analysis*, USA, 2006. CRC Press.
42. Deng K, Pan P, Lam A and Xue Y, *A simplified model for analysis of high-rise buildings equipped with hysteresis damped outriggers*. The Structural Design of Tall and Special Buildings, 2013. **23**(15): p. 1158-1170.
43. Spencer BF, Dyke SJ, Sain MK and Carlson JD, *Phenomenological model for magnetorheological dampers*. Journal of Engineering Mechanics, 1997. **123**(3): p. 230-238.
44. Yang G, Spencer BF, Carlson JD and Sain MK, *Large-scale MR fluid dampers: Modeling and dynamic performance considerations*. Engineering Structures, 2002. **23**(3): p. 309-323.
45. Yang G, Spencer BF, Jung HJ and Carlson JD, *Dynamic modeling of large-scale magnetorheological damper systems for civil engineering applications*. Journal of Engineering Mechanics, 2004. **130**(9): p. 1107-1114.
46. Mendis P, Ngo T, Haritos N, Hira A, Samali B and Cheung John CK *Wind loading on tall buildings*. Electronic Journal of Structural Engineering, Special Issue: Loading on Structures, 2007.p. 41-54.
47. Li HN, Liu Y, Li C and Zheng XW, *Multihazard fragility assessment of steel-concrete composite frame structures with buckling-restrained braces subjected to combined earthquake and wind*. The Structural Design of Tall and Special Buildings, 2020. **e1746**: p. 1-19.
48. Luongo A and Zulli D, *Parametric, external and self-excitation of a tower under turbulent wind flow*. Journal of Sound and Vibration, 2011. **330**(13): p. 3057-3069.
49. Anague Tabejieu LM, Nana Nbandjo BR and Filatrella G, *Effect of the fractional foundation on the response of beam structure submitted to moving and wind loads*. Chaos, Solitons and Fractals, 2019. **127**: p. 178-188.
50. Lin YK and Li QC, *Stochastic stability of wind excited structures*. Journal of Wind Engineering and Industrial Aerodynamics, 1995. **54/55**: p. 75-82.
51. Cai GQ and Wu C, *Modeling of bounded stochastic processes*. Probabilistic Engineering Mechanics, 2004. **19**(30): p. 197-203
52. Xie WC and Ronald MCSO, *Parametric resonance of a two-dimensional system under bounded noise excitation*. Nonlinear Dynamics, 2004. **36**(2-4): p. 437-453.
53. Fan FG and Ahmadi G, *Nonstationary Kanai-Tajimi models for El Centro 1940 and Mexico City 1985 earthquakes*. Probabilistic Engineering Mechanics, 1990. **5**(4): p. 171-181.
54. Moustafa A and Takewaki I, *Response of nonlinear single-degree-of-freedom structures to random acceleration sequences*. Engineering Structures, 2011. **33**(4): p. 1251-1258.
55. Ndemanou BP, Nana Nbandjo BR and Dorka U, *Quenching of vibration modes on two interconnected buildings subjected to seismic loads using magneto rheological device*. Mechanical Research Communication, 2016. **78**: p. 6-12.
56. Dyke SJ, Spencer BF, Sain MK and Carlson JD, *An experimental study of MR dampers for seismic protection*. Smart Materials and Structures, 1998. **7**(5): p. 693-703.

Appendix

$$b_1 = \int_0^1 \phi^2(X) dX, b_3 = \int_0^1 \phi''''(X) dX, b_4 = \int_0^1 \phi(X) dX,$$

$$\int_0^1 b_5 = \int_0^1 \phi^3(X) dX, b_6 = \int_0^1 \phi^4(X) dX, \sigma = \frac{b_4}{den}$$

**Research Article**

Numerical assessment of the performance of different constitutive models used to predict liquefiable soil behavior

Selçuk Demir ^{a,*} 

^aBolu Abant İzzet Baysal University, Engineering Faculty, Department of Civil Engineering, 14030, Bolu, Turkey

ARTICLE INFO*Article history:*

Received 01 February 2021

Revised 27 April 2021

Accepted 14 May 2021

Keywords:

DeepSoil

Liquefaction

MKZ Model

OpenSees

PDMY02 Model

ABSTRACT

Liquefaction has caused severe damages to structures such as excessive settlements, tilting, lateral spreading etc., all over the world during many past earthquakes. Hence, the efficient prediction of liquefiable soil behavior is crucial for liquefaction-induced hazard evaluation of existing structures and the design of new structures in seismically active regions. In this study, a series of nonlinear effective stress analyses are carried out using the DeepSoil and OpenSees opensource software with Modified Kondner–Zelasko (MKZ) and Pressure Dependent Multi Yield02 (PDMY02) constitutive models to evaluate their capabilities in terms of predicting liquefiable soil behavior. The performance of the models has been evaluated by comparing the results between the numerical predictions and a centrifuge study from literature in terms of excess pore water pressures, acceleration-time histories, spectral accelerations, lateral displacements and maximum profile responses at specific depths. The results clearly illustrate that the excess pore water pressure predictions from nonlinear analyses are reasonably close to centrifuge measurements, but the accelerations and lateral displacements are slightly different. It is also observed that dissimilarities in the predictions of the numerical simulations are more obvious for OpenSees simulations with respect to DeepSoil ones.

© 2021, Advanced Researches and Engineering Journal (IAREJ) and the Author(s).

1. Introduction

Soil liquefaction is a complex phenomenon that has been observed in many historical earthquakes in its various aspects [1]. When a soil deposit is liquefied, the excess pore pressures in the soil become equal to the effective stress of soil then the strength and stiffness of the soil reduce dramatically. Different consequences of soil liquefaction may be seen during and after an earthquake such as excessive settlements, tilting, and lateral spreading [2]. These consequences are the main reasons behind the massive damage to structures and life.

A wide range of case studies, experimental tests, or numerical models have been employed in recent years to highlight soil liquefaction and its effects on structures. Evaluation of liquefiable soil behavior with experimental tests may be thought an ideal method under realistic earthquake conditions. However, these tests are generally costly and too complex to put into practice. On the other

hand, numerical analysis or modeling offers an economical solution to simulate soil behavior with different parametric variables.

Reliable prediction of the behavior of a liquefiable soil profile (i.e., excess pore pressures, accelerations, and deformations) remains a major challenge in geotechnical earthquake engineering. In this regard, numerical modeling is an efficient tool for practitioners to predict liquefiable soil behavior and prevent liquefaction-induced failures in the future. Provided that constitutive soil models sufficiently cover the real soil behavior under seismic loading, the liquefiable soil behavior can be reasonably simulated via numerical studies. In other words, considerable attention is needed during the calibration of constitutive soil models in order to properly represent the soil nonlinearity.

A key issue of assessing the accuracy of a numerical simulation is to compare results of the case history or experiment data with computed results. In recent decades,

* Corresponding author. Tel.: +90-374-254-4831; Fax: +90-374-253-4558.

E-mail address: selcukdemir@ibu.edu.tr (S. Demir)

ORCID: 0000-0003-2520-4395 (S. Demir)

DOI: 10.35860/iarej.871429

This article is licensed under the CC BY-NC 4.0 International License (<https://creativecommons.org/licenses/by-nc/4.0/>).

researchers have been performed numerous numerical efforts using dynamic centrifuge model test results [3-7] to predict the liquefiable soil behavior due to the increasing availability of computational resources and constitutive soil models [8-16].

Popescu and Prevost [3] and Byrne et al. [4] presented the comparison of numerical modeling predictions using constitutive soil models and measured centrifuge model response to investigate soil liquefaction. Also, Taiebat et al. [5] presented numerical analysis results of a liquefiable sand using two types of plasticity models. They concluded that the capabilities of the two numerical models producing pore pressures in the liquefiable sand are consistent with observations of the centrifuge test. Ramirez et al. [6] investigated the predictive capabilities of two constitutive soil models namely PDMY02 (OpenSees) and SANISAND (Flac) by using element tests and centrifuge test results in a liquefiable soil profile. They concluded that although PDMY02 and SANISAND models are capable of predicting excess pore pressures and accelerations, liquefaction induced volumetric settlements still remain poorly. Demir and Özener [7] numerically simulated a centrifuge test with UBC3D-PLM model implemented in Plaxis and their results showed that excess pore water pressure development and time history of accelerations are consistent with experimental observations, unlike excess pore pressure dissipation and displacements.

This paper aims to study the capabilities of the MKZ and PDMY02 soil constitutive models for predicting the one-layered liquefiable soil behavior and provide a calibration guide of the two numerical models for accurate modeling of liquefiable soils. To this end, a numerical study was carried out in open-source software DeepSoil and OpenSees. Results of numerical simulations have been compared with results of a centrifuge test from the literature. At the end of the simulations, the performance of numerical models is discussed.

2. Details of Numerical Modeling

Performance of the numerical models was investigated through results of a centrifuge test conducted on saturated liquefiable soil by Taboada and Dobry [17] during the VELACS project (Model No: 1). Figure 1 shows a schematic representation of the laminar box, including instrumentations used during the centrifuge test. One-layered uniform Nevada Sand ($D_r = 40\%$) with 10 m thick was adopted in the centrifuge study. The groundwater table (GWT) was located at the ground surface. The laminar box was subjected to a centrifuge acceleration of 50 g. A sinusoidal input motion with a maximum value of 0.235g shown in Figure 1(b) was excited during the test. Pore water pressures, accelerations, and horizontal displacements were recorded in different locations during

the centrifuge test using piezometers (P), horizontal accelerometers (AH), and horizontal displacement transducers (LVDT), respectively.

Two different open-source computational platforms were chosen for this study, DeepSoil and OpenSees. The Pressure Dependent Modified Kondner–Zelasko (MKZ) and Pressure Dependent Multi-Yield02 (PDMY02) nonlinear constitutive soil models were considered in DeepSoil and OpenSees simulations, respectively. Details of the modeling procedures of constitutive models were described below. Figure 2 simply shows the simulated soil profile for two numerical models.

2.1 DeepSoil

Nonlinear analyses were employed using the software DeepSoil v7.0 [18]. The soil column was discretized one-dimensionally (1D) as a multi-degree-of-freedom (MDOF) lumped mass model. Each layer was represented by a corresponding mass, a nonlinear spring, and a dashpot. The nonlinear soil behavior was modeled using pressure-dependent Modified Kondner–Zelasko (MKZ) hyperbolic-type model with non-Masing hysteretic Re/Un-loading formulation. MKZ model developed by Matasovic and Vucetic [19] is a widely preferred nonlinear soil model in order to define the soil backbone characteristic and cyclic loading-unloading behavior. In DeepSoil simulations, a frequency-independent viscous damping formulation proposed by Phillips and Hashash [20] was used to represent small-strain damping.

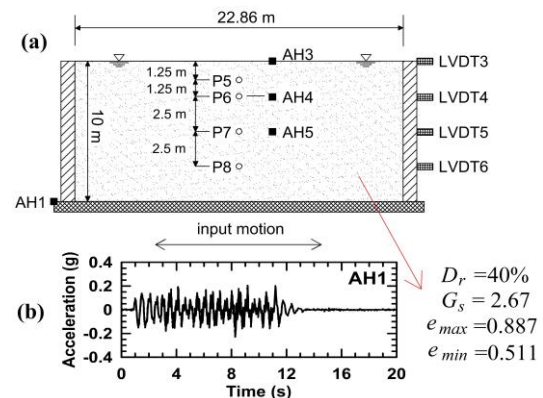


Figure 1. (a) Illustration of the centrifuge test (Model No: 1) and instrumentation layout with index properties [17], (b) applied input motion

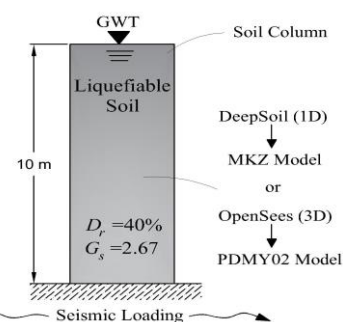


Figure 2. Schematic view of the simulated soil profile

Modulus reduction and damping curves of the soil were defined by using Darendeli [21] model for each layer in the soil column. MRDF with Darandeli reduction factor fitting tool was utilized to agree with the empirical nonlinear curves obtained from the Darendeli [21] curves.

Darendeli model requires five inputs that are plasticity index (PI), overconsolidation ratio (OCR), lateral earth pressure coefficient at rest (K_0), number of loading cycles (N_c), and frequency ($Freq$). The simulated soil was considered normally consolidated and non-plastic soil ($OCR=1$ and $PI=0$). N_c and $Freq$ were set 10 and 1.0 as recommended by [21], respectively. The value of K_0 was estimated using Jaky's [22] equation (Equation 1):

$$K_0 = 1 - \sin\phi' \quad (1)$$

where effective friction angle, $\phi' = 32^\circ$ for $D_r = 40\%$ was considered from the empirical relationship given in [23].

Note that modulus reduction curves obtained from [21] are only valid for small shear strains (up to 0.3%). The implied shear strength procedure proposed by Hashash et al. [24] was applied to represent the real (target) shear strength of the soil for large shear strains. In this procedure, the original modulus reduction curve (G/G_{max}) for each layer computed from Darendeli's [21] equation was modified to reach target shear strength levels at large strains by adjusting the data points manually. The Mohr–Coulomb failure criterion was utilized to estimate the target shear strength of the soil ($\tau = \sigma' \tan\phi + c'$, here c' assumed zero and $\phi' = 32^\circ$).

The soil profile was divided into 12 layers to ensure the frequency of each layer greater than 30 Hz which is the maximum frequency criteria recommended by [18]. The base of the soil profile was modeled as a rigid half-space. The shear wave velocity (V_s) of each soil layer was computed using Equation (2) that was generated from the resonant column test results performed by [25]. Figure 3 presents the distribution of V_s , maximum frequency, and implied friction angle with depth.

$$V_s = 99(z)^{0.25} \quad (2)$$

Vucetic and Dobry [26] model implemented in DeepSoil which was initially developed by Dobry et al. [27] and modified by Vucetic and Dobry [26] was used to estimate pore water pressure generation and dissipation of the soil used in the model as expressed in Equation (3):

$$r_{u,N} = \frac{pfN_cF(\gamma_c - \gamma_{tvp})^2}{1 + fN_cF(\gamma_c - \gamma_{tvp})} \quad (3)$$

where $r_{u,N}$ is residual pore water pressure ratio after N_c cycles; F , s , and p are the curve fitting parameters; f is equal to 1.0 or 2.0 depending on 1D or 2D shaking; γ_c is cyclic shear strain; γ_{tvp} is volumetric threshold shear strain. F is obtained to be 1.7 from the chart proposed by [28].

Similarly, s was assigned to be 1.0 based on [28]. p and γ_{tvp} was assumed as 1.15 and 0.05%, respectively. Table 1 summarizes all of the pore water pressure model parameters used in this study.

Two degradation indices proposed by Matasovic [19] were utilized in DeepSoil analyses (Equations 4 and 5) to simulate the shear strength and shear stiffness degradation of the soil depend on excess porewater pressure ratio:

$$\delta_G = \sqrt{1 - r_u} \quad (4)$$

$$\delta_\tau = 1 - (r_u)^v \quad (5)$$

in which δ_G and δ_τ are shear modulus and shear stress degradation functions, v is curve-fitting parameter. In this study, $v=1.0$ was used to better simulate the shear strength degradation.

In DeepSoil, the dissipation of excess pore water pressure is taken into account using Terzaghi's 1D consolidation theory. This theory requires the coefficient of consolidation (c_v) of the soil for evaluating pore water pressure dissipation. For Nevada sand, c_v of each layer was computed through Equation (6):

$$c_v = \frac{k(1 + e_0)}{\gamma_w a_v} \quad (6)$$

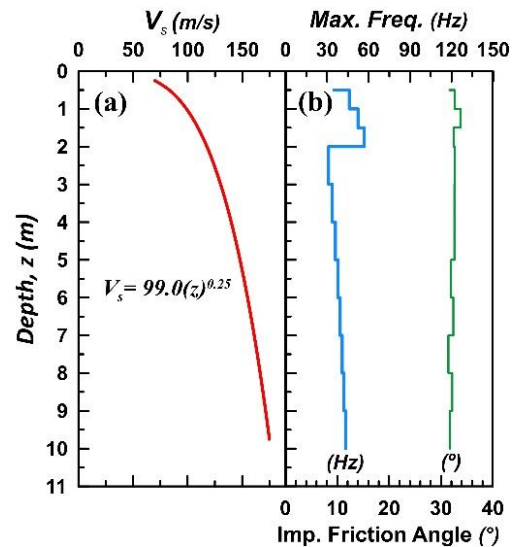


Figure 3. (a) V_s profile (b) maximum frequency and implied friction angle of the profile used in DeepSoil simulations

Table 1. Pore water pressure model parameters of the sand ($D_r = 40\%$) used in simulations

	Value	Reference
F	1.7	[28]
s	1	[28]
p	1.15	-
f	1	-
γ_{tvp}	0.05	-
v	1	-
c_v	Equation (6)	-

In Equation 6, the symbol γ_w is the unit weight of the water and k is the permeability coefficient of the soil. e_0 is the initial void ratio, and a_v is the compressibility coefficient of the soil. k and e_0 was used to be 6.6×10^{-5} m/s and 0.74, respectively [25]. a_v was estimated using Equation (7) which was generated based on laboratory studies on Nevada sand by Gibson [29] (Figure 4). The coefficient of consolidation (c_v) of each soil layer was increased by 50 times due to the acceleration used in the centrifuge test.

$$a_v = 8.95 \times 10^{-3} (\sigma'_v + 4.4)^{-0.93} \quad (7)$$

2.2 OpenSees

The open-source finite element (FE) analysis program OpenSees [30] was used to simulate the liquefiable soil behavior. The soil column was modeled using 3D eight-node brick elements. The element sizes of the model were suitably selected to be equal to or smaller than one-eighth of the minimum wavelength (λ_{min}) corresponding to the highest cut-off frequency (f_{max}) [31]. The 10 m soil profile was discretized in 1.0 m horizontal and 0.625 m vertical direction. At the bottom of the model was separately fixed in horizontal and vertical directions and formed as a rigid base to apply earthquake motion from this layer. Nodes at the same location on the lateral boundaries were tied to move together in all directions using equalDOF command in OpenSees.

Soil layers were constructed out of 8 node Brick UP elements to simulate fully coupled soil response. Each node has four degrees of freedom (DOFs), one for pore water pressure (p) and the others for translational displacements (u). An advanced constitutive model, Pressure Dependent Multi Yield02 (PDMY02) [32, 33] was employed to represent the nonlinear soil response. This material model is an elastoplastic model and can simulate the dilatancy and cyclic mobility behavior of sandy soils earthquake loading. The model uses a non-associative rule to define the dilative or contractive behavior of the soil.

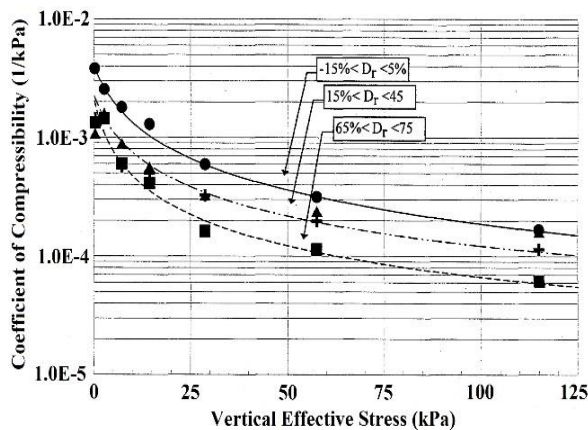


Figure 4. Variation of compressibility coefficients of Nevada Sand with vertical effective stress, [29]

The PDMY02 model has a total of 15 parameters and includes elastic, nonlinear and dilatancy properties, as listed in Table 2. Octahedral shear modulus of the soil ($G_{max,oct}$) were calculated using small strain shear modulus, $G_0 = \rho V_s^2$, as described in [34]. Bulk modulus of the soil (B_r) was derived from $G_{max,oct}$ and Poisson's ratio (ν). The default parameters were selected for $\gamma_{max,r}$, d , and NYS as suggested by Lu et al. [35]. Appropriate values was assigned for phase transformation angle (ϕ'_{pt}), contraction (c_1, c_2, c_3), and dilation parameters (d_1, d_2, d_3) as recommended by [30, 35].

Prior to seismic loading, static analysis was performed to apply the gravitational load and provide initial stress condition. Subsequently, the input motion was applied to the model by performing dynamic analysis. Simulations are carried with Rayleigh damping of 3% to apply low strain damping of the model. The Newmark integrator method was utilized to integrate the equations of motion.

3. Evaluation of Performance of Constitutive Soil Models

The performance of the numerical models to predict nonlinear liquefiable soil behavior was investigated through comparison of simulation and centrifuge test results. Comparison results were evaluated in terms of excess pore water pressure, acceleration-time history, spectral acceleration, and lateral displacement. In addition, maximum soil profile responses were presented to compare numerical simulation results and measured data throughout the soil profile.

Table 2. Selected PDMY02 model parameters during simulations

Parameter	Description	Value
ρ (ton/m ³)	Density	1.96
p_{ref} (kPa)	Reference effective confining stress	100
$G_{max,oct}$ (MPa)	Octahedral low-strain shear modulus	50
$\gamma_{max,r}$ (%)	Maximum octahedral shear strain	0.1
B_r (MPa)	Bulk modulus	122
d	Pressure dependency coefficient	0.5
c (kPa)	Cohesion	0.1
ϕ'_{txc}	Triaxial friction angle	32
ϕ'_{pt}	Phase transformation angle	27
c_1, c_2, c_3	Contraction and dilation coefficients	0.025, 4.5, 0.2
d_1, d_2, d_3		0.1, 3.0, 0.0
NYS	Number of yield surface	20

3.1 Excess Pore Water Pressure

The behavior of liquefiable soil is basically governed by the development and dissipation of excess pore pressures. Thus, it is important to adequately simulate excess pore pressures during seismic shaking to obtain the liquefiable soil behavior realistically.

Figure 5 shows measured and predicted excess pore pressures time histories at different locations. In general, MKZ (DeepSoil) and PDMY02 (OpenSees) models reasonably predicted the generation and dissipation of excess pore pressures at all depths.

3.2 Acceleration-Time Histories

Figure 6 compares acceleration-time histories results obtained from the measured and predicted data. Acceleration values predicted from numerical simulations are almost identical throughout the entire time history with the experimental study results, except amplitudes of accelerations. At the soil surface, numerical simulations overestimated the amplitude of accelerations to the centrifuge study. However, predicted acceleration-time histories were closer to measured data at 2.5 and 5 m depths. Besides, at 5 m depth, high dilation spikes were observed in the centrifuge test, while the phenomenon was not observed from predicted results.

3.3 Spectral Accelerations (S_a)

In Figure 7, measured and predicted spectral accelerations (S_a) at depths of 1.25, 2.5, and 5.0 m are presented. As seen from Figure 7, MKZ and PDMY02 models overestimated S_a values at the soil surface (AH3) between periods of 0.01 to 1.0s. As mentioned in Section 3.2, overestimation of S_a at the soil surface due to prediction of amplitude of accelerations higher than their experimental counterparts. On the other hand, two soil models showed a better match with centrifuge measurements at 2.5 and 5.0m depths as compared to soil surface records. Overall, the MKZ model exhibited better performance to predict spectral accelerations with respect to the PDMY02 model at three locations.

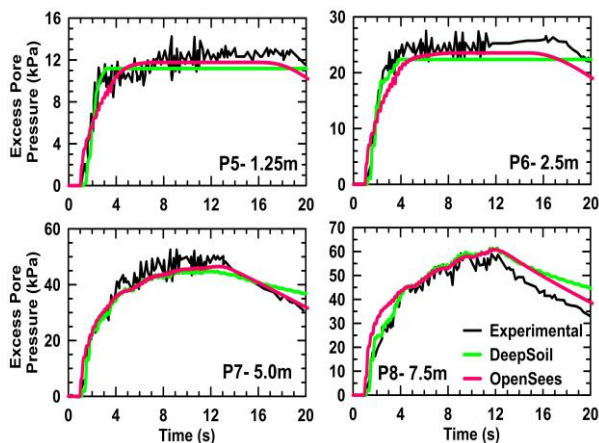


Figure 5. Comparison of excess pore water pressures obtained from numerical simulations and the centrifuge test

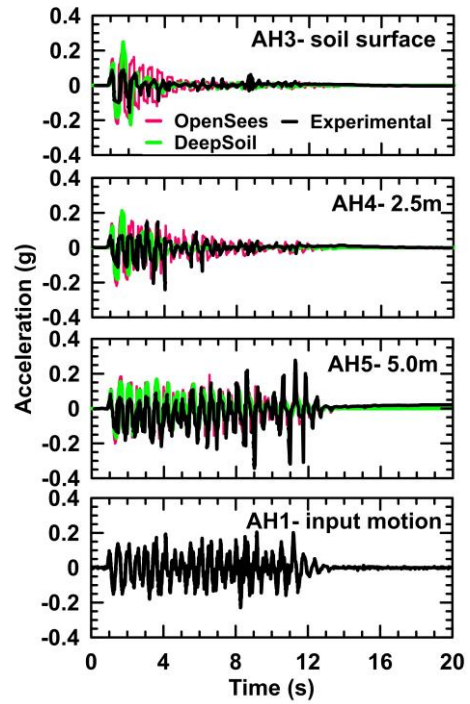


Figure 6. Variation of acceleration-time histories at different depths

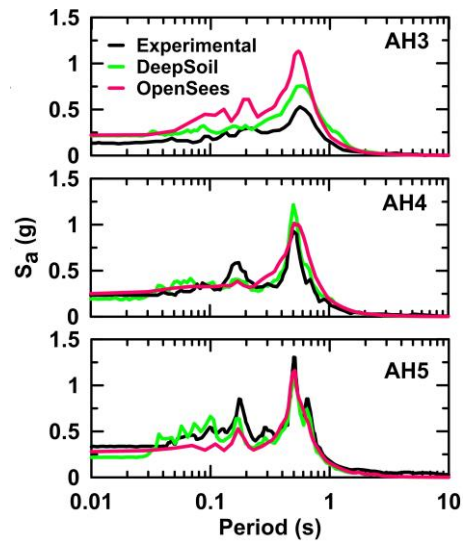


Figure 7. Comparison of simulated and measured spectral accelerations

Residual spectral accelerations were plotted for AH3, AH4, and AH5 to clearly assess the difference of the predicted spectral accelerations during the applied motion. Residuals of S_a between MKZ and PDMY02 models were computed in a logarithmic space as follows:

$$Residual S_a = \log \frac{S_{a,DeepSoil}}{S_{a,OpenSees}} \quad (8)$$

Positive values indicate that OpenSees (PDMY02) simulations underestimate S_a values with respect to DeepSoil (MKZ) ones, or vice versa. Figure 8 presents the residuals of spectral accelerations computed from numerical simulations.

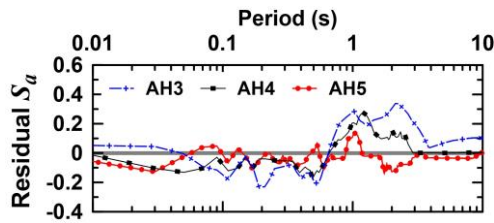


Figure 8. Residuals between the DeepSoil and OpenSees spectral accelerations (S_a)

During the simulations at 5.0 m depth (AH5), residual S_a was computed nearly zero for all periods which indicates that MKZ and PDMY02 models exhibited similar responses. On other hand, PDMY02 model overestimated spectral accelerations in periods between $T=0.03-0.5s$ at the ground surface (AH3). Nevertheless, at high periods (low frequencies), spectral accelerations were underestimated from OpenSees simulations as compared to DeepSoil ones. At 2.5 m depth, PDMY02 model overestimated (negative residuals) S_a values up to $T=0.5s$, after that spectral accelerations were underestimated with respect to MKZ model predictions.

3.4 Lateral Displacements

Figure 9 compares lateral soil displacement results obtained from the centrifuge test and numerical simulations. The magnitude of predicted lateral displacements at each time step is consistent with the experimental measurements. In particular, MKZ model indicated more satisfactorily results with the experimental results as against PDMY02 model simulations.

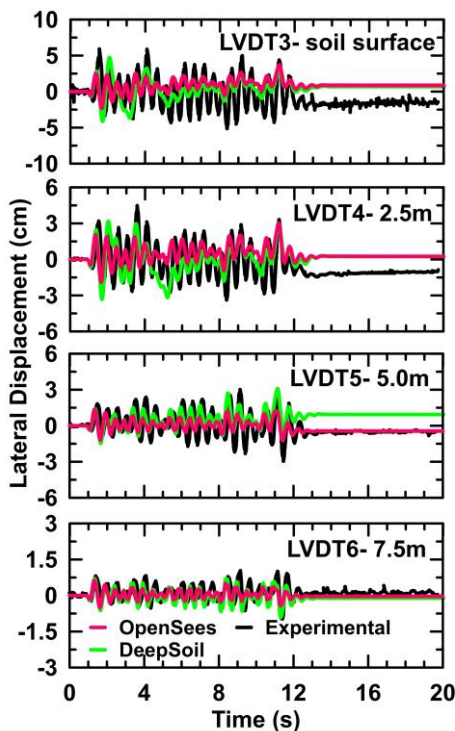


Figure 9. Variation of lateral displacements at different depths

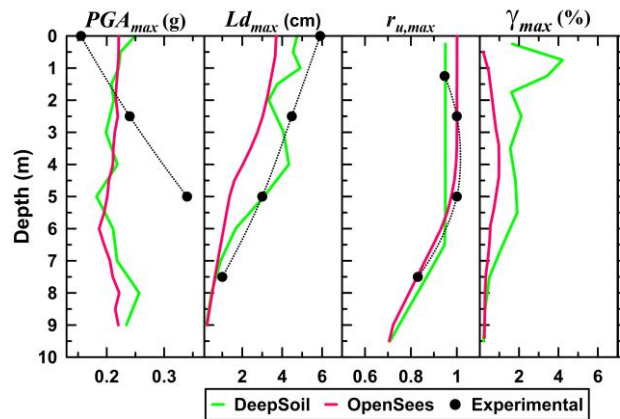


Figure 10. Maximum profile responses of numerical simulations and the centrifuge test

3.5 Maximum Profile Responses

Figure 10 compares the maximum profile response of numerical simulations in terms of maximum horizontal acceleration (PGA_{max}), maximum lateral displacements (Ld_{max}), maximum excess pore pressure ratio ($r_{u,max}$), and maximum shear strain (γ_{max}). The predicted PGA_{max} values from nonlinear DeepSoil analyses exhibited similar behavior with nonlinear OpenSees simulations through the soil profile. Nevertheless, numerical simulations generally underestimated the centrifuge results in terms of PGA_{max} except at soil surface measurement. At the soil surface, PGA_{max} values were overestimated from OpenSees (PDMY02) and DeepSoil (MKZ) simulations about 1.4 and 1.6 times smaller than the measured one, respectively. DeepSoil analyses provided a similar trend to the Ld_{max} measurements obtained from the centrifuge test but predicted Ld_{max} values from OpenSees simulations were about 37% lower than the measured Ld_{max} values. Besides, the predicted $r_{u,max}$ from numerical simulations were nearly the same to the experimental measurements. When compared the γ_{max} values obtained from numerical simulations, γ_{max} values increased up through the soil profile and reached the maximum value of 4.2% at about 1.0 m depth from DeepSoil analyses. However, computed maximum shear strains from OpenSees analyses were smaller than those obtained from DeepSoil analyses. The maximum shear strain was computed approximately $\gamma_{max} = 1.0\%$ at 4.0 m depth from OpenSees analyses.

4. Conclusions

In this paper, results from two different constitutive soil models were compared with centrifuge test measurements regarding their capability to predict one-layered liquefiable soil behavior with regard to excess pore water pressures, accelerations, lateral displacements, and maximum profile responses under a seismic shaking. The major findings from

this study are as follows:

- MKZ (DeepSoil) and PDMY02 (OpenSees) models are reasonable simulated generation and dissipation of excess pore pressures during seismic shaking when the calibration methodologies of the models are applied sufficiently.
- Acceleration-time histories and spectral accelerations at the ground surface were overestimated in both DeepSoil and OpenSees simulations. On the other hand, the predicted accelerations at deeper depths were in reasonable agreement with the centrifuge test results.
- DeepSoil model simulated the magnitudes of lateral displacements observed in the centrifuge experiment better than OpenSees ones. Similar results were obtained at different depths during maximum profile response simulations in terms of Ld_{max} and $r_{u,max}$.

The paper concluded that the models predict key responses of the liquefiable soil during seismic shaking. These models can be acceptably utilized to predict one-layered liquefiable soil behavior. Nevertheless, the MKZ model stands out in terms of properly predicting the relevant responses of the liquefiable soil and its simplicity in defining the input parameters as compared to the PDMY02 model. For future studies, the numerical models used in the current study should also be extended and validated for multi-layered soil profiles to evaluate liquefiable soil behavior accurately.

Declaration

The author declared no potential conflicts of interest with respect to the research, authorship, and/or publication of this article. The author also declared that this article is original, was prepared in accordance with international publication and research ethics, and ethical committee permission or any special permission is not required.

Author Contributions

S. Demir is responsible for all section of the study

Nomenclature

a_v	: Compressibility coefficient
B_r	: Bulk modulus of the soil
c'	: Effective cohesion
c_1, c_2, c_3	: Contraction parameters
C_u	: Coefficient of uniformity
d	: Pressure dependence coefficient
d_1, d_2, d_3	: Dilation parameters
D_r	: Relative density
e_0	: Initial void ratio
f	: Model constant
f_1, f_2	: Corner frequencies
f_{max}	: Highest cut-off frequency
F, s, p	: Curve fitting parameters
$Freq$: Frequency

$G_{max,oct}$: Octahedral shear modulus of the soil
G/G_{max}	: Modulus reduction curve
k	: Permeability
K_0	: Lateral earth pressure at rest
Ld_{max}	: Maximum lateral displacement
NYS	: Number of yield surface
N_c	: Number of loading cycles
OCR	: Over consolidation ratio
PGA_{max}	: Maximum horizontal acceleration
PI	: Plasticity index
p	: Pore water pressure
p_{ref}	: Reference effective confining stress
r_u	: Excess pore water pressure ratio
$r_{u,max}$: Maximum excess pore water pressure ratio
$r_{u,N}$: Residual pore water pressure ratio after N_c cycles
u	: Displacement
v	: Curve-fitting parameter
V_s	: Shear wave velocity
β, γ	: Parameters for integrator Newmark
δ_G	: Shear modulus degradation function
δ_G	: Shear stress degradation function
ϕ'	: Effective friction angle
ϕ'_{txc}	: Triaxial friction angle
ϕ'_{pt}	: Phase transformation angle
γ_c	: Cyclic shear strain
γ_{max}	: Maximum shear strain
$\gamma_{max,r}$: Maximum octahedral shear strain
γ_{tvp}	: Volumetric threshold shear strain
γ_w	: Unit weight of the water
λ_{min}	: Minimum wavelength
ν	: Poisson's ratio
σ'	: Effective stress
ρ	: Saturated mass density

References

1. Kramer, S. and A. Elgamel, *Modeling soil liquefaction hazards for performance based earthquake engineering. Report 2001/13, Pacific Earthquake Engineering Research Center.* University of California, Berkeley, 2001. p.165
2. Kramer, S.L., *Geotechnical earthquake engineering.* Prentice-Hall Civil Engineering and Engineering Mechanics Series. 1996, Upper Saddle River, NJ: Pearson 653.
3. Popescu, R. and J.H. Prevost, *Centrifuge validation of a numerical model for dynamic soil liquefaction.* Soil Dynamics and Earthquake Engineering, 1993. **12**(2): p. 73-90.
4. Byrne, P.M., Park, S.S., Beaty, M., Sharp, M., Gonzalez, L. and Abdoun, T., *Numerical modeling of liquefaction and comparison with centrifuge tests.* Canadian Geotechnical Journal, 2004. **41**(2): p. 193-211.
5. Taiebat, M., H. Shahir, and A. Pak, *Study of pore pressure variation during liquefaction using two constitutive models for sand.* Soil Dynamics and Earthquake Engineering, 2007. **27**(1): p. 60-72.
6. Ramirez, J., et al., *Site response in a layered liquefiable deposit: evaluation of different numerical tools and methodologies with centrifuge experimental results.* Journal of Geotechnical and Geoenvironmental Engineering, 2018. **144**(10): p. 1-22.

7. Demir, S. and P. Özener, *Estimation of Liquefaction with UBC3D-PLM Model: A Centrifuge Test Example*. Teknik Dergi, 2019. **30**(5): p. 9421-9442.
8. Prevost, J.H., *A simple plasticity theory for frictional cohesionless soils*. International Journal of Soil Dynamics and Earthquake Engineering, 1985. **4**(1): p. 9-17.
9. Matasović, N. and M. Vucetic, *Cyclic characterization of liquefiable sands*. Journal of Geotechnical Engineering, 1993. **119**(11): p. 1805-1822.
10. Beaty, M. and P.M. Byrne, *An Effective Stress Model for Predicting Liquefaction Behaviour of Sand*. in *Geotechnical Earthquake Engineering and Soil Dynamics III*. 1998. ASCE. pp. 766-777
11. Yang, Z., A. Elgamal, and E. Parra, *Computational model for cyclic mobility and associated shear deformation*. Journal of Geotechnical and Geoenvironmental Engineering, 2003. **129**(12): p. 1119-1127.
12. Dafalias, Y.F. and M.T. Manzari, *Simple plasticity sand model accounting for fabric change effects*. Journal of Engineering mechanics, 2004. **130**(6): p. 622-634.
13. Petalas, A. and V. Galavi, *Plaxis Liquefaction Model UBC3DPLM*. Plaxis Report, 2013.
14. Ziotopoulou, K. and R. Boulanger, *Calibration and implementation of a sand plasticity plane-strain model for earthquake engineering applications*. Soil Dynamics and Earthquake Engineering, 2013. **53**: p. 268-280.
15. Khosravifar, A., Elgamal, A., Lu, J. and Li, J., *A 3D model for earthquake-induced liquefaction triggering and post-liquefaction response*. Soil Dynamics and Earthquake Engineering, 2018. **110**: p. 43-52.
16. Yang, M., M. Taiebat, and Y. Dafalias, *A New Sand Constitutive Model for Pre-and Post-liquefaction Stages*. in *International Conference of the International Association for Computer Methods and Advances in Geomechanics*. IACMAG 2021. **129**:p. 718-726.
17. Taboada, V. and R. Dobry, *Experimental results of model no. p. 1 at RPI*, in Arulanandan K, Scott RF, editors. *Verification of numerical procedures for the analysis of soil liquefaction problems*. 1993, Rotterdam, A.A. Balkema. p. 3-18.
18. Hashash, Y.M., et al., *DEEPSOIL 7.0, User Manual*. Urbana, IL, Board of Trustees of University of Illinois at Urbana-Champaign. 2016. p. 170.
19. Matasovic, N., *Seismic response of composite horizontally-layered soil deposits*. 1993, University of California. p. 452.
20. Phillips, C. and Y.M. Hashash, *Damping formulation for nonlinear 1D site response analyses*. Soil Dynamics and Earthquake Engineering, 2009. **29**(7): p. 1143-1158.
21. Darendeli, M.B., *Development of a new family of normalized modulus reduction and material damping curves*, in *Civil Engineering*. 2001, University of Texas at Austin. p. 362.
22. Jaky, J., *The coefficient of earth pressure at rest*. J. of the Society of Hungarian Architects and Engineers, 1944: p. 355-358.
23. Meyerhof, G.G., *Compaction of sands and bearing capacity of piles*. Transactions of the American Society of Civil Engineers, 1959. **126**(1): p. 1292-1322.
24. Hashash, Y., C. Phillips, and D.R. Groholski, *Recent advances in non-linear site response analysis*. in *5th Int. Conf. in Recent Advances in Geotechnical Earthquake Engineering and Soil Dynamics*. 2010. Missouri Univ. of Science and Technology, Rolla, MO. p. 1-22.
25. Arulmoli, K., Muraleetharan, K. K., Hossain, M. M. and Fruth, L. S., *VELACS: Verification of liquefaction analyses by centrifuge studies, laboratory testing program*. Soil data report, 1992.
26. Vucetic, M. and R. Dobry, *Pore pressure build-up and liquefaction at level sandy sites during earthquakes*. 1986: Research Rep. No. CE-86-3. Troy, NY: Dept. of Civil Engineering, Rensselaer Polytechnic Institute. p. 616.
27. Dobry, R., Pierce, W.G., Dyvik, R., Thomas, G.E. and Ladd, R.S., *Pore pressure model for cyclic straining of sand*, in *Rensselaer Polytechnic Institute, Troy, New York*. 1985: Research Report 1985-06.
28. Mei, X., S.M. Olson, and Y.M. Hashash, *Empirical porewater pressure generation model parameters in 1-D seismic site response analysis*. Soil Dynamics and Earthquake Engineering, 2018. **114**: p. 563-567.
29. Gibson, A.D., *Physical scale modeling of geotechnical structures at one-G*. 1997, California Institute of Technology. p. 397.
30. Mazzoni, S., McKenna F, Scott M.H, and Fenves G.L., *Open system for earthquake engineering simulation user command-language manual—OpenSees version 2.0*. Pacific Earthquake Engineering Research Center, Univ. of California, Berkeley, CA, 2009. p. 451.
31. Kuhlemeyer, R.L. and J. Lysmer, *Finite element method accuracy for wave propagation problems*. Journal of Soil Mechanics & Foundations Div, 1973. **99**(5): p.421-427.
32. Parra, E., *Numerical modeling of liquefaction and lateral ground deformation including cyclic mobility and dilative behavior in soil systems*. 1996, Department of Civil Engineering, Rensselaer Polytechnic Institute, Troy, NY.
33. Yang, Z., J. Lu, and A. Elgamal, *OpenSees soil models and solid-fluid fully coupled elements user's manual*. 2008. p. 1-25.
34. Khosravifar, A., *Analysis and design for inelastic structural response of extended pile shaft foundations in laterally spreading ground during earthquakes*. 2012, University of California, Davis. p. 310.
35. Lu, J., A. Elgamal, and Z. Yang, *OpenSeesPL: 3D lateral pile-ground interaction user manual (Beta 1.0)*. Department of Structural Engineering, University of California, San Diego, 2011. p. 147.

**Research Article**

Application of the Muskingum-Cunge routing method with variable parameters in a gauged creek reach

Hülya Çakır ^{a,*}  and Mustafa Erol Keskin ^b 

^aGraduate School of Natural and Applied Sciences, Süleyman Demirel University, Isparta, 32260, Turkey

^bDepartment of Civil Engineering, Süleyman Demirel University, Isparta, 32260, Turkey

ARTICLE INFO*Article history:*

Received 23 October 2020

Revised 14 February 2021

Accepted 26 April 2021

Keywords:

Flood routing

HEC-HMS

Muskingum-Cunge

Variable parameter

ABSTRACT

In general, the Muskingum-Cunge method is used to route floods when observed flood data are not available. In this study, applicability of the Variable Parameter Muskingum-Cunge (VPMC) flood routing method was investigated in a gauged creek reach. The reach was between two stream gauging stations. Some physical characteristics of the reach, such as length, bed slope, cross sections, and Manning's coefficient (n), were determined by using digital topographical map of the reach, inflow, and also outflow data of the two stream gauging stations. The HEC-HMS hydrological model was used to route the inflow hydrograph through using the VPMC method. In conclusion, observed and computed outflow hydrographs were compared and it was seen that the VPMC flood routing method was suitable for the gauged creek reach, which was the subject of this study.

© 2021, Advanced Researches and Engineering Journal (IAREJ) and the Author(s).

1. Introduction

Flood or flow routing is a method used to predict the time and magnitude of flood/flow in a river or a channel based on available upstream inflow data. Flood routing is classified into two types: hydrologic routing and hydraulic routing.

In hydrologic routing, flow is only time-dependent, while in hydraulic routing, flow is space and time-dependent [1]. In hydraulic routing, topographical data are needed to solve complex equations, while in hydrologic routing, equations are uncomplicated compared to those in hydraulic routing and there is less need for topographical data [2].

In 1848 Barré de Saint-Venant first put forward a solution to the hydraulic flood routing problem. In this solution, the continuity equation and the "momentum equation" statement of Newton's Second Law are solved for a differential volume of one-dimensional flow. Inertia, pressure, gravity, and friction forces acting on the control volume are taken into account and mass is maintained in the solution [3].

In hydrologic routing, continuity equation and the relation among inflow, outflow, and storage are used to solve the routing problem. The solution process is relatively simple and results are satisfactory in general [4]. The Muskingum method, proposed by McCarthy in 1938 [5], is one of the well-known hydrologic routing methods in the literature. The method establishes a linear relationship among storage, inflow, and outflow including two parameters [6]. The parameters of this linear function are determined by observed inflow and outflow data. In the absence of observed flow data, parameters of the Muskingum flood routing method may be determined by the Muskingum-Cunge flood routing method [1]. When the parameters of the Muskingum-Cunge method change with respect to space and time, the method is called the Variable Parameter Muskingum-Cunge (VPMC) method.

The Muskingum-Cunge Method has been studied by several scholars in recent years. Todini proposed a new algorithm to overcome the mass balance problem in the Muskingum-Cunge method and to eliminate contradictory values for the water volume stored in the channel. The

* Corresponding author. Tel.: +90-505-758-5879

E-mail addresses: d1640101001@ogr.sdu.edu.tr (F. Author), erolkeskin@sdu.edu.tr (S. Author)

ORCID: 0000-0001-9731-5989 (H. Çakır), 0000-0003-3749-5169 (M.E. Keskin)

DOI: 10.35860/iarej.813766

This article is licensed under the CC BY-NC 4.0 International License (<https://creativecommons.org/licenses/by-nc/4.0/>).

performance of the proposed model was tested by various time and space intervals, cross-section types, roughness coefficients, and bed slopes. The results were satisfactory in terms of mass balance when they are compared to the results of Saint-Venant equations. The results were also in line with the results of Muskingum equations [7].

Barati et al. investigated the performance of constant and variable parameter Muskingum-Cunge methods in terms of volume conservation and also in terms of the attenuation value and the lag time of the peak outflow. Available flow data for Karun River in Iran were used for conducting numerical experiments. Results were compared to those of kinematic wave, dynamic wave, and Muskingum model. It was concluded that with moderate values of roughness coefficients and bed slopes, Muskingum-Cunge methods were more accurate in ungauged catchments [8].

Ponce and Lugo developed a looped-rating Muskingum-Cunge model by modifying the four-point variable-parameter Muskingum-Cunge model. In the proposed model, local water surface slope and Vedernikov number were used to generate the looped ratings. In order to test the accuracy of the model, numerical experiments were made. The looped ratings calculated by the Muskingum-Cunge model and the outflow hydrographs generated by this model were compared with the results of the dynamic wave model. It was concluded that both models were capable of producing accurate looped ratings and outflow hydrographs [9].

Szel and Gaspar applied the Muskingum-scheme to the one-dimensional unsteady advection-diffusion equation. The scheme did not contain weighting parameters explicitly but contained Courant and Peclet numbers. It was shown that when negative parameters were defined in the scheme they did not affect the accuracy of the scheme. In addition, it was revealed that numerical instabilities could be eliminated by establishing a relationship between Courant and Peclet numbers [10].

Perumal and Sahoo investigated the volume conservation problem of the VPMC method and compared the method with the variable parameter Muskingum discharge hydrograph (VPMD) method. In order to analyze the problem, 6400 experiments were conducted using hypothetical data. It was concluded that the VPMC method was not as mass conservative as the VPMD method. Furthermore, the VPMC method was not successful at producing accurate peak outflow and time to peak outflow, while the VPMD method gave satisfactory results [11].

2. Variable Parameter Muskingum-Cunge Method

As mentioned above, when the parameters of the Muskingum-Cunge method change with respect to space and time, the method is called the variable parameter

Muskingum-Cunge (VPMC) method. Variations of the VPMC method have been used in flood routing phenomena [7, 9, 12-18].

In this study, the VPMC method was used to model the flood routing process in a gauged creek. Basic equations of the method are described in HEC-HMS Technical Reference Manual [19] as below:

The VPMC method is solved using the continuity equation and momentum equation. The continuity equation is written as follows:

$$\frac{\partial A}{\partial t} + \frac{\partial Q}{\partial x} = 0 \quad (1)$$

where A is cross sectional area (m^2), Q is discharge (m^3/s), t is time (s), and x is space (m).

The finite-difference form of continuity equation is as follows:

$$\left(\frac{I_{t-1} + I_t}{2} \right) - \left(\frac{O_{t-1} + O_t}{2} \right) = \left(\frac{S_t - S_{t-1}}{\Delta t} \right) \quad (2)$$

where I_{t-1} , O_{t-1} and S_{t-1} are inflow (m^3/s), outflow (m^3/s) and storage (m^3) at time $t-1$ respectively, while I_t , O_t and S_t are inflow (m^3/s), outflow (m^3/s) and storage (m^3) at time t respectively. Δt is routing time step or time (s) between t and $t-1$.

When there is lateral inflow contribution to the system, equation 1 becomes:

$$\frac{\partial A}{\partial t} + \frac{\partial Q}{\partial x} = q_L \quad (3)$$

where q_L is the lateral inflow (m^3/s).

The diffusion form of the momentum equation is written as follows:

$$S_f = S_0 - \frac{\partial y}{\partial x} \quad (4)$$

where S_f is friction slope (m/m) and S_0 is channel bed slope (m/m).

After combining these two equations and after a linearization process, a convective diffusion equation is derived as [20]:

$$\frac{\partial Q}{\partial t} + c \frac{\partial Q}{\partial x} = \mu \frac{\partial^2 Q}{\partial x^2} + cq_L \quad (5)$$

where c is wave celerity (m/s), μ is hydraulic diffusivity (m^2/s). They are expressed as follows:

$$c = \frac{dQ}{\partial A} \quad (6)$$

and

$$\mu = \frac{Q}{2BS_0} \quad (7)$$

where B is top width of the water surface (m).

Storage is defined in the Muskingum model as follows:

$$S_t = K[XI_t + (1 - X)O_t] \tag{8}$$

where K is a proportionality coefficient (s) and X is a weighting factor.

When Equation (2) is substituted in Equation (8), Equation (9) is obtained:

$$O_t = \left(\frac{\Delta t - 2KX}{2K(1 - X) + \Delta t}\right)I_t + \left(\frac{\Delta t + 2KX}{2K(1 - X) + \Delta t}\right)I_{t-1} + \left(\frac{2K(1 - X) - \Delta t}{2K(1 - X) + \Delta t}\right)O_{t-1} \tag{9}$$

A finite difference approximation of the partial derivatives, combined with Equation (9) yields:

$$O_t = C_1I_{t-1} + C_2I_t + C_3O_{t-1} + C_4(q_L \Delta x) \tag{10}$$

The coefficients C₁, C₂, C₃ and C₄ are expressed as follows:

$$C_1 = \frac{\frac{\Delta t}{K} + 2X}{\frac{\Delta t}{K} + 2(1 - X)} \tag{11}$$

$$C_2 = \frac{\frac{\Delta t}{K} - 2X}{\frac{\Delta t}{K} + 2(1 - X)} \tag{12}$$

$$C_3 = \frac{2(1 - X) - \frac{\Delta t}{K}}{\frac{\Delta t}{K} + 2(1 - X)} \tag{13}$$

$$C_4 = \frac{2\left(\frac{\Delta t}{K}\right)}{\frac{\Delta t}{K} + 2(1 - X)} \tag{14}$$

In the above equations the parameters K and X are [21], [14]:

$$K = \frac{\Delta x}{c} \tag{15}$$

$$X = \frac{1}{2} \left(1 - \frac{Q}{BS_0 c \Delta x} \right) \tag{16}$$

Since c, Q, and B are time dependent, C₁, C₂, C₃ and C₄ must change in every time step. By using Ponce’s algorithm, HEC-HMS recalculates c, Q and B at each time and distance step, Δt and Δx respectively [22].

Determination of Δt and Δx is essential for stability of the VPMC method. Therefore, minimum Δt is selected among other Δt values. Minimum Δt criteria is described in the literature [19].

After Δt is selected, Δx is calculated as follows:

$$\Delta x = c \Delta t \tag{17}$$

But Δx must ensure the criteria given below:

$$\Delta x < \frac{1}{2} \left(c \Delta t + \frac{Q_0}{BS_0 c} \right) \tag{18}$$

where Q₀ is reference inflow (m³/s):

$$Q_0 = Q_B + \frac{1}{2} (Q_{peak} - Q_B) \tag{19}$$

where Q_B is base inflow (m³/s) and Q_{peak} is peak inflow (m³/s).

3. Study Area and Materials

Çaydere Creek is located in Isparta Province of Turkey. Catchment area of Çaydere Creek basin covers 102 km². Study area is located in lower reach of this creek. The creek flows from southeast toward Lake Eğirdir which is also known as the “Seven Colored Lake”. In the study area, there are two stream gauging stations. Distance between upper gauging station (D09A601) and lower gauging station (D09A602) is 1764 meters in length (Figure 1). There is no lateral inflow or outflow between the stations.

The two gauging stations were installed in 2017. The inflow and outflow hydrographs chosen for this study belong to flood event occurred in 2018 spring because the two hydrographs had good hydrograph shapes during that flood event. Gauging stations are installed to measure the flow stages in 5-min intervals. 5-min interval inflow and outflow hydrographs are produced with the help of available rating curves. Afterwards, inflow and outflow hydrographs are calibrated to 30-min time steps. Elapsed time of the two hydrographs is 9 hours. They have single peak flows. Time to peak flow in the inflow hydrograph is 3 hours and lag of time to peak in the outflow hydrograph is 0.5 hours.

In this study, a 1:1000 scale digital topographical map of the study area was used. Based on the topographical map, bed slope between upper and lower gauging stations was calculated as 0.006236. The value of Manning roughness coefficient (n) is derived from the well-known Manning equation given below:

$$n = \frac{R^{2/3} J^{0.5} A}{Q} \tag{20}$$

In equation (20), R (m) is the hydraulic radius of various flows at the upper and lower gauging stations, J (m/m) is bed slopes in the vicinity of upper and lower gauging stations, A (m²) is cross-sectional area of various flows at the upper and lower gauging stations, and Q (m³/s) various flows in the inflow and outflow hydrographs. Thus, “n” is calculated for different values of R, J, A, and Q. As a result of the calculations, it was seen that the results are in the vicinity of 0.037. Therefore, “n” was calculated as 0.037.



Figure 1. Study area © Google Earth

Since the creek bed is lined with gravels and stones, the calibrated value of “ n ” is compatible with “Manning roughness coefficients for various open channel surfaces” [1].

In 2000, a bank protection project was constructed within the lower basin of Çaydere Creek including the study area. The project consists of grading the Çaydere Creek bank to a 2V:5H slope along 2500 meters of the eroded bank, and it is made of riprap (Figure 2 and 3).



Figure 2. Stream gauging station D09A601

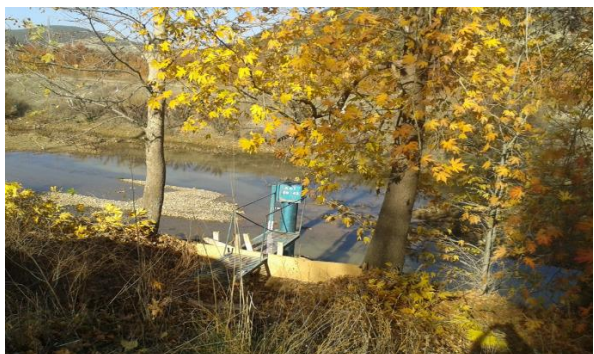


Figure 3. Stream gauging station D09A602

4. HEC-HMS Model

In flood routing performed using the VPMC method, all of the required physical components for the HEC-HMS model are calculated based on the flow and topographical data.

In Figure 4, length is the distance between upper and lower gauging stations and it is 1764 meters. Slope is the average bed slope between the two stations and it was calculated as 0.006236. “ n ” roughness coefficient is the average value for the whole reach and it was calculated as 0.037. Invert is the river bed elevation where the upper gauging station is installed. Cross section is the average cross-section (eight-point) representing the cross-sectional shape of the reach.

Reach		Routing		Options	
Basin Name: CAYDERE					
Element Name: CAYDERE					
Time Step Method:	Automatic Fixed Interval				
*Length (M)	1764				
*Slope (M/M)	0.006236				
*Manning's n:	0.037				
Invert (M)	945.23				
Shape:	Eight Point				
*Left Manning's n:	0.037				
*Right Manning's n:	0.037				
*Cross Section:	Table 1				

Figure 4. HEC-HMS Component editor for VPMC method

5. Results and Discussion

After the simulation, HEC-HMS gave the computed outflow hydrograph. The observed inflow hydrograph and computed outflow hydrograph are given in Figure 5. There is attenuation in the peak discharge due to routing, and lag time (0.50 hours) can be seen clearly between inflow peak discharge and computed outflow peak discharge.

In Figure 6, the observed and computed outflow hydrographs are shown. The computed outflow hydrograph has good agreement with the observed outflow hydrograph, and their times to peak are the same.

Although visual comparison of the observed and computed outflow hydrographs gives a positive opinion about the accuracy of the VPMC method in Çaydere Creek, statistical analyses are needed to support this opinion.

The root-mean-square error (RMSE) equation and the mean absolute error (MAE) equation are used to determine the difference between the observed and computed hydrographs (Equations 21 and 22).

$$RMSE = \sqrt{\frac{\sum_{i=1}^n (Q_c - Q_o)^2}{n}} \quad i=1, 2, 3, \dots, n \quad (21)$$

$$MAE = \frac{\sum_{i=1}^n |Q_c - Q_o|}{n} \quad i=1, 2, 3, \dots, n \quad (22)$$

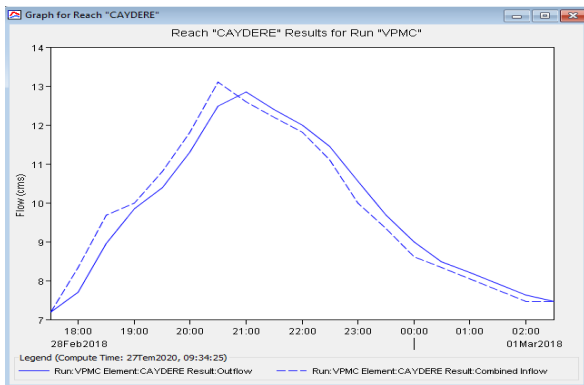


Figure 5. Inflow hydrograph and computed outflow hydrograph

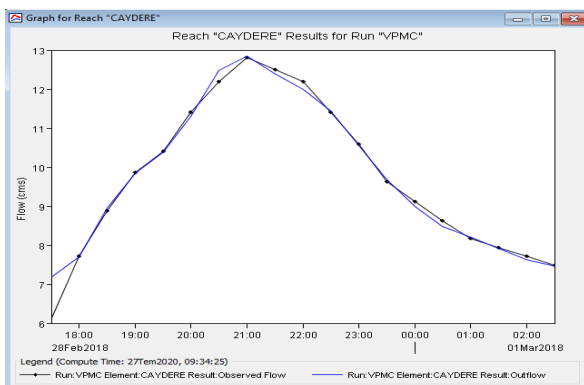


Figure 6. Observed outflow hydrograph and computed outflow hydrograph

Relative errors of 1) peak flow, 2) time to peak and 3) volume are computed as shown in Equations 23, 24, and 25.

$$\sigma_{peak} = \left(\frac{Q_{pc}}{Q_{po}} - 1\right)100 \quad (23)$$

$$\sigma_{time} = \left(\frac{t_{pc}}{t_{po}} - 1\right)100 \quad (24)$$

$$\sigma_{volume} = \left(\frac{V_c}{V_o} - 1\right)100 \quad (25)$$

where:

Q_c = Computed flows in the outflow hydrograph (m^3/s)

Q_o = Observed flows in the outflow hydrograph (m^3/s)

σ_{peak} = Relative error of peak flow (%)

Q_{pc} = Computed peak outflow (m^3/s)

Q_{po} = Observed peak outflow (m^3/s)

σ_{time} = Relative error of time to peak flow (%)

t_{pc} = time to peak flow in the computed outflow hydrograph (h)

t_{po} = time to peak flow in the observed outflow hydrograph (h)

σ_{volume} = Relative error of total volume (%)

V_c =Total volume of the computed hydrograph (m^3)

V_o =Total volume of the observed hydrograph (m^3)

In order to compare the shape of the inflow and outflow hydrographs, Nash–Sutcliffe model efficiency coefficient (E) is calculated (26). If the computed flows are the same as the observed flows, E is expected to be 1. If E is between 0 and 1, it means that there are deviations between observed and computed flows. If E is negative, it means that the computed flows are too far off from the accuracy.

$$E = \frac{\sum_{i=1}^n (Q_o - Q_{mo})^2 - \sum_{i=1}^n (Q_o - Q_c)^2}{\sum_{i=1}^n (Q_o - Q_{mo})^2} \quad i=1, \dots, n \quad (26)$$

Q_{mo} = Mean of the observed outflows (m^3/s)

Results of statistical analyses are shown in Table 1 and 2. Finally, relationship between the observed and computed outflows is shown by a scatter plot in Figure 7.

Table 1. RMSE, MAE, Q_{pc} , Q_{po} and σ_{peak} values

RMSE (m^3/s)	MAE (m^3/s)	Q_{pc} (m^3/s)	Q_{po} (m^3/s)	σ_{peak} (%)
0,26	0,13	12,84	12,80	0,04

Table 2. t_{pc} , t_{po} , σ_{time} , V_c , V_o , σ_{vol} and E values

t_{pc} (h)	t_{po} (h)	σ_{time} (%)	V_c (m^3)	V_o (m^3)	σ_{vol} (%)	E
3,50	3,50	0	320634	320310	0,10	0,98

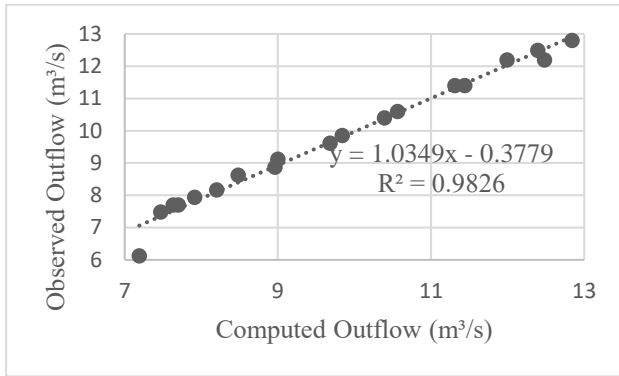


Figure 7. Scatter plot of the observed and computed outflows

According to results obtained from statistical analyses (Table 1 and 2), the three relative errors (peak, time, and volume) are acceptable. In addition, the value of the efficiency coefficient is close to 1, which indicates that the computed flow hydrograph's shape is similar to the observed hydrograph's shape.

Finally, according to the scatter plot in Figure 7, there is a positive, strong, and linear relationship between the observed and computed outflows.

6. Conclusions

In this study, the VPMC flood routing method was used in Çaydere creek reach. The reach was between two stream gauging stations. Inflow and outflow hydrographs were available and they belonged to the flood event occurred in the spring of 2018. 1/1000 scale topographical map of the study area was also available. The HEC-HMS model was used to derive the computed hydrograph. Statistical analysis was conducted to measure the accuracy of the VPMC method in the study area. Based on the results obtained from the analysis, it can be said that the VPMC method seems to produce reliable flood routing data, such as peak outflow, time to peak outflow, total volume, and hydrograph shape. Thus, it can be concluded that the VPMC method can be used in flood routing studies in the Çaydere basin when topographical and outflow data are not available. This method can also be applied to reaches that have similar physical characteristics with Çaydere reach.

Declaration

The authors declared no potential conflicts of interest with respect to the research, authorship, and/or publication of this article. The authors also declared that this article is original, was prepared in accordance with international publication and research ethics, and ethical committee permission or any special permission is not required.

Author Contributions

H. Çakır collected hydrological and survey data, performed the analysis and wrote the manuscript. M. E.

Keskin supervised and improved the study.

References

1. Chow, V.T., Maidment, D.R., Mays, L.W., *Applied Hydrology*. 1988, USA; McGraw-Hill Inc.
2. Zhang, S., L. Kang, L. Zhou, X. Guo, *A new modified nonlinear Muskingum model and its parameter estimation using the adaptive genetic algorithm*. Hydrology Research, 2016. **48**(1): p. 17-27.
3. Heatherman, W.J., *Flood routing on small streams: A review of Muskingum-Cunge, cascading reservoirs, and full dynamic solutions*. The degree of Doctor of Philosophy, University of Kansas, 2008, USA.
4. Shaw, E.M., *Hydrology in Practice*. 2005, USA: Taylor&Francis Group.
5. McCarthy G.T., *The unit hydrograph and flood routing*. Unpublished m/s conference of US Army Corps of Engineers. 1938, USA.
6. Perumal, M., G. Tayfur, C.M. Rao, G. Gürarlan, *Evaluation of a physically based quasi-linear and a conceptually based nonlinear Muskingum methods*. Journal of Hydrology, 2017. **546**: p. 437-449.
7. Todini, E., *A mass conservative and water storage consistent variable parameter Muskingum-Cunge approach*. Hydrology and Earth System Sciences Discussions, 2007. **11**: p. 1645-1659.
8. Barati, R., G.H. Akbari, S. Rahimi, *Flood routing of an unmanaged river basin using Muskingum-Cunge model; field application and numerical experiments*. Caspian Journal of Applied Sciences Research, 2013. **2**(6): p. 8-20.
9. Ponce, V.M., A. Lugo, *Modeling looped ratings in Muskingum-Cunge routing*. Journal of Hydrologic Engineering, 2001. **6**(2): p. 119-125.
10. Szel, S., C. Gaspar, *On the negative weighting factors in the Muskingum-Cunge scheme*. Journal Of Hydraulic Research, 2000. **38**(4): p. 299-306.
11. Perumal, M., B. Sahoo, *Volume conservation controversy of the variable parameter Muskingum-Cunge method*. Journal of Hydraulic Engineering, 2008. **134**(4): p. 475-485.
12. Price, R.K., *Flood routing methods for British rivers*. Proceedings of the Institution of Civil Engineers, 1973. **55**(12): p. 913-930.
13. Price, R.K., *Flood routing*. Developments in Hydraulic Engineering. 1985. **3**: p. 129-173.
14. Ponce, V.M., V. Yevjevich, *Muskingum-Cunge method with variable parameters*. Journal of Hydr. Div., 1978. **104**(12): p. 1663-1667.
15. Ponce, V.M., F.D. Theurer, *Accuracy criteria in diffusion routing*. J. Hydr.Div., 1982. **1086**: p. 747-757.
16. Ponce, V.M., P.V. Chaganti, *Variable-parameter Muskingum-Cunge method revisited*. J. Hydrol., 1994. **162**(3-4): p. 433-439.
17. Ponce, V.M., A.K. Lohani, C. Scheyhing, *Analytical verification of Muskingum-Cunge routing*. J. Hydrol., 1996. **174**(3-4): p. 235-241.
18. Franchini, M., A. Bernini, S. Berbetta, T. Moramarco, *Forecasting discharges at the downstream end of a river*

reach through two simple Muskingum based procedures.
Journal of Hydrology, 2011. **546**: p. 437-449.

19. HEC-HMS, version 4.2.1; *Hydrologic Modeling System-Technical Reference Manual*, U.S. Army Corps of Engineers, Hydrologic Engineering Center, 2000, USA.
20. Miller, W.A., J.A. Cunge, *Simplified equations of unsteady flow. Unsteady flow in open channels*. Water Resources Publications, 1975.1: p. 216-242,
21. Cunge, J.A., *On the subject of a flood propagation method*. Hydraulics Res. IAHR., 1969. **7**: p. 205-230.
22. Ponce, V.M., *Diffusion wave modeling of catchment dynamics*. J. Hydr. Engrg., 1986. **112**(8): p. 716-727.



Research Article

Analysis and modified function projective synchronization of integer and fractional-order autonomous Morse jerk oscillator

Eric Donald Dongmo ^a , Cyrille Ainamon ^b , Alex Stephane Kemnang Tsafack ^{c,*} ,
Nasr Saeed ^d , Victor Kamdoun Tamba ^e  and Sifeu Takougang Kingni ^f 

^aDepartment of Mechanical Engineering, College of Technology, University of Buea, P. O. Box: 63 Buea, Cameroon

^bInstitute of Mathematics and Physical Sciences, University of Abomey-Calavi, P. O. Box: 613, Porto Novo, Benin

^cResearch unit of Condensed Matter of Electronics and Signal Processing, Department of Physics, Faculty of Sciences, University of Dschang, P.O. Box: 67, Dschang, Cameroon

^dDepartment of Physics, College of Education, Nyala University, P.O. Box: 155, Nyala, Sudan

^eDepartment of Telecommunication and Network Engineering, IUT-Fotso Victor of Bandjoun, University of Dschang, P. O. Box: 134, Bandjoun, Cameroon

^fDepartment of Mechanical, Petroleum and Gas Engineering, Faculty of Mines and Petroleum Industries, University of Maroua, P.O. Box: 46, Maroua, Cameroon

ARTICLE INFO

Article history:

Received 07 January 2021

Revised 29 April 2021

Accepted 21 May 2021

Keywords:

Chaos

Electronic implementation

Integer and fractional-order

Modified function projective

Morse jerk oscillator

Periodic spiking oscillations

Synchronization

ABSTRACT

Dynamical analysis and modified function projective synchronization (MFPS) of integer and fractional-order Morse jerk oscillator are investigated in this paper. Integer-order Morse jerk oscillator generates periodic behaviors, periodic spiking and two different shapes of chaotic attractors. The periodic spiking and chaotic behaviors obtained during numerical simulations of integer-order Morse jerk oscillator is ascertained by using electronic implementation. The numerical simulations results qualitatively agree with the Orcad-PSpice results. Moreover, MFPS of identical and mismatched chaotic Morse jerk oscillators is numerically investigated. At last, the theoretical investigation of fractional-order Morse jerk oscillator reveals the existence of chaos in Morse jerk oscillator for order greater or equal to 2.85.

© 2021, Advanced Researches and Engineering Journal (IAREJ) and the Author(s).

1. Introduction

Chaotic systems are highly sensitive to petty perturbations [1]. Chaos can be observed in various physical systems [2-5] and it is useful in many fields [6, 7]. The construction of chaotic oscillators with simple structures [8-14] is an interesting field of research. There is two types of simple chaotic oscillators: Non-autonomous [9] and autonomous oscillators [10-14]. Sprott in [14] proposed various new chaotic jerk oscillators with diverse nonlinearities and easy electronic implementation.

Following the idea of proposing new autonomous chaotic oscillators with easy electronic implementation,

several research works have been conducted on new autonomous chaotic jerk oscillators [12-17]. The authors of [15-17] introduced autonomous chaotic jerk oscillators using Duffing and Van der Pol dynamics washed into a jerk system. The authors of [15, 16] proposed an autonomous chaotic Van der Pol jerk oscillator based on second-order-equation of Van der Pol oscillator. The authors of [17] proposed an autonomous chaotic Duffing jerk oscillator based on second-order-equation of Duffing oscillator. Inspired by [12-17], Morse jerk oscillator is designed based on the second-order autonomous Morse oscillator in this paper. Then dynamical analysis, synchronization, circuit design of integer and fractional-

* Corresponding author. Tel.: +237-698-022-585.

E-mail addresses: eric.dongmo90@gmail.com (E.D. Dongmo), ainamoncyrille@yahoo.fr (C. Ainamon), alexstephanekemnang@gmail.com (A.S.K. Tsafack), nasrsaeed19@yahoo.com (N. Saeed), y.kamdoun@gmail.com (V.K. Tamba), stkingni@gmail.com (S.T. Kingni)

ORCID: 0000-0002-0203-2829 (E.D. Dongmo), 0000-0002-3656-1614 (C. Ainamon), 0000-0002-4602-9293 (A.S.K. Tsafack),

0000-0002-5123-5139 (N. Saeed), 0000-0002-0835-4722 (V.K. Tamba), 0000-0003-1547-6856 (S.T. Kingni)

DOI: 10.35860/iarej.854623

This article is licensed under the CC BY-NC 4.0 International License (<https://creativecommons.org/licenses/by-nc/4.0/>).

order Morse jerk oscillator are studied. The fractional-order of autonomous Morse jerk oscillator is analysed by using analytical [18] and numerical methods [19, 20]. Morse oscillator is used to describe molecular vibrations [21, 22]. The present work contributes to the dynamical analysis, the modified function projective synchronization (MFPS) of integer and fractional-order Morse jerk oscillator. Integer-order of this jerk oscillator generates periodic behaviors, periodic spiking and chaotic attractors. Investigations of fractional-order Morse jerk oscillator reveals the existence of chaos in Morse jerk oscillator for order less than three.

This paper is organized as follows: In the Section 2, the Morse jerk oscillator is analysed and implemented on Orcad-PSpice software. The MFPS of identical and mismatched coupled chaotic Morse jerk oscillators is investigated in Section 3. Section 4 deals with the analysis of fractional-order Morse jerk oscillator. Section 5 presents the conclusion.

2. Dynamical Analysis of Morse Jerk Oscillator

The two-dimensional Morse equation [22] can be transformed to a jerk oscillator:

$$\begin{aligned} \dot{x} &= y, \\ \dot{y} &= \delta z, \\ \dot{z} &= -\gamma y - z - \beta[1 - \exp(-\alpha x)] \exp(-\alpha x) \end{aligned} \tag{1}$$

where $\alpha, \gamma, \beta, \delta$ are positive parameters, $\ddot{x}(t) = z(t)$ and $\dot{x}(t) = y(t)$. For $\delta = \alpha = 1, \gamma = 0.16$ and by increasing the parameter β , system (2) exhibits steady state behaviour up to $\gamma = \beta = 0.16$ where a Hopf bifurcation appears followed by limit cycle and periodic spiking oscillations as illustrated in Figure 1.

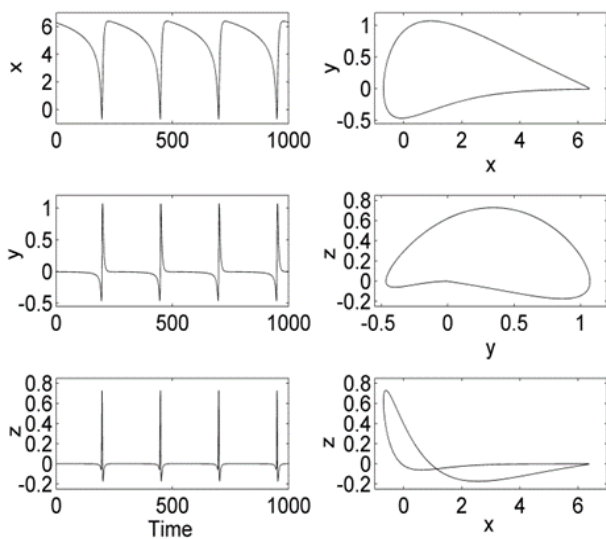


Figure 1. Time traces (left panel) and phase portraits (right panel) for $\alpha = 1, \gamma = 0.16$ and $\beta = 0.5$ and the initial conditions $(x(0), y(0), z(0)) = (0.1, 0.1, 0.1)$

The periodic spiking oscillations are depicted in Figure 1. System (1) is dissipative and has single equilibrium point $O(0,0,0)$. The characteristic equation at the equilibrium point $O = (0,0,0)$ is:

$$\lambda^3 + \lambda^2 + \gamma\delta\lambda + \alpha\beta\delta = 0. \tag{2}$$

Based on Routh-Hurwitz criteria, the single equilibrium point is stable if $\gamma > \alpha\beta$ and unstable for $\gamma < \alpha\beta$ because $\delta > 0$.

Figure 2 presents the two parameters bifurcation diagram of system (1) for $\alpha = 1$ and $\gamma = 0.16$.

System (1) exhibits periodic (grey color) and chaotic (black color) behaviors as depicted in Figure 2. Figure 3 presents the phase portraits of chaotic behaviors for given values of β and δ .

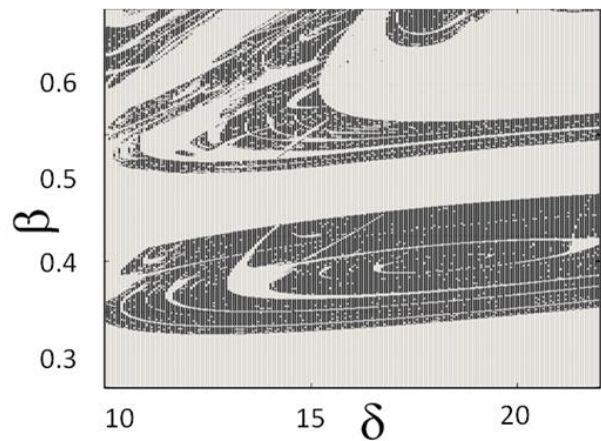


Figure 2. Two parameters (δ, β) bifurcation diagram for $\alpha = 1$ and $\gamma = 0.16$.

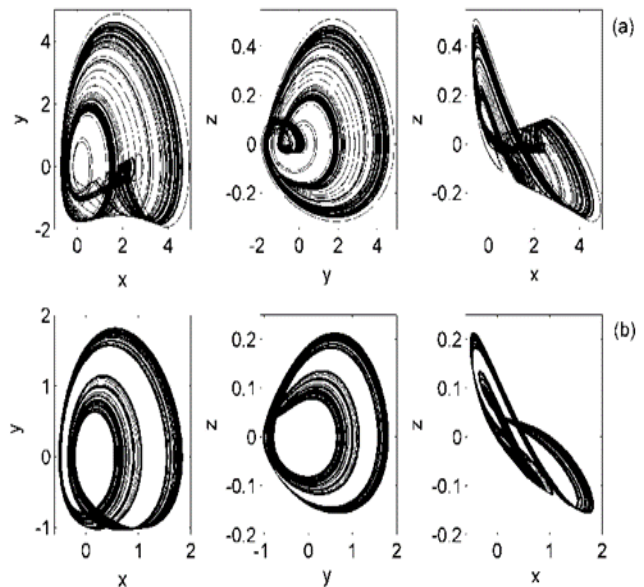


Figure 3. Phase portraits of system (1) for given values of δ and β : (a) $\beta = 0.6, \delta = 18$ and (b) $\beta = 0.345, \delta = 12.85$. The others parameters are $\alpha = 1$ and $\gamma = 0.16$. The initial conditions are $(x(0), y(0), z(0)) = (0.1, 0.1, 0.1)$

From Figure 3, it emerges two different forms of chaotic attractors for given values of β and δ . The circuit of system (1) is depicted in Figure 4. This figure includes of analog multiplier device (ADJ633), operational amplifiers (TL084), capacitors, resistors and battery. The exponential black box is built by an operational amplifier associated with a resistor and a single diode. The phase portraits obtained from the Orcard-PSPice software are shown in Figure 5.

The obtained PSPice results of Figure 5 are in agreement with the numerical results of the right panel of Figure 1 and Figure 3.

3. Modified Function Projective Synchronization of Chaotic Morse Jerk Oscillators

To achieve the MFPS [23, 24] of unidirectional coupled chaotic Morse jerk oscillators, the controllers are designed for MFPS of identical and mismatched Morse jerk oscillators. The numerical simulations are included in each case to ascertain the effectiveness of the control method. The chaotic drive and response systems are described by Equations (3) and (4), respectively.

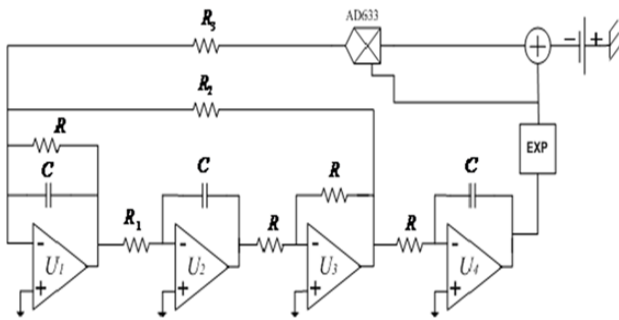


Figure 4. Circuit illustrating system (1)

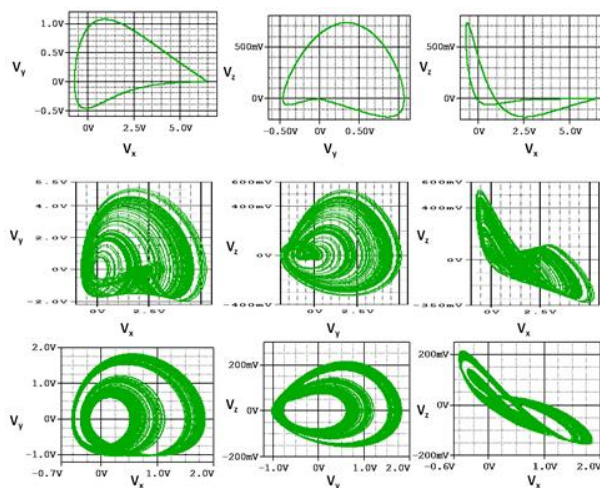


Figure 5. Phase portraits of periodic and chaotic attractors obtained on Orcard-PSPICE. Resistors and capacitor values are $C = 10nF, R_1 = R = 10k\Omega, R_3 = 20k\Omega, R_2 = 62.50k\Omega$ (first line reproduces the right panel of Figure 1), $R_3 = 16.16k\Omega, R = 10k\Omega, R_1 = 555.5k\Omega, R_2 = 62.5k\Omega, C = 10nF$ (second line agrees with Figure 3(a)) and $R = 10k\Omega, R_1 = 778.21k\Omega, R_2 = 62.5k\Omega, R_3 = 28.98k\Omega$ (third line agrees with Figures 3(b)).

$$\dot{x} = f(x) + \Delta f(x) \tag{3}$$

$$\dot{y} = f(y) + D(y, \tilde{g}) \tag{4}$$

where $x, y \in R^n$ are the state vectors, f is the differentiable vector function, $\Delta f(x)$ is the mismatched term and equal to zero for identical oscillators. The coupling function $D(y, \tilde{g})$ is given by Equation (5).

$$D(y, \tilde{g}) = \Lambda_i m(t) \dot{x}(t) + \Lambda_i \dot{m}(t) x(t) - f(\tilde{g}) + (H - JF(\tilde{g}(t)))(y - \Lambda_i m(t) x(t)) \tag{5}$$

where the constant diagonal matrix is $\Lambda_i = \text{diag}(\Lambda_1, \Lambda_2, \dots, \Lambda_n)$, $m(t)$ is a differentiable function with $m(t) \neq 0$ for all t , $\tilde{g}(t)$ is the goal dynamics function which is defined by Equation (6).

$$\tilde{g}(t) = [g_1(t), g_2(t), \dots, g_n(t)]^T = [\Lambda_1 m(t) x_1(t), \Lambda_2 m(t) x_2(t), \dots, \Lambda_n m(t) x_n(t)]^T \tag{6}$$

where H is an arbitrary constant Hurwitz matrix ($n \times n$) whose eigenvalues all have negative real parts and $\frac{J=\partial}{\partial \tilde{g}}$ is the Jacobian matrix of the dynamical system. The error state vector of MFPS is given by Equation (7).

$$e(t) = y(t) - \tilde{g}(t) \tag{7}$$

The challenge is to build the response jerk oscillator in order its synchronize with the drive jerk oscillator for given scaling diagonal matrix and $m(t)$:

$$\lim_{t \rightarrow \infty} \|y(t) - \Lambda_i m(t) x(t)\| = 0 \tag{8}$$

3.1 MFPS of Unidirectional Coupled Identical Chaotic Morse Jerk Oscillators

The drive chaotic Morse jerk oscillator is described by Equation (9).

$$\begin{aligned} \dot{x}_1 &= x_2, \\ \dot{x}_2 &= \delta x_3, \end{aligned} \tag{9}$$

$$\dot{x}_3 = -\gamma x_2 - x_3 - \beta [1 - \exp(-\alpha x_1)] \exp(-\alpha x_1).$$

By applying the OPCL coupling, the response oscillator is given by Equation (10).

$$\begin{aligned} \dot{y}_1 &= y_2 + m(t)(\Lambda_1 - \Lambda_2)x_2 + \Lambda_1 \dot{m}(t)x_1 - e_1 - e_2, \\ \dot{y}_2 &= \delta y_3 + m(t)(\Lambda_2 - \Lambda_3)\delta x_3 + \Lambda_2 \dot{m}(t)x_2 - e_2 - \delta e_3, \\ \dot{y}_3 &= -y_3 - \gamma y_2 - \beta [1 - \exp(-\alpha y_1)] \exp(-\alpha y_1) + m(t)(\Lambda_2 - \Lambda_3)\gamma x_2 + \Lambda_3 \dot{m}(t)x_3 + \beta [1 - \exp(-\alpha \Lambda_1 m(t)x_1)] \exp(-\alpha \Lambda_1 m(t)x_1) - b e_1 + \gamma e_2. \end{aligned} \tag{10}$$

where $a = \alpha\beta[1 - 2 \exp(-\alpha x_1)] \exp(-\alpha x_1)$ and $b = \alpha\beta[1 - 2 \exp(-\alpha\Lambda_1 m(t)x_1)] \exp(-\alpha\Lambda_1 m(t)x_1)$. The parameter values using during numerical simulations of the drive and response jerk oscillator are those of Figure 3 (a) for which the oscillator presents a chaotic behavior. The constant diagonal matrix is taken arbitrary as $\Lambda = \text{diag}(0.1, 0.2, 0.3)$ whereas the differentiable function is $m(t) = 3 + 1.5 \sin(2\pi t/10)$. The numerical simulations results are presented in Figure 6. Figure 6 (a) presents the time traces of the state vector x_1 (solid line for the drive jerk) and y_1 (dashed line the response jerk oscillator) respectively for the drive and the response oscillators. Figure 6 (b) shows the time traces of MFPS errors $e_i(t) i = 1,2,3$ tending to zero asymptotically showing the achievement of MFPS between drive and response systems. Figure 6 (c) shows that $\frac{\|y\|}{\|x\|}$ tends to the differentiable function $m(t)$ indicating MFPS.

3.2 MFPS of Two Mismatched Chaotic Morse Jerk Oscillators

For $\alpha = 1$, the mismatched chaotic Morse jerk oscillator is defined by Equation (11).

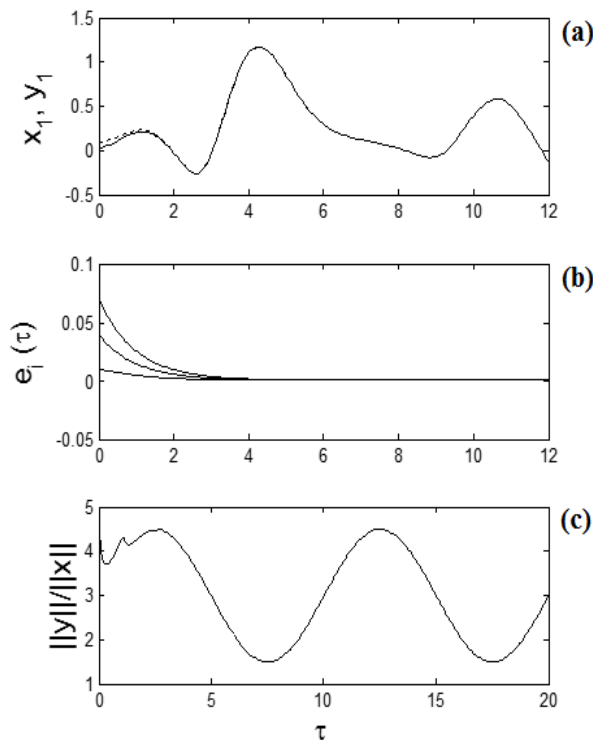


Figure 6. MFPS of identical chaotic Morse jerk oscillators: (a) Time traces of the state vector x_1 (solid line) and y_1 (dashed line), (b) evolution errors and

(c) ratio $\frac{\|y\|}{\|x\|}$. The initial conditions are $(y_1(0), y_2(0), y_3(0)) = (0.1, 0.1, 0.1)$ and $(x_1(0), x_2(0), x_3(0)) = (0.1, 0.1, 0.1)$.

$$\begin{aligned} \dot{x}_1 &= x_2, \\ \dot{x}_2 &= \delta x_3 + \Delta\delta x_3, \\ \dot{x}_3 &= -x_3 - \gamma x_2 - \beta[1 - \exp(-x_1)] \exp(-x_1) \\ &\quad - \Delta\gamma x_2 \\ &\quad - \Delta\beta[1 - \exp(-x_1)] \exp(-x_1). \end{aligned} \tag{11}$$

System (11) is still chaotic for $\beta = 0.6, \Delta\beta = 0.3, \gamma = 0.16, \Delta\gamma = 0.1, \delta = 18$ and $\Delta\delta = 3$. Considering (11) as the drive jerk, the response jerk is given by Equation 12.

$$\begin{aligned} \dot{y}_1 &= y_2 + m(t)(\Lambda_1 - \Lambda_2)x_2 + \Lambda_1 \dot{m}(t)x_1 - e_1 - e_2, \\ \dot{y}_2 &= \delta y_3 + \Delta\delta y_3 + m(t)(\Lambda_2 - \Lambda_3)\delta x_3 + \\ &\quad m(t)(\Lambda_2 - \Lambda_3)\Delta\delta x_3 + \Lambda_2 \dot{m}(t)x_2 - e_2 - \delta e_3, \\ \dot{y}_3 &= -y_3 - \gamma y_2 - \beta \exp(-y_1) [1 - \exp(-y_1)] \\ &\quad - \Delta\gamma y_2 \\ &\quad - \Delta\beta \exp(-y_1) [1 - \exp(-y_1)] \\ &\quad + m(t)(\Lambda_2 - \Lambda_3)\gamma x_2 + \Lambda_3 \dot{m}(t)x_3 \\ &\quad - \Lambda_3 m(t)(\beta + \Delta\beta)[1 \\ &\quad - \exp(-x_1)] \exp(-x_1) \\ &\quad + m(t)(\Lambda_2 - \Lambda_3)\Delta\gamma x_2 \\ &\quad + (\beta + \Delta\beta)[1 \\ &\quad - \exp(-\Lambda_1 m(t)x_1)] \exp(-\Lambda_1 m(t)x_1) \\ &\quad - c e_1 + \gamma e_2, \end{aligned} \tag{12}$$

$$c = \beta[1 - 2 \exp(-\Lambda_1 m(t)x_1)] \exp(-\Lambda_1 m(t)x_1).$$

The parameter values using during numerical simulations of the drive and response jerks are those of Figure 3 (a). The mismatch parameters are chosen as $\Delta\delta = 1, \Delta\gamma = 0.1$ and $\Delta\beta = 0.2$. The constant diagonal matrix is taken arbitrary as $\Lambda = \text{diag}(0.3, 0.2, 0.1)$ while the differentiable function as $m(t) = 5 + 2 \sin(2\pi t/10)$. Sample numerical simulations results are presented in Figure 7.

Figure 7 (a) presents the time traces of the state vector x_1 (solid line) and y_1 (dashed line). Figure 7 (b) shows that the time traces of MFPS errors $e_i(t) i = 1,2,3$ tend to zero asymptotically indicating MFPS between drive and response oscillators in presence of mismatch parameters. Figure 7 (c) shows that $\frac{\|y\|}{\|x\|}$ tends to $m(t)$ confirming MFPS.

4. Fractional-Order of Chaotic Morse Jerk Oscillator

The rate-equations describing of the fractional order of

$$\begin{aligned} \frac{d^{q_1} x}{dt^{q_1}} &= y, \\ \frac{d^{q_2} y}{dt^{q_2}} &= \delta z, \\ \frac{d^{q_3} z}{dt^{q_3}} &= -\gamma y - z - \beta \exp(-ax) [1 - \exp(-ax)]. \end{aligned} \tag{13}$$

system (1) is given by Equation (13).

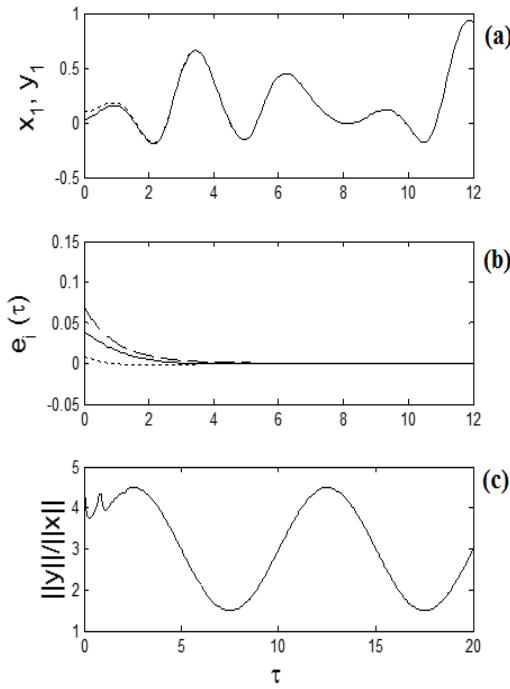


Figure 7. MFPS of mismatched chaotic Morse jerk oscillators. (a) Time traces of the state vector x_1 (solid line) and y_1 (dashed line) and in presence of mismatch parameters, (b) evolution errors and (c) ratio $\frac{\|y\|}{\|x\|}$. The initial conditions are $(x_1(0), x_2(0), x_3(0)) = (0.1, 0.1, 0.1)$ and $(y_1(0), y_2(0), y_3(0)) = (0.1, 0.1, 0.1)$.

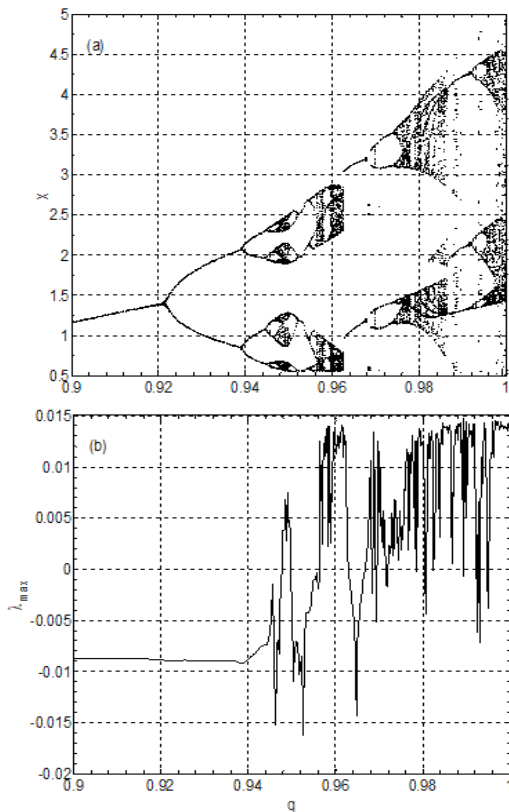


Figure 8. Bifurcation diagram of x (a) and LLE (b) of system (13) as function of the parameter q with $\alpha = 1, \gamma = 0.16, \delta = 18$ and $\beta = 0.6$.

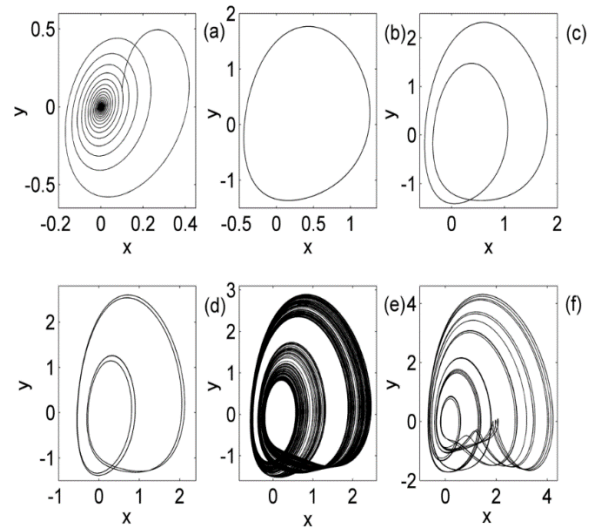


Figure 9. Phase portraits of fractional order system (13) for specific values of parameter q : (a) $q = 0.83$, (b) $q = 0.91$, (c) $q = 0.93$, (d) $q = 0.941$, (e) $q = 0.95$ and (f) $q = 0.99$.

where $q_1 = q_2 = q_3 = q (0 < q < 1)$ is the commensurate fractional order. For $\alpha = 1, \gamma = 0.16, \delta = 18$ and $\beta = 0.6$, the eigenvalues of equilibrium point $O(0,0,0)$ are given as $\lambda_1 = -2.091656729, \lambda_{2,3} = 0.5458283647 \pm 2.205774816j$. Based on Eq. (17) in [21], the fractional-order system (13) exhibits chaos if $3q_0 \geq 2.536703964$. The bifurcation diagram representing the local maxima of $x(t)$ and LLE versus of parameter q are plotted in Figure 8.

In Figure 8, system (13) exhibits limit cycle and period-doubling route to chaos incrustated with periodic windows. So, system (13) exhibits chaos for $3q_0 \approx 2.85$. Figure 9 depicts the phase portraits of system (13) for given value of parameter q .

Figure 9 exhibits steady state behavior at $q = 0.83$ (see Figure 9 (a)), limit cycle at $q = 0.941$ (see Figure 9 (b)), period doubling attractors (see Figures 9 (c) and (d)) to chaotic attractors (see Figures 9 (e) and (f)).

5. Conclusions

This paper investigated the dynamics and modified function projective synchronization of integer and fractional-order Morse jerk oscillator. Interesting dynamics such as periodic oscillations, periodic spiking and two different shapes of chaotic attractors emerged by tuning the parameters. The designed circuit of autonomous Morse jerk oscillator was realized on the Orcad-PSpice software to ascertain the numerical simulations results. Next, numerical simulations of identical and mismatched chaotic Morse jerk oscillators were done to denote the effectiveness of the modified function projective synchronization. At last, the theoretical investigation of fractional-order Morse jerk

oscillator revealed the existence of chaos in Morse jerk oscillator for order greater or equal to 2.85.

Declaration

The authors declared no potential conflicts of interest with respect to the research, authorship, and/or publication of this article. The authors also declared that this article is original, was prepared in accordance with international publication and research ethics, and ethical committee permission or any special permission is not required.

Author Contributions

N. Saeed, V.K. Tamba and S.T. Kingni conceived this study. E.D. Dongmo, C. Ainamon and A.S.K. Tsafack did the calculations and computers simulations. E. D. Dongmo and A.S.K. Tsafack did the analogsimulations. E.D. Dongmo, C. Ainamon and A.S.K. Tsafack wrote the manuscript. N. Saeed, V.K. Tamba and S.T. Kingni checked the results obtained in this study.

References

- Ivancevic V.G. and T.T. Ivancevic, *Complex nonlinearity: chaos, phase transitions, topology change, and path integrals*. 2008, Berlin: Springer Science & Business Media.
- Rial J.A., *Abrupt climate change: chaos and order at orbital and millennial scales*. Global and planetary change, 2004. **41**: p. 95-109.
- Carlen E., R. Chatelin, P. Degond and B. Wennberg, *Kinetic hierarchy and propagation of chaos in biological swarm models*. Physica D: Nonlinear Phenomena, 2013. **260**: p. 90-111.
- Callan K. L., L. Illing, Z. Gao, D. J. Gauthier and E. Schöll, *Broadband chaos generated by an optoelectronic oscillator*. Physical Review Letters, 2010. **104**: 113901.
- Kingni S. T., G. Van der Sande, I. V. Ermakov and J. Danckaert, *Theoretical analysis of semiconductor ring laser with short and long time-delayed optoelectronic and incoherent feedback*. Optics Communications, 2015. **341**: p. 147-154.
- Nana B., P. Wofo and S. Domngang, *Chaotic synchronization with experimental application to secure communications*. Communications in nonlinear science and Numerical Simulation, 2009. **14**: p. 2266-2276.
- Kingni S. T., J. H. TallaMbé and P. Wofo, *Semiconductor lasers driven by self-sustained chaotic electronic oscillators and applications to optical chaos cryptography*. Chaos, 2012. **22**: p. 033108-033115.
- Sprott J. C., *Elegant Chaos Algebraically Simple Flows*. 2010, Singapore: World Scientific.
- Lindberg E., K. Murali and A. Tamasevicius, *The smallest transistor-based nonautonomous chaotic circuit*. IEEE Transactions on Circuits and Systems II: Express Briefs, 2005. **52**: p. 661-664.
- Tchitnga R., H. B. Fotsin, B. Nana, P. H. L. Fotso and P. Wofo, *Hartley's oscillator: the simplest chaotic two-component circuit*. Chaos Solitons Fractals, 2012. **45**: p. 306-313.
- Muthuswamy B. and L. O. Chua, *Simplest chaotic circuit*. International Journal of Bifurcation and Chaos, 2010. **20**: p. 1567-1580.
- Piper J. R. and J. C. Sprott, *Simple autonomous chaotic circuits*, IEEE Transactions on Circuits and Systems II: Express Briefs, 2010. **57**: p. 730-734.
- Srisuchinwong B. and B. Munmuangsaen, *Current-tunable chaotic jerk oscillator*. Electronics letters, 2012. **48**: p. 1051-1053.
- Sprott J.C., *Simple chaotic systems and circuits*. American Journal of Physics, 2000. **68**: p. 758-763.
- Acho L., J. Rolon and S. Benitez, *Synchronization of mechanical systems with a new Van der Pol chaotic oscillator*. WSEAS Transactions on Circuits and Systems, 2004. **3**: p. 198-199.
- Benitez S., L. Acho and R. J. R. Guerra, *Chaotification of the Van der Pol system using Jerk architecture*. IEICE Transactions on Fundamentals of Electronics, Communications and Computer Sciences, 2006. **89**: p. 1088-1091.
- Kengne J., Z. T. Njitacke and H. B. Fotsin, *Dynamical analysis of a simple autonomous jerk system with multiple attractors*, Nonlinear Dynamics, 2016. **83**(1): p. 751-765.
- Tavazoei M. S., M. Haeri, *A necessary condition for double scroll attractor existence in fractional-order systems*. Physics Letters A, 2007. **367**(1-2): p.102-13.
- Caponetto R., R. Dongola, L. Fortuna and I. Petráš, *Fractional-order system: Modelling and control applications*. 2010, World scientific series on nonlinear science, series A, vol. **72**.
- Diethelm K., N. J. Ford, D. Freed, *A predictor-corrector approach for the numerical solution of fractional differential equations*. Nonlinear Dynamics 2002. **29**(1): p. 3-22.
- Wu J. and J. Cao, *Linear and nonlinear response functions of the Morse oscillator: Classical divergence and the uncertainty principle*, The Journal of Chemical Physics, 2001. **115**(12): p. 5381-5392.
- Jing Z., J. Deng and J. Yang, *Bifurcations of periodic orbits and chaos in damped and driven Morse oscillator*. Chaos, Solitons & Fractals, 2008. **35**(3): p. 486-505.
- Sudheer K.S. and M. Sabir, *Modified function projective synchronization of hyperchaotic systems through open-plus-closed-loop coupling*. Physics Letters A, 2010. **374**(19-20): p. 2017-2023.
- Kamdoum Tamba V., H. B. Fotsin, J. Kengne, F Kapche Tagne and P. K. Talla, *Coupled inductors-based chaotic Colpitts oscillators: Mathematical modeling and synchronization issues*. The European Physical Journal Plus, 2015. **130**(7):137.

**Research Article**

A new region-of-interest (ROI) detection method using the chan-veese algorithm for lung nodule classification

Ali Cinar ^{a,*} , Bengisu Topuz ^b  and Semih Ergin ^c 

^aDept. of Electrical and Electronics Engineering, Kastamonu University, Kastamonu, Turkey

^bBioengineering Division, Institute of Science, Hacettepe University, Ankara, Turkey

^cDept. of Electrical and Electronics Engineering, Eskisehir Osmangazi University, Eskisehir, Turkey

ARTICLE INFO*Article history:*

Received 12 January 2021

Revised 17 April 2021

Accepted 24 June 2021

Keywords:

Chest x-ray classification

Nodule classification

Nodule detection

Rib detection

Rib suppression

ROI detection

ABSTRACT

Suspicious regions in chest x-rays are detected automatically, and these regions are classified into three types, including “malignant nodule”, “benign nodule”, and “no nodule” in this study. Firstly, the areas except the lung tissues are removed in each chest x-ray using the thresholding method. Then, Poisson noise was removed from the images by applying the gradient filter. Ribs may overlap onto nodules. Since this circumstance will make the detection of a nodule difficult, it is necessary to distinguish and suppress the ribs. The location of the rib bones is determined by a template matching method, and then the corresponding bones are suppressed by applying the Gabor filter. After this stage, suspicious tissues in the chest x-rays are specified using the Chan-Vese active contour without edges. Then, some features are extracted from these suspicious regions. Six different features are extracted: Statistical, Histogram of Oriented Gradients (HOG)-based, Local Binary Pattern (LBP)-based, Geometrical, Gray Level Co-Occurrence Matrix (GLCM) Texture-based and Dense Scale Invariant Feature Transform (DSIFT)-based. Then, the classification stage is achieved using these features. The best classification result is obtained using statistical, LBP-based, and HOG-Based features. The classification results are evaluated with sensitivity, accuracy, and specificity analyses. K-Nearest Neighbour (KNN), Decision Tree (DT), Random Forest (RF), Logistic Linear Classifier (LLC), Support Vector Machines (SVM), Fisher’s Linear Discriminant Analysis (FLDA), and Naive Bayes (NB) methods are used for the classification purpose separately. The random forest classifier gives the best results with 57% sensitivity, 66% accuracy, 81% specificity values.

© 2021, Advanced Researches and Engineering Journal (IAREJ) and the Author(s).

1. Introduction

Lung cancer is one of the most wide spread causes of death in the World [1]. Structurally, it is based on an uncontrolled proliferation of cells from normal lung tissue to form a mass within the lung. This nodule structure on the lung is often noticed during radiological imaging of the lung rather than as a symptom. The shape and structure of the nodule roughly indicate whether the nodule may be benign or malignant. However, for definitive diagnosis, extract of the nodule and pathological examinations are essential.

Today, different imaging methods (x-ray, tomography, MRI, etc.) are utilized depending on the structure of the nodules and their location in the tissue. However, as this

nodule structure varies from patient to patient in general and is difficult to detect, new approaches are needed in imaging systems. As with other types of cancer, early diagnosis is critical to overcome lung cancer. The X-ray imaging system is one of the oldest and widely used diagnostic systems in the world. In the images obtained from this system, the bones appear black, and the soft tissue appears lighter. Thanks to this contrast difference, the nodule within the bones and soft tissue can be easily distinguished. In addition, the low cost and easy access to x-ray, less radiation, and allowing more frequent follow-up of nodule development make it more preferred than other imaging systems [2].

In the literature, there are many works on lung-based illnesses detection and classification. Abbas et al. developed

* Corresponding author. Tel.: +90-366-280-2932.

E-mail addresses: alicinar@outlook.com.tr (A.Cinar), bengisutopuz@gmail.com (B.Topuz), sergin@ogu.edu.tr (S.Ergin)

ORCID: 0000-0002-3947-7848 (A.Cinar), 0000-0001-6698-5154 (B.Topuz), 0000-0002-7470-8488 (S.Ergin)

DOI: 10.35860/iarej.857579

This article is licensed under the CC BY-NC 4.0 International License (<https://creativecommons.org/licenses/by-nc/4.0/>).

a computer-aided diagnosis (CAD) system for detecting lung nodule cancer earlier. They enhanced the contrast of images using contrast limited adaptive histogram equalization. The segmentation process was done using Otsu's thresholding method. Then, some morphological filters were used to remove background and other geometrical objects. After that, denoised images were obtained using Discrete Wavelet Transform. GLCM was used for feature extraction, and some features were extracted, such as correlation, energy, etc. Principal component analysis was used for feature selection. SVM was used for the classification of benign or malignant tumors. Classification results were given in terms of accuracy, specificity, sensitivity, peak signal to noise ratio, and root mean square errors [3]. Parveen and Khan developed a CAD system for the detection and classification of pneumonia in chest x-ray images. Features are extracted using the HOG technique. SVM, DT and RF were used as classifiers. Classification results were given in terms of accuracy, recall, precision, and F1 score [4]. Gonzalez and Ponomaryov developed a CAD system for lung cancer detection. Firstly, the background tissue was eliminated using the thresholding technique and morphological operations. Then, suspicious regions were calculated using priori information and Hounsfield Units. After that, shape and textural features were extracted. Shape features include area, eccentricity, circularity, and fractal dimension. Texture features include mean, variance, energy, entropy, inverse difference moment, kurtosis, skewness, contrast, smoothness, and correlation. SVM was used as a classifier. Classification results were given in terms of sensitivity, specificity, and accuracy [5]. Tun and Khaing developed a CAD system for lung cancer detection and classification. Median filter was used for preprocessing. Otsu's thresholding method was used for segmentation. Physical dimension measures and the GLCM method were used for feature extraction. Physical dimension measures include area, perimeter, and eccentricity. GLCM-based features are entropy, contrast, correlation, energy, and homogeneity. The artificial neural network was used for classification [6].

The purpose of this study is to detect and classify the different tissues in chest x-rays. At the end of the study, chest x-rays are classified as benign, malignant, and with no nodules. In this context, the database prepared by the Japanese Radiological Technology Association was used [7]. This dataset was chosen because it is free and a public dataset. Moreover, this dataset was used in many works, and thus it gives the advantage to compare with the other works' results.

This study includes 7 sections. In section 2, preprocessing of chest x-ray images is expressed. Detection of suspicious regions is explained in section 3, and feature extraction methods are declared in section 4. In section 5, classification results are given. Conclusions are given in section 6, and discussion is given in section 7. The block diagram shows how the algorithm classifies chest x-ray images in Figure 1.

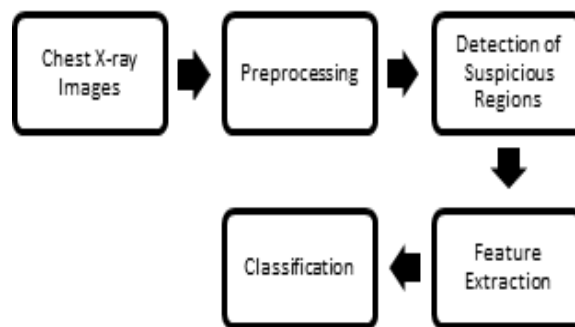


Figure 1. Block Diagram

Nodules appear spherical on chest x-rays. Roughly defined, generally benign nodules have a uniform shape, and malignant nodules have an irregular shape. The greater the diameter of the nodule, the more likely it is to be malignant. In X-rays, ribs may overlap with the nodular region. This is undesirable and may prevent accurate detection of the nodular region. For this reason, the image is preprocessed in order to suppress the ribs. Preprocessing plays a crucial role in image processing and improves the characteristics of the image, and ensures better classification results. After preprocessing, ribs' positions are detected and then suppressed. Subsequently, suspicious regions are specified in the lung and features are extracted from these suspected regions, and the classification stage starts. Different feature extraction methods are tried, and it is seen that which features express benign nodule, malignant nodule, or non-nodule region well according to classification results. Many different classifiers are employed in the classification stage, and it is seen which classifier makes the best classification. Thus, a new region-of-interest (ROI) detection method using the chan-veise algorithm is developed for lung nodule classification. Classification results are given with respect to sensitivity, accuracy and specificity as in the other studies in the literature using the database akin to this study. So as to compare the results obtained with other studies in the literature in a fair manner, only the studies using this database are considered.

2. Preprocessing of Chest X-ray Images

2.1 Segmentation and Denoising of Lung Area

A random chest x-ray is shown in Figure 2a. To segment only lung area, a pixel value 45 was chosen as a threshold value, and all pixel values under 45 changed with 0. Thus, mostly lung area was extracted. However, some non-lung tissues were still visible. A weighted gradient filter was applied to the segmented image to remove Poisson noise, and a gradient image was obtained [8]. Then, a Gaussian weighted filter was applied to the gradient image for smoothing [8]. The segmented denoised image is demonstrated in Figure 2b.

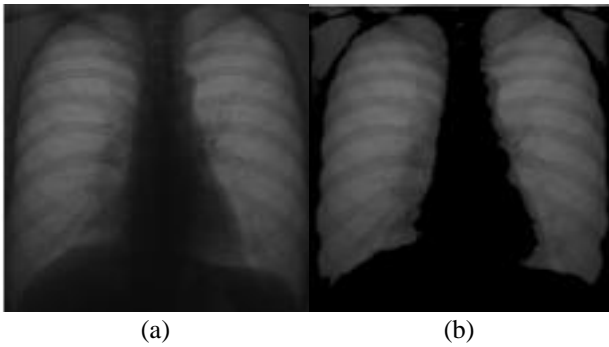


Figure 2. a) The Original image, b) The Segmented denoised image

2.2 Rib Detection and Suppression

200x200 median filter [9] was used to smooth the segmented denoised image [10]. The difference between median filtered and segmented denoised images is shown in Figure 3a [10]. Then, binarization was applied [10]. A threshold value of 0.0005 was chosen for binarization. The pixels with a value of less than 0.0005 were transformed into 0, whereas the ones with a greater value than 0.0005 were changed into 1 as can be seen in Figure 3b. Thus, only the ribs area was extracted.

By completing the binarization operation, ribs were extracted, but there were tissues connected to the ribs. Then, some morphological operations (i.e., closing and opening) were applied to eliminate non-rib tissues. Firstly, a closing operation was applied. The line-shaped structure element with a radius of 20 pixels was created for this operation, and the gaps got filled as in Figure 4a. Afterward, an opening operation was performed.

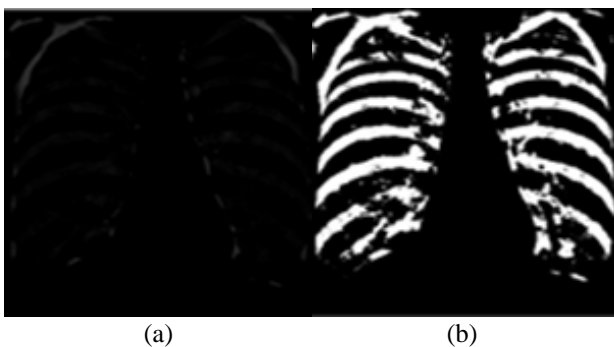


Figure 3. a) The difference between median filtered and the segmented image, b) The binarization applied image

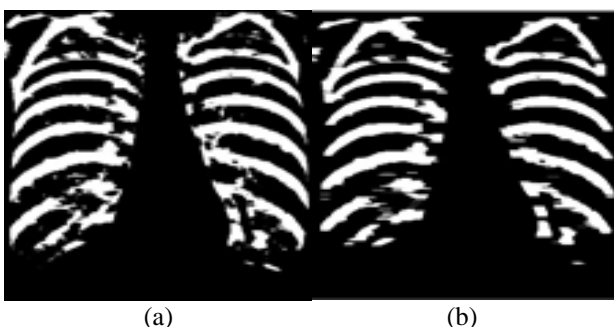


Figure 4. a) The image after the closing operation, b) The image after the opening operation

The line-shaped structure element with a radius of 40 pixels was formed for this operation, and the lines having a radius less than 40 pixels were removed, as can be seen in Figure 4b.

There were still some tissues connected to the ribs. To remove these tissues and record ribs' positions, template matching was applied. Totally two templates were utilized. One of the rib bones from the left side of the lung and one of the rib bones from the right side of the lung were used as a template. The rib bone template, which was selected from the left side of the lung, was used to extract rib bones from the left side of the lung, and the rib bone template which was chosen from the right side of the lung was employed to extract the rib bones from right the side of the lung. For the left side of the lung, the template is shown to the image pixel by pixel. A threshold value was determined to detect rib bones. In each iteration, the amount of overlap between the template and the image was examined. If this amount was larger than the threshold value, the rib bones were detected, and their position was recorded. Thus, more smooth rib structures with reduced tissue were obtained. The same operation was applied to the right side of the lung. Later, the recorded rib bones' pixel values were changed with their original value. After template matching, the detected ribs with their original values are shown in Figure 5a.

Detected ribs should be suppressed. Gabor filter is used for that purpose [11]. The Gabor Filter with a 2 wavelength in pixels/cycle and 0° orientation was applied to the image (see Figure 5a) in order to suppress ribs and the magnitude response of the filter was obtained as seen in Figure 5b [12].

Then, the images in Figure 5a and Figure 5b were summed in the form of a matrix summation. The summation of images is shown in Figure 6a. The new ribs in Figure 6a were replaced with the ribs in the original image which is Figure 2a and Figure 6b illustrates the placement.

The black pixels (non-rib) in Figure 6b were replaced with their original values in Figure 2b, and the new image was obtained in Figure 7a. 3x3 median filter was applied to the image in Figure 7a, and the median filtered image is shown in Figure 7b. Afterwards, an opening operation was applied to the image in Figure 7b. The line-shaped structure element with a radius of 10 pixels is created for this operation.

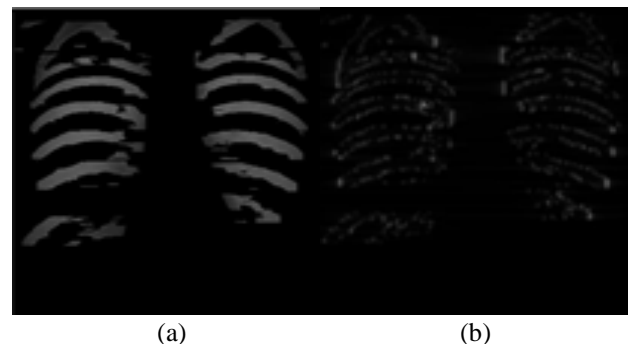


Figure 5. a) The detected ribs, b) The magnitude response of the filter

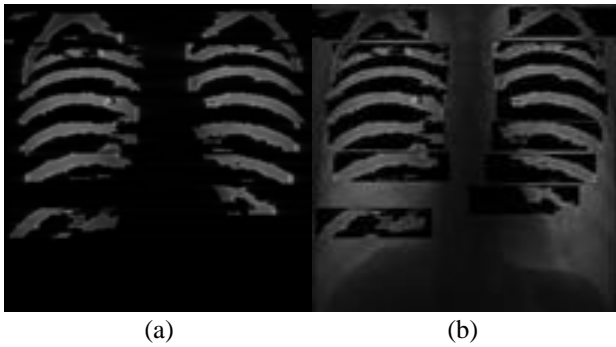


Figure 6. a) The summation of image matrices, b) The placement of the new ribs to the original image

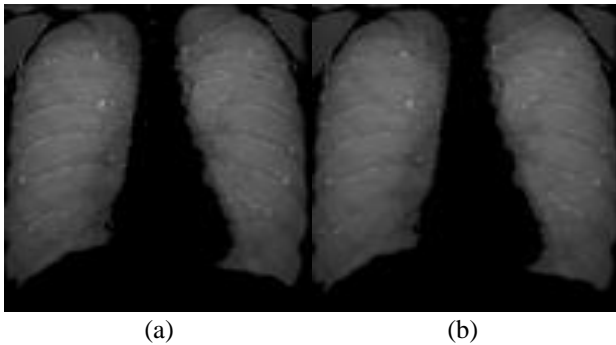


Figure 7. a) The replacement of black pixels with their original values, b) The image after median filtered

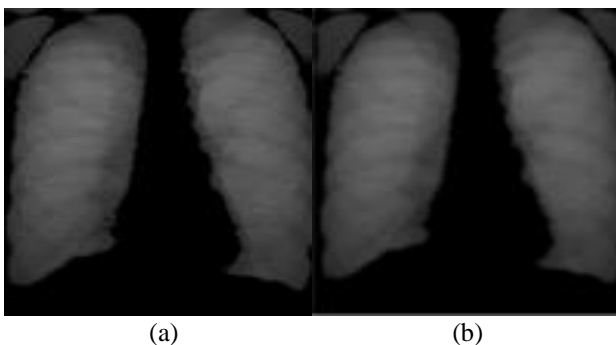


Figure 8. a) The image after the opening operation, b) The ribs suppressed image

The lines having a radius less than 10 pixels were eliminated removed as seen in Figure 8a. Finally, Gaussian Filter [13] with a standard deviation of 2 was applied to the image in Figure 13, thus suppressed ribs of the image are shown in Figure 8b [12].

3. Detection of Suspicious Regions in Chest X-ray Images

3.1 The Chan-Vese Algorithm-Based Approach

In order to obtain more accurate results in the classification of nodules, the suspicious areas on the lung were specified, and feature extraction was made in these suspicious areas. In this study, Chan-Vese active contour without edges method was made use of. The Chan-Vese active contour method without edges is based on the segmentation problem formulated by Mumford and Shah [14].

Equation (1) gives the function that minimizes energy compared to c_1 , c_2 , and C [14]. u_0 represents the image, c_1 can be interpreted as the average value of everything inside the C contour, and c_2 can be interpreted as the average value of everything outside the C contour. Ω_1 refers to the area within the contour, and Ω_2 refers to the area outside the contour.

$$F(c_1, c_2, C) = \int_{\Omega_1=w} (u_0(x, y) - c_1)^2 dx dy + \int_{\Omega_2=\Omega-w} (u_0(x, y) - c_2)^2 dx dy + v|C|, C = \partial w, w \subset \Omega \quad (1)$$

Chan and Vese interpreted the first two terms in Equation (2) as two forces in the article [14]. The first term forces the contour to reduce, and the second term forces the contour to expand. These two forces are compensated when the contour reaches the boundary of the object of interest. The logic of the algorithm is shown in Figure 9 in four cases.

$$F(c_1, c_2, C) = \int_{inside(C)} |u_0 - c_1|^2 dx + \int_{outside(C)} |u_0 - c_2|^2 dx = F_1(C) + F_2(C) \quad (2)$$

In the images in Figure 9, the black parts are indicated by -1, and the gray parts are indicated by 1. When the case (a) is examined in Figure 9, the first contour covers the entire object (-1) and some gray regions (+1). Therefore, c_1 is approximately 0, and c_2 is 1. Subtracting c_2 from the image outside the contour yields 0. Thus, the term F_2 is zero. Since c_1 approaches zero, a large positive number is reached when subtracting c_1 from the image remaining in the contour and finding the sum of the squares as shown by the formula. Therefore, $F_1 > 0$. For $F_1 > 0$ and $F_2 = 0$, the contour will narrow in the next step. The other cases in Figure 9 can be interpreted in this way.

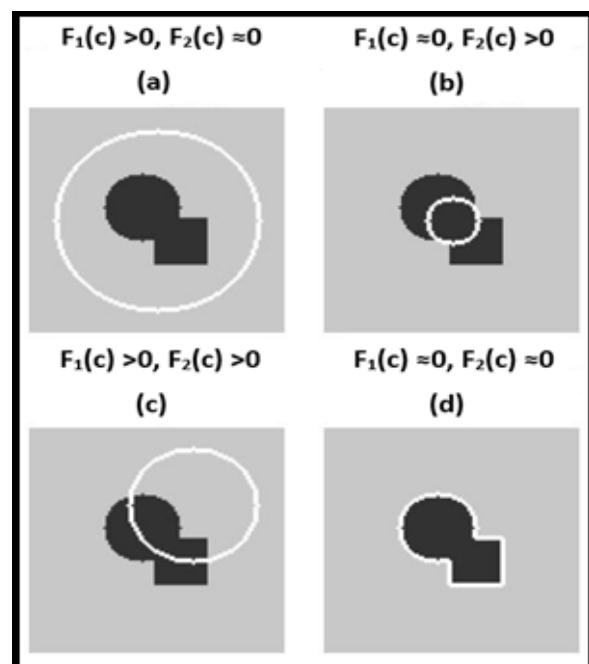


Figure 9. The procedure of the chan-veese algorithm [14]

In the Chan-Vese active contour without edge algorithm, the level set function shows the contour values $\phi(x, y)$. The mathematical expression of the contour curve C is given in Equation (3).

$$C = \{(x, y) : \phi(x, y) = 0\}, \forall(x, y) \in u_0 \quad (3)$$

The change of the contour over time according to the level set function is given in Equation (4).

$$\frac{\partial C}{\partial t} = \frac{\partial \phi(x, y)}{\partial t} \quad (4)$$

4. Feature Extraction Methods

4.1 Statistical Features

Statistical features' success has been explained in many papers. They are extracted from suspicious regions These features are given in Table 1. The feature vector has a dimension that is 12x1 [15]. In Table 1, x_i represents its sample, and N represents the total sample number.

Table 1. The statistical features and their mathematical representations

Statistical Features	Mathematical Representations
Energy	$\sum_{i=1}^N x_i^2$
Mean	$\mu = \frac{1}{N} \sum_{i=1}^N x_i$
Variance	$\frac{1}{N-1} \sum_{i=1}^N (x_i - \mu)^2$
Maximum	$\max\{x_i, 1 \leq i \leq N\}$
Minimum	$\min\{x_i, 1 \leq i \leq N\}$
Standard Deviation	$\sigma = \sqrt{\frac{1}{N-1} \sum_{i=1}^N (x_i - \mu)^2}$
Skewness	$\frac{\frac{1}{N} \sum_{i=1}^N (x_i - \mu)^3}{\sigma^3}$
Kurtosis	$\frac{\frac{1}{N} \sum_{i=1}^N (x_i - \mu)^4}{\sigma^4}$
Area Descriptor [16]	σ / μ
Mean Energy	$\mu_{Energy} = \frac{1}{N} \sum_{i=1}^N x_i^2$
Energy Variance	$\frac{1}{N} \sum_{i=1}^N (X_i^2 - \mu_{Energy})^2$
Entropy	$\sum_{i=1}^N p(X_i) \log_2 p(X_i)$

4.2 Histogram of Oriented Gradients (HOG)-Based Features

HOG-based features yield good results in biomedical pattern recognition problems [17]. HOG-based features are extracted from suspicious regions.

The image gradient vector is defined as a metric for each pixel containing pixel intensity changes on both the x-axis and the y-axis. The definition is given by the gradient of a continuous multivariate function, a vector of partial derivatives of all variables. Suppose that position $F(x, y)$ records the intensity value of the pixel at (x, y) , the gradient vector of the pixel (x, y) is defined as in Equation (5).

$$\nabla f(x, y) = \begin{pmatrix} g_x \\ g_y \end{pmatrix} = \begin{pmatrix} \frac{\partial f}{\partial x} \\ \frac{\partial f}{\partial y} \end{pmatrix} = \begin{pmatrix} f(x+1, y) - f(x-1, y) \\ f(x, y+1) - f(x, y-1) \end{pmatrix} \quad (5)$$

The expression $\partial f / \partial x$ is a partial derivative in the + x direction, calculated as the difference in intensity between adjacent pixels on the left and right of the target pixel. Similarly, $\partial f / \partial y$ is a partial derivative in the + y direction, calculated as the difference in intensity between adjacent pixels above and below the target pixel. The magnitude is the L2 norm of the vector and is calculated as in Equation (6). The orientation is the arctangent of the ratio of partial derivatives to each other in two directions and is calculated as in Equation (7).

$$\nabla f(x, y) = \sqrt{g_x^2 + g_y^2} \quad (6)$$

$$\theta = \arctan\left(\frac{g_y}{g_x}\right) \quad (7)$$

4.3 Local Binary Pattern (LBP)-Based Features

LBP-based features are extracted from suspicious regions. LBP is plain yet a useful tissue operator that marks the pixels of an image by thresholding the neighbourhood of each pixel and sees the result as a binary number [18]. Due to its discriminatory strength and computational simplicity, the LBP tissue operator has become a popular approach in a variety of applications. The most significant aspect of the LBP operator in actual applications is its robustness to monotonic grayscale changes.

The LBP operator replaces the value of pixels of an image with decimal numbers named LBP codes encoding the local structure around each pixel. Each center pixel is compared with its eight neighbours. The neighbours smaller than the value of the central pixel have bit 0, and the other neighbours greater than or equal to the value of the central pixel have bit 1. For each given central pixel, a binary number is generated by combining all of these binary bits clockwise, starting from one of the upper left neighbours. The resulting decimal value of the generated binary number replaces the central pixel value.

The LBP representation of an image is calculated as in Equation (8). In the equation, R is the radius of the circle, P is the number of pixels in the neighbourhood, u is the unit step function, g_i represents the intensity value of the i th neighbouring pixel and g_c stands for the intensity value of the central pixel in the neighbourhood.

$$LBP(P, R) = \sum_{i=0}^{P-1} u(g_i - g_c) \cdot 2^i \quad (8)$$

If the binary pattern consists of no more than two 0-1 or 1-0 transitions, the local binary pattern is called uniform. The rotation-independent patterns are reached by rotating each bit circularly to the minimum value. The rotation-independent patterns are calculated as in Equation (9). The expression U in the equation expresses the uniform criterion.

$$LBP^{riu2}(P, R) = \begin{cases} \sum_{i=0}^{P-1} u(g_i - g_c) U(LBP(P, R)) \leq 2 \\ P + 1 & U(LBP(P, R)) \leq 2 \end{cases} \quad (9)$$

4.4 Geometrical Features

Geometrical features are derived from the suspicious regions in the images. The largest interconnected tissue is specified in the suspicious region, and features; orientation, major axis length, minor axis length, eccentricity, solidity, fullness ratio, diameter, convex area, area, roundness, ovality, and perimeter are extracted.

Area refers to the total number of pixels in the suspicious tissue. The convex area is determined by plotting the smallest convex to contain the suspicious tissue and finding the total number of pixels within that convex. The solidity is found by dividing the total number of pixels (area) within the suspicious tissue into the convex area. The fullness ratio is determined by plotting the smallest rectangle to contain the suspicious tissue and dividing the total number of pixels in the suspicious tissue by the total number of pixels in the rectangle. While the major and minor axis lengths are found, an ellipse is drawn to cover the suspicious tissue. The major axis refers to the length of the ellipse's x-axis in pixels. The minor axis refers to the length of the ellipse's y-axis in pixels. The orientation is the angle between the x-axis and the x-axis of the ellipse. Eccentricity is the ratio of the distance between the foci of the ellipse and the major axis length. The perimeter gives the total number of pixels around the suspicious tissue. The diameter is calculated in Equation (10) as the diameter of a circle that has the same area with the suspected tissue.

$$D = \sqrt{\frac{4 * Area}{\pi}} \quad (10)$$

Ovality indicates how close the suspicious tissue is to the oval shape and is calculated as in Equation (11) [19].

$$O = 2 * \frac{major\ axis\ length - minor\ axis\ length}{major\ axis\ length + minor\ axis\ length} \quad (11)$$

Roundness is calculated as in Equation (12). r is the major axis length divided by the minor axis length [19].

$$Y = \frac{Area}{\pi r^2} \quad (12)$$

4.5 Gray Level Co-Occurrence Matrices (GLCM)-Based Texture Features

GLCM is used for tissue analysis [20]. GLCM, a square matrix, yields certain properties about the spatial distribution of gray levels in the tissue. Each element (i, j) of the GLCM matrix is the number of repetitions of the i and j pixel values at a distance d in Θ direction to each other. An example of how the GLCM matrix is generated is given in Figure 10.

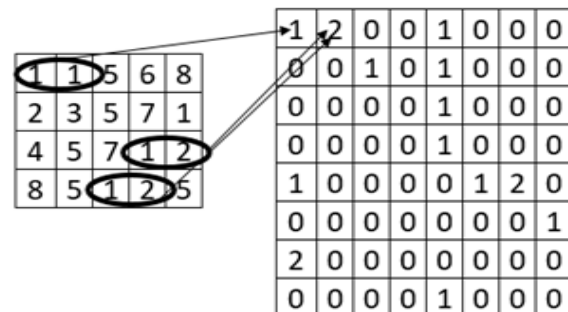


Figure 10. Creating a GLCM matrix

Figure 10 illustrates how often i and j pixel values repeat for $d = 1$ and $\Theta = 0^\circ$. When the i and j pixel values are 1, 1 is written to the first column of the first row in the GLCM matrix since there are no elements in the matrix where the other i and j pixels are equal to 1. Likewise, since there are 2 pairs of pixels in the matrix with a pixel value of $i = 1$ and $j = 2$, 2 is written to the second column of the first row in the GLCM matrix.

Within the scope of the study [20-22], the features extracted from the GLCM matrices were utilized. Equations used for feature extraction are given in Table 2. Features and their mathematical expressions are given in Table 3. A total of 22 different features are extracted from the GLCM matrix [23]. The features given in the table are calculated using the equations given at the beginning of the table. As seen in Table 2; $P(i,j)$ represents elements of the GLCM matrix, and Ng represents the row or column number of the GLCM matrix.

4.6. Dense Scale Invariant Feature Transform (DSIFT)-Based Features

DSIFT descriptors is a well known method to extract features from lesions [24]. DSIFT performs scale invariant feature transform on non-overlapping image blocks with the given radius and returns a 128-dimensional feature vector for each [24].

Table 2. The required equations

$P(i, j): GLCM = \begin{bmatrix} P(1,1) & \dots & P(1, N_g) \\ \vdots & \ddots & \vdots \\ P(N_g, 1) & \dots & P(N_g, N_g) \end{bmatrix}$
$P_x(i) = \sum_{j=1}^{N_g} P(i, j) \quad , \quad P_y(i) = \sum_{i=1}^{N_g} P(i, j)$
$P_{x+y}(k) = \sum_{i=1}^{N_g} \sum_{j=1}^{N_g} P_{i+j=k}(i, j) \quad , k = 2, 3, \dots, 2N_g$
$P_{x-y}(k) = \sum_{i=1}^{N_g} \sum_{j=1}^{N_g} P_{i-j=k}(i, j) \quad , k = 0, 1, \dots, N_g - 1$
$\mu_x = \sum_i \sum_j i \cdot P(i, j) \quad , \quad \mu_y = \sum_i \sum_j j \cdot P(i, j)$
$\sigma_x = \sum_i \sum_j (i - \mu_x)^2 \cdot P(i, j)$
$\sigma_y = \sum_i \sum_j (j - \mu_y)^2 \cdot P(i, j)$

Table 3. The GLCM texture features and their mathematical representations

GLCM Texture Features	Mathematical Representations
Autocorrelation [21]	$\sum_i \sum_j (i \cdot j) \cdot P(i, j)$
Contrast [20, 21]	$\sum_{n=0}^{N_g-1} n^2 \left\{ \sum_{i=1}^{N_g} \sum_{\substack{j=1 \\ i-j =n}}^{N_g} P(i, j) \right\}$
Correlation (MATLAB SUITE)	$\frac{\sum_i \sum_j (i - \mu_x) \cdot (j - \mu_y) \cdot (P(i, j))}{\sigma_x \cdot \sigma_y}$
Korelasyon [20, 21]	$\frac{\sum_i \sum_j (i \cdot j) \cdot P(i, j) - \mu_x \cdot \mu_y}{\sigma_x \cdot \sigma_y}$
Cluster Prominence [21]	$\sum_{i=0}^{N_g-1} \sum_{j=0}^{N_g-1} \{i + j - \mu_x - \mu_y\}^4 \cdot P(i, j)$
Cluster Shade [21]	$\sum_{i=0}^{N_g-1} \sum_{j=0}^{N_g-1} \{i + j - \mu_x - \mu_y\}^3 \cdot P(i, j)$
Dissimilarity [21]	$\sum_i \sum_j i - j \cdot P(i, j)$
Energy [20, 21]	$\sum_i \sum_j \{P(i, j)\}^2$
Entropy [21]	$-\sum_{i=0}^{N_g-1} \sum_{j=0}^{N_g-1} P(i, j) \cdot \log\{P(i, j)\}$
Homogeneity (MATLAB SUITE)	$\sum_i \sum_j \frac{1}{1 + i - j ^2} \cdot P(i, j)$
Homogeneity [21]	$\sum_i \sum_j \frac{1}{1 + (i - j)^2} \cdot P(i, j)$

Table 3. The GLCM texture features and their mathematical Representations (continue)

Maximum Probability [21]	$\max_{i,j} P(i, j)$
Variance [20]	$\sum_i \sum_j (i - \mu)^2 \cdot P(i, j)$
Sum Average [20]	$\sum_{i=2}^{2N_g} i \cdot P_{x+y}(i)$
Sum Variance [20]	$\sum_{i=2}^{2N_g} (i - \text{Sum Average})^2 \cdot P_{x+y}(i)$
Sum Entropy [20]	$-\sum_{i=2}^{2N_g} P_{x+y}(i) \cdot \log\{P_{x+y}(i)\}$
Difference Entropy [20]	$-\sum_{i=2}^{2N_g} P_{x-y}(i) \cdot \log\{P_{x-y}(i)\}$
Information Measure of Correlation 1 [20]	$\frac{HXY - HXY1}{\max\{HX; HY\}}$ $HXY = -\sum_i \sum_j P(i, j) \cdot \log(P(i, j))$ $HXY1 = -\sum_i \sum_j P(i, j) \cdot \log(p_x(i) \cdot p_y(j))$ <p><i>HX and HY are entropies of p_x and p_y</i></p>
Information Measure of Correlation 2 [20]	$(1 - \exp[-2 \cdot (HXY2 - HXY)])^{1/2}$ $HXY2 = -\sum_i \sum_j P_x(i) \cdot P_y(j) \cdot \log\{P_x(i) \cdot P_y(j)\}$
Inverse Difference Normalized [22]	$\sum_i \sum_j \frac{1}{1 + i - j ^2 / N_g^2} \cdot P(i, j)$
Inverse Difference Moment Normalized [22]	$\sum_i \sum_j \frac{1}{1 + (i - j)^2 / N_g^2} \cdot P(i, j)$

5. Experimental Study

5.1 Database

The database [10] of Japanese Society of Radiological Technology (JSRT) was used for this study. It is a digital public database with and without lung nodules. It contains 247 chest x-rays, among which 154 x-rays are abnormal, and 93 x-rays are normal. Out of 156 abnormal x-rays, 100 of them contain malignant nodules, and 54 of them contain benign nodules. Nodule diameters vary from 1mm to 60 mm. All x-ray images have a size of 2048×2048 pixels and a gray-scale color depth of 8 bits [10].

5.2. Revealing of Suspicious Tissue Regions

In all of the images, the Chan-Vese active contour without edge algorithm made the same number of iterations and

found suspicious regions. For each suppressed rib image like in Figure 8b, the suspected regions of the left lung and the right lung were specified separately, and the starting contour was applied in the same manner.

The initial contour was taken as in Figure 11. The pixel value of the black pixels (pixel value=0) in each suppressed rib image was changed to 118 before suspicious regions were specified. For the left lung, the replacement of black pixels in a suppressed rib image with the value of 118 pixels is given in Figure 12a. The Chan-Vese algorithm had 1500 iterations, and suspicious regions were segmented. The white areas in Figure 12b show the locations that the algorithm found suspicious. The same procedures were performed in the right lung. Some examples that how the algorithm found suspicious regions were given in Figure 13a and Figure 13b.

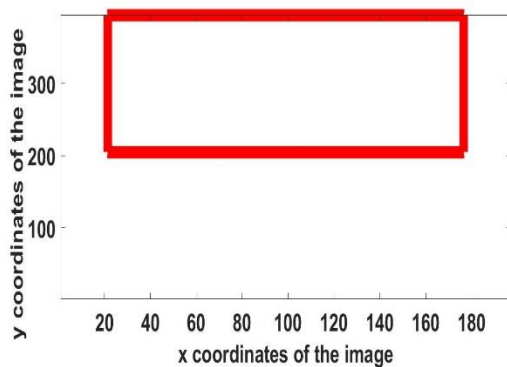


Figure 11. The frame (red colored rectangle) for the initial Contour

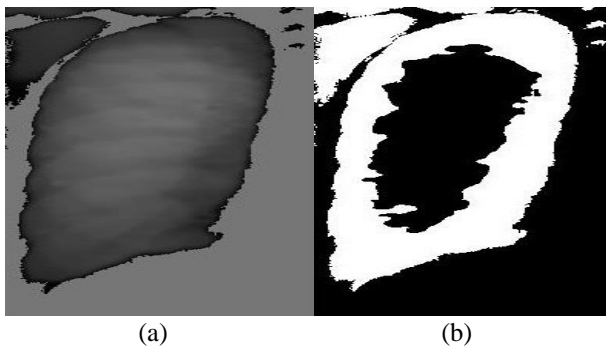


Figure 12. a) The image after the replacement of black pixels with the value of 118, b) The segmentation of the suspicious region

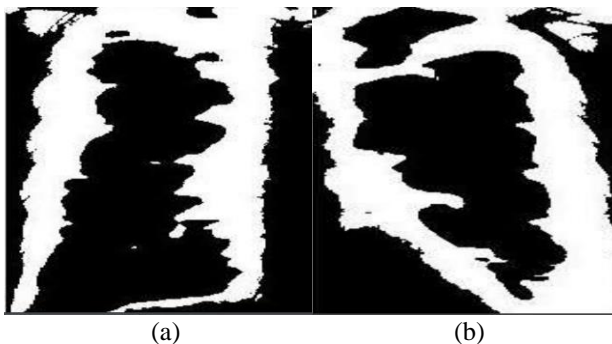


Figure 13. a) The example of how the algorithm found suspicious regions on left lung, b) The example of how the algorithm found suspicious regions on right lung

5.3. Feature Extraction and Classification of Detected Suspicious Tissues

The regions with a size of 32x32 were selected randomly from the suspicious regions in each image, and feature vectors were created from these regions. For each image, first, all of the feature extraction methods described in subsection 4 were extracted separately, and the classification success of each feature vector was examined. Then, the feature vector was created by using the features with high success, and the classification successes were explored again.

The method of 10-fold cross-validation was utilized in the classification. 90% of the images in each class were used for the training and 10% for the test purposes. The classification was completed in 10 stages. At each stage, 10% of each class entered the test phase, and the classification success was calculated on the basis of sensitivity, accuracy, and specificity. Then, these values were summed and averaged, so the system's sensitivity, accuracy, and specificity were found. The formulas for performance evaluation metrics (sensitivity, accuracy, and specificity) are given in the Table 4. Classifiers used; KNN (k = 5) [25], RF(number of trees = 100) [26], DT [27], NB [28], LLC [29], SVM [30], and FLDA [31].

Specificity percentage shows that how the algorithm is well enough to identify lungs without disease. Sensitivity percentage shows that how the algorithm is well enough to identify lungs with disease. Accuracy percentage shows that how the algorithm differentiates disease and without disease conditions correctly.

Firstly, all feature extraction methods described in subsection 4 was used separately to see which method gave the best result. The region with a size of 32x32 was converted to 1024x1 size of vector, and the statistical features were generated from 1024x1 vector. The feature vector obtained using only statistical properties has a size of 12x1. All the other features were extracted from the region with a size of 32x32 without converting to a vector. The GLCM matrix was formed by taking $d = 2$ and $\Theta = 0^\circ$. The GLCM-based texture features were extracted from this GLCM matrix.

Table 4. The evaluation criteria and their mathematical expressions

Evaluation Criteria	Mathematical Expressions
	TP: True Positive, TN: True Negative FP: False Positive, FN: False Negative S: Class Number, V_j = data number who belongs to jth class
Sensitivity (SNS)	$SNS\% = \frac{TP}{TP+FN} \cdot 100$
Specificity (SPC)	$SPC\% = \frac{TN}{TN+FP} \cdot 100$
Accuracy (ACC)	$ACC\% = \frac{\sum_{j=1}^S SNS_j \cdot V_j}{\sum_{j=1}^S V_j}$

The feature vector created using GLCM-based texture features only has a size of 22x1. The rotation invariant LBP-based features were extracted. The radius of the circle is 1, and the number of pixels in the neighbourhood is 8. The feature vector obtained using LBP-based features only has a size of 10x1. The geometrical features were extracted. The feature vector obtained using only geometrical features has a size of 12x1. 16x16 cell size HOG was applied to the region with a size of 32x32, and the features were obtained. The feature vector obtained using HOG only has a size of 36x1. DSIFT-based features were extracted. The feature vector created using only DSIFT-based features has a size of 64x1. All feature vectors' sensitivity, accuracy, and specificity values for each classifier were calculated and presented in Table 5.

As seen in table 5, statistical features gave the best results. Then, statistical features were combined with the other features, and it was found which combination gave the best result. Statistical and HOG-based features were used together, and a 48x1 size vector was obtained.

Table 5. The sensitivity, accuracy, and specificity values for each classifier and feature vectors

	Criteria	KNN	FLDA	RF	DT	SVM	NB	LLC
Statistical Features	ACC%	53%	59%	60%	56%	33%	59%	43%
	SNS%	50%	49%	51%	50%	26%	51%	33%
	SPC%	76%	78%	79%	78%	63%	79%	67%
GLCM-based texture features	ACC%	39%	43%	44%	38%	48%	45%	49%
	SNS%	36%	37%	39%	34%	39%	43%	40%
	SPC%	70%	71%	71%	68%	71%	73%	71%
LBP-based features	ACC%	42%	50%	54%	46%	52%	45%	52%
	SNS%	41%	41%	47%	42%	42%	40%	43%
	SPC%	71%	72%	75%	72%	73%	71%	73%
Geometrical Features	ACC%	40%	48%	46%	44%	48%	47%	47%
	SNS%	38%	40%	39%	41%	39%	40%	39%
	SPC%	70%	71%	71%	72%	71%	72%	70%
HOG-based features	ACC%	43%	49%	53%	43%	55%	45%	55%
	SNS%	38%	43%	44%	40%	46%	39%	45%
	SPC%	72%	73%	74%	71%	75%	72%	75%
DSIFT-based features	ACC%	50%	45%	58%	45%	47%	51%	51%
	SNS%	45%	41%	48%	41%	37%	43%	41%
	SPC%	75%	72%	77%	72%	69%	74%	72%

Table 6. The sensitivity, accuracy, and specificity values for each classifier and combination of feature vectors

	Criteria	KNN	FLDA	RF	DT	SVM	NB	LLC
Statistical and HOG-based Features	ACC%	52%	57%	64%	54%	32%	52%	43%
	SNS%	50%	51%	55%	49%	25%	47%	33%
	SPC%	76%	78%	81%	77%	62%	76%	67%
Statistical and LBP-based Features	ACC%	52%	51%	60%	54%	32%	53%	41%
	SNS%	50%	43%	51%	50%	25%	48%	33%
	SPC%	76%	74%	79%	77%	62%	77%	66%
Statistical and DSIFT-based Features	ACC%	51%	45%	59%	50%	32%	51%	43%
	SNS%	48%	39%	49%	46%	25%	43%	34%
	SPC%	76%	72%	78%	75%	62%	75%	67%
Statistical, HOG- and DSIFT-based Features	ACC%	51%	43%	60%	51%	32%	53%	42%
	SNS%	49%	39%	49%	46%	26%	45%	34%
	SPC%	76%	74%	79%	77%	62%	77%	66%
Statistical, HOG- and LBP-based Features	ACC%	54%	55%	66%	50%	32%	53%	43%
	SNS%	51%	49%	57%	46%	27%	50%	33%
	SPC%	78%	78%	81%	75%	64%	77%	67%

Statistical and LBP-based features were used together, and a 22x1 size vector was obtained. Statistical and DSIFT-based features were used together, and a 76x1 size vector was obtained. It was seen that the combination of statistical and HOG-based features gave the best results. Afterwards, DSIFT-based features and LBP-based features were added to the combination of statistical and Hog-based features separately to see which gave the best results. Statistical, HOG-based, and DSIFT-based features were used together, and a 112x1 size vector was obtained. Statistical, HOG-based, and LBP-based features are used together, and 58x1 size vector is obtained. Sensitivity, accuracy, and specificity values for each classifier and combination of feature vectors were calculated and presented in Table 6.

6. Discussion

The findings are in line with the literature. If the classification results (accuracy=66%, sensitivity=57%, and specificity=81%) are compared to the studies' results which use the same JSRT database in the literature, it gives the top

eight result among the other up to date works [10]. It is important to compare the proposed study with other studies that only used the JSRT database in terms of being fair because the choice of the database directly affects the results. Moreover, all the manuscripts that compared use image processing techniques. It is also essential in terms of making a fair comparison because it is known that many deep learning algorithms are used in this area.

7. Conclusions

In this study, a new region of interest (ROI) detection method using the Chan-Vese algorithm for lung nodule classification was proposed. Firstly, chest x-rays were preprocessed to suppress ribs. Then, suspicious tissue regions were determined in each x-ray by applying the Chan-Vese algorithm. The suspicious regions were successfully specified with a sensitivity score of 73%. The regions with a size of 32x32 were selected randomly from suspicious regions for each image, and then, different feature vectors were extracted from these selected regions. Finally, the chest x-rays were classified into three groups, including no nodule, benign nodule, and malignant nodule.

As seen in Table 6, the whole aggregation of the HOG-, LBP-based and statistical features yielded the best classification results (accuracy=66%, sensitivity=57%, and specificity=81%) with the random forest classifier when tree number was 100. Thus, starting from the best individual performance among all the types of the features, the dual combinations of the features in which the statistical features remain constant in every possible case were tested. Then the best triplet combination was constructed using the best dual combinations of the features according to accuracy, sensitivity, and specificity performances. This manner of increase in the number of features is an elaborative search in order to identify the most suitable feature-classifier combination. The random forest classifier mostly generated better classification results compared to the other classifiers.

Declaration

The authors declared no potential conflicts of interest with respect to the research, authorship, and/or publication of this article. The authors also declared that this article is original, was prepared in accordance with international publication and research ethics, and ethical committee permission or any special permission is not required.

Author Contributions

S. Ergin supervised and guided the study. B. Topuz did some preprocessing operations on chest x-ray images, interpreted the JSRT database, and adjusted parameters in the chan-vese algorithm. A. Cinar did some preprocessing, feature extraction, classification, and detected suspicious regions.

References

1. Stewart, B., C.P. Wild, *World Cancer Report 2014*. 2015, WHO Press.
2. Garfinkel, L., G. Murphy, W.J. Lawrence, R.J. Lenhard, *American Cancer Society Textbook of Clinical Oncology*. 1995, The Society Press.
3. Abbas, W., K.B. Khan, M. Aqeel, M.A. Azam, M.H. Ghouri, F.H. Jaskani, *Lungs Nodule Cancer Detection Using Statistical Techniques*. IEEE 23rd International Multitopic Conference, 2020, Pakistan. p. 1-6.
4. Parveen, S., K.B. Khan, *Detection and classification of pneumonia in chest X-ray images by supervised learning*. IEEE 23rd International Multitopic Conference, 2020, Pakistan, p. 1-5.
5. Gonzalez, E.R., V. Ponomaryov, *Automatic Lung nodule segmentation and classification in CT images based on SVM*. 9th International Kharkiv Symposium on Physics and Engineering of Microwaves, Millimeter and Submillimeter Waves, 2016, Ukraine. p. 1-4.
6. Tun, K.M.M, A.S. Khaing, *Feature Extraction and Classification of Lung Cancer Nodule using Image Processing Techniques*. International Journal of Engineering Research & Technology, 2014. **3**(3): p. 2204-2210.
7. Shiraishi, J., S. Katsuragawa, J. Ikezoe, T. Matsumoto, T. Kobayashi, K. Komatsu, M. Matsui, H. Fujita, Y. Kodera, K. Doi, *Development of a digital image database for chest radiographs with and without a lung nodule: Receiver operating characteristic analysis of radiologists' detection of pulmonary nodules*. AJR, 2000. **174**(1): p. 71-74.
8. Khan, K.B., A.A. Khaliq, M. Shadid, J.A. Shah, *A new approach of weighted gradient filter for denoising of medical images in the presence of Poisson noise*. Tehnički vjesnik, 2016. **23** (6): p. 1755-62.
9. Gallagher, N., G. Wise, *A theoretical analysis of the properties of median filters*. IEEE Transaction on Acoustic Speech Signal Processing, 1981. **29** (6): p. 1135-1141.
10. Wang, C., A. Elazab, J. Wu, Q. Hua, *Lung nodule classification using deep feature fusion in chest radiography*. Computerized Medical Imaging and Graphics, 2017. **57**: p. 10-18.
11. Gabor, D., *Theory of communication*. Journal of the Institution of Electrical Engineers- Part III: Radio and Communication Engineering, 1946. **93**(26): p. 429-457.
12. Soleymanpour, E., H.R. Pourreza, E. Ansariour, M. Sadooghi, *Fully Automatic Lung Segmentation and Rib Suppression Methods to Improve Nodule Detection in Chest Radiographs*. Journal of Medical Signals and Sensors, 2011. **1**(3): p. 191-199.
13. Haddad, R.A., A.N. Akansu, A, *Class of Fast Gaussian Binomial Filters for Speech and Image Processing*, IEEE Transactions on Acoustics, Speech and Signal Processing, 1991. **39**(3): p. 723-727.
14. Chan, T.F., L.A. Vese, *Active contours without edges*. IEEE Transactions on Image Processing, 2001. **10**(2): p. 266-277.
15. Esener, I.I., S. Ergin, T. Yuksel, *A New Feature Ensemble with a Multistage Classification Scheme for Breast Cancer Diagnosis*. Journal of Healthcare Engineering, 2017. **2017**: p. 1-15.
16. Ahonen, T., A. Hadid, M. Pietkäinen, *Face description with local binary patterns: Application to face recognition*. IEEE Transactions on Pattern Analysis and Machine Intelligence,

2006. **28**(12): p. 2037-2041.
17. Song, L., X. Liu, L. Ma, C. Zhou, X. Zhao, Y. Zhao, *Using HOG-LBP features and MMP learning to recognize imaging signs of lung lesions*. 25. International Symposium On Computer-Based Medical Systems, 2012, Italy. p. 1-4.
 18. Wang, L., D.C. He, *Texture Classification Using Texture Spectrum*, Pattern Recognition, 1990. **23**(8): p. 905-910.
 19. Esener, I.I., *The Identification of Suspicious Regions on Mammography Images for Breast Cancer and the Classification of Breast Cancer Type*. PhD Thesis, Eskisehir Osmangazi University, 2017.
 20. Haralick, R.M., K. Shanmugam, I. Dinstein, *Textural features of image classification*. IEEE Transactions on Systems, Man, and Cybernetics, 1973. **SMC-3**(6): p. 610-621.
 21. Soh, L., C. Tsatsoulis, *Texture analysis of SAR sea ice imagery using gray level co-occurrence matrices*. IEEE Transactions on Geoscience and Remote Sensing, 1999. **37**(2): p. 780-795.
 22. Clausi, D.A., *An analysis of co-occurrence texture statistics as a function of grey level quantization*. Canadian Journal of Remote Sensing, 2002. **28**(1): p. 45-62.
 23. Esener, I.I., S. Ergin, T. Yuksel, *A Genuine GLCM-based Feature Extraction for Breast Tissue Classification on Mammograms*. International Journal of Intelligent Systems and Applications in Engineering, 2016. **4**(Special Issue): p. 124-129.
 24. Ergin, S., O. Kilinc, *Using DSIFT and LCP features for detecting breast lesions*. ISCSE, 2013. International Symposium on Computing in Science & Engineering. Proceedings: Izmir. p. 216-220.
 25. Kim, J., B.S. Kim, S. Savarese, *Comparing image classification methods: K-nearest-neighbor and support-vector-machines*. 6. WSEAS International Conference on Computer Engineering and Applications, 2012, World Scientific and Engineering Academy and Society: USA. p. 133-138.
 26. Akar, O., O. Gungor, *Classification of multispectral images using Random Forest Algorithm*. Journal of Geodesy and Geoinformation, 2012. **1**(2): p. 105-112.
 27. Safavian, S.R., D. Landgrebe, *A survey of decision tree classifier methodology*. IEEE Transactions on Systems, Man, and Cybernetics, 1991. **21**(3): p. 660-674.
 28. Rish, I., *An empirical study of the naive Bayes classifier*. IJCAI Workshop on Empirical Methods in artificial intelligence, 2001, IBM New York: USA. p. 41-46.
 29. Webb, A.R., *Linear discriminant analysis in Statistical Pattern Recognition*. 2002, John Wiley & Sons.
 30. Ozkan, K., S. Ergin, S. Isik, I. Isikli, *A new classification scheme of plastic wastes based upon recycling labels*, Waste Management, 2015. **35**: p. 29-35.
 31. Fisher, R.A., *The use of multiple measurements in taxonomic problems*. Annals of Eugenics, 1936. **7**(2): p. 179-188.

**Research Article**

A comparative study on appliance recognition with power parameters by using machine learning algorithms

Yılmaz Güven^{a,*} 

^aVocational School of Technical Science, Kırklareli University, Kırklareli 39100, Turkey

ARTICLE INFO*Article history:*

Received 03 February 2021

Revised 24 May 2021

Accepted 18 June 2021

Keywords:

Appliance recognition

Data pre-processing

Feature extraction

Grey relational analysis

Machine learning

ABSTRACT

Recently, machine Learning algorithms are widely used in many fields. Especially, they are really good to create prediction models for problems which are not easy to solve with conventional programming techniques. Although, there are many different kinds of machine learning algorithms, results of applications are varying depend on type of data and correlation of information. In this study, different machine learning algorithms have been used for appliance recognition. The measurement data of Appliance Consumption Signatures database and some derivative values have been used for training and testing. Additionally, a data pre-processing technique and its effects on results have been presented. Filtering corrupted data and removing uncertain measurement value has improved the quality of machine learning. Combination of machine learning algorithms is best way to work with uncertain values. Different feature extraction methods and data pre-processing techniques are crucial in machine learning. Therefore, this study aims to develop a high accurate appliance recognition technique by combining grey relational analysis and an ensemble classification method. The results of this new method have been presented comparatively to show the improvement for itself and previous studies that uses the same database.

© 2021, Advanced Researches and Engineering Journal (IAREJ) and the Author(s).

1. Introduction

Energy saving techniques are current discussions because of increased energy consumption rates. Nearly, half of all energy consumption is related to buildings and houses all over the world. That is why, attentions to smart homes and smart energy distribution system are on high demand. The main purpose of a smart system is being aware of all information around it. This way it can calculate, predict and make planning for better working conditions.

In this study, we have focused on appliance recognition techniques for buildings and houses. It is crucial to know which appliance is working and how often it is on for prediction of energy consumption. On the other hand, this information might be useful for other smart system such as security, telemetry and smart grids. There are many recognition and prediction methods in data science. Engineering methods, Statistical methods, neural

networks, support vector machines and grey models are commonly used [1]. Home energy management system with load monitoring and power scheduling has already facilitated [2]. Prototype of low-cost power smart meter has been developed for photovoltaic prosumers [3].

Furthermore, many datasets have been established for appliance recognition and identification. The most recent one is a voltage and current measurement dataset for plug loads [4]. This data set contains 17 different appliances from 330 different makes and models. The another one is

ACS (Appliance Consumption Signatures) database [5]. We have preferred to use this database for our study because of its low sampling frequency. This database contains 15 different appliances from 225 brands. It also has two separate measurement sessions for training and testing. Some other researchers have also focused on real-time recognition and profiling by using a single electricity sensor [6]. All these works show us that future of electric

* Corresponding author. Tel.: +90 288 214 1845; Fax: +90 288 214 1495.

E-mail addresses: yilmaz.guven@klu.edu.tr (Y. Güven)

ORCID: 0000-0002-8205-2490 (Y. Güven)

DOI: 10.35860/iarej.873644

This article is licensed under the CC BY-NC 4.0 International License (<https://creativecommons.org/licenses/by-nc/4.0/>).

energy delivery and management systems cannot be apart from information system and internet technologies [7].

Previous studies show that it is hard to detect some appliance while some are easy. Different data preparation techniques have been used for better accuracy. For example, moving average technique has been used with machine learning algorithms [8]. Result of this work was promising but dataset was limited. Some other researchers who have been using the extended database for developing automatic household appliances identification [9] have achieved relatively better results. On the other hand, non-intrusive methods show that more than one identification techniques improve the accuracy of the system [10].

Future of intelligent power system is depending on machine learning algorithms. Identifying loads and forecasting electricity consumption is crucial. Ensemble machine learning based artificial neural networks can be used for load forecasting [11]. Non-intrusive appliance recognition techniques can be applied by using machine learning for better and low-cost intelligent measurement device [12]. It is really important to identify power consumption of different appliance from a single metering point in smart buildings [13].

Building automation and management systems require real-time, end to end solutions for appliance recognition as internet of things device [14]. Smart outlets are easiest way to measure and identify each individual appliance with simple machine learning techniques [15].

All these studies show that data preparation techniques and classification methods must be choose wisely. In this study, some popular machine learning algorithms have been compared by using latest ACS dataset for appliance recognition. The advantages of different data pre-processing and feature extraction techniques have been cited.

2. Material and Method

2.1 The Database

The ACS database contains electrical consumption signatures of 15 different appliance categories with 225 different brands. The measurements (Table 1) of real power, reactive power, frequency, phase angle, RMS current and RMS voltage were recorded at low sampling frequency as 0,1 Hz [16]. Low sampling rate is good for both energy saving and reducing the data size.

Table 1. The measurement detail of dataset

Value	Symbol	Unit
Frequency	F	Hz
Phase Angle	φ	°
Real Power	P	W
Reactive Power	Q	VAR
RMS Current	IRMS	A
RMS Voltage	VRMS	V

The database has two distinct session for different measurements. The first one is for using as training data and the second one is for testing purpose. This way, we can test the system with new unknown data. The database contains hours of measurement data which provide us more than eighty thousand samples of 15 different appliances.

2.2 Pre-processing

Real world data must be pre-processed for preparation before analysis. There are many different types of data pre-processing techniques. The main purposes of these techniques are removing errors, noises and inconsistent data as much as normalize and improve the quality of the data [17].

All measurements contain samples in time series so they need to be expressed with dynamic coefficients. The coefficient can be calculated by using different methods such as moving average, velocity and acceleration or standard deviation. On the other hand, normalization of these data is another step of data preparation. This study will demonstrate a combined data preparation technique which does both calculating dynamic coefficients and normalize the data at the same time.

Grey Relational Analysis (GRA) is a new approach in grey system theory. It is good for calculating the relation between multiple factors and variable. Since our data has different range with different units, it is good to use GRA for pre-processing. You can choose whether higher-better as in Equation (1) or lower-better as in Equation (2) approach in GRA. It means that your data will reference 0 or 1 depends on your approach [18].

$$X_i(k) = \frac{X_i - \min X_i}{\max X_i - \min X_i} \quad (1)$$

$$X_i(k) = \frac{\max X_i - X_i}{\max X_i - \min X_i} \quad (2)$$

Where i represent the original sequence index number and k represent after pre-processing, max and min are the maximum and minimum value of the data sequence.

Then the deviation sequences as in Equation (3) and grey relational coefficient can be calculated by using Equation (4).

$$\Delta_i(k) = |X_i(k) - X_0(k)| \quad (3)$$

$$C_i(k) = \frac{\Delta_{\min} + q\Delta_{\max}}{\Delta_i(k) + q\Delta_{\max}} \quad (4)$$

Where X_0 is reference sequence, Δ_{\min} and Δ_{\max} minimum and maximum values of Δ_i and q is adjustment coefficient which is between 0 and 1 (normally 0.5).

Finally, grey relational grade (GRG) for each sample can be calculate as in Equation (5).

$$Y_i(k) = \frac{1}{n} \sum_{k=1}^n C_i(k) \quad (5)$$

Where Y_i represents GRG, which is the correlation level of normalised inputs, $k=1\dots n$; n is the number of the parameters, $i=1\dots m$; m is the number of the data items in the sequence.

2.3 Machine Learning

Machine learning (ML) can be describe as building a model from previous experience to predict outcomes of future problems. Most popular applications of ML are used for classification, data preparation, supervised learning, generalization, support vector machines, decision trees, nearest neighbour and clustering. For better accuracy and speed more than one technique can be used combined for ensemble learning such as boosting, bagging, random subspace and predictors ensemble [19].

A learning algorithm can be supervised, unsupervised or reinforcement. Supervised means input and target vectors are together in the training set while unsupervised learning doesn't contain target vector in the training set. This is also known as labelling. The reinforcement learning doesn't need labels as it takes action in order to maximize notion of cumulative reward [20].

Decision trees are fast and use less memory but they have low predictive accuracy. Discriminant analysis methods are fast and accurate but they are not flexible. Support Vector Machines are hard to interpret and use large amount of memory. Nearest neighbour classifiers generally have good results in low size data with high memory usage. For these reasons, ensemble classifiers are generally used to combine more than one learning technique to build a high-quality model (Figure 1).

Although, there are many ensemble methods by manipulating error function, labels, feature space, training or test parameters; three general approaches emerge [21]. The first approach is Majority voting as in Equation (6) which is the simplest one because it neither requires previous data nor complex computation. However, it can make poorly decisions because it votes all classifier equally so a weighted voting as in Equation (7) can improve the result by reducing effect of poor classifiers. Furthermore, a Bayesian combination as in Equation (8) makes each classifiers' error can affect the result with different weights by using previous knowledge [22].

$$C_e = \arg \max \{ \sum_{n=1}^k S_i C_n \} \tag{6}$$

$$C_e = \arg \max \{ \sum_{n=1}^k W_n S_i C_n \} \tag{7}$$

$$C_e = \arg \max \{ \mu \prod_{n=1}^k P(C_i | C_n) \} \tag{8}$$

Where C_e ensemble output, C_n is the class, S_i is the classifier ($1 \leq i \leq m$), W_n is the weight of n th classifier as follows in Equation (9).

$$W_n = \frac{1 - E_n}{\sum_k (1 - E_k)} \tag{9}$$

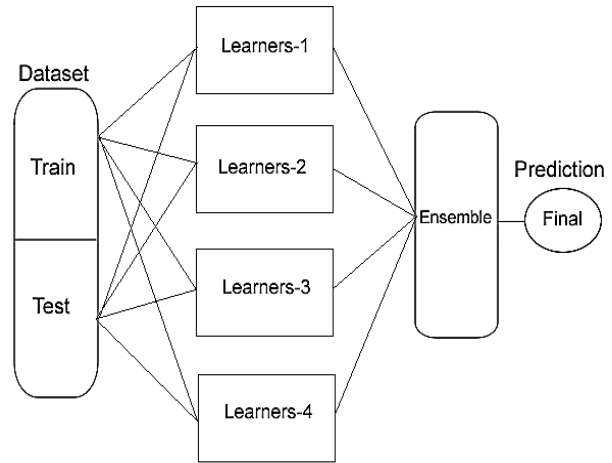


Figure 1. Ensemble Techniques Diagram

Where E_n is the error of n th classifier and E_k is the error of combined classifiers.

3. Result and Discussion

The database contains 15 different appliance types with 15 different brands. Active and reactive power distribution of the appliances is shown in Figure 2. For better feature extraction, derivative values such as apparent power as in Equation (10), power factor as in Equation (11), active as in Equation (12) and reactive power as in Equation (13) have been created by using database measurement data.

$$S = \sqrt{P^2 + Q^2} \tag{10}$$

$$\cos \varphi = \frac{P}{S}, \sin \varphi = \frac{Q}{S} \tag{11}$$

$$P = V_{RMS} \cdot I_{RMS} \cdot \cos \varphi \tag{12}$$

$$Q = V_{RMS} \cdot I_{RMS} \cdot \sin \varphi \tag{13}$$

Where S is apparent power, P is active power, Q is reactive power, φ is power factor, V_{rms} and I_{rms} are root mean square value of voltage and current.

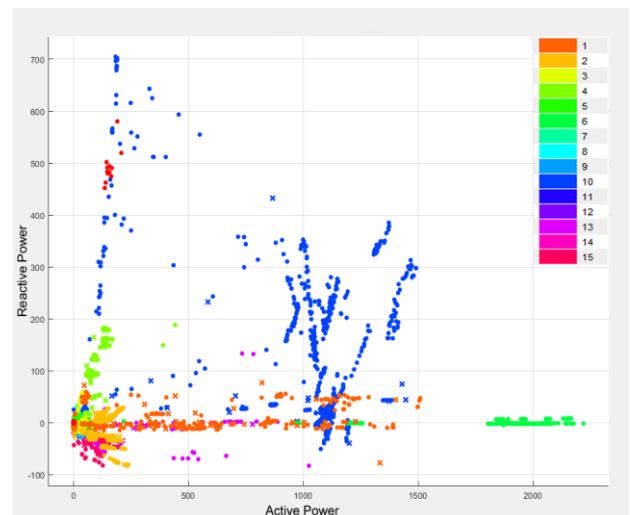


Figure 2. Distribution of classes

Table 2. Raw data and 6 features

Classifier	Type	Train	Test	Drop
Decision Tree	Fine	63.9%	57.7%	6.20%
Discriminant	Linear	26.6%	26.15%	0.45%
Naïve Bayes	Kernel	55%	53.06%	1.94%
Support Vector Machine	Fine Gaussian	76.7%	64.53%	12.17%
k-Nearest Neighbor	Fine	77.6%	62.51%	15.09%
Ensemble Method	Bagged Trees	81.4%	72.9%	8.50%

Table 3. Raw data and 12 features

Classifier	Type	Train	Test	Drop
Decision Tree	Fine	67.9%	62.95%	4.95%
Discriminant	Linear	39%	38.45%	0.55%
Naïve Bayes	Kernel	56.5%	54.09%	2.41%
Support Vector Machine	Fine Gaussian	79%	69.38%	9.62%
k-Nearest Neighbor	Fine	78.9%	64.22%	14.68%
Ensemble Method	Bagged Trees	80%	73.05%	6.95%

Table 4. GRA data and 6 features

Classifier	Type	Train	Test	Drop
Decision Tree	Fine	85%	81.65%	3.35%
Discriminant	Linear	54%	51.2%	2.80%
Naïve Bayes	Kernel	40.7%	35.6%	5.10%
Support Vector Machine	Fine Gaussian	91.8%	80.16%	11.64%
k-Nearest Neighbor	Fine	98%	80.93%	17.07%
Ensemble Method	Bagged Trees	98.8%	88.28%	10.52%

Table 5. GRA data and 12 features

Classifier	Type	Train	Test	Drop
Decision Tree	Fine	85.3%	81.88%	3.42%
Discriminant	Linear	62.4%	52.23%	10.17%
Naïve Bayes	Kernel	41.4%	36.98%	4.46%
Support Vector Machine	Fine Gaussian	97.3%	85.08%	12.22%
k-Nearest Neighbor	Fine	98.7%	84.08%	14.62%
Ensemble Method	Bagged Trees	99.2%	93.5%	5.70%

As it can be seen from Figure 2, distribution of classes is too complex for one classification techniques. For this reason, we have used an ensemble machine learning technique. This way, results of more than one classifier could be combine for better classification as it was stated before. Furthermore, derivative features have been extracted from measured values. This improves the accordance between training and test accuracy. However, it can be seen that derivative features do not help to improve the total accuracy of the classifier. This can be seen on Table 2 and Table 3.

On the other hand, data pre-processing technique which is grey relational analysis here, has helped the machine learning algorithm to get better accuracy rating. This is because the invalid measurement data have been removed by comparing measured and derivative data. Grey Relational Analysis is a normalization technique which also provide a dynamic coefficient for correlation of input data. This way, input values can be pre-classified as grey values between 0 and 1 as they are normalized at same time. The results of machine learning algorithms with grey relational analysis with 12 features proves that data pre-processing and better feature extraction are both crucial for machine learning. When Table 4 and Table 5 are examined, it can be seen clearly that drop rates between training and testing have decreased dramatically. This shows that both features extraction and data preprocessing play important role on machine learning.

All these studies show that ensemble techniques such as bagging, boosting and stacking are best for imbalanced data. A powerful data pre-processing technique is also needed with better feature extraction method. Test results of ensemble classifier can be seen on confusion matrixes below. Figure 3 shows the result of ensemble classifier with six features extracted from raw data directly. Accuracy of the model is around 73% because of raw data with less features. Figure 4 shows the test result of ensemble classifier with more features extracted from this raw data directly. Six of these features are derivative values. Accuracy of the model is around 73% again because of raw data. There is no effective change in total accuracy. However, it can be seen that drop rate between training and testing has reduced because of derivative features.

This raw data contains corrupt and unnecessary measurement values. A grey relational coefficient has been determined to get rid of these measurement data. A new class has been created for this reason and labeled as zero class. All transient regime measurements of appliance have been ignored. This improve both training and testing accuracy ratings as can be observed in Figure 5 and Figure 6 below.

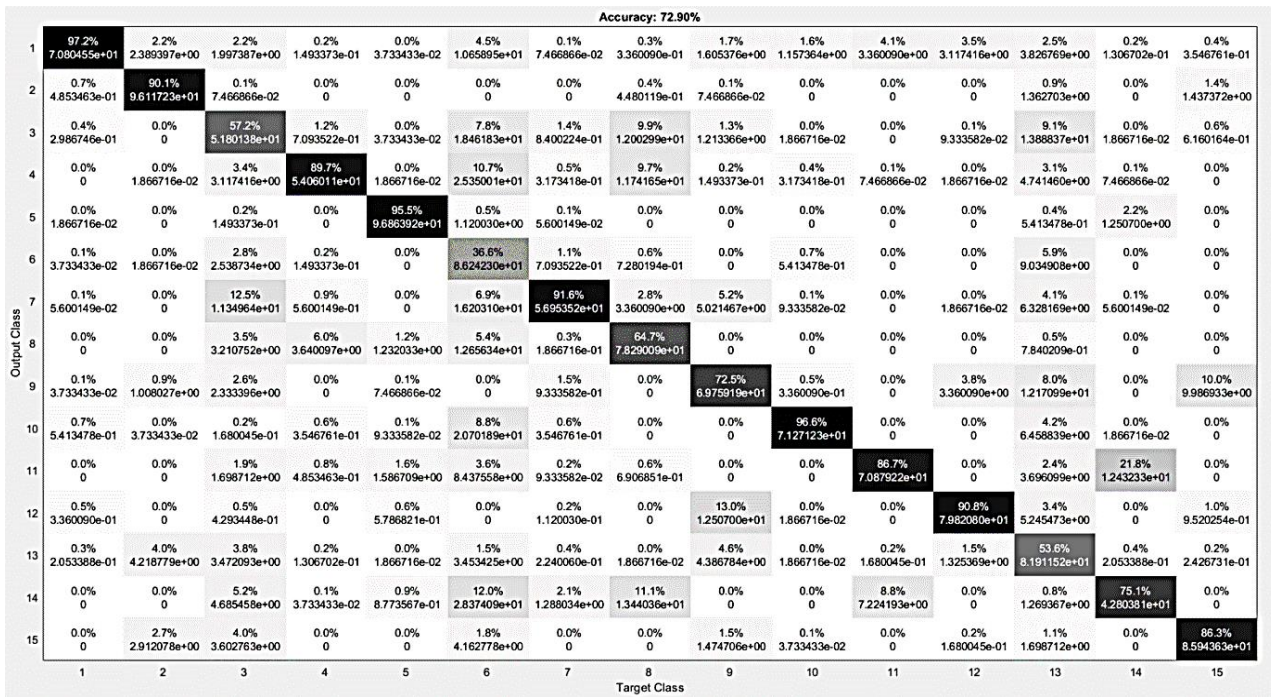


Figure 3. Test Result of Ensemble classifier with six features and raw data

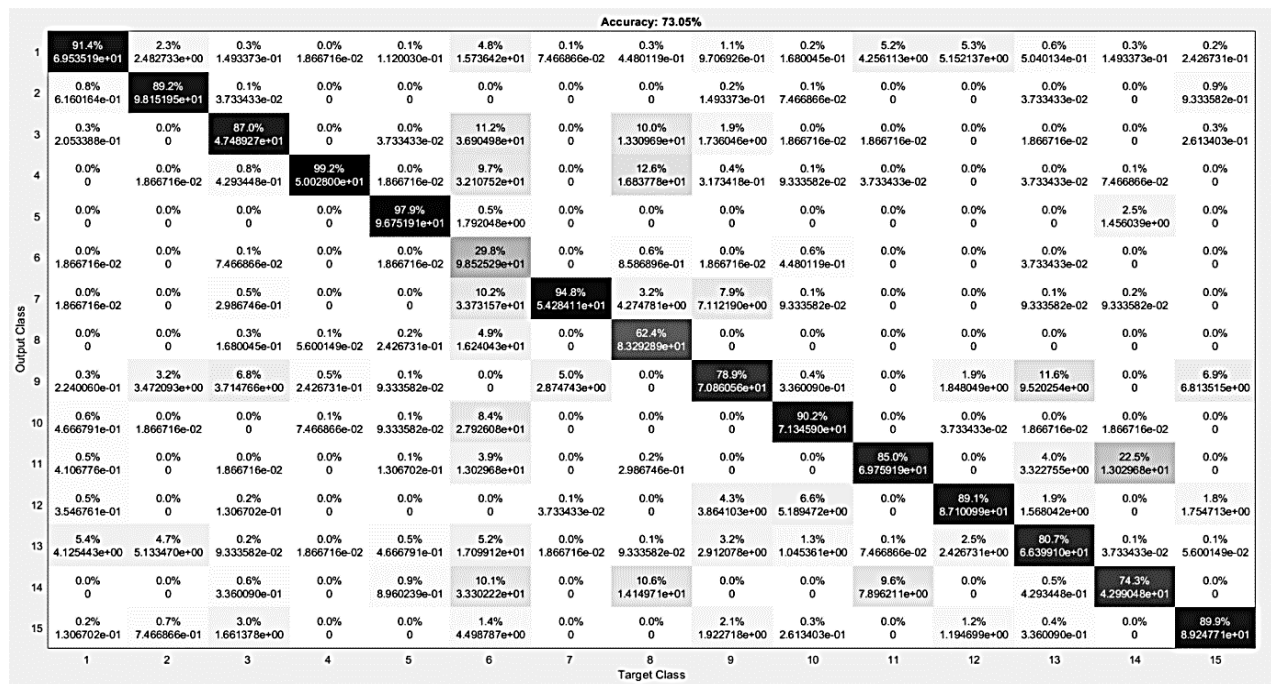


Figure 4. Test Result of Ensemble classifier with twelve features and raw data

It is obvious that feature extraction has positive effect on accordance between training and testing. On the other hand, it is necessary to use a data pre-processing technique for achieving better accuracy result. Figure 6 shows that GRA has increased the accuracy of the model dramatically. However, drop between training and testing is still high. Using more features to train the system will overcome this problem.

As it was presented before, the ensemble classifiers have the best accuracy rate in both training and testing

data. The receiver operating characteristic (ROC) shows the performance of a classification model for each class [23]. The ROC curve has two parameters; true positive rate as in Equation (14) and false positive rate as in Equation (15). These parameters give proportional correlation of correct and false prediction of the model.

$$TPR = \frac{TP}{TP+FN} \tag{14}$$

$$FPR = \frac{FP}{FP+TN} \tag{15}$$

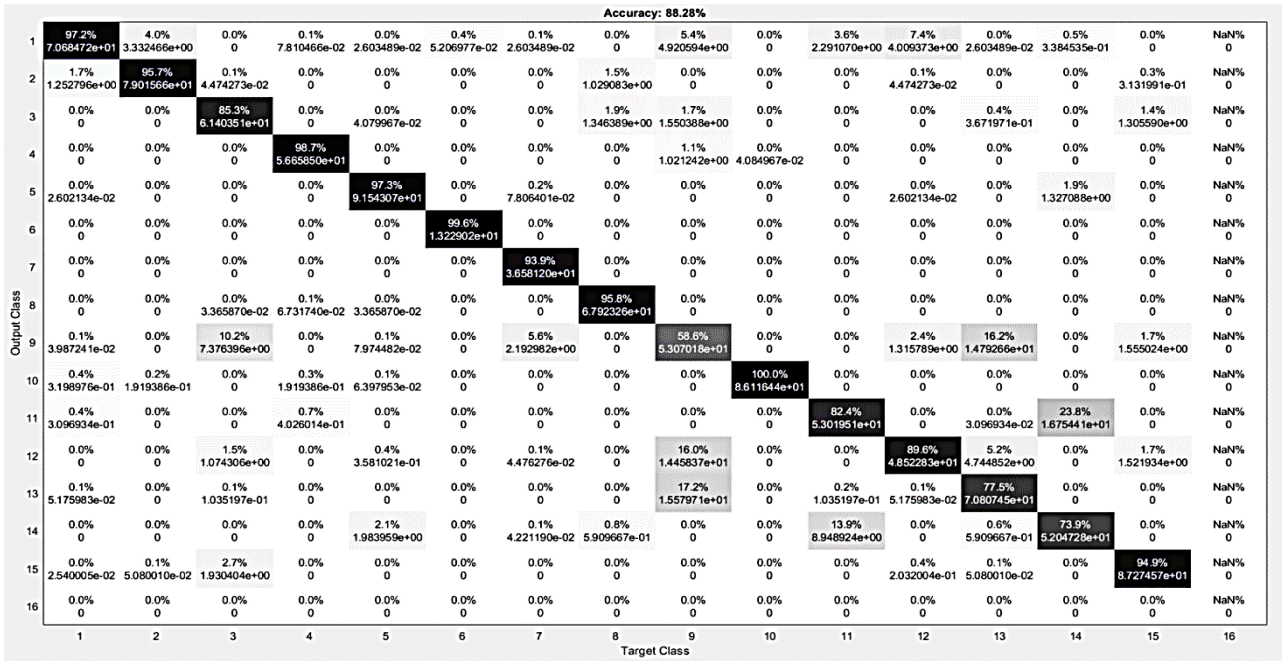


Figure 5. Test Result of Ensemble classifier with six features and GRA data

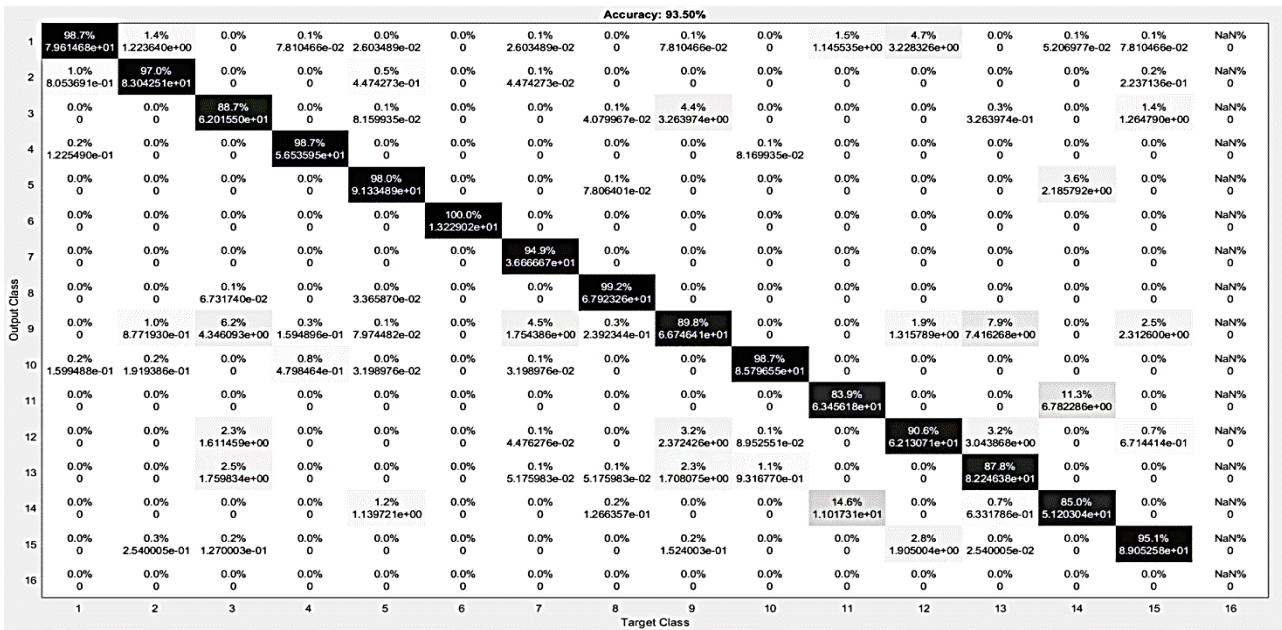


Figure 6. Test Result of Ensemble classifier with twelve features and GRA data

Where TPR is true positive rate, FPR is false positive rate, TP is true positive result, FP is false positive result, FN is false negative results and FP is false positive results.

Distribution of model prediction can be seen on Figure 7. The confusion matrixes show the detail of true and predicted classes on Figure 8 and Figure 9. Here, we create another class named zero. This class represent values which is no good for prediction because the appliance is neither in steady regime nor working at all. The GRA helps to detect these measurements and label them as class 0 at pre-processing. This way accuracy of the model has been increased.

The area under the ROC curve (AUC) represents the quality of the prediction model for each class

independently. The AUC should be equal to 1.0 for perfect prediction rate. As it is shown on table 6, the ensemble classifier is highly successful on prediction for each class except for 14. Shaving machine has lower AUC value because it has low number of samples in the dataset.

Figure 7 shows correct prediction as dot and false prediction as cross symbol. It can be seen that some appliances have been mixed with others commonly when we examine the confusion matrixes in Figure 8. Especially, second matrixes in both Figure 8 and Figure 9 show how grey relational analysis improves the prediction quality by ignoring corrupt data.

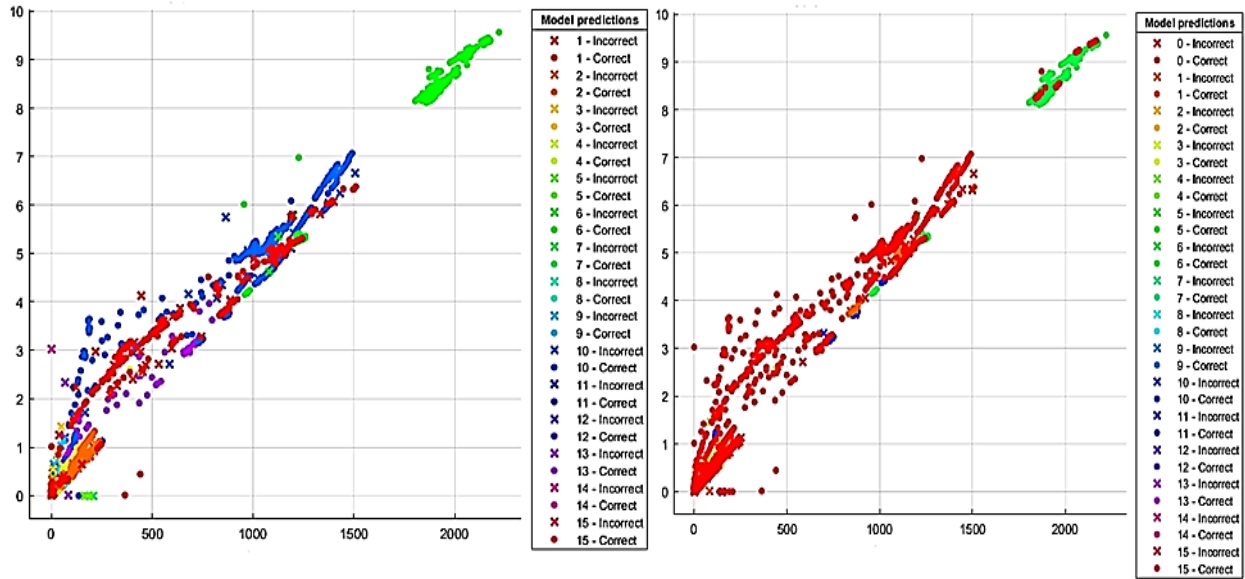


Figure 7. Distributions of prediction results (Raw data on left, GRA data on right)

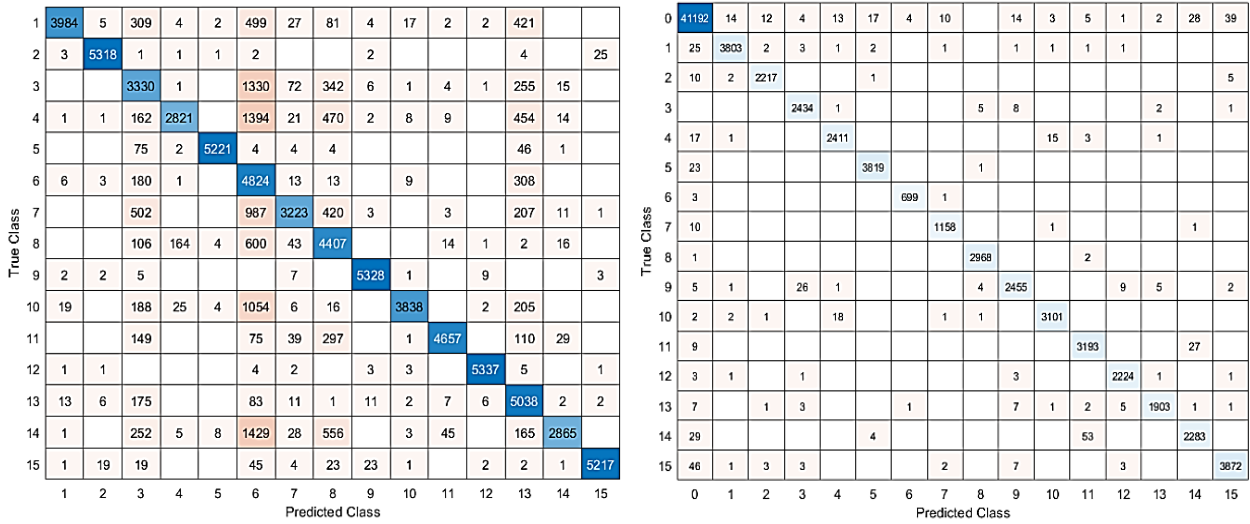


Figure 8. Confusion matrix for classes (Raw data on left, GRA data on right)

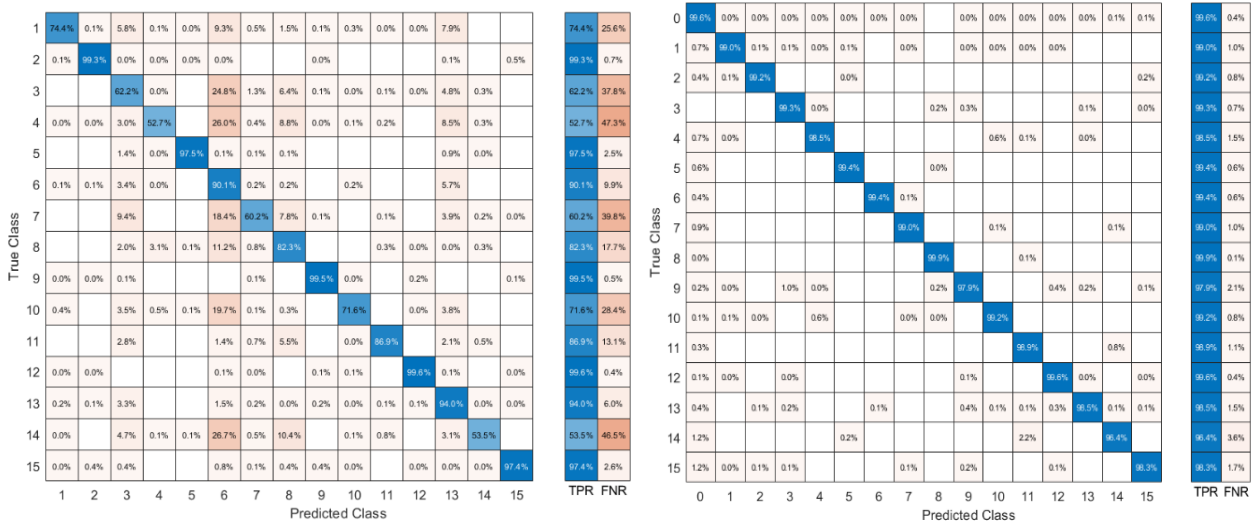


Figure 9. Confusion matrix for accuracy (Raw data on left, GRA data on right)

Table 6. ROC curve results for each class

Class	Label	AUC
1	Coffee Machine	0.990
2	Computer Station	0.992
3	Fan	0.993
4	Fridge and Freezer	0.985
5	Hi-Fi System	0.994
6	Kettle	0.994
7	Compact Fluorescent	0.990
8	Incandescent Lamp	0.999
9	Laptop Charger	0.979
10	Microwave Oven	0.992
11	Phone Charger	0.989
12	Monitor	0.996
13	Printer	0.985
14	Shaving Machine	0.964
15	Television	0.983

Table 7. Comparison with previous studies

Study	Pre-process	Classifier	Accuracy
Ridi [5]	Acceleration and Velocity	KNN GMM	83.1% 89.7%
Ruzzelli [6]	None	Bayesian Markov chain	84%
Mpawenimana [8]	Moving Average	KNN Random Forest	99.1%
Qaisar [9]	Compression Gain	Naïve Bayes	91.9%
Hamid [10]	NILM	Decision Trees	99%
This Study	GRA	Ensemble (Bagged Trees)	99.2%

4. Conclusion

It is important to pre-processes the data before machine learning. Better feature extraction is another important step to get best prediction results. A dynamic coefficient that shows the variant of the data would be used along with an effective normalization method. Previous studies show that data preparation techniques play important role in the results. Although, there are many different types of classifiers, each one has its own characteristic so they give different results with different dataset. The accuracy of studies which are presented in first section can be summarized as on Table 7. They all have used different pre-processing techniques and classifiers but accuracy levels are varying.

In this study, grey-relational analysis has been used for feature extraction from ACS dataset. This quite improve the quality of data. In addition, measurement data have been filtered by removing inconsistent measurement values. Then different machine learning algorithms have been used for appliance recognition task by using only power parameters. Best result has been obtained by an ensemble (Bagged Trees) classification learner with 1%

loss between training and testing phase. The confusion matrix shows that the most misclassification is on class 14 due to few measurement samples. Other than that, prediction model is highly accurate.

This study has demonstrated a supervised machine learning method with a different data pre-processing technique. Grey Relational Analysis can be used to analyze multivariable system. It normalizes the data while calculates the variation. Ensemble classification methods are best resulting machine learning algorithms. They are combination of different classification method with weighted voting algorithms. This method can be improved by implementing an artificial neural network which is another application of machine learning.

Declaration

The author(s) declared no potential conflicts of interest with respect to the research, authorship, and/or publication of this article. The author(s) also declared that this article is original, was prepared in accordance with international publication and research ethics, and ethical committee permission or any special permission is not required.

Author Contributions

Y. Güven is responsible for all section of the study.

References

- Zhaou, H. X., Magoules F., A review on the prediction of building energy consumption. *Renewable and Sustainable Energy Reviews*, 2012. **16**: p.3586-3592.
- Lin, Y. H., Tsai, M. S., An Advanced Home Energy Management System Facilitated by Nonintrusive Load Monitoring with Automated Multiobjective Power Scheduling. *IEEE Transactions on Smart Grid*, 2015. **6**: p.1839-1851.
- Sanchez-Sutil, F., Cano-Ortega, A., Hernandez, J.C., Rus-Casas, C., Development and Calibration of an Open Source, Low-Cost Power Smart Meter Prototype for PV Household-Prosumers, *MDPI Electronics*, 2019. **8**: p.878.
- Medico, R., De Baets, L., Gao, J. et al., A voltage and current measurement dataset for plug load appliance identification in households, *Nature Scientific Data*, 2020. **7**: p.49.
- Ridi, A., Gisler, C., Hennebert, J., ACS-F2 A new database of appliance consumption signatures. 6th International Conference of Soft Computing and Pattern Recognition (SoCPaR), 2017. **6**: p.145-150.
- Ruzzelli, A. G., Nicolas, C., Schoofs, A., O'Hare, G. M. P., Real-Time Recognition and Profiling of Appliances through a Single Electricity Sensor. 7th Annual IEEE Communications Society Conference on Sensor, Mesh and Ad Hoc Communications and Networks (SECON), 2017. **7**: p.1-9.
- Huang, A. Q., Crow, M. L., Heydt, G. T., Zheng, J. P., Dale, S. J., The Future Renewable Electric Energy Delivery and Management (FREEDM) System: The Energy Internet, *Proceedings of the IEEE*, 2011. **99**(1): p.133-148.

8. Mpawenimana, I., Pegatoquet, A., Soe, W. T., Belleudy, C., Appliances Identification for Different Electrical Signatures using Moving Average as Data Preparation. Ninth International Green and Sustainable Computing Conference (IGSC), 2018. **9**: p.1-6.
9. Qaisar, S. M., Alsharif, F., An Adaptive Rate Time-Domain Approach for a Proficient and Automatic Household Appliances Identification. International Conference on Electrical and Computing Technologies and Applications (ICECTA), 2019, p.1-4.
10. Hamid, O., Barbarosou, M., Papageorgas, P., Prekas, K., Salame, C-T., Automatic recognition of electric loads analysing the characteristic parameters of the consumed electric power through a Non-Intrusive Monitoring methodology. Energy Procedia, 2017. **119**: p.742-751.
11. Khawaja, A.S., Anpalagan, A., Naeem, M., Venkatesh, B. Joint bagged-boosted artificial neural networks: Using ensemble machine learning to improve short-term electricity load forecasting, Electric Power Systems Research, 2020. **179**: p.1-7.
12. Himeur, Y., Alsalemi, A., Bensaali, F., Amira A., Robust event-based non-intrusive appliance recognition using multi-scale wavelet packet tree and ensemble bagging tree, Applied Energy, 2020. **267**: p.1-16.
13. Huchtkoetter, J., Tepe, M.A., Reinhardt, A. The Impact of Ambient Sensing on the Recognition of Electrical Appliances. Energies 2021. **14**: p.188.
14. Mihailescu, R-C., Hurtig, D., Olsson, C., End-to-end anytime solution for appliance recognition based on high-resolution current sensing with few-shot learning, Internet of Things, 2020. **11**: p.1-10.
15. Shin, E., Khamesi, A. R., Bahr, Z., Silvestri, S. and Baker, D. A., A User-Centered Active Learning Approach for Appliance Recognition, IEEE International Conference on Smart Computing (SMARTCOMP), 2020. p. 208-213.
16. Institute of Complex Systems [Cites 2020 11 June]; Available from: <https://icosys.ch/acs-f2>.
17. Zhang, S., Zhang, C., Yang, Q., Data preparation for data mining. Applied Artificial Intelligence, 2003 **17**(5-6): p.375-381.
18. Sallehuddin, R. Shamsuddin, S. M. H., Hashim, S. Z. M., Application of Grey Relational Analysis for Multivariate Time Series. Eighth International Conference on Intelligent Systems Design and Applications, 2008. **8**: p.432-437.
19. Voyant, C., Notton, G., Kalogirou, S., Nivet, M-L., Paoli, C., Motte, F., Fouilloy, A., Machine learning methods for solar radiation forecasting: A review. Renewable Energy, 2017. **105**: p. 569-582.
20. Mahdavinejad, M. S., Rezvan, M., Barekatin, M., Adibi, P., Barnaghi, P., Sheth, A. P., Machine learning for internet of things data analysis: a survey. Digital Communications and Networks, 2018. **4**(3): p.161-175.
21. Rahman, A., Tasnim, S., Ensemble Classifiers and Their Applications: A Review. International Journal of Computer Trends and Technology, 2014. **10**(1): p.31-35.
22. Kim, K-J., Cho, S. B., Ensemble classifiers based on correlation analysis for DNA microarray classification. Neurocomputing, 2006. **70**: p.187-199.
23. Machine Learning Crash Course [Cited 2020 2 February]; Available from: <https://developers.google.com/machine-learning/crash-course>
24. Tshitoyan V. [Cited 2020 27 April]; Available from: <https://www.github.com/vtshitoyan/plotConfMat>



Research Article

A novel formula derived by using ABC algorithm for calculation of the average fiber diameter of electrospun poly (ϵ -caprolactone) scaffolds

Çağdas Yılmaz^a , Didem Demir^b , Nimet Bölgen^b , Ali Akdağlı^{a,*} 

^a Department of Electrical-Electronics Engineering, Mersin University, Mersin 33110, Turkey.

^b Department of Chemical Engineering, Mersin University, Mersin 33110, Turkey.

ARTICLE INFO

Article history:

Received 27 November 2020

Revised 08 March 2021

Accepted 26 April 2021

Keywords:

ABC Algorithm
Electrospinning
Fiber Diameter
Optimization
PCL

ABSTRACT

The characteristics of a scaffold that is the basic component of tissue engineering are considerably influenced by the fiber diameter of the fibrous scaffolds. Since the significant effect of the fiber diameter on the scaffold properties, many researchers have focused on estimating the fiber diameter based on the electrospinning parameters. With similar motivation, in this paper, a new and simple closed-form expression, which can help researchers in fabricating the electrospun poly (ϵ -caprolactone) (PCL) scaffold with desired fiber diameter, is presented. In order to construct the expression proposed, an experimental study has been performed to obtain the data set, in which 25 experimental data including average fiber diameter (AFD) values dependent on different combinations of parameters such as voltage, solution concentration, tip to collector (TTC) distance, and flow rate. Then, an expression has been constructed that is used to estimate the AFD of the electrospun PCL, and the coefficients of the expression were determined by using the artificial bee colony (ABC) algorithm. In order to validate the estimation ability of the expression, the metrics such as mean absolute error (MAE) and mean absolute percentage error (MAPE) have been used, and the optimization and test errors were respectively obtained as 3.30% and 1.27% in terms of MAPE. In addition, the results obtained were compared with those reported in the literature. Results show that our new expression can be successfully used to estimate the AFD of electrospun PCL prior to the electrospinning process. Thus, the number of test repetitions could be reduced by using the expression proposed, and time, cost, and labor could be saved in this way. This study contributes to the literature because there have been only a limited number of studies that focus on estimating the AFD of PCL nanofiber despite many studies about various polymers.

© 2021, Advanced Researches and Engineering Journal (IAREJ) and the Author(s).

1. Introduction

Electrospinning derived from “electrostatic spinning” is a well-known and widely used technique for producing fibrous structures with ultrafine fiber diameters ranging from hundreds of nanometers to several micrometers [1]. In a classical electrospinning procedure, a polymer is forced to pass through a thin nozzle under a high electric field, and thus continuous and uniform polymeric fibers are obtained [2]. The most important advantages of the electrospinning method over other fiber production techniques (phase separation and self-assembly) are to be

relatively fast, simple and economical in fabricating fibrous and porous materials in a variety of shapes, topographies, and sizes. Another notable important feature of the electrospinning process is its versatility which allows nanofibers' production of diverse compositions with controlled structures. The morphological network, particularly the diameter of the fibers, can be influenced by several parameters, including viscosity, conductivity, temperature, humidity, electric field, TTC distance, and nozzle/needle size. All these factors affecting the fiber diameter are grouped under three main headings: solution characteristics (conductivity, viscosity, surface tension,

* Corresponding author. Tel.: +90 324 361 00 01; Fax: +90 324 361 00 32.

E-mail addresses: bmmcagdas@gmail.com (C. Yilmaz), didemdemir@mersin.edu.tr (D. Demir), nimet@mersin.edu.tr (N. Bölgen), akdagli@mersin.edu.tr (A. Akdagli)

ORCID: 0000-0001-6373-2768 (C. Yilmaz), 0000-0002-2977-2077 (D. Demir), 0000-0003-3162-0803 (N. Bölgen), 0000-0003-3312-992X (A. Akdagli)

DOI: 10.35860/iarej.832439

This article is licensed under the CC BY-NC 4.0 International License (<https://creativecommons.org/licenses/by-nc/4.0/>).

concentration, molecular weight, and dielectric coefficient of the solvent), processing parameters (applied voltage, feed rate, type of collector, and TTC distance) and ambient conditions (humidity, temperature, and airflow rate) [3-5].

Due to unique features such as a high surface area to volume ratio, controllable membrane thickness, tensile strength, adjustable porosity, and extensibility of the materials produced from electrospun fibers, several applications in protective clothing [6], sensors [7], food packaging [8], water filtration [9], drug delivery [10] and tissue engineering [11] have been proposed and investigated in the literature. Particularly in tissue engineering, electrospun polymeric materials have been of great interest. The fibrous and porous structures, which are similar to an extracellular matrix of natural tissues, serve as scaffolds for supporting cell adhesion and delivering growth factors [12]. The architecture of an electrospun scaffold, such as fiber diameter, porosity, and surface topography, is related to the characteristics and the biological response of the scaffold, which affects many vital functions of the cells like cell-to-cell communication, cell growth, cell adhesion, proliferation, differentiation and migration [13]. Moreover, the mechanical stability of the scaffold is associated with its fiber size and density [14]. Therefore, preparing fibrous scaffolds in the targeted fiber diameter by optimization of the electrospinning parameters is highly desirable.

The significant effect of the fiber diameter on the properties of the scaffold has motivated researchers to investigate the effect of electrospinning parameters on the fiber diameter. However, since electrospinning is a very complex and nonlinear process, it is quite difficult to determine precisely the diameter of the electrospun fibers. Therefore, different modeling techniques are used that capable of giving convergent results even if they don't give precise results for estimating the diameter of the electrospun fibers. When the studies conducted to estimate the AFD are examined, it is seen that response surface methodology (RSM) and artificial neural network (ANN) are used mostly. RSM is a practical modeling technique using together statistical and mathematical techniques to establish a correlation between the electrospinning parameters and the AFD [15-17]. Since ANN is a simulation of the biological neural system is an effective method that can be modeling highly complicated functions and automatically learning the structure of data, it is used to estimate the fiber diameter of the mats fabricated by electrospinning, which is a complex process [18, 19]. In spite of the fact that ANN can generally estimate the AFD successfully, its disadvantage is a black box structure that is not giving any explicit expression. On the contrary, in RSM, although the polynomial expression used for estimating can be accessible, high accuracy to estimate AFD may not be achieved. Studies on the estimation of

AFD of various polymers using ANN and RSM techniques are given in Table 1. Although ANN and RSM are predominantly used in studies on the estimation of AFD, as seen in Table 1, there are studies in which different techniques such as Adaptive Neuro-Fuzzy Inference Systems (ANFIS), Support Vector Machines (SVMs), and Gene Expression Programming (GEP) methods are used. Nurwaha et al. [20] used methods of ANFIS, SVMs, and GEP to estimate the AFD of electrospun PEO. They reported that the SVMs model was better predictive power in comparison with both ANFIS and Gene Expression Programming models. In the study conducted by Khatti et al. [21] in 2019, they stated that although there were studies to model the electrospinning process of the various nanofiber, no study had been performed on the PCL. In the current literature review, no new study was found for the estimation of AFD of electrospun PCL other than the Khatti's et al. [21] study. Therefore, the validity of the presented study has been ensured by comparing it with the results of Khatti's study.

Khatti et al. [21] had been tried to estimate the AFD of electrospun PCL using ANN and RSM techniques in their study. While the Box-Behnken design was used in RSM, which was used to develop a mathematical model, the Levenberg-Marquardt backpropagation algorithm was used to develop the artificial neural network. They reported that although both models had good agreement with experimental data, the RSM model had a slightly lower error than the ANN model. The comparison of the results of the presented study with the results found by Khatti et al. [21] has been given in section 3.

In this study, a simple and novel expression has been derived for accurately estimating the fiber diameter, and the unknown coefficients of this expression have been optimally determined by the ABC algorithm that is one of the swarm-based algorithms.

Table 1. Summary of studies on the estimation of AFD

Nanofiber	Year	Method	Reference
PCL	2019	ANN, RSM	[21]
PVDF	2018	ANN	[22]
Kefiran	2017	ANN	[23]
PVA	2018	ANN	[24]
Ferrofluid/ polyvinyl alcohol	2020	ANN	[18]
Chitosan-Collagen	2018	RSM	[16]
Titanium Oxide	2017	RSM	[17]
PET-PVP	2018	RSM	[25]
PEO	2019	ANFIS, SVMs, GEP	[20]

Swarm intelligence algorithms that can produce solutions for many different optimization problems have become increasingly popular in recent years. These algorithms, which are inspired by various social behaviors performed by animal groups, do not guarantee the exact solution to the problem, but they can produce very successful solutions in a reasonable time. The ABC algorithm, which introduced by Karaboğa in 2005 [26]. ABC algorithm has been developed by inspiring honey bees' cooperative feeding behavior. Because of its simple structure and good performance, ABC has become a widely used optimization algorithm. Details on the ABC algorithm and its engineering application can be found in [26-32].

This study aims to derive a simple expression by using the ABC algorithm to estimate the average diameter of electrospun fibers that have the potential to be utilized in tissue engineering. To fabricate the fibrous scaffolds using electrospinning, PCL, which is a Food and Drug Administration (FDA) approved synthetic polymer, was used due to its biocompatibility, biodegradability, good processability, and high mechanical properties [10, 33]. Another reason is that there are not enough studies that can be used to estimate the AFD of electrospun PCL. The effects of main factors such as TTC distance, voltage, polymer concentration, and flow rate on the AFD of PCL were studied. The number and variety of experiments were determined using RSM. Morphological characteristics of fibers fabricated at the different process and solution parameters were examined using scanning electron microscopy (SEM). The AFD of the scaffolds as experimental results were calculated using SEM images that have been used for the optimization process. Then, a closed-form expression, determined the unknown coefficient of the derived expression using the ABC algorithm, was derived for calculating AFD of the electrospun PCL scaffolds.

The article is organized into the following sections: Firstly, the materials and methods used are described in Section 2. Explanations about the preparation of fibers, planning the experiments using RSM, measurement studies of AFD are given in this section. Section 3 discusses the numerical AFD results from SEM images and the derivation of the AFD expression to be used in estimating fiber diameter. In addition, it discusses the comparison of the results of the presented study with the results found by another study with similar motivation. Finally, the results from the study are summarized in Section 4.

2. Materials and Methods

2.1 Materials

PCL in pellet form with an average molecular weight of 80 kDa was supplied from Sigma-Aldrich (United

Kingdom). Chloroform and dimethylformamide used as solvents were obtained from Tekkim (Turkey) and Carlo Erba Reagents (France), respectively. All reagents have analytical purity and were used as received, without further purification.

2.2 Fabrication of PCL Nanofibers Using Electrospinning Technique

Fibrous membranes were first produced under different conditions to estimate the AFD of the nanofibers to be produced by changing the electrospinning parameters (polymer concentration, applied voltage, tip-to-collector distance, and flow rate).

For the experiments in this study, a horizontal electrospinning set-up was used with a high voltage power supply (Gamma, ES40P, USA) and a microfluidic syringe pump (New Era, NE-1002X, USA), as illustrated in Figure 1.

In the premise of ensuring the quality of the electrospun fiber membranes, the parameter values of various electrospinning factors were determined at the maximum and minimum ranges as a result of the preliminary optimization studies carried out by Bölgen et al. [34]. Considering that study, the value interval for the setup parameter such as the concentration of PCL, voltage, TTC distance, and the flow rate was used as 11-15 (% w/v) 11-15 (kV), 8-12 (cm) and 1-3 (mL/h), respectively.

To prepare the different concentrations of polymer solution (11, 13, and 15%, w/v) for electrospinning, a calculated amount of PCL was firstly dissolved into 3 mL of chloroform. After PCL was completely dissolved, 7 mL of dimethylformamide was added to the PCL-chloroform solution. The PCL-chloroform-dimethylformamide solution was stirred for 2 hours until a homogeneous mixture was obtained. The prepared solution in a 2 mL portion was loaded in a plastic syringe with a metal capillary needle. The syringe was placed in the syringe pump to ensure a controlled flow rate. The needle tip was connected to the high voltage power supply operating at 11, 13, and 15 kV. The polymer solution was fed at different rates of 1, 2, and 3 mL/h. The voltage was applied for 15 min to fabricate electrospun fibers. TTC was varied from 8, 10, and 12 cm. All experiments were performed in triplicate at room temperature ($27\pm 1^\circ\text{C}$) with relative humidity at about 45%.

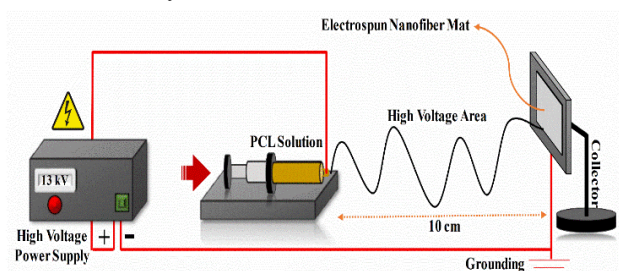


Figure 1. Schematic representation of the horizontal set-up of electrospinning apparatus

2.3 Morphological Observations and Fiber Diameter Analysis

The morphological structure of the produced nanofibers at the different processes and solution conditions was evaluated by using SEM. Before analysis, the samples were sputter-coated with platinum. Images of the samples were taken at 20.00 and 50.00 KX magnifications. The diameters of individual fibers were measured using Image-J Software from SEM images. The average diameter of fibers was calculated using at least 50 measurements per group. The standard deviation was determined and used as a measure of the uniformity of the collected fibers.

3. Results and Discussion

3.1 Derivation of the AFD Expression

In order to derive the expression that calculates AFD of the electrospun PCL scaffolds, 25 experimental data given in Table 2 have been used. The fiber sizes of each electrospun PCL membrane were measured using Image-J Software. Several SEM images yielded with the experiments, which have different setup parameters resulting in different fiber diameters, are shown in Figure 2.

In the optimization process, while 22 samples are used to construct the AFD expression, the remaining 3 ones are used for the verification. The experimental results, calculated using the SEM images, for the fiber diameter of the electrospun PCL scaffolds are presented in Table 2.

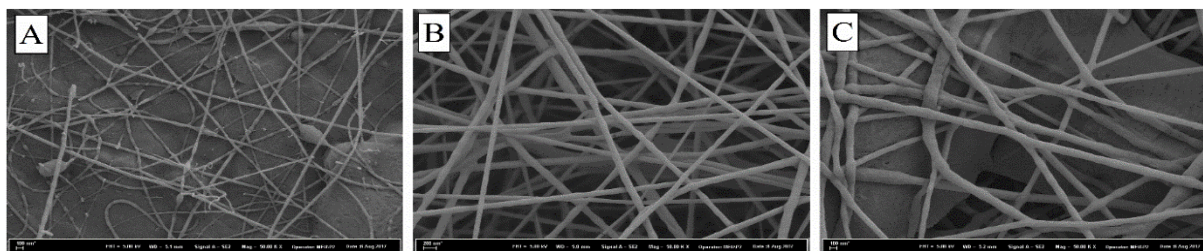


Figure 2. SEM image samples belonging to the electrospun PCL nanofibrous scaffolds fabricated at different electrospinning parameters: A) PCL concentration: 11%, Voltage: 11 kV, TTC distance: 12 cm and Flow rate: 1 mL/h; B) PCL concentration: 13%, Voltage: 13 kV, TTC distance: 10 cm and Flow rate: 2 mL/h; C) PCL concentration: 13%, Voltage: 13 kV, TTC distance: 8 cm and Flow rate: 2 mL/h

Table 2. Electrospinning setup parameters corresponding to the AFD values

Exp. No	Process and solution parameters				AFD	
	P ₁ PCL concentration (%, w/v)	P ₂ Voltage (kV)	P ₃ TTC Distance (cm)	P ₄ Flow rate (mL/h)	Mean (nm)	Std. dev. (nm)
1	11	11	12	1	45	7.9
2	15	11	8	3	106	8.8
3	15	11	8	1	103	9.9
4	13	13	8	2	141	14.1
5	11	15	12	1	37	5.3
6	11	15	8	3	74	7.2
7	15	13	10	2	115	11.6
8	13	13	10	3	138	31.6
9	13	13	10	1	99	15.1
10	11	13	10	2	63	9.3
11	15	15	8	1	87	3.8
12	11	15	12	3	53	7.3
13	13	13	12	2	119	16.2
14	11	11	12	3	67	9.2
15	13	15	10	2	99	10.4
16	15	15	12	3	75	10.3
17	15	15	12	1	68	6.9
18	15	11	12	1	89	13.0
19	15	15	8	3	89	13.1
20	11	11	8	1	69	6.5
21	11	11	8	3	90	11.3
22	13	13	10	2	105	12.4
23	13	11	10	2	123	12.6
24	11	15	8	1	59	3.1
25	15	11	12	3	93	9.8

Table 3. The optimization parameters and the values associated with these parameters used in the ABC algorithm

Parameters	Assigned values
Number of dimensions (D)	11
Population size (NP)	50
Maximum iteration number	3000
Trial number	NP*D

For simplicity in expression, the concentration of PCL, the voltage, the TTC distance, and the flow rate is denoted as P₁, P₂, P₃, and P₄, respectively. ABC is a flexible algorithm that provides to optimize according to the different metrics. Therefore, the metrics are given below, including MAPE and MAE, have been utilized.

$$MAPE = \frac{1}{n} \sum_{i=1}^n \left| \frac{AFD_M - AFD_C}{AFD_M} \right| \times 100 \quad (1)$$

$$MAE = \frac{1}{n} \sum_{i=1}^n |AFD_M - AFD_C| \quad (2)$$

where AFD_M and AFD_C are the measured and computed AFD values, respectively. The number n indicates the experiment number. Optimization parameters of the ABC algorithm used in this study and the values associated with these parameters are given in Table 3.

To achieve the best model corresponding to the AFD, several trials are performed. The following AFD expression, which is giving satisfactory results, is obtained Equation (A.1) (in Appendix).

Note that the AFD expressions that are simpler and more complex according to the one proposed have also been tried. Simpler ones showed poor concordance with the experimental results, while more complex ones provided minor improvement in error values.

In Table 4, the coefficient values obtained for considering 22 experiment samples are listed. The coefficients of the expression are optimally determined by the agency of the ABC algorithm so as to minimize the error between the calculated results and the experimental ones.

3.2 Numerical Results

The AFD expression obtained by substituted x values (Table 4) into Equation (A.1) (in Appendix) is presented. The values of AFD calculated using the expression proposed given by (A.2) (in Appendix) are presented in Table 5.

When this table, which also includes the experimental results of the AFD of the electrospun PCL scaffolds, is analyzed, it is clearly seen that the experimental results agree well with the calculated using the expression proposed ones. MAPE and MAE were achieved as 1.27% and 1.14, respectively, for 22 experiments. This good agreement supports the accuracy and reliability of the AFD formula proposed in this work. Results are also given

graphically in Figure 3 and Figure 4 to show the performance of the expression proposed. When Figure 3 is examined, it can be seen that the expression proposed yields quite acceptable results. As well, the correlation graph showing the close relationship between the calculated AFD and the experimental ones is presented in Figure 4 (adjusted correlation coefficient: 0.995). To evaluate the success of the expression, the AFD was computed for test data, and MAPE and MAE were obtained as 3.30% and 2.66, respectively. For simplicity, the value coefficients with the use of ABC according to only the MAPE are given in Table 4. In order to ensure the validity of the presented expression, the error values obtained in this study were compared with those reported by Khatti et al. [21]. Details of this comparison are presented for the optimization and testing phase in Table 6.

As seen in Table 6, the results of RSM and ANN models presented by Khatti et al. [21] for estimating the AFD of electrospun PCL have been in good agreement with the experimental results. Although there was not a great difference between the results obtained with the expression presented in this study and the results presented by Khatti et al. [21], the expression presented in this study has estimated the AFD of electrospun PCL more successfully.

Thus, the validity of the proposed expression was confirmed by comparing the results of a similarly motivated study published in the literature with the results obtained in this study.

Table 4. The coefficient values for the AFD expression determined by the ABC algorithm

X ₁	X ₂	X ₃	X ₄
-5.561	1000	5.400	1.099
X ₅	X ₆	X ₇	X ₈
999.90	-1.167	-1000	-0.006
X ₉	X ₁₀	X ₁₁	X ₁₂
8.06	-14.536	-29.515	57.088
X ₁₃	X ₁₄	X ₁₅	X ₁₆
5.987	-10.505	-17.375	6.852

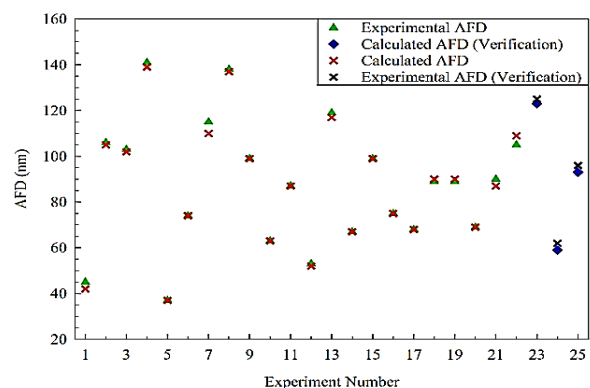


Figure 3. The comparative results of the calculated and experimental AFD

Table 5. Comparison of experimental AFD and calculated AFD (*: test data)

Exp. No	AFD (nm)		METRICS	
	Experimental	Calculated	Absolute Percentage Error	Absolute Error
1	45	42	6.7	3
2	106	105	0.9	1
3	103	102	1	1
4	141	139	1.4	2
5	37	37	0	0
6	74	74	0	0
7	115	110	4.3	5
8	138	137	0.7	1
9	99	99	0	0
10	63	63	0	0
11	87	87	0	0
12	53	52	1.9	1
13	119	117	1.7	2
14	67	67	0	0
15	99	99	0	0
16	75	75	0	0
17	68	68	0	0
18	89	90	1.1	1
19	89	90	1.1	1
20	69	69	0	0
21	90	87	3.3	3
22	105	109	3.8	4
23*	123	125	1.6	2
24*	59	62	5.1	3
25*	93	96	3.2	3
			MAPE	MAE
		Optimization	1.27%	1.14
		Test	3.30%	2.66

Table 6. The comparison of the results obtained in this study with those obtained in the other study [21]

	Metrics	Khatti et al. [21]		
		This Study	RSM	ANN
Optimization	MAPE	1.27%	4.34%	5.91%
Phase	MAE	1.14	11.29	14.58
Test Phase	MAPE	3.30%	4.44%	3.41%
	MAE	2.66	13.00	9.66

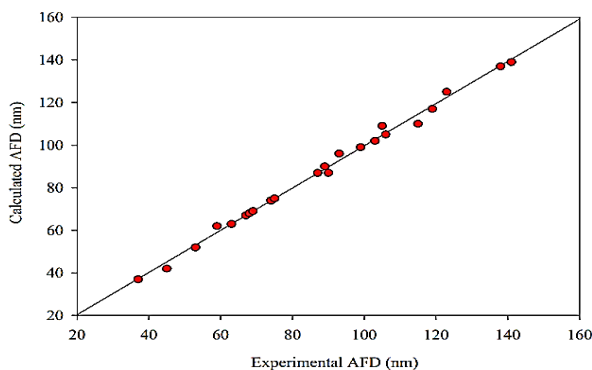


Figure 4. Correlation graph between calculated and experimental AFD

Therefore, it is of great importance to be able to predict the domain of process parameters by which the target fiber diameter can be obtained.

4. Conclusions

In order to produce a scaffold with the desired fiber size and morphology, it is necessary to model the process by changing the electrospinning conditions and polymer properties. Depending on this change, many experiments should be done. However, this process is very time-consuming and costly.

In this study, the goal was to establish a simple and novel expression for accurately estimating the AFD of the electrospun PCL fibers with the help of the ABC algorithm. First, the experimental studies (based on changing the electrospinning process and polymer parameters) which planning within the context of RSM were carried out to produce PCL fibers. Then, the produced scaffolds were examined by SEM, and a data set which is containing AFD values depending on different combinations of the parameters (concentration of PCL, voltage, TTC distance,

and the flow rate) was obtained. Utilizing this data set, a closed-form expression is derived to be used to calculate the AFD of the electrospun PCL scaffolds. The optimum determination of the coefficients of the derived expression was performed with the ABC algorithm, which is one of the swarm intelligence techniques. The metrics such as MAPE and MAE applied to determine the success of the proposed expression, and the expression was seen to be very robust and successful. In addition, the results obtained in this study were compared with those reported elsewhere. As a result of this comparison, it was determined that the expression proposed was estimating the AFD more successfully. It is concluded that the expression presented in the study can be contributed to obtaining the electrospun PCL scaffold with the desired fiber diameter. The presented article is valuable because although there are many studies in the literature to estimate the AFD values of various electrospun fibers, it is one of the rare articles that can be referenced to estimate the fiber diameter of PCL. The predictive effect of each parameter on fiber formation and the estimation of AFD of the membranes that will be produced depending on the change of these parameters can be useful for a cheap, short time, and high amount of fabrication.

Declaration

The authors declared no potential conflicts of interest with respect to the research, authorship, and/or publication of this article. The authors also declared that this article is original, was prepared in accordance with international publication and research ethics, and ethical committee permission or any special permission is not required.

Author Contributions

C. Yilmaz; methodology, investigation, writing of original draft. D. Demir; methodology, investigation, writing of original draft. N. Bolgen; visualization, editing, supervision. A. Akdagli; the corresponding author, visualization, editing, supervision.

Acknowledgment

This work was supported by the Scientific Research Projects Unit of Mersin University (2018-1-AP2-2785).

Nomenclature

<i>ABC</i>	: Artificial bee colony
<i>AFD</i>	: Average fiber diameter
<i>ANFIS</i>	: Adaptive Neuro-Fuzzy Inference Systems
<i>ANN</i>	: Artificial neural network
<i>GEP</i>	: Gene Expression Programming
<i>MAE</i>	: Mean absolute error
<i>MAPE</i>	: Mean absolute percentage error
<i>PCL</i>	: Poly (ϵ -caprolactone)
<i>RSM</i>	: Response surface methodology
<i>SEM</i>	: Scanning electron microscopy

SVMs : Support Vector Machines

TTC : Tip to collector

References

- Mishra, R. K., et al., *Electrospinning production of nanofibrous membranes*. Environmental Chemistry Letters, 2019. **17**(2): p. 767-800.
- Bölgen, N., D. Demir, and A. Vaseashta, *Nanofibers for the Detection of VOCs*, in *Nanoscience Advances in CBRN Agents Detection, Information and Energy Security*. 2015, Springer: Dordrecht. p. 159-165.
- Amariei, N., et al., *The Influence of Polymer Solution on the Properties of Electrospun 3D Nanostructures*. IOP Conference Series: Materials Science and Engineering, 2017. **209**: p. 12092-12100.
- Angel, N., et al., *Effect of Processing Parameters on the Electrospinning of Cellulose Acetate Studied by Response Surface Methodology*. Journal of Agriculture and Food Research, 2019. **2**.
- Haider, A., S. Haider, and I.-K. Kang, *A comprehensive review summarizing the effect of electrospinning parameters and potential applications of nanofibers in biomedical and biotechnology*. Arabian Journal of Chemistry, 2018. **11**(8): p. 1165-1188.
- Serbezeanu, D., et al., *Preparation and characterization of thermally stable polyimide membranes by electrospinning for protective clothing applications*. Textile Research Journal, 2015. **85**(17): p. 1763-1775.
- Zhao, G., et al., *Piezoelectric polyacrylonitrile nanofiber film-based dual-function self-powered flexible sensor*. ACS Applied Materials & Interfaces, 2018. **10**(18): p. 15855-15863.
- Diez-Pascual, A. and A. Diez-Vicente, *Antimicrobial and sustainable food packaging based on poly(butylene adipate-co-terephthalate) and electrospun chitosan nanofibers*. RSC Adv., 2015. **5**(113): p. 93095-93107.
- Faccini, M., et al., *Electrospun Carbon Nanofiber Membranes for Filtration of Nanoparticles from Water*. Journal of Nanomaterials, 2015. **2015**.
- Demir, D., et al., *Magnetic nanoparticle-loaded electrospun poly(ϵ -caprolactone) nanofibers for drug delivery applications*. Applied Nanoscience, 2018. **8**(6): p. 1461-1469.
- İşoğlu, İ. A., et al., *Stem cells combined 3D electrospun nanofibrous and macrochannelled matrices: a preliminary approach in repair of rat cranial bones*. Artificial Cells, Nanomedicine, and Biotechnology, 2019. **47**(1): p. 1094-1100.
- Bölgen, N., S. Ceylan, and D. Demir, *Influence of fabrication temperature on the structural features of chitosan gels for tissue engineering applications*. International Advanced Researches and Engineering Journal, 2019. **3**(3): p. 170-174.
- Hong, Y., *Electrospun Fibrous Polyurethane Scaffolds in Tissue Engineering*, in *Advances in polyurethane biomaterials*. 2016, Woodhead. p. 543-559.
- Wu, J. and Y. Hong, *Enhancing cell infiltration of electrospun fibrous scaffolds in tissue regeneration*. Bioactive Materials, 2016. **1**(1): p. 56-64.
- Maleki, H., et al., *The influence of process parameters on the properties of electrospun PLLA yarns studied by the response surface methodology*. Journal of Applied Polymer Science, 2015. **132**(5).

16. Amiri, N., et al., *Modeling and process optimization of electrospinning of chitosan-collagen nanofiber by response surface methodology*. Materials Research Express, 2018. **5**(4).
17. Tang, Z. S., et al., *Response Surface Modeling of Electrospinning Parameters on Titanium Oxide Nanofibers' Diameter: A Box-Behnken Design (BBD)*. Advanced Science Letters, 2017. **23**(11): p. 11237-11241.
18. Maurya, A., et al., *Modeling the relationship between electrospinning process parameters and ferrofluid/polyvinyl alcohol magnetic nanofiber diameter by artificial neural networks*. Journal of Electrostatics, 2020. **104**.
19. Naghibzadeh, M. and M. Adabi, *Evaluation of effective electrospinning parameters controlling gelatin nanofibers diameter via modelling artificial neural networks*. Fibers and Polymers, 2014. **15**(4): p. 767-777.
20. Nurwaha, D. and X.J.G.J.T.O. Wang, *Modeling and Prediction of Electrospun Fiber Morphology using Artificial Intelligence Techniques*. Global Journal of Technology & Optimization, 2019. **10**(1): p. 237-243.
21. Khatti, T., et al., *Application of ANN and RSM techniques for modeling electrospinning process of polycaprolactone*. Neural Computing & Applications, 2019. **31**(1): p. 239-248.
22. Abolhasani, M.M., et al., *Towards predicting the piezoelectricity and physiochemical properties of the electrospun P (VDF-TrFE) nanogenerators using an artificial neural network*. Polymer Testing, 2018. **66**: p. 178-188.
23. Esnaashari, S.S., et al., *Evaluation of the effective electrospinning parameters controlling Kefiran nanofibers diameter using modelling artificial neural networks*. Nanomedicine research journal, 2017. **2**(4): p. 239-249.
24. Naghibzadeh, M., et al., *Evaluation of the effective forcespinning parameters controlling polyvinyl alcohol nanofibers diameter using artificial neural network*. Advances in polymer technology, 2018. **37**(6): p. 1608-1617.
25. Shahrabi, S.S., J. Barzin, and P.J.M.R.E. Shokrollahi, *Statistical approach to estimate fiber diameter of PET/PVP blend electrospun using Taguchi method and fitting regression model*. Materials research express, 2018. **6**(2).
26. Karaboga, D., *An Idea Based on Honey Bee Swarm for Numerical Optimization, Technical Report - TR06*. Technical Report, Erciyes University, 2005.
27. Biçer, M. and A. Akdagli, *An experimental study on microwave imaging of breast cancer with the use of tumor phantom*. Applied Computational Electromagnetics Society Journal, 2017. **32**(10): p. 941-947.
28. Hetmaniok, E., D. Słota, and A. Zielonka, *Restoration of the cooling conditions in a three-dimensional continuous casting process using artificial intelligence algorithms*. Applied Mathematical Modelling, 2015. **39**(16): p. 4797-4807.
29. Li, G., et al., *Artificial bee colony algorithm with gene recombination for numerical function optimization*. Applied Soft Computing, 2017. **52**: p. 146-159.
30. Ustun, D. and A. Akdagli, *Design of a dual-wideband monopole antenna by artificial bee colony algorithm for UMTS, WLAN, and WiMAX applications*. International Journal of Microwave and Wireless Technologies, 2017. **9**(5): p. 1197-1208.
31. Zhao, H. and S. Yin, *Inverse analysis of geomechanical parameters by the artificial bee colony algorithm and multi-output support vector machine*. Inverse Problems in Science and Engineering, 2016. **24**(7): p. 1266-1281.
32. Karaboga, D., et al., *A comprehensive survey: artificial bee colony (ABC) algorithm and applications*. Artificial Intelligence Review, 2014. **42**(1): p. 21-57.
33. Rad, Z.P., et al., *Fabrication and characterization of PCL/zein/gum arabic electrospun nanocomposite scaffold for skin tissue engineering*. Materials Science and Engineering, 2018. **93**: p. 356-366.
34. Bölgen, N., et al., *In vitro and in vivo degradation of non-woven materials made of poly(ϵ -caprolactone) nanofibers prepared by electrospinning under different conditions*. Journal of Biomaterials Science, Polymer Edition, 2005. **16**(12): p. 1537-1555.

Appendix

$$AFD = \omega + \sigma$$

$$\omega = x_1 * \sin(P_1 * P_2 * P_4) + x_2 + x_3 * (P_1^{x_4}) + x_5 * (P_2 * P_3)^{x_6} + x_7 * P_4^{x_8} \quad (A.1)$$

$$\sigma = x_9 * \sin\left(\frac{x_{10} * P_1 * P_4}{P_2 * P_3}\right) + x_{11} * \sin\left(\frac{P_1 * x_{12}}{P_3}\right) + x_{13} * \sin\left(x_{14} * \frac{P_2}{P_3}\right) + x_{15} * \sin\left(\frac{P_2 * x_{16}}{P_4}\right)$$

$$AFD = \omega + \sigma$$

$$\omega = -5.561 * \sin(P_1 * P_2 * P_4) + 1000 + 5.4 * (P_1^{1.099}) + 999.90 * (P_2 * P_3)^{-1.167} - 1000 * P_4^{-0.006} \quad (A.2)$$

$$\sigma = 8.06 * \sin\left(\frac{-14.536 * P_1 * P_4}{P_2 * P_3}\right) - 29.515 * \sin\left(\frac{P_1 * 57.088}{P_3}\right) + 5.987 * \sin\left(-10.505 * \frac{P_2}{P_3}\right) - 17.375 * \sin\left(\frac{P_2 * 6.852}{P_4}\right)$$



Review Article

Review of machine learning and deep learning models in agriculture

Fatih Bal ^{a,*}  and Fatih Kayaalp ^b 

^aDepartment of Software Engineering, Kirklareli University, Kirklareli 39010, Turkey

^bDepartment of Computer Engineering, Duzce University, Duzce 81620, Turkey

ARTICLE INFO

Article history:

Received 28 December 2020

Revised 17 March 2021

Accepted 13 April 2021

Keywords:

Analysis
Artificial Intelligence
Agriculture
Deep Learning
Machine Learning
Prediction
Smart Farm

ABSTRACT

Machine learning (ML) refers to the processes that enable computers to think based on various learning methods. It can be also called domain which is a subset of Artificial Intelligence (AI). Deep learning (DL) has been a promising, new and modern technique for data analysis in recent years. It can be shown as the improved version of Artificial Neural Networks (ANN) which is one of the popular AI methods of today. The population of the world is increasing day by day and the importance of agriculture is also increasing in parallel. Because of this, many researchers have focused on this issue and have tried to apply machine learning and deep learning methods in agriculture under the name of smart farm technologies both to increase agricultural production and to solve some challenges of agriculture. In this study, it is aimed to give detailed information about these up-to-date studies. 77 articles based on machine learning and deep learning algorithms in the agriculture field and published in IEEE Xplore, ScienceDirect, Web of Science and Scopus publication databases between 2016 and 2020 years were reviewed. The articles were classified under five categories as plant recognition, disease detection, weed and pest detection, soil mapping-drought index, and yield forecast. They were examined in detail in terms of machine learning/deep learning architectures, data sets, performance metrics (Accuracy, Precision, Recall, F-Score, R^2 , MAPE, RMSE, MAE), and the obtained experimental results. Based on the examined articles, the most popular methods, used data sets/types, chosen performance criteria, and performance results among the existing studies are presented. It is seen that the number of AI-based applications related to agriculture is increasing compared to the past and the sustainability in productivity is so promising.

© 2021, Advanced Researches and Engineering Journal (IAREJ) and the Author(s).

1. Introduction

The mind is formed by the combination of thinking, comprehension, understanding, decision-making, reasoning, and knowledge power [1]. Intelligence combines all these goals and making them suitable for the situation [2]. Artificial intelligence brings in all these abilities to the machine. Artificial intelligence is an effort to make the computer do what people do [3]. Today, artificial intelligence studies conducted in many fields are also carried out in the field of agriculture. Given the fact that the world population is increasing rapidly, agricultural products and nutrition are critical for the continuation of human life. People have made radical changes in agricultural products by the discovery of modern

agriculture [4]. Besides, the supply and production of agricultural products have a great importance in the global economy [5]. The decrease in agricultural production due to the effect of global warming, drying of wetlands, unconscious irrigation and unconscious agriculture poses a great danger to world population. Because of these effects, the amount of nutrition is increasing in parallel with the rapid increase in the world. Looking at the developments, it seems that smart farming has become critical to overcome the challenges [6].

Machine learning (ML) has emerged with big data and high performance and is actively used in many areas of the industrial environment such as entertainment and commerce [7]. Machine learning has started to create opportunities in agricultural fields by using the learning

* Corresponding author. Tel.: +90-288-214-0514; Fax: +90-288-214-0516.

E-mail addresses: fatihbal@klu.edu.tr (Fatih Bal), fatihkayaalp@duzce.edu.tr (Fatih Kayaalp)

ORCID: 0000-0002-7179-1634 (Fatih Bal), 0000-0002-8752-3335 (Fatih Kayaalp)

DOI: 10.35860/iarej.848458

This article is licensed under the CC BY-NC 4.0 International License (<https://creativecommons.org/licenses/by-nc/4.0/>).

abilities of measuring and understanding data. Deep learning (DL) is a branch of machine learning that tries to model abstractions with a series of algorithms by using a deep layer with multiple processing layers [8]. Deep learning, which is of great interest in the field of artificial intelligence, has come to the fore in natural language processing and image classification. In this study, previous studies on deep learning and machine learning in agriculture applications were examined. Articles published between 2016 and 2020 in the most well-known and used databases (IEEE Xplore, Science Direct, Web of Science, Scopus) were searched using the keywords “Machine Learning in Agriculture” and “Deep Learning in Agriculture”. 7 studies from 2016, 9 studies from 2017, 14 studies from 2018, 29 studies from 2019, and 18 studies from 2020 were examined. While 71% (55 articles) of the 77 articles were related to the United States, United Kingdom, China, India, Spain and Australia, 29% of them (22 articles) were related to other countries.

While ML and the most used ML methods were defined in the *second section*, DL and the most used DL methods were defined in the *third section*. Articles and applications related to ML and DL in agriculture were reviewed in the *fourth section*.

2. Machine Learning

ML refers to the process of creating a mathematical model on sample data sets called training data to make predictions and decisions [9]. ML, a sub-branch of artificial intelligence [90] and developed based on learning models, is a system that investigates the working principle of algorithms that can make predictions through data (Figure 1). The data to be used for prediction is trained and classified (Dataset) with a ML algorithm. The test (sample) data are appropriately classified according to the data being trained (Figure 2). Depending on their learning skills, ML algorithms are divided into three separate categories as Supervised, Unsupervised and Reinforcement Learning. Classification and Regression Models are examined in the *supervised learning* category. Clustering and Dimensionality Reduction are examined in the *unsupervised learning* category and Real-Time Decisions models are examined in the *reinforcement learning* category. Supervised learning makes predictions over the designed model by using input data. Unsupervised learning performs more complex processing tasks. Dimension reduction is a method that can be analyzed with both supervised and unsupervised learning methods. PCA (Principal Component Analysis), PLSR (Partial Least Squares Regression) and LDA (Linear Discriminant Analysis) are the most known and used dimensional reduction algorithms. ML techniques are generally used to analyze human behavior benefiting from available data, enable businesses to carry out production accordingly, and

also to create business models and decision support systems. Especially, behaviors of individuals are analyzed through online shopping, social media, e-mail contents, etc. and characteristics of human behavior can be determined. Today, many cellphones, laptops and electronic devices use various ML-based applications for different purposes.

3. Deep Learning

Deep learning (DL), first pronounced by Igor Aizenberg in the early 2000s, became more popular in 2016 [10]. DL gives more depth and complexity to the model and improves the classic ML model through transforming data into various levels of abstraction by using artificial neural network (ANN) or similar ML algorithms [11].

DL is a much more advanced model of ANNs. While ANNs consist of three layers (input, output and hidden layers), networks with more than one hidden layer number are called deep learning. DL produces an output by self-learning the information passed through hidden layers as seen in Figure 3. It has algorithms such as Convolutional Neural Networks, Recurrent Neural Networks, Restricted Boltzmann Machine, and Deep Belief Network [12]. DL has the advantages of processing unstructured data at the maximum level, producing high quality results, and avoiding unnecessary costs. On the other hand, it has some disadvantages such as needing much larger amount of data and high cost for software and hardware. It is used in a wide range of areas including natural language processing, driverless vehicles, image processing, face recognition, and personalized shopping planning.

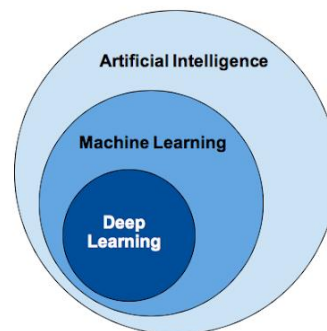


Figure 1. Relationship between DL and ML

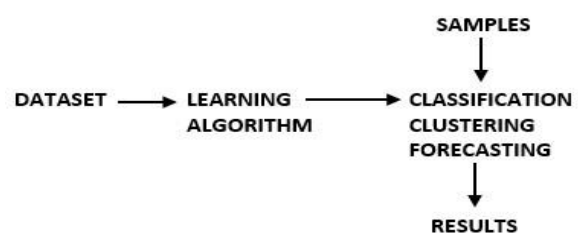


Figure 2. Machine Learning Architecture

4. Methodology

We carried out literature review of academic articles indexed on the Scopus, Web of Science, Science Direct and IEEE Xplore to assess the extent to which ML and DL features with in the agriculture. We have analyzed and classified articles in two fields which are ML and DL. These articles have been explored in details based on various features such as years of the studies, aim of the studies (plant recognition, disease detection, weed and pest detection, soil mapping-drought index and yield forecasting), properties of the datasets used in the studies, architectures, performance criteria examined in the studies and received results.

4.1. Data

As mentioned in methodology, the study contains articles from four well-known databases such as Scopus, Science

Direct, Web of Science and IEEE Xplore. The main reason for selection of these databases is that they are considered to include the highest quality and up-to-date publications. In order to list the up-to-date publications to readers, data used for this study were collected from January to June 2020 for the years from 2016 to 2020 with the keywords “*Machine Learning in Agriculture*”, “*Deep Learning in Agriculture*”. The study was conducted as a doctoral thesis. As the final dataset, 77 articles within the scope of studies similar to doctoral thesis have been reviewed. Of the total 77 articles reviewed, 10 were on plant recognition, 16 were on disease detection, 9 were on weed and pest detection, 26 were on yield forecasting and 16 were on soil mapping, drought index and other studies.

4.2. Studies on ML and DL

In this section studies related to ML and DL are classified according to their fields. Of the total 77 articles reviewed, 10 were on *Plan Recognition*, 16 were on *Disease Detection in Plants*, 9 were on *Weed and Pest Detection*, 26 were on *Yield Forecasting* categories, and 16 were on *Soil Mapping, Drought Index and Other Studies*.

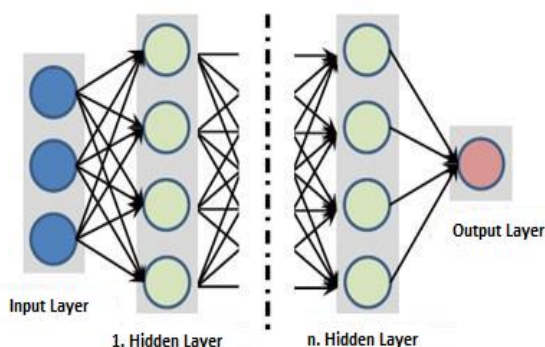


Figure 3. Deep Learning Architecture [8]

4.2.1. Plant Recognition

Identification of the plant species has been realized with ML and DL methods depending on classification algorithms in smart agriculture applications based on artificial intelligence (Table A.1 in Appendix). 126 citrus images obtained in different sizes and under various lighting conditions were trained with ML algorithms and a study was carried out to determine the green citrus fruit [13]. Plant species were classified using DL algorithms on many images obtained from 1200 Turkey TARBIL station [14]. Similarly, a various plant type was classified with DL algorithms by using the half-hour images obtained from the Turkey TARBIL system [15]. Coffee leaf rust was modeled with images obtained using a hand-made spectroradiometer [16]. Product type recognition was carried out with ML algorithms using 126 Rice, Corn and Soybean plant images obtained from 2017 Sentinel-II satellite [17]. Determination of wheat nitrogen and water status was carried out using data combined with annual rainfall data [18]. Using DL algorithm, 450 images of Lycopersicon were classified into three different level as mature, semi-mature, and immature [19]. In order to detect *Convolvulus Sepium* plant in sugar beet fields and to detect changes in the appearance of sugar beet plants, necessary detection process was performed on 2271 synthetic images of 452 areas [20]. A hybrid algorithm was developed to estimate size of rice kernels, and data sets containing long, medium and short grain rice images were used in three separate data sets for training model [21]. Flaws of the lemon fruit were detected by using ML and DL methods on 341 images (185 healthy shaped, 156 damaged shaped) of sour lemon with different shapes, and accordingly lemons were classified [22].

4.2.2. Disease Detection in Plants

One of the most important problems in agriculture and the production of agricultural products is plant diseases. To prevent this, pesticides are sprayed homogeneously on the crops, or weeds are cleaned with the help of manpower to prevent and control harmful organisms. However, while doing this, labor, financial issues and time costs are high. In order to prevent these diseases and reduce time and cost, studies have been carried out on smart farming systems with ML and DL-based algorithms (Table A.2 in Appendix). In literature; the hybrid model developed for multi-class classification problems was applied on the traits that trigger oilseed disease [23]. Multicolor fluorescent imaging was applied together with thermography in order to detect soft rot caused by *Dickeya Dadantii* (Negative Bacteria) in the pumpkin plant [24]. An improved moth flame approach was proposed to detect tomato diseases, and the proposed algorithm ensured the highest classification accuracy [25]. A technique for disease detection and classification was explained with the

aid of ML mechanisms and image processing tools [26]. Symptomatic recognition of four diseases of cucumber (anthracnose, downy mildew, powdery mildew, leaf spots) was tried to be detected using DL algorithms [27]. Detection of diseased melon leaves was performed using ML-based algorithms on numerical data provided through various imaging techniques [28]. It was aimed to develop an automated proof of concept by using images of A. Psidii disease in lemon tree [29]. A new Exponential Spider Monkey Optimization, which was used to fix important features from high dimensional features created by SPAM, and supported by SVM was developed, and it was compared with other ML algorithms to classify plants as healthy and diseased images [30]. It was aimed to detect diseases in red vine leaves by using yellowing and severe symptoms of grape leaves on color images of Grapevine Yellow leaves [31]. A multi-layer DL algorithm was developed to identify anthracnose disease and symptoms in mango leaves [32]. A model using the ML algorithm was proposed to detect rice blast disease in the early stages of cultivation [33]. A method was developed to detect diseases through plant leaf images by using the TensorFlow object detection API [34]. An automatic identification method was developed for diseases, such as healthy, downy mildew, powdery mildew and rot, in various leaf sample images corresponding to different product types [35]. An onion area was regularly monitored through the established monitoring system and the symptoms of the disease were tried to be determined by creating four different models based on the images obtained [36]. Disease detection was performed with DL algorithms over a data set containing various disease images in order to detect disease types in tomato, potato, corn, and apple plants [37]. Cassava plant diseases have been tried to be determined by using the category of cassava leaf disease [38].

4.2.3. Weed and Pest Detection

Weed and pest detection is one of the major problems in agriculture for crop production and has turned into a serious problem for many producers. Weed and pest detection is crucial for sustainable agriculture. For this purpose, in studies related to smart agriculture, detection studies have been carried out by using ML and DL methods (Table A.3 in Appendix). In literature; a hybrid algorithm consisting of Deep-CNN and SVM was used to identify and classify 22 different Lepidoptera (Butterfly) species on 1301 images [39]. Anastrepha fruit fly species were determined by using ML algorithms in order to avoid insect analysis time and economic losses related to agricultural pests [40]. For pest detection, a DL-based algorithm was proposed for the development of an agricultural pest identification system based on computer vision technology [41]. A DL-based approach aimed at

weed specific herbicide application was proposed to detect weeds on soybean images and classify weeds [42]. The characteristics of the pest images were determined from a large number of unlabeled image structures by using unsupervised learning methods [43]. Spanish phytosanitary products were classified using four separate ML algorithm methods in order to classify pesticide regulations correctly [44]. An ML-based algorithm was developed for weed and crop separation, and their accuracies were compared with NDVI values [45]. A large-scale study was conducted at 336 French sites to determine crop damage caused by the presence of wireworm and raiding species [46]. DL-based approaches were used for foreign object analysis through images obtained with UAV at four different times in two different rice fields [47].

4.2.4. Soil Mapping, Drought Index and Determining Agricultural Vehicles

It is important to determine suitable soil types for agriculture and to prepare drought index. In this context, studies conducted for soil mapping and determination of drought index were analyzed. The reviewed articles related to weed and pest detection are presented Table A.4 (in Appendix); A variance-based solution was proposed to identify the central pivot irrigation system and position the center of each central pivot system at a more effective point [48]. A geoparser-based soil mapping was proposed, and by applying ML methods, establishing the relationship between the phosphorus in the soil and the environment was tried [49]. SDAP model was proposed to predict drought areas without meteorological data and assuming no rainfall. This study was carried out for short-term drought prediction [50]. The temporal behavior of the soil ground was estimated using two separate ML algorithms, and Meteorological data were used as input [51]. A DL-based model named AMTNet was designed for the identification and classification of agricultural machinery [52]. A medium resolution imaging spectroradiometer was used to measure the surface temperature of the land up to 90 meters and to make a comparison between ML-based algorithms by scaling the image [53]. Neural networks offer real-time computational flow. The load on the neural network was restrained and the pretreatment by removing the plants from the background was briefly discussed [54]. A hybrid heuristic method was developed to estimate the irrigation time and find the most suitable decision tree to model the farmers' behavior [55]. To monitor agricultural drought data in Southeast Australia, an attempt was made to estimate drought over wheat yield by using SPEI data sensed remotely by the Tropical Rainfall Measuring Mission and MODIS satellite [56]. ML algorithms were used to define the relationships between soil properties and multiple common variables that can be detected in the

landscape, and the most appropriate ML algorithm was selected for digital soil mapping (DSM) [57]. New approaches were proposed to map the agricultural drought hazard by using machine learning methods [58]. The potential of the DL approach to automatically draw agricultural plot boundaries from orthophoto images in large areas with a heterogeneous landscape was explored [59]. The crop drought mapping system was implemented by evaluating crop stress with RGB images obtained from UAV vehicles [60]. DL-based models were examined to calculate the crop water stress index (CWSI) which is one of the parameters obtained from the vegetation temperature and measured in open irrigation [61]. A new drought index (IDI) that defines the multivariate relationship between agricultural drought conditions was proposed [62]. A hybrid model was developed by combining the global climate model and ML-based model to forecast 90-day weather on field scale [63].

4.2.5. Yield Forecasting

Depending on the increasing world population, increasing agricultural productivity has come to a very important point. The reviewed articles related to yield forecasting are presented in Table A.5 (in Appendix). It was tried to predict wheat yield through images obtained from different soil and crop sensors by using an unsupervised learning algorithm [64]. An ML-based model was applied to estimate the NDVI values of large pastures in the USA. The prediction model consisted of data on vegetation index and meteorological factors [65]. A hybrid approach was proposed to perform yield classification of sugarcane based on various soil and climate parameters [66]. A classification model was developed to predict the production in an orchard and determine the effects of ML-based models and factors on production [67]. Two separate artificial intelligence models were developed to predict ET₀ (Evapotranspiration) by using only temperature data in Sichuan region of China [68]. ML-based models were used to define the importance of remotely sensed image variables in the spatial prediction of soil and maize yield [69]. A collection of 76 regressors was proposed for the estimation of soil organic carbon productivity indices of four important soil nutrients [70]. An ML-based prediction model was developed to determine and map cotton lint yield in a 73-hectare field in Tennessee, USA [71]. Three separate DL-based simulation models were carried out to predict the rapeseed (canola) plant before harvest and to determine the most important independent variables affecting the yield of rapeseed [72]. The possibility of using ML algorithms was examined on the satellite images obtained to evaluate the spatial variation of corn grain yield in cropland scale, and the measured yield was analyzed [73]. An attempts was made to estimate wheat

yield in Australia by looking at time series-based climate records and satellite images [74]. A DL-based model was developed to estimate the number of seeds from soybean images [75]. Participants were asked to predict their yield performance using data from 2017, and a model based on DL algorithms was developed at the Syngenta Crop Competition in 2018 [76]. Yield estimation study was carried out using data on wheat, barley and canola crops as a case study on a large farm in Western Australia [77]. Phenotype characteristics of trees belonging to 25 different rootstock varieties on orange yield were determined using high-type phenotyping system on images obtained by UAV [78]. A software called AirSurf, which was an open-source hybrid system, was developed to automatically measure yield related phenotypes on ultra-large aerial images for lettuce [79]. A ML-based model was developed to estimate the amount of carbamazepine (CBA) and diclofenac (DCF) in tissues of lettuce plants irrigated with water recovered from water treatment plants [80]. ML methods were used to estimate interpolation accuracy by using greenhouse environment data, and the results were compared with each other [81]. An ML approach was used to increase crop yields based on crop planting dates and to estimate the annual crop planting date [82]. ML approaches were used to estimate ET₀ (Evapotranspiration) by using data from the Verde Grande River basin [83]. A new criterion was introduced to determine daily ET₀, improve classification efficiency, educate, and validate for the regions of Hoshiarpur and Patiala, Punjab state of India [84]. A segmentation method based on DL model was implemented to automatically perform the segmentation task [85]. A case study on maize production was conducted to predict global warming and eutrophication effects, and ML algorithms were compared to determine the most efficient and accurate model [86]. An ML-based prediction model was developed to measure global warming and eutrophication effects on the life cycle of corn production [87]. ML-based models were used to evaluate moisture content and fruit quality for apple and mango plants [88]. An architectural model was developed to assess soil fertility and productivity and to make farming more efficient and productive with minimal impact on the environment [89].

5. Results and Discussions

It was determined that while 50% of the reviewed studies on *plant recognition* involved DL models, other studies involved the use of ML methods and the comparison of the results of the performance metrics of these methods. While the most preferred DL models were CNN-based models, SVM and ANN algorithms were used more in ML methods. It was seen that 10% of the studies on plant recognition were carried out by implementing a hybrid model using ML algorithms. The hybrid model was

created with the combination of five different ML algorithms (SVM, ANN, RF, KRR, and KNN). It was observed that models were mainly evaluated by looking at accuracy, precision, recall, and F1-Score metric values in the studies performed using both methods (ML and DL). The most studied agricultural product was rice in plant recognition.

While 37% of the examined studies on *disease detection* in plants were carried out with DL models, 50% of them were realized with ML algorithms and 13% were carried out by using hybrid models. While studies on DL were carried out with CNN and CNN-based models, ML studies were carried out using SVM and ANN algorithms. While one of the two studies created using hybrid models was performed with DL, CNN-based models were used as a model. Another hybrid model was realized with ML methods and this model was a combination of logistic regression and naive bayes algorithms. The most studied agricultural product was tomato.

While 55% of the studies on *weed and pest detection in plants* were carried out on pest detection, 45% was carried out on weed detection. 50% of the studies carried out with *pest detection* was realized with DL methods, the other 50% was realized with ML methods. CNN and CNN based AlexNet, ResNet-50, and ResNet-101 models were used as ML methods. MLP, SVM, LR and RF algorithms were used as ML algorithms. While CNN and CNN-based FCNN and AlexNet were preferred as DL methods in studies carried out with *weed detection*, SVM, LR and RF algorithms were preferred as ML algorithms. The results obtained by all methods were compared with each other's performance criteria and the best model was selected.

While 11 of 16 studies on *soil mapping, drought index and determination of agricultural vehicles* were carried out for the detection of agricultural drought, 4 of them were for soil mapping, and 1 of them was for identification of agricultural vehicles. Of the 11 studies conducted for the *detection of agricultural drought*, 4 were carried out with DL methods, 5 were carried out with ML methods, and 2 were implemented with hybrid models developed with ML methods. CNN and CNN based LeNet, AlexNet, VGGNet, SegNet models were used as DL models. ANN, RF, SVM, MLP algorithms were used as ML models. While one of the implemented hybrid models consisted of the combination of decision tree and genetic algorithm, the other hybrid model was created by combining ELM and GloSea5GC2 climate model. *Of 4 studies conducted for soil mapping*, 1 was carried out with DL methods, the others were carried out with ML methods. CNN algorithms were used as DL model, ANN, SVM and RF algorithms were used as ML models. Only one study was carried out for *determining agricultural vehicles*, and Google Inception v3 and ResNet-50 models were used for that study. Accuracy, precision and error averages of

models and algorithms were examined throughout the studies and algorithms, and models were compared based on these values.

73% of the applications realized for yield forecasting were carried out with ML methods. The most used ML algorithms were ANN, SVM, Decision Tree, LR, RF, and MLP. CNN and CNN-based model, which was SegNet, were used as a DL method. MAE, R^2 , RMSE, and correlation coefficient values were checked to compare the results of the algorithms and models in general. The most studied agricultural products in terms of yield were corn, wheat, lettuce crop amount, and Evapotranspiration value.

It is seen that the use of image data obtained from different sources is widespread thanks to the advances in image processing methods in ML and DL. Especially CNN based architectures are so popular.

The articles reviewed in the presented paper has been classified according to the aims of the studies and shown in Table 1. And another classification according to the years of studies in publication databases and shown in Table 2 below. When the two tables are examined, it is seen that most of the presented studies aims on yield forecasting. Most of the papers about agriculture has been listed in Scopus. As the end of the article collection process was June of 2020, number of listed studies in 2020 is smaller than 2019. But it is generally seen that the number of studies are increasing in recent years. It is thought that scientific studies in agriculture have increased due to the increasing importance of agriculture.

Table 1. Classification of Studies by Years and Aims

Years	Plant Recognition	Disease Detection	Weed and Pest Detection	Soil Mapping	Yield Forecast	Total
2016	2	2	0	0	3	7
2017	1	2	4	0	2	9
2018	1	4	4	2	3	14
2019	3	5	0	8	13	29
2020	3	3	1	6	5	18
Total	10	16	9	16	26	77

Table 2. Reviewed Articles in Academic Databases by Years (WOS: Web of Science, SD: Science Direct, IEEE: IEEE Xplore, SCO: Scopus)

Years	WOS	SD	IEEE	SCO	Total
2016	0	1	0	6	7
2017	0	0	0	9	9
2018	0	4	0	10	14
2019	4	4	5	16	29
2020	9	6	1	2	18
Total	13	15	6	43	77

6. Conclusion

ML and DL are two of the popular subsets of today's AI technology and used in various areas such as health, manufacturing, network, etc. As importance of agriculture is increasing in parallel with the population of the world, the scientists have focused on increasing the productivity in agriculture. Many studies about this topic have been conducted in the literature. For the purpose of providing up-to-date information to researchers, ML and DL-based articles about agriculture published in well-known publication databases, such as IEEE Xplore, ScienceDirect, Web of Science and Scopus, between 2016 and 2020 years were reviewed and presented in this study.

The articles were classified according to their main purposes, such as plant recognition, disease detection, weed and pest detection, soil mapping-drought index-determining agricultural vehicles, and yield forecasting. The review of the studies showed that while the most preferred ML models were SVM, ANN, and RF, the most preferred DL models were CNN-based models which were AlexNet, LeNet, and ResNet-50. However, hybrid models of DL and ML were also used. Generally used performance criteria for both ML and DL models were accuracy, precision, F1-score, and recall. The most popular plant and agricultural products used in experiments were wheat, corn, rice, tomato, sugarcane, and soybean. Although most of the studies used images taken from drones or satellites, some studies also used meteorological data.

It is seen that the number of AI based-applications in agriculture is increasing compared to the past and this is very promising in terms of the sustainability in productivity.

Declaration

The authors declared no potential conflicts of interest with respect to the research, authorship, and/or publication of this article. The authors also declared that this article is original, was prepared in accordance with international publication and research ethics, and ethical committee permission or any special permission is not required.

Author Contributions

This study was prepared within the scope of a doctoral thesis. F. Bal is the PhD student and the F. Kayaalp is the supervisor. Conception and design of the study has been implemented by F. Kayaalp. After the acquisition of data, analysis and drafting of the manuscript has been carried out by F. Bal. Revising the manuscript critically in terms of important intellectual content has been performed by F. Kayaalp.

Nomenclature

AlexNet	: An another model of CNN (Designed by Alex Krizhevsky)
AMTNet	: A version of Inception_v3 Network
ANFIS	: Adaptive Network Based Fuzzy Inference System
ANN	: Artificial Neural Networks
API	: Application Programming Interface
BP Network	: Back Propagation Network
BRT	: Boosted Regression Tree
CART	: Classification and Regression Trees
CNN	: Convolutional Neural Networks
CWSI	: Crop Water Stress Index
D-CNN	: Deep CNN
DL	: Deep Learning
DSM	: Digital Soil Mapping
D-Tree	: Decision Tree
ELM	: Extreme Learning Machine
ET0	: Evapotranspiration
FCNN	: Fully Convolutional Neural Networks
KNN	: K-Nearest Neighbors
KRR	: Kernel Ridge Regression
LDA	: Latent Dirichlet Algorithms
LeNet	: An another model of CNN (Designed by Yann LeCun)
LR	: Logistic Regression
MAE	: Mean Absolute Error
MAPE	: Mean Absolute Percentage Error
MARS	: Multivariate Adaptive Regression Spline
ML	: Machine Learning
MLP	: Multi-Layer Perceptron
MODIS	: Moderate Resolution Imaging Spectroradiometer
NB	: Naive Bayes
NDVI	: Normalized Difference Vegetation Index
PLSR	: Partial Least Squared Regression
PSO	: Particle Swarm Optimization
RBF	: Radial Basis Function
RF	: Random Forest
RGB	: Red-Green-Blue colors
RMSE	: Root Mean Squared Error
SDAP	: Severe Drought Area Prediction
SegNet	: Semantic Segmentation
SPAM	: Subtractive Pixel Adjacency Model
SPEI	: Standardized Precipitation-Evapotranspiration Index
SVM	: Support Vector Machine
TARBIL	: Tarımsal İzleme ve Bilgi Sistemi (Agricultural Monitoring and Information System)
UAV	: Unmanned Aerial Vehicle
USA	: United States of America
VGGNet	: Visual Geometry Group (Designed by VGG from Oxford University)

References

1. Elmas, Ç., *Yapay Zekâ Uygulamaları [Artificial Intelligence Applications]*, Turkey: Seçkin Yayınları, 2016, s. 21. (In Turkish).

2. Oleron, P., *Zekâ [L'Intelligence]*, İletişim Yayınları/Çeviri [Translator]– Ela Güngören, 1996, s. 26. (In Turkish)
3. Nabyev, V. V., *Yapay Zekâ [Artificial Intelligence]*, Turkey: Seçkin Yayınları, 2016, s. 25. (In Turkish).
4. Gülgönül, A. and Akiş, E., *Sınır Ötesi Tarım Yatırımlarının Geleceği ve Ülkelerin Sınır Ötesi Tarım Yatırımı İhtiyacının Tespiti İçin Bir Yaklaşım*. Atatürk Üniversitesi İktisadi ve İdari Bilimler Dergisi, 2020. **34** (2): p. 531-553.
5. Liakos, K. G., Busato, P., Moshou, D., Pearson, S. and Bochtis, D., *Machine Learning in Agriculture: A Review*. Sensors, 2018. **18**(8): p. 2674.
6. Avinash, C. Tyagi, *Towards a second green revolution*. Irrigation and Drainage, 2016. **65**(4): p. 388-389.
7. Michael, S., Ronay, A. and Thomas, H., *A survey of the advancing use and development of machine learning in smart manufacturing*. Journal of Manufacturing Systems, 2018. **48**: p. 170-179.
8. Kaya, U., Yılmaz, A. and Dikmen, Y., *Sağlık alanında kullanılan derin öğrenme yöntemleri*. European Journal of Science and Technology, 2019. **16**: p. 792-808.
9. Mitchell, T. M., *Machine learning*, McGrawHill, [Cited 2021, 9 April]; Available from: <http://www.cs.cmu.edu/~tom/>
10. Goodfellow, I., Bengio, Y. and Courville, A., *Deep Learning* [Cited 2021, 9 April]; Available from: <https://www.deeplearningbook.org/>
11. Schmidhuber J., *Deep learnign in neural networks: An overview*. IDSIA, 2020, **61**: p. 85-117.
12. Şeker, A., Diri, B. and Balık, H. H., *Derin öğrenme yöntemleri ve uygulamaları hakkında bir inceleme*. Gazi Mühendislik Bilimleri Dergisi, 2017. **3**(3): p. 47-64.
13. Zhao, C., Lee, W. S. and He, D., *Immature green citrus detection based on color feature and sum of absolute transformed difference (SATD) using color images in the citrus grove*. Computers and Electronics in Agriculture, 2016. **124**: p. 243-253.
14. Dyrmann, M., Karstoft, H. and Midtiby, H. S., *Plant classification using convolutional neural networks*. Biosystems Engineering, 2016. **151**: p. 72-80.
15. Yalcin, H., *Plant phenology recognition using deep learning: Deep-Pheno*. 2017 6th International Conference on Agro-Geoinformatics, 2017: p. 1-5.
16. Chemura, A., Mutanga, O. and Sibanda, M., *Machine learning prediction of coffee rust severity on leaves using spectroradiometer data*. Tropical Plant Pathology, 2018. **43**: p. 117-127.
17. Siwen, F. and Jianjun, Z., *Crop type identification and mapping using machine learning algorithms and Sentinel-II time series data*. IEEE Journal of Selected Topics in Applied Earth Observations and Remote Sensing, 2019. **12**(9): p. 1-12.
18. Tavakoli, H. and Gebbers, R., *Assesing nitrogen and water status of winter wheat using a digital camera*. Computers and Electronics in Agriculture, 2019. **157**: p. 558-567.
19. Kao, I. H. et al., *Determination of Lycopersicon maturity using convolutional autoencoders*. Scientia Horticulturae, 2019. **256**: p. 108538.
20. Gao, J. and Andrew, P. F., *Deep convolutional networks for image-based Convolvulus sepium detection in sugar beet fields*. Plant Methods 16, 2020. **29**.
21. Samrendra, K. and Sriram, K., *Machine learnt image processing to predict weight and size of rice kernels*. Journal of Food Engineering, 2020. **274**: p. 109828.
22. Jahanbakhshi, A., Momeny, M., Mahmoudi, M. and Zhang, Y. D., *Classification of sour lemons based on apparent defects using stochastic pooling mechanism in deep convolutional neural networks*. Scientia Horticulturae, 2020. **263**: p. 109133.
23. Chaudhary, A. and Kolhe, S., *A hybrid ensemble for classification in multiclass datasets: An application to oilseed disease dataset*. Computers and Electronics in Agriculture, 2016. **124**: p. 65-72.
24. Perez-Bueno M. L., Pineda, M., Francisco, C. M. and Baron, M., *Multicolor Fluorescence imaging as candidate for disease detection in plant phenotyping*. Frontiers in Plant Science, 2016. **7**: p. 1790.
25. Hassaniien, A. E. and Gaber, T., *An improved moth flame optimization algorithm based on rough sets for tomato diseases detection*. Computers and Electronics in Agriculture, 2017. **136**: p. 86-96.
26. Pooja, V., Das, R. and Kanchana, V., *Identification of plant leaf diseases using image processing techniques*. 2017 IEEE Technological Innovations in ICT for Agriculture and Rural Development (TIAR), 2017: pp. 130-133.
27. Ma J. et al., *A recognition method for cucumber diseases using leaf symptom images based on deep convolutional neural network*. Computers and Electronics in Agriculture, 2018. **154**: p 18-24.
28. Perez-Bueno M. L., Pineda, M., Francisco, C. M. and Baron, M., *Detection of bacterial infection in melon plants by classification methods based on imaging data*. Frontiers in Plant Science, 2018. **9**: p. 164.
29. Heim, R. et al., *Detecting myrtle rust (Austropuccinia psidii) on lemon myrtle trees using spectral signatures and machine learning*, Plant pathology, 2018: **67**(5): p. 1114-1121.
30. Kumar, S. and Sharma, B., *Plant leaf disease identification using exponential spider monkey optimization*. Sustainable Computing: Informatics and Systems, 2018. **28**: p. 100283.
31. Cruz, A., Ampatzidis, Y., Materazzi, A. and Luvisi, A., *Detection of grapevine yellows symptoms in Vitis vinifera L. with artificial intelligence*. Computers and Electronic in Agriculture, 2019. **157**: p. 63-67.
32. Singh, U. P., Chouhan, S. S. and Jain, S., *Multilayer Convolution Neural Network for the Classification of Mango Leaves Infected by Anthracnose Disease*. IEEE Access, 2019. **7**: p. 43721-43729.
33. Dharmar, V., *Application of Machine Learning in Detection of Blast Disease in South Indian Rice Crops*. Journal of Phytology, 2019. **11**(1): p. 31-37.
34. Cynthia, S. T. et al., *Automated Detection of Plant Diseases Using Image Processing and Faster R-CNN Algorithm*. 2019 International Conference on Sustainable Technologies for Industry 4.0 (STI), 2019: p. 1-5.
35. Pantazi, X.E., Moshou, D. and Tamourido A. A., *Automated leaf disease detection in different crop species through image features analysis and One Class Classifiers*. Computers and Electronics in Agriculture, 2019. **156**: p. 96-104.
36. Kim, W. S. et al., *Machine vision-based automatic disease symptom detection of onion downy mildew*. Computers and

- Electronics Agriculture, 2020. **168**: p. 105538.
37. Yang, H. et al., *Experimental analysis and evaluation of wide residual networks based agricultural disease identification in smart agriculture system*. J Wireless Com Network, 2019. **292**.
 38. Sambasivam, G. and Opiyo G. G., *A predictive machine learning application in agriculture: Cassave disease detection and classification with imbalanced dataset using CNNs*. Egyptian Informatics Journal, 2020. **22**(1): p. 27-34.
 39. Zhu, L. Q. et al., *Hybrid deep learning for automated lepidopteran insect image classification*. Oriental Insects, 2017. **51**(2): p. 79-91.
 40. Leonardo M. M. et al., *Mid-level Image Representation for Fruit Fly Identification (Diptera: Tephritidae)*. 2017 IEEE 13th International Conference on e-Science (e-Science), 2017: p. 202-209.
 41. Cheng, X. et al., *Pest identification via deep residual learning in complex background*. Computers and Electronics in Agriculture, 2017. **141**: p. 351-356.
 42. dos Santos Ferreira, A., Freitas, D. M., da Silva, G. G., Pistori, H. and Folhes, M. T., *Weed detection in soybean crops using ConvNets*. Computers and Electronics in Agriculture, 2017. **143**: p. 314-324.
 43. Xie C. et al., *Multi-level learning features for automatic classification of field crop pests*. Computers and Electronics in Agriculture, 2018. **152**: p. 233-241.
 44. Borja E. G. et al., *Machine learning for automatic rule classification of agricultural regulations: A case study in Spain*. Computers and Electronics in Agriculture, 2018. **150**: p. 343-352.
 45. Akbarzadeh, S., Paap, A., Ahderom, S., Apopei, B. and Alameh, K., *Plant discrimination by SVM classifier based on spectral reflectance*. Computers and Electronics in Agriculture, 2018. **148**: p. 250-258.
 46. Ramendra, P., Deo, R. C., Li, Y. and Marasemi, T., *Soil moisture forecasting by a hybrid machine learning technique: ELM integrated with ensemble mode decomposition*. Geoderma, 2018. **330**: p. 136-161.
 47. Huang H. et al., *Deep learning versus Object-based Image Analysis (OBIA) in weed mapping of UAV imagery*. International Journal of Remote Sensing, 2020. **41**(9): p. 3446-3479.
 48. Zhang, C. et al., *Automatic Identification of Center Pivot Irrigation Systems from Landsat Images Using Convolutional Neural Networks*. Agriculture, 2018. **8**: p. 100147.
 49. Dong, W. et al., *Digital Mapping of Soil Available Phosphorus Supported by AI Technology for Precision Agriculture*. 2018 7th International Conference on Agro-geoinformatics (Agro-geoinformatics), Hangzhou, 2018: p. 1-5.
 50. Park, H., Kim, K. and Lee D. K., *Prediction of Severe Drought Area Based on Random Forest: Using Satellite Image and Topography Data*. Water, 2019. **11**: p. 705.
 51. Termite, L. F., Garinei, A., Marini, A., Marconi, M. and Biondi, L., *Combining satellite data and Machine Learning techniques for irrigation Decision Support Systems*. 2019 IEEE International Workshop on Metrology for Agriculture and Forestry, 2019: p. 291-296.
 52. Zhang, Z. et al., *Deep learning-based automatic recognition network of agricultural machinery images*. Computers and Electronics in Agriculture, 2019. **166**: p. 104978.
 53. Li, W. et al., *Evaluation of Machine Learning Algorithms in Spatial Downscaling of MODIS Land Surface Temperature*. IEEE Journal of Selected Topics in Applied Earth Observations and Remote Sensing, 2019. **12**(7): p. 2299-2307.
 54. Knoll, F. J., Vitali, C., Harders, L. O. and Hussmann, S., *Real-time classification of weeds in organic carrot production using deep learning algorithms*. Computers and Electronics in Agriculture, 2019. **167**: p. 105097.
 55. Perea, R. G., Poyato E. C., Montesinos, P. and Diaz J. A. R., *Prediction of irrigation event occurrence of farm level using optimal decision trees*. Computers and Electronics in Agriculture, 2019. **157**: p. 173-180.
 56. Feng, P. et al., *Machine learning-based integraton of remoted-sensed droguht factors can improve this the estimation of agricultural drought in South-Eastern Australia*. Agricultural Systems, 2019. **173**: p. 303-316.
 57. Khaledian, Y. and Miller, B. A., *Selecting appropriate machine learning methods for digital soil mapping*. Applied Mathematical Modelling, 2020. **81**: p. 401-418.
 58. Rahmati, O. et al., *Machine learning approaches for spatial modeling of agricultural droughts is the south-east region of Queensland Australia*. Science of The Total Environment, 2020. **699**: p. 134230.
 59. Pedrero, A. G., Saavedra, M. L., Esparragon, D. R. and Martin, C. G., *Deep Learning for Automatic Outlining Agricultural Parcels: Exploiting the Land Parcel Identification System*. IEEE Access, 2019. **7**: p. 158223-158236.
 60. Su, J. et al., *Machine learning-based crop drought mapping system by UAV remote sensing RBG imagery*. World Scientific, 2020. **08**: p. 71-83.
 61. Gallego, J. G. et al., *Segmentation of Multiple Tree Leaves Pictures with Natural Backgrounds using Deep Learning for Image-Based Agriculture Applications*, Applied Sciences, 2020. **10**: p. 202.
 62. Liu, X. et al., *A remote sensing and artificial neural network-based integrated agricultural drought index: Index development and applications*. Catena, 2020. **186**: p. 104934.
 63. Shin, J. Y., Kim, K. R. and Ha, J. C., *Seasonal forecasting of daily mean air temperatures using a coupled global climate model and machine learning algorithm for field-scale agriculture management*. Agricultural and Forest Meteorology, 2020. **281**: p. 107858.
 64. Pantazi, X. E., Moshou, D. and Alexandridis, T., *Wheat yield production using machine learning and advanced sensing techniques*. Computers and Electronics in Agriculture, 2016. **121**: p. 57-65.
 65. Kang, L. et al., *Forecasting vegetation index based on vegetation-meteorological factor interactions with artificial neural network*. 2016 Fifth International Conference on Agro-Geoinformatics, 2016: p. 1-6.
 66. Natarajan, R., Subramanian J. and Papageorgiou, E. I., *Hybrid learning of fuzzy cognitive maps for sugarcane yield classification*. Computers and Electronics in Agriculture, 2016. **127**: p. 147-157.
 67. Diaz, I. et al., *Machine learning applied to the prediction of citrus production*, Spanish Journal of Agricultural Research, 2017. **15**(2): p. e0205.

68. Feng, Y. et al., *Modeling reference evapotranspiration using extreme learning machine and generalized regression neural network only with temperature data*. Computers and Electronics in Agriculture, 2017. **136**: p. 71-78.
69. Khanal, S., Fulton, J., Klopfenstein, A., Douridas, N. and Shearer, S., *Integration of high resolution remotely sensed data and machine learning techniques for spatial prediction of soil properties*. Computers and Electronics in Agriculture, 2018. **153**: p. 213-225.
70. Sirsat, M. S., Cernadas, E., Delgado, M. F. and Barro, S., *Automatic prediction of village-wise soil fertility for several nutrients in india using a wide range of regression methods*. Computers and Electronics in Agriculture, 2018. **154**: p. 120-133.
71. Haghverdi, A., Allen, R. A. W., Leib, B. G., *Prediction of cotton lint yield from phenology of crop indices using ANN*. Computers and Electronics in Agriculture, 2018. **152**: p. 186-197.
72. Niedbala, G. et al., *Application of ANN for yield modeling of winter rapeseed based on combined quantitative and qualitative data*. Agronomy, 2019. **9**(12): p. 781.
73. Kayad, A., Sozzi, M., Gatto, S., Marinello, F. and Pirotti, F., *Monitoring Within-Field Variability of corn yield using Sentinel-II and Machine learning techniques*. Remote Sensing, 2019. **11**(23): p. 2873.
74. Kamir, E., Waldner, F. and Hochman, Z., *Estimating wheat yields in Australia using climate records satellite image time series and machine learning methods*. ISPRS Journal of Photogrammetry and Remote Sensing, 2019. **160**: p. 124-135.
75. Li, Y. et al., *Soybean Seed Counting Based on Pod Image Using Two-Column Convolution Neural Network*. IEEE Access, 2019. **7**: p. 64177-64185.
76. Khaki, S. and Wang, L., *Crop yield prediction using deep neural networks*. Frontiers in Plant Science, 2019. **10**: p. 621.
77. Filippi, P. et al., *An approach to forecast grain crop yield using multi-layered, multi-farm data sets and machine learning*. Precision Agriculture, 2019: p. 1015-1029.
78. Ampatzidis, Y., Partel, V., Meyering, B. and Albrecht, U., *Citrus rootstock evaluation utilizing UAV based remote sensing and artificial intelligence*. Computers and Electronics in Agriculture, 2019. **164**: p. 104900.
79. Bauer, A. et al., *Combining computer vision and deep learning to enable ultra-scale aerial phenotyping and precision agriculture: A case study of lettuce production*. Horticulture Research, 2019. **70**.
80. Garcia, M. G., Lopez, C. F., Crespo, A. B. and Espana, R. M., *Extreme learning machine-based prediction of uptake of pharmaceuticals in reclaimed water irrigation lettuces in the region of murcia, spain*. Biosystems Engineering, 2019. **177**: p. 78-89.
81. Taewon M. et al., *Interpolation of greenhouse environment data using multilayer perceptron*. Computers and Electronics in Agriculture, 2019. **166**: p. 105023.
82. Zhang, C., Di, L., Lin, L. and Guo, L., *Machine-learned prediction annual crop planting in the U.S. Corn belt based on historical crop planting maps*. Computers and Electronics in Agriculture, 2019. **166**: p. 104989.
83. Reis, M. M. et al., *Empirical and learning machine approaches to estimating reference evapotranspiration based on temperature data*. Computers and Electronics in Agriculture, 2019. **165**: p. 104937.
84. Saggi, M. D. and Sushma, J., *Reference evapotranspiration estimation and modeling of the Punjab Northern India using deep learning*. Computers and Electronics in Agriculture, 2019. **156**: p. 387-398.
85. Majeed, Y. et al., *Deep learning-based segmentation for automated training of apple trees on trellis wires*, Computers and Electronics in Agriculture, 2020. **170**: p. 105277.
86. Romeiko, X. X., Guo, Z., Pang, Y., Lee, E. K. and Zhang, X., *Comparing machine learning approaches for predicting spatially explicit life cycle global warming and Eutrophication impacts from corn production*. Sustainability, 2020. **12**(4): p. 1481.
87. Lee, E. K. et al., *Projecting life-cycle environmental impacts on corn production in the U.S. Midwest under future climate scenarios using a machine learning approach*. Science of The Total Environment, 2020. **714**: p. 136697.
88. Ren, A. et al., *Machine learning driven approach towards the quality assessment of fresh fruits using non-invasive Sensing*. IEEE Sensors Journal, 2020. **20**(4): p. 2075-2083.
89. Helfer, G. A., Barbosa J. L., dos Santos, R. and da Costa A. B., *A computational model for soil fertility prediction in ubiquitous agriculture*. Computers and Electronics in Agriculture, 2020. **175**: p. 105602.
90. Sevlı, O. and Kemaloğlu, N., *Turkish sign language digits classification with CNN using different optimizers*, International Advanced Researches and Engineering Journal, 2020, **4**(3): p. 200-207.

Appendix

Table A.1. Studies on plant recognition

Article	Year	Plant	Dataset	Model/Algorithm	Result
[13]	2016	Citrus	RGB images of 126 citrus fruits	SVM	Accuracy SVM: 83%
[14]	2016	Various Plant Images	Images obtained from 1200 Turkey TARBIL stations	CNN, SVM-Kernel, SVM-Polynomial Kernel	Accuracy CNN: 100%, SVM: 91.2%, D-Tree: 81.5%, ANN: 93%, kNN: 83.6%
[15]	2017	Various Plant Images	The half-hour AlexNet images obtained from Turkey TARBIL system		For Wheat: CNN Precision: 82.62%, Recall: 83.64%, F1-Score 83.68%, Accuracy: 83.64%, MEF-BA precision: 75.51%, Recall: 74.53%, F1-Score: 74.57%, Accuracy: 74.53%; For Barley, CNN Precision: 79.32%, Recall 77.34% F1-Score: 78.43%, Accuracy: 77.15% MEF-BA Precision: 72.21%, Recall 71.68%, F1-Score: 72.21%, Accuracy: 71.43%
[16]	2018	Various Plant Images	Images obtained using a spectrodiameter	RBF-PLS, CLR	For RBF-PLS; R ² : 0.27, RMSE: 18.7 For CLR; R ² : 0.92, RMSE: 6.1
[17]	2019	Rice, Corn, Soybean	Images of Rice, Corn, Soybeans obtained from Sentinel-II satellite in 2017	RF, SVM	Accuracy RF: 88.6%, SVM: 98%
[18]	2019	Wheat	Average annual rainfall data for the years 2012, 2013, 2014 and combined data	PLSR	Accuracy RF: 88.6%, SVM: 98%
[19]	2019	Tomato	450 images obtained on ImageNet	CAE, CNN, SoftMax	F1-Score CNN+SoftMax: 99.63% CAE+CNN+SoftMax: 100% CNN+SVM: 100% CAE+CNN+SVM 100%
[20]	2020	Sugarcane	2271 Synthetic images in 452 different area	CNN Algoritmları: Yolo v3, Yolo v3-Tiny	MAPE Values; Yolo v3: 0.832 Yolo v3-Tiny: 0.810
[21]	2020	Rice	CL153 (Long grain dataset) Jupiter (Medium grain data) Calhikari 202 (Short grain dataset)	SEM Hibrit Modeli: RF, ANN, SVM, kRR, kNN	MEAN ERROR For CL153 dataset: 4.1% Jupiter dataset: 2.9% Calhikari for dataset: 4.3% has error rate.
[22]	2020	Sour Lemon	341 Sour lemon images (185 health shapes, 156 damages shapes)	CNN, SVM, D-Tree, ANN, kNN	Accuracy CNN: 100%, SVM: 91.2% D-Tree: 81.5%, ANN: 93% kNN: 83.6%

Table A.2. Studies on detection of plant diseases

Article	Year	Plant	Dataset	Model/Algorithm	Result
[23]	2016	Various Plant Images	A total of 13360 images from different sources	Hybrid Model (Logistic Regression and Naive Bayes)	Accuracy Hybrid Model: 94.73%
[24]	2016	Pumpkin	Many images of the pumpkin plant	Logistic Regression, ANN	LR, high dose-infiltrated leaves; YSA, low dose-infiltrated leaves. High accuracy predicted by rates.
[25]	2017	Tomato	Adult, Zoo, Lung, taken from the UCI ML pool Soybean-small, Monk's datasets	KNN, SVM	MFORS-kNN Accuracy:84%, Precision:84.2%, Recall: 83%; MFORS-SVM Accuracy: 84%, Precision 86%, Recall 87%
[26]	2017	Various Plant Images	250 images of 5 different diseases	SVM	Accuracy SVM: 94.2%
[27]	2018	Cucumber	14208 symptom images	D-CNN, RF, SVM, AlexNet	Accuracy D-CNN: 92.2%, AlexNet: 82.6%, SVM: 81.9%, RF 84.8%
[28]	2018	Melon	358 images between 3-7 DPI	LR, ANN, SVM	Accuracy LRA: 96.5%, SVM: 98.3%, ANN 99.1%
[29]	2018	Lemon	135 images of untreated lemon trees	RF	Accuracy RF: 95%

Article	Year	Plant	Dataset	Model/Algorithm	Result
[30]	2018	Various Plant Images	Image dataset from PlantVillage (500 healthy, 500 unhealthy)	SVM, LDA, kNN, ZeroR	Accuracy ESMO-SVM: 92.12%, ESMO-LDA: 80.79%, ESMO-kNN: 84.76%, ESMO-ZeroR: 49.32%
[31]	2019	Grape	Image dataset from PlantVillage in Tuscon region between July and October	AlexNet, GoogleNet, Google Inception v3, ResNet-50, ResNet-101, SqueezeNet	Accuracy AlexNet: 97.63%, GoogleNet: 96.36%, Google Inception v3: 98.43%, ResNet-50: 99.18%, ResNet-101: 99.33%, SqueezeNet: 93.77%
[32]	2019	Mango	1070 real-time environment images, 1130 images from the PlantVillage dataset. 2200 images in total	PSO, SVM, RBF, MCNN	Accuracy PSO: 88.39%, SVM: 92.75%, RBFNN: 94.20%, MCNN: 97.13%
[33]	2019	Rice	350 images for rice	kNN, ANN	Accuracy kNN for explosion image 85%, for normal image 86%; ANN for explosion image 99%, for normal image 100%
[34]	2019	Various Plant Images	236 healthy plants images; COCO dataset	R-CNN	Accuracy R-CNN: 67.34%
[35]	2019	Various Plant Images	Images obtained from smart phone and tablet	One Class SVM	Accuracy SVM: 95%
[36]	2020	Onion	Obtained real time images for onion	CNN	MAP; For A model: 75.0% For B model: 74.1% For C model: 81.8% For D model: 87.2%
[37]	2020	Tomato, Potato, Corn, Apple	Images of plant diseases 36,000 images	Wide Residual Networks, Google Inception v4	Accuracy WRN: 91.03% Google Inc. v4: 57.26%
[38]	2020	Cassava	10,000 images of 5 fine-grained Cassava roots	CNN	Accuracy CNN: 94%

Table A.3. Studies on weed and pest detection

Article	Year	Plant	Dataset	Model/Algorithm	Result
[39]	2017	Lepidoptera (Butterfly)	1301 images of 22 Lepidoptera species	CNN	LLC and CART method 95% His own methods 100%
[40]	2017	Anastrepha (Fruit Fly Pest)	301 images divided into different categories	MLP, NB, D-Tree, NB-Tree, kNN, Simple LR, SVM	Accuracy MLP: 88.9%, NB: 58.9%, D-Tree: 70.6%, NB-Tree: 71.6%, kNN: 79.5%, Simple-LR: 79.2%, SVM 87.7%
[41]	2017	Various Pest Images	Pest Images obtained from mixed agricultural land	SVM, BP-NN, AlexNet, ResNet-50, ResNet-101	Accuracy ResNet-101: 98.67%, ResNet-50: 94.67%, AlexNet: 86.67%, SVM: 44.00%, BP-NN: 42.67%
[42]	2017	Weed	Images acquired between 08:00 and 10:00 in the morning between December 2015 and March 2016	CaffeNet, SVM, AdaBoost, RF	Precision CaffeNet: 98%, SVM: 95%, AdaBoost: 96%, RF: 95%
[43]	2018	Various Pest Images	4500 pest images for D0 area 1440 butterfly images for D1 area 60 images of 24 pest kind pest images for D2 area 225 insect images for D3 area	Unsupervised Dictionary Learning	Accuracy For D0: 83.5% For D1: 97.2% For D2: 90.0% For D3: 91.5%
[44]	2018	Weed	Consisting of 25 420 words and 1135 rules a data set	LR, SVM, RF	Accuracy LR: 84.46%, RF: 84.04%, SVM 72.12%
[45]	2018	Weed, Beet, Corn	146 images of beet and corn plants	Gauss-SVM	Accuracy Gauss-SVM: 97%, NDVI: 70%
[46]	2018	Wireworm	14% of the land area and Data from Murray-Darling Basin covering 67% of agricultural land	ELM, RF	For ELM R values: 0.641, RMSE: 0.641, MAE: 0.055; For RF R values: 0.829, RMSE 0.056, MAE: 0.044
[47]	2020	Weed	364 pest images in F1 area, 240 pest images in F2 area	BP Network, SVM, RF, FCNN	In OBIA analysis MIU values 66.6% and 2343.5 inference speed, and FCN 80.2% and 326.8 inference speed

Table A.4. Studies on soil mapping, drought index and determining agricultural vehicles

Article	Year	Plant	Dataset	Model/Algorithm	Result
[48]	2018	Drought	Images obtained from Landsat 5-TM satellite between 1986-2000	LeNet, AlexNet, VGGNet	Accuracy LeNet: 100%, AlexNet 99.92%, VGGNet 99.93%
[49]	2018	Soil Mapping	69562 images of multispectral area	ANN, RF	For ANN; ME 2.85, RMSE 23.64 For RF; ME 3.19, RMSE 22.53
[50]	2019	Drought	Images obtained from the 97-day Landsat-8 satellite between March 2017 and June 2017	RF	First model; RMSE: 0.052, MAE: 0.039, R ² : 0.91. Second model; RMSE 0.382, MAE: 0.375, R ² : 0.58
[51]	2019	Drought	Meteorological data obtained from SWI	ANN, ANFIS	For ANN; NSE: 0.371, RMSE: 2.654 For ANFIS; NSE 0.460, RMSE 2.459
[52]	2019	Agricultural Machinery Classification	7 models of agricultural machines are divided into 6 types according to shooting angle; 125,000 images in total	Inception v3, RestNet-50, AMTNet	For Top_1 Dataset: 97.83%, For Top_5 Dataset: 100%
[53]	2019	Soil Mapping	DEM data obtained from NASA's Shuttle Radar Topography	ANN, SVM, RF	For RMSE; ANN: 2.62, SVM: 2.82, RF 2.22
[54]	2019	Drought	80,000 images of 12,517 plant	CNN	For Carrot; Precision: 99.68%, Recall: 99.56, F-Score: 0.9962. For Herb; Precision: 99.57%, Recall: 99.68%, F-Score: 0.9962
[55]	2019	Drought	Values for 228,855 irrigation events were used in the 365-day evaluation of the 2,891-hectare Sector 2 in Spain's 21,141 hectare Canal del Zujar (CZD) region.	Hibrit (D-Tree ve Genetik Algoritma)	Accurate irrigation events between 68%-100%, Inaccurate irrigation events between 93%-100%
[56]	2019	Drought	SPI (Standardized Precipitation Evapotranspiration Index), TRMM (Tropical Rainfall Measuring Mission) and MODIS data between 2001-2017.	Bias-corrected random forest, SVM, MLP Neural Network	Looking at the RMSE; Bias-corrected is more effective results from Random Forest
[57]	2020	Soil Mapping	Dataset A includes 200 sample data. Dataset B is a subset of A and includes 50 sample data. Dataset C includes 25 data of dataset B with largest residuals. Dataset D includes 25 data of dataset B with least residuals.	MLR, kNN, SVM, SVR, Cubist, RF, ANN	Calculation time is not important ANN works best. If the data set is less than 100 Cubist, RF, SVM, kNN good result gives.
[58]	2020	Drought	Hydraulic environmental datasets between 1994-2013	CART, MARS, BRT, RF	Looking at the ROC analysis RF is the best result the other models to 97.7%
[59]	2019	Soil Mapping	LPIS (Land-Parcel Identification System) data	CNN	To forecast field areas 89%, To field border 69%
[60]	2020	Drought	Average temperature, precipitation sunny day rate and RGB field images from UAV, Chine Meteorological Administration in Dixing County	SVM	The pixel classification provided only 82.8% accuracy, with a low F1 score of 71.7%. Using spectral densities, it provided an accuracy of 89.9% with an F1 score of 87.7%.
[61]	2020	Drought	A total of 372 images taken in winter from lemon, orange, almond, olive, malt, fig, strawberry, cherry and walnut trees in Murcia, Spain (251 for SVM, 121 for deep learning)	SVM, SegNet	F1-Score; SVM: 83.11%, SegNet: 86.27%
[62]	2020	Drought	China Meteorological Information Center Meteorological data, agrometeorological data, remote sensing data and biophysical data between 2003-2014.	BP Neural Network	Recommended IDI system, SPI-3 and results close to SPEI-3 data produced.
[63]	2020	Drought	It was used by comparing Korea Meteorological Administration (KMA) forecast data and Met Office Global Seasonal Forecast Model v5 data.	Hybrid Model (Combined Extreme Learning Machine and GloSea5GC2 climate model)	Looking at the RMSE; Hybrid Model results between 1.02 and 3.35, and Climate Model results between 1.61 and 3.37

Table A.5. Studies on yield forecasting

Article	Year	Plant	Dataset	Model/Algorithm	Result
[64]	2016	Wheat	Online satellite image	Counter-program ANN, XY-Fused Networks, Supervised Kohen Networks	CP-ANN: %78.3, XY-Fs – 80%, SKN 81.65%
[65]	2016	Three Different Vegetations	3 different vegetation index (AVHRR, MODIS, SPOT-4) for 32 years from NASA measures NDVI	ANN	Develop a model for daily in 16, 32, 48, 64 days and examine RMSE and MAPE values to each model
[66]	2016	Sugarcane	Nitrogen, Phosphorus, Potassium, Sulfur and total 20 data in Sugarcane field	Hybrid Model (DDNHL-GA), FCM-GA, GCM-DDHNL, NB, RBF Network, MLP, j48, Random Tree, LMT	Accuracy DDNHL-GA: 94.7%, FCM-GA: 93.4%, FCM-DDNHL: 92.1%, NB: 89.4%, RBF: 85.5%, MLP: 81.57%, J48: 73.68%, Random Tree: 71.05%, LMT: 86.84%
[67]	2017	Lemon, Mandarin, Orange	94 lemon images, 364 mandarin images, 509 orange images	M5 Prime	R (Correlation coefficient) Lemon 0.813, Mandarin 0.744, Orange 0.828 RMSE Lemon 0.072, Mandarin 0.165, Orange 0.297 MAE Lemon 0.107, Mandarin 0.081, Orange 0.102
[68]	2017	Evapotranspiration	Meteorological data between 1961-2014 years in Sichuan, China	ELM, GRNN	1. Model ELM RMSE 0.198, MAE 0.267; GRNN RMSE 0.220, MAE 0.314 2. Model ELM RMSE 0.209, MAE 0.301; GRNN RMSE 0.194, MAE 0.263
[69]	2018	Corn	SOM, CEC, Mg, K and PH values for 200 soil at 2013, October 1 in Molly Caren Farm, Ohio	Linear Regression, RF, Neural Network, Radial SVM, Linear SVM, Gradient Boosting Model, CU	Cross-Validation R ² ; Linear 0.34, RF 0.53, SVM-R 0.45, SVM-L 0.33, GBM 0.41, NN 0.37, CU 0.52 RMSE Linear 1.15, RF 0.97, SVM-R 1.16, SVM-L 1.05, GBM 1.08, NN 1.12, CU 0.98
[70]	2018	Soil Fertility	372 data in Maharashtra, India	Neural Network, Deep Learning, SVM, RF, Boosting, Bagging, Bayesian Models, Extremely Randomized Regression Trees (extraTrees)	The best result is extraTrees for RMSE values between 0,57 and 0,70
[71]	2018	Cotton	400 images from 100 different cotton field and NCDC climate data between 2013-2014	ANN	ANN correlation R=0,68 and MAE: %11
[72]	2019	Canola	Canola plant data between 2008-2015 and three separate datasets with 21 to 27 variables (QQWR15_4, QQWR31_5, QQWR30_6)	MLP	QQWR15_4 model MAE 0.2870, MAPE6.88, QQWR31_5 model MAE 0.4353, MAPE 9.87, QQWR30_6 model MAE 0.4118, MAPE 7.69
[73]	2019	Corn	721 images in 2016, 1552 images in 2017, 1566 images in 2018 obtained from Sentinel-II satellite	MR, RF, SVM, GNDVI	The highest R ² GNDVI 0.48, The best results of R ² for ML are RF which is 0.6. The best time to have a high corn yield is between 105 and 135 days after October
[74]	2019	Wheat	Satellite images and climate data of NDVI between 2009 and 2015 at an altitude of 250 meters, daily precipitation and weather data from SILO and images provided by farmers	RF, CUB, XB, SVM Linear, SVM Radial Basis, MLP, MARS, GP, kNN	Looking at the RMSE; The best result of RMSE is SVM Radial Basis Function (0.545.
[75]	2019	Soybean	500 Soybean images 32126 images containing seeds	CNN (3x3) CNN (5x5)	MSE; CNN (3x3): 23.49, CNN (5x5): 20.79, TCNN: 13.21
[76]	2019	Corn	2267 genotype of corn hybrid between 2008-2016 in 2247 location	DNN, Lasso, Shallow Neural Networks, Regression Tree	DNN RMSE 10.55, r 88.3; Lasso RMSE 20.28, r 36.68; SNN RMSE 12.96, r 80.21 RT RMSE 14.31, r 76.7
[77]	2019	Wheat, Barley, Canola	Precipitation and MODIS national-global dataset	RF	Correlation 0.89

Article	Year	Plant	Dataset	Model/ Algorithm	Result
[78]	2019	Orange	4931 tree images belonging to 25 rootstock varieties	CNN	Accuracy CNN: 99.9%
[79]	2019	Lettuce	Over 10000 training datasets with 20x20 pixels	Hybrid Model (AlexNet and CNN)	Accuracy 98%
[80]	2019	Lettuce	In a greenhouse with controlled temperature and humidity data followed for two weeks to determine CBZ and DCF intake by growing three types of lettuce	Hybrid Model (ELM and FFNN)	Accuracy for Hybrid Model 95%
[81]	2019	Mango	Mango greenhouse data from October 2016 and May 2018	MLP, RF, Spline, MVR, Linear	R ² values In short term Linear %95, Long-term MLP %96
[82]	2019	Crop Forecast	Cropland Data Layer (CDL) data	Multi-layer ANN	Accuracy: %88 R ² : 0.9
[83]	2019	Evapotranspiration	INMET data between 1996 and 2016 in Verde Grande River	HS, ANN, MLR, ELM	R (correlation coefficient) HS 0.661, MLR 0.731, ELM 0.724, ANN 0.718 RRMSE HR 0.171 MLR 0.091, ELM 0.151, ANN 0.165
[84]	2019	Evapotranspiration	Meteorological data between 1978-1999 and 2007-2016 in Hoshiarpur, and between 1970-1999 and 2007-2016 in Patiala	ELM, GBM, GLM, DL-MLP	Nash-sutcliffe efficiency (NSE) 0.95-0.98, R ² 0.95-0.99, ACC 85-95, MSE 0.0369- 0.1215, RMSE 0.1921- 0.2691
[85]	2020	Various many plant images	365 images contain Simple-RGB and Foreground-RGB	SegNet	For Simple-RGB; Mean Accuracy 0.89, IoU 0.52, Boundary-F1 0.81 For Foreground-RGB; Mean Accuracy 0.94, IoU 0.58, Boundary F1 0.92
[86]	2020	Corn	For monthly weather forecast data; 4000 data to Scenario A and 6000 data to Scenario B	Linear Regression, SVM, MLP, GBM, Regression Tree, EGB	To Scenario A, GW Effects; Cross-validation correlation (CV CORR) values (LR-0.45, SVR-0.68, ANN-0.64, GBRT-0.80, XGBoost-0.78) To Scenario A, EU Effects; CV CORR values (LR-0.65, SVR-0.80, ANN-0.74, GBRT-0.87, XGBoost-0.86). To Scenario B, GW Effects; CV CORR values (LR-0.35, SVR-0.63, ANN-0.64, GBRT-0.78, XGBoost-0.76) Scenario B, EU Effects; CV CORR values (LR-0.63, SVR-0.74, ANN-0.74, GBRT-0.84, XGBoost-0.83)
[87]	2020	Corn	NASS fertilizer data, SSURGO data for soil type, NCDC monthly average temperature and precipitation data	The BRT model has been developed according to the life cycle of maize production for a period of 9 years.	Correlation coefficient between 0.87- 0.99, R ² between 0.78- 0.82
[88]	2020	Apple and Mango	Terahertz data and Swissto2 data (0.75 and 1.1 Thz frequency)	SVM, kNN, D-Tree	Accuracy For Apple SVM: 97.0%, kNN: 86.4%, D-Tree: 93.2; For Mango SVM: 93.4%, kNN: 86.4%, D-Tree: 92.5%
[89]	2020	Barley	Climatic events between 2001-2015 and data on 450 soils	PLSR (Partial Least Square Regression)	For Wheat RMSEC 0.20, R ² : 0.54 For organic matter; R ² : 0.9345, RMSECV 0.54%

**Review Article****A survey: blockchain utilization for securing healthcare system****Elnaz Dadvar^{a,*} and Kubra Kalkan^a** ^a*Ozyegin University, Faculty of Engineering, Computer Science Department, Istanbul 34794, Turkey*

ARTICLE INFO

Article history:

Received 13 October 2020

Revised 19 March 2021

Accepted 23 May 2021

Keywords:

Blockchain Technology

Healthcare System

IoMT

Privacy

Security

ABSTRACT

Nowadays healthcare systems have started to be integrated with Internet of Things (IoT) in order to deliver some benefits in diagnosis and treatment process, such as remote patient monitoring and data usage for analytics and fast treatment. With the rise of IoT healthcare devices, number of electronic health records are increased to a rate that it is estimated to exceed billions in the next few years. Although cloud computing is a practical solution for processing this kind of data, healthcare records contain confidential and sensitive patient data which makes this system very vulnerable to the security and privacy threats, so it needs more investigation. For making this critical information more secure, researchers have come up with a solution of applying blockchain technology in healthcare. In this paper, we review the latest literature of blockchain application in healthcare from the security and privacy perspective. Several existing works have been discussed and a comparative study is done among the published works, along with potential future perspectives.

© 2021, Advanced Researches and Engineering Journal (IAREJ) and the Author(s).

1. Introduction

Healthcare has a vital role in today's society, because it is concerned with improving the quality of life. Traditionally, healthcare information recording was paper based, which was prone to alteration and missing, it was also hard and time taking to access data when required. Researchers came up with the idea of digitizing the medical data and integrating it with IoT, to perform the tasks that may lead to serious breakthrough in healthcare, including (1) automated healthcare record system; (2) sharing reliable information between trusted parties; (3) analysing big data; and (4) collaboration in clinical practice and diagnosis [1]. However, along with these advancements a lot of security and privacy challenges have been risen. For example, there is storage limitation in databases for this huge and ever-growing amount of data which are also exposed to cyberattacks. Patient's sensitive data may be accessed by attackers which then can be altered or utilized to the detriment of the patient. So, it is not reliable to utilize a centralized database system, because chance of cyberattacks is rising in a centralized system. This is where a peer-to-peer (P2P) network comes

in handy to enable the decentralization feature [2]. Therefore, blockchain technology has risen as a practical solution and transparent mechanism for storing and distributing the data with the potentiality of dealing with data security, privacy, and integrity issues in medical healthcare, such as tampering and data leakage threats [3]. Blockchain technology provides a distributed, immutable, and secure system for all transactions. it can revolutionize medical database interoperability. Overall blockchain technology has the potential to dramatically improve medical care [4]. This distributed ledger technology can guarantee reliability by itself. And if we utilize this technology together with cloud computing, storage issues can be solved, because cloud is known for being trustworthy for data storage and processing. Rehman et al. [5] has employed a secure mechanism for providing services in IoT devices which preserves the security of edge servers of these devices with the contribution of smart contracts. Based on a study done at [6], blockchain is also proved to be a practical tool for improving the security issues of cloud computing environment.

Some literature review articles are proposed in recent

* Corresponding author. Tel.: +90-216-564-9150.

E-mail addresses: : elnaz.dadvar@ozu.edu.tr (E. Dadvar) , kubra.kalkan@ozyegin.edu.tr (K. Kalkan)

ORCID: 0000-0003-0092-8901 (E. Dadvar), 0000-0003-1918-8587 (K. Kalkan)

DOI: 10.35860/iarej.809797

This article is licensed under the CC BY-NC 4.0 International License (<https://creativecommons.org/licenses/by-nc/4.0/>).

years. They covered blockchain technology application in healthcare domain comprehensively [7-9]. As compared to these studies and other available state-of-the-art comprehensive surveys in this area, this survey focuses precisely on the security and privacy aspects of healthcare systems along with blockchain-based proposed solutions in the most recent years. This paper offers a baseline for researchers by giving a general overview of blockchain technology use case for securing different aspects of sensitive medical data management such as storing, accessing, sharing, and monitoring, while considering the privacy of users. It also offers a concise comparison between recent schemes proposed for securing healthcare systems using blockchain and identifying the gaps and limitations in the existing solutions. We have also proposed a new prototype for a potential future research direction.

The study initially starts by giving a brief background of blockchain technology and its characteristics, then we will discuss how blockchain can contribute to the medical system for solving potential security and privacy issues in healthcare systems. Afterwards, we will propose a new prototype and discuss around it. And finally, we conclude this review by comparing and discussing the related studies of blockchain application in healthcare and provide a perspective for future study directions.

2. Blockchain Background

Blockchain technology originally has been introduced as an infrastructure for cryptocurrencies in 2008 [10]. This technology's infrastructure is a peer-to-peer network [11]. Blockchain is a decentralized and distributed ledger which is shared among different parties in a system that records transactions. The main features of this technology are decentralization, reliability, and immutability, which are required for managing medical records [12]. The framework of blockchain technology is distributed in which we have a real-time sharing of captured data among trusted parties. In all transactions, each block holds a timestamp, transaction data, and a hash value as a pointer to the previous block [13]. Another characteristic of blockchain is transparency which makes the system autonomous and eliminates the need for any intermediary or third-party [14]. In blockchain, when a node receives the message it checks for accuracy of the message, if it is confirmed it will be stored in a separate block, then the consensus algorithm is applied for confirming the stored data in blocks; this action is called "Proof-of-work (PoW)". When the algorithm is finalized a new block joins into the chain. This process continues until it gets all network node's admission on the chain. Blockchain is a decentralized framework that applies strong and different encryption algorithms to store digital data in a transparent, secure, and anonymous way [15].

Blockchain has been introduced initially for the financial sector, however, researchers have embedded it with other technologies, so that it can be utilized in different fields. One of the useful and emerging integrations is the utilization of blockchain along with IoT and cloud computing which makes the best fit for solving healthcare security problems.

2.1. Compatible Characteristics of Blockchain For Healthcare System

In this section we provided important characteristics of blockchain that makes it suitable for healthcare system [1]:

- **Decentralized:** This is the main feature of blockchain that gives the system the opportunity to give open access control to anybody associated with the network. Due to this feature there is no single point of failure in blockchain, this means if a node fails then other nodes are able to continue accessing their data
- **Immutable:** When records are stored in blockchain they cannot be modified or deleted subsequently without having the admission of more than 51% of the system users.
- **Secure:** In blockchain encryption algorithms are utilized to encrypt data in order to give data access only to the authorized participants. Also, data integrity is satisfied from the very beginning process until the end.
- **Autonomous:** Every block can act independently; means they can alter their own data securely and safely. The execution of distributed transactions are done automatically under user-defined conditions.
- **Anonymous:** When data transferring takes place between nodes the identity of nodes remains anonymous which makes system more reliable.
- **Synchronized:** All nodes in blockchain have the same chance of accessing exactly the same data at the same time.

2.2. Blockchain Types

Basically, blockchain is divided into two types: private and public. However, we have some other variations too, such as consortium and hybrid blockchains. Based on every system's requirement each one of these can be selected, but they all have some features in common, and that is each blockchain operates on a P2P network and has a cluster of nodes in which each node keeps a copy of the shared ledger and updates it promptly. Nodes has the capability to verify transactions, initiate or receive any process in the system independently [16]. Some detailed explanation of blockchain types are discussed as follows [11].

1. **Public Blockchain:** This is a permission-less distributed ledger system. That means anyone can join the network and be an authorized node in the system. Public blockchains are secure only if the clients follow the

security conventions. Examples of this type of blockchain are: Bitcoin (BTC) and Ethereum (ETH).

2. Private Blockchain: This type of blockchain is also called permissioned blockchain which operates only in a closed network. Private blockchain's usage is very similar to public blockchain, but its network is much smaller and restrictive. Examples of this type of blockchain are: Ripple (XRP), Multichain and Hyperledger (Fabric, Sawtooth), Corda, etc.

3. Consortium Blockchain: Consortium blockchain has semi-decentralized framework. In contrast to private blockchain, here there is more than one organization managing the network. And each one can act as an independent node. Examples of consortium blockchain can be: Quorum, Energy Web Foundation, R3, etc.

4. Hybrid Blockchain: This blockchain is created by merging private and public blockchain. It also integrates the features of both types of blockchains in a way that user can have both a private permission-based system along with a public permission-less system. Employing this network helps users to have control over who gets access to which data in the blockchain. Only partial data is allowed to be publicly available, but the rest of records are kept confidential using the private network. So, this type of blockchain can communicate with outer world easily while preserving network's privacy. Hybrid blockchain has gained a vast usage domain, Dragonchain can be a good example of a hybrid blockchain.

Each of these blockchain technologies can be utilized based on the system requirements. Most of the research studies on applying blockchain in the healthcare domain have primarily focused on utilizing permissionless Ethereum blockchain technology, but this type of blockchain has some downsides such that it consumes heavy energy, it is very restricted in scalability, and the network throughput is very low. For fulfilling these gaps there is a crucial need for a much scalable, fault-tolerant, timely managed, secure, and private blockchain to meet the demands of the healthcare systems. Based on the researches done so far, a permissioned blockchain has proved to be more compatible for healthcare data management with the results of reducing the computational overhead and so lowering energy consumption, by meeting the security and privacy factors much efficiently in compared with Ethereum blockchain.

3. How Blockchain Meets Healthcare Requirements

Blockchain provides a 'secure by design' approach in which security is considered the primary factor of the architecture. Blockchain satisfies required security, and by integrating with other supporting solutions it opens up other complexities of the system. The reference architecture applied to healthcare system is as follows: The user of blockchain syncs up with other nodes in the

network. Then a particular server manages the transaction records. Data integrity and provenance is fulfilled by applying cryptographical algorithms. The massive scale of operation of blockchain software makes it almost impossible to break into the framework or other applications which are running on it. Hence, there is no need for a central third party to issue, authenticate and validate ownership of the data. When there is two or more nodes possessing same blocks in their own databases, we can consider them to be in consensus. So, according to the blockchain features and applications it can feasibly meet the healthcare requirements such as security, interoperability, data access and data sharing. For better understanding, we designed a general flowchart for a potential blockchain-based healthcare system, Figure 1. It shows all technical and functional platforms of the architecture for applying blockchain in healthcare. This platform consists of four main layers, the very first layer is public network, which includes user interface applications that are utilized to collect user data. In the second layer cloud network, the gathered data from patients or doctors are first encrypted and then pushed to the cloud for secure storing. All data are hashed before transferring in order to avoid data leakage during transferring process to the blockchain service. In blockchain service layer there is a consensus algorithm which helps at reaching to a common agreement between all participated nodes of the network by approving the transactions. There are multiple methods of reaching consensus; the frequently used ones are proof of work, proof of stake and multisignature schemes. A shared ledger in this layer holds approved and authenticated transactions and distributes data among other confirmed members, thus user's privacy is guaranteed. In this layer smart contract holds and executes the coded agreements of blockchain network. During these processes data security are assured by applying cryptographic algorithms. Ultimately, communication between blockchain and enterprise network layer is accomplished using an appropriate API.

4. Comparison of Related Studies

As we mentioned before, healthcare data is very sensitive, and it is crucial to protect them in means of privacy and security. So, for processing, sharing, storing and handling medical information a secure platform should be designed [17]. Blockchain technology has been proposed and explained by several research studies in recent years for dealing with security and privacy risks, due to its potential to promote better data sharing and management and its assistance in treatment process.

Azaria et al. [18] have proposed MedRec as a novel system which utilizes blockchain for managing large medical data.

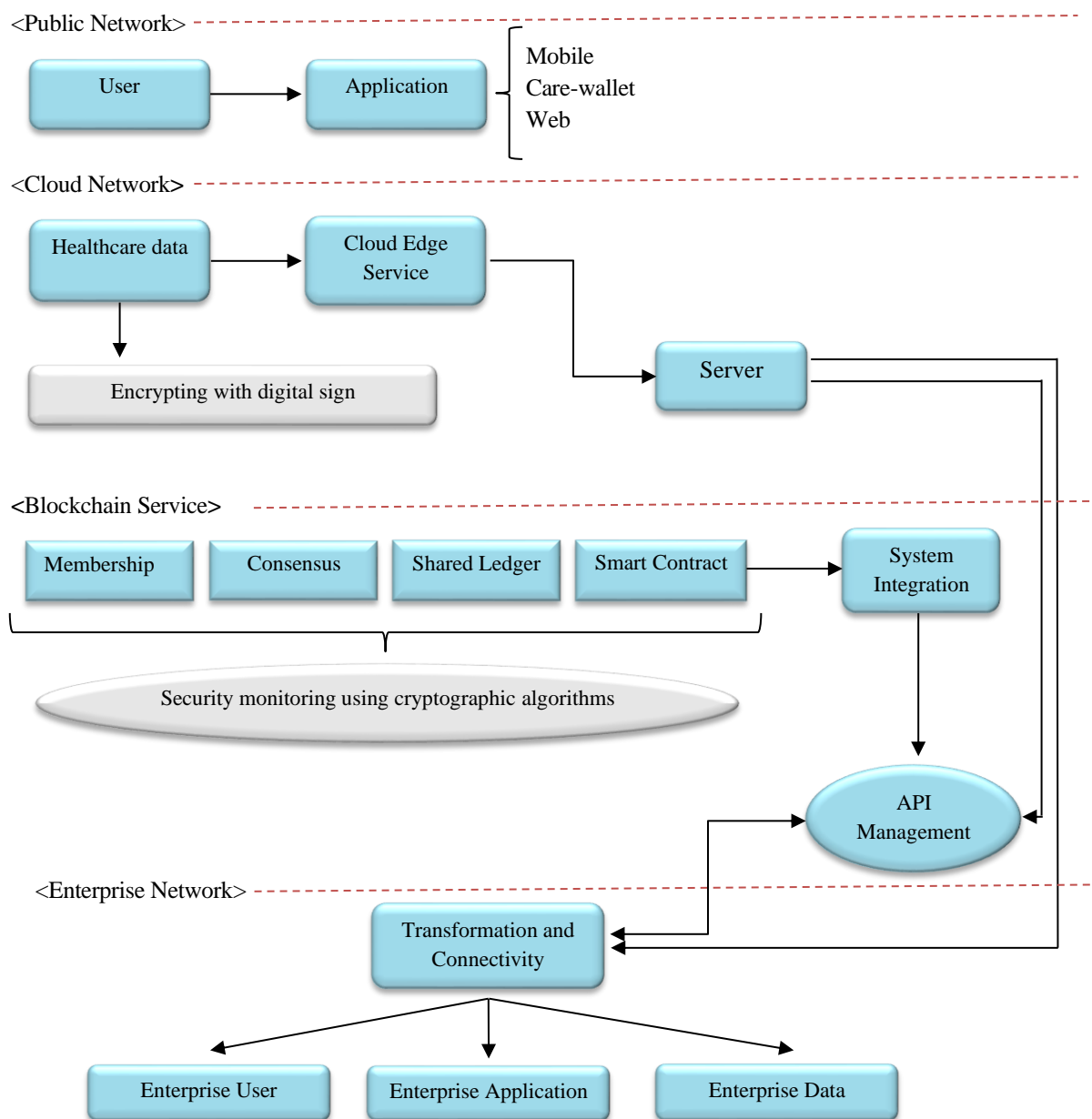


Figure 1. Blockchain-based healthcare system flowchart

It provides easy access to data and feasible patient data sharing. Theodouli et al. [19] has facilitated a Healthcare system that enables sharing data in a private and auditable manner by considering patient pseudonymity and hiding the identity of the user whose data is shared. A 3-layered architecture is also proposed for respectively storing patient’s data in a web or cloud platform. In this architecture there is a cloud middleware layer which its task is data fetching from the cloud layer to the next layer, which is blockchain network, by utilizing an API and interacting with smart contracts. A smart contract is a self-executing protocol which is coded and executed inside of a blockchain and it contains terms and conditions of an agreement between peers. It also consists of rules that helps to keep medical data secure in a way that the data is accessible only to the authorized person by digital

signature [20]. The Ethereum platform is utilized for executing smart contracts. Liu et al. [21] has improved security and privacy related issues in biomedical systems by designing a blockchain and distributed ledger based secure scheme. Authors have proved that this system is capable of maximizing the data sharing ratio while minimizing the computation and response time by ensuring the privacy of users.

Zhang et al. [22] has proved that smart contract can be a potential solution to tackle the challenges of interoperability in healthcare, so that medical data are shared and communicated in a secure way. Ethereum smart contracts is also being used in [23], to design a MedRec prototype which is a proof-of-concept system, and to manage the access to healthcare records. Researchers in [24], have applied smart contract in their unique architecture, which is independent of

any previously designed blockchain platforms, in this system they could guarantee the integrity in the records of EHR systems, and they enhanced the interoperability of the system. Smart contracts are considered to be dynamic in nature, so they are best fit to be employed in designing access control policies for example, authors in [25], proposed an Enhanced Bell–LaPadula model to classify the healthcare data and access control policies and so implement a scalable and secure healthcare network. Some hybrid methods are recently proposed by researchers in which they combine the power of blockchain technology with other existing technologies to fulfil the security and privacy gaps of healthcare system. Chakraborty et al. [26] has utilized Blockchain technology along with machine learning to provide a secure framework in order to store and maintain patient's data such as providing accurate and authentic health records. In this system machine learning is applied to detect any anomaly in the newly generated data of patients. De Oliverira et al. [27] provides an approach for a private and scalable EMR storage by the incorporation of Public Key Infrastructure (PKI) with blockchain technology. Zhao et al. [28] developed a key management scheme for healthcare blockchain to enhance security and privacy in healthcare system. They integrated Body Sensor Network (BSN) with health blockchain and created an efficient recovery strategy for managing the keys. Another study related to key management by blockchain is done recently in [29], researchers designed a new sharing scheme based on blockchain for privacy protection and enhancing access control management process through symmetric and attribute-based encryption. Healthcare data are dynamic, and they are changing constantly and there should be a system that can adopt to the metadata alteration efficiently. Shen et al. [30] proposed a scheme called MedChain that integrates blockchain, digest chain and P2P network aspects to provide an efficient system for data sharing in healthcare. Xia et al. [31] has also utilized blockchain to propose a framework for sensitive medical data sharing which is stored in cloud. The blockchain type used in this system is permissioned blockchain that gives access only to the verified users. Putting encrypted medical data into blockchain is first proposed by [32], an App was also designed to this purpose. Researchers in [33], have proposed the requirements along with their potential solution for having an efficient healthcare system with combining blockchain and cryptographic algorithms. And the details for applied cryptographic techniques are discussed at [34]. For example, ARX Symmetric Encryption Algorithm has been applied in order to have an efficient encryption of the sensitive data of blockchain. Digital Signature is used in authentication process and for keeping the users anonymous and protecting the privacy of users Digital Ring Signature is applied. A three-layered architecture is proposed in [35], for ensuring a private and secure data management in healthcare

IoT devices. The layers include Sensing, NEAR processing, and FAR processing layer. Sensing layer is for patient data acquisition and transmitting to IoT devices. NEAR processing layer is used for sensing the IoT devices, and FAR processing layer includes servers for cloud and high computations. Digital Ring Signature and SSS is applied in this system to fulfil security requirements in healthcare agent's communication process. Authors of [36], set up a shared key for providing a private access to medical data to be used in the process of diagnosis and treatment. This shared key is created using sibling intractable function families (SIFF). The key is utilized for encrypting and storing data in a blockchain for protecting data. The evaluation of proposed system proves to have a good efficiency in aspects of integrity, availability, and privacy of medical data. In a most recent study [37], a Multi-Modal Secure Data Dissemination Framework is proposed for data access control management in IoMT devices. In this scheme data is encrypted in blockchain and decrypted only by private key of patient. By employing blockchain in this framework security and privacy is enhanced significantly compared to previously proposed methods. Due to the ever-growing amount of medical data in the world, security and privacy issues of health data have become a major research topic for academicians and security engineers. Figure 2. depicts the global picture of security related research areas. Proposals in the literature can be classified mostly in the concept of data sharing and access management in a secure manner. In Table A.1 (in Appendix). we carried out a detailed summary of the current blockchain-based healthcare systems proposed by researchers so far along with their contribution and gaps to form a point of comparison between methods.

5. A New Prototype For Enhancing The Security of Healthcare In Emergency Condition

In the conventional healthcare systems for any medical process patient authorizes access to the healthcare records, in other words most of the proposed systems have implemented to be patient-centric in data sharing and accessing in order to keep data private and secure. But these systems may act poorly in emergency cases. When the patient loses his/her consciousness, its hard and almost impossible to be able to issue any access authorization or share health related data with a medical service provider which may lead to a delay in diagnosis and treatment process and put a patient's life in danger. We have proposed a prototype for handling this issue. In this prototype we classified system users into three categories based on their access level permissions to patient's sensitive health data. The main focus lies on generating a group of trusted parties and transferring the personal medical data's partial- ownership to these parties in emergency cases, these parties may be a healthcare provider, family member or another trusted party which is pre-specified by the real data owner.

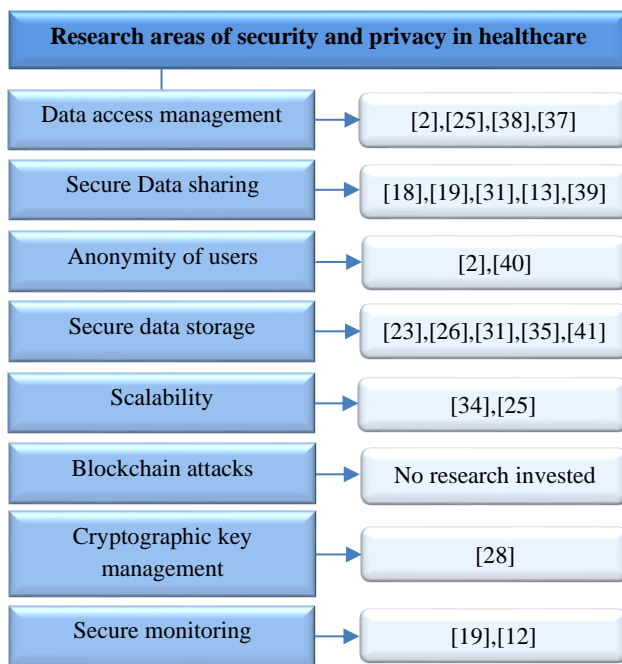


Figure 2. Classification of Security in healthcare studies

If the trusted party is a related medical service provider, diagnosis and treatment process takes place, if not the case they will authorize the access and share only required data with a third-level party which may be EMT staff or agencies. A potential architecture for our proposed prototype is provided in Figure 3. As it is observed in this figure, the user who can be the patient, doctors, nurses, health organizations or emergency staff makes data request in emergency condition, this request then would be validated through edge service and be sent to the transaction manager. The pre-defined policies in smart contract along with identity access management will be processed in order to make the authorization and accept or reject the request, then the status of the request (accept/reject) would be sent to the requester user and the partial access to the data would be issued. For our future research direction, we are planning to apply this system on a private blockchain, Hyperledger platform to form a feasible protocol for emergency access authorization while considering patient's privacy and data security.

6. Discussion and Future Perspectives

- A fundamental concern in modern healthcare systems, such as Electronic Medical Record (EMR) systems is patient's data security and privacy. In health systems data storing process should be done securely and keep the system safe from unauthorized users. These issues are addressed using different cryptographic algorithms along with adopting blockchain technology to the system. For example [18], have utilized blockchain for managing the medical data access, but they have not investigated enough on the database security.
- Scalability can be a critical issue in EMR systems. Because of the growing number of patients, the data is

increasing exponentially, so we need a scalable system that can be adopted to this increasing rate which existing works have not investigated enough in this area.

- One research challenge that needs more investigation can be cryptographic key management and replacement in case of any loss or change.
- Research study on the specific blockchain attacks that can affect whole functionality of the system, have not been investigated.
- Research is needed to focus on authorization issue. The proposed systems so far have given the data access permission confirmation only to patients, in other words the access process is patient centric. But they have not considered the likelihood of emergency cases. So, there should be some protocols for emergency cases that allows authorized doctors to have access to the data.
- The studies done so far in this area are mostly a proof-of-concept research. So, one of the main research gaps that can be seen in the published papers used in this review study is the lack of implementation and experiment on real-world healthcare data so that the proposed solutions and systems can be evaluated for real.

Overall, implementing blockchain technology needs a decent framework along with experts. These might be considered as technical barriers to achieving success in the healthcare industry.

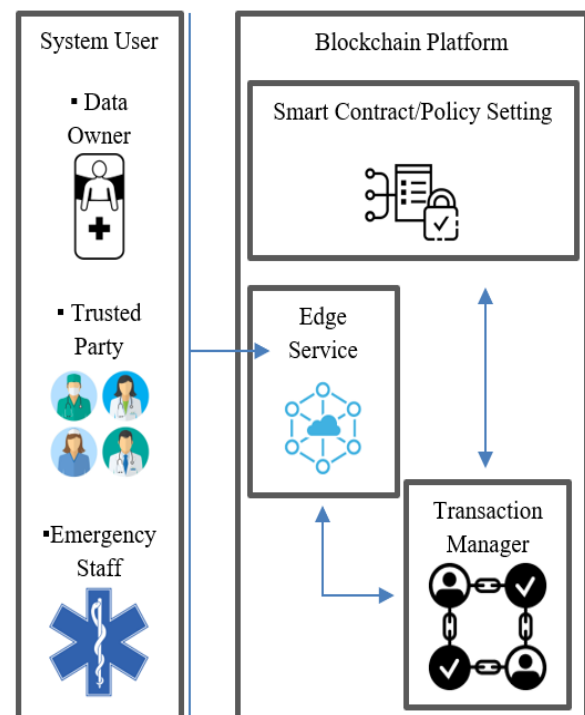


Figure 3. Architecture of proposed prototype for PHR access in emergency condition using blockchain

6. Conclusion

Healthcare has been a crucial part of human life and so the medical data. These data include the personal details of the patient's health condition, so it should not be shared with third parties to protect from being misused. This is where blockchain technology is proposed to deal with security and privacy issues. Blockchain has made a huge contribution to the healthcare handling many difficulties such as providing secure and efficient data storing, sharing, and accessing and also data integrity is fully satisfied. Blockchain technology is now setting new standards for patient care.

In this study, a general and clear classification is provided about the global research studies related to securing healthcare systems. We also reviewed current researches done on maintaining health data and how blockchain can affect and empower patients in controlling the sharing process of their personal health data. A consensus has been observed among most papers that blockchain will help in authentication process and the data will be exclusively managed by patient. In this paper we carried out a literature study and reviewed all possible works on the medical healthcare using blockchain technology with a comparative study. We proposed a new prototype for improving the privacy and security of patients in emergency conditions of healthcare, we also covered major research initiatives and future research opportunities. Some major issues are still open, like mining incentives and specific blockchain attacks, which form the core mechanism of a blockchain have not been fully investigated in these studies, whereas these problems can break the entire system.

Blockchain technology is an emerging technology, and its utilization in healthcare system is started to be investigated from 2016 up to now. However, initial studies in this area only defined general terms and then moved to the proof-of-concept phase. Most recently initial experiments have been started in a testable system for applying blockchain for patient data sharing and patient monitoring system to provide some real work security guarantee. Nevertheless, there are still many open challenges in this area that demand further and precise investigation.

Declaration

The authors declared no potential conflicts of interest with respect to the research, authorship, and/or publication of this article. The authors also declared that this article is original, was prepared in accordance with international publication and research ethics, and ethical committee permission or any special permission is not required. The authors declare that they have no known competing financial interests or personal relationships that could have appeared to influence the work reported in this paper.

Author Contributions

E. Dadvar: conceptualization, methodology, writing the

original draft, visualization, investigation, writing - review and editing. K. Kalkan: conceptualization, methodology, visualization, supervision, investigation, writing - review and editing.

References

1. Roman-Belmonte, J. M., H. De la Corte-Rodriguez, and E. C. Rodriguez-Merchan, *How blockchain technology can change medicine*. Postgraduate medicine, 2018. **130**(4), p. 420-427.
2. Al Omar, A., M. S. Rahman, A. Basu, and S. Kiyomoto, *Medibchain: A blockchain based privacy preserving platform for healthcare data*. International conference on security, privacy and anonymity in computation, communication, and storage. Springer, Cham, 2017. Volume 10658, pp. 534-543.
3. Yaeger, K., M. Martini, J. Rasouli, and A. Costa, *Emerging blockchain technology solutions for modern healthcare infrastructure*. Journal of Scientific Innovation in Medicine, 2019. **2**(1):1.
4. Heston, T.F., *Why Blockchain Technology Is Important for Healthcare Professionals*. SSRN Electronic Journal, 2017. SSRN 3006389. pp. 1-4.
5. Rehman, M., N. Javai, M. Awais, M. Imran, and N. Naseer, *Cloud based Secure Service Providing for IoTs using Blockchain*. IEEE Global Communications Conference (GLOBECOM), 2019. pp. 1-7.
6. Gupta, A., S.T. Siddiqui, S. Alam, and M. Shuaib, *Cloud Computing Security using Blockchain*. J. Emerging Technol. Innovative Res., 2019. **6**(6): p. 791-794
7. Soltanisehat, L., R. Alizadeh, H. Hao, and K. K. R. Choo, *Technical, Temporal, and Spatial Research Challenges and Opportunities in Blockchain-Based Healthcare: A Systematic Literature Review*. IEEE Transactions on Engineering Management, 2020. p. 0018-9391
8. Khezz, S., M. Moniruzzaman, A. Yassine, and R. Benlamri, *Blockchain Technology in Healthcare: A Comprehensive Review and Directions for Future Research*. Applied sciences, 2019. **9**(9): p. 1736.
9. Zubaydi, H. D., Y.W. Chong, K. Ko, S. M. Hanshi, and S. Karuppayah, *A review on the role of blockchain technology in the healthcare domain*. Electronics, 2019. **8**(6): p. 679.
10. Nakamoto S., *Bitcoin: A peer-to-peer electronic cash system*. Available from: <http://bitcoin.org/bitcoin.pdf>, 2009.
11. Hölbl, M., M. Kompara, A. Kamišalić, and L. N. Zlatolas, *A systematic review of the use of blockchain in healthcare*. Symmetry, 2018. **10**(10): p. 470.
12. Griggs, K. N., O. Ossipova, C. P. Kohlios, A. N. Baccarini, E. A. Howson, and T. Hayajneh, *Healthcare blockchain system using smart contracts for secure automated remote patient monitoring*. Journal of medical systems, 2018. **42**(7): p.130.
13. Zhang, A., and X. Lin, *Towards secure and privacy-preserving data sharing in e-health systems via consortium blockchain*. Journal of medical systems, 2018. **42**(8): p.140.
14. Rennock, M., A. Cohn, and J. R. Butcher, *Blockchain technology and regulatory investigations*. Practical Law Litigation, 2018. pp. 35-44.
15. Lin, I. C., and T. C. Liao, *A survey of blockchain security issues and challenges*. IJ Network Security, 2017. **19**(5): p. 653-659.
16. Zheng, Z., S. Xie, H. N. Dai, X. Chen, and H. Wang, *Blockchain challenges and opportunities: A survey*. International Journal of Web and Grid Services, 2018. **14**(4): p. 352-375.

17. Puppala, M., T. He, X. Yu, S. Chen, R. Ogunti, and S. T. Wong, *Data security and privacy management in healthcare applications and clinical data warehouse environment*. IEEE-EMBS International Conference on Biomedical and Health Informatics (BHI), 2016. pp. 5-8.
18. Azaria, A., A. Ekblaw, T. Vieira, and A. Lippman, *Medrec: Using blockchain for medical data access and permission management*. 2nd International Conference on Open and Big Data (OBD), 2016. pp. 25-30.
19. Theodouli, A., S. Arakliotis, K. Moschou, K. Votis, and D. Tzovaras, *On the design of a Blockchain-based system to facilitate Healthcare Data Sharing*. IEEE International Conference On Trust, Security And Privacy In Computing And Communications (TrustCom/BigDataSE), 2018. pp. 1374-1379.
20. Wohrer, M., and U. Zdun, *Smart contracts: security patterns in the ethereum ecosystem and solidity*. International Workshop on Blockchain Oriented Software Engineering (IWBOSE), 2018. pp. 2-8.
21. Liu, H., R. G. Crespo, and O. S. Martínez, *Enhancing Privacy and Data Security across Healthcare Applications Using Blockchain and Distributed Ledger Concepts*. Multidisciplinary Digital Publishing Institute, 2021. **8**(3): p. 243.
22. Zhang, P., J. White, D. C. Schmidt, and G. Lenz, *Applying Software Patterns to Address Interoperability in Blockchain-Based Healthcare Apps*. arXiv preprint arXiv:1706.03700, 2017.
23. Ekblaw, A., A. Azaria, J. D. Halamka, and A. Lippman, *A Case Study for Blockchain in Healthcare: "MedRec" prototype for electronic health records and medical research data*. In Proceedings of IEEE open & big data conference, 2016. **(13)**: p. 13.
24. Yang, G., C. Li, and K. E. Marstein, *A blockchain-based architecture for securing electronic health record systems*. Concurrency and Computation: Practice and Experience, Wiley, 2019. e5479, **31**.
25. Kumar, R., and R. Tripathi, *Scalable and secure access control policy for healthcare system using blockchain and enhanced Bell-LaPadula model*. Journal of Ambient Intelligence and Humanized Computing, 2020. pp. 1-18.
26. Chakraborty, S., S. Aich, and H. C. Kim, *A secure healthcare system design framework using blockchain technology*. IEEE International Conference on Advanced Communication Technology (ICACT), 2019. pp. 260-264.
27. de Oliveira, M. T., L. H. Reis, R. C. Carrano, F. L. Seixas, D. C. Saade, C. V. Albuquerque, N. C. Fernandes, S. D. Olabarriga, D. S.V. Medeiros, and D. M. F. Mattos, *Towards a blockchain-based secure electronic medical record for healthcare applications*. IEEE International Conference on Communications (ICC), 2019. pp. 1-6.
28. Zhao, H., P. Bai, Y. Peng, and R. Xu, *Efficient key management scheme for health blockchain*. CAAI Transactions on Intelligence Technology, 2018. **3**(2): p. 114-118.
29. Wang, S., D. Zhang, and Y. Zhang, *Blockchain-based personal health records sharing scheme with data integrity verifiable*. IEEE Access, 2018. **7**: p. 102887-102901.
30. Shen, B., J. Guo, and Y. Yang, *MedChain: Efficient healthcare data sharing via blockchain*. Applied sciences, 2019. **9**(6): p. 1207.
31. Xia, Q., E. B. Sifah, A. Smahi, S. Amofa, and X. Zhang, *BBDS: Blockchain-based data sharing for electronic medical records in cloud environments*. Information, 2017. **8**(2): p. 44.
32. Yue, X., H. Wang, D. Jin, M. Li, and W. Jiang, *Healthcare data gateways: found healthcare intelligence on blockchain with novel privacy risk control*. Journal of medical systems, 2016. **40**(10): p. 1-8.
33. Srivastava, G., J. Crichigno, and S. Dhar, *A light and secure healthcare blockchain for iot medical devices*. IEEE Canadian conference of electrical and computer engineering (CCECE), 2019. pp. 1-5.
34. Dwivedi, A. D., G. Srivastava, S. Dhar, and R. Singh, *A decentralized privacy-preserving healthcare blockchain for IoT*. Sensors, 2019. **19**(2): p. 326.
35. Uddin, M. A., A. Stranieri, I. Gondal, and V. Balasubramanian, *Blockchain leveraged decentralized iot ehealth framework*. Internet of Things, 2020. **9**: p. 100159.
36. Tian, H., J. He, and Y. Ding, *Medical data management on blockchain with privacy*. Journal of medical systems, 2019. **43**(2): p. 26.
37. Arul, R., Y. D. Al-Otaibi, W. S. Alnumay, U. Tariq, U. Shoab, and M. J. Piran, *Multi-modal secure healthcare data dissemination framework using blockchain in IoMT*. Personal and Ubiquitous Computing, 2021. pp. 1-13.
38. Chakraborty, S., S. Aich, and H. C. Kim, *A secure healthcare system design framework using blockchain technology*. International Conference on Advanced Communication Technology (ICACT), 2019. pp. 260-264.
39. Fan, K., S. Wang, Y. Ren, H. Li, and Y. Yang, *Medblock: Efficient and secure medical data sharing via blockchain*. Journal of medical systems, 2018. **42**(8): p. 136.
40. Li, H., L. Zhu, M. Shen, F. Gao, X. Tao, and S. Liu, *Blockchain-based data preservation system for medical data*. Journal of medical systems, 2018. **42**(8): p. 141.
41. Kaur, H., M. A. Alam, R. Jameel, A. K. Mourya, and V. Chang, *A proposed solution and future direction for blockchain-based heterogeneous medicare data in cloud environment*. Journal of medical systems, 2018. **42**(8): p. 156.
42. Ismail, L., H. Materwala, and S. Zeadally, *Lightweight blockchain for healthcare*. IEEE Access 7, 2019. P. 149935-149951.

Appendix

Table A.1. Comparison of the current studies on blockchain-based healthcare system security and privacy

Reference Article	Concept	Secured Information data type	Use Case In Healthcare	Blockchain Type	Contribution	Gaps
[12]	Smart contracts for secure remote patient monitoring	PHI	Managing medical sensors	<ul style="list-style-type: none"> ▪ Permitted blockchain ▪ Public Ethereum blockchain 	Patient's data validation using PBFT consensus mechanism	<ul style="list-style-type: none"> ▪ Lack of verification step in consensus mechanism ▪ Inefficient data
[41]	Blockchain usage in cloud environment for storing and managing the EMRs	EHR	Medical data stored in cloud	Undefined	Maintaining and storing the heterogeneous medical data in distributed form	Key generation is not addressed
[31]	Blockchain framework for sharing data of EMRs system in cloud environment	EMR	Shares medical data into cloud for secure access	Permitted blockchain	Guaranteeing user anonymity using identity-based authentication along with key agreement protocol	Communication and authentication protocols are not fully investigated
[2]	Blockchain-based mechanism for the privacy of health data	Healthcare data	Securing the interaction between patient and system	Permitted blockchain	Patient-centric system for healthcare data management by ensuring pseudonymity and anonymity using cryptographic primitives	Key generation in the protocols are not fully addressed
[13]	Providing e-health system based on blockchain for secure data sharing	PHI	Diagnosis process improvements in e-health system	<ul style="list-style-type: none"> ▪ Consortium blockchain ▪ Private blockchain 	Secure sharing of PHR using cryptographic primitives for improving the diagnosis	Scalability in private blockchains is not addressed
[38]	Timely remote data fetching by considering the data privacy and security of patients	EMR	Real-time data delivery to medical practitioner	Consortium blockchain	Protecting the system from stakeholder's data manipulation and leakage while providing a timely mannered and secured access to data	Security and cryptographic details are not discussed
[18]	Sharing and managing medical data using blockchain	EMR	Gives patients easy access to treatment sites	Ethereum blockchain	Patient data sharing and mining incentives is addressed	No key replacement capability, and legal issues are not addressed
[19]	Blockchain-based system for sharing the medical data	Healthcare Data	Used for data sharing between patients and medical research centers	Consortium blockchain	<ul style="list-style-type: none"> ▪ Enables private data sharing ▪ Enhances security by access permission management 	Cryptographic techniques are not discussed
[39]	Blockchain-based framework for protecting the electronic medical record while data sharing	EMR	Patients can access to different hospital EMRs through this framework	Public blockchain	Guaranteeing privacy by combining access control protocol with encryption algorithms	PBFT consensus is not fully investigated
[40]	Data preservation system for Medical Data	Medical Data Records	Storing medical data in a reliable system	Ethereum blockchain	Ensuring verifiability of stored data while protecting users' privacy	Authentication protocol is not fully investigated
[22]	Software patterns for addressing interoperability issues in healthcare apps	Medical Records	Enhancing communication between users and medical applications	Ethereum blockchain	Maximizing sharing of resources and application scalability by applying foundational software patterns	Privacy and security concerns are not investigated enough
[23]	Blockchain-based record management system for handling EHR	EHR	Provides easy data access to patients	Ethereum blockchain	Secure and interoperable medical record access system	Cryptographic techniques are not discussed
[33]	Blockchain-based security approaches for remote patient monitoring	Healthcare Data	Remote patient monitoring for diagnosis and treatment process	Undefined	Security and privacy is provided for IoT-based patient monitoring utilizing cryptographic algorithms	Cryptographic algorithms are not implemented in a testable system

[42]	Scalable and efficient blockchain architecture to meet healthcare data management issues	EHR	Managing healthcare data	Permissioned blockchain	The architecture reduces the computational and communication delay in a more scalable environment	Security and privacy performance in this architecture is not fully investigated
[21]	Enhanced blockchain and distributed ledger based secure scheme for secure data sharing	EHR	Used for maximizing the secure sharing rate along with minimizing the complexity in EHRs	Undefined	Classification-based authentication reduced the computation time and provides a secure and private data sharing	Scalability is not addressed
[24]	A new scalable and adoptable architecture for dealing with interoperability	EHR	Recording the healthcare data while considering the integrity	Private blockchain	Guarantees the integrity of healthcare records with a multiple access system for block creation	Consensus mechanism detail is not fully investigated
[25]	Enhanced Bell-LaPadula model to classify the healthcare data and access control policies	Healthcare Data	Accessing healthcare data in a secure and private manner	Permissioned blockchain	Secure and scalable healthcare network by dynamic access control policies	No gap identified
[26]	Secure framework for storing and maintaining patient's data	PHR	Remote data fetching from patient's wearable devices and insurance companies	Consortium blockchain	Accurate and authentic health records	There may be delays in treatment process because system is patient-centric
[27]	Integrating blockchain with public key Infrastructure for maximizing privacy and security	EMR	Securing EMR's for healthcare applications	Permissioned blockchain	private and scalable EMR storage	There may be latency problem in treatment and diagnosis process
[28]	Key management scheme for healthcare blockchain	Undefined	Not specified	Undefined	Efficient encryption key backup and recovery scheme enhances security	System may not be timely mannered
[29]	Health data sharing while considering the integrity	PHR	Encrypting personal health records for secure data sharing	Ethereum blockchain	Privacy protection and sharing, enhanced access control management process through symmetric encryption and attribute-based encryption.	Interoperability is not investigated
[30]	Efficient and secure data sharing scheme	EHR	Secure data sharing between medical laboratories and institutions	Consortium blockchain	Integrating blockchain, digest chain and P2P network to provide an efficient system for data sharing in healthcare	Proposed system is not fully automated
[32]	Healthcare Data Gateway App for private data control by patient	Personal Electronic Medical Data	A mobile app to maintain the control and sharing process of personal electronic medical data	Private blockchain	Access control model which enables patients to possess, and share their own data while preserving privacy	No consideration for emergency situations
[35]	Architecture for private and secure data management in IoMT devices	EHR, EMR, PHR	Storing medical data generated from IoMT devices	Ethereum blockchain	Contributing to a secure and private communication by proposing a layered architecture	High storage overhead
[36]	A shared key is proposed for protecting medical data privacy	PHR	Private medical data sharing for diagnosis and treatment process	Private blockchain	Protecting data by storing encrypted data into blockchain	Scalability is not addressed
[37]	Framework for access control management in IoMT devices	Healthcare Data	Managing health related data collected by IoMT devices	Private blockchain	A key-based framework for a private and secure data access	Interoperability is not investigated in details